

**Optical Diagnostics of the Motion of Spherical, Cylindrical and Irregularly Shaped
Particles within variable Flow Media**

by

Lisa Karen Kinsale

A thesis submitted in partial fulfillment of the requirements for the degree of

Doctor of Philosophy

Department of Mechanical Engineering
University of Alberta

© Lisa Karen Kinsale, 2022

Abstract

The shape of non-spherical or irregularly shaped particles have been a challenging factor to include in mathematical models that describe particle motion in a fluid. In many studies in the literature, irregularly shaped particles have been modelled essentially as spheres. This thesis is an experimental study that investigates the hypothesis that using the spherical assumption to model non-spherical or irregularly shaped particles is invalid. The optical diagnostic technique that was used to evaluate the particle motion is particle shadowgraph velocimetry (PSV). The objectives of this research was to: (1) determine an appropriate length scale to define the particle Reynolds number and coefficient of drag of long aspect ratio particles, (2) identify the important aspects of particle motion in an industrial application known as steam assisted gravity drainage (SAGD), (3) highlight the impact of particle shape and rotation on particle deposition and build-up in SAGD operations.

A commonly used correlation in the literature to determine the coefficient of drag of non-spherical particles is the Haider and Levenspiel model. This is a generalized model that has been often used as a reference or starting point for other empirical correlations that have been developed in the literature. The Haider and Levenspiel model utilizes the equivalent diameter, which is a method of modelling non-spherical particles with respect to a perfect sphere. In this research, experiments were undertaken to investigate the suitability of using the equivalent diameter as a length scale for long aspect ratio particles. A guillotine chopper was used to manufacture cylindrical particles from opaque, black, constant diameter mono-filament. Spherical particles of various sizes and densities were also included in the analysis. The terminal settling velocity of particles used in the Haider and Levenspiel model were determined by estimating the ratio of the average distance travelled by the

particle to the average time of travel. However, in this research, a custom image processing technique was used to track the particles and calculate the localized velocities in order to identify when the particles reached the terminal settling velocity. The results showed that the ratio of the volume to the surface area of the particle is a more suitable length scale to define the particle Reynolds number and coefficient of drag for long aspect ratio particles in comparison to using the equivalent diameter.

One of the industrial applications in which particle motion is relevant is SAGD operations. SAGD is a method that is used to extract and produce oil sands. Particle deposition is one of the failure mechanisms of downhole equipment that is used in SAGD operations. The general approach in the literature to analyze particle transport during SAGD operations is a bulk type approach known as ‘core flooding’. In this process, particle transport is analyzed by injecting fluid into a rock sample known as a core and then evaluating the effluent. Therefore, the localized impact of particle motion is unknown. This study seeks to demonstrate the effect of the localized motion of the particles during SAGD by evaluating the motion of both spherical and irregularly shaped particles. The results showed that particle rotation of micro-sized particles can lead to particle deposition and build-up, affecting the flow field of the surrounding fluid. It was also observed that particle rotation depends on particle shape, the initial orientation and the relative location of the particles within the flow field. This study shows that the core flooding approach is inadequate to capture significant aspects of particle motion such as rotation and deposition in SAGD operations.

The thesis shows that long aspect ratio cylindrical particles falling in the direction of gravity within a fluid media can be well modeled as spheres using the ratio of the volume to the surface area of the particles as a length scale. This was observed because a more complete non-dimensionalization of the particle Reynolds number and the coefficient of drag was achieved as the experimental

spherical and non-spherical data overlapped well with the predictive model. However, in more complex flow geometries in which a co-flow is introduced, the spherical assumption neglects some important aspects of particle motion. As the results showed, particle shape and rotation can lead to deposition and build-up, which is one of the failure mechanisms in SAGD operations.

Preface

This thesis document presents the original work by Lisa Karen Kinsale. The experiments and image processing methodologies were developed using the facilities of the Applied Thermofluids Laboratory in the Mechanical Engineering Department of the University of Alberta under the supervision of Professor David S. Nobes. In Chapter 3 in this thesis research, I was responsible to designing and building several component of the experimental set-up, manufacturing the particles, data collecting and developing post-processing codes to analyze the results. Professor David S. Nobes assisted with designing the guillotine chopper used to manufacture the cylindrical particles and developing the image processing codes to process the raw data.

Chapters 4 and 5 has partly funded by an industrial partner RGL Reservoir Management Inc. The results in Chapter 4 was published in as a conference paper ‘Kinsale, L. and Nobes, D.S. (2017) "The Development Of An Online System To Measure Sand Production Through Thin Slots In SAGD Operations Using PSV", Okanagan Fluid Dynamics Meeting, Kelowna, British Columbia, Canada, Aug 22-23, 2017’. I was responsible for the work performed in this study in which Professor David S. Nobes was the supervisory author.

Chapter 5 was a research collaboration with Dr. Mohammad Amin Kazemi, Professor Janet A. W. Elliott and Professor David S. Nobes. The results were published in a journal paper ‘Kinsale, L.K., Kazemi, M., Elliott, J.A.W. and Nobes, D.S. (2019) Transportation and Deposition of Spherical and Irregularly Shaped Particles Flowing Through a Porous Network into a Narrow Slot, Exp Therm Fluid Sci, Vol 109, 109894’. I was responsible for the preparation of the manuscript, designing and building components for the experimental set-up, data processing and a portion of the data processing techniques used in this study. Dr. Mohammad Amin Kazemi assisted with preparing the figures, development of the image processing codes that were used to analyze the experimental data and review. Professor David S. Nobes and Professor Janet A. W. Elliott were the supervisory authors.

The results of this thesis have been published to scientific journals and conference proceedings with the supervision and guidance from Professor David S. Nobes. Lisa is the lead author in the following publications:

1. L.K. Kinsale ¹, M.A. Kazemi, J.A.W. Elliott, D.S. Nobes, Transportation and deposition of spherical and irregularly shaped particles flowing through a porous network into a narrow slot, *Exp. Therm. Fluid Sci.* 109 (2019) 109894. doi:10.1016/j.expthermflusci.2019.109894
2. L. Kinsale ², D.S. Nobes, The study of flow through porous media within the near-slot region of SAGD operations using PSV, in: 5th Int. Conf. Exp. Fluid Mech. , Munich, Ger. July 2-4, 2018: pp. 573–578 (*Invited paper: from Experimental Thermal and Fluid Science for the Special Issue of the 5th International Conference of Experimental Fluid Mechanics (ICEFM) in Munich, 2018*)
3. L. Kinsale ³, D.S. Nobes, Development of an online system to measure sand production through mini-slots in SAGD operations using PSV, in: Okanagan Fluid Dyn. Meet. Kelowna, Br. Columbia, Canada. August 21-24, 2017: pp. 182–186 (*Best presentation award*)
4. L. Kinsale ⁴, M.A. Kazemi, Y.A. Yusuf, S. Ansari and D.S. Nobes, The study of flow through porous media within the near-slot region of SAGD operations using PSV, in: 4th American Society of Thermal and Fluids Engineering (ASTFE) Conference, Las Vegas, NV, USA, April 14-17, 2019

I also contributed to the research works of several colleagues in the following publications:

1. S. Ansari, Y. Yusuf, L. Kinsale ⁵, R. Sabbagh and D.S. Nobes, Visualization of fines migration in the flow entering apertures through the near-wellbore porous media, SPE Thermal Well Integrity and Design Symposium, Banff, Canada, Nov 27-29, 2018
2. Y. Yusuf, L. Kinsale ⁶, S. Ansari and D.S. Nobes, The convergent path of streamlines for the flow approaching a rectangular orifice through a porous region, Proceedings of the 4th Thermal and Fluid Engineering Conference, TFEC-2019-28074, Las Vegas, USA, April 14-17, 2019

¹ Contributions: Review of the literature, preparation of manuscripts, designing and building components for the experimental set-up, experimental data collection and a portion of the data processing techniques

² Contributions: Preparation of manuscripts, designing and building components for the experimental set-up, experimental data collection, image processing and analysis of results

³ Contributions: Preparation of manuscripts, experimental data collection, image processing, analysis and interpretation of results

⁴ Contributions: Experimental data collection, preparation of manuscripts and presentation

⁵ Contributions: Building experimental components, a portion of the writing and review

⁶ Contributions: Preparing some figures and review

*In loving memory of my mom, Nerescia Kinsale, who died three weeks before my Ph.D. defense,
she always stood by me with much strength, love and prayer*

*In loving memory of my dad, Lloyd Sylvester Kinsale, who passed away in 2011, I will forever
cherish his love and never-ending support*

To Almighty God and my Lord, Who has keep me through it all

Acknowledgements

I would like to express sincere gratitude to my Ph.D. supervisor Professor David S. Nobes for his constant support, motivation, advice, mentorship and patience. I truly admire his wisdom, professionalism, respect and consideration to others. Dr. Nobes is honestly one of the best supervisors any graduate student can ask for, I would truly like to make him proud as I begin my career. I would also like to thank Dr. Carlos Lange and Dr. Jaime Wong for being apart of my supervisory committee. I really appreciate the time they dedicated for discussions and I truly benefitted from their advice and honest feedback. Special thanks to Professor Janet A. W. Elliott and Dr. Mohammad Amin Kazemi as it was definitely an honor to co-author a paper with you both. I would also like to acknowledge the financial support from the Natural Sciences and Engineering Research Council (NSERC) of Canada, the Alberta Ingenuity Fund, and the Canadian Foundation for Innovation (CFI).

I would like to dearly thank my lab mates and colleagues who I met at the University of Alberta: Yeganeh Saffar, Sina Kashanj, Reza Azadi, Pavan Kamble, Beatriz Bravo, David Serrano, Gabriel Salata, Hiran Soltani, Calynn Stumpf, Jason Michaud, Carlos Mendez, Linda Hasanovich, Jason Der, Jake Hadfield, Matthias Lottmann, Jan Raffel, Dr. Yishak Yusuf, Dr. Shadi Ansari, Dr. Guilherme Bessa, Dr. Masoud Ebrahimian and Dr. Seyedehfatemeh Razavi. Leaving my home country and coming to Canada was a much bigger decision than I realized and I am truly thankful to each of them for their friendship, support and advice.

Words cannot express how truly grateful I am to my family and dear friends for their constant support and prayers: Julien Mervin Kinsale, Lori Kinsale, Esmarolda Guerra, Julien Guerra, Jillian Guerra, Courtney Wallace, Mayrose Peterson, Buddy George, Albertina Debra George, Ricardo Crovador, Nicholas Ragbir, Joanne Taylor, Caren Dyall, Keith Tyson, Althea Tyson-Edwards, Earl Tyson, Tina Clavijo, Nixon Dyall, Damali Cox, Kambiri Cox, Jeanette Sutherland-Finley, David Charles, Kerna Charles, Kiayann Forbes, Ann Marie Forbes, Neil Richardson, Donna Gannon, Anne Magee, Tim Magee, Mohammed Batou Ndiaye, Nahid Mina Elyasi, Kenneth Oppon Jr, Joel Agarwal, Riwo Egor, Jeremy Thomas, Mikaela Epp, Randell Jackman, Meryl La Touche Mohammed , Heidi Williams Thomas, Abena Abraham, Gemma Gordon, Jacqueline Abraham, Elizabeth George, Paula Chin Fong, Gloria McMillan,

Peter Tyrell, Tramaine Harrison, Patricia Moses, Shenelle Moses, Lanalisa Jackson-George, Ryan Baseanoo, Alana Krahn, Apostle Randolph Joseph, Pastor Eric Brooks, Pastor Pam Reichenbach, Dr. Proscovia Mugaba, Arabat Kasangaki, Thelma Reid, Lena Walker, Valerie Kennedy, Shelley Utz, Joe Lover, Yanitza Wilson, Jemila James Nunes, Bernadette Alexander and Norris Alexander. I am truly thankful to the village of support that I had during my Ph.D.

My both parents are not alive to witness this accomplishment but I could not have reached this far in my journey without the selfless love, support, sacrifice and dedication that they showed throughout their lives. My dear mother, Nerescia Kinsale, passed away three weeks before my defense but she selflessly stood by me throughout my entire Ph.D. I want to express in writing how much I am grateful for the times she pushed me when I felt like giving up. She was an amazing, phenomenal woman and my very best friend. My dear dad, Lloyd Sylvester Kinsale died five years before I started my Ph.D. but yet he showed me that he was already extremely proud of me and he truly believed in me. I am truly thankful for my father's constant patience, love and support.

Table of Contents

Abstract	ii
Preface	v
Acknowledgements	viii
Table of Contents	x
List of Figures	xxix
List of Tables	xxvi
1 Background	1
1.1 Motivation	1
1.2 Hypotheses.....	4
1.3 Research Objectives	4
2 Literature Review	6
2.1 Modeling Particle Motion in a Fluid	6
2.1.1 Particle Reynolds Number	6
2.1.2 Modeling the Coefficient of Drag of Particles	7
2.1.3 Terminal Settling Velocity of Particles.....	11
2.1.4 Particle Motion in Steam Assisted Gravity Drainage (SAGD) Operations	12
2.1.5 Particle Rotation.....	14
2.2 Evaluating Particle Motion using Particle Shadowgraph Velocimetry (PSV).....	15
2.3 Thesis Overview	16
3 Terminal Settling Velocity and Coefficient of Drag of Spherical and Cylindrical Particles using Particle Shadowgraph Velocimetry	18
3.1 Introduction	18
3.2 Description of the Particles, Fluids and the Flow Geometry.....	19

3.2.1	Spherical Particles	19
3.2.2	Cylindrical Particles	20
3.3	Flow geometry	23
3.4	Optical Experimental Set-up	25
3.5	Data Processing: Calculates and Quantifies Particle Motion	29
3.5.1	Initialization	30
3.5.2	Pre-processing and Image Processing	31
3.5.3	Calculations: Displacement, Velocity and Acceleration from the Raw Images	33
3.5.4	Methodology of Obtaining the Terminal Settling Velocity of Particles from Experiments.....	35
3.6	Experimental Results and Analyses	37
3.6.1	Spherical Particles: Particle Trajectory, Displacement, Velocity and Acceleration	37
3.6.2	Cylindrical Particles: Particle Trajectory, Displacement, Velocity and Acceleration	39
3.6.3	Spherical Particles: Terminal settling velocity and the Coefficient of Drag Obtained from Experimental Data	40
3.6.4	Uncertainty of the Experimental Terminal Settling Velocity Measurements	42
3.6.5	Cylindrical Particles: Terminal Settling Velocity and the Coefficient of Drag Obtained from Experimental Data	47
3.6.6	Values of the Length Scales and the Four Parameters (<i>A</i> , <i>B</i> , <i>C</i> and <i>D</i>) which were used to calculate the Coefficient of Drag	49
3.6.7	The Equivalent Diameter as a Length Scale to determine the Particle Reynolds Number and Coefficient of Drag.....	51
3.6.8	Volume/Area as a Length Scale to determine the Particle Reynolds Number and Coefficient of Drag.....	53
3.7	Conclusions	56
4	The Motion of a Particle through Narrow Slots	57

4.1	Introduction	57
4.2	Description of the Fluid, Particles and the Flow Geometry	58
4.3	Optical Experimental Set-up	59
4.4	Image Processing.....	60
4.4.1	Particle Characterization	61
4.4.2	The Velocity Field of the Surrounding Fluid.....	63
4.5	Experimental Results and Analysis	64
4.5.1	The Equivalent Diameter and the Aspect Ratio of the Particles	64
4.5.2	The Velocity Field of the Surrounding Fluid around the Particles	66
4.6	Conclusion.....	70
5	Particle Transportation and Deposition within a Porous Network into a Narrow Slot.....	71
5.1	Introduction	71
5.2	Description of the Fluid, Particles and the Flow Geometry	72
5.3	Optical Experimental Set-up	74
5.4	Image Processing.....	75
5.4.1	Particle Detection and the Fitted Ellipse Approach	75
5.4.2	Particle Tracking	76
5.4.3	Particle Characterization	76
5.4.4	Velocity Field Measurements of the Continuous Phase.....	79
5.4.5	Build-up Tests: Obtaining the Thickness of the Deposited Layer of Particles	80
5.5	Experimental Results and Analyses	81
5.5.1	Velocity Vector Field of the Continuous Phase	81
5.5.2	Particle Deposition	83
5.5.3	Particle Rotation.....	87
5.6	Conclusion.....	92

6	Conclusions	93
6.1	Future Work.....	95
7	References	96
8	Appendices	107
8.1	Appendix 1: 4mm Diameter Delrin Spheres in Water	107
8.1.1	Particle Displacement, Particle Velocity and Particle Acceleration for 4mm Diameter Delrin Spheres in Water	107
8.1.2	x -Velocity (V_x), y -Velocity (V_y) and Magnitude of Velocity ($ V $) for 4mm Diameter Delrin Spheres in Water	108
8.1.3	x -Acceleration (A_x), y -Acceleration (A_y) and Magnitude of Acceleration ($ A $) for 4mm Diameter Delrin Spheres in Water	109
8.2	Appendix 2: 4mm Delrin Spheres in 20%–80% Glycerol–Water.....	110
8.2.1	Particle Displacement, Particle Velocity and Particle Acceleration for 4mm Diameter Delrin Spheres in 20%–80% Glycerol–Water	110
8.2.2	x -Velocity (V_x), y -Velocity (V_y) and Magnitude of Velocity ($ V $) for 4mm Diameter Delrin Spheres in 20%–80% Glycerol–Water	111
8.2.3	x -Acceleration (A_x), y -Acceleration (A_y) and Magnitude of Acceleration ($ A $) for 4mm Diameter Delrin Spheres in 20%–80% Glycerol–Water.....	112
8.3	Appendix 3: 4mm Delrin Spheres in 40%–60% Glycerol–Water.....	113
8.3.1	Particle Displacement, Particle Velocity and Particle Acceleration for 4mm Diameter Delrin Spheres in 40%–60% Glycerol–Water	113
8.3.2	x -Velocity (V_x), y -Velocity (V_y) and Magnitude of Velocity ($ V $) for 4mm Diameter Delrin Spheres in 40%–60% Glycerol–Water	114
8.3.3	x -Acceleration (A_x), y -Acceleration (A_y) and Magnitude of Acceleration ($ A $) for 4mm Diameter Delrin Spheres in 40%–60% Glycerol–Water.....	115
8.4	Appendix 4: 4mm Delrin Spheres in 70%–30% Glycerol–Water.....	116

8.4.1	Particle Displacement, Particle Velocity and Particle Acceleration for 4mm Diameter Delrin Spheres in 70%–30% Glycerol–Water	116
8.4.2	x -Velocity (V_x), y -Velocity (V_y) and Magnitude of Velocity ($ V $) for 4mm Diameter Delrin Spheres in 70%–30% Glycerol–Water	117
8.4.3	x -Acceleration (A_x), y -Acceleration (A_y) and Magnitude of Acceleration ($ A $) for 4mm Diameter Delrin Spheres in 70%–30% Glycerol–Water.....	118
8.5	Appendix 5: 4mm Delrin Spheres in Canola Oil.....	119
8.5.1	Particle Displacement, Particle Velocity and Particle Acceleration for 4mm Diameter Delrin Spheres in Canola Oil	119
8.5.2	x -Velocity (V_x), y -Velocity (V_y) and Magnitude of Velocity ($ V $) for 4mm Diameter Delrin Spheres in Canola Oil	120
8.5.3	x -Acceleration (A_x), y -Acceleration (A_y) and Magnitude of Acceleration ($ A $) for 4mm Diameter Delrin Spheres in Canola Oil.....	121
8.6	Appendix 6: 2mm Diameter Delrin Spheres in Water	122
8.6.1	Particle Displacement, Particle Velocity and Particle Acceleration for 2mm Diameter Delrin Spheres in Water	122
8.6.2	x -Velocity (V_x), y -Velocity (V_y) and Magnitude of Velocity ($ V $) for 2mm Diameter Delrin Spheres in Water	123
8.6.3	x -Acceleration (A_x), y -Acceleration (A_y) and Magnitude of Acceleration ($ A $) for 2mm Diameter Delrin Spheres in Water	124
8.7	Appendix 7: 2mm Delrin Spheres in 20%–80% Glycerol–Water.....	125
8.7.1	Particle Displacement, Particle Velocity and Particle Acceleration for 2mm Diameter Delrin Spheres in 20%–80% Glycerol–Water	125
8.7.2	x -Velocity (V_x), y -Velocity (V_y) and Magnitude of Velocity ($ V $) for 2mm Diameter Delrin Spheres in 20%–80% Glycerol–Water	126
8.7.3	x -Acceleration (A_x), y -Acceleration (A_y) and Magnitude of Acceleration ($ A $) for 2mm Diameter Delrin Spheres in 20%–80% Glycerol–Water.....	127
8.8	Appendix 8: 2mm Delrin Spheres in 40%–60% Glycerol–Water.....	128

8.8.1	Particle Displacement, Particle Velocity and Particle Acceleration for 2mm Diameter Delrin Spheres in 40%–60% Glycerol–Water	128
8.8.2	x -Velocity (V_x), y -Velocity (V_y) and Magnitude of Velocity ($ V $) for 2mm Diameter Delrin Spheres in 40%–60% Glycerol–Water	129
8.8.3	x -Acceleration (A_x), y -Acceleration (A_y) and Magnitude of Acceleration ($ A $) for 2mm Diameter Delrin Spheres in 40%–60% Glycerol–Water.....	130
8.9	Appendix 9: 2mm Delrin Spheres in 70%–30% Glycerol–Water.....	131
8.9.1	Particle Displacement, Particle Velocity and Particle Acceleration for 2mm Diameter Delrin Spheres in 70%–30% Glycerol–Water	131
8.9.2	x -Velocity (V_x), y -Velocity (V_y) and Magnitude of Velocity ($ V $) for 2mm Diameter Delrin Spheres in 70%–30% Glycerol–Water	132
8.9.3	x -Acceleration (A_x), y -Acceleration (A_y) and Magnitude of Acceleration ($ A $) for 2mm Diameter Delrin Spheres in 70%–30% Glycerol–Water.....	133
8.10	Appendix 10: 2mm Delrin Spheres in Canola Oil	134
8.10.1	Particle Displacement, Particle Velocity and Particle Acceleration for 2mm Diameter Delrin Spheres in Canola Oil	134
8.10.2	x -Velocity (V_x), y -Velocity (V_y) and Magnitude of Velocity ($ V $) for 2mm Diameter Delrin Spheres in Canola Oil	135
8.10.3	x -Acceleration (A_x), y -Acceleration (A_y) and Magnitude of Acceleration ($ A $) for 2mm Diameter Delrin Spheres in Canola Oil.....	136
8.11	Appendix 11: 2mm Diameter Aluminum Spheres in Water.....	137
8.11.1	Particle Displacement, Particle Velocity and Particle Acceleration for 2mm Diameter Aluminum Spheres in Water	137
8.11.2	x -Velocity (V_x), y -Velocity (V_y) and Magnitude of Velocity ($ V $) for 2mm Diameter Aluminum Spheres in Water	138
8.11.3	x -Acceleration (A_x), y -Acceleration (A_y) and Magnitude of Acceleration ($ A $) for 2mm Diameter Aluminum Spheres in Water	139
8.12	Appendix 12: 2mm Diameter Aluminum Spheres in 20%–80% Glycerol–Water	140

8.12.1	Particle Displacement, Particle Velocity and Particle Acceleration for 2mm Diameter Aluminum Spheres in 20%–80% Glycerol–Water	140
8.12.2	x -Velocity (V_x), y -Velocity (V_y) and Magnitude of Velocity ($ V $) for 2mm Diameter Aluminum Spheres in 20%–80% Glycerol–Water	141
8.12.3	x -Acceleration (A_x), y -Acceleration (A_y) and Magnitude of Acceleration ($ A $) for 2mm Diameter Aluminum Spheres in 20%–80% Glycerol–Water	142
8.13	Appendix 13: 2mm Diameter Aluminum Spheres in 40%–60% Glycerol–Water	143
8.13.1	Particle Displacement, Particle Velocity and Particle Acceleration for 2mm Diameter Aluminum Spheres in 40%–60% Glycerol–Water	143
8.13.2	x -Velocity (V_x), y -Velocity (V_y) and Magnitude of Velocity ($ V $) for 2mm Diameter Aluminum Spheres in 40%–60% Glycerol–Water	144
8.13.3	x -Acceleration (A_x), y -Acceleration (A_y) and Magnitude of Acceleration ($ A $) for 2mm Diameter Aluminum Spheres in 40%–60% Glycerol–Water	145
8.14	Appendix 14: 2mm Diameter Aluminum Spheres in 70%–30% Glycerol–Water	146
8.14.1	Particle Displacement, Particle Velocity and Particle Acceleration for 2mm Diameter Aluminum Spheres in 70%–30% Glycerol–Water	146
8.14.2	x -Velocity (V_x), y -Velocity (V_y) and Magnitude of Velocity ($ V $) for 2mm Diameter Aluminum Spheres in 70%–30% Glycerol–Water	147
8.14.3	x -Acceleration (A_x), y -Acceleration (A_y) and Magnitude of Acceleration ($ A $) for 2mm Diameter Aluminum Spheres in 70%–30% Glycerol–Water	148
8.15	Appendix 15: 2mm Diameter Aluminum Spheres in Canola Oil	149
8.15.1	Particle Displacement, Particle Velocity and Particle Acceleration for 2mm Diameter Aluminum Spheres in Canola Oil	149
8.15.2	x -Velocity (V_x), y -Velocity (V_y) and Magnitude of Velocity ($ V $) for 2mm Diameter Aluminum Spheres in Canola Oil	150
8.15.3	x -Acceleration (A_x), y -Acceleration (A_y) and Magnitude of Acceleration ($ A $) for 2mm Diameter Aluminum Spheres in Canola Oil	151

8.16	Appendix 16: 1.30 mm Diameter and 1:1 Aspect Ratio ($AR = d_p/l_p$) Nylon Cylindrical Particles in Water	152
8.16.1	Particle Displacement, Particle Velocity and Particle Acceleration for 1.30 mm Diameter and 1:1 Aspect Ratio ($AR = d_p/l_p$) Nylon Cylindrical Particles in Water.....	152
8.16.2	x -Velocity (V_x), y -Velocity (V_y) and Magnitude of Velocity ($ V $) for 1.30 mm Diameter and 1:1 Aspect Ratio ($AR = d_p/l_p$) Nylon Cylindrical Particles in Water.....	153
8.16.3	x -Acceleration (A_x), y -Acceleration (A_y) and Magnitude of Acceleration ($ A $) for 1.30 mm Diameter and 1:1 Aspect Ratio ($AR = d_p/l_p$) Nylon Cylindrical Particles in Water	154
8.17	Appendix 17: 1.30 mm Diameter and 1:1 Aspect Ratio ($AR = d_p/l_p$) Nylon Cylindrical Particles in 20%–80% Glycerol–Water.....	155
8.17.1	Particle Displacement, Particle Velocity and Particle Acceleration for 1.30 mm Diameter and 1:1 Aspect Ratio ($AR = d_p/l_p$) Nylon Cylindrical Particles in 20%–80% Glycerol–Water	155
8.17.2	x -Velocity (V_x), y -Velocity (V_y) and Magnitude of Velocity ($ V $) for 1.30 mm Diameter and 1:1 Aspect Ratio ($AR = d_p/l_p$) Nylon Cylindrical Particles in 20%–80% Glycerol–Water	156
8.17.3	x -Acceleration (A_x), y -Acceleration (A_y) and Magnitude of Acceleration ($ A $) for 1.30 mm Diameter and 1:1 Aspect Ratio ($AR = d_p/l_p$) Nylon Cylindrical Particles in 20%–80% Glycerol–Water.....	157
8.18	Appendix 18: 1.30 mm Diameter and 1:1 Aspect Ratio ($AR = d_p/l_p$) Nylon Cylindrical Particles in 40%–60% Glycerol–Water.....	158
8.18.1	Particle Displacement, Particle Velocity and Particle Acceleration for 1.30 mm Diameter and 1:1 Aspect Ratio ($AR = d_p/l_p$) Nylon Cylindrical Particles in 40%–60% Glycerol–Water	158
8.18.2	x -Velocity (V_x), y -Velocity (V_y) and Magnitude of Velocity ($ V $) for 1.30 mm Diameter and 1:1 Aspect Ratio ($AR = d_p/l_p$) Nylon Cylindrical Particles in 40%–60% Glycerol–Water	159

8.18.3	x -Acceleration (A_x), y -Acceleration (A_y) and Magnitude of Acceleration ($ A $) for 1.30 mm Diameter and 1:1 Aspect Ratio ($AR = d_p/l_p$) Nylon Cylindrical Particles in 40%–60% Glycerol–Water.....	160
8.19	Appendix 19: 1.30 mm Diameter and 1:1 Aspect Ratio ($AR = d_p/l_p$) Nylon Cylindrical Particles in Canola Oil.....	161
8.19.1	Particle Displacement, Particle Velocity and Particle Acceleration for 1.30 mm Diameter and 1:1 Aspect Ratio ($AR = d_p/l_p$) Nylon Cylindrical Particles in Canola Oil.....	161
8.19.2	x -Velocity (V_x), y -Velocity (V_y) and Magnitude of Velocity ($ V $) for 1.30 mm Diameter and 1:1 Aspect Ratio ($AR = d_p/l_p$) Nylon Cylindrical Particles in Canola Oil.....	162
8.19.3	x -Acceleration (A_x), y -Acceleration (A_y) and Magnitude of Acceleration ($ A $) for 1.30 mm Diameter and 1:1 Aspect Ratio ($AR = d_p/l_p$) Nylon Cylindrical Particles in Canola Oil	163
8.20	Appendix 20: 1.30 mm Diameter and 1:3 Aspect Ratio ($AR = d_p/l_p$) Nylon Cylindrical Particles in Water	164
8.20.1	Particle Displacement, Particle Velocity and Particle Acceleration for 1.30 mm Diameter and 1:3 Aspect Ratio ($AR = d_p/l_p$) Nylon Cylindrical Particles in Water.....	164
8.20.2	x -Velocity (V_x), y -Velocity (V_y) and Magnitude of Velocity ($ V $) for 1.30 mm Diameter and 1:3 Aspect Ratio ($AR = d_p/l_p$) Nylon Cylindrical Particles in Water.....	165
8.20.3	x -Acceleration (A_x), y -Acceleration (A_y) and Magnitude of Acceleration ($ A $) for 1.30 mm Diameter and 1:3 Aspect Ratio ($AR = d_p/l_p$) Nylon Cylindrical Particles in Water	166
8.21	Appendix 21: 1.30 mm Diameter and 1:3 Aspect Ratio ($AR = d_p/l_p$) Nylon Cylindrical Particles in 20%–80% Glycerol–Water.....	167
8.21.1	Particle Displacement, Particle Velocity and Particle Acceleration for 1.30 mm Diameter and 1:3 Aspect Ratio ($AR = d_p/l_p$) Nylon Cylindrical Particles in 20%–80% Glycerol–Water	167
8.21.2	x -Velocity (V_x), y -Velocity (V_y) and Magnitude of Velocity ($ V $) for 1.30 mm Diameter and 1:3 Aspect Ratio ($AR = d_p/l_p$) Nylon Cylindrical Particles in 20%–80% Glycerol–Water	168

8.21.3	x -Acceleration (A_x), y -Acceleration (A_y) and Magnitude of Acceleration ($ A $) for 1.30 mm Diameter and 1:3 Aspect Ratio ($AR = d_p/l_p$) Nylon Cylindrical Particles in 20%–80% Glycerol–Water.....	169
8.22	Appendix 22: 1.30 mm Diameter and 1:3 Aspect Ratio ($AR = d_p/l_p$) Nylon Cylindrical Particles in 40%–60% Glycerol–Water.....	170
8.22.1	Particle Displacement, Particle Velocity and Particle Acceleration for 1.30 mm Diameter and 1:3 Aspect Ratio ($AR = d_p/l_p$) Nylon Cylindrical Particles in 40%–60% Glycerol–Water.....	170
8.22.2	x -Velocity (V_x), y -Velocity (V_y) and Magnitude of Velocity ($ V $) for 1.30 mm Diameter and 1:3 Aspect Ratio ($AR = d_p/l_p$) Nylon Cylindrical Particles in 40%–60% Glycerol–Water.....	171
8.22.3	x -Acceleration (A_x), y -Acceleration (A_y) and Magnitude of Acceleration ($ A $) for 1.30 mm Diameter and 1:3 Aspect Ratio ($AR = d_p/l_p$) Nylon Cylindrical Particles in 40%–60% Glycerol–Water.....	172
8.23	Appendix 23: 1.30 mm Diameter and 1:3 Aspect Ratio ($AR = d_p/l_p$) Nylon Cylindrical Particles in Canola Oil.....	173
8.23.1	Particle Displacement, Particle Velocity and Particle Acceleration for 1.30 mm Diameter and 1:3 Aspect Ratio ($AR = d_p/l_p$) Nylon Cylindrical Particles in Canola Oil.....	173
8.23.2	x -Velocity (V_x), y -Velocity (V_y) and Magnitude of Velocity ($ V $) for 1.30 mm Diameter and 1:3 Aspect Ratio ($AR = d_p/l_p$) Nylon Cylindrical Particles in Canola Oil.....	174
8.23.3	x -Acceleration (A_x), y -Acceleration (A_y) and Magnitude of Acceleration ($ A $) for 1.30 mm Diameter and 1:3 Aspect Ratio ($AR = d_p/l_p$) Nylon Cylindrical Particles in Canola Oil	175
8.24	Appendix 24: 1.30 mm Diameter and 1:5 Aspect Ratio ($AR = d_p/l_p$) Nylon Cylindrical Particles in Water.....	176
8.24.1	Particle Displacement, Particle Velocity and Particle Acceleration for 1.30 mm Diameter and 1:5 Aspect Ratio ($AR = d_p/l_p$) Nylon Cylindrical Particles in Water.....	176
8.24.2	x -Velocity (V_x), y -Velocity (V_y) and Magnitude of Velocity ($ V $) for 1.30 mm Diameter and 1:5 Aspect Ratio ($AR = d_p/l_p$) Nylon Cylindrical Particles in Water.....	177

8.24.3	x -Acceleration (A_x), y -Acceleration (A_y) and Magnitude of Acceleration ($ A $) for 1.30 mm Diameter and 1:5 Aspect Ratio ($AR = d_p/l_p$) Nylon Cylindrical Particles in Water	178
8.25	Appendix 25: 1.30 mm Diameter and 1:5 Aspect Ratio ($AR = d_p/l_p$) Nylon Cylindrical Particles in 20%–80% Glycerol–Water.....	179
8.25.1	Particle Displacement, Particle Velocity and Particle Acceleration for 1.30 mm Diameter and 1:5 Aspect Ratio ($AR = d_p/l_p$) Nylon Cylindrical Particles in 20%–80% Glycerol–Water	179
8.25.2	x -Velocity (V_x), y -Velocity (V_y) and Magnitude of Velocity ($ V $) for 1.30 mm Diameter and 1:5 Aspect Ratio ($AR = d_p/l_p$) Nylon Cylindrical Particles in 20%–80% Glycerol–Water	180
8.25.3	x -Acceleration (A_x), y -Acceleration (A_y) and Magnitude of Acceleration ($ A $) for 1.30 mm Diameter and 1:5 Aspect Ratio ($AR = d_p/l_p$) Nylon Cylindrical Particles in 20%–80% Glycerol–Water.....	181
8.26	Appendix 26: 1.30 mm Diameter and 1:5 Aspect Ratio ($AR = d_p/l_p$) Nylon Cylindrical Particles in 40%–60% Glycerol–Water.....	182
8.26.1	Particle Displacement, Particle Velocity and Particle Acceleration for 1.30 mm Diameter and 1:5 Aspect Ratio ($AR = d_p/l_p$) Nylon Cylindrical Particles in 40%–60% Glycerol–Water	182
8.26.2	x -Velocity (V_x), y -Velocity (V_y) and Magnitude of Velocity ($ V $) for 1.30 mm Diameter and 1:5 Aspect Ratio ($AR = d_p/l_p$) Nylon Cylindrical Particles in 40%–60% Glycerol–Water	183
8.26.3	x -Acceleration (A_x), y -Acceleration (A_y) and Magnitude of Acceleration ($ A $) for 1.30 mm Diameter and 1:5 Aspect Ratio ($AR = d_p/l_p$) Nylon Cylindrical Particles in 40%–60% Glycerol–Water.....	184
8.27	Appendix 27: 1.30 mm Diameter and 1:5 Aspect Ratio ($AR = d_p/l_p$) Nylon Cylindrical Particles in Canola Oil.....	185
8.27.1	Particle Displacement, Particle Velocity and Particle Acceleration for 1.30 mm Diameter and 1:5 Aspect Ratio ($AR = d_p/l_p$) Nylon Cylindrical Particles in Canola Oil.....	185

8.27.2	x -Velocity (V_x), y -Velocity (V_y) and Magnitude of Velocity ($ V $) for 1.30 mm Diameter and 1:5 Aspect Ratio ($AR = d_p/l_p$) Nylon Cylindrical Particles in Canola Oil.....	186
8.27.3	x -Acceleration (A_x), y -Acceleration (A_y) and Magnitude of Acceleration ($ A $) for 1.30 mm Diameter and 1:5 Aspect Ratio ($AR = d_p/l_p$) Nylon Cylindrical Particles in Canola Oil	187
8.28	Appendix 28: 1.50 mm Diameter and 1:1 Aspect Ratio ($AR = d_p/l_p$) Nylon Cylindrical Particles in Water	188
8.28.1	Particle Displacement, Particle Velocity and Particle Acceleration for 1.50 mm Diameter and 1:1 Aspect Ratio ($AR = d_p/l_p$) Nylon Cylindrical Particles in Water.....	188
8.28.2	x -Velocity (V_x), y -Velocity (V_y) and Magnitude of Velocity ($ V $) for 1.50 mm Diameter and 1:1 Aspect Ratio ($AR = d_p/l_p$) Nylon Cylindrical Particles in Water.....	189
8.28.3	x -Acceleration (A_x), y -Acceleration (A_y) and Magnitude of Acceleration ($ A $) for 1.50 mm Diameter and 1:1 Aspect Ratio ($AR = d_p/l_p$) Nylon Cylindrical Particles in Water	190
8.29	Appendix 29: 1.50 mm Diameter and 1:1 Aspect Ratio ($AR = d_p/l_p$) Nylon Cylindrical Particles in 20%–80% Glycerol–Water.....	191
8.29.1	Particle Displacement, Particle Velocity and Particle Acceleration for 1.50 mm Diameter and 1:1 Aspect Ratio ($AR = d_p/l_p$) Nylon Cylindrical Particles in 20%–80% Glycerol–Water	191
8.29.2	x -Velocity (V_x), y -Velocity (V_y) and Magnitude of Velocity ($ V $) for 1.50 mm Diameter and 1:1 Aspect Ratio ($AR = d_p/l_p$) Nylon Cylindrical Particles in 20%–80% Glycerol–Water	192
8.29.3	x -Acceleration (A_x), y -Acceleration (A_y) and Magnitude of Acceleration ($ A $) for 1.50 mm Diameter and 1:1 Aspect Ratio ($AR = d_p/l_p$) Nylon Cylindrical Particles in 20%–80% Glycerol–Water.....	193
8.30	Appendix 30: 1.50 mm Diameter and 1:1 Aspect Ratio ($AR = d_p/l_p$) Nylon Cylindrical Particles in 40%–60% Glycerol–Water.....	194

8.30.1 Particle Displacement, Particle Velocity and Particle Acceleration for 1.50 mm Diameter and 1:1 Aspect Ratio ($AR = d_p/l_p$) Nylon Cylindrical Particles in 40%–60% Glycerol–Water	194
8.30.2 x -Velocity (V_x), y -Velocity (V_y) and Magnitude of Velocity ($ V $) for 1.50 mm Diameter and 1:1 Aspect Ratio ($AR = d_p/l_p$) Nylon Cylindrical Particles in 40%–60% Glycerol–Water	195
8.30.3 x -Acceleration (A_x), y -Acceleration (A_y) and Magnitude of Acceleration ($ A $) for 1.50 mm Diameter and 1:1 Aspect Ratio ($AR = d_p/l_p$) Nylon Cylindrical Particles in 40%–60% Glycerol–Water	196
8.31 Appendix 31: 1.50 mm Diameter and 1:1 Aspect Ratio ($AR = d_p/l_p$) Nylon Cylindrical Particles in Canola Oil.....	197
8.31.1 Particle Displacement, Particle Velocity and Particle Acceleration for 1.50 mm Diameter and 1:1 Aspect Ratio ($AR = d_p/l_p$) Nylon Cylindrical Particles in Canola Oil.....	197
8.31.2 x -Velocity (V_x), y -Velocity (V_y) and Magnitude of Velocity ($ V $) for 1.50 mm Diameter and 1:1 Aspect Ratio ($AR = d_p/l_p$) Nylon Cylindrical Particles in Canola Oil.....	198
8.31.3 x -Acceleration (A_x), y -Acceleration (A_y) and Magnitude of Acceleration ($ A $) for 1.50 mm Diameter and 1:1 Aspect Ratio ($AR = d_p/l_p$) Nylon Cylindrical Particles in Canola Oil	199
8.32 Appendix 32: 1.50 mm Diameter and 1:3 Aspect Ratio ($AR = d_p/l_p$) Nylon Cylindrical Particles in Water	200
8.32.1 Particle Displacement, Particle Velocity and Particle Acceleration for 1.50 mm Diameter and 1:3 Aspect Ratio ($AR = d_p/l_p$) Nylon Cylindrical Particles in Water.....	200
8.32.2 x -Velocity (V_x), y -Velocity (V_y) and Magnitude of Velocity ($ V $) for 1.50 mm Diameter and 1:3 Aspect Ratio ($AR = d_p/l_p$) Nylon Cylindrical Particles in Water.....	201
8.32.3 x -Acceleration (A_x), y -Acceleration (A_y) and Magnitude of Acceleration ($ A $) for 1.50 mm Diameter and 1:3 Aspect Ratio ($AR = d_p/l_p$) Nylon Cylindrical Particles in Water	202
8.33 Appendix 33: 1.50 mm Diameter and 1:3 Aspect Ratio ($AR = d_p/l_p$) Nylon Cylindrical Particles in 20%–80% Glycerol–Water.....	203

8.33.1 Particle Displacement, Particle Velocity and Particle Acceleration for 1.50 mm Diameter and 1:3 Aspect Ratio ($AR = d_p/l_p$) Nylon Cylindrical Particles in 20%–80% Glycerol–Water	203
8.33.2 x -Velocity (V_x), y -Velocity (V_y) and Magnitude of Velocity ($ V $) for 1.50 mm Diameter and 1:3 Aspect Ratio ($AR = d_p/l_p$) Nylon Cylindrical Particles in 20%–80% Glycerol–Water	204
8.33.3 x -Acceleration (A_x), y -Acceleration (A_y) and Magnitude of Acceleration ($ A $) for 1.50 mm Diameter and 1:3 Aspect Ratio ($AR = d_p/l_p$) Nylon Cylindrical Particles in 20%–80% Glycerol–Water	205
8.34 Appendix 34: 1.50 mm Diameter and 1:3 Aspect Ratio ($AR = d_p/l_p$) Nylon Cylindrical Particles in 40%–60% Glycerol–Water	206
8.34.1 Particle Displacement, Particle Velocity and Particle Acceleration for 1.50 mm Diameter and 1:3 Aspect Ratio ($AR = d_p/l_p$) Nylon Cylindrical Particles in 40%–60% Glycerol–Water	206
8.34.2 x -Velocity (V_x), y -Velocity (V_y) and Magnitude of Velocity ($ V $) for 1.50 mm Diameter and 1:3 Aspect Ratio ($AR = d_p/l_p$) Nylon Cylindrical Particles in 40%–60% Glycerol–Water	207
8.34.3 x -Acceleration (A_x), y -Acceleration (A_y) and Magnitude of Acceleration ($ A $) for 1.50 mm Diameter and 1:3 Aspect Ratio ($AR = d_p/l_p$) Nylon Cylindrical Particles in 40%–60% Glycerol–Water	208
8.35 Appendix 35: 1.50 mm Diameter and 1:3 Aspect Ratio ($AR = d_p/l_p$) Nylon Cylindrical Particles in Canola Oil	209
8.35.1 Particle Displacement, Particle Velocity and Particle Acceleration for 1.50 mm Diameter and 1:3 Aspect Ratio ($AR = d_p/l_p$) Nylon Cylindrical Particles in Canola Oil	209
8.35.2 x -Velocity (V_x), y -Velocity (V_y) and Magnitude of Velocity ($ V $) for 1.50 mm Diameter and 1:3 Aspect Ratio ($AR = d_p/l_p$) Nylon Cylindrical Particles in Canola Oil	210
8.35.3 x -Acceleration (A_x), y -Acceleration (A_y) and Magnitude of Acceleration ($ A $) for 1.50 mm Diameter and 1:3 Aspect Ratio ($AR = d_p/l_p$) Nylon Cylindrical Particles in Canola Oil	211

8.36	Appendix 36: 1.50 mm Diameter and 1:5 Aspect Ratio ($AR = d_p/l_p$) Nylon Cylindrical Particles in Water	212
8.36.1	Particle Displacement, Particle Velocity and Particle Acceleration for 1.50 mm Diameter and 1:5 Aspect Ratio ($AR = d_p/l_p$) Nylon Cylindrical Particles in Water.....	212
8.36.2	x -Velocity (V_x), y -Velocity (V_y) and Magnitude of Velocity ($ V $) for 1.50 mm Diameter and 1:5 Aspect Ratio ($AR = d_p/l_p$) Nylon Cylindrical Particles in Water.....	213
8.36.3	x -Acceleration (A_x), y -Acceleration (A_y) and Magnitude of Acceleration ($ A $) for 1.50 mm Diameter and 1:5 Aspect Ratio ($AR = d_p/l_p$) Nylon Cylindrical Particles in Water	214
8.37	Appendix 37: 1.50 mm Diameter and 1:5 Aspect Ratio ($AR = d_p/l_p$) Nylon Cylindrical Particles in 20%–80% Glycerol–Water.....	215
8.37.1	Particle Displacement, Particle Velocity and Particle Acceleration for 1.50 mm Diameter and 1:5 Aspect Ratio ($AR = d_p/l_p$) Nylon Cylindrical Particles in 20%–80% Glycerol–Water	215
8.37.2	x -Velocity (V_x), y -Velocity (V_y) and Magnitude of Velocity ($ V $) for 1.50 mm Diameter and 1:5 Aspect Ratio ($AR = d_p/l_p$) Nylon Cylindrical Particles in 20%–80% Glycerol–Water	216
8.37.3	x -Acceleration (A_x), y -Acceleration (A_y) and Magnitude of Acceleration ($ A $) for 1.50 mm Diameter and 1:5 Aspect Ratio ($AR = d_p/l_p$) Nylon Cylindrical Particles in 20%–80% Glycerol–Water.....	217
8.38	Appendix 38: 1.50 mm Diameter and 1:5 Aspect Ratio ($AR = d_p/l_p$) Nylon Cylindrical Particles in 40%–60% Glycerol–Water.....	218
8.38.1	Particle Displacement, Particle Velocity and Particle Acceleration for 1.50 mm Diameter and 1:5 Aspect Ratio ($AR = d_p/l_p$) Nylon Cylindrical Particles in 40%–60% Glycerol–Water	218
8.38.2	x -Velocity (V_x), y -Velocity (V_y) and Magnitude of Velocity ($ V $) for 1.50 mm Diameter and 1:5 Aspect Ratio ($AR = d_p/l_p$) Nylon Cylindrical Particles in 40%–60% Glycerol–Water	219

8.38.3	x -Acceleration (A_x), y -Acceleration (A_y) and Magnitude of Acceleration ($ A $) for 1.50 mm Diameter and 1:5 Aspect Ratio ($AR = d_p/l_p$) Nylon Cylindrical Particles in 40%–60% Glycerol–Water.....	220
8.39	Appendix 39: 1.50 mm Diameter and 1:5 Aspect Ratio ($AR = d_p/l_p$) Nylon Cylindrical Particles in Canola Oil.....	221
8.39.1	Particle Displacement, Particle Velocity and Particle Acceleration for 1.50 mm Diameter and 1:5 Aspect Ratio ($AR = d_p/l_p$) Nylon Cylindrical Particles in Canola Oil.....	221
8.39.2	x -Velocity (V_x), y -Velocity (V_y) and Magnitude of Velocity ($ V $) for 1.50 mm Diameter and 1:5 Aspect Ratio ($AR = d_p/l_p$) Nylon Cylindrical Particles in Canola Oil.....	222
8.39.3	x -Acceleration (A_x), y -Acceleration (A_y) and Magnitude of Acceleration ($ A $) for 1.50 mm Diameter and 1:5 Aspect Ratio ($AR = d_p/l_p$) Nylon Cylindrical Particles in Canola Oil	223
8.40	Appendix 40 The Predicted Theoretical Values of the Terminal Settling Velocity of the 4 mm Delrin Spheres in Water.....	224
8.41	Appendix 41 Measured Mass, Diameter and Density of 4 mm Delrin Spherical Particles	226
8.42	Appendix 42 Measured Diameter, Mass and Density of 2 mm Aluminium Spherical Particles	227
8.43	Appendix 43 Particle Reynolds Number and the Coefficient of Drag of the Cylindrical Particles using the Ratio of Volume to the Surface Area of the Particle as a Length Scale	228
8.44	Appendix 44: Stokes' Number and Gravitational Terminal settling velocity for the Multiple Particles within the Near-Slot Region in SAGD Operations.....	230
8.45	Appendix 45: Image Processing Code – Image Preprocessing and Boundary Fitted Approach.....	232
8.46	Appendix 46: Image Processing Code – Tracking the Centroid of the Particles and Calculating the Particle Displacement, Velocity and Acceleration	238
8.47	Appendix 47: Solid Modeling.....	244

List of Tables

Table 1 The material, density and diameter of the spherical particles used in this phase of the study	19
Table 2 The densities and viscosities of the of the five (5) fluids that were used to spherical particles experiments [74–77]. All the liquids were degassed using a vacuum pump (Labconco 117) having a vacuum chamber attached. (Tap water was used in the experiments)	20
Table 3 The material, density, diameter, length and aspect ratios of the cylindrical particles that were made using the set-up in Figure 4.....	23
Table 4 The densities and viscosities of the of the four (4) fluids that were used to cylindrical particles experiments [74–77].	23
Table 5 Specifications of the PSV imaging system used for the short channel	26
Table 6 Specifications of the PSV imaging system used for the tall channel. The camera (4M180NCL, IO Industries Inc.) sensor size was cropped in order to achieve higher frames.	28
Table 7 This table shows the average terminal settling velocity within the terminal settling velocity region of the 15 spherical particles for each experimental condition. The terminal settling velocity were obtain from the plots of the particle displacement versus the particle velocity (magnitude) for the spherical particles as shown in Section 8.1 – Appendix 2 to Section 8.15 – Appendix 16. The particle Reynolds Number and the coefficient of drag were calculated based on the average terminal settling velocity values. The coefficient of drag was calculated based on the model in [16].	41
Table 8 This table shows the average terminal settling velocity within the terminal settling velocity region of the 1.30 mm Diameter 25 nylon cylindrical particles for each experimental condition. The terminal settling velocity were obtain from the plots of the particle displacement versus the particle velocity (magnitude) for the spherical particles as shown in Section 8.16 – Appendix 17 to Section 8.27 – Appendix 28. The particle Reynolds Number and the coefficient of drag were calculated based on the average terminal settling velocity values and the <i>equivalent diameter</i> of the particle. The coefficient of drag was calculated based on the model in [16]......	47
Table 9 This table shows the average terminal settling velocity within the terminal settling velocity region of the 1.50 mm Diameter 25 nylon cylindrical particles for each experimental condition. The terminal settling velocity were obtain from the plots of the particle displacement versus the particle velocity (magnitude) for the spherical particles as shown in Section 8.28 – Appendix 18 to	

Section 8.39 – Appendix 39. The particle Reynolds Number and the coefficient of drag were calculated based on the average terminal settling velocity values and the *equivalent diameter* of the particle. The coefficient of drag was calculated based on the model in [16].48

Table 10 The values of the four parameters A, B, C and D to determine the coefficient of drag using the Haider and Levenspiel model. The values of A, B, C and D dependent on the particle sphericity, ϕ , which is the ratio of the surface area of a sphere having the same volume as the particle, s , to the surface area of the particle, S49

Table 11 This table shows the values of the two length scales that were used to determine the coefficient of drag of the particles and the particle Reynolds number of the cylinders i.e. the equivalent diameter of the cylinders and the ratio of the volume to the surface area of the cylinders.50

Table 12 Specifications of the PSV system, Figure 26, which was used to study the motion of single particles within the near-slot region in SAGD operations60

Table 13 Specifications of the PSV system, shown in Figure 36, which used to study the motion of multiple particles within the near-slot region in SAGD operations.75

Table 14 The aspect ratio and roundness of the six particles (a)-(f) shown in Figure 43 [11]88

Table 15 The predicted theoretical values of the terminal settling velocity and the coefficient of drag of the 4 mm delrin particles in water.225

Table 16 The measured mass, diameter, volume and density of the 4 mm delrin spheres.226

Table 17 The measured mass, diameter, volume and density of the 2 mm aluminum spheres. ..227

Table 18 This table shows the average terminal settling velocity within the terminal settling velocity region of the 1.30 mm Diameter 25 nylon cylindrical particles for each experimental condition. The terminal settling velocity were obtain from the plots of the particle displacement versus the particle velocity (magnitude) for the spherical particles as shown in Section 8.16 – Appendix 16 to Section 8.27 – Appendix 27. The particle Reynolds Number and the coefficient of drag were calculated based on the average terminal settling velocity values and *the ratio of the volume to the surface area of the particle as a length scale*. The coefficient of drag was calculated based on the model in [16].228

Table 19 This table shows the average terminal settling velocity within the terminal settling velocity region of the 1.50 mm Diameter 25 nylon cylindrical particles for each experimental condition. The terminal settling velocity were obtain from the plots of the particle displacement

versus the particle velocity (magnitude) for the spherical particles as shown in Section 8.28 – Appendix 18 to Section 8.39 – Appendix 39. The particle Reynolds Number and the coefficient of drag were calculated based on the average terminal settling velocity values and *the ratio of the volume to the surface area of the particle as a length scale*. The coefficient of drag was calculated based on the model in [16].229

Table 20 Diameter, density, particle–fluid density difference and terminal settling velocity of the three particles used in Chapter 5 and discussed in Section 5.5.2 namely, tracer particles (polystyrene spherical microbeads), spherical particles (glass beads) and irregularly shaped (silicon carbide). Note the equivalent diameter was used as the length scale to characterize the irregularly shaped particles.230

List of Figures

Figure 1 A schematic of steam assisted gravity drainage (SAGD) process which also includes an illustration of the slotted liner. Some of the flow geometries that were used in this study include one single slot of the slotted liner.....3

Figure 2 A schematic of a core sample used in the core flooding test. This is a bulk approach in which fluid is injected into the core sample and the effluent is assessed. The core flooding approach is analyzed using Darcy’s Law..... 13

Figure 3 A schematic of the particles that were used in each of the three experimental analyses performed. The cylindrical particles were manufactured in-house. In this thesis research the hypothesis that using the spherical assumption to model non-spherical particles is invalid was tested by studying particle motion in: (1) an open flow area i.e. a rectangular channel, (2) particle motion through narrow slots and (3) particle motion within a porous network into a narrow slots. 17

Figure 4 Particle chopper used to make cylindrical particles of diameters 1.30 mm and 1.50 mm and aspect ratios, ($AR = d_p/l_p$) 1:1, 1:3 and 1:5. The micrometer on the XY Translation Stage was adjusted to create a spacing equal to the particle length. Then a razor blade attached to a lever performed the cutting action. The particle chopper is a modified design of a jewelry wire guillotine cutter tool (AL Findings Limited).....21

Figure 5 Sample two-dimensional images of the cylindrical particles that were manufactured for this study. This figure shows images of the 1.30 mm diameter opaque, black, constant diameter mono-filament (fishing lines, Hi-Seas Grand Slam) at aspect ratios, ($AR = d_p/l_p$) of 1:1, 1:3 and 1:5. The histograms shows the distributed of the projected areas of the particles that were calculated from the two-dimensional images of the particles.22

Figure 6 The rectangular flow channels: (a) short channel and (b) tall channel. The channels were made of acrylic sheet. The particle inlet was 3D printed using a clear photopolymer resin.....24

Figure 7 Particle shadowgraph velocimetry (PSV) experimental set-up for the short channel (Figure 6 (a)).One (1) high speed camera was sufficient to capture the motion of the falling particles within a field of view of 50 mm × 200 mm. An LED panel was used to illuminate the field of view. This set-up was used for the cylindrical particles in water and 20%-80% glycerol-water.26

Figure 8 Particle shadowgraph velocimetry (PSV) experimental set-up for the tall channel (Figure 6 (b)). Two (2) high speed cameras were needed in order to capture the field of view. The field of view of the falling particles was 50 mm × 600 mm. A projector was used as the light source to illuminate such a large field of view. This set-up was used for the cylindrical particles in 40%-60% glycerol-water and canola oil and all of the spherical particles experiments.....27

Figure 9 This is a flow chart describes image processing steps that were used to quantify particle motion. The spherical or cylindrical particles were delineated in the image processing script with a function that defines the minimal boundary of the particles [78]. Particle motion was determined by tracking the centroid of the falling particle. The displacement, velocity and acceleration of the particle was found by applying a derivativeFit function [79] to the tracked centroid locations. ...29

Figure 10 The initialization stage of the image processing: (a) A sample raw image in which the region of interest within the rectangular channel was identified and highlighted by the red dashed lines, (b) The region of interest was cropped from the raw image, (c) The cropped image was binarized using a coarse threshold and (d) The image was inverted and the boundary and the centroid of the particle were identified. A localized boxed region centered at the centroid of the particle was defined as highlighted by the solid red line. This localized region is the basis of the subsequent image processing steps.30

Figure 11 The processing steps of the fitted circle approach. This method which begins with a localized region around the particle. The images are inverted and the intensity values are stretched. A circle is fitted to the boundary of the particle and the centroid is identified and tracking in subsequent images.....32

Figure 12 The processing steps of the boundary fitted approach. This method begins with a localized cropped region around the particle. The images are inverted and the intensity values are stretched. The images are then binarized and a minimal bounding objects function [78] was used to fit a square to the 2D images of the spherical particles and a rectangle to the 2D images of the cylindrical particles. The centroid is identified and tracking in subsequent images.....33

Figure 13 Particle velocity in the x -direction V_x , y -direction V_y , and the magnitude $\sqrt{V_x^2 + V_y^2}$ of the particle velocity $|V|$ for 1.50 mm Diameter Nylon Cylindrical Particles with Aspect Ratio, A.R. = 1:5 (25 particles) in Water. The average terminal settling velocity, U_t is 51.61 mm/s.....35

Figure 14 Particle acceleration in the x -direction A_x , y -direction A_y , and the magnitude $\sqrt{A_x^2 + A_y^2}$ of the particle acceleration $|A|$ for 1.50 mm Diameter Nylon Cylindrical Particles with Aspect Ratio,

A.R. = 1:5 (25 particles) in Water. The acceleration was observed to be zero within the region that was used to determine the average terminal settling velocity in Figure 13.36

Figure 15 (a) The general trend of the particle trajectory that was observed for the spherical particles falling within all of the fluids. (b) particle displacement, y , versus time, (c) the y component of the particle velocity and (d) the y component of the particle acceleration for 4 mm delrin spheres in Water. 15 particles were used in the original experiment however, two particles appeared as outliers and were omitted from this plot. This experimental condition was performed within the tall channel as shown in Figure 6 (b) in order to allow the particles to reach terminal settling velocity.38

Figure 16 (a) The general trend of the particle trajectory that was observed for the cylindrical particles falling within all of the fluids. (b) particle displacement, y , versus time, (c) the y component of the particle velocity and (d) the y component of the particle acceleration for 1.50 mm Diameter Nylon Cylindrical Particles with Aspect Ratio, A.R. = 1:5 (25 particles) in Water. In this experimental condition the particles reached terminal settling velocity within the short channel as shown in Figure 6 (a).40

Figure 17 The theoretical terminal settling velocities, U_t (Theoretical), plotted against the experimental terminal settling velocities, U_t (experimental), of the spherical particles that were discussed in section 3.6.3 and shown in Table 7. The dotted black line represents a plot of $y = x$ which was used to evaluate the agreement between the theoretical values and the experimental values of the terminal settling velocity. The minimum values of the measured density of delrin and aluminum were used to calculate U_t (Theoretical). This resulted in the closest fit between the experimental and theoretical values.44

Figure 18 The theoretical terminal settling velocities, U_t (Theoretical), plotted against the experimental terminal settling velocities, U_t (experimental), of the spherical particles that were discussed in section 3.6.3 and shown in Table 7. The dotted black line represents a plot of $y = x$ which was used to evaluate the agreement between the theoretical values and the experimental values of the terminal settling velocity. The maximum values of the measured density of delrin and aluminum were used to calculate U_t (Theoretical). The data points deviated further away from the $y = x$ line compared to the plot obtained in Figure 17 which was obtained using the minimum values of the measured density.45

Figure 19 The theoretical terminal settling velocities, U_t (Theoretical), plotted against the experimental terminal settling velocities, U_t (experimental), of the spherical particles that were discussed in section 3.6.3 and shown in Table 7. The dotted black line represents a plot of $y = x$ which was used to evaluate the agreement between the theoretical values and the experimental values of the terminal settling velocity. The median values of the measured terminal settling velocity of delrin and aluminum were used to calculate U_t (Theoretical). The experimental and theoretical data points had a closer fit compared to Figure 18 where the maximum value of the measured density was used to determine U_t (Theoretical).46

Figure 20 A plot of the coefficient of drag of the particles, C_D plotted versus the particle Reynolds number Re_p which were obtained from experimental data. The coefficient of drag and the particle Reynolds number were calculated based on the *equivalent diameter* of the particles as a length scale. The five curves were obtained from the Haider and Levenspiel model for the coefficient of drag, plotted for five different values of particle sphericity, ϕ i.e. 1, 0.906, 0.846, 0.806, 0.670. The particle sphericity is ratio of the surface area of a sphere having the same volume as the particle to the actual surface area of the particle.51

Figure 21 Illustrates the variation of the coefficient of drag, C_D , and the cylindrical particle Reynolds number Re_p with respect to the aspect ratio of the cylindrical particles. The coefficient of drag and the particle Reynolds number were calculated based on the *equivalent diameter* of the cylindrical particles as a length scale.52

Figure 22 A plot of the coefficient of drag of the particles, C_D plotted versus the particle Reynolds number Re_p which were obtained from experimental data. The coefficient of drag and the particle Reynolds number were calculated using *the ratio of the volume to the surface area of the cylindrical particles as a length scale*. The data points overlapped more closely compared to Figure 20. The five curves were obtained from the Haider and Levenspiel model for the coefficient of drag, plotted for five different values of particle sphericity, ϕ i.e. 1, 0.906, 0.846, 0.806, 0.670. The particle sphericity is ratio of the surface area of a sphere having the same volume as the particle to the actual surface area of the particle.53

Figure 23 Illustrates the variation of the coefficient of drag, C_D , and the cylindrical particle Reynolds number Re_p with respect to the aspect ratio of the cylindrical particles. The coefficient of drag and the particle Reynolds number were calculated based on *the ratio of the volume to the*

surface area of the cylindrical particles as a length scale. The data points overlapped more closely when compared to using the equivalent diameter as a length scale in Figure 21.54

Figure 24 This figure focuses on the particle trajectories within the terminal settling regions for the spherical particle in Figure 15 and the cylindrical particle in Figure 16. It can be seen that the cylindrical particle moved in a horizontal position within the region of terminal velocity. This indicates that the equivalent diameter is not a suitable length scale to obtain the particle Reynolds number for long aspect ratio particles. Shows the particle trajectory of the 4 mm delrin spherical particle falling within water whereby the average terminal settling velocity of the particles was 196.82 mm/s. The plot of the magnitude of velocity was obtained from the 13 spherical particles shown in Figure 15 and (b) Shows the particle trajectory of the 1.50 mm diameter cylinders with an aspect ratio of 1:5 falling within water whereby the average terminal settling velocity of the particles is 51.61 mm/s. The plot of the magnitude of velocity was obtained from the 25 cylindrical particles shown in Figure 16. The raw image in (b) is wider as this experiment was performed in the shorter channel whereby the camera was closer to the test section compared to the tall channel used for the raw image in (a).....55

Figure 25 (a) A schematic of the exploded flow cell assembly and (b) An enlarged image to clearly highlight the dimensions of the field of view. The section within the dashed red lines is the region of interest (ROI) which was considered in the analysis of the single particle motion.58

Figure 26 A schematic of the Particle Shadowgraph Velocimetry (PSV) experimental set-up for the single particles60

Figure 27 A sample processed image of the spherical glass beads particle. The particle fell in the direction of gravity within a 70%–30% glycerol–water solution. The diameter of the sphere in this image is 3.213 mm. The yellow lines highlight the shortest and longest lengths that were used to determine the aspect ratio of the particle. The outline/diameter of the particle is also highlighted with the yellow circle.62

Figure 28 A sample processed image of the irregularly shaped glass beads particle. The particle fell in the direction of gravity within a 70%–30% glycerol–water solution. The equivalent diameter of the particle in this image is 2.66 mm. The yellow lines highlight the shortest and longest lengths that were used to determine the aspect ratio of the particle. The equivalent diameter of the particle is also highlighted with the yellow circle.....62

Figure 29 The equivalent diameter, D_e of both the irregularly shaped particle and the spherical particle. For each particle D_e was calculated for every subsequent frame as the particles fell through the fluid. D_e was plotted versus the vertical y location of the particle which was non-dimensionalized with the length, l , of the slot.....65

Figure 30 The aspect ratio of both the spherical particle and the irregularly shaped particle. For each particle the aspect ratio was calculated for every subsequent frame as the particles fell through the fluid. The aspect ratio was plotted versus the vertical y location of the particle which was non-dimensionalized with the length, l , of the slot.....65

Figure 31 The velocity field of the surrounding fluid around the spherical particle shown at four (4) vertical locations as the particle fell through the fluid. The diameter of the sphere is 3.213 mm.67

Figure 32 The velocity field of the surrounding fluid around the irregularly shaped particle shown at four (4) vertical locations as the particle fell through the fluid. The equivalent diameter of the irregularly shaped particle is 2.66 mm.67

Figure 33 Illustrates the velocity vector field of the surrounding fluid within a localized region around the spherical particle at the four (4) different vertical locations (a), (b), (c), and (d) corresponding to four (4) positions shown in Figure 31 as the particle fell within the fluid.68

Figure 34 Illustrates the velocity vector field of the surrounding fluid within a localized region around the irregularly shaped particle at the four (4) different vertical locations (a), (b), (c), and (d) corresponding to four (4) positions shown in Figure 32 as the particle fell within the fluid.69

Figure 35 A schematic of the flow cell used in this study. (a) The exploded view of the flow cell assembly, (b) the flow channel where the region of interest (ROI) is highlighted with a red box and (c) enlarged images of the ROI to demonstrate the three inlet conditions: (1) the open slot and pillars which were 2 mm in height aimed to simulate porous media: (2) 1 mm diameter cylindrical pillars and (3) diamond shaped pillars circumscribed into 1 mm diameter circles. The field of view (FOV) for the continuous phase velocity measurements are highlighted in the blue boxes. Note that the FOV for the build-up tests was slightly wider than the FOV for the velocity measurements of the continuous phase [11]. A detailed drawing is given in Section 8.47–Appendix 47.....73

Figure 36 A schematic of the Particle Shadowgraph Velocimetry (PSV) experimental set-up for the multiple particles analysis74

Figure 37 To determine the particle characteristics of the irregularly shaped silicon carbide particles (AGSCO Corp.), 2D images were taken of 2213 particles. (a) One sample images selected from the 55 2D images that were taken. (b) The particle size distribution (equivalent diameter) of the particles whereby the average particle size is 43 μm . (c) The distribution of the aspect ratios of the particles (i.e. the ratio of the minor axes to the major axes of the fitted ellipses). The average particle aspect ratio was 0.68. (d) The distribution of the roundness of the particles. The average round is 0.40.....78

Figure 38 The velocity field within the region of interest for the three flow cell configurations (the open slot and inlet conditions aimed to simulate porous media using cylindrical pillars or diamond shaped pillars). The colors in the background represent the velocity magnitude ($\sqrt{u^2+v^2}$) and the black arrows represent the velocity vector field. The low velocity regions are selected with red boxes and the average velocities U_{ave} within the low velocity regions are shown.[11].....82

Figure 39 A plot of the average velocity U_{ave} within the low velocity regions, represented by the red boxes in Figure 38, versus Reynolds number ($Re = 0.1, 1.0$ and 10) for the three flow cell configurations (the open slot and inlet conditions aimed to simulate porous media using cylindrical pillars or diamond shaped pillars). [11]83

Figure 40 Particle deposition which occurred during the 12 seconds of data collection, starting at time $t = 0$ and then at time $t = 16$ minutes. This figure shows the particle deposition for both spherical and irregularly shaped particles in three flow cell configurations: open slot, cylindrical pillars, and diamond shaped pillars, at $Re = 0.1$ [11].....84

Figure 41 Particle deposition which occurred during the 12 seconds of data collection, starting at time $t = 0$ and then at time $t = 16$ minutes. This figure shows the particle deposition for both spherical and irregularly shaped particles in three flow cell configurations: open slot, cylindrical pillars, and diamond shaped pillars, at $Re = 1$ [11].....85

Figure 42 Particle deposition which occurred during the 12 seconds of data collection, starting at time $t = 0$ and then at time $t = 16$ minutes. This figure shows the particle deposition for both spherical and irregularly shaped particles in three flow cell configurations: open slot, cylindrical pillars, and diamond shaped pillars, at $Re = 10$ [11].....86

Figure 43 Factors that influenced the rotation of six selected particles flowing through the slot of the open channel at $Re = 1$. The velocity vector field and the streamlines of the continuous phase are shown at left corner. The six grayscale figures are snapshots of selected particles at every 4th

frame to avoid overlapping images of particles. The line plots are vertical locations of the center of the fitted ellipse to the particle plotted versus the absolute value of the difference between the angle of rotation of the particles, θ , (in every 4th frame) and the initial angle, θ_i , of each particle [11].89

Figure 44 The trajectory of two particles that are transported through a porous network into a narrow slot at $Re = 0.1$. The images were edited to exclude the surrounding particles. P_1 and P_2 flowed at two different times in the experiments and therefore, they were not in physical contact. [11].91

Figure 45 Particle displacement, y , velocity, V_y , and acceleration, A_y , for 4mm Diameter Delrin (15 particles) in Water. Two particles (represented by the light blue and mustard lines) were outliers because the velocity plots exhibited unusual trends within 375 mm and 450 mm of the particle displacement. The outliers in the original data were removed and plotted in Figure 46 and Figure 47 in order to obtain a better estimate of the terminal settling velocity and average constant acceleration..... 107

Figure 46 Particle velocity in the x -direction V_x , y -direction V_y , and the magnitude $\sqrt{V_x^2 + V_y^2}$ of the particle velocity $|V|$ for 4mm Diameter Delrin in Water. The average terminal settling velocity, U_t is 196.82 mm/s. Note: the two (2) outliers shown in Figure 45 were omitted in order to obtain a better estimate of the terminal settling velocity. Therefore only 13 particles are shown in this plots. 108

Figure 47 Particle acceleration in the x -direction A_x , y -direction A_y , and the magnitude $\sqrt{A_x^2 + A_y^2}$ of the particle acceleration $|A|$ for 4mm Diameter Delrin in Water. Note: the two (2) outliers shown in Figure 45 were omitted in order to obtain a better estimate of the average acceleration within the terminal velocity region. Therefore only 13 particles are shown in this plots. 109

Figure 48 Particle displacement, y , velocity, V_y , and acceleration, A_y , for 4mm Diameter Delrin (15 particles) in 20%–80% Glycerol–Water. 110

Figure 49 Particle velocity in the x -direction V_x , y -direction V_y , and the magnitude $\sqrt{V_x^2 + V_y^2}$ of the particle velocity $|V|$ for 4mm Diameter Delrin (15 particles) in 20%–80% Glycerol–Water. The average terminal settling velocity, U_t is 152.99 mm/s. 111

Figure 50 Particle acceleration in the x -direction A_x , y -direction A_y , and the magnitude $\sqrt{A_x^2 + A_y^2}$ of the particle acceleration $|A|$ for 4mm Diameter Delrin (15 particles) in 20%–80% Glycerol–Water. 112

Figure 51 Particle displacement, y , velocity, V_y , and acceleration, A_y , for 4mm Diameter Delrin (15 particles) in 40%–60% Glycerol–Water. 113

Figure 52 Particle velocity in the x -direction V_x , y -direction V_y , and the magnitude $\sqrt{V_x^2 + V_y^2}$ of the particle velocity $|V|$ for 4mm Diameter Delrin (15 particles) in 40%–60% Glycerol–Water. The average terminal settling velocity, U_t is 108.37 mm/s. 114

Figure 53 Particle acceleration in the x -direction A_x , y -direction A_y , and the magnitude $\sqrt{A_x^2 + A_y^2}$ of the particle acceleration $|A|$ for 4mm Diameter Delrin (15 particles) in 40%–60% Glycerol–Water. 115

Figure 54 Particle displacement, y , velocity, V_y , and acceleration, A_y , for 4mm Diameter Delrin (15 particles) in 70%–30% Glycerol–Water. The outliers at displacement 260 mm occurred within the overlap between the two cameras. In this region there was a variation in the light distribution compared to the rest of the field of view. A uniform distribution of light was not achieved with the projector and kite paper as shown in Figure 8 and describe in Section 3.5.1. This affected the binarization of the particle within that region and thereby a slight shift in the location of the centroid of the particle from the image processing scheme. 116

Figure 55 Particle velocity in the x -direction V_x , y -direction V_y , and the magnitude $\sqrt{V_x^2 + V_y^2}$ of the particle velocity $|V|$ for 4mm Diameter Delrin (15 particles) in 70%–30% Glycerol–Water. The average terminal settling velocity, U_t is 34.68 mm/s. The outliers at displacement 260 mm occurred within the overlap between the two cameras. In this region there was a variation in the light distribution compared to the rest of the field of view. A uniform distribution of light was not achieved with the projector and kite paper as shown in Figure 8 and describe in Section 3.5.1. This affected the binarization of the particle within that region and thereby a slight shift in the location of the centroid of the particle from the image processing scheme. 117

Figure 56 Particle acceleration in the x -direction A_x , y -direction A_y , and the magnitude $\sqrt{A_x^2 + A_y^2}$ of the particle acceleration $|A|$ for 4mm Diameter Delrin (15 particles) in 70%–30% Glycerol–Water. The outliers at displacement 260 mm occurred within the overlap between the two cameras. In this region there was a variation in the light distribution compared to the rest of the field of view. A uniform distribution of light was not achieved with the projector and kite paper as shown in Figure 8 and describe in Section 3.5.1. This affected the binarization of the particle within that region and thereby a slight shift in the location of the centroid of the particle from the image processing scheme. 118

Figure 57 Particle displacement, y , velocity, V_y , and acceleration, A_y , for 4mm Diameter Delrin (15 particles) in Canola Oil. The outliers at displacement 260 mm occurred within the overlap between the two cameras. In this region there was a variation in the light distribution compared to the rest of the field of view. A uniform distribution of light was not achieved with the projector and kite paper as shown in Figure 8 and describe in Section 3.5.1. This affected the binarization of the particle within that region and thereby a slight shift in the location of the centroid of the particle from the image processing scheme. 119

Figure 58 Particle velocity in the x -direction V_x , y -direction V_y , and the magnitude $\sqrt{(V_x^2 + V_y^2)}$ of the particle velocity $|V|$ for 4mm Diameter Delrin in Canola Oil. The average terminal settling velocity, U_t is 54.86 mm/s. The outliers at displacement 260 mm occurred within the overlap between the two cameras. In this region there was a variation in the light distribution compared to the rest of the field of view. A uniform distribution of light was not achieved with the projector and kite paper as shown in Figure 8 and describe in Section 3.5.1. This affected the binarization of the particle within that region and thereby a slight shift in the location of the centroid of the particle from the image processing scheme. 120

Figure 59 Particle acceleration in the x -direction A_x , y -direction A_y , and the magnitude $\sqrt{(A_x^2 + A_y^2)}$ of the particle acceleration $|A|$ for 4mm Diameter Delrin in Canola Oil. The outliers at displacement 260 mm occurred within the overlap between the two cameras. In this region there was a variation in the light distribution compared to the rest of the field of view. A uniform distribution of light was not achieved with the projector and kite paper as shown in Figure 8 and describe in Section 3.5.1. This affected the binarization of the particle within that region and thereby a slight shift in the location of the centroid of the particle from the image processing scheme. 121

Figure 60 Particle displacement, y , velocity, V_y , and acceleration, A_y , for 2mm Diameter Delrin (15 particles) in Water. Four particles (represented by the pink, blue, light green and purple lines) were outliers because the velocity plots exhibited unusual trends within 360 mm and 420 mm of the particle displacement. The outliers in the original data were removed and plotted in Figure 61 and Figure 62 in order to obtain a better estimate of the terminal settling velocity and average constant acceleration. 122

Figure 61 Particle velocity in the x -direction V_x , y -direction V_y , and the magnitude $\sqrt{(V_x^2 + V_y^2)}$ of the particle velocity $|V|$ for 2mm Diameter Delrin in Water. The average terminal settling velocity, U_t is 114.18 mm/s. Note: the four (4) outliers shown in Figure 60 were omitted in order to obtain

a better estimate of the terminal settling velocity. Therefore only 11 particles are shown in this plots. 123

Figure 62 Particle acceleration in the x -direction A_x , y -direction A_y , and the magnitude $\sqrt{(A_x^2 + A_y^2)}$ of the particle acceleration $|A|$ for 2mm Diameter Delrin in Water. Note: the four (4) outliers shown in Figure 60 were omitted in order to obtain a better estimate of the average acceleration within the terminal velocity region. Therefore only 11 particles are shown in this plots. 124

Figure 63 Particle displacement, y , velocity, V_y , and acceleration, A_y , for 2mm Diameter Delrin (15 particles) in 20%–80% glycerol–water. The outliers at displacement 260 mm occurred within the overlap between the two cameras. In this region there was a variation in the light distribution compared to the rest of the field of view. A uniform distribution of light was not achieved with the projector and kite paper as shown in Figure 8 and describe in Section 3.5.1. This affected the binarization of the particle within that region and thereby a slight shift in the location of the centroid of the particle from the image processing scheme. 125

Figure 64 Particle velocity in the x -direction V_x , y -direction V_y , and the magnitude $\sqrt{(V_x^2 + V_y^2)}$ of the particle velocity $|V|$ for 2mm Diameter Delrin in 20%–80% glycerol–water. The average terminal settling velocity, U_t is 78.84 mm/s. The outliers at displacement 260 mm occurred within the overlap between the two cameras. In this region there was a variation in the light distribution compared to the rest of the field of view. A uniform distribution of light was not achieved with the projector and kite paper as shown in Figure 8 and describe in Section 3.5.1. This affected the binarization of the particle within that region and thereby a slight shift in the location of the centroid of the particle from the image processing scheme. 126

Figure 65 Particle acceleration in the x -direction A_x , y -direction A_y , and the magnitude $\sqrt{(A_x^2 + A_y^2)}$ of the particle acceleration $|A|$ for 2mm Diameter Delrin in 20%–80% glycerol–water. The outliers at displacement 260 mm occurred within the overlap between the two cameras. In this region there was a variation in the light distribution compared to the rest of the field of view. A uniform distribution of light was not achieved with the projector and kite paper as shown in Figure 8 and describe in Section 3.5.1. This affected the binarization of the particle within that region and thereby a slight shift in the location of the centroid of the particle from the image processing scheme. 127

Figure 66 Particle displacement, y , velocity, V_y , and acceleration, A_y , for 2mm Diameter Delrin (15 particles) in 40%–60% glycerol–water. The outliers at displacement 260 mm occurred within

the overlap between the two cameras. In this region there was a variation in the light distribution compared to the rest of the field of view. A uniform distribution of light was not achieved with the projector and kite paper as shown in Figure 8 and describe in Section 3.5.1. This affected the binarization of the particle within that region and thereby a slight shift in the location of the centroid of the particle from the image processing scheme. 128

Figure 67 Particle velocity in the x -direction V_x , y -direction V_y , and the magnitude $\sqrt{V_x^2 + V_y^2}$ of the particle velocity $|V|$ for 2mm Diameter Delrin (15 particles) in 40%–60% glycerol–water. The average terminal settling velocity, U_t is 49.85 mm/s. The outliers at displacement 260 mm occurred within the overlap between the two cameras. In this region there was a variation in the light distribution compared to the rest of the field of view. A uniform distribution of light was not achieved with the projector and kite paper as shown in Figure 8 and describe in Section 3.5.1. This affected the binarization of the particle within that region and thereby a slight shift in the location of the centroid of the particle from the image processing scheme. 129

Figure 68 Particle acceleration in the x -direction A_x , y -direction A_y , and the magnitude $\sqrt{A_x^2 + A_y^2}$ of the particle acceleration $|A|$ for 2mm Diameter Delrin (15 particles) in 40%–60% glycerol–water. The outliers at displacement 260 mm occurred within the overlap between the two cameras. In this region there was a variation in the light distribution compared to the rest of the field of view. A uniform distribution of light was not achieved with the projector and kite paper as shown in Figure 8 and describe in Section 3.5.1. This affected the binarization of the particle within that region and thereby a slight shift in the location of the centroid of the particle from the image processing scheme 130

Figure 69 Particle displacement, y , velocity, V_y , and acceleration, A_y , for 2mm Diameter Delrin (15 particles) in 70%–30% glycerol–water. The outliers at displacement 260 mm occurred within the overlap between the two cameras. In this region there was a variation in the light distribution compared to the rest of the field of view. A uniform distribution of light was not achieved with the projector and kite paper as shown in Figure 8 and describe in Section 3.5.1. This affected the binarization of the particle within that region and thereby a slight shift in the location of the centroid of the particle from the image processing scheme. 131

Figure 70 Particle velocity in the x -direction V_x , y -direction V_y , and the magnitude $\sqrt{V_x^2 + V_y^2}$ of the particle velocity $|V|$ for 2mm Diameter Delrin (15 particles) in 70%–30% glycerol–water. The average terminal settling velocity, U_t is 12.07 mm/s. The outliers at displacement 260 mm occurred

within the overlap between the two cameras. In this region there was a variation in the light distribution compared to the rest of the field of view. A uniform distribution of light was not achieved with the projector and kite paper as shown in Figure 8 and describe in Section 3.5.1. This affected the binarization of the particle within that region and thereby a slight shift in the location of the centroid of the particle from the image processing scheme. 132

Figure 71 Particle acceleration in the x -direction A_x , y -direction A_y , and the magnitude $\sqrt{(A_x^2 + A_y^2)}$ of the particle acceleration $|A|$ for 2mm Diameter Delrin (15 particles) in 70%–30% glycerol–water. The outliers at displacement 260 mm occurred within the overlap between the two cameras. In this region there was a variation in the light distribution compared to the rest of the field of view. A uniform distribution of light was not achieved with the projector and kite paper as shown in Figure 8 and describe in Section 3.5.1. This affected the binarization of the particle within that region and thereby a slight shift in the location of the centroid of the particle from the image processing scheme. 133

Figure 72 Particle displacement, y , velocity, V_y , and acceleration, A_y , for 2mm Diameter Delrin (15 particles) in Canola Oil. In this region there was a variation in the light distribution compared to the rest of the field of view. A uniform distribution of light was not achieved with the projector and kite paper as shown in Figure 8 and describe in Section 3.5.1. This affected the binarization of the particle within that region and thereby a slight shift in the location of the centroid of the particle from the image processing scheme. 134

Figure 73 Particle velocity in the x -direction V_x , y -direction V_y , and the magnitude $\sqrt{(V_x^2 + V_y^2)}$ of the particle velocity $|V|$ for 2mm Diameter Delrin (15 particles) in Canola Oil. The average terminal settling velocity, U_t is 17.30 mm/s. In this region there was a variation in the light distribution compared to the rest of the field of view. A uniform distribution of light was not achieved with the projector and kite paper as shown in Figure 8 and describe in Section 3.5.1. This affected the binarization of the particle within that region and thereby a slight shift in the location of the centroid of the particle from the image processing scheme. 135

Figure 74 Particle acceleration in the x -direction A_x , y -direction A_y , and the magnitude $\sqrt{(A_x^2 + A_y^2)}$ of the particle acceleration $|A|$ for 2mm Diameter Delrin (15 particles) in Canola Oil. In this region there was a variation in the light distribution compared to the rest of the field of view. A uniform distribution of light was not achieved with the projector and kite paper as shown in Figure 8 and describe in Section 3.5.1. This affected the binarization of the particle within that region and

thereby a slight shift in the location of the centroid of the particle from the image processing scheme. 136

Figure 75 Particle displacement, y , velocity, V_y , and acceleration, A_y , for 2mm Diameter Aluminum (15 particles) in Water. 137

Figure 76 Particle velocity in the x -direction V_x , y -direction V_y , and the magnitude $\sqrt{V_x^2 + V_y^2}$ of the particle velocity $|V|$ for 2mm Diameter Aluminum (15 particles) in Water. The average terminal settling velocity, U_t is 289.97 mm/s. 138

Figure 77 Particle acceleration in the x -direction A_x , y -direction A_y , and the magnitude $\sqrt{A_x^2 + A_y^2}$ of the particle acceleration $|A|$ for 2mm Diameter Aluminum (15 particles) in Water. 139

Figure 78 Particle displacement, y , velocity, V_y , and acceleration, A_y , for 2mm Diameter Aluminum (15 particles) in 20%–80% glycerol–water. 140

Figure 79 Particle velocity in the x -direction V_x , y -direction V_y , and the magnitude $\sqrt{V_x^2 + V_y^2}$ of the particle velocity $|V|$ for 2mm Diameter Aluminum (15 particles) in 20%–80% glycerol–water. The average terminal settling velocity, U_t is 241.99 mm/s. 141

Figure 80 Particle acceleration in the x -direction A_x , y -direction A_y , and the magnitude $\sqrt{A_x^2 + A_y^2}$ of the particle acceleration $|A|$ for 2mm Diameter Aluminum (15 particles) in 20%–80% glycerol–water. 142

Figure 81 Particle displacement, y , velocity, V_y , and acceleration, A_y , for 2mm Diameter Aluminum (15 particles) in 40%–60% Glycerol–Water. The outliers at displacement 260 mm occurred within the overlap between the two cameras. In this region there was a variation in the light distribution compared to the rest of the field of view. A uniform distribution of light was not achieved with the projector and kite paper as shown in Figure 8 and describe in Section 3.5.1. This affected the binarization of the particle within that region and thereby a slight shift in the location of the centroid of the particle from the image processing scheme. 143

Figure 82 Particle velocity in the x -direction V_x , y -direction V_y , and the magnitude $\sqrt{V_x^2 + V_y^2}$ of the particle velocity $|V|$ for 2mm Diameter Aluminum in 40%–60% Glycerol–Water. The average terminal settling velocity, U_t is 184.59 mm/s. The outliers at displacement 260 mm occurred within the overlap between the two cameras. In this region there was a variation in the light distribution compared to the rest of the field of view. A uniform distribution of light was not achieved with the projector and kite paper as shown in Figure 8 and describe in Section 3.5.1. This affected the

binarization of the particle within that region and thereby a slight shift in the location of the centroid of the particle from the image processing scheme. 144

Figure 83 Particle acceleration in the x -direction A_x , y -direction A_y , and the magnitude $\sqrt{(A_x^2 + A_y^2)}$ of the particle acceleration $|A|$ for 2mm Diameter Aluminum in 40%–60% Glycerol–Water. The outliers at displacement 260 mm occurred within the overlap between the two cameras. In this region there was a variation in the light distribution compared to the rest of the field of view. A uniform distribution of light was not achieved with the projector and kite paper as shown in Figure 8 and describe in Section 3.5.1. This affected the binarization of the particle within that region and thereby a slight shift in the location of the centroid of the particle from the image processing scheme. 145

Figure 84 Particle displacement, y , velocity, V_y , and acceleration, A_y , for 2mm Diameter Aluminum (15 particles) in 70%–30% Glycerol–Water. The outliers at displacement 260 mm occurred within the overlap between the two cameras. In this region there was a variation in the light distribution compared to the rest of the field of view. A uniform distribution of light was not achieved with the projector and kite paper as shown in Figure 8 and describe in Section 3.5.1. This affected the binarization of the particle within that region and thereby a slight shift in the location of the centroid of the particle from the image processing scheme. 146

Figure 85 Particle velocity in the x -direction V_x , y -direction V_y , and the magnitude $\sqrt{(V_x^2 + V_y^2)}$ of the particle velocity $|V|$ for 2mm Diameter Aluminum in 70%–30% Glycerol–Water. The average terminal settling velocity, U_t is 75.25 mm/s. The outliers at displacement 260 mm occurred within the overlap between the two cameras. In this region there was a variation in the light distribution compared to the rest of the field of view. A uniform distribution of light was not achieved with the projector and kite paper as shown in Figure 8 and describe in Section 3.5.1. This affected the binarization of the particle within that region and thereby a slight shift in the location of the centroid of the particle from the image processing scheme. 147

Figure 86 Particle acceleration in the x -direction A_x , y -direction A_y , and the magnitude $\sqrt{(A_x^2 + A_y^2)}$ of the particle acceleration $|A|$ for 2mm Diameter Aluminum in 70%–30% Glycerol–Water. The outliers at displacement 260 mm occurred within the overlap between the two cameras. In this region there was a variation in the light distribution compared to the rest of the field of view. A uniform distribution of light was not achieved with the projector and kite paper as shown in Figure 8 and describe in Section 3.5.1. This affected the binarization of the particle within that region and

thereby a slight shift in the location of the centroid of the particle from the image processing scheme. 148

Figure 87 Particle displacement, y , velocity, V_y , and acceleration, A_y , for 2mm Diameter Aluminum (15 particles) in Canola Oil. 149

Figure 88 Particle velocity in the x -direction V_x , y -direction V_y , and the magnitude $\sqrt{V_x^2 + V_y^2}$ of the particle velocity $|V|$ for 2mm Diameter Aluminum in Canola Oil. The average terminal settling velocity, U_t is 60.41 mm/s. 150

Figure 89 Particle acceleration in the x -direction A_x , y -direction A_y , and the magnitude $\sqrt{A_x^2 + A_y^2}$ of the particle acceleration $|A|$ for 2mm Diameter Aluminum in Canola Oil. 151

Figure 90 Particle displacement, y , velocity, V_y , and acceleration, A_y , for 1.30 mm Diameter Nylon Cylindrical Particles with Aspect Ratio, A.R. = 1:1 (25 particles) in Water. 152

Figure 91 Particle velocity in the x -direction V_x , y -direction V_y , and the magnitude $\sqrt{V_x^2 + V_y^2}$ of the particle velocity $|V|$ for 1.30 mm Diameter Nylon Cylindrical Particles with Aspect Ratio, A.R. = 1:1 (25 particles) in Water. The average terminal settling velocity, U_t is 43.62 mm/s. 153

Figure 92 Particle acceleration in the x -direction A_x , y -direction A_y , and the magnitude $\sqrt{A_x^2 + A_y^2}$ of the particle acceleration $|A|$ for 1.30 mm Diameter Nylon Cylindrical Particles with Aspect Ratio, A.R. = 1:1 (25 particles) in Water. 154

Figure 93 Particle displacement, y , velocity, V_y , and acceleration, A_y , for 1.30 mm Diameter Nylon Cylindrical Particles with Aspect Ratio, A.R. = 1:1 (25 particles) in 20%–80% Glycerol–Water. 155

Figure 94 Particle velocity in the x -direction V_x , y -direction V_y , and the magnitude $\sqrt{V_x^2 + V_y^2}$ of the particle velocity $|V|$ for 1.30 mm Diameter Nylon Cylindrical Particles with Aspect Ratio, A.R. = 1:1 (25 particles) in 20%–80% Glycerol–Water. The average terminal settling velocity, U_t is 21.17 mm/s. 156

Figure 95 Particle acceleration in the x -direction A_x , y -direction A_y , and the magnitude $\sqrt{A_x^2 + A_y^2}$ of the particle acceleration $|A|$ 1.30 mm Diameter Nylon Cylindrical Particles with Aspect Ratio, A.R. = 1:1 (25 particles) in 20%–80% Glycerol–Water. 157

Figure 96 Particle displacement, y , velocity, V_y , and acceleration, A_y , for 1.30 mm Diameter Nylon Cylindrical Particles with Aspect Ratio, A.R. = 1:1 (25 particles) in 40%–60% Glycerol–Water. 158

Figure 97 Particle velocity in the x -direction V_x , y -direction V_y , and the magnitude $\sqrt{V_x^2 + V_y^2}$ of the particle velocity $|V|$ for 1.30 mm Diameter Nylon Cylindrical Particles with Aspect Ratio, A.R. = 1:1 (25 particles) in 40%–60% Glycerol–Water. The average terminal settling velocity, U_t is 2.03 mm/s. 159

Figure 98 Particle acceleration in the x -direction A_x , y -direction A_y , and the magnitude $\sqrt{A_x^2 + A_y^2}$ of the particle acceleration $|A|$ for 1.30 mm Diameter Nylon Cylindrical Particles with Aspect Ratio, A.R. = 1:1 (25 particles) in 40%–60% Glycerol–Water. 160

Figure 99 Particle displacement, y , velocity, V_y , and acceleration, A_y , for 1.30 mm Diameter Nylon Cylindrical Particles with Aspect Ratio, A.R. = 1:1 (25 particles) in Canola Oil..... 161

Figure 100 Particle velocity in the x -direction V_x , y -direction V_y , and the magnitude $\sqrt{V_x^2 + V_y^2}$ of the particle velocity $|V|$ for 1.30 mm Diameter Nylon Cylindrical Particles with Aspect Ratio, A.R. = 1:1 (25 particles) in Canola Oil. The average terminal settling velocity, U_t is 4.69 mm/s..... 162

Figure 101 Particle acceleration in the x -direction A_x , y -direction A_y , and the magnitude $\sqrt{A_x^2 + A_y^2}$ of the particle acceleration $|A|$ for 1.30 mm Diameter Nylon Cylindrical Particles with Aspect Ratio, A.R. = 1:1 (25 particles) in Canola Oil..... 163

Figure 102 Particle displacement, y , velocity, V_y , and acceleration, A_y , for 1.30 mm Diameter Nylon Cylindrical Particles with Aspect Ratio, A.R. = 1:3 (25 particles) in Water. 164

Figure 103 Particle velocity in the x -direction V_x , y -direction V_y , and the magnitude $\sqrt{V_x^2 + V_y^2}$ of the particle velocity $|V|$ for 1.30 mm Diameter Nylon Cylindrical Particles with Aspect Ratio, A.R. = 1:3 (25 particles) in Water. The average terminal settling velocity, U_t is 47.64 mm/s..... 165

Figure 104 Particle acceleration in the x -direction A_x , y -direction A_y , and the magnitude $\sqrt{A_x^2 + A_y^2}$ of the particle acceleration $|A|$ for 1.30 mm Diameter Nylon Cylindrical Particles with Aspect Ratio, A.R. = 1:3 (25 particles) in Water. 166

Figure 105 Particle displacement, y , velocity, V_y , and acceleration, A_y , for 1.30 mm Diameter Nylon Cylindrical Particles with Aspect Ratio, A.R. = 1:3 (25 particles) in 20%–80% Glycerol–Water. 167

Figure 106 Particle velocity in the x -direction V_x , y -direction V_y , and the magnitude $\sqrt{V_x^2 + V_y^2}$ of the particle velocity $|V|$ for 1.30 mm Diameter Nylon Cylindrical Particles with Aspect Ratio, A.R. = 1:3 (25 particles) in 20%–80% Glycerol–Water. The average terminal settling velocity, U_t is 26.51 mm/s. 168

Figure 107 Particle acceleration in the x -direction A_x , y -direction A_y , and the magnitude $\sqrt{(A_x^2 + A_y^2)}$ of the particle acceleration $|A|$ for 1.30 mm Diameter Nylon Cylindrical Particles with Aspect Ratio, A.R. = 1:3 (25 particles) in 20%–80% Glycerol–Water..... 169

Figure 108 Particle displacement, y , velocity, V_y , and acceleration, A_y , for 1.30 mm Diameter Nylon Cylindrical Particles with Aspect Ratio, A.R. = 1:3 (25 particles) in 40%–60% Glycerol–Water. The outliers at displacement 500 mm occurred in this region there was a low light compared to the rest of the field of view. A uniform distribution of light was not achieved with the projector and kite paper as shown in Figure 8 and describe in Section 3.5.1. This affected the binarization of the particle within that region and thereby a slight shift in the location of the centroid of the particle from the image processing scheme. 170

Figure 109 Particle velocity in the x -direction V_x , y -direction V_y , and the magnitude $\sqrt{(V_x^2 + V_y^2)}$ of the particle velocity $|V|$ for 1.30 mm Diameter Nylon Cylindrical Particles with Aspect Ratio, A.R. = 1:3 (25 particles) in 40%–60% Glycerol–Water. The average terminal settling velocity, U_t is 3.31 mm/s. The outliers at displacement 500 mm occurred in this region there was a low light compared to the rest of the field of view. A uniform distribution of light was not achieved with the projector and kite paper as shown in Figure 8 and describe in Section 3.5.1. This affected the binarization of the particle within that region and thereby a slight shift in the location of the centroid of the particle from the image processing scheme. 171

Figure 110 Particle acceleration in the x -direction A_x , y -direction A_y , and the magnitude $\sqrt{(A_x^2 + A_y^2)}$ of the particle acceleration $|A|$ for 1.30 mm Diameter Nylon Cylindrical Particles with Aspect Ratio, A.R. = 1:3 (25 particles) in 40%–60% Glycerol–Water. The outliers at displacement 500 mm occurred in this region there was a low light compared to the rest of the field of view. A uniform distribution of light was not achieved with the projector and kite paper as shown in Figure 8 and describe in Section 3.5.1. This affected the binarization of the particle within that region and thereby a slight shift in the location of the centroid of the particle from the image processing scheme. 172

Figure 111 Particle displacement, y , velocity, V_y , and acceleration, A_y , for 1.30 mm Diameter Nylon Cylindrical Particles with Aspect Ratio, A.R. = 1:3 (25 particles) in Canola Oil. The outliers at displacement 260 mm occurred within the overlap between the two cameras. In this region there was a variation in the light distribution compared to the rest of the field of view. A uniform distribution of light was not achieved with the projector and kite paper as shown in Figure 8 and

describe in Section 3.5.1. This affected the binarization of the particle within that region and thereby a slight shift in the location of the centroid of the particle from the image processing scheme.....173

Figure 112 Particle velocity in the x -direction V_x , y -direction V_y , and the magnitude $\sqrt{V_x^2 + V_y^2}$ of the particle velocity $|V|$ for 1.30 mm Diameter Nylon Cylindrical Particles with Aspect Ratio, A.R. = 1:3 (25 particles) in Canola Oil. The magnitude of velocity deviated slightly to the left between 490 mm and 520 mm. Therefore the average was calculated between 430 mm and 475 mm in order to obtain a more accurate representation of the terminal settling velocity. The average terminal settling velocity, U_t is 7.63 mm/s. The outliers at displacement 260 mm occurred within the overlap between the two cameras. In this region there was a variation in the light distribution compared to the rest of the field of view. A uniform distribution of light was not achieved with the projector and kite paper as shown in Figure 8 and describe in Section 3.5.1. This affected the binarization of the particle within that region and thereby a slight shift in the location of the centroid of the particle from the image processing scheme.174

Figure 113 Particle acceleration in the x -direction A_x , y -direction A_y , and the magnitude $\sqrt{A_x^2 + A_y^2}$ of the particle acceleration $|A|$ for 1.30 mm Diameter Nylon Cylindrical Particles with Aspect Ratio, A.R. = 1:3 (25 particles) in Canola Oil. The outliers at displacement 260 mm occurred within the overlap between the two cameras. In this region there was a variation in the light distribution compared to the rest of the field of view. A uniform distribution of light was not achieved with the projector and kite paper as shown in Figure 8 and describe in Section 3.5.1. This affected the binarization of the particle within that region and thereby a slight shift in the location of the centroid of the particle from the image processing scheme.....175

Figure 114 Particle displacement, y , velocity, V_y , and acceleration, A_y , for 1.30 mm Diameter Nylon Cylindrical Particles with Aspect Ratio, A.R. = 1:5 (25 particles) in Water.176

Figure 115 Particle velocity in the x -direction V_x , y -direction V_y , and the magnitude $\sqrt{V_x^2 + V_y^2}$ of the particle velocity $|V|$ for 1.30 mm Diameter Nylon Cylindrical Particles with Aspect Ratio, A.R. = 1:5 (25 particles) in Water. The average terminal settling velocity, U_t is 60.41 mm/s.....177

Figure 116 Particle acceleration in the x -direction A_x , y -direction A_y , and the magnitude $\sqrt{A_x^2 + A_y^2}$ of the particle acceleration $|A|$ for 1.30 mm Diameter Nylon Cylindrical Particles with Aspect Ratio, A.R. = 1:5 (25 particles) in Water.178

Figure 117 Particle displacement, y , velocity, V_y , and acceleration, A_y , for 1.30 mm Diameter Nylon Cylindrical Particles with Aspect Ratio, A.R. = 1:5 (25 particles) in 20%–80% Glycerol–Water. 179

Figure 118 Particle velocity in the x -direction V_x , y -direction V_y , and the magnitude $\sqrt{(V_x^2 + V_y^2)}$ of the particle velocity $|V|$ for 1.30 mm Diameter Nylon Cylindrical Particles with Aspect Ratio, A.R. = 1:5 (25 particles) in 20%–80% Glycerol–Water. The average terminal settling velocity, U_t is 27.40 mm/s. 180

Figure 119 Particle acceleration in the x -direction A_x , y -direction A_y , and the magnitude $\sqrt{(A_x^2 + A_y^2)}$ of the particle acceleration $|A|$ for 1.30 mm Diameter Nylon Cylindrical Particles with Aspect Ratio, A.R. = 1:5 (25 particles) in 20%–80% Glycerol–Water. 181

Figure 120 Particle displacement, y , velocity, V_y , and acceleration, A_y , for 1.30 mm Diameter Nylon Cylindrical Particles with Aspect Ratio, A.R. = 1:5 (25 particles) in 40%–60% Glycerol–Water. The outliers at displacement 260 mm occurred within the overlap between the two cameras. In this region there was a variation in the light distribution compared to the rest of the field of view. A uniform distribution of light was not achieved with the projector and kite paper as shown in Figure 8 and describe in Section 3.5.1. This affected the binarization of the particle within that region and thereby a slight shift in the location of the centroid of the particle from the image processing scheme. 182

Figure 121 Particle velocity in the x -direction V_x , y -direction V_y , and the magnitude $\sqrt{(V_x^2 + V_y^2)}$ of the particle velocity $|V|$ for 1.30 mm Diameter Nylon Cylindrical Particles with Aspect Ratio, A.R. = 1:5 (25 particles) in 40%–60% Glycerol–Water. The average terminal settling velocity, U_t is 5.33 mm/s. The outliers at displacement 260 mm occurred within the overlap between the two cameras. In this region there was a variation in the light distribution compared to the rest of the field of view. A uniform distribution of light was not achieved with the projector and kite paper as shown in Figure 8 and describe in Section 3.5.1. This affected the binarization of the particle within that region and thereby a slight shift in the location of the centroid of the particle from the image processing scheme. 183

Figure 122 Particle acceleration in the x -direction A_x , y -direction A_y , and the magnitude $\sqrt{(A_x^2 + A_y^2)}$ of the particle acceleration $|A|$ for 1.30 mm Diameter Nylon Cylindrical Particles with Aspect Ratio, A.R. = 1:5 (25 particles) in 40%–60% Glycerol–Water. The outliers at displacement 260 mm occurred within the overlap between the two cameras. In this region there was a variation

in the light distribution compared to the rest of the field of view. A uniform distribution of light was not achieved with the projector and kite paper as shown in Figure 8 and describe in Section 3.5.1. This affected the binarization of the particle within that region and thereby a slight shift in the location of the centroid of the particle from the image processing scheme. 184

Figure 123 Particle displacement, y , velocity, V_y , and acceleration, A_y , for 1.30 mm Diameter Nylon Cylindrical Particles with Aspect Ratio, A.R. = 1:5 (25 particles) in Canola Oil. The outliers at displacement 260 mm occurred within the overlap between the two cameras. In this region there was a variation in the light distribution compared to the rest of the field of view. A uniform distribution of light was not achieved with the projector and kite paper as shown in Figure 8 and describe in Section 3.5.1. This affected the binarization of the particle within that region and thereby a slight shift in the location of the centroid of the particle from the image processing scheme. 185

Figure 124 Particle velocity in the x -direction V_x , y -direction V_y , and the magnitude $\sqrt{(V_x^2 + V_y^2)}$ of the particle velocity $|V|$ for 1.30 mm Diameter Nylon Cylindrical Particles with Aspect Ratio, A.R. = 1:5 (25 particles) in Canola Oil. The magnitude of velocity deviated slightly to the left between 470 mm and 520 mm. Therefore the average was calculated between 340 mm and 460 mm in order to obtain a more accurate representation of the terminal settling velocity. The average terminal settling velocity, U_t is 8.68 mm/s. The outliers at displacement 260 mm occurred within the overlap between the two cameras. In this region there was a variation in the light distribution compared to the rest of the field of view. A uniform distribution of light was not achieved with the projector and kite paper as shown in Figure 8 and describe in Section 3.5.1. This affected the binarization of the particle within that region and thereby a slight shift in the location of the centroid of the particle from the image processing scheme. 186

Figure 125 Particle acceleration in the x -direction A_x , y -direction A_y , and the magnitude $\sqrt{(A_x^2 + A_y^2)}$ of the particle acceleration $|A|$ for 1.30 mm Diameter Nylon Cylindrical Particles with Aspect Ratio, A.R. = 1:5 (25 particles) in Canola Oil. The outliers at displacement 260 mm occurred within the overlap between the two cameras. In this region there was a variation in the light distribution compared to the rest of the field of view. A uniform distribution of light was not achieved with the projector and kite paper as shown in Figure 8 and describe in Section 3.5.1. This affected the binarization of the particle within that region and thereby a slight shift in the location of the centroid of the particle from the image processing scheme. 187

Figure 126 Particle displacement, y , velocity, V_y , and acceleration, A_y , for 1.50 mm Diameter Nylon Cylindrical Particles with Aspect Ratio, A.R. = 1:1 (25 particles) in Water. 188

Figure 127 Particle velocity in the x -direction V_x , y -direction V_y , and the magnitude $\sqrt{(V_x^2 + V_y^2)}$ of the particle velocity $|V|$ for 1.50 mm Diameter Nylon Cylindrical Particles with Aspect Ratio, A.R. = 1:1 (25 particles) in Water. The average terminal settling velocity, U_t is 46.76 mm/s..... 189

Figure 128 Particle acceleration in the x -direction A_x , y -direction A_y , and the magnitude $\sqrt{(A_x^2 + A_y^2)}$ of the particle acceleration $|A|$ for 1.50 mm Diameter Nylon Cylindrical Particles with Aspect Ratio, A.R. = 1:1 (25 particles) in Water. 190

Figure 129 Particle displacement, y , velocity, V_y , and acceleration, A_y , for 1.50 mm Diameter Nylon Cylindrical Particles with Aspect Ratio, A.R. = 1:1 (25 particles) in 20%–80% Glycerol–Water. 191

Figure 130 Particle velocity in the x -direction V_x , y -direction V_y , and the magnitude $\sqrt{(V_x^2 + V_y^2)}$ of the particle velocity $|V|$ for 1.50 mm Diameter Nylon Cylindrical Particles with Aspect Ratio, A.R. = 1:1 (25 particles) in 20%–80% Glycerol–Water. The average terminal settling velocity, U_t is 23.56 mm/s..... 192

Figure 131 Particle acceleration in the x -direction A_x , y -direction A_y , and the magnitude $\sqrt{(A_x^2 + A_y^2)}$ of the particle acceleration $|A|$ for 1.50 mm Diameter Nylon Cylindrical Particles with Aspect Ratio, A.R. = 1:1 (25 particles) in 20%–80% Glycerol–Water..... 193

Figure 132 Particle displacement, y , velocity, V_y , and acceleration, A_y , for 1.50 mm Diameter Nylon Cylindrical Particles with Aspect Ratio, A.R. = 1:1 (25 particles) in 40%–60% Glycerol–Water. 194

Figure 133 Particle velocity in the x -direction V_x , y -direction V_y , and the magnitude $\sqrt{(V_x^2 + V_y^2)}$ of the particle velocity $|V|$ for 1.50 mm Diameter Nylon Cylindrical Particles with Aspect Ratio, A.R. = 1:1 (25 particles) in 40%–60% Glycerol–Water. The average terminal settling velocity, U_t is 3.02 mm/s..... 195

Figure 134 Particle acceleration in the x -direction A_x , y -direction A_y , and the magnitude $\sqrt{(A_x^2 + A_y^2)}$ of the particle acceleration $|A|$ for 1.50 mm Diameter Nylon Cylindrical Particles with Aspect Ratio, A.R. = 1:1 (25 particles) in 40%–60% Glycerol–Water..... 196

Figure 135 Particle displacement, y , velocity, V_y , and acceleration, A_y , for 1.50 mm Diameter Nylon Cylindrical Particles with Aspect Ratio, A.R. = 1:1 (25 particles) in Canola Oil..... 197

Figure 136 Particle velocity in the x -direction V_x , y -direction V_y , and the magnitude $\sqrt{V_x^2 + V_y^2}$ of the particle velocity $|V|$ for 1.50 mm Diameter Nylon Cylindrical Particles with Aspect Ratio, A.R. = 1:1 (25 particles) in Canola Oil. The magnitude of velocity deviated slightly to the left between 390 mm and 520 mm. Therefore the average was calculated between 140 mm and 380 mm in order to obtain a more accurate representation of the terminal settling velocity. The average terminal settling velocity, U_t is 5.77 mm/s. 198

Figure 137 Particle acceleration in the x -direction A_x , y -direction A_y , and the magnitude $\sqrt{A_x^2 + A_y^2}$ of the particle acceleration $|A|$ for 1.50 mm Diameter Nylon Cylindrical Particles with Aspect Ratio, A.R. = 1:1 (25 particles) in Canola Oil..... 199

Figure 138 Particle displacement, y , velocity, V_y , and acceleration, A_y , for 1.50 mm Diameter Nylon Cylindrical Particles with Aspect Ratio, A.R. = 1:3 (25 particles) in Water. 200

Figure 139 Particle velocity in the x -direction V_x , y -direction V_y , and the magnitude $\sqrt{V_x^2 + V_y^2}$ of the particle velocity $|V|$ for 1.50 mm Diameter Nylon Cylindrical Particles with Aspect Ratio, A.R. = 1:3 (25 particles) in Water. The average terminal settling velocity, U_t is 60.41 mm/s..... 201

Figure 140 Particle acceleration in the x -direction A_x , y -direction A_y , and the magnitude $\sqrt{A_x^2 + A_y^2}$ of the particle acceleration $|A|$ for 1.50 mm Diameter Nylon Cylindrical Particles with Aspect Ratio, A.R. = 1:3 (25 particles) in Water. 202

Figure 141 Particle displacement, y , velocity, V_y , and acceleration, A_y , for 1.50 mm Diameter Nylon Cylindrical Particles with Aspect Ratio, A.R. = 1:3 (25 particles) in 20%–80% Glycerol–Water. 203

Figure 142 Particle velocity in the x -direction V_x , y -direction V_y , and the magnitude $\sqrt{V_x^2 + V_y^2}$ of the particle velocity $|V|$ for 1.50 mm Diameter Nylon Cylindrical Particles with Aspect Ratio, A.R. = 1:3 (25 particles) in 20%–80% Glycerol–Water. The average terminal settling velocity, U_t is 28.57 mm/s. 204

Figure 143 Particle acceleration in the x -direction A_x , y -direction A_y , and the magnitude $\sqrt{A_x^2 + A_y^2}$ of the particle acceleration $|A|$ for 1.50 mm Diameter Nylon Cylindrical Particles with Aspect Ratio, A.R. = 1:3 (25 particles) in 20%–80% Glycerol–Water..... 205

Figure 144 Particle displacement, y , velocity, V_y , and acceleration, A_y , for 1.50 mm Diameter Nylon Cylindrical Particles with Aspect Ratio, A.R. = 1:3 (25 particles) in 40%–60% Glycerol–Water. 206

Figure 145 Particle velocity in the x -direction V_x , y -direction V_y , and the magnitude $\sqrt{(V_x^2 + V_y^2)}$ of the particle velocity $|V|$ for 1.50 mm Diameter Nylon Cylindrical Particles with Aspect Ratio, A.R. = 1:3 (25 particles) in 40%–60% Glycerol–Water. The average terminal settling velocity, U_t is 6.71 mm/s.207

Figure 146 Particle acceleration in the x -direction A_x , y -direction A_y , and the magnitude $\sqrt{(A_x^2 + A_y^2)}$ of the particle acceleration $|A|$ for 1.50 mm Diameter Nylon Cylindrical Particles with Aspect Ratio, A.R. = 1:3 (25 particles) in 40%–60% Glycerol–Water.....208

Figure 147 Particle displacement, y , velocity, V_y , and acceleration, A_y , for 1.50 mm Diameter Nylon Cylindrical Particles with Aspect Ratio, A.R. = 1:3 (25 particles) in Canola Oil. The outliers at displacement 260 mm occurred within the overlap between the two cameras. In this region there was a variation in the light distribution compared to the rest of the field of view. A uniform distribution of light was not achieved with the projector and kite paper as shown in Figure 8 and describe in Section 3.5.1. This affected the binarization of the particle within that region and thereby a slight shift in the location of the centroid of the particle from the image processing scheme.209

Figure 148 Particle velocity in the x -direction V_x , y -direction V_y , and the magnitude $\sqrt{(V_x^2 + V_y^2)}$ of the particle velocity $|V|$ for 1.50 mm Diameter Nylon Cylindrical Particles with Aspect Ratio, A.R. = 1:3 (25 particles) in Canola Oil. The magnitude of velocity deviated slightly to the left between 490 mm and 520 mm. Therefore the average was calculated between 390 mm and 480 mm in order to obtain a more accurate representation of the terminal settling velocity. The average terminal settling velocity, U_t is 8.94 mm/s. The outliers at displacement 260 mm occurred within the overlap between the two cameras. In this region there was a variation in the light distribution compared to the rest of the field of view. A uniform distribution of light was not achieved with the projector and kite paper as shown in Figure 8 and describe in Section 3.5.1. This affected the binarization of the particle within that region and thereby a slight shift in the location of the centroid of the particle from the image processing scheme.210

Figure 149 Particle acceleration in the x -direction A_x , y -direction A_y , and the magnitude $\sqrt{(A_x^2 + A_y^2)}$ of the particle acceleration $|A|$ for 1.50 mm Diameter Nylon Cylindrical Particles with Aspect Ratio, A.R. = 1:3 (25 particles) in Canola Oil. The outliers at displacement 260 mm occurred within the overlap between the two cameras. In this region there was a variation in the light distribution compared to the rest of the field of view. A uniform distribution of light was not

achieved with the projector and kite paper as shown in Figure 8 and describe in Section 3.5.1. This affected the binarization of the particle within that region and thereby a slight shift in the location of the centroid of the particle from the image processing scheme.....211

Figure 150 Particle displacement, y , velocity, V_y , and acceleration, A_y , for 1.50 mm Diameter Nylon Cylindrical Particles with Aspect Ratio, A.R. = 1:5 (25 particles) in Water.212

Figure 151 Particle velocity in the x -direction V_x , y -direction V_y , and the magnitude $\sqrt{(V_x^2 + V_y^2)}$ of the particle velocity $|V|$ for 1.50 mm Diameter Nylon Cylindrical Particles with Aspect Ratio, A.R. = 1:5 (25 particles) in Water. The average terminal settling velocity, U_t is 51.61 mm/s.....213

Figure 152 Particle acceleration in the x -direction A_x , y -direction A_y , and the magnitude $\sqrt{(A_x^2 + A_y^2)}$ of the particle acceleration $|A|$ for 1.50 mm Diameter Nylon Cylindrical Particles with Aspect Ratio, A.R. = 1:5 (25 particles) in Water.214

Figure 153 Particle displacement, y , velocity, V_y , and acceleration, A_y , for 1.50 mm Diameter Nylon Cylindrical Particles with Aspect Ratio, A.R. = 1:5 (25 particles) in 20%–80% Glycerol–Water.215

Figure 154 Particle velocity in the x -direction V_x , y -direction V_y , and the magnitude $\sqrt{(V_x^2 + V_y^2)}$ of the particle velocity $|V|$ for 1.50 mm Diameter Nylon Cylindrical Particles with Aspect Ratio, A.R. = 1:5 (25 particles) in 20%–80% Glycerol–Water. The average terminal settling velocity, U_t is 28.66 mm/s.....216

Figure 155 Particle acceleration in the x -direction A_x , y -direction A_y , and the magnitude $\sqrt{(A_x^2 + A_y^2)}$ of the particle acceleration $|A|$ for 1.50 mm Diameter Nylon Cylindrical Particles with Aspect Ratio, A.R. = 1:5 (25 particles) in 20%–80% Glycerol–Water.....217

Figure 156 Particle displacement, y , velocity, V_y , and acceleration, A_y , for 1.50 mm Diameter Nylon Cylindrical Particles with Aspect Ratio, A.R. = 1:5 (25 particles) in 40%–60% Glycerol–Water.218

Figure 157 Particle velocity in the x -direction V_x , y -direction V_y , and the magnitude $\sqrt{(V_x^2 + V_y^2)}$ of the particle velocity $|V|$ for 1.50 mm Diameter Nylon Cylindrical Particles with Aspect Ratio, A.R. = 1:5 (25 particles) in 40%–60% Glycerol–Water. The average terminal settling velocity, U_t is 7.24 mm/s.....219

Figure 158 Particle acceleration in the x -direction A_x , y -direction A_y , and the magnitude $\sqrt{(A_x^2 + A_y^2)}$ of the particle acceleration $|A|$ for 1.50 mm Diameter Nylon Cylindrical Particles with Aspect Ratio, A.R. = 1:5 (25 particles) in 40%–60% Glycerol–Water.....220

Figure 159 Particle displacement, y , velocity, V_y , and acceleration, A_y , for 1.50 mm Diameter Nylon Cylindrical Particles with Aspect Ratio, A.R. = 1:5 (25 particles) in Canola Oil. The outliers at displacement 260 mm occurred within the overlap between the two cameras. In this region there was a variation in the light distribution compared to the rest of the field of view. A uniform distribution of light was not achieved with the projector and kite paper as shown in Figure 8 and describe in Section 3.5.1. This affected the binarization of the particle within that region and thereby a slight shift in the location of the centroid of the particle from the image processing scheme. Note: 25 particles were used in this experiment however the light distribution was particularly problematic for this experimental condition so there were 15 outliers which were omitted from this plot.....221

Figure 160 Particle velocity in the x -direction V_x , y -direction V_y , and the magnitude $\sqrt{(V_x^2 + V_y^2)}$ of the particle velocity $|V|$ for 1.50 mm Diameter Nylon Cylindrical Particles with Aspect Ratio, A.R. = 1:5 (25 particles) in Canola Oil. The average terminal settling velocity, U_t is 10.67 mm/s. The outliers at displacement 260 mm occurred within the overlap between the two cameras. In this region there was a variation in the light distribution compared to the rest of the field of view. A uniform distribution of light was not achieved with the projector and kite paper as shown in Figure 8 and describe in Section 3.5.1. This affected the binarization of the particle within that region and thereby a slight shift in the location of the centroid of the particle from the image processing scheme. Note: 25 particles were used in this experiment however the light distribution was particularly problematic for this experimental condition so there were 15 outliers which were omitted from this plot.....222

Figure 161 Particle acceleration in the x -direction A_x , y -direction A_y , and the magnitude $\sqrt{(A_x^2 + A_y^2)}$ of the particle acceleration $|A|$ for 1.50 mm Diameter Nylon Cylindrical Particles with Aspect Ratio, A.R. = 1:5 (25 particles) in Canola Oil. The outliers at displacement 260 mm occurred within the overlap between the two cameras. In this region there was a variation in the light distribution compared to the rest of the field of view. A uniform distribution of light was not achieved with the projector and kite paper as shown in Figure 8 and describe in Section 3.5.1. This affected the binarization of the particle within that region and thereby a slight shift in the location of the centroid

of the particle from the image processing scheme. Note: 25 particles were used in this experiment however the light distribution was particularly problematic for this experimental condition so there were 15 outliers which were omitted from this plot.....223

1 Background

1.1 Motivation

Particle motion is useful in a number of applications in science and engineering. In medical research, the motion of inhaled particles is analyzed so that the performance of drug delivery can be determined [1,2]. Researchers have also investigated particle transport and deposition during abrasion to understand the history of sedimentary deposits [3]. Analyzing the transport of particles is a task in which many researchers have been investigating [4–11]. One of the challenges has been to consider the exact shape of non-spherical or irregularly shaped particles to fully account for the motion of particles within a fluid [8,12]. A simplification that has been used in the literature is to assume that the particles are perfect spheres [4,13]. The motivation of this thesis research is to investigate the validity of using the spherical assumption to model non-spherical or irregularly shaped particles. In this analysis particle motion was also studied in an industrial application which is used in the oil and gas industry.

The sphere is considered as an ‘ideal’ shape with a known length scale and it is often used to describe non-spherical or irregularly shaped particles [8,14]. The difficulty of modelling irregularly shaped particles arises due to the challenge of accurately determining the area or volume of an irregular shape [8]. One of the approaches in literature to address non-spherical or irregularly shaped particles is the development of parameters to define their size and shape. The size of non-spherical or irregularly shaped particles are commonly characterized using the equivalent diameter. That is, the diameter of a sphere which has an equivalent volume to the particle [2,15]. The mathematical formulae that are used to describe parameters such as the coefficient of drag and the terminal settling velocity of particles were originally derived for spheres [4]. As a result, in the literature researchers have developed correlations of non-dimensional parameters to describe the motion of particles of various shapes [16,17]. However, the challenge has been to obtain non-dimensional plots in which particles of various shapes overlap exactly [16,17].

Using the assumption that the particles are spheres can be also considered as an over simplification of particle motion within a fluid because it neglects important factors such as the rotational motion of the particles [18]. Particle size, shape and rotational motion have been shown to affect the

general behavior of particles in fluids. For example in aerosol technology, the rotation of the aerosol particles led to particle deposition or sedimentation [9]. Particle deposition is either desirable or undesirable depending on the application. For example, particle deposition is useful for the purpose of delivering inhaled particles into the human body as medical treatment for conditions such as asthma and diabetes [19,20]. Conversely, particle deposition contributes to the failure of sand control devices and can lead to an overall reduction in productivity in steam assisted gravity drainage (SAGD) operations [21–23].

SAGD is a method used to produce oil sands whereby two parallel horizontal wells are drilled into the reservoir which are 750 to 1,000 meters in length and 5 meters apart [24]. Steam is injected into the oil sand formation through the upper or ‘injection’ well [25]. The steam creates a high-temperature steam chamber which reduces the viscosity of the oil [25]. The oil sand then becomes mobilized and with the assistance of gravity it is drained into the lower or ‘production’ well to be pumped to the surface facilities [25]. Figure 1 shows a schematic of the SAGD process. Oil sand refers to sandstones or friable sands (quartz) that are saturated with bitumen, water and large amounts of sand and clay particles [26]. Generally, sand particles found in SAGD operations can be categorized into fines ($< 45 \mu\text{m}$) and coarse particles ($> 45 \mu\text{m}$) [27,28]. The clay particles consist of kaolinite, montmorillonite, illite, mica and fine sand particles which are usually non-spherical or irregularly shaped [29,30]. These clay particles together are known as ‘fines’ or ‘migratory fine particles’ [30]. The oil sand reservoir is therefore considered as a porous media.

Sand control devices (SCD) are necessary in SAGD operations due to the unconsolidated in nature of oil sands [31]. Sand production is undesirable as it causes erosion of the production equipment which thereby increases the maintenance costs due to well shut-ins, cleaning and servicing of downhole equipment [31,32]. The slotted liner is a SCD that is used extensively in SAGD operations in western Canada due to its mechanical strength [33] and relatively low cost [34]. Figure 1 shows an illustration of the slotted liner within the SAGD process. It is a well casing that contains a series of longitudinal slots that are arranged in a specified pattern throughout the length and circumference of the liner [35]. These are high aspect ratio slots which are typically 0.30 to 6.4 mm in width and 50 to 70 mm in length [35,36]. The dimensions of the slots are determined based on the grains size distribution of the reservoir [34,35].

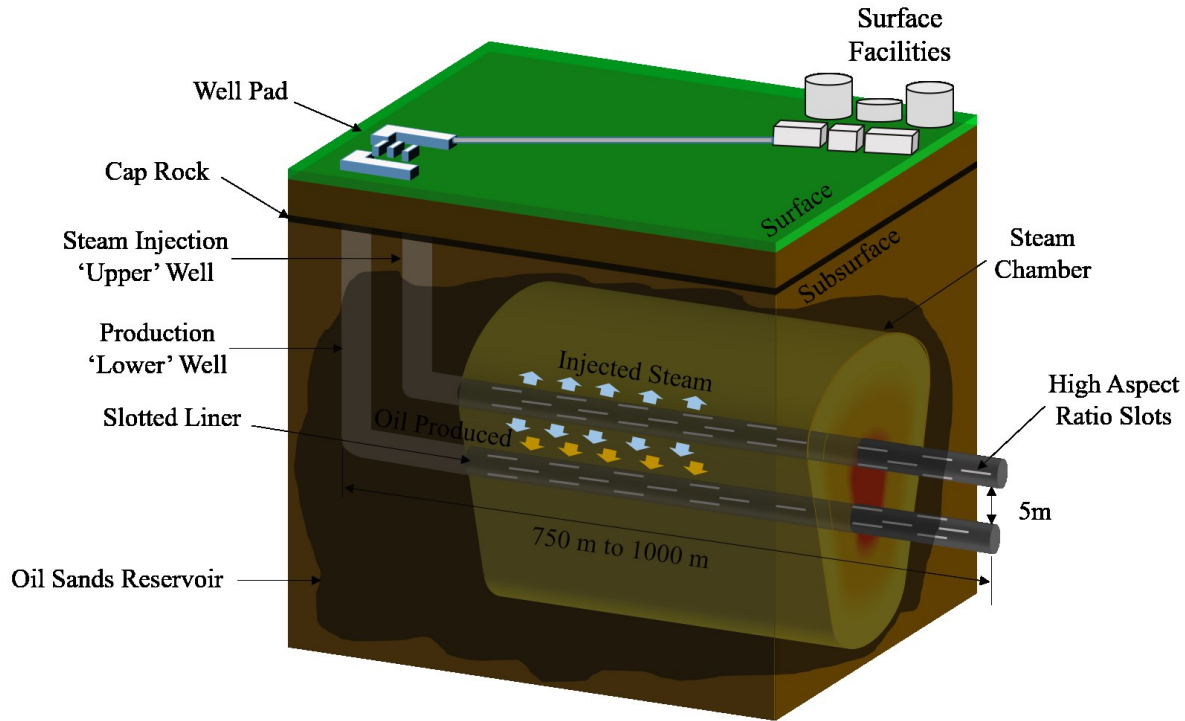


Figure 1 A schematic of steam assisted gravity drainage (SAGD) process which also includes an illustration of the slotted liner. Some of the flow geometries that were used in this study include one single slot of the slotted liner.

One of the common failure mechanisms of the slotted liners is the plugging of the slots [37–39]. The occurrence of plugging can hinder the flow of fluids into or out of the reservoir, which is an integral part of the SAGD process [34,35,37]. Plugging can occur as a result of residual drilling mud on the surface of the wellbore, surface roughness of the slot [38], scaling [40] and fines migration [35,38]. Fines migration occurs as fluid flow mobilizes the fine sand particles within the reservoir [41]. These fines can settle or deposit within the reservoir or within the near-slot region [11,21,38]. The near-slot is the transition area where the flow converges from the porous media within the reservoir and enters into the slots. The deposition of the fines can lead to a build-up of particles with time, which thereby creates blockages within the pore spaces of the reservoir [21] and within the near-slot region of the well [11,38]. Fines migration thereby causes an overall reduction in the productivity of the well [21,22,42]. It has been shown in a case study that fines migration can contribute to fully plugged slots, that is a complete blockage of flow within the open flow area in the near-slot region [38].

There is little information in literature concerning the localized changes within the reservoir due to fines migration. Instead, a global or bulk type approach that is based on ‘core flooding’ type experiments is used to analyze many problems within petroleum engineering such as fines migration [23,42]. Core flooding tests are performed by injecting fluid into a rock sample from the reservoir of interest [43,44]. This a porous media sample known as a core and it is usually obtained during the drilling/exploration process [45]. The core flooding approach has been used to quantify and assess fines migration by evaluating the effluent from the core as well as the flow rates and pressure differentials across the core [42]. Therefore, the factors that influence the localize transport and deposition of fines within the core would be unknown.

1.2 Hypotheses

The thesis research thereby investigates the following objectives:

1. Using the assumption that non-spherical shaped particles can be modeled as spheres is invalid.
2. Dimensionless coefficients such as the coefficient of drag and the particle Reynolds number of non-spherical particles can be modeled as spheres if the correct length scale is used.
3. A bulk analysis is inadequate to study the particle motion in SAGD operations
4. Particle deposition and build-up within the near-slot region depends on particle shape and rotation

1.3 Research Objectives

The overall goals of this study were defined in order to address the gaps in literature that were outlined in Section 1.1. Thereby the research objectives are as follows:

1. Examine the validity of using the spherical assumption to define the motion of non-spherical particles
2. To calculate the terminal settling velocity, the coefficient of drag and the particle Reynolds number of spherical and cylindrical particles from experimental data

3. Determine an appropriate length scale to calculate the coefficient of drag and the particle Reynolds number of non-spherical particles
4. To demonstrate the importance of considering the exact shape of the particle
5. Identify factors that influence particle deposition and build-up in SAGD operations
6. Illustrate the significance of considering particle rotation

2 Literature Review

2.1 Modeling Particle Motion in a Fluid

Modelling non-spherical particles as spheres is a simplification that is often used in the literature because this approach uses a single length scale to characterize the geometry, an approach used in a number of research works [46–49]. Starting from as early as 212-287 BC where Archimedes during his lifetime developed the formula for the volume of a sphere as two thirds that of a cylinder which as described in [50]. In the 1800s George Stokes derived a formula for the drag force acting on a sphere within a fluid, presented in [51] and in 1983 the equations of motion of a sphere within a flow field were developed [52]. Therefore, the assumption that particles can be modeled as spheres is an opportunity to utilize the extensive work that is available in the literature on the motion of spheres in fluids [4].

Some of the common parameters used to describe the motion of particles in a fluid include: the particle Reynolds number, the drag force acting on the particle, the coefficient of drag and the terminal settling velocity of the particle. The mathematical formulae that are used to describe these parameters were developed with the assumption that the particles are spherical [4,6]. The following sub-sections review the approaches in the literature which have been used to define these three parameters for non-spherical particles and the research questions for this thesis research were identified:

2.1.1 Particle Reynolds Number

The particle Reynolds number is the ratio of the inertial forces of the particle to the viscous forces of the fluid [53] and can be defined as:

$$\text{Localized Particle Reynolds Number, } Re_{p(\text{localized})} = \frac{\rho_f V d_p}{\mu_f} \quad \text{Equation 1}$$

where ρ_f is the density of the fluid, V is the velocity of the particle, d_p is the diameter of the particle and μ_f is the viscosity of the fluid. However, the terminal settling velocity is often used to obtain a generalized definition of the particle Reynolds number [16,54,55] since the $Re_{p(\text{localized})}$ of the

particle remains constant after the particle reaches the terminal settling velocity. Thereby, the particle Reynolds number is often defined in the literature as:

$$\text{Particle Reynolds Number, } Re_p = \frac{\rho_f U_t d_p}{\mu_f} \quad \text{Equation 2}$$

where U_t is the terminal settling velocity of the particle. For spherical particles it is convenient to define the Re_p since the diameter can be used as the characteristic length scale. As a result in the literature, Re_p for non-spherical or irregularly shaped particles have been modelled as spheres with the use of the equivalent diameter [16,56,57]. The equivalent is the diameter of a sphere which has the same volume as the particle [2,15] and it is sometimes referred to as the volume-equivalent-sphere diameter or nominal diameter [58], given as:

$$\text{Equivalent Diameter of a Non – Spherical Particle, } d_{eq} = \sqrt[3]{\frac{6 V_p}{\pi}} \quad \text{Equation 3}$$

where V_p is the volume of the non-spherical particle. The Re_p has also been defined based on the surface equivalent sphere diameter which is found based on the projected area of imaged particles [58]. Another approach found in the literature was to define Re_p in terms of a shape correction factor developed by Loth [59]. The shape correction factor is a non-dimensional parameter which is the ratio of the coefficient of drag of the non-spherical particle to the coefficient of drag of a spherical particle [59]. Loth [59] examined this approach using particles in the shape of spheres, disks, needles, cubes, cones, octahedrons and tetrahedrons. Using this definition for Re_p , the results in Loth showed that their model for determining the drag coefficient of the particle did not allow complete non-dimensionalization as the non-spherical data did not collapse and overly the model exactly [59]. The review of the approaches used in literature to determine the particle Reynolds number leads to the current research question: to determine an appropriate length scale to define the particle Reynolds number of non-spherical particles based on experimental data.

2.1.2 Modeling the Coefficient of Drag of Particles

The particle Reynolds number is often used to define other parameters of motion such as the drag coefficient. Solid particles moving through a fluid experience a resistive force known as drag [60].

The drag force is a function of a number of variables such as the density of the fluid, the size, shape and orientation of the particle [60]. Therefore, the coefficient of drag, C_D , is a dimensionless parameter that is used to quantify the drag force acting on the particle [60]. There are several approaches in the literature to define C_D of non-spherical particles [16,58,59]. In the literature, one of the approaches to define the coefficient of drag for non-spherical or irregularly shapes is the development of empirical correlations.

Tran-Cong et al. [58] developed a correlation for the C_D for various shapes of agglomerates of spheres. This model explores two length scales to define C_D including the ratio of the equivalent diameter to the surface equivalent sphere diameter and the particle circularity [58]. The particle circularity is calculated based on the surface equivalent sphere diameter and the projected area of the particle [58]. Tran-Cong et al. [58] found that the plot of C_D versus Re_p for the various shape of agglomerates of spheres overlapped more closely with their model at lower values of Re_p , typically < 10 when the ratio of the equivalent diameter to the surface equivalent sphere diameter was used as a length scale. However, at higher Re_p the particle circularity parameter was introduced in order to achieve a closer overlap. It should be noted that the non-spherical particles that were used in this study were an amalgamation of spherical particles, thereby it was convenient to define the length scales using the diameter of the spheres.

Dioguardi et. al [54] developed a one-equation model for the drag coefficient of irregular shaped particles and compared the results to five other models found in the literature. Dioguardi et. al [54] used a shape factor which incorporates the ratio of the diameter of an equivalent sphere to the surface area of the particle and the ratio of the maximum projected perimeter to the perimeter of a circle of equivalent maximum projected area of the particle. The plots of the C_D versus Re_p showed that the particles of various shapes and sizes overlapped closely for $Re_p < 10$ and deviations within the range $10 < Re_p < 10,000$ were observed [54].

One of the most commonly used correlations for the drag coefficient of non-spherical particles in the literature was developed by Haider and Levenspiel [16] as:

$$\text{Coefficient of Drag, } C_D = \frac{24}{Re_p} [1 + A Re_p^B] + \frac{C}{\left[1 + \frac{D}{Re_p}\right]} \quad \text{Equation 4}$$

where Re_p is the particle Reynolds number (using the equivalent diameter of the particles) and the parameters A , B , C and D are directly dependent on the particle sphericity, ϕ , which is given as:

$$\text{Particle Sphericity, } \phi = \frac{\text{Surface Area of a Sphere of Equivalent Volume}}{\text{Surface Area of the Particle}} = \frac{S}{\bar{S}} \quad \text{Equation 5}$$

The parameters A , B , C and D in the Haider and Levenspiel [16] are:

$$A = \exp(2.3288 - 6.4581 \phi + 2.4486 \phi^2) \quad \text{Equation 6}$$

$$B = 0.0964 + 0.5565 \phi \quad \text{Equation 7}$$

$$C = \exp(4.905 - 13.8944 \phi + 18.4222 \phi^2 - 10.2599 \phi^3) \quad \text{Equation 8}$$

$$D = \exp(1.4681 + 12.2584 \phi - 20.7322 \phi^2 + 15.8855 \phi^3) \quad \text{Equation 9}$$

The Haider and Levenspiel model was developed as a generalized expression for non-spherical particles. The non-spherical particles that were used as the experimental data to validate the Haider and Levenspiel model included spheres, disks and isometric particles namely: cube octahedrons, octahedrons, cubes and tetrahedrons. The particle Reynolds number for the non-spherical particles used in the Haider and Levenspiel model was defined using the equivalent diameter as the length scale. In this regard, the non-spherical particles were modelled in relation to a perfect sphere.

In the original study where the model was developed [16], the particle Reynolds number was plotted versus the coefficient of drag model for various values of ϕ . Disk shaped particles overlapped with the Haider and Levenspiel model curves at ϕ values of 0.026, 0.043, 0.123 and 0.230. The cube octahedrons, octahedrons, cubes and tetrahedrons overlapped with the Haider and Levenspiel model curves at ϕ values of 0.670, 0.806, 0.846 and 0.906. The spheres overlapped with the Haider and Levenspiel model curves at a ϕ value of 1. Overall the non-spherical particles used in Haider and Levenspiel [16] overlapped with their model at the corresponding ϕ values of the

particles. It was also noted that using the equivalent diameter was used as the length scale, the non-spherical data deviated away from the spherical curve at a ϕ value of 1 [16].

Madhav and Chhabra [61] investigated the coefficient of drag of cylinders made of stainless steel, perspex (plastic) and glass and rectangular prisms made of perspex (plastic). This study performed measurements on the coefficient of drag of the particles falling within castor oil, a glucose–water solution and silicone oil. Madhav and Chhabra [61] considered two length scales to define the non-spherical particles to analyzed the cylindrical particles. These include the ratio of the equivalent diameter to the diameter of a circle having the same area as the projected area of the particle and secondly the sphericity factor which is defined as:

$$\text{Sphericity Factor, } \phi = \frac{d_{eq}^2}{dL + (d^2/2)} \quad \text{Equation 10}$$

where d_{eq} is the equivalent diameter, d is the diameter of the cylinder and L is the length of the cylinder. Madhav and Chhabra [61] compared the results of the study to the Haider and Levenspiel model [16] and the Thompson and Clark model [53]. Whereby, Thompson and Clark [53] developed a modified correlation of Haider and Levenspiel [16] by introducing a shape parameter known as the scruple. The scruple parameter is the ratio of the coefficient of drag of the particle to the coefficient of drag of a sphere [53]. Madhav and Chhabra [61] reported that their experimental data only agreed with both models [16,53] for $Re_p < 100$ and $\phi < 0.55$. However for $Re_p > 100$ and $\phi > 0.55$, Madhav and Chhabra [61] experimental results deviated from the models in [16,53] by almost 100%. Madhav and Chhabra [61] also developed a correlation for the coefficient of drag, however, the results of the cylindrical particles still did not overlap well in the plot of C_D versus Re_p .

Bagheri and Bonadonna [56] also developed a correlation to predict the drag coefficient of non-spherical particle in terms of particle flatness, elongation and equivalent diameter. This model was developed with reference to Haider and Levenspiel [16]. This study considered disks, ellipsoid, cylinders, spheres and irregularly shaped particles. The study presented a non-dimensionalized plot of the ratio of the coefficient of drag of the particles to a drag correction coefficient versus the product of the particle Reynolds number and the drag correction coefficients. The drag coefficient correction factors were defined as the ratio of the coefficient of drag of the particle to the coefficient

of drag of a sphere with equivalent volume to the particle. The results showed that the non-dimensionalized plots of particles of various shaped did not overlap exactly for $Re_p > 10$.

The Haider and Levenspiel [16] is the most general model for the coefficient of drag of non-spherical particles and has been often used as a reference or starting point for other empirical correlations that has been developed in the literature [54,56,61]. From the review of the models developed in literature it was found that many correlations to predict the coefficient of drag of non-spherical particles were developed using shape parameters that were referenced to perfect spheres. This leads to the current research question: to determine the suitability of using a spherical shape parameter as a length scale to define particle motion of non-spherical particles.

2.1.3 Terminal Settling Velocity of Particles

Another parameter that is used to describe particle motion is the terminal settling velocity. This velocity occurs when a balance of forces is achieved and the particle is no longer accelerating as it falls through the fluid [6]. The terminal settling velocity can be found using:

$$\text{Terminal Settling Velocity, } U_t = \frac{g d_p^2 (\rho_p - \rho_f)}{18 \mu} \quad \text{Equation 11}$$

where g is the acceleration due to gravity, d_p is the diameter of the particle, ρ_p is the density of the particle, ρ_f is the density of the fluid and μ is the viscosity of the fluid [62,63]. This was derived using Stokes' law and assuming that the particles to be a perfect sphere [4].

In the literature, the terminal settling velocity of non-spherical particles were found using developed correlations [16] or by using experimental measurements [64,65]. Cheng [57] developed a correlation for predicting the terminal settling velocity of particles. This correlation utilizes a dimensionless particle diameter which is defined in terms of the diameter of the particle, the kinematic viscosity of the fluid and the acceleration due to gravity. The calculated terminal settling velocities from the correlation developed by Cheng [57] were comparable to other measured experimental data in the literature. However, this correlation does not account for the terminal settling velocity of non-spherical or irregularly shaped particles since the particle diameter is incorporated in to the model.

The terminal settling velocity of the discs which were superimposed onto the Haider and Levenspiel model was obtained by measuring the time it takes for the discs to fall within a predetermined distance [16,64]. Here, it was proposed that the discs were oriented in a horizontal position in the settling region [64]. The terminal settling velocity of the isometric particles that were also superimposed onto the Haider and Levenspiel model were obtained using photos of the shadow of the particle which were reflected on a graduated glass plate as the particles fell in front of a beam of light [65]. The camera and graduate glass plate approach have also been used in other studies for example to find the settling velocity of a single sphere in a drilling fluid [66]. In these methods the terminal settling velocity was obtained without tracking the localized velocity of the particle, which should be undertaken in order to ensure that the particle reached within a region of constant velocity. This leads to another research question: to develop an experimental methodology to track the entire trajectory of the particle, calculate the localized velocities and the terminal settling velocity of the particles.

2.1.4 Particle Motion in Steam Assisted Gravity Drainage (SAGD) Operations

This thesis work is particularly motivated by the behavior and deposition of solid particles transported in (SAGD) operations that can affect the flow characteristics and general productivity of the well. One of the failure mechanisms of the downhole equipment in SAGD operations is caused by the transport of particles that occurs during the production and extraction of oil sand [35,38]. The transport of particles during SAGD operations is referred to as fines migration [42]. One of the approaches that is used to analyze fines migration or particle transport are core flooding tests. In these tests, fluids are injected into a porous media sample known as a core sample as shown in Figure 2. Petroleum reservoirs are porous networks. One of the basic requirements of a petroleum reservoir is the presence of migratory pathways or flow paths [67]. Two intrinsic properties of the migratory pathways in petroleum reservoirs are porosity and permeability. Porosity refers to the void spaces or pore spaces in which liquids are stored within the reservoir [68]. If the pore spaces within the reservoir are interconnected this allows fluid flow within the

reservoir which is essentially permeability [68]. During core flooding tests, permeability measurements are taken and these are used to assess fines migration.

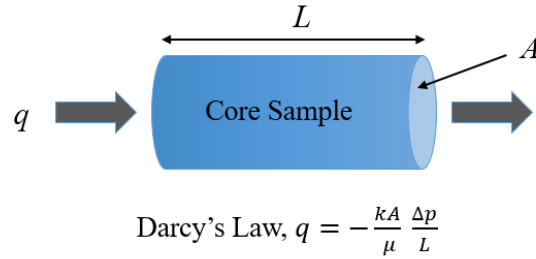


Figure 2 A schematic of a core sample used in the core flooding test. This is a bulk approach in which fluid is injected into the core sample and the effluent is assessed. The core flooding approach is analyzed using Darcy's Law.

Permeability measurements are obtained using core samples with the application of Darcy's Law which states that the flow rate through a porous media is directly proportional to the permeability and pressure drop across the core sample [68] as:

$$q = -\frac{kA}{\mu} \frac{dp}{L} \quad \text{Equation 12}$$

where q is the flow rate through the porous medium, k is the permeability of the porous medium, A is the cross-sectional area the porous media or core sample, $\frac{dp}{L}$ is the pressure drop per unit length of the core sample and μ is the viscosity of the fluid.

The core flooding approach has been used to quantify the amount of fines produced and to predict the likelihood for fines migration [42]. This can be achieved by flowing fluid into the core and placing a suitable filter mechanism placed at the outlet of the core sample [42]. There are challenges associated with this bulk type approach and there are studies that were focused on optimizing core flooding testing [43,69,70]. Some of the factors that were observed were that increased flowrates during core floods result in an immediate change in the permeability within the core which indicates that the fines are mobilized simultaneously [69]. It was also noted that the inclusion of surge testing is important in core floods since it accounts for the effect of sudden pressure changes that may occur in the near wellbore region during production operations on the well [43]. In another study, an analytical model was developed based on existing equations for fines migration, for the slow migration of suspended fines during core flooding [70]. With the use of mass balance, a

filtration coefficient to account for particle capture or entrapment and Darcy's equation to account for any decline in permeability, an analytical model was developed for (1) the total concentration of fines that were captured within the pore throats and (2) the history of permeability decline throughout the core flood.

The general approach in the literature to quantify fines migration is based on evaluating the effluent from the core as well as the flow rates and pressure differentials across the core. However, an understanding of the factors that influence the transport and deposition of fines locally within the core would be unknown. This leads to research questions to determine: (1) the effect of particle properties such as shape (or irregularity) on particle transport during SAGD operations and (2) to identify factors that influence the localized motion of the particles.

2.1.5 Particle Rotation

The assumption that the non-spherical particles are spheres neglects important aspects such as the rotational motion of the particles [18]. Particle size, shape and rotational motion have been shown to affect the general behavior of particles in fluids in turbulent flows [18], aerosol technology [9], and co-firing biomass applications [71]. In turbulent flows, it has been observed that the different drag coefficients were obtained for particles with similar equivalent diameters [18]. This difference was attributed to the shape and orientation or rotation of the particles which was observed from the results of a numerical simulation of a particle laden flow in a rectangular channel [18].

Another study investigating the rotation and translation of non-spherical particles within a turbulent flow observed that long aspect ratio particles experienced a significant variation in angular velocity during motion within a fluid [72]. The rotation and translation of non-spherical aerosol particles was investigated in [9] using a theoretical model with experimental validation. The results of that study indicated that the rotation of the aerosol particles led to particle deposition or sedimentation [9]. Particle rotation was accounted within a numerical model of the design for co-firing biomass applications [71]. It was shown that particle rotation or orientation affects the drag and lift of non-spherical particles [71].

Section 2.1.4 describes the bulk approach that has been used in literature to study the motion of particles within SAGD operations. There is very little information in literature about the occurrence

and impact of particle rotation during fines migrations in SAGD operations. Thereby, the review of the significance of particle rotation in other applications such as turbulent flows, aerosol technology, and co-firing biomass applications leads to the research question: to determine the impact of particle rotation during SAGD operations.

2.2 Evaluating Particle Motion using Particle Shadowgraph Velocimetry (PSV)

A summary of the research questions/objectives that were identified for this thesis research based on a review of the approaches used in the literature to model particle motion include:

1. to determine the suitability of using a spherical shape parameter as a length scale to obtain parameters which describe particle motion,
2. to develop an experimental methodology to track the entire trajectory of the particle in order to calculate the localized velocities and the terminal settling velocity of the particles,
3. to determine the effect of particle properties such as shape (or irregularity) on particle transport during SAGD operations,
4. to identify factors that influence the localized motion of the particles.
5. to determine the impact of particle rotation during SAGD operations.

Therefore, the overall goal is to select a suitable measuring technique to analyze particle motion in various flow media. Thereby the experimental analyses that were performed in this thesis research were achieved using an optical diagnostic technique known as particle shadowgraph velocimetry (PSV).

Shadowgraphy is a non-invasive technique that is used to analyze fluid flow in a number of different applications [73]. In this technique the light source is placed behind the test-section to provide back-illumination. Thereby, in the images obtained from this system, the test objects appear dark against a bright background [60]. A shadowgraph image is an illustration of the difference in refractive index between the test object and the surrounding medium [73]. In this

thesis research thesis PSV was used to capture the localized motion of the particles and several image processing techniques were developed in order to:

1. track the centroid of the particles,
2. calculate the localized velocities of the particles,
3. calculate the terminal settling velocity of the particles,
4. understand the flow field around particle motion during SAGD operations,
5. identify the factors that led to particle rotation,
6. demonstrate the impact of particle rotation on deposition and build-up during SAGD operations.

2.3 Thesis Overview

In this thesis research three different PSV experimental set-ups were used to test the hypothesis that using the spherical assumption to model non-spherical particles is invalid. Three experimental analyses were performed including:

1. falling spherical particles and cylindrical particles within a rectangular channel in order to calculate the coefficient of drag and particle Reynolds number,
2. spherical and irregularly shaped particles flowing within a single slot in SAGD operations in order to investigate the impact of particle shape and rotation on the surrounding flow field and
3. spherical and irregularly shaped particles flowing within a porous network to determine factors that influence particle deposition within the near-slot region in SAGD operations.

Figure 3 gives an overview of the three experimental analysis and it gives a schematic of all the particles that were used in this thesis research. The cylindrical particles were manufactured in-house.

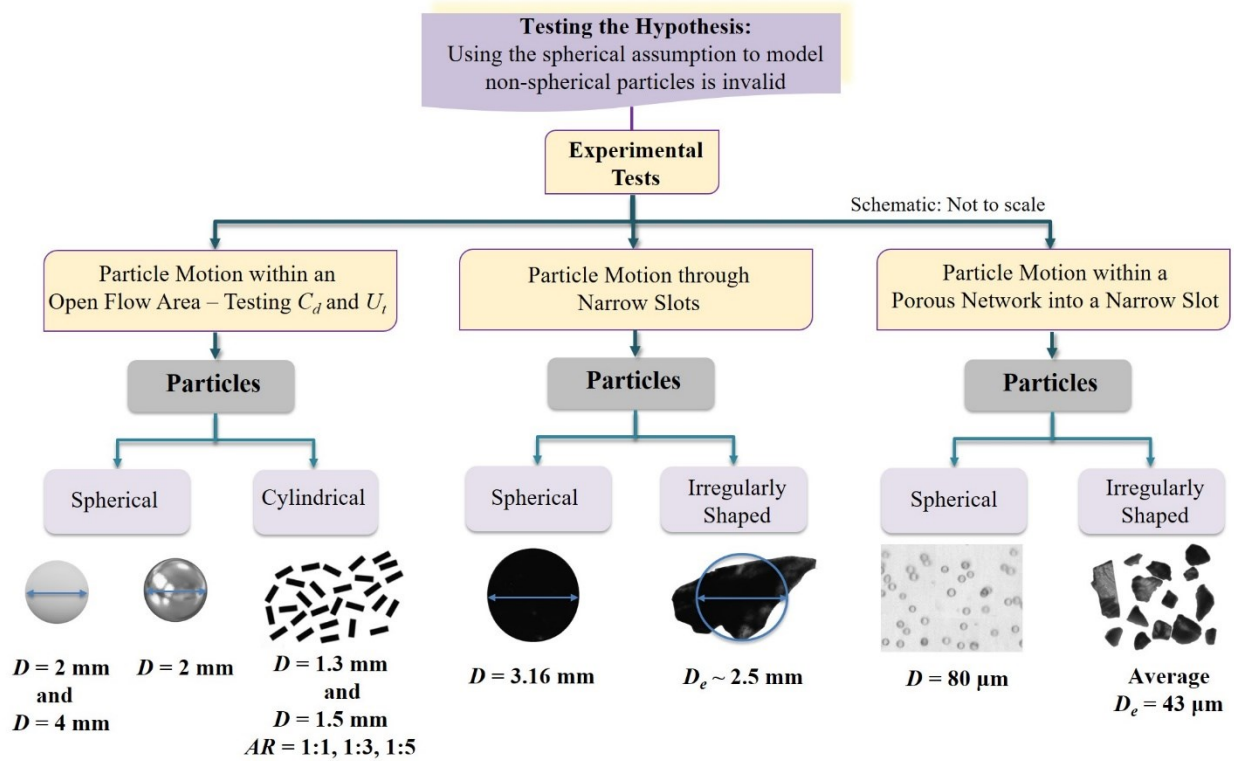


Figure 3 A schematic of the particles that were used in each of the three experimental analyses performed. The cylindrical particles were manufactured in-house. In this thesis research the hypothesis that using the spherical assumption to model non-spherical particles is invalid was tested by studying particle motion in: (1) an open flow area i.e. a rectangular channel, (2) particle motion through narrow slots and (3) particle motion within a porous network into a narrow slots.

3 Terminal Settling Velocity and Coefficient of Drag of Spherical and Cylindrical Particles using Particle Shadowgraph Velocimetry

3.1 Introduction

This chapter illustrates the impact of particle shape on some of the fundamental parameters used to define particle motion. The focus is on three parameters namely the settling velocity, the coefficient of drag and the Reynolds number of the particle. This is an experimental study which was performed by evaluating the motion of spherical particles and cylindrical particles falling within a rectangular channel. The objectives of the study were to: (1) determine an appropriate measuring technique and image processing approach to obtain the settling velocity of the particles experimentally, (2) evaluate the dynamics of the falling particles and (3) select and provide justification for an appropriate length scale to define the Reynolds number and coefficient of drag of the particles.

The motivation of this study was to evaluate parameters, which can be used to describe the motion of non-spherical particles with comparison to spherical particles. Spheres have a known length scale, the diameter of the sphere, which can be easily used to define the physical properties and the dynamics of motion of spherical particles. Conversely, shape parameters have been developed and used as length scales to describe non-spherical particles [14]. One of the common length scales that is used to describe non-spherical particles is the equivalent diameter [2,14]. This chapter evaluates the coefficient of drag and particle Reynolds number based on experimental results with comparison to the Haider and Levenspiel model [16] in order to determine a suitable length scale to model the particles. The non-spherical particles used in this study were cylinders that were manufactured manually using a guillotine chopping technique. Cylinders of various aspect ratios were manufactured in order to obtain different particle shapes and the results were compared to spherical particles. A PSV experimental set-up was used to capture the motion of the falling particles and image processing techniques were developed to calculate parameters that describe particle motion.

3.2 Description of the Particles, Fluids and the Flow Geometry

Three (3) different spherical particles and six (6) different cylindrical particles were used in this analysis. The experiments were performed in fluids with densities ranging between 919.44 kg/m³ to 1191.0 kg/m³ and viscosities ranging between 0.000914 Pa.s to 0.0809 Pas. The spherical particles used in this study had a higher density than the cylindrical particles. Thereby the spherical particles were evaluated in five (5) different fluids within the full range of fluid densities mentioned above. However, the cylindrical particles were evaluated in four (4) different fluids because the particles floated in the fluid with a density of 1191.0 kg/m³.

A total of 39 experimental conditions were evaluated based on the particle and fluid combinations. For each experimental condition, the experiments were repeated 15 times for the spherical particles and 25 times for the cylindrical particles. Thereby, 825 experiments were performed. This was done to ensure the repeatability of the experiments and to obtain some statistics of the particle motion. The cylindrical particles were manufactured in lab as part of this thesis research. The length of each particles varied slightly. Therefore, more repetitions were used in the cylindrical particle experiments to minimize the uncertainty in the calculations and data analyses. The spherical particles had a much smaller variation in size. Therefore, fewer repetitions were used in these experiments. The particle and fluid properties are given in the following sub-sections.

3.2.1 Spherical Particles

The properties of the three spherical particles used in this study are shown in Table 1 below. The motion of each of these particles were examined in five different fluids. The densities and viscosities of the five (5) fluids [74–77] at room temperature ($\approx 24^{\circ}\text{C}$) are given in. Table 2.

Table 1 The material, density and diameter of the spherical particles used in this phase of the study

Particle	Particle Density, ρ_p (kg/m ³)
2mm Diameter Delrin (McMaster-Carr)	1411.68
4mm Diameter Delrin (McMaster-Carr)	1411.68
2mm Diameter Aluminum (McMaster-Carr)	2710

Table 2 The densities and viscosities of the of the five (5) fluids that were used to spherical particles experiments [74–77]. All the liquids were degassed using a vacuum pump (Labconco 117) having a vacuum chamber attached. (Tap water was used in the experiments)

Fluid	Fluid Density, ρ_f(kg/m³)	Fluid Viscosity, μ_f(Pa.s)
Water	997.14	0.000914
20%–80% Glycerol–Water	1055.4	0.00178
40%–60% Glycerol–Water	1112.5	0.00419
70%–30% Glycerol–Water	1191.0	0.0283
Canola Oil	919.44	0.0809

3.2.2 Cylindrical Particles

The cylindrical particles were made from 1.30 mm and 1.50 mm diameter opaque, black, constant diameter mono-filament (fishing line, Hi-Seas Grand Slam). Additional components were attached to a jewelry wire guillotine cutter tool (AL Findings Limited) in order to cut the mono-filament into specified lengths as shown in Figure 4. This set-up was used to make cylindrical particles of aspect ratios ranging from 1:1 to 1:5. The aspect ratio is defined by the ratio of the particle diameter, d_p , to the length of the particle, l_p as:

$$\text{Aspect Ratio, } AR = \frac{\text{Particle Diameter}}{\text{Particle Length}} = \frac{d_p}{l_p} \quad \text{Equation 13}$$

The base of the jewelry wire guillotine cutter tool was fixed onto an optical breadboard (Thorlabs). The particle length ‘stop’ in Figure 4 has two projecting metal rods (not visible in the figure) that is fixed within a clamp that is connected to the optical XY translation stage (Thorlabs). The micrometer on the optical XY translation stage moved the particle length ‘stop’ forward to create a spacing, that is equal to the length of the particle, in between the ‘stop’ and the acrylic sheet. This acrylic sheet was fixed to the guillotine cutter and it contained particle guide holes equal to the diameter of the particles. It also allowed for more than one particle to be cut in a single stroke of the guillotine level.

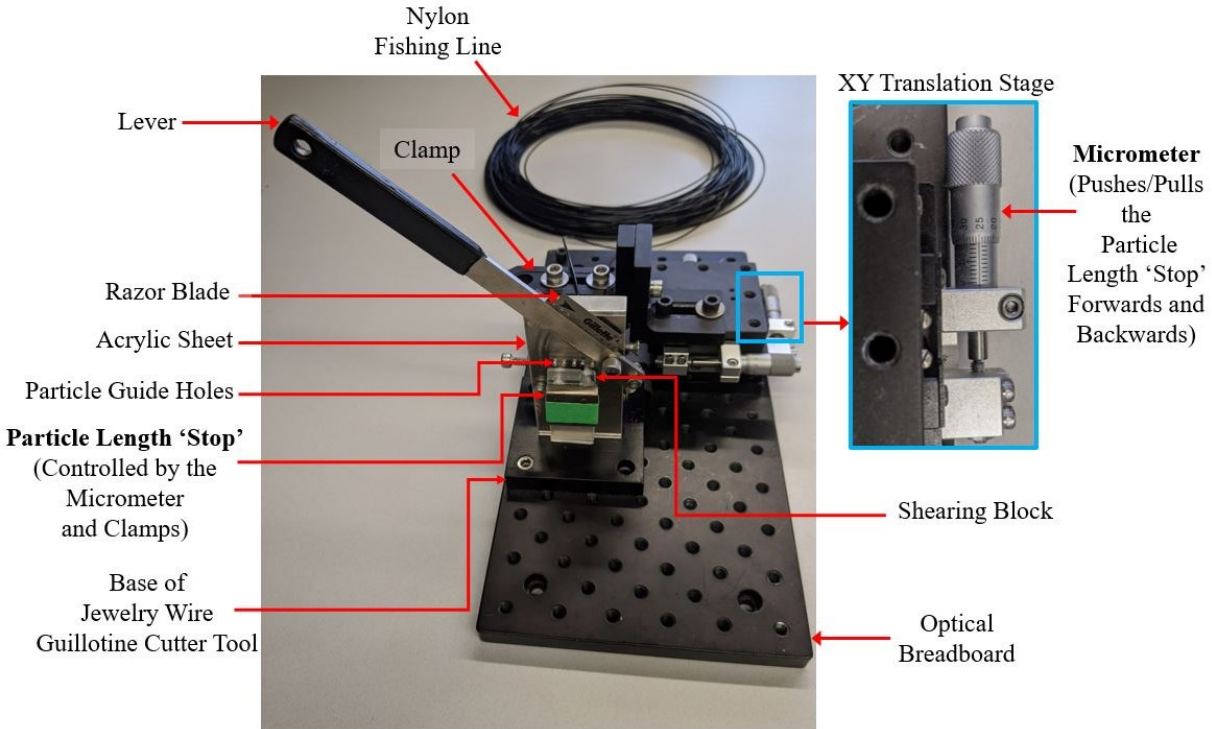


Figure 4 Particle chopper used to make cylindrical particles of diameters 1.30 mm and 1.50 mm and aspect ratios, ($AR = d_p/l_p$) 1:1, 1:3 and 1:5. The micrometer on the XY Translation Stage was adjusted to create a spacing equal to the particle length. Then a razor blade attached to a lever performed the cutting action. The particle chopper is a modified design of a jewelry wire guillotine cutter tool (AL Findings Limited).

The lever and the attached razor blade (Gillette) shown in Figure 4 were used to perform the cutting action to make particles of specified lengths. In Figure 4, the shearing block, also made of acrylic, was placed right at the base of the particle guide holes. Therefore, as the mono-filament were fed through the acrylic sheet it immediately rested on the shearing block. The purpose of the shearing block was to create a shearing cutting action to ensure that the ends of the particles were flat. A piece of tape was placed around the shearing block in order to create a very thin space in between the acrylic sheet and the shearing block to make room for the razor blade to perform the cutting action. Figure 5 shows two-dimensional images that were taken of the nylon cylindrical particles that were manufactured using the set-up in Figure 4. The particles were placed on a microscopic glass slide and the sample images were taken using a lens (50× microscopic lens). The images were calibrated by capturing an image of a ruler, whereby 1 mm is equivalent to 22 pixels.

Figure 5 shows a sample image of each of the aspect ratios of the 1.30 mm diameter cylindrical particles. The 2D projected area can be considered as the particle diameter \times the particle length. Therefore the expected projected areas of the 1.30 mm diameter nylon cylindrical particles at aspect ratios of 1:1, 1:3 and 1:5 are 1.69 mm², 5.07 mm² and 8.45 mm² respectively. The histograms of the projected areas of the cylindrical particles that were calculated from the two-dimensional images. The histogram values show that the projected area of the actual manufactured particles were slightly larger than the expected values. This can be due to a slight uncertainty in the distance between the particle length ‘stop’ and the shearing block shown in Figure 4. The properties of all the cylindrical particles used in this study are given in Table 3. The properties of the four fluids used for the cylindrical particles are given in Table 4.

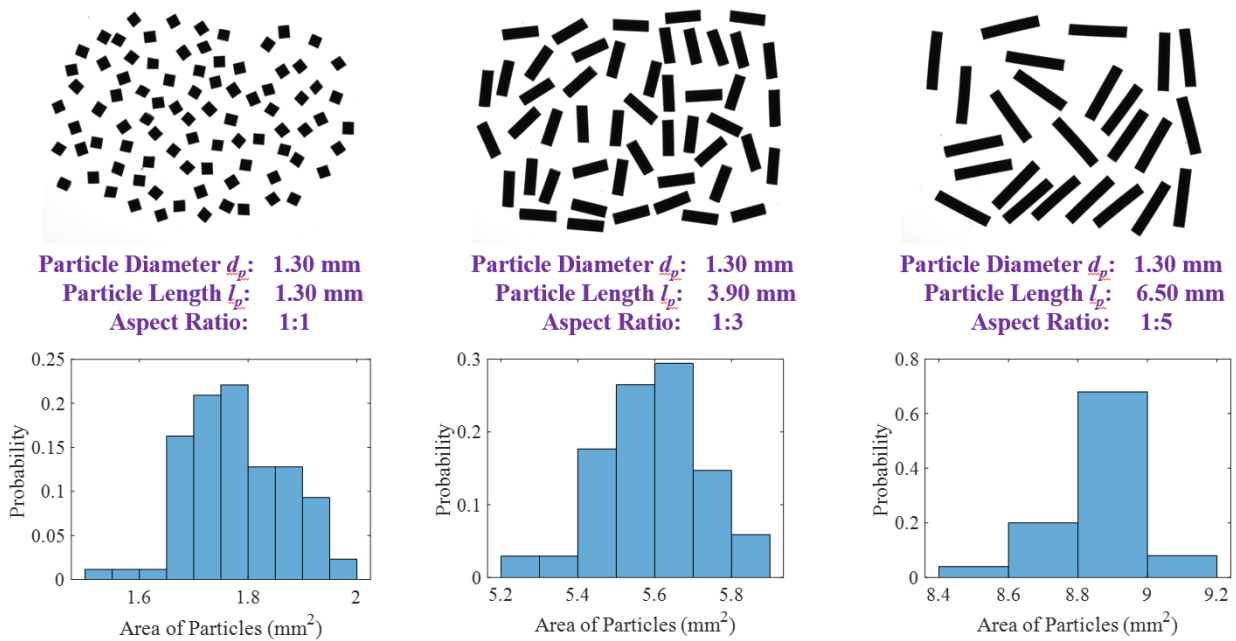


Figure 5 Sample two-dimensional images of the cylindrical particles that were manufactured for this study. This figure shows images of the 1.30 mm diameter opaque, black, constant diameter monofilament (fishing lines, Hi-Seas Grand Slam) at aspect ratios, ($AR = d_p/l_p$) of 1:1, 1:3 and 1:5. The histograms shows the distributed of the projected areas of the particles that were calculated from the two-dimensional images of the particles.

Table 3 The material, density, diameter, length and aspect ratios of the cylindrical particles that were made using the set-up in Figure 4

Particle Material	Particle Density, ρ_p (kg/m ³)	Particle Diameter, d_p (mm)	Particle Length, l_p (mm)	Aspect Ratios, ($AR = d_p/l_p$)
Mono-filament (Fishing lines, Hi-Seas Grand Slam) Colour: Black	1140	1.30	1.30	1:1
			3.90	1:3
			6.50	1:5
		1.50	1.50	1:1
			4.50	1:3
			7.50	1:5

Table 4 The densities and viscosities of the of the four (4) fluids that were used to cylindrical particles experiments [74–77].

Fluid	Fluid Density, ρ_f (kg/m ³)	Fluid Viscosity, μ_f (Pa.s)
Water	997.14	0.000914
20%–80% Glycerol–Water	1055.4	0.00178
40%–60% Glycerol–Water	1112.5	0.00419
Canola Oil	919.44	0.0809

3.3 Flow geometry

Two rectangular flow channels were used in the experiments. The short channel shown in Figure 6 (a) was used for the cylindrical particles in water and 20%-80% glycerol-water. However, in other experimental conditions, the channel height in Figure 6 (a) was insufficient to allow the particles to reach terminal velocity. Thereby, the taller channel shown in Figure 6 (b) was designed and fabricated and used for the remainder of the experiments.

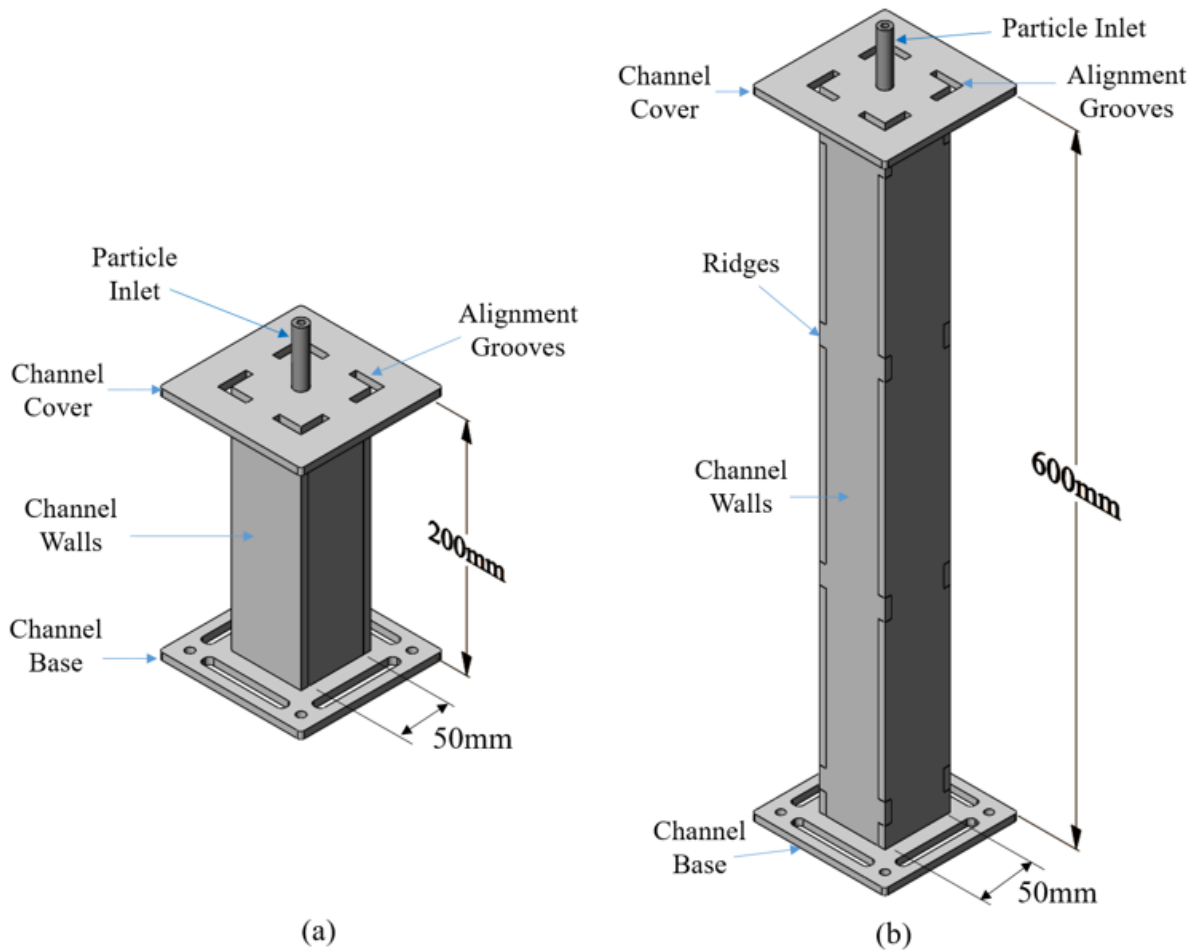


Figure 6 The rectangular flow channels: (a) short channel and (b) tall channel. The channels were made of acrylic sheet. The particle inlet was 3D printed using a clear photopolymer resin.

Both channels were 50mm square. The channel widths were made wide enough to reduce the wall effects. The short channel in Figure 6 (a) was 200 mm in height and the tall channel in Figure 6 (b) was 600 mm in height. The channels were made of 6.35 mm thick acrylic sheets and fabricated with a laser cutter (VLS3.50, Universal Laser). The channel were glued together with clear liquid acrylic cement (Model No. 3, SCIGRIP adhesives). For the tall channel ridges were added to the channel walls in Figure 6 (b) to ensure proper alignment for the gluing process. The channel walls were also glued onto the channel base.

The particle inlets shown in Figure 6 were manufactured using an additive manufacturing process (Form 3, Formlabs Inc.) with a clear photopolymer resin. The particle inlet was placed at the center of the channel cover which had alignment grooves to ensure that the particles began falling at the

center of the channel. The channel cover was loose and removable to allow the channel to be filled with fluid and to be cleaned at the end of each experiment.

3.4 Optical Experimental Set-up

Two PSV experimental set-ups were used to perform the experiments. One set-up was designed for the short channel, as shown in Figure 7, and the other was designed for the tall channel, as shown in Figure 8. One high speed camera was sufficient to capture the field of view in the short channel. However, the height of the field of view of the tall channel in Figure 6 (b) was three (3) times larger than the height of the field of view of the short channel in Figure 6 (a). Therefore, for the tall channel it was necessary to use two cameras to capture the entire trajectory of the particles and a different light source was needed in order to illuminate a field of view with a height of 600 mm.

The method of experiment was the same for both experimental set-ups whereby the flow channels in Figure 6 were initially filled with each of the fluids given in Table 2. Each of the particles in Table 1 and Table 3 were individually released from the particle inlet. This was done by filling the syringes shown in Figure 7 and Figure 8 with the desirable fluid and the particles were pumped into a tubing that had the opposite end fixed into the particle inlet. The particles were pumped at a very low flow rate of 0.5 ml/min using a syringe pump (11 plus, Harvard Apparatus Inc.). The base of the channels were tightly secured onto channel stands that were 3D printed (Ultimaker 2+). The channel stands were secured on an optical table to avoid motion or vibrations during the experiments as shown in Figure 7 and Figure 8.

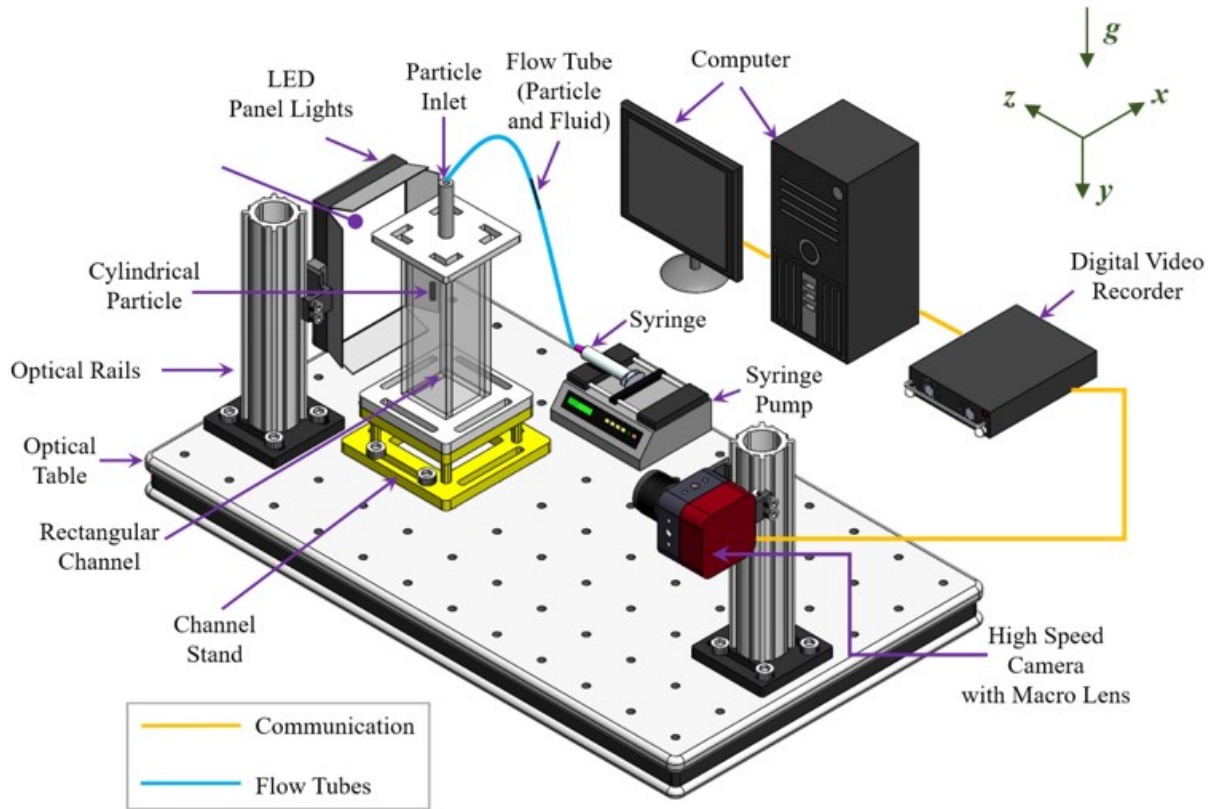


Figure 7 Particle shadowgraph velocimetry (PSV) experimental set-up for the short channel (Figure 6 (a)). One (1) high speed camera was sufficient to capture the motion of the falling particles within a field of view of $50 \text{ mm} \times 200 \text{ mm}$. An LED panel was used to illuminate the field of view. This set-up was used for the cylindrical particles in water and 20%-80% glycerol-water.

Table 5 Specifications of the PSV imaging system used for the short channel

Camera sensor size	2048×2048 pixels
Field-of-view ($w \times h$)	204.8×204.8 mm
Working Distance	990 mm
Magnification	0.055
Digital resolution	$0.10 \text{ mm pixels}^{-1}$

Particles fell in the direction of gravity and high speed cameras with a 2048×2048 pixel array (4M180NCL, IO Industries Inc.) with macro lens (50 mm f/1.4D, AF Nikkor) were used to capture the motion of the falling particles in the stationary fluids. The cameras were connected to a computer and a digital video recorder storage (DVR Express Core 2, IO Industries Inc.) to store

the captured images of the trajectories of the particles. The frame rates ranged between 14 frames per second (fps) to 155.12 fps, depending on the experimental conditions. Higher frame rates were required in order to capture the particle motion in fluids of lower density such as water because the particles fell quickly and covered the field of view in less than 10 seconds. However, for fluids of higher density such as 40%–60% glycerol–water, the particles took more than 1 minute to fall. So lower frame rates were adequate to freeze the motion of the particles.

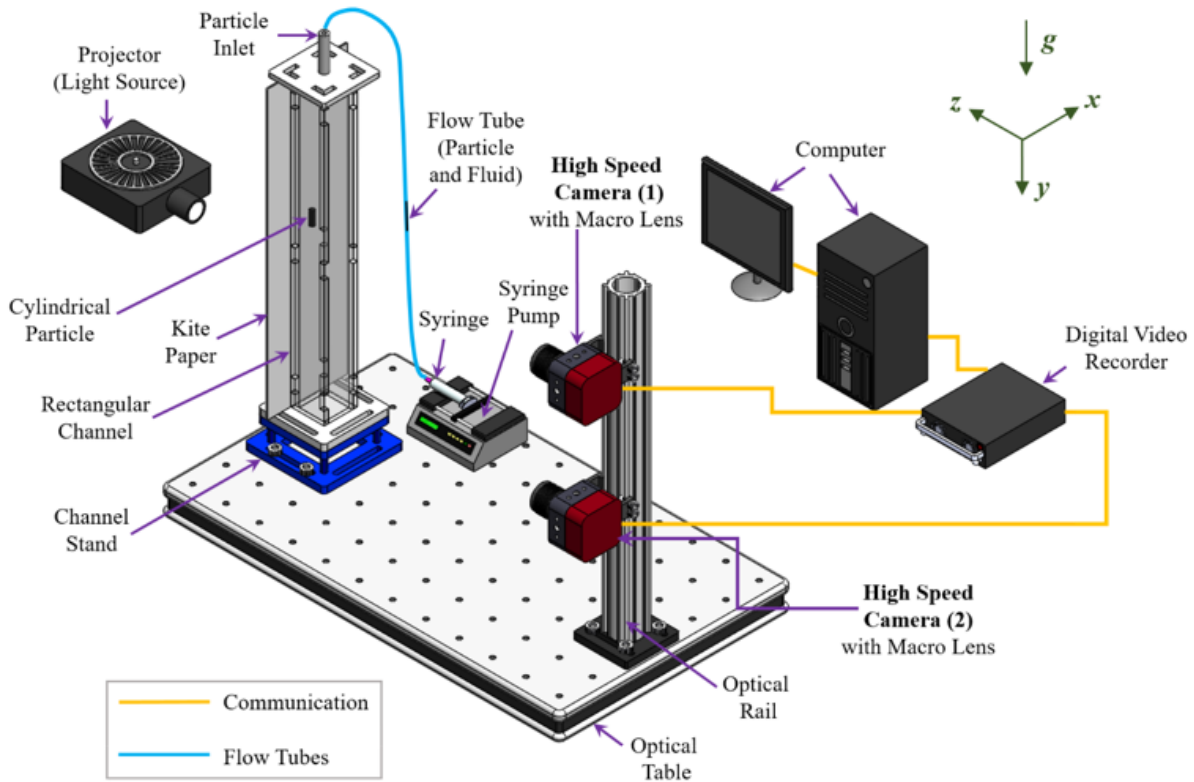


Figure 8 Particle shadowgraph velocimetry (PSV) experimental set-up for the tall channel (Figure 6 (b)). Two (2) high speed cameras were needed in order to capture the field of view. The field of view of the falling particles was 50 mm × 600 mm. A projector was used as the light source to illuminate such a large field of view. This set-up was used for the cylindrical particles in 40%-60% glycerol-water and canola oil and all of the spherical particles experiments.

Table 6 Specifications of the PSV imaging system used for the tall channel. The camera (4M180NCL, IO Industries Inc.) sensor size was cropped in order to achieve higher frames.

Camera sensor size	1200 × 1976 pixels
Field-of-view ($w \times h$)	170 × 280 mm
Working Distance	1385 mm
Magnification	0.04
Digital resolution	0.14 mm pixels ⁻¹

An LED panel light source (Yongnuo Digital YN600L) was used to provide back illumination to the field of view for the short channel as shown in Figure 7. The LED panel light was covered with two sheets of standard printing paper in order to achieve a more uniform light distribution and to block out excessive light that may cause damage to the camera. A slide projector (Carousel 850, Kodak) was used as the light source for the tall channel as shown in Figure 8. The slide projector was placed behind the rectangular channel to provide back illumination for shadowgraphy. A double layer of kite paper was attached to the back wall of the rectangular channel. The kite paper was used to distribute the light coming from the slide projector throughout the field of view and to prevent excessive light that may cause damage to the camera.

3.5 Data Processing: Calculates and Quantifies Particle Motion

This section describes the image processing techniques that were used to quantify the motion of the particle. Particle motion was described as displacement, velocity and acceleration. These parameters were obtained by tracking the centroid of the falling particle within the fluid. In-house image processing codes (Matlab, The MathWorks Inc.) were developed which incorporated the use of a minimal bounding objects function [78] and a derivativeFit function [79] as shown in Sections 8.45–Appendix 45 and 8.46–Appendix 46. The twelve (12) steps that were used in the image processing scheme are illustrated in Figure 9. The following sub-sections describes the four phases of the image processing scheme shown in Figure 9: (1) Initialization of the code, (2) Pre-processing of the image, (3) Image processing and (4) Calculations which quantified particle motion. All four stages are performed within one image processing script.

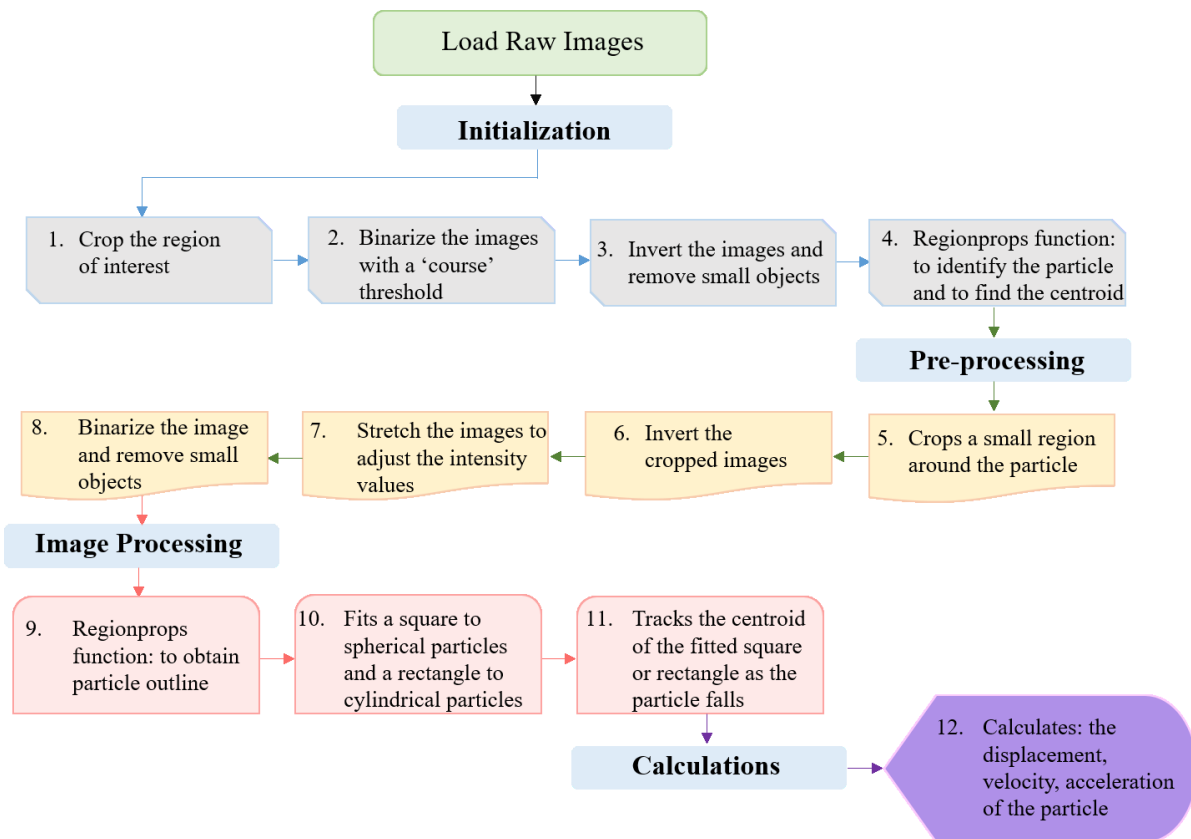


Figure 9 This is a flow chart describes image processing steps that were used to quantify particle motion. The spherical or cylindrical particles were delineated in the image processing script with a function that defines the minimal boundary of the particles [78]. Particle motion was determined by tracking the centroid of the falling particle. The displacement, velocity and acceleration of the particle was found by applying a derivativeFit function [79] to the tracked centroid locations.

3.5.1 Initialization

Sheets of paper were used to diffuse the light from the light sources as shown in Figure 7 and Figure 8. As a result, the background illumination in the raw shadowgraphy images were not perfectly uniform. Therefore, the purpose of the initialization stage, shown in steps 1–4 in Figure 9, was to identify a region around the particle in each subsequent image within which the image processing was performed. This localized image processing technique was used to assess the intensity differences between the particle and the background within a small localized region instead of considering the entire image as illustrated in Figure 10.

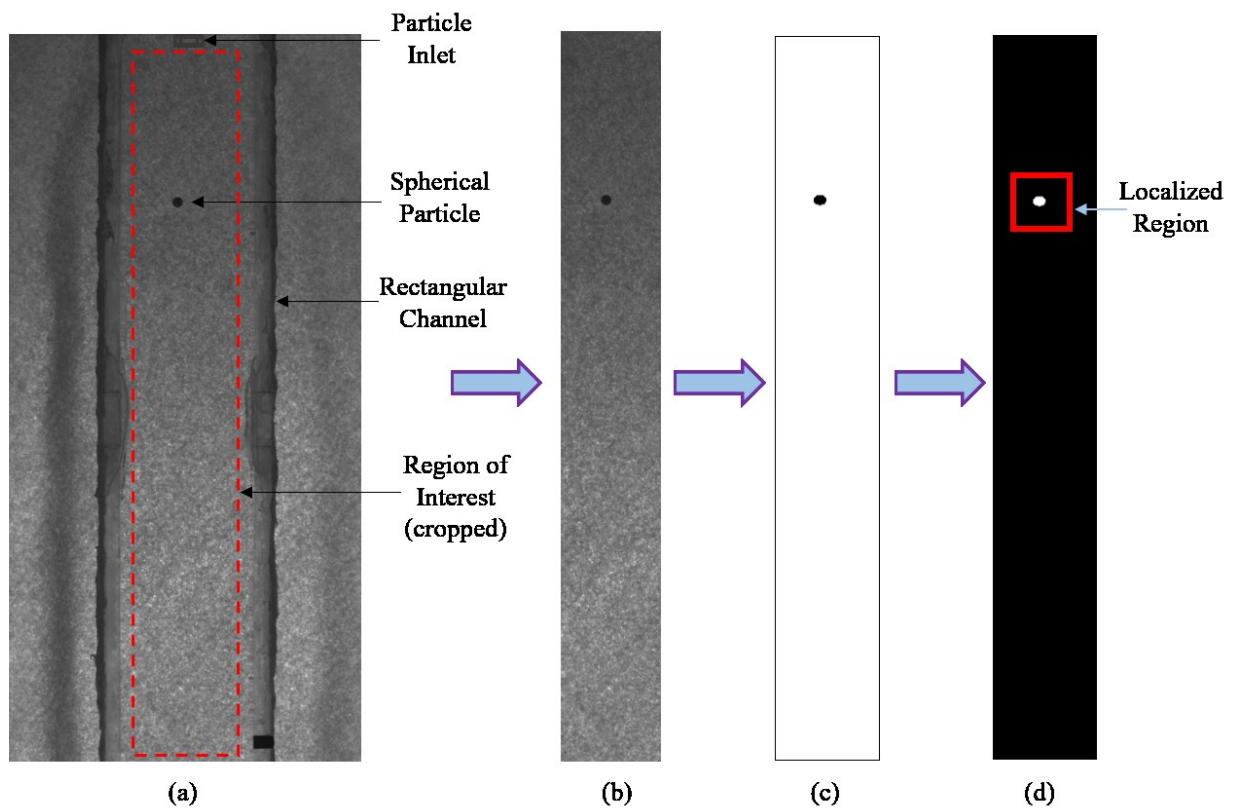


Figure 10 The initialization stage of the image processing: (a) A sample raw image in which the region of interest within the rectangular channel was identified and highlighted by the red dashed lines, (b) The region of interest was cropped from the raw image, (c) The cropped image was binarized using a coarse threshold and (d) The image was inverted and the boundary and the centroid of the particle were identified. A localized boxed region centered at the centroid of the particle was defined as highlighted by the solid red line. This localized region is the basis of the subsequent image processing steps.

In the initialization stage, the raw images were first uploaded sequentially and the region of interest, highlighted by the red dashed lines in Figure 10 (a) was cropped. The cropped region of interest was binarized based on a coarse threshold. The images were inverted, then the boundary and the centroid of the particle in each subsequent image were identified using a built-in function (*regionprop*, Matlab, The Mathworks) and a minimal bounding objects function [78]. A small boxed localized region centered at the centroid of the particle was identified as highlighted by the solid red line in Figure 10 (d).

3.5.2 Pre-processing and Image Processing

The localized region in Figure 10 (d) was used as the initial step of the remaining stages of the image processing scheme. The localized region was first inverted so that the particle appears bright on a dark background as shown in Figure 11. The intensity values in the images were then ‘stretched’ to increase the contrast of the images. This was achieved by remapping the intensity values of the image to fit closely to a range of 0 to 255 counts. Thereafter, two approaches were employed to identify the boundary and the centroid of the particle: (1) a fitted circle approach and (2) a boundary fitted approach based on the shape of the particle.

The fitted circle approach was performed using a built-in function (*viscircles*, Matlab, The Mathworks) by fitting a circle to the intensity stretched images of the spherical particles, shown in Figure 11. The function identifies the centroid of the spherical particles and calculates the particle diameter. Then the centroid of the particles in each subsequent image can be tracked. The processing steps of the fitted circle approach are shown in Figure 11. The fitted circle approach was used to validate the boundary fitted approach.

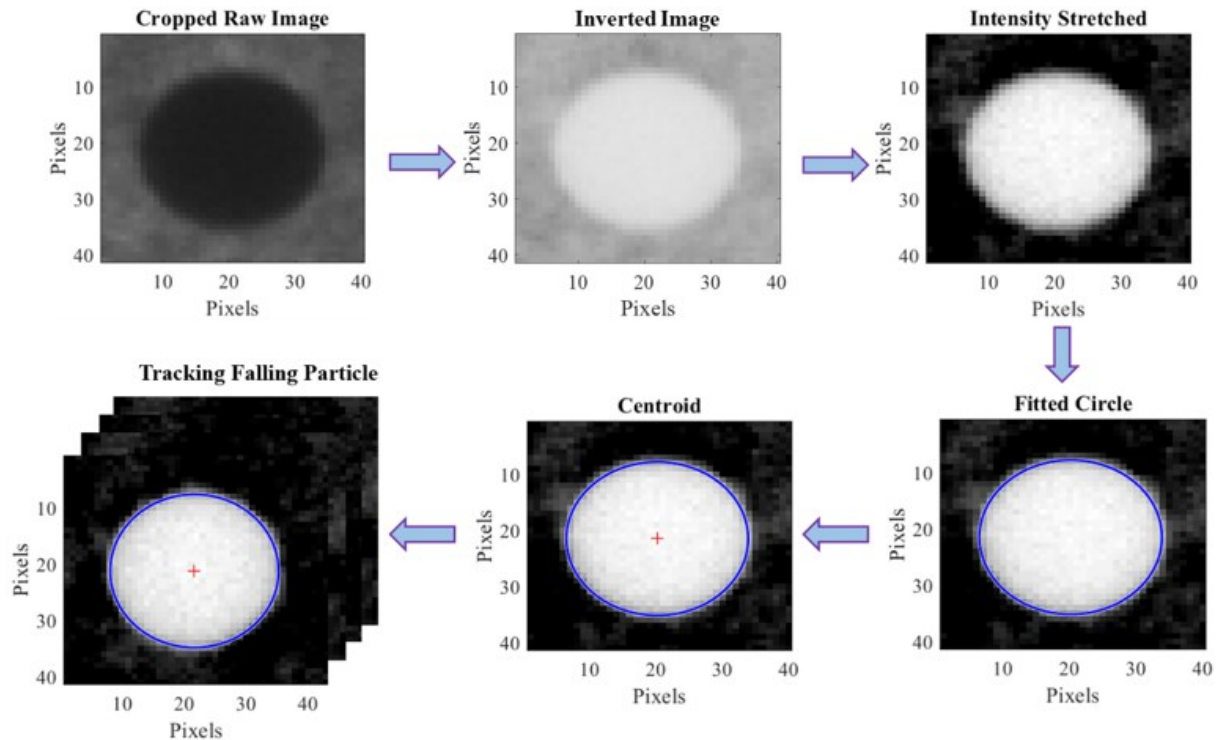


Figure 11 The processing steps of the fitted circle approach. This method which begins with a localized region around the particle. The images are inverted and the intensity values are stretched. A circle is fitted to the boundary of the particle and the centroid is identified and tracking in subsequent images.

The boundary fitted approach was achieved using a minimal bounding objects function [78]. This approach was necessary as it fits a minimal bounding outline depending on the shape of the particle appearing on the images obtained from the experiments. This tool fits a square to the 2D projected images of the spherical particles and a rectangle to the 2D projected images of the cylindrical particles. The cylindrical particles rotate while falling through the fluid. Therefore, throughout the trajectory of the particles, the boundary fitted approach was needed to capture the outline of the various shapes that would appear on the 2D projected images of the rotating cylindrical particles. For the boundary fitted approach, the intensity stretched images were binarized with a specified threshold. The 2D projected area was obtained and the boundary of the particle was traced using a built-in function (*bwboundaries*, Matlab, The Mathworks). The minimal bounding objects function [78] then fits a square/rectangle to the particles. Finally the centroid of the particles in each subsequent image was identified and tracked. The processing steps of the boundary fitted approach are shown in Figure 12.

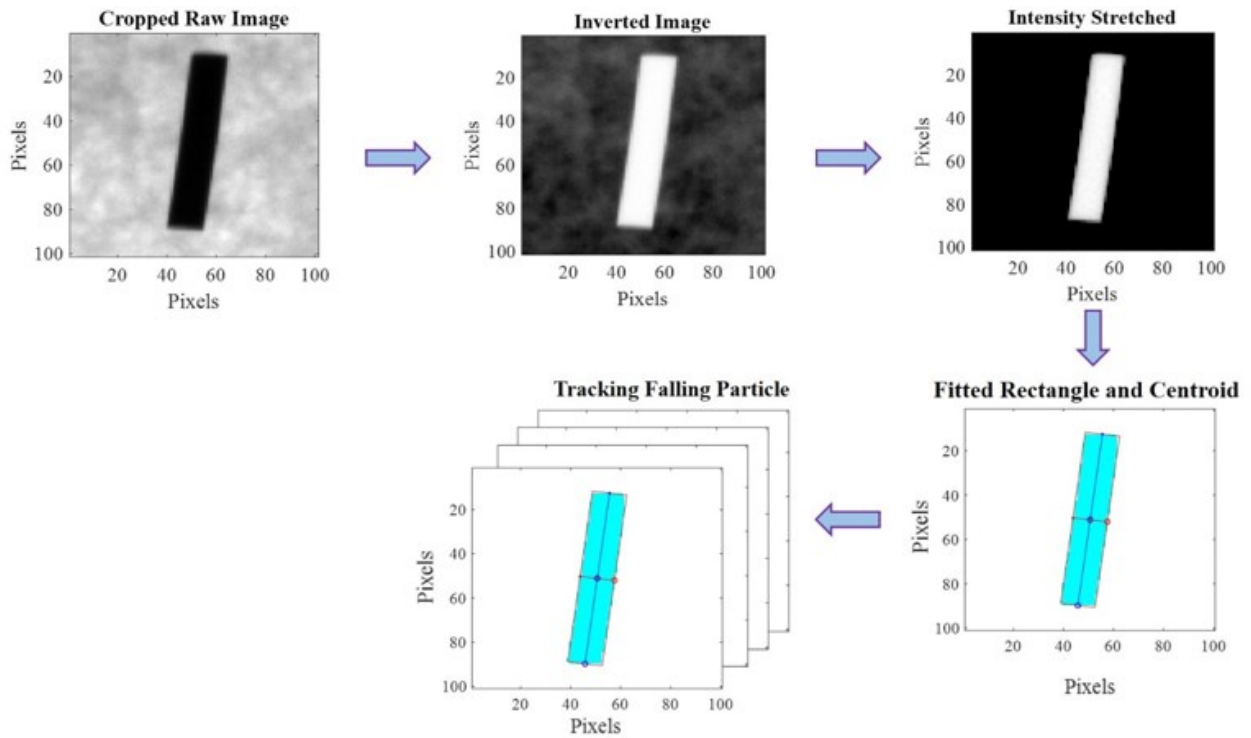


Figure 12 The processing steps of the boundary fitted approach. This method begins with a localized cropped region around the particle. The images are inverted and the intensity values are stretched. The images are then binarized and a minimal bounding objects function [78] was used to fit a square to the 2D images of the spherical particles and a rectangle to the 2D images of the cylindrical particles. The centroid is identified and tracking in subsequent images.

3.5.3 Calculations: Displacement, Velocity and Acceleration from the Raw Images

The location of the centroid of the particle in each frame was identified and plotted as described in Section 3.5.2. A derivativeFit function [79] was used to calculate and plot the velocity and acceleration of the particle. First, the displacement plot is determined by plotting the location of the centroid. Then the derivativeFit function was used to find the first derivative of the displacement plot in order to obtain the particle velocity, ds , and the second derivative of the displacement plot in order to obtain the particle acceleration, dds . The derivativeFit function, shown in Equation 14, obtains the first and second derivatives by calculating the gradient of a curve fitted over $1+2n$ points.

$$[ds, dds] = \text{derivativeFit} (t, s, n, \text{order}) \quad \text{Equation 14}$$

The 1-D array inputs to the derivativeFit function are shown in Equation 14 where t represents the values of time, t , at each frame/image obtained within the data set. s represents the values of the particle displacement which was obtained by tracking the centroid of the particle in each subsequent frame. n is the number of points around a specific data point (one data point will be one specific location of the centroid of the particle) in which the curve fitting will be performed. The *order* defines the polynomial fit curve used, which can be linear or quadratic.

The experiments were performed at high frame rates. As a result the data points used to obtain the displacement plot were tightly packed. Therefore, the value of n for the curve fitting was selected to be equal to the number of frames it took for the spherical particles to move one particle diameter and the number of frames it took for the cylindrical particles to move one particle length. Therefore, at one specific data point in the displacement plot, a linear curve will be fitted to $1 - n$ to $1 + n$ data points i.e. one particle diameter forwards and backwards for the spherical particles and one particle length forwards and backwards for the cylindrical particles. The velocity was obtained by finding the gradient or the first derivative of the fitted linear curve and the acceleration was found by finding the second derivative.

3.5.4 Methodology of Obtaining the Terminal Settling Velocity of Particles from Experiments

The x and y components of the particle velocity were calculated from experimental data using the image processing technique described in Section 3.5.3. Thereafter, the magnitude of velocity, $|V|$, was calculated. The average magnitude of the velocity within the constant velocity region was calculated for each of the 25 particles within one experimental condition. The terminal settling velocity, U_t , was obtained by finding the average of the constant velocities of the 25 cylindrical particles as shown in the example in Figure 13. The plot of the magnitude of acceleration, $|A|$, shown in Figure 14 confirms that the particles experienced zero acceleration within the terminal settling velocity region. It was also observed that the 25 particles followed a similar trend for the particle velocity and acceleration in the y direction. However, in the x direction the particle velocity and acceleration exhibited different trends before reaching to the terminal settling velocity.

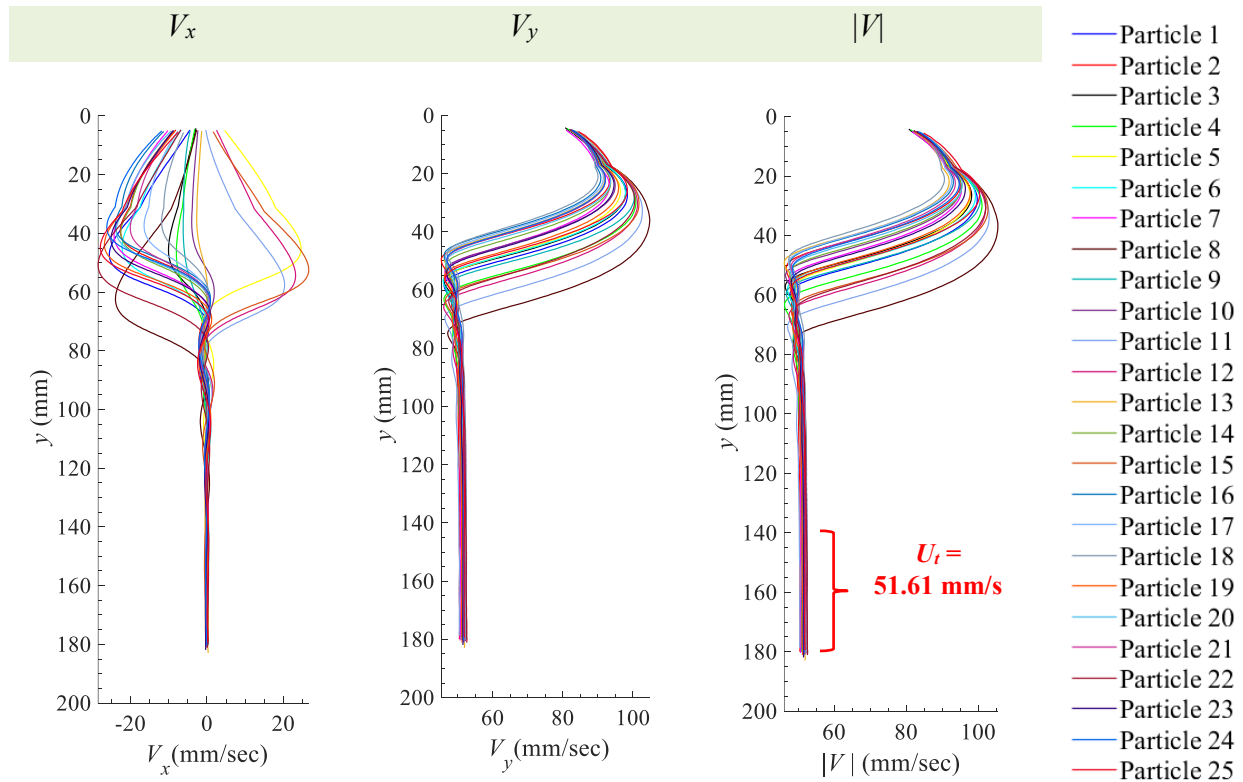


Figure 13 Particle velocity in the x -direction V_x , y -direction V_y , and the magnitude $\sqrt{(V_x^2 + V_y^2)}$ of the particle velocity $|V|$ for 1.50 mm Diameter Nylon Cylindrical Particles with Aspect Ratio, A.R. = 1:5 (25 particles) in Water. The average terminal settling velocity, U_t is 51.61 mm/s.

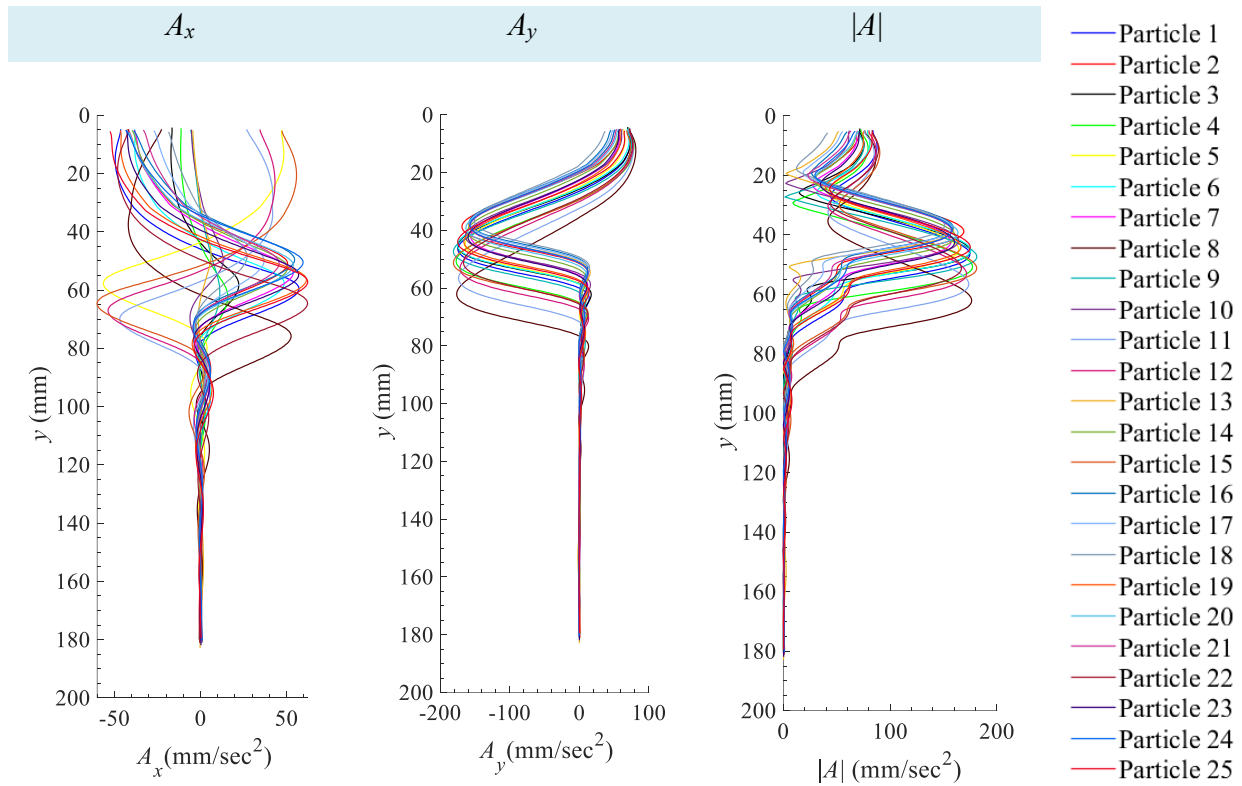


Figure 14 Particle acceleration in the x -direction A_x , y -direction A_y , and the magnitude $\sqrt{A_x^2 + A_y^2}$ of the particle acceleration $|A|$ for 1.50 mm Diameter Nylon Cylindrical Particles with Aspect Ratio, A.R. = 1:5 (25 particles) in Water. The acceleration was observed to be zero within the region that was used to determine the average terminal settling velocity in Figure 13.

3.6 Experimental Results and Analyses

The processed images were used to obtain the displacement, velocity and acceleration of the particles as shown in Section 8.1–Appendix 1 to Section 8.39–Appendix 39. In this section, the terminal settling velocity of both the spherical and cylindrical particles, obtained from experimental data, were presented. Thereafter, the coefficient of drag and the particle Reynolds number were obtained together with an evaluation to determine an appropriate length scale that can be used to assess the motion of non-spherical particles.

3.6.1 Spherical Particles: Particle Trajectory, Displacement, Velocity and Acceleration

The particle trajectory for one of the 4 mm delrin spheres falling within water is shown in Figure 15 (a). Two cameras were mounted vertically to image the motion of the particles falling within the tall rectangular channel as shown in Figure 6. The tall channel was used to ensure that the particles reach their terminal settling velocity. The cameras were mounted such that the two field of views were slightly overlapped. The overlap region is shown in Figure 15 (a). Generally the spherical particles moved back and forth in the x -direction before reaching their terminal settling velocity. The amount of movement in the x -direction was dependent on the viscosity of the fluid whereby for less viscous fluids the particles experienced more motion in the x -direction.

It was also observed that there was a very slight change in the gradient of the displacement plots within the first 100 mm of the trajectory of the particle as shown in Figure 15 (b). This showed a corresponding change in the particle velocity and acceleration as shown in Figure 15 (c) and (d). The particle velocity plot showed that the 4 mm delrin particles reached their terminal settling velocity at approximately 300 mm where the particle velocity reached an average constant value and the average acceleration was zero. However, there were minor fluctuations in the velocity and acceleration plots. These fluctuations may be attributed to the presence of vortex shedding as the particles fell within the fluid or these can be due to digitization errors within the image processing. The diameter of the 4 mm delrin particle is equivalent to 28 pixels, therefore when the raw images were binarized there is a possibility that some pixels were lost during the image processing scheme.

This can result in a slight shift in the location of the centroid of the particle that would impact the calculation of the local velocity and acceleration of the particle.

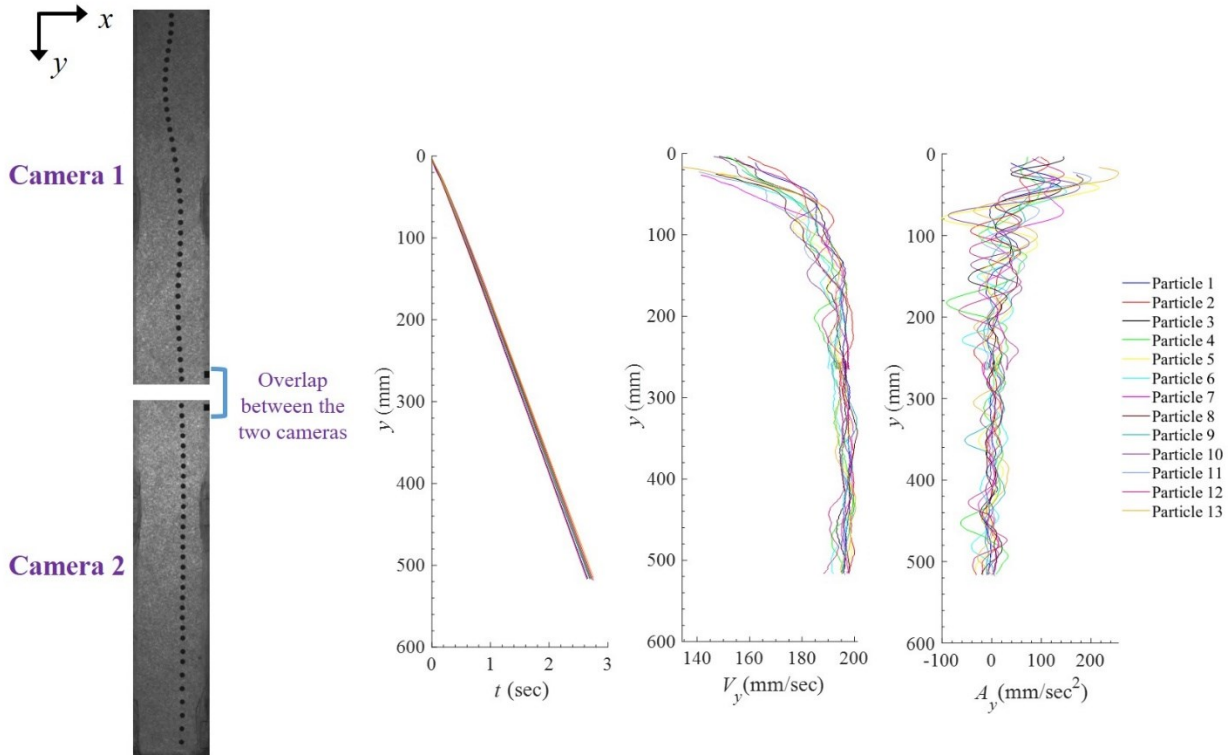


Figure 15 (a) The general trend of the particle trajectory that was observed for the spherical particles falling within all of the fluids. (b) particle displacement, y , versus time, (c) the y component of the particle velocity and (d) the y component of the particle acceleration for 4 mm delrin spheres in Water. 15 particles were used in the original experiment however, two particles appeared as outliers and were omitted from this plot. This experimental condition was performed within the tall channel as shown in Figure 6 (b) in order to allow the particles to reach terminal settling velocity.

3.6.2 Cylindrical Particles: Particle Trajectory, Displacement, Velocity and Acceleration

Cylindrical particles with aspect ratios 1:3 and 1:5 exhibited a similar particle trajectory while falling through the fluid. Figure 16 (a) illustrates the general trend that was observed. The cylindrical particles entered the rectangular channel vertically after exiting the particle inlet. The particles maintained this vertical orientation within the first few frames as shown in Figure 16 (a). Subsequently the particles experienced rotation in each subsequent frame, due to the unbalance of forces, until it reached a new orientation and its terminal settling velocity. In this regard, each cylindrical particle presented a different cross-sectional area towards the fluid within the three different orientations throughout the particle trajectory shown in Figure 16 (a). This is in contrast to the spherical particles which presents the same cross-sectional area towards the fluid regardless of its orientation [80].

Figure 16 also shows the particle displacement, velocity and acceleration for the 1.50 mm diameter nylon cylindrical particles with an aspect ratio of 1:5 falling within water. The 25 particles that were used in this experimental condition followed a similar trend. Whereby in Figure 16 (b) there was a slight change in the gradient of the displacement versus time plot within the region where the particle experienced rotation. Figure 16 (c) shows that the particles entered the rectangular channel with an initial velocity. This is because the particles were pumped into the particle inlet at the top of the rectangular channel using a syringe pump and the flow tube, as shown in Figure 7 and Figure 8. The particle velocity slightly increased within the first few frames and then decreased in each subsequent frame until the particles reach their terminal settling velocity. The particle also decelerates after entering the rectangular channel and then accelerations until it reaches the terminal settling velocity region where it experiences constant acceleration as shown in Figure 16 (d).

Please note: the short channel PSV set-up with one camera as shown in Figure 7 was used for the cylindrical particles falling in water and 20%–80% glycerol–water. For all other particles in this study, the PSV set-up with two cameras mounted vertically together with the tall channel, as shown in Figure 8, was used. Thereby the particle displacement in Figure 16 is representative of the short channel whereas the particle displacement in Figure 15 is representative of the tall channel.

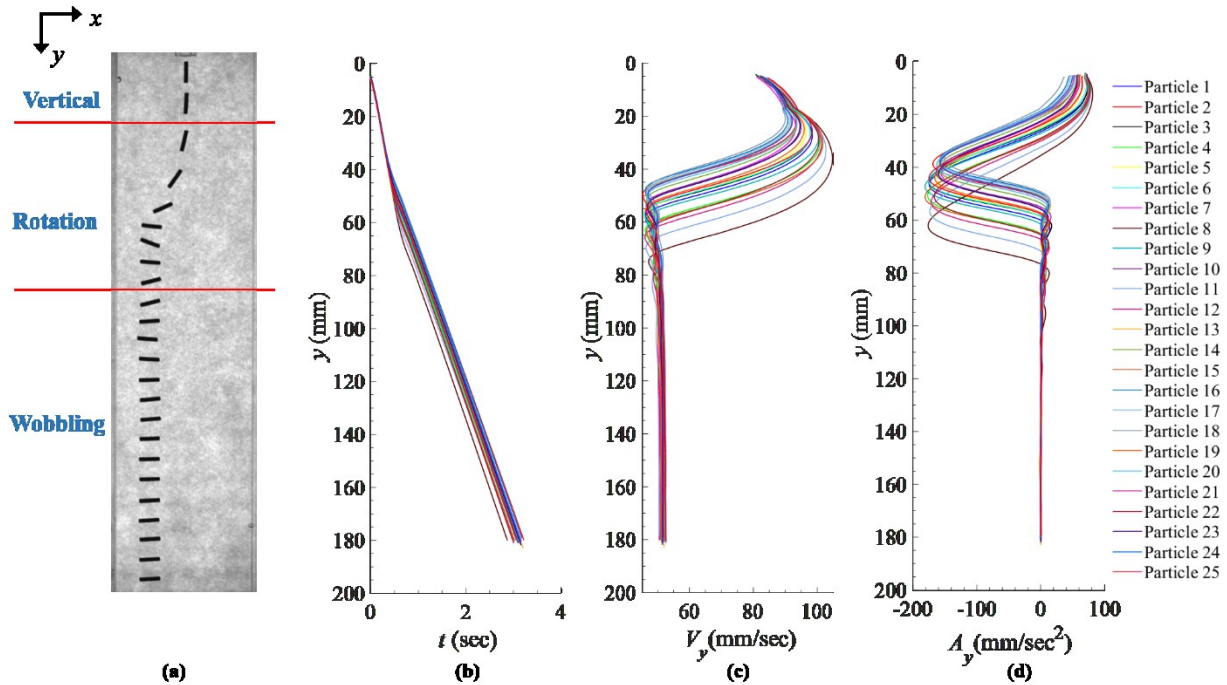


Figure 16 (a) The general trend of the particle trajectory that was observed for the cylindrical particles falling within all of the fluids. (b) particle displacement, y , versus time, (c) the y component of the particle velocity and (d) the y component of the particle acceleration for 1.50 mm Diameter Nylon Cylindrical Particles with Aspect Ratio, A.R. = 1:5 (25 particles) in Water. In this experimental condition the particles reached terminal settling velocity within the short channel as shown in Figure 6 (a).

3.6.3 Spherical Particles: Terminal settling velocity and the Coefficient of Drag Obtained from Experimental Data

The terminal settling velocity of the particles were used to calculate the particle Reynolds number in each experimental condition. For the spherical particles the coefficient of drag was calculated using the Haider and Levenspiel model [16] as described in Section 2.1.2. The values of the coefficients A, B, C and D are dependent on the particle sphericity, ϕ , which is the ratio of the surface of a sphere having the same volume of the particle to the actual surface area of the particle. Therefore, the particle sphericity of the spherical particles was always 1. The values of the average terminal settling velocity that were obtained from the 15 spherical particles at each experimental condition along with the corresponding values of the particle Reynolds number and the coefficient of drag are shown in Table 7.

Table 7 This table shows the average terminal settling velocity within the terminal settling velocity region of the 15 spherical particles for each experimental condition. The terminal settling velocity were obtain from the plots of the particle displacement versus the particle velocity (magnitude) for the spherical particles as shown in Section 8.1 – Appendix 2 to Section 8.15 – Appendix 16. The particle Reynolds Number and the coefficient of drag were calculated based on the average terminal settling velocity values. The coefficient of drag was calculated based on the model in [16].

Particle	Fluid	Average Terminal Settling Velocity, U_t (mm/s) 15 particles	Particle Reynolds Number, Re_p	Coefficient of Drag, C_D
			$\frac{\rho_f U_t d_p}{\mu_f}$	$\frac{24}{Re} [1 + A Re^B] + \frac{C}{[1 + \frac{D}{Re}]}$
4 mm Delrin	Water	196.82	859.36	0.50
	20%–80% Glycerol–Water	152.99	363.68	0.66
	40%–60% Glycerol–Water	108.37	115.23	1.08
	70%–30% Glycerol–Water	34.68	5.84	6.53
	Canola Oil	54.86	2.49	12.88
2 mm Delrin	Water	114.18	249.27	0.77
	20%–80% Glycerol–Water	78.84	93.71	1.19
	40%–60% Glycerol–Water	49.85	26.50	2.34
	70%–30% Glycerol–Water	12.07	1.02	28.05
	Canola Oil	17.30	0.39	67.23
2 mm Aluminum	Water	289.97	633.04	0.55
	20%–80% Glycerol–Water	241.99	287.62	0.73
	40%–60% Glycerol–Water	184.59	98.14	1.16
	70%–30% Glycerol–Water	75.25	6.34	6.14
	Canola Oil	60.41	1.37	21.48

3.6.4 Uncertainty of the Experimental Terminal Settling Velocity Measurements

The uncertainty of the experimental terminal settling velocity measurements was analyzed by plotting the experimental values against the predicted theoretical values. This allows a comparison of the data points with a 45 degree line through the origin ($y = x$) represented by the black dotted line shown in Figure 17, Figure 18 and Figure 19. The spherical data was used to validate the experimental measurements since it has a known length scale, which is the sphere diameter. The model that was used to determine the theoretical terminal settling velocity takes into account the balance of forces, that is, the drag force, buoyant force and weight of the spherical particles which is given as:

$$\text{Theoretical Terminal Settling Velocity, } U_t(\textit{Theoretical}) = \sqrt{\frac{\pi r g (\rho_p - \rho_f)}{c_d \rho_f}} \quad \text{Equation 15}$$

where r is the radius of the particle, ρ_p is the density of the particle, ρ_f is the density of the fluid, g is the acceleration due to gravity and c_d is the coefficient of drag of the particle. The theoretical terminal settling velocity model is an implicit equation because $U_t(\textit{Theoretical})$ is a function of c_d which is a function of Re_p . Additionally, Re_p is a function of $U_t(\textit{Theoretical})$. Therefore, $U_t(\textit{Theoretical})$ cannot be solved without a direct value or simplified expression for c_d .

$U_t(\textit{Theoretical})$ was thereby obtained using an iteration process. This process was performed by first calculating the Re_p using the particle and fluid properties and then c_d using Haider and Levenspiel model. The c_d value was then used to calculate the $U_t(\textit{Theoretical})$. This value of $U_t(\textit{Theoretical})$ was used to calculate a new value of Re_p which was then used to calculate a new value of c_d and $U_t(\textit{Theoretical})$. This iterative process was repeated until the values of $U_t(\textit{Theoretical})$ converged. Section 8.40 – Appendix 40 shows an example of the iteration process, whereby the $U_t(\textit{Theoretical})$ was 213.413 mm/s for the 4 mm delrin particles in water. This approach was used to find the $U_t(\textit{Theoretical})$ for the three different spheres falling in the five different fluids used in this analysis as described in Section 3.2.1 – Table 1 and Table 2.

The particle density values for the delrin and aluminum spheres that were given in Section 3.2.1 – Table 1 were obtained from the manufacturer data. However, the density of the

particles were also measured and the values are presented in Section 8.41 – Appendix 41 and Section 8.42 – Appendix 42. The mass of the each individual particle was measured using a scale (Ohaus EX124 Explorer Analytical Balance) and the diameter of each particle was measured with a digital Vernier caliper. The volume and density of the particles were then calculated using the measured mass and diameter of the particles.

Section 8.41 – Appendix 41 shows the measured density of 20 individual 4 mm delrin particles. The minimum measured density was 1.31 g/cm^3 and the maximum measured density was 1.40 g/cm^3 . Thereby the median value of the measured particle density of the 4 mm delrin particles was 1.36 g/cm^3 . Section 8.42 – Appendix 42 shows the measured density of 20 individual 2 mm aluminum particles. The minimum measured density was 2.12 g/cm^3 , the maximum measured density was 2.59 g/cm^3 and the median value of the measure particle density of the 2 mm aluminum particles was 2.35 g/cm^3 . The standard density values for delrin and aluminum as shown in Section 3.2.1 – Table 1 are 1.41 g/cm^3 and 2.71 g/cm^3 respectively. The standard density values are different to the measured values of density probably because of changes in the material properties of the particles during the manufacturing process. The minimum, maximum and medium values of the measured particle densities were used in the calculation of $U_t(\text{Theoretical})$ and compared to the measured experimental values of the terminal settling velocity as shown in Figure 17, Figure 18 and Figure 19.

In Figure 17, the minimum density values of delrin and aluminum was used to calculate $U_t(\text{Theoretical})$. A close fit was established between the measured values of the terminal settling velocities from the experimental data and the predicted theoretical values of the terminal settling velocities of the particles. Similarly in Figure 18 and Figure 19, $U_t(\text{Theoretical})$ was determined using the maximum and median values respectively of the measured values of the densities of delrin and aluminum. Figure 18 and Figure 19 shows that a slight change in the particle density ranging from 0.04 g/cm^3 to 0.24 g/cm^3 resulted in a significant shift in the $U_t(\text{Theoretical})$ data points. The minimum and median values of the measured density values yielded a fairly close fit of the predicted theoretical values compared to the experimental values of the terminal settling velocities as shown in Figure 17 and Figure 19. This shows that the experimental method that was used to determine the terminal settling velocity of both the spherical particles and the long aspect ratio cylindrical particles is reliable.

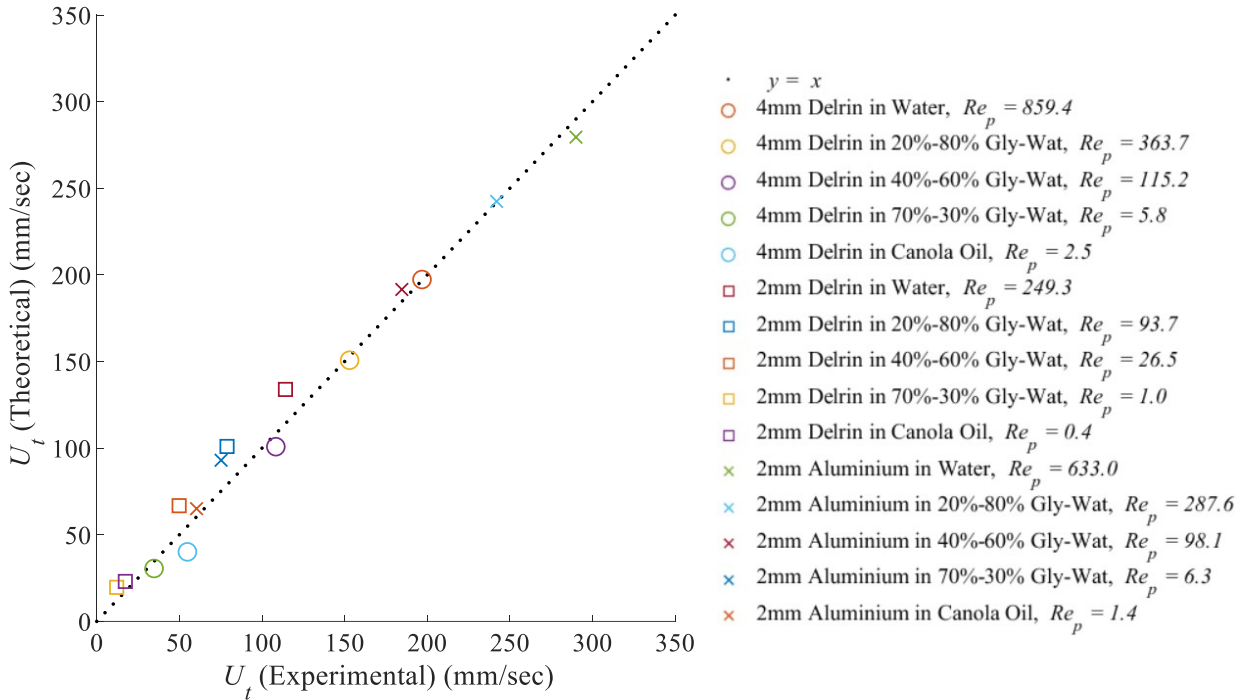


Figure 17 The theoretical terminal settling velocities, U_t (Theoretical), plotted against the experimental terminal settling velocities, U_t (Experimental), of the spherical particles that were discussed in section 3.6.3 and shown in Table 7. The dotted black line represents a plot of $y = x$ which was used to evaluate the agreement between the theoretical values and the experimental values of the terminal settling velocity. The minimum values of the measured density of delrin and aluminum were used to calculate U_t (Theoretical). This resulted in the closest fit between the experimental and theoretical values.

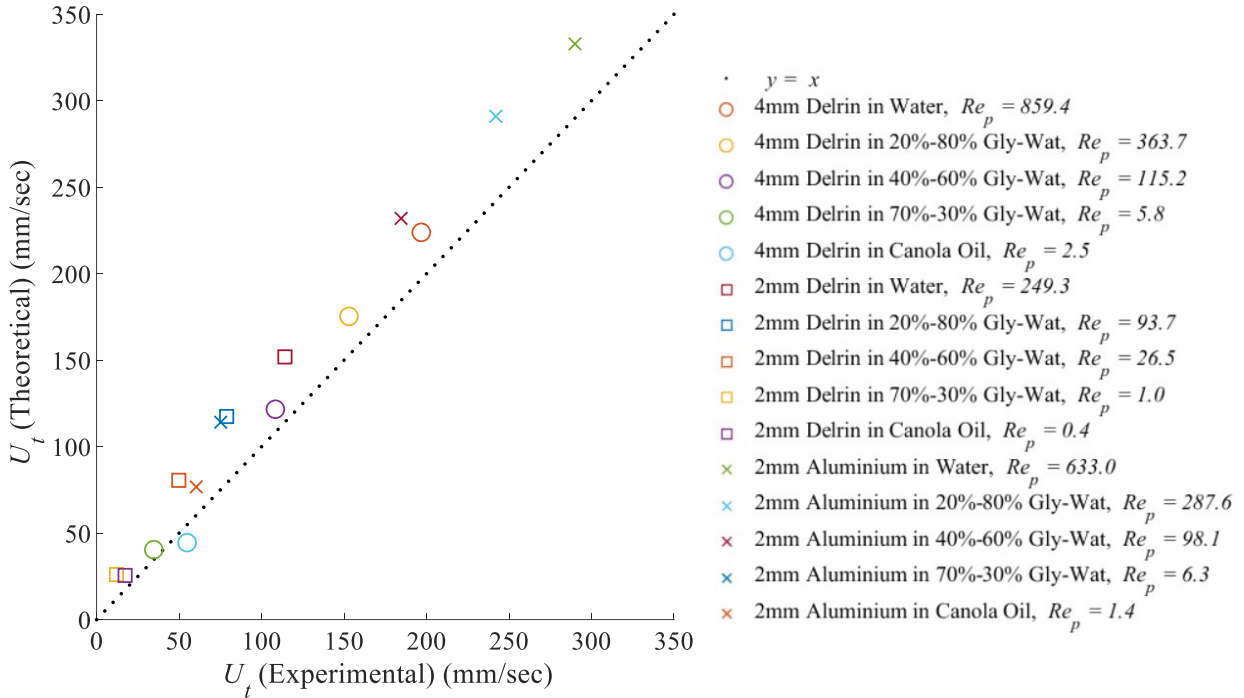


Figure 18 The theoretical terminal settling velocities, U_t (Theoretical), plotted against the experimental terminal settling velocities, U_t (Experimental), of the spherical particles that were discussed in section 3.6.3 and shown in Table 7. The dotted black line represents a plot of $y = x$ which was used to evaluate the agreement between the theoretical values and the experimental values of the terminal settling velocity. The maximum values of the measured density of delrin and aluminum were used to calculate U_t (Theoretical). The data points deviated further away from the $y = x$ line compared to the plot obtained in Figure 17 which was obtained using the minimum values of the measured density.

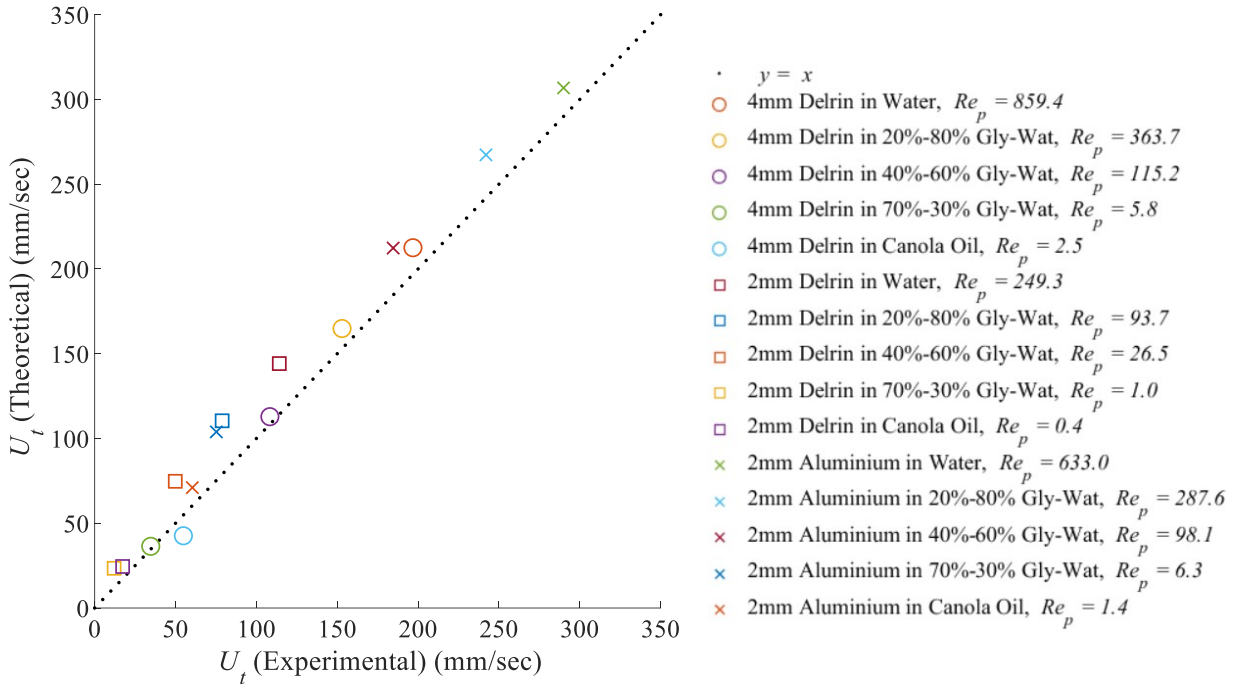


Figure 19 The theoretical terminal settling velocities, U_t (Theoretical), plotted against the experimental terminal settling velocities, U_t (Experimental), of the spherical particles that were discussed in section 3.6.3 and shown in Table 7. The dotted black line represents a plot of $y = x$ which was used to evaluate the agreement between the theoretical values and the experimental values of the terminal settling velocity. The median values of the measured terminal settling velocity of delrin and aluminium were used to calculate U_t (Theoretical). The experimental and theoretical data points had a closer fit compared to Figure 18 where the maximum value of the measured density was used to determine U_t (Theoretical).

3.6.5 Cylindrical Particles: Terminal Settling Velocity and the Coefficient of Drag Obtained from Experimental Data

The settling velocities, particle Reynolds numbers and coefficient of drag of the 1.30 mm diameter and 1.50 mm diameter cylindrical particles which were obtained from experimental data are shown in Table 8 and Table 9. The particle Reynolds number and the coefficient of drag were first calculated using the equivalent diameter in Table 8 and Table 9 and secondly using the ratio of the volume to the surface area of the particle as a length scale as shown in Section 8.43 – Appendix 43.

Table 8 This table shows the average terminal settling velocity within the terminal settling velocity region of the 1.30 mm Diameter 25 nylon cylindrical particles for each experimental condition. The terminal settling velocity were obtain from the plots of the particle displacement versus the particle velocity (magnitude) for the spherical particles as shown in Section 8.16 – Appendix 17 to Section 8.27 – Appendix 28. The particle Reynolds Number and the coefficient of drag were calculated based on the average terminal settling velocity values and the *equivalent diameter* of the particle. The coefficient of drag was calculated based on the model in [16].

Particle	Fluid	Average Terminal Settling Velocity, U_t (mm/s)	Particle Reynolds Number, Re_p	Coefficient of Drag, C_D
		25 particles	$\frac{\rho_f U_t d_p}{\mu_f}$	$\frac{24}{Re} [1 + A Re^B] + \frac{C}{[1 + \frac{D}{Re}]}$
Nylon	Water	43.62	70.82	1.36
Cylinders:	20%–80% Glycerol–Water	21.17	18.73	2.97
Dia. 1.30 mm	40%–60% Glycerol–Water	2.03	0.80	36.10
AR 1:1	Canola Oil	4.75	0.08	314.88
Nylon	Water	47.64	111.55	1.33
Cylinders:	20%–80% Glycerol–Water	26.51	33.81	2.19
Dia. 1.30 mm	40%–60% Glycerol–Water	3.31	1.89	18.02
AR 1:3	Canola Oil	7.63	0.19	144.65
Nylon	Water	48.11	133.55	1.70
Cylinders:	20%–80% Glycerol–Water	27.40	41.43	2.24
Dia. 1.30 mm	40%–30% Glycerol–Water	5.33	3.60	11.33
AR 1:5	Canola Oil	8.68	0.25	113.99

Table 9 This table shows the average terminal settling velocity within the terminal settling velocity region of the 1.50 mm Diameter 25 nylon cylindrical particles for each experimental condition. The terminal settling velocity were obtain from the plots of the particle displacement versus the particle velocity (magnitude) for the spherical particles as shown in Section 8.28 – Appendix 18 to Section 8.39 – Appendix 39. The particle Reynolds Number and the coefficient of drag were calculated based on the average terminal settling velocity values and the *equivalent diameter* of the particle. The coefficient of drag was calculated based on the model in [16].

Particle	Fluid	Average Terminal settling velocity, U_t (mm/s)	Particle Reynolds Number, Re_p	Coefficient of Drag, C_D
		25 particles	$\frac{\rho_f U_t d_p}{\mu_f}$	
Nylon	Water	46.76	87.58	1.23
Cylinders:	20%–80% Glycerol–Water	23.56	24.04	2.52
Dia. 1.50 mm	40%–60% Glycerol–Water	3.02	1.38	22.39
AR 1:1	Canola Oil	5.77	0.11	227.09
Nylon	Water	52.55	141.98	1.27
Cylinders:	20%–80% Glycerol–Water	28.57	42.05	1.95
Dia. 1.50 mm	40%–60% Glycerol–Water	6.71	4.42	8.99
AR 1:3	Canola Oil	8.94	0.25	108.98
Nylon	Water	51.61	165.31	1.69
Cylinders:	20%–80% Glycerol–Water	28.66	50.00	2.07
Dia. 1.50 mm	40%–60% Glycerol–Water	7.24	5.65	7.98
AR 1:5	Canola Oil	10.67	0.36	82.76

3.6.6 Values of the Length Scales and the Four Parameters (*A*, *B*, *C* and *D*) which were used to calculate the Coefficient of Drag

The four parameters *A*, *B*, *C* and *D* used to obtain the coefficient of drag in the Haider and Levenspiel model [16] are obtained from Equation 6, Equation 7, Equation 8 and Equation 9 as described in Section 2.1.2. The value of ϕ for the spherical particles is 1. However, ϕ varied for each aspect ratio for the cylinders. It was noted that the values of the ϕ of the 1.30 mm diameter and 1.50 mm diameter cylinders were the similar since the ratio of the surface area of the particle to the surface area of a sphere of equivalent volume were equivalent. Table 10 shows the values of ϕ , *A*, *B*, *C* and *D* for all the particles used in this study. Table 11 includes the values of the two length scales that were compared to calculate the particle Reynolds number and the coefficient of drag of the particles used in this study, i.e. (1) equivalent diameter and (2) the ratio of the volume to the surface area of the particle.

Table 10 The values of the four parameters A, B, C and D to determine the coefficient of drag using the Haider and Levenspiel model. The values of A, B, C and D dependent on the particle sphericity, ϕ , which is the ratio of the surface area of a sphere having the same volume as the particle, *s*, to the surface area of the particle, *S*.

	Particle Diameter d_p (mm)	Aspect Ratio	Surface area of the particle, <i>S</i> (mm ²)	Surface area of a sphere with equivalent volume as the particle, <i>s</i> (mm ²)	Particle Sphericity ϕ	A	B	C	D
Nylon Cylinders	1.30	1:1	7.96	6.96	0.87	0.236	0.583	0.986	1038.469
		1:3	18.58	14.47	0.78	0.297	0.530	1.509	381.346
		1:5	29.20	20.34	0.70	0.375	0.484	2.008	203.767
	1.50	1:1	10.60	9.26	0.87	0.236	0.583	0.986	1038.469
		1:3	24.74	19.27	0.78	0.297	0.530	1.509	381.346
		1:5	38.88	27.08	0.70	0.375	0.484	2.008	203.767
Delrin Spheres	4.00	-	50.26	50.26	1.00	0.186	0.653	0.437	7185.354
	2.00	-	12.57	12.57	1.00	0.186	0.653	0.437	7185.354
Aluminum Spheres	2.00	-	12.57	12.57	1.00	0.186	0.653	0.437	7185.354

Table 11 This table shows the values of the two length scales that were used to determine the coefficient of drag of the particles and the particle Reynolds number of the cylinders i.e. the equivalent diameter of the cylinders and the ratio of the volume to the surface area of the cylinders.

	Particle Diameter d_p (mm)	Aspect Ratio	Volume (mm ³)	Equivalent Diameter (mm)	Surface area of the particle, S (mm ²)	Volume/Surface Area (mm)
Nylon Cylinders	1.30	1:1	7.96	6.96	7.96	0.22
		1:3	18.58	14.47	18.58	0.28
		1:5	29.20	20.34	29.20	0.30
	1.50	1:1	10.60	9.26	10.60	0.25
		1:3	24.74	19.27	24.74	0.32
		1:5	38.88	27.08	38.88	0.34

3.6.7 The Equivalent Diameter as a Length Scale to determine the Particle Reynolds Number and Coefficient of Drag

Figure 20 illustrates the coefficient of drag plotted versus the particle Reynolds number using the values given in Table 7, Table 8 and Table 9. The data points are representative of the results that were obtained for all the particles at each experimental condition. The experimental data obtained from this study was superimposed onto the Haider and Levenspiel model at $\phi = 1, 0.906, 0.846, 0.806, 0.670$. The values of ϕ in Figure 20 matched the values used to plot the correlation in Haider and Levenspiel [16] whereby, a value of $\phi = 1$ is for spherical particles. The particle Reynolds Number was found by using the equivalent diameter of the particle. It can be observed that at lower values of the particle Reynolds number, i.e. between 10^{-2} and 10^1 in Figure 20, the cylindrical particles overlapped with the spherical particles more closely when compared to the particles have a particle Reynolds number $>10^1$.

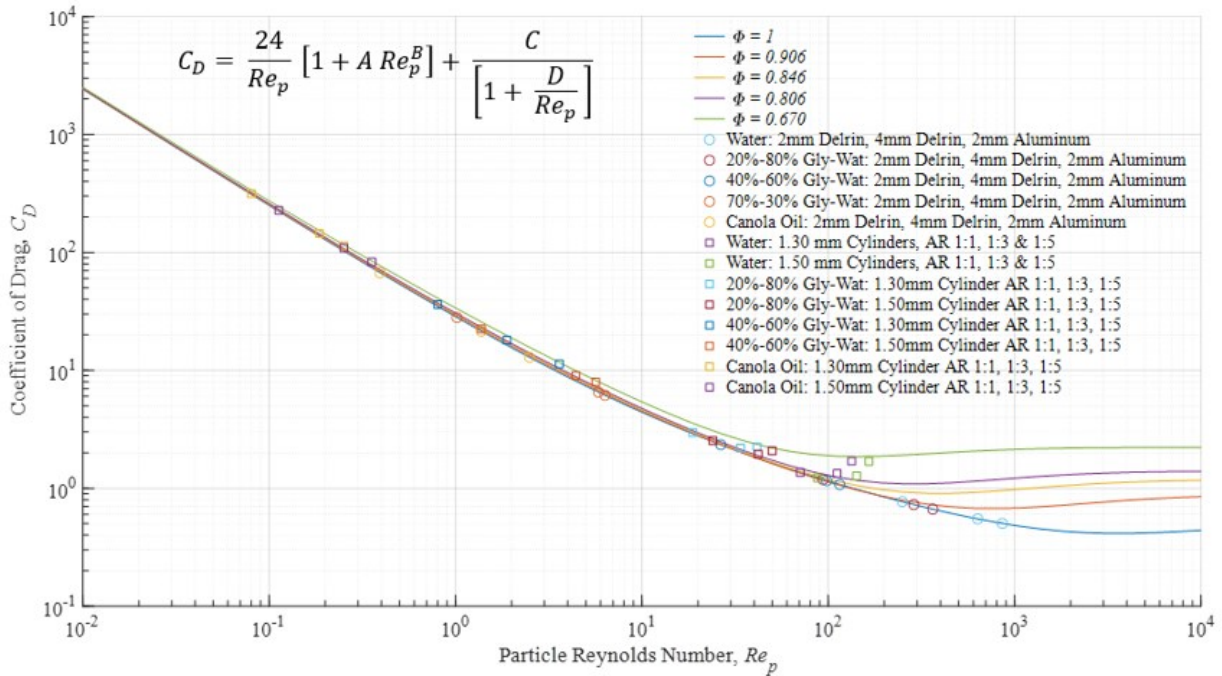


Figure 20 A plot of the coefficient of drag of the particles, C_D plotted versus the particle Reynolds number Re_p which were obtained from experimental data. The coefficient of drag and the particle Reynolds number were calculated based on the *equivalent diameter* of the particles as a length scale. The five curves were obtained from the Haider and Levenspiel model for the coefficient of drag, plotted for five different values of particle sphericity, ϕ i.e. 1, 0.906, 0.846, 0.806, 0.670. The particle sphericity is ratio of the surface area of a sphere having the same volume as the particle to the actual surface area of the particle.

The experimental data is replotted in Figure 21 for the cylindrical particles only with Reynolds number $>10^1$ in order to demonstrate the impact of the aspect ratio of the particles. It was observed that both the 1.30 mm diameter and 1.50 mm diameter cylinders with aspect ratio 1:1 overlapped with the coefficient of drag curve at $\phi = 1$. The cylindrical particles of aspect ratio 1:3 and 1:5 deviated further away from the $\phi = 1$. Figure 21 shows that using the equivalent diameter as a length scale does not result in an exact overlap of the non-dimensional parameters particles Reynolds number and the coefficient of drag.

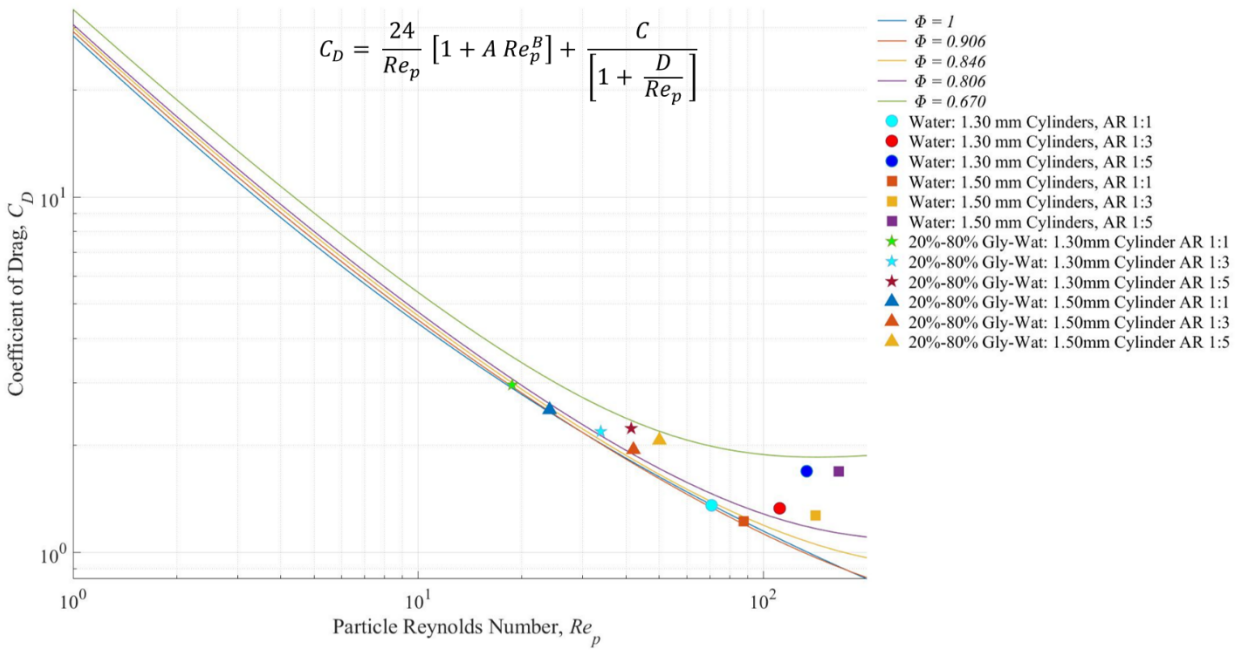


Figure 21 Illustrates the variation of the coefficient of drag, C_D , and the cylindrical particle Reynolds number Re_p with respect to the aspect ratio of the cylindrical particles. The coefficient of drag and the particle Reynolds number were calculated based on the *equivalent diameter* of the cylindrical particles as a length scale.

3.6.8 Volume/Area as a Length Scale to determine the Particle Reynolds Number and Coefficient of Drag

The particle Reynolds number and the coefficient of drag of the particles were then calculated using: (1) the ratio of the volume to the surface area of the particles as a length scale and (2) the average terminal settling velocity values obtained from experimental data given in Table 7, Table 18 and Table 19. The results are presented in Figure 22. It was observed that the non-dimensional plot overlapped more closely as compared to the plots in Figure 20 and Figure 21. This indicates that the ratio of the volume to the surface area of the particle is a more appropriate length scale to define the particle Reynolds number and the coefficient of drag of the cylindrical particles used in this study. The deviations that were observed for higher aspect ratio cylinders (i.e. 1:3 and 1:5) in Figure 21 were significantly reduced when using the ratio of the volume to the surface area of the particles as a length scale.

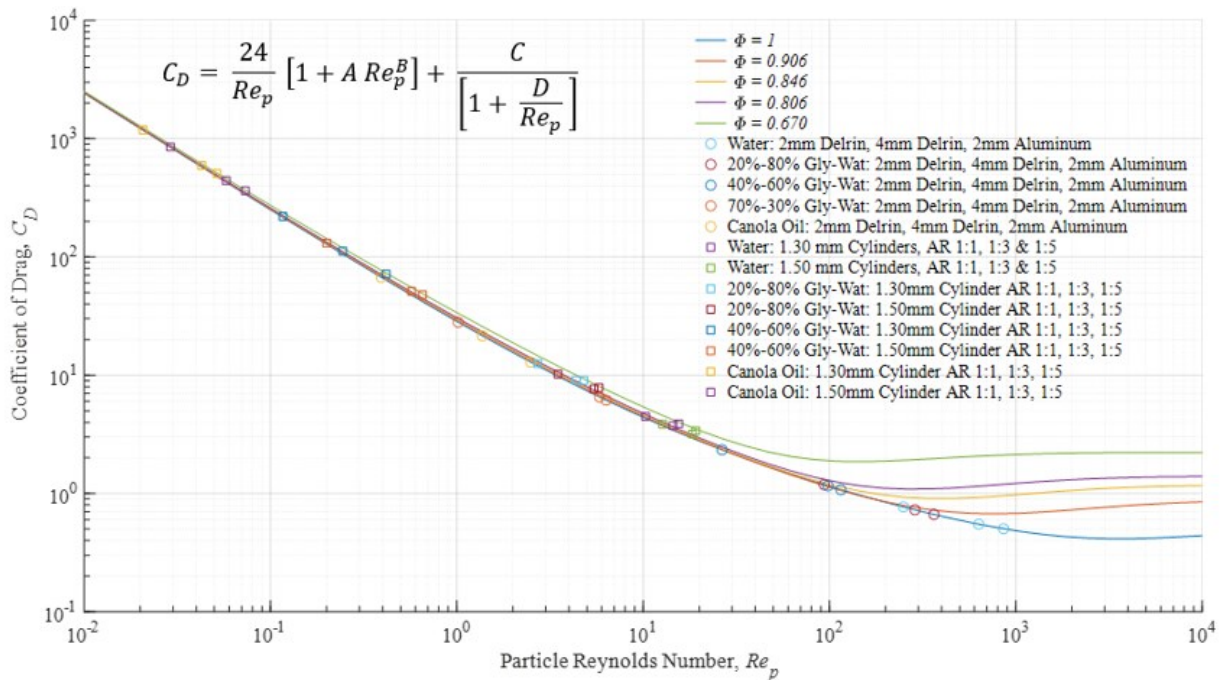


Figure 22 A plot of the coefficient of drag of the particles, C_D plotted versus the particle Reynolds number Re_p which were obtained from experimental data. The coefficient of drag and the particle Reynolds number were calculated using *the ratio of the volume to the surface area of the cylindrical particles as a length scale*. The data points overlapped more closely compared to Figure 20. The five curves were obtained from the Haider and Levenspiel model for the coefficient of drag, plotted for five different values of particle sphericity, ϕ i.e. 1, 0.906, 0.846, 0.806, 0.670. The particle sphericity is ratio of the surface area of a sphere having the same volume as the particle to the actual surface area of the particle.

The experimental data, in which the ratio of the volume to the surface area of the particles was used as a length scale, is replotted in Figure 23 in order to demonstrate the impact on the aspect ratio of the particles. It was observed that the particle Reynolds number was approximately seven times lower when the ratio of the volume to the surface area of the particles was used as a length scale, as shown in Table 18 and Table 19 compared to when the equivalent diameter was used as a length scale as shown in Table 8 and Table 9. Additionally, the coefficient of drag was approximately three times higher using the volume to the surface area was used as a length scale compared to using the equivalent diameter. Thereby all the experimental data points in the dimensionless plot in Figure 21 was shifted to the left as shown in Figure 23. The range of particle Reynolds numbers decreased by an order of magnitude with the ratio of the volume to the surface area of the particles was used as a length scale as shown in Figure 23 compared to Figure 21.

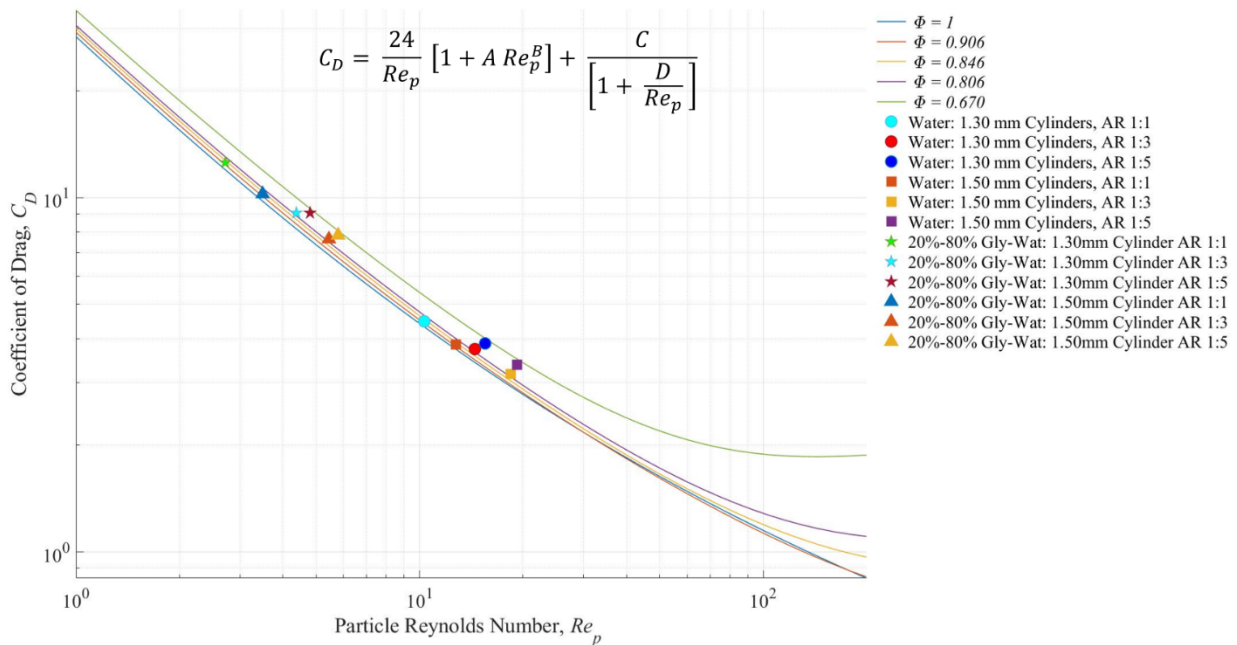


Figure 23 Illustrates the variation of the coefficient of drag, C_D , and the cylindrical particle Reynolds number Re_p with respect to the aspect ratio of the cylindrical particles. The coefficient of drag and the particle Reynolds number were calculated based on *the ratio of the volume to the surface area of the cylindrical particles as a length scale*. The data points overlapped more closely when compared to using the equivalent diameter as a length scale in Figure 21.

The cylindrical data obtained in Madhav and Chhabra [61] deviated from the Haider and Levenspiel model [16] for $Re_p > 100$ and $\phi > 0.55$ by almost 100% with the use of the sphericity

factor, φ as the length scale. The results of this thesis research shows that Haider and Levenspiel model [16] can be improved for cylindrical particles by using the ratio of the volume to the surface area of the particles as a length scale as was observed in Figure 23.

Figure 24 shows the particle trajectories within the terminal settling velocity region for the 4 mm delrin spherical particle and the 1.50 mm diameter cylindrical particle with aspect ratio of 1:5. The particle Reynolds number $Re_p = \frac{\rho_f U_t d_p}{\mu_f}$ is directly proportional to the terminal velocity and the length scale used to define the particles. It was observed that the cylindrical particle moved in a horizontal position within the region of terminal velocity as shown in Figure 24.

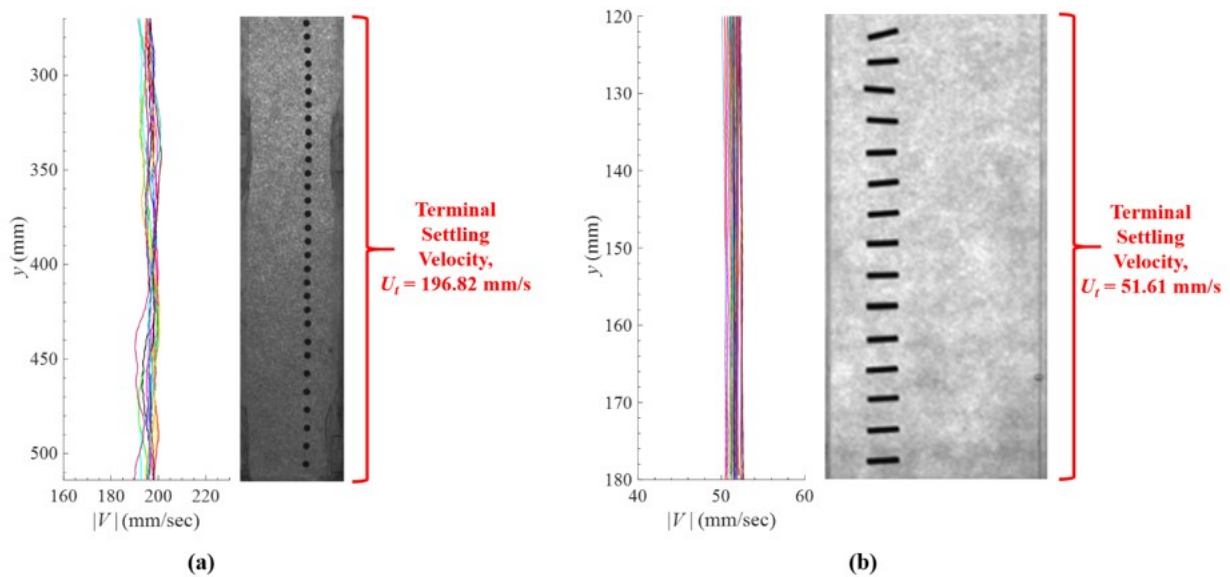


Figure 24 This figure focuses on the particle trajectories within the terminal settling regions for the spherical particle in Figure 15 and the cylindrical particle in Figure 16. It can be seen that the cylindrical particle moved in a horizontal position within the region of terminal velocity. This indicates that the equivalent diameter is not a suitable length scale to obtain the particle Reynolds number for long aspect ratio particles. Shows the particle trajectory of the 4 mm delrin spherical particle falling within water whereby the average terminal settling velocity of the particles was 196.82 mm/s. The plot of the magnitude of velocity was obtained from the 13 spherical particles shown in Figure 15 and (b) Shows the particle trajectory of the 1.50 mm diameter cylinders with an aspect ratio of 1:5 falling within water whereby the average terminal settling velocity of the particles is 51.61 mm/s. The plot of the magnitude of velocity was obtained from the 25 cylindrical particles shown in Figure 16. The raw image in (b) is wider as this experiment was performed in the shorter channel whereby the camera was closer to the test section compared to the tall channel used for the raw image in (a).

The cylindrical particle has a cross-sectional area of a long aspect ratio rectangle acting on the fluid when compared to the circular cross-section of the sphere. Thereby, the equivalent diameter is not a suitable length scale to model long aspect ratio cylindrical particles. This is because the equivalent diameter is used to model non-spherical particles as spheres and the trajectory of the cylindrical particle in Figure 24 shows that the spherical assumption would not account for the rectangular cross-section of the particle that is acting on the fluid within the terminal velocity region.

3.7 Conclusions

This chapter evaluated three parameters that are used to describe particle motion including: the terminal settling velocity, the coefficient of drag and the particle Reynolds number. Two shape parameters were considered to define the non-spherical particles used in this study. The results showed that the ratio of the volume to the surface area of the particles is a more appropriate length scale to define the particle Reynolds number and the coefficient of drag of the particles. This was noted as the non-dimensionalized plot overlapped more closely with the model of Haider and Levenspiel [16] when using the ratio of the volume to the surface area of the particles compared to using the equivalent diameter for the particle Reynolds number length scale. The equivalent diameter was more appropriate for the cylindrical particles with aspect ratio 1:1. However, the ratio of the volume to the surface area of the particles was appropriate for the cylindrical particles with aspect ratios 1:3 and 1:5 within the full range of particle Reynolds numbers that were used in this study.

4 The Motion of a Particle through Narrow Slots ¹

4.1 Introduction

The experimental results in the previous chapter demonstrates the occurrence of particle rotation in non-spherical particles in a wide open channel. In this chapter, particle rotation will be investigated in a channel geometry relevant to the industrial application SAGD. The analysis of the motion of single particles flowing through a narrow slot which was published in [81]. The objective of this study was to test the hypothesis that using the spherical assumption to model irregularly shaped particles is invalid.

The narrow slot used in the experiments was designed based on the geometry of the slots within the slotted liners used in SAGD operations. The kaolinite, montmorillonite, illite and mica clay particles which a found in oil sand reservoirs are typically non-spherical or irregularly shaped [29,30]. Thereby, two particle shapes were considered in the analysis including: a spherical particle and an irregularly shaped particle in order to demonstrate the impact of particle shape. A PSV measurement system was used to evaluate the motion of each particle within a single slot. The particle properties were derived and analyzed based on the two dimensional projected images obtained from the experiments. The flow field around the particles were evaluated.

¹ Components of this chapter have been published in:

L. Kinsale, D.S. Nobes, Development of an online system to measure sand production through mini-slots in SAGD operations using PSV, in: Okanagan Fluid Dyn. Meet. Kelowna, Br. Columbia, Canada. August 21-24, 2017: pp. 182–186

4.2 Description of the Fluid, Particles and the Flow Geometry

Two particles were used in this study: (1) spherical glass beads with a diameter of 3.16 mm and (2) irregularly shaped glass beads with equivalent diameter ~ 2.5 mm. These particles were individually released from the particle inlet into a vertically mounted flow cell and allowed to move in the direction of gravity in a stationary fluid as shown in Figure 25. The flow cell was initially filled with a 70%–30% glycerol–water solution. The glycerol–water solution was seeded with 20 μm diameter polystyrene spherical microbeads tracer particles (Dynoseeds TS20, Microbeads AS) in order to track the velocity of the surrounding fluid as the particles fell in the direction of gravity. The density and dynamic viscosity of the fluid were 1191.6 kg/m^3 and 0.0298 Ns/m^2 , respectively [82].

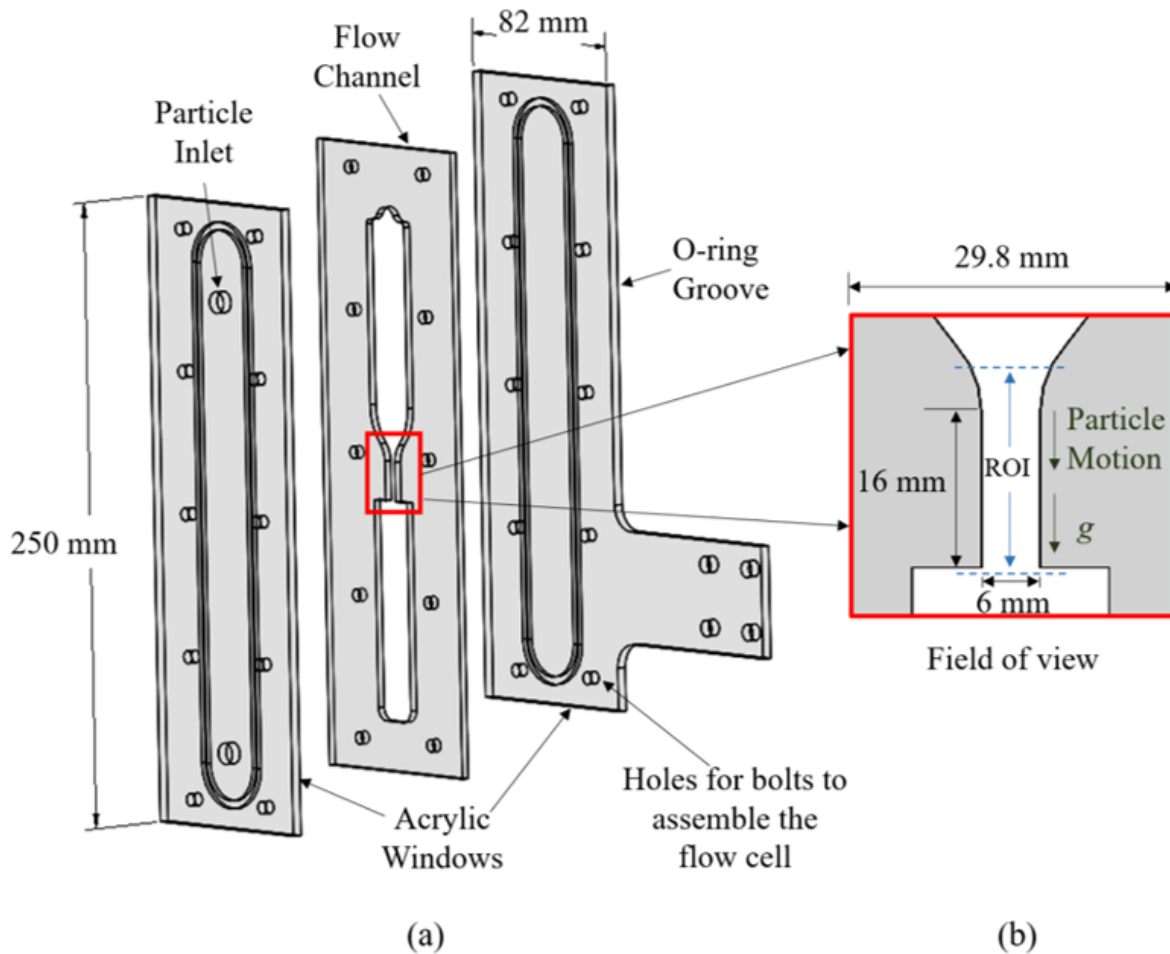


Figure 25 (a) A schematic of the exploded flow cell assembly and (b) An enlarged image to clearly highlight the dimensions of the field of view. The section within the dashed red lines is the region of interest (ROI) which was considered in the analysis of the single particle motion.

The flow cell is a sandwich of two windows and one flow channel which were all made of acrylic sheets as illustrated in Figure 25 (a). The transparency of the acrylic sheets allowed optical access to particle motion within the fluid. The flow channel was placed in between the two optical windows and an o-ring was used to seal the fluid within the flow channel as shown in Figure 25 (a). The assembly in Figure 25 (a) was then bolted together and filled with the fluid. The test section or field of view is highlighted within the red box in Figure 25 (b). The depth of the flow channel was 6.35 mm. The particle motion within the region of interest (ROI), as highlighted within the blue dashed lines in Figure 25 (b), was considered in the analysis. The ROI contained a single slot with a width of 6 mm and a height of 16 mm with a converging inlet to ensure that the particle would flow into the ROI.

4.3 Optical Experimental Set-up

The PSV experimental set-up shown in Figure 26 was used to capture the motion of the particles within the flow cell. The set-up consisted of a high speed camera (SP-5000C-PMCL, JAI) with 2560×2048 pixel resolution coupled with a macro lens (105mm f/2.8 DG Macro, Sigma). The specifications of the imaging system are given in Table 12. A function generator was used in conjunction with the camera to acquire images of the moving particles. A continuous LED light source (Model BX404-520, Advanced Illumination Inc.) was used to provide back illumination to the field of view. The camera captured the motion of the particles at a rate of 88 frames per second as the particles fell in the direction of gravity as shown in Figure 26.

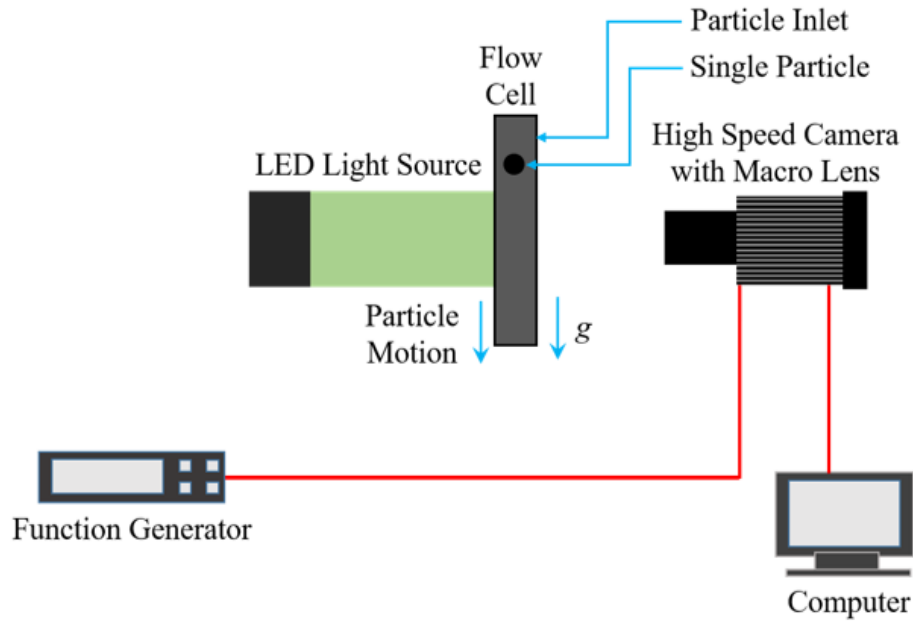


Figure 26 A schematic of the Particle Shadowgraph Velocimetry (PSV) experimental set-up for the single particles

Table 12 Specifications of the PSV system, Figure 26, which was used to study the motion of single particles within the near-slot region in SAGD operations

Camera sensor size	2560 × 2048 pixels
Field-of-view ($w \times h$)	29.8 × 23.8 mm
Magnification	0.43
Digital resolution	0.012 mm pixels ⁻¹
Image acquisition frequency	88 fps

4.4 Image Processing

Approximately 250 raw images were captured for each data set of the particle falling in the direction of gravity as shown in Figure 26. The following sub-sections describe the image processing steps that were used to analyze the data in the 250 images. In-house processing codes (Matlab, The MathWorks Inc.) together with a commercial software (Davis 8.3.1 LaVision GmbH) coupled with in-house processing scripts were used to: (1) quantify the characteristics of the particles and (2) quantify the velocity field around the particle.

4.4.1 Particle Characterization

The raw images were processed to determine: the diameter of the sphere, the equivalent area diameter of the irregularly shaped particle and the aspect ratio of the particles. These processing steps were performed using a commercial software (Davis 8.3.1 LaVision GmbH) whereby a recognition filter was used to detect the particles. This filter detected the particles based on a defined minimal particle size and aspect ratio. Within the illuminated test-section, the particle appeared dark and the 70%–30% glycerol–water solution which was seeded with 20- μm diameter tracer particles appeared bright. Thereby, the particles were also detected based on the difference between the intensity counts within the 2D projected area of the particle compared to that of the surrounding fluid.

The properties of the particles were observed for every frame during the motion of the particle. Thereby the equivalent diameter and aspect ratio was calculated in each vertical position as the particle fell. This was done using the software. Figure 27 shows a sample processed image of the spherical particle. The diameter of the sphere was calculated to be 3.213 mm and the yellow lines (not drawn to scale) represents the lines that were used to calculate the aspect ratio of the sphere as shown in Figure 27. Figure 28 shows a sample processed image of the irregularly shaped particle. The equivalent diameter of the 2D projected area of the irregularly shaped particle is 2.66 mm and the yellow lines (not drawn to scale) represent the shortest and longest length of the particles which were used to determine the aspect ratio of the particles. The yellow circle (not drawn to scale) represents the equivalent diameter of the irregularly shaped particle.

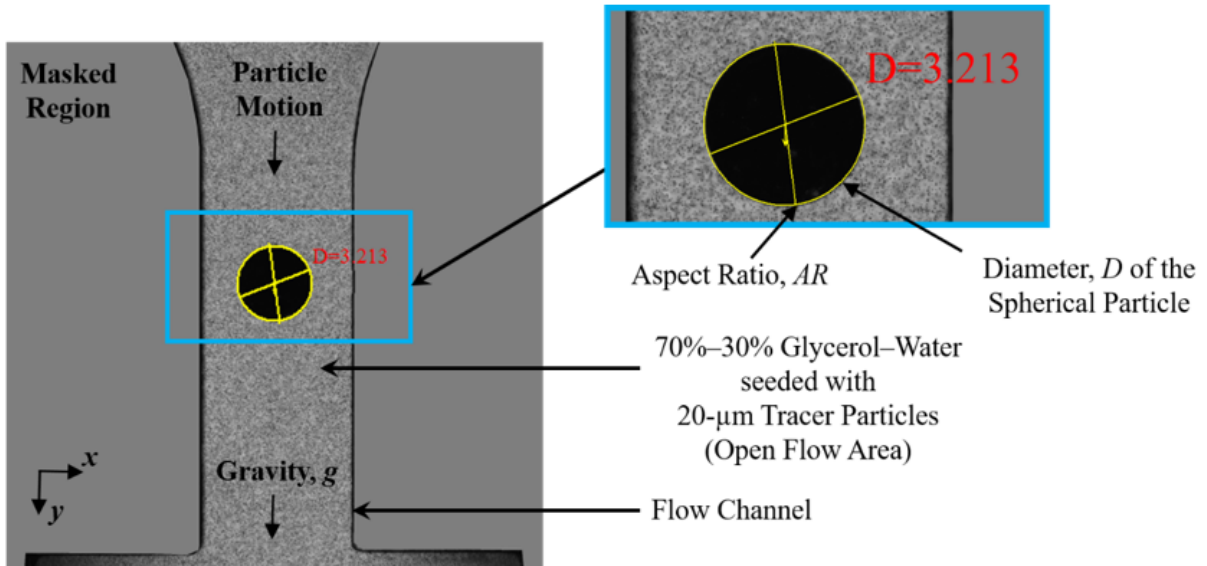


Figure 27 A sample processed image of the spherical glass beads particle. The particle fell in the direction of gravity within a 70%–30% glycerol–water solution. The diameter of the sphere in this image is 3.213 mm. The yellow lines highlight the shortest and longest lengths that were used to determine the aspect ratio of the particle. The outline/diameter of the particle is also highlighted with the yellow circle.

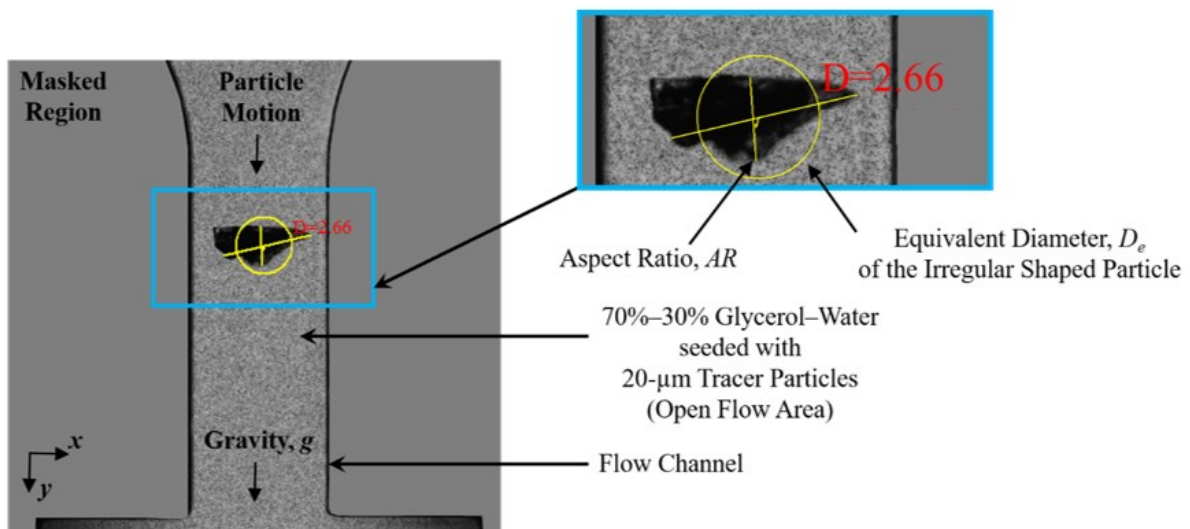


Figure 28 A sample processed image of the irregularly shaped glass beads particle. The particle fell in the direction of gravity within a 70%–30% glycerol–water solution. The equivalent diameter of the particle in this image is 2.66 mm. The yellow lines highlight the shortest and longest lengths that were used to determine the aspect ratio of the particle. The equivalent diameter of the particle is also highlighted with the yellow circle.

4.4.2 The Velocity Field of the Surrounding Fluid

The velocity field of the fluid around the surrounding falling particle was also calculated in commercial software (DaVis 8.3.1, LaVision GmbH). A geometric polygon mask was used to mask out the regions outside of the open flow area as shown in Figure 27 and Figure 28. The particle also appeared dark on a bright background. Therefore the intensity counts below a specified value was set to zero in order to mask out the particle so that the velocity calculations would capture only the motion of the surrounding fluid. A particle image velocimetry (PIV) time series multi-pass cross-correlation algorithm was applied to consecutive images to calculate the velocity vector field. Elliptical interrogation windows with 87% overlap were used to perform the cross-correlation. First, an interrogation window size of 128×128 pixels were used to capture the larger changes in the fluid velocity. Then an interrogation window size of 64×64 pixels were applied to sequential images to complete the cross-correlation. The fluid velocity vector field that was obtained from this software was plotted using an in-house post-processing code using functions found in [83] (PIVMat Matlab, The MathWorks Inc.).

4.5 Experimental Results and Analysis

Processed images were used to obtain the equivalent diameter and aspect ratio of the particles in each subsequent frame as the particles fell within the fluid. This section also analyzes the velocity vector field of the surrounding fluid around the particle. The results in this section is aimed to evaluate if the spherical assumption is adequate to model the motion of non-spherical particles within confined flow geometries as can be found in SAGD operations.

4.5.1 The Equivalent Diameter and the Aspect Ratio of the Particles

The equivalent diameter and the aspect ratio were plotted against the vertical y location of the particle which was non-dimensionalized with the length, l , of the slot as shown in Figure 29 and Figure 30 respectively. The results shown in Figure 29 indicate that the diameter of the sphere remains constant throughout all the images. This is expected as the sphere does not change shape or size as it falls through the fluid. However, the slight variation in the diameter plot for the sphere in Figure 29 can be attributed to the uncertainty in the image processing technique.

Conversely, there was significant variation in the equivalent diameter plot for the irregularly shaped particle in Figure 29. This variation occurred because the 2D projected area of the irregularly shaped particle changed in each frame. This is evidence of particle rotation. Similar trends were observed in the aspect ratio plots of both particles as shown in Figure 30. The aspect ratio of the spherical particles in Figure 30 are slightly less than 1, this can be possibly be due to having insufficient pixels within the 2D projected image of the particle to adequately describe the shape of the particle [84]. The irregularly shaped particle displayed much more variation than the spherical particle in Figure 30. This is also evidence of particle rotation in the irregularly shaped particle.

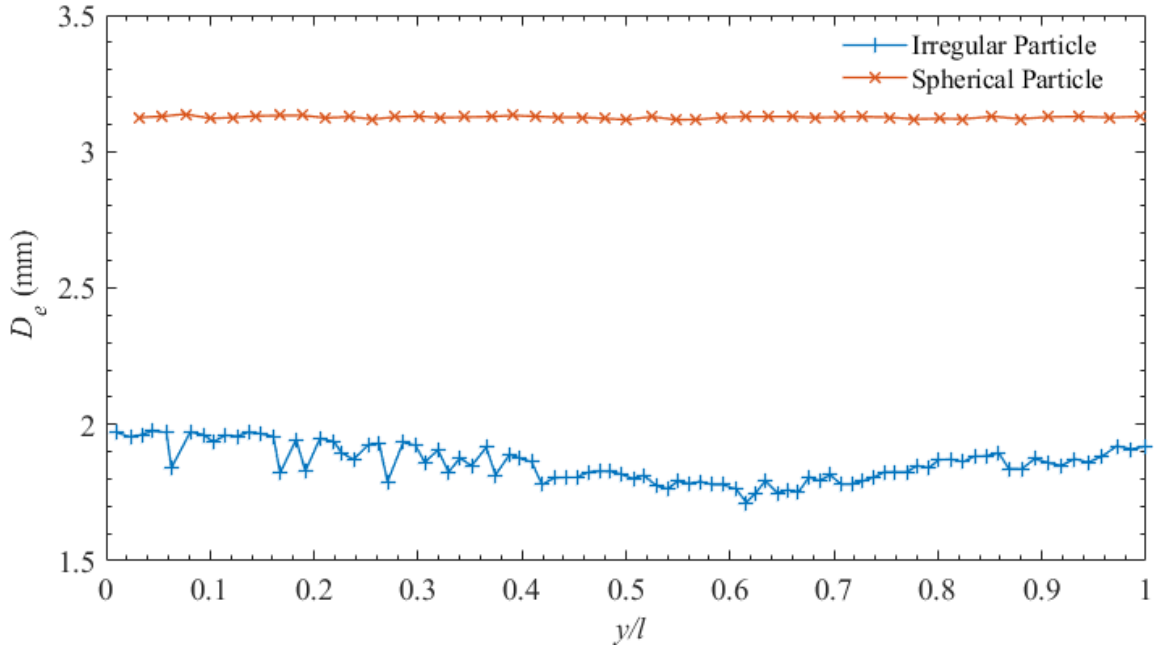


Figure 29 The equivalent diameter, D_e of both the irregularly shaped particle and the spherical particle. For each particle D_e was calculated for every subsequent frame as the particles fell through the fluid. D_e was plotted versus the vertical y location of the particle which was non-dimensionalized with the length, l , of the slot.

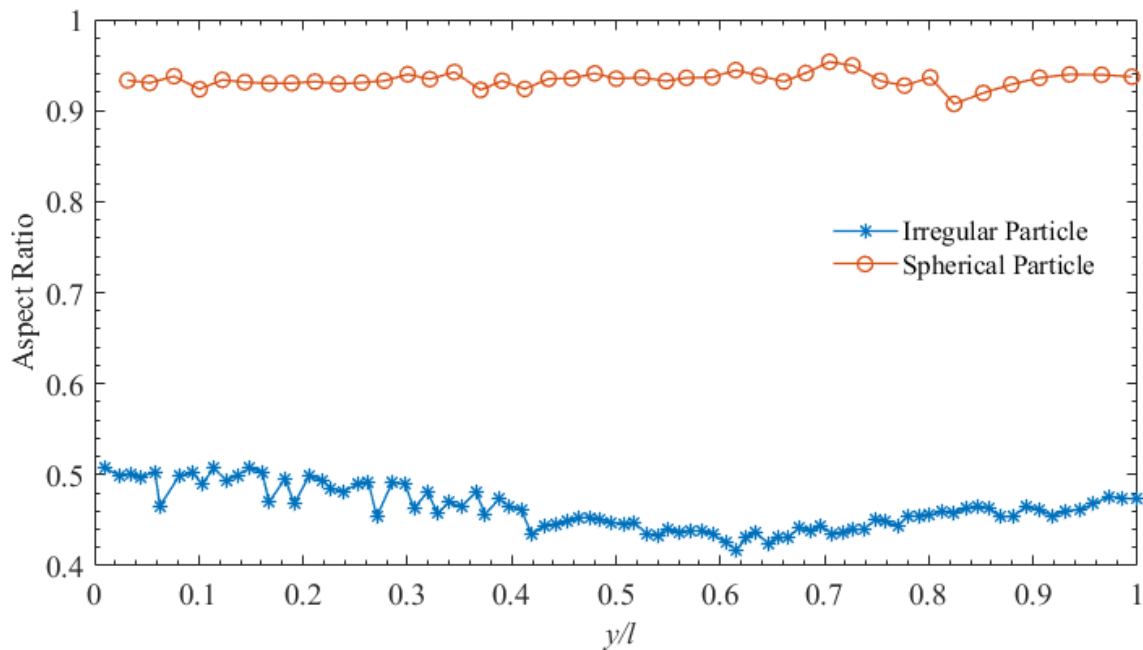


Figure 30 The aspect ratio of both the spherical particle and the irregularly shaped particle. For each particle the aspect ratio was calculated for every subsequent frame as the particles fell through the fluid. The aspect ratio was plotted versus the vertical y location of the particle which was non-dimensionalized with the length, l , of the slot.

4.5.2 The Velocity Field of the Surrounding Fluid around the Particles

Figure 31 and Figure 32 shows the velocity profiles of the surrounding fluid around the spherical particle and the irregularly shaped particle respectively at four different vertical locations. For the spherical particle, the maximum flow velocity occurred at similar places at the four different locations, that is, at the left side and at the right side of the particle as shown in Figure 31. The velocity field around the spherical particle were also very similar, the slight variations may be due to the difficulty in measuring the flow field closest to the boundary of the particle or possibly due to particle rotation in the out of plane direction. The variations in the velocity profile around the spherical particle could be attributed to the subtle particle movement in the x -direction toward the walls of the slot. The velocity flow field around the spherical particle in Figure 31 was also somewhat symmetrical at the four different locations.

Conversely at all four locations, the velocity profiles around the irregularly shaped particles in Figure 32 were not symmetrical. The spherical assumption indicates that the velocity field of the fluid surrounding the particle should be symmetrical. However, Figure 32 illustrates that particle shape and rotation impacts the flow field around the particle which resulted in different non-symmetrical velocity profiles at the four different vertical locations. Thereby, using the spherical assumption to model the motion of irregularly shaped particles within confined flow geometries as can be found in SAGD operations is inadequate. It was also observed that the magnitude of the velocity of the surrounding fluid was generally less for the irregularly shaped particle compared to the spherical particle. Additionally, the distribution of the velocity field around the irregularly shaped particle varied at each vertical position in Figure 32. Whereby, the maximum velocity occurred closest to the sharpest edge of the particle, which moved in every frame as the particle rotates.

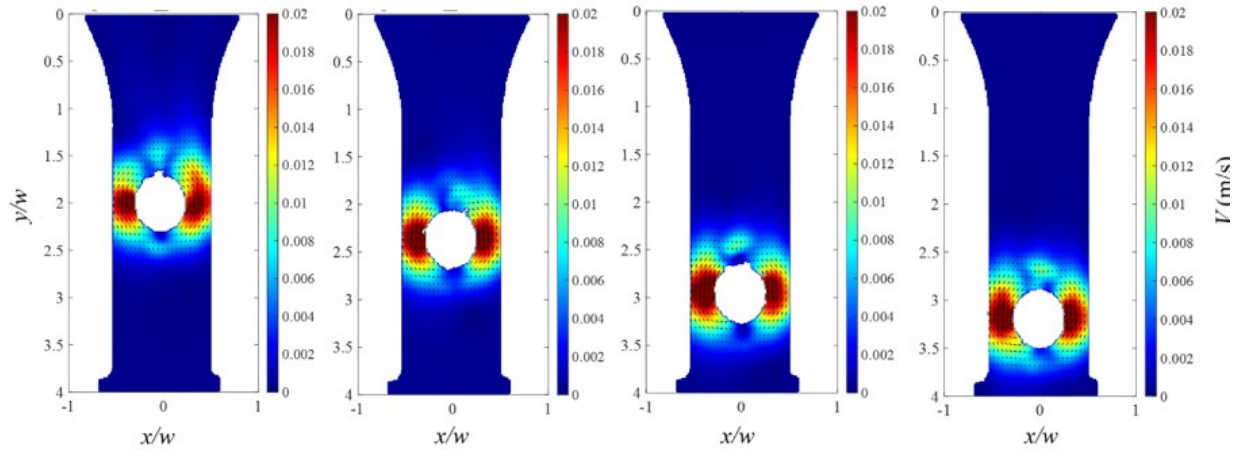


Figure 31 The velocity field of the surrounding fluid around the spherical particle shown at four (4) vertical locations as the particle fell through the fluid. The diameter of the sphere is 3.213 mm.

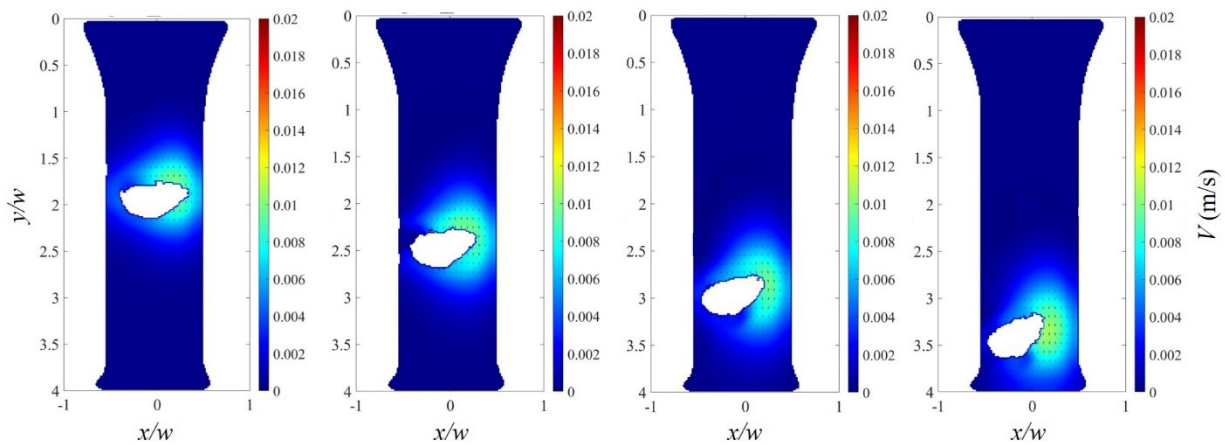


Figure 32 The velocity field of the surrounding fluid around the irregularly shaped particle shown at four (4) vertical locations as the particle fell through the fluid. The equivalent diameter of the irregularly shaped particle is 2.66 mm.

Figure 33 and Figure 34 zooms in on the velocity vector field of the surrounding fluid around the spherical particle and the irregularly shaped particle at the four different locations shown in Figure 31 and Figure 32 respectively. For the spherical particle, the distribution of the magnitudes of the fluid velocity as indicated by the color map and the direction of the velocity vectors indicated by the black arrows in Figure 33 were similar at the four vertical locations, (a), (b), (c) and (d). A symmetrical velocity profile was also observed at each location.

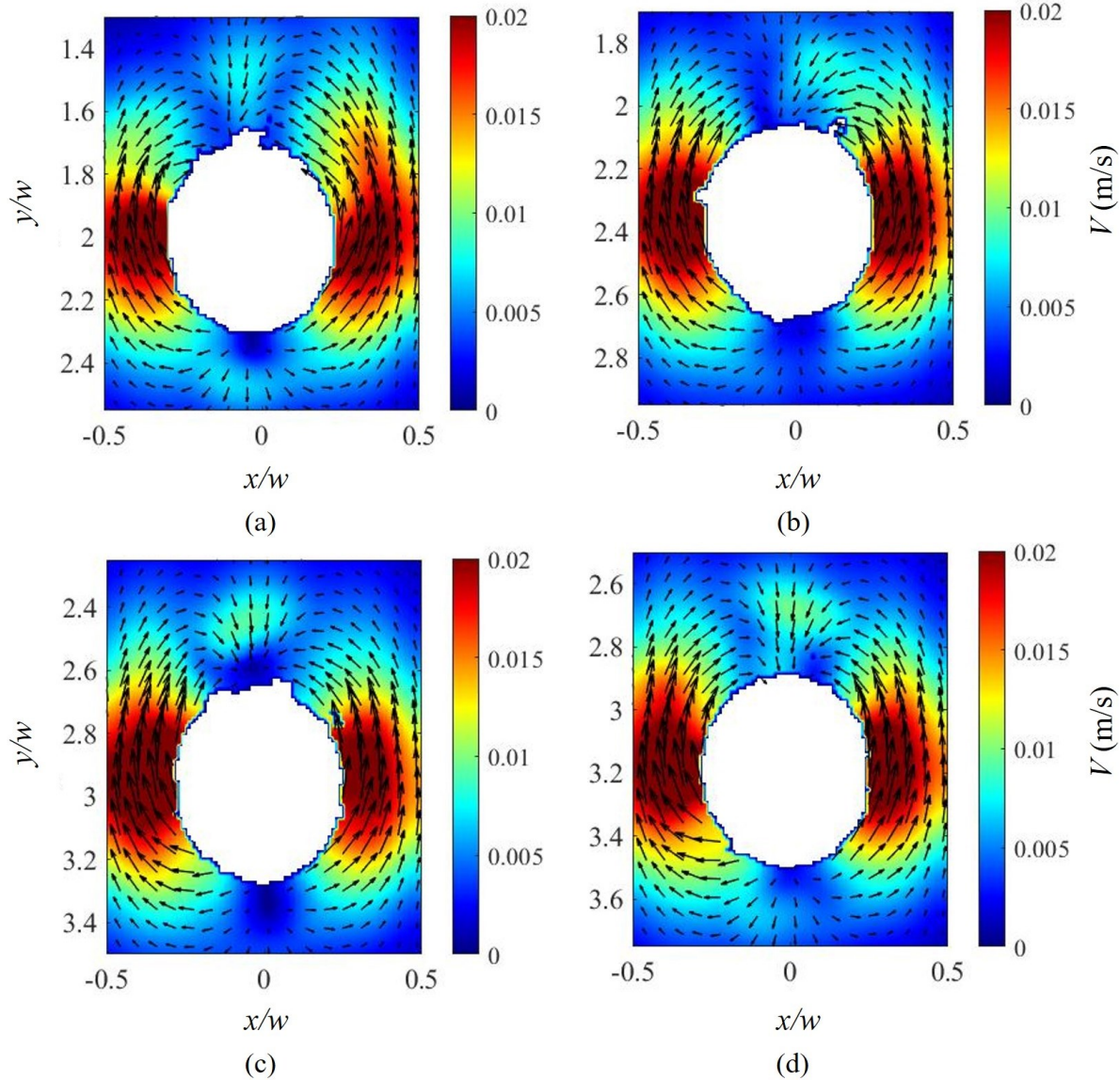


Figure 33 Illustrates the velocity vector field of the surrounding fluid within a localized region around the spherical particle at the four (4) different vertical locations (a), (b), (c), and (d) corresponding to four (4) positions shown in Figure 31 as the particle fell within the fluid.

The length of the velocity vectors of the surrounding fluid around the irregularly shaped particle which are indicated by the black arrows in Figure 34 are shorter compared to the velocity vectors around the spherical particle in Figure 33. This shows that the overall velocity of the surrounding fluid was less around the irregularly shaped particle compared to the spherical particle. Additionally, the distribution of the magnitudes of the fluid velocity around the irregularly shaped particle as indicated by the color map in Figure 34 were different at the four vertical locations, (a), (b), (c) and (d) as the particle rotates. Also a slightly different non-symmetrical velocity profile

was observed at each location. The results in Chapter 3 showed that the drag coefficient of non-spherical particles falling in a wide-open flow area can be modelled as spheres if the correct length scale is used. However, for industrial applications such as SAGD operations which consist of confined flow geometries, using the spherical assumption to model irregularly shaped particles will be inadequate to capture significant aspects of particle motion. This was noted as Figure 33 and Figure 34 demonstrate the impact of particle shape and rotation on the surrounding fluid flow field.

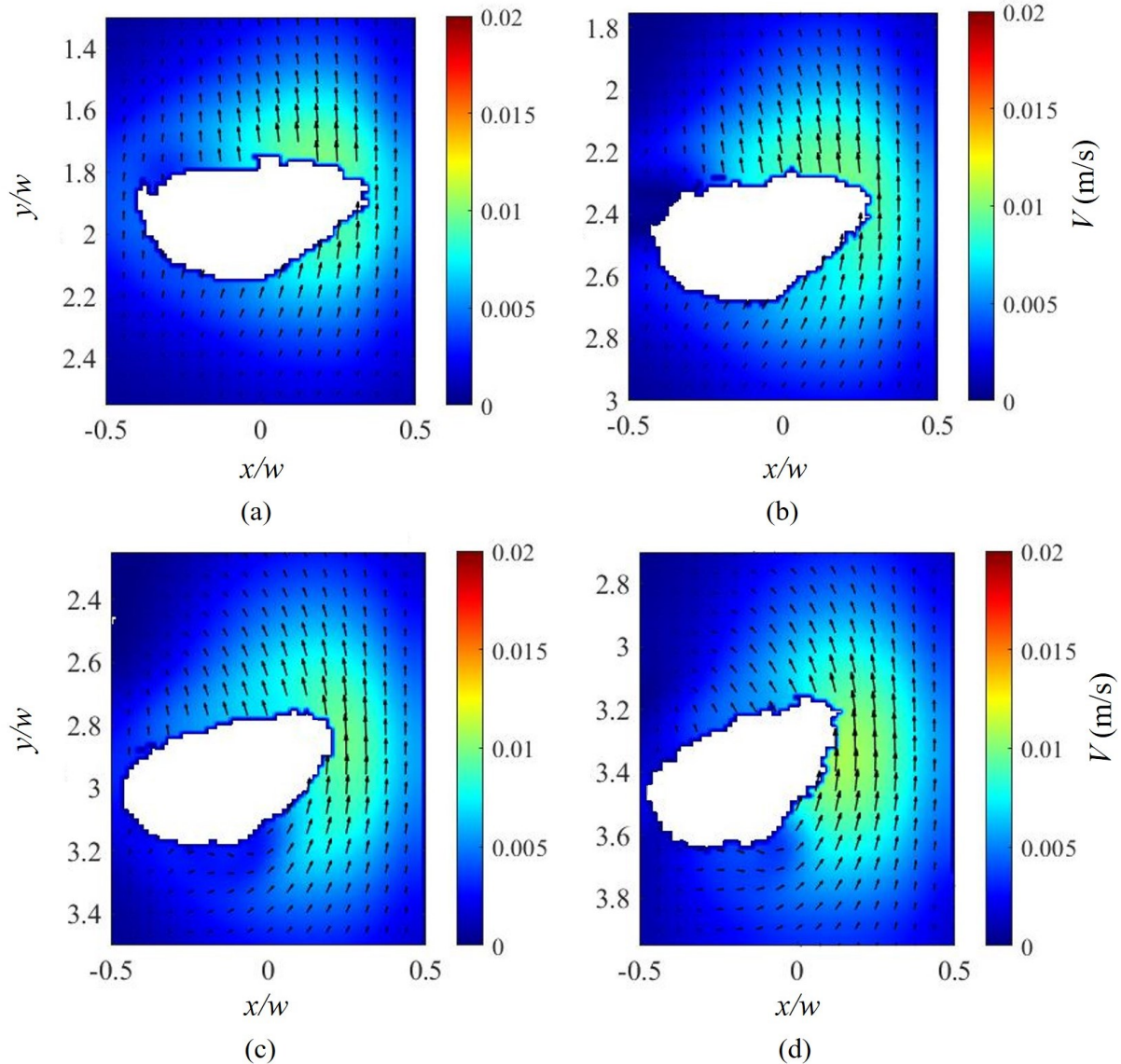


Figure 34 Illustrates the velocity vector field of the surrounding fluid within a localized region around the irregularly shaped particle at the four (4) different vertical locations (a), (b), (c), and (d) corresponding to four (4) positions shown in Figure 32 as the particle fell within the fluid.

4.6 Conclusion

This chapter evaluated whether the use of the spherical assumption is adequate to model the motion of non-spherical particles within confined flow geometries in an industrial application known as SAGD. An experimental analysis was performed to evaluate the motion of a spherical particle as well as an irregularly shaped particle falling within a single narrow slot flow geometry which is applicable in sand control devices in SAGD operations. The analysis of particle motion through the single narrow slot demonstrated the importance of considering the exact shape of the particle. The presence of particle rotation was confirmed by the fluctuation in the plots of the equivalent diameter and the aspect ratio of the irregularly shaped particle falling through the fluid.

Previously, the analysis in Chapter 3 was performed in an open flow geometry which was more than ten times wider than the diameter of the particles. The results showed that the drag coefficient of non-spherical particles can be modelled as spheres if the correct length scale is used. However, in this chapter, the results demonstrated the limitations of using the spherical assumption to model the motion of irregularly shaped particles a confined flow geometry. It was observed that for irregularly shaped particles, as small as 2.66 mm, the spherical assumption will not account for the impact of particle shape and rotation on the surrounding fluid flow field. The spherical assumption also implies that the velocity profile around the particle should be symmetrical. However, a non-symmetric velocity profile was also observed around the irregularly shaped particle. This chapter simplifies particle motion within SAGD operation by analyzing individual particles falling within a slot. However, in real conditions in SAGD operations, multiple particles are transported with the fluid flow, therefore the occurrence of particle rotation of non-spherical particles which affects the flow field around the particle can also influence the transport of near-by particles as well.

5 Particle Transportation and Deposition within a Porous Network into a Narrow Slot²

5.1 Introduction

The previous chapter highlighted the significance of particle shape and rotation using a single particle within an open flow geometry. This chapter is an experimental study of multiple particles flowing within a porous network into a narrow slot which is a replication of the flow geometries found in SAGD. The results of this study was published in [11]. The objective of this study is to identify important features of particle transport that need to be included in any modelling effort.

To provide a relevant set of conditions, this investigation explores the behavior of solid particles transported by a viscous fluid in a complex geometry. The geometry is a simulated 2D porous media with a region of converging flow into a narrow slot. To characterize particle shape and motion of the discrete, transported phase as well as the continuous phase, PSV and several image processing techniques were employed. The continuous phase was seeded with tracer particles and two types of larger particles including spherical and irregularly shaped particles of greater densities were used to represent the fines found in oil sand reservoirs.

The goal is to identify the various factors that can impact particle deposition or build-up within a flow area by analyzing the velocity vector field of the continuous phase as well as the general motion of individual particles. A complete understanding of the rotation of particles is a complex task that requires calculation of the forces acting on the body and the surface of each particle, which is beyond the scope of this research. Here however, the problem was simplified and three parameters were identified and investigated that could influence particle rotation, namely the initial particle orientation, the location of the particle in the flow relative to solid bodies, and the shape of the particle.

² Components of this chapter have been published in:

L.K. Kinsale, M.A. Kazemi, J.A.W. Elliott, D.S. Nobes, Transportation and deposition of spherical and irregularly shaped particles flowing through a porous network into a narrow slot, *Exp. Therm. Fluid Sci.* 109 (2019) 109894. doi:10.1016/j.expthermflusci.2019.109894

5.2 Description of the Fluid, Particles and the Flow Geometry

This experimental study includes both velocity measurements of the continuous phase using only tracer particles and build-up tests using larger spherical and irregularly shaped particles. Three geometries were used including an open slot, and two inlet conditions aimed to simulate porous media using cylindrical pillars and diamond shaped pillars as shown in Figure 35. For every geometry, experiments were performed at three flow conditions of different Reynolds numbers (Re) 0.1, 1 and 10. These Re correspond to flow rates (Q) of 0.3, 3 and 30 ml/min. Therefore, a total of 27 experimental runs were performed in this study.

The flow conditions in the experiments were determined by matching the Re at the entrance of the slot. The Re which is defined by ($Re = \rho UL/\mu$) was calculated based on the density (ρ) and dynamic viscosity (μ) of the liquid at room temperature (≈ 24 °C), the width of the slot (L) and the average velocity in the slot ($U = Q/A$). The density and dynamic viscosity of the 70%–30% glycerol–water solution were 1191.6 kg/m³ and 0.0298 Ns/m², respectively [82]; the width of the slot (L) was 1 mm and depth 2 mm giving a cross-sectional area of the slot (A) of 2 mm². The average fluid flow velocities in this study were: 0.0025 m/s, 0.025 m/s and 0.25 m/s for $Re = 0.1$, 1 and 10 respectively.

The experiments were performed with three different types of particles: 20- μ m diameter polystyrene spherical microbeads (Dynoseeds TS20, Microbeads AS) tracer particles to determine the continuous phase fluid velocity, and 80- μ m diameter spherical glass beads and 40- μ m diameter silicon carbide irregularly shaped particles (AGSCO Corp.) to mimic particle transport and to perform the build-up tests. The particles mixed in the fluid were injected from the top of the flow cell at constant flow rates using a syringe pump (70-2002 PHD 2000, Harvard Apparatus Inc.), in the same direction as gravity. Figure 35 shows the flow cell assembly and the three different geometries used in the experiments.

Each flow cell was a sandwich of a flow channel and a transparent window to allow optical access. The window, as shown in Figure 35 (a) was made of a 6.35-mm thick acrylic sheet and fabricated with a laser cutter (VLS3.50, Universal Laser). The flow channel shown in Figure 35 (a) and (b) was manufactured using an additive manufacturing process (Form 2, Formlabs Inc.) with a clear photopolymer resin. The arranged slots shown in Figure 35 (b) were included into the top section

of the flow channel to allow distribution of the solid particles across the field of view. Three different configurations of the flow cell were used in this study as shown in Figure 35 (c). These include: (i) an open slot, (ii) equally spaced cylindrical pillars of 1-mm diameter and 2-mm depth, and (iii) equally spaced diamond shaped pillars circumscribed into 1 mm diameter circles and 2 mm in depth. These geometries were selected to study the phenomena that occur in the near-slot region in the SAGD oil recovery process. The open slot geometry was compared to the simulated porous media geometries to investigate the effect of the presence of the simulated porous media on the flow field and particle build-up. The circular pillars and diamond shaped pillars were included to evaluate whether a change in the shape of the simulated porous network would significantly impact the flow field and the deposition of particles within the near-slot region. Section 8.47–Appendix 47 presents detailed drawings of the flow cells shown in Figure 35.

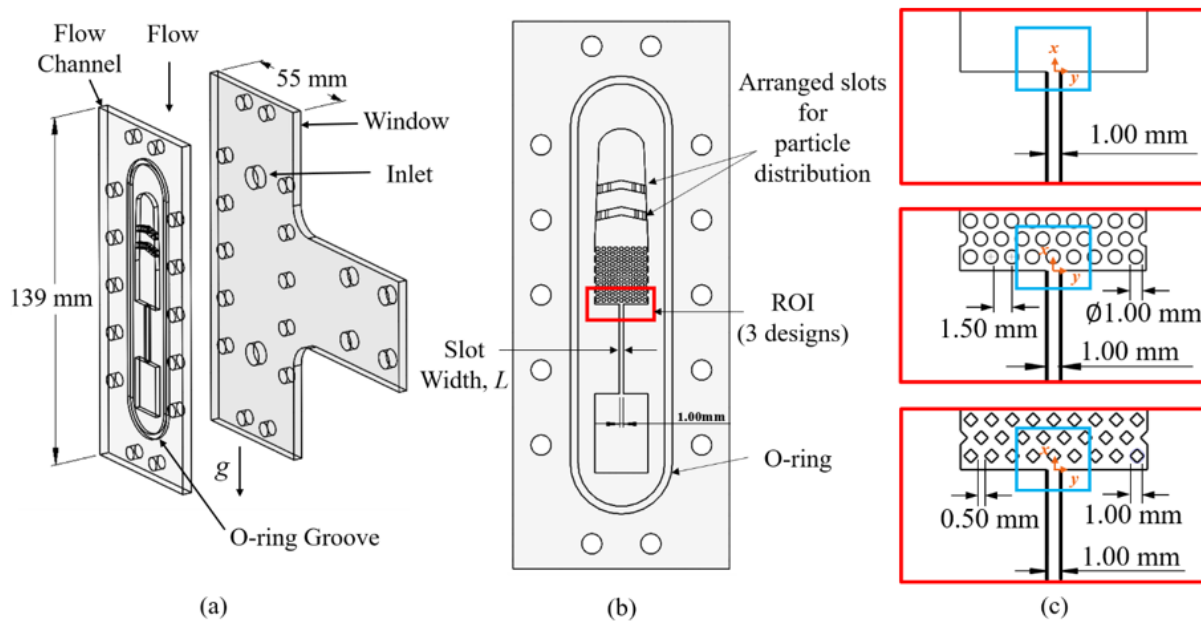


Figure 35 A schematic of the flow cell used in this study. (a) The exploded view of the flow cell assembly, (b) the flow channel where the region of interest (ROI) is highlighted with a red box and (c) enlarged images of the ROI to demonstrate the three inlet conditions: (1) the open slot and pillars which were 2 mm in height aimed to simulate porous media: (2) 1 mm diameter cylindrical pillars and (3) diamond shaped pillars circumscribed into 1 mm diameter circles. The field of view (FOV) for the continuous phase velocity measurements are highlighted in the blue boxes. Note that the FOV for the build-up tests was slightly wider than the FOV for the velocity measurements of the continuous phase [11]. A detailed drawing is given in Section 8.47–Appendix 47.

5.3 Optical Experimental Set-up

The experimental set-up as illustrated in Figure 36 consists of a camera imaging the flow cell in a shadowgraph configuration illuminated by a high-current LED light source. A high speed camera (Photron FastCam Mini WX 50) with 2048×2048 pixel resolution was used to capture velocity measurements of the continuous phase. The continuous phase flow velocity measurements at $Q = 0.3$ ml/min and 3 ml/min were performed at a frame rate of 125 fps. However, at the highest flowrate $Q = 30$ ml/min the images were captured at a frame rate of 750 fps in order to freeze the motion of the tracer particles added to the flow field. A second camera with the same 2048×2048 pixel resolution (4M180, IO Industries Inc.) was used for imaging particle build-up over longer time periods. This camera was connected to a digital video recorder storage (DVR Express Core 2, IO Industries Inc.) and a computer. For the build-up tests, two sets of images were collected for 12 seconds at 36 frames per second (fps) and exposure time of $150 \mu\text{s}$ with 16 minutes interval between each recording. Each camera was combined with a macro lens (105 mm $f/2.8$, Sigma) to image the field of view illuminated by an LED light source (BX0404-520 nm; Advanced Illumination Inc.) which provided uniform back illumination.

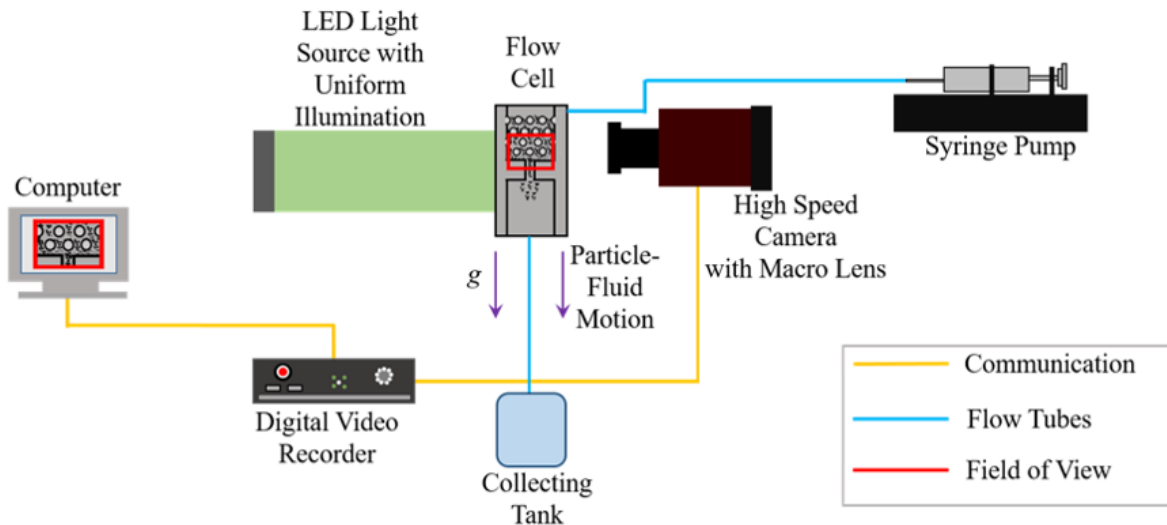


Figure 36 A schematic of the Particle Shadowgraph Velocimetry (PSV) experimental set-up for the multiple particles analysis

Table 13 Specifications of the PSV system, shown in Figure 36, which used to study the motion of multiple particles within the near-slot region in SAGD operations.

Camera sensor size	2048 × 2048 pixels
Field-of-view ($w \times h$)	16 × 16 mm
Magnification	0.704
Digital resolution	0.008 mm pixels ⁻¹

5.4 Image Processing

Several image processing techniques were employed to detect and track the particles within the region of interest and to determine parameters such as the fluid velocity field, particle deposition, particle size distribution, and particle rotation. All image processing was performed using commercial software (DaVis 8.3.1 LaVision GmbH) and in-house post-processing scripts (Matlab, The MathWorks Inc.). The following sections describe the techniques used to process and analyze the experimental data.

5.4.1 Particle Detection and the Fitted Ellipse Approach

Particle detection is the first data processing step that was used in order to assess particle motion within the near-slot region. Five image processing steps were used to detect the particles and to fit ellipses to the irregularly shaped particles: (1) A 2D Gaussian smoothing filter with a kernel size of 31 pixels and a standard deviation of 0.2 was applied to the raw shadowgraph images to invert the images and to reduce the noise. (2) The local standard deviation of the smoothed image was normalized between 0 and 1 and the scaled standard deviation was multiplied by itself thrice. (3) The smoothed image itself was also normalized between 0 and 1 and the resulting scaled image was multiplied by itself. (4) The images obtained in step 2 and 3 were averaged and the resultant image was binarized. (5) The particles were detected and an ellipse was fitted to each particle using a built-in function (*regionprop*, Matlab, The Mathworks). Subsequently the location of the centroid of each ellipses fitted to the particles was also identified using (*regionprop*, Matlab, The Mathworks). The angular orientation of each ellipse with respect to the vertical axis was also determined.

5.4.2 Particle Tracking

Images were pre-processed using the technique described in Section 5.4.1 for particle detection. From this step, the coordinates of the centroid of every individual particle were detected in each image. A built-in function (*regionprop*, Matlab, The Mathworks) was used to determine the coordinates of the centroid of every individual ellipse as well as the orientation of each ellipse with respect to the vertical axis. Finally, particle tracking was performed using a method developed in reference [85] which is a modified approach based on that by Baek and Lee [86]. Particles within a user defined radius are assumed to have similar displacement in direction and magnitude and based on the most probable trajectory, the velocity of an individual particle is determined. If there are no neighboring particles within the radius, then the nearest-neighbor-in-the-next-frame approach is used. The displacements of individual ellipses were obtained by identifying each particle in the subsequent frame.

5.4.3 Particle Characterization

The particles suspended in the flow contained a variety of particle sizes and shapes. Figure 37 (a) shows an image of a sample of the irregularly shaped 40- μm silicon carbide particles. To determine the general particle characteristics, 2D images were taken of 2213 particles, which were placed on microscope glass slides in order to obtain an approximation of the size and shape distributions. The images used in the size and shape analysis were taken using a lens (50 \times microscopic lens) with a higher magnification than the macro lens used for the experimental analysis.

There are several parameters in the literature which can be used to characterize particle size or shape [14,15,87–92]. For the purpose of identifying the size or degree of irregularity of the particles used in this study, some of the more commonly used parameters in the literature namely equivalent diameter, aspect ratio and roundness, are used [14,15,87–93].

The equivalent diameter was determined from the projected area of each particle in the 2D images by calculating the diameter of a circle having the same area [46]. The particle size distribution obtained is shown in Figure 37 (b) where the average particle size of the sample was 43 μm , which

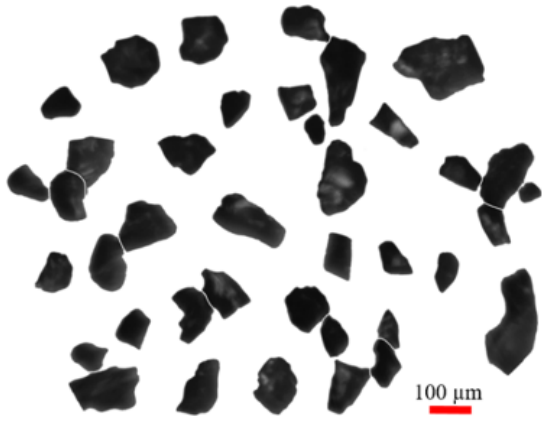
is comparable to the particle size of 40 μm in the manufacturer specifications (AGSCO Corporation).

Among the various methods available in the literature to determine the aspect ratio [15,87,89], the method selected and used in this study is the calculation of the ratio of the minor axis to the major axis of a fitted ellipse to the particles [14,90]. The average aspect ratio obtained from the sample of 2213 particles was 0.68 as shown in Figure 37 (c). In some studies the aspect ratio is referred to by different names such as sphericity [92] or elongation [14]. However, the mathematical definition is similar which is given as:

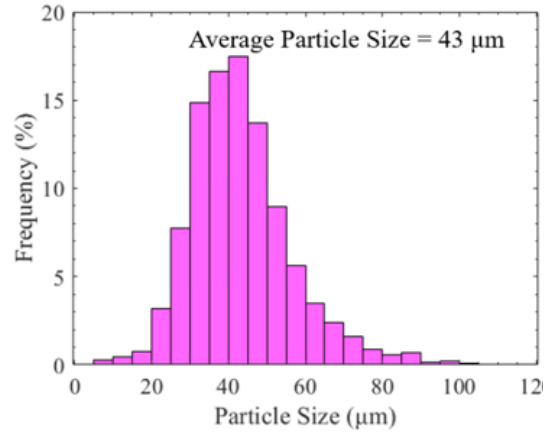
$$\text{Aspect Ratio} = \frac{\text{Minor Axis of Fitted Ellipse}}{\text{Major Axis of Fitted Ellipse}} = \frac{d_1}{d_2} \quad \text{Equation 16}$$

where d_1 and d_2 are the ‘width’ and ‘length’ of a particle. Since measuring d_1 and d_2 for each particle was difficult, the equivalent dimensions of the fitted ellipse to each particle were used to calculate the aspect ratio, where d_1 and d_2 were the minor and major axes of the fitted ellipses [14]. The aspect ratio varies from 0 to 1, where a value of 1 indicates that the particle is a perfect sphere [14,90]. The aspect ratio was calculated using a customized code developed in the study in reference [92] using reference [94].

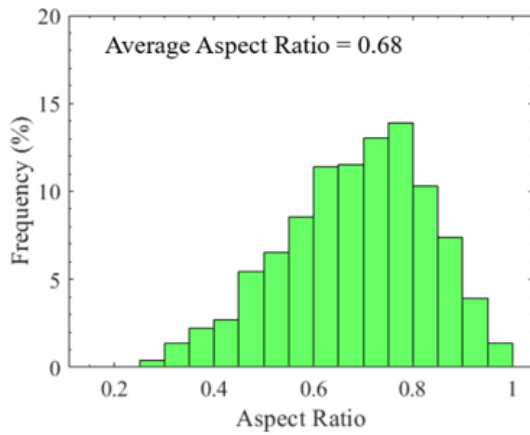
Roundness is a parameter that indicates the degree to which the shape or outline of a particle deviates from a circle. It is an indication of the smoothness of the edges of the particle [14,92,95,96]. In some studies, roundness is referred to by different names such as circularity [87], sphericity [15], or shape factor [97]. However, the implications or mathematical definitions are similar. Traditionally, the roundness is calculated using the ratio of the projected area to the perimeter of the particle squared [14,87,93]. Alternatively, another approach to attain the roundness for two-dimensional images was developed in [91,92]. This approach was used to define the roundness of the particles used in this study. The approach calculates the roundness using the ratio of the average radius of curvature of the outline of a particle to the radius of the maximum inscribed circle. This was done using a circle fitting method to the corners of the particle [91,92,95]. The value of roundness ranges from 0 to 1. The value of roundness decreases from 1 as the outline of the particle deviates from a perfect circle [14]. The average roundness calculated for the 2213 particles was 0.40 as shown from the distribution in Figure 37 (d).



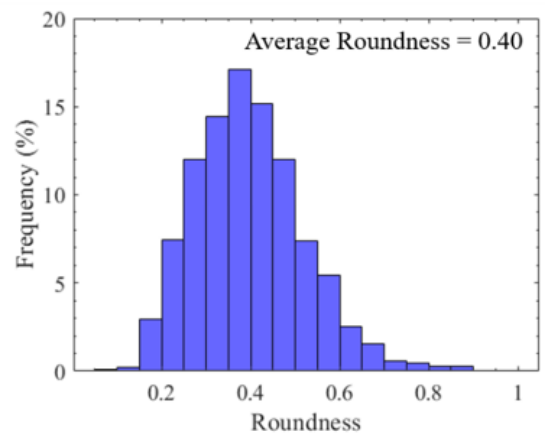
(a)



(b)



(c)



(d)

Figure 37 To determine the particle characteristics of the irregularly shaped silicon carbide particles (AGSCO Corp.), 2D images were taken of 2213 particles. (a) One sample images selected from the 55 2D images that were taken. (b) The particle size distribution (equivalent diameter) of the particles whereby the average particle size is 43 μm . (c) The distribution of the aspect ratios of the particles (i.e. the ratio of the minor axes to the major axes of the fitted ellipses). The average particle aspect ratio was 0.68. (d) The distribution of the roundness of the particles. The average round is 0.40.

5.4.4 Velocity Field Measurements of the Continuous Phase

The velocity vector field was calculated using particle image velocimetry (PIV) image processing using commercial software (DaVis 8.3.1, LaVision GmbH). Several pre-processing techniques were used to remove background noise and to allow the tracer particles to appear bright on a dark background. The images were first inverted and the inverted images were multiplied by themselves. An average of the product was calculated and subtracted from the multiplied images, and then the velocity field processing was performed.

A single-frame time-series sum-of-correlation vector calculation was applied to the pre-processed images. A multi-pass cross-correlation, with decreasing interrogation windows sizes, was applied to sequential pre-processed images to calculate the velocity field. Initially, three passes were performed using an interrogation window size of 128×128 pixels with 87% window overlap to capture large changes in the velocity field. This was followed by another three passes using a 64×64 pixels interrogation window size with 87% window overlap between sequential correlations. The interrogation window sizes were selected to allow the particles to move at least one half of the interrogation window size between subsequent frames [98]. The average of the processed images was calculated to determine the velocity vector field. Finally, an in-house post-processing code using functions found in [83] (PIVMat Matlab, The MathWorks Inc.) was used for post-processing and plotting of the velocity vector maps.

It is important to note that there is uncertainty related to the processing interrogation window size and cross-correlation that are used to find the average velocity field [99,100]. It has been found in literature that in an ideal case a symmetric correlation peak would be achieved if particles were matched perfectly during the cross-correlation of images. However, in reality a perfect match may not be achieved resulting in a non-symmetric correlation peak [100]. In this study, the uncertainty of the average velocity field was attained using:

$$U_x = \frac{\sigma_x}{\sqrt{N}} \quad \text{Equation 17}$$

where, U_x is the uncertainty of the average velocity, σ_x is the standard deviation, and N is the number of measured variables, that is the number of available vectors [101]. The uncertainty of the average velocity vector was calculated using (DaVis 8.3.1, LaVision GmbH). The maximum

uncertainty was estimated to range from 1.33 % of the maximum velocities for the low Re case to 5.73 % of the maximum velocities at high Re .

5.4.5 Build-up Tests: Obtaining the Thickness of the Deposited Layer of Particles

The thickness of the deposited layers in the vicinity of the slot was obtained by processing individual images with custom approaches (Matlab, The Mathworks). To demonstrate the variation of the layer thickness with time, two datasets of 432 images were collected. The first dataset consisted of images collected from time $t = 0$ seconds to $t = 12$ seconds and the second dataset consisted of images collected from $t = 16$ minutes to time $t = 16.2$ minutes. For each data set, the average of the 432 images was calculated to eliminate the moving particles and focus solely on the deposited layers along the entrance of the slot. The average of the images calculated for each data set was converted to a binary image where the particles appeared as white ‘blobs’ on a black background. All the white blobs except the two significantly largest ones, which represented the deposited layers at the entrance of the slot, were removed. Thereby the deposited layer could be observed.

5.5 Experimental Results and Analyses

5.5.1 Velocity Vector Field of the Continuous Phase

The velocity field measurements were performed, using 20- μm tracer particles, for nine experimental conditions as shown in Figure 38. The FOV used for analysis in this study represents the flow convergence zone into a confined narrow 2D slot [102,103]. Each row in Figure 38 shows the flow field for different geometries at the same $Re = 0.1, 1$ or 10 . Over the range of the experiments the velocity varied by two orders of magnitude. To highlight this, logarithmic colormaps are used in Figure 38 to allow better observation of the lower velocity regions in the flow. Each column in Figure 38 compares the flow field in a specific geometry at different Re .

It can be seen in Figure 38 that the velocity distribution for each experimental condition is almost symmetric about the centerline of the slot, $x = 0$. In general, the flow characteristics are similar for each Re but are strongly influenced by the particular flow geometry. A parabolic velocity profile was observed within the rectangular slots which is in agreement with the theoretically calculated velocities in the range of Re investigated here [104]. The velocity increased within the near-slot region due to the change in the cross-sectional area which provides a smaller open flow area at the entrance of the slot.

Within the porous region, the relative maximum velocities occurred diagonally between the pore spaces, while the minimum relative velocity within the porous region occurred at the walls of the pillars and along the entrance of the slot as indicated by the red arrows in Figure 38. The average local velocities (U_{ave}) within the low velocity regions adjacent to the wall on one side of the entrance of the slot indicated by the red boxes shown in Figure 38 were then plotted against Re for all three geometry configurations as shown in Figure 39.

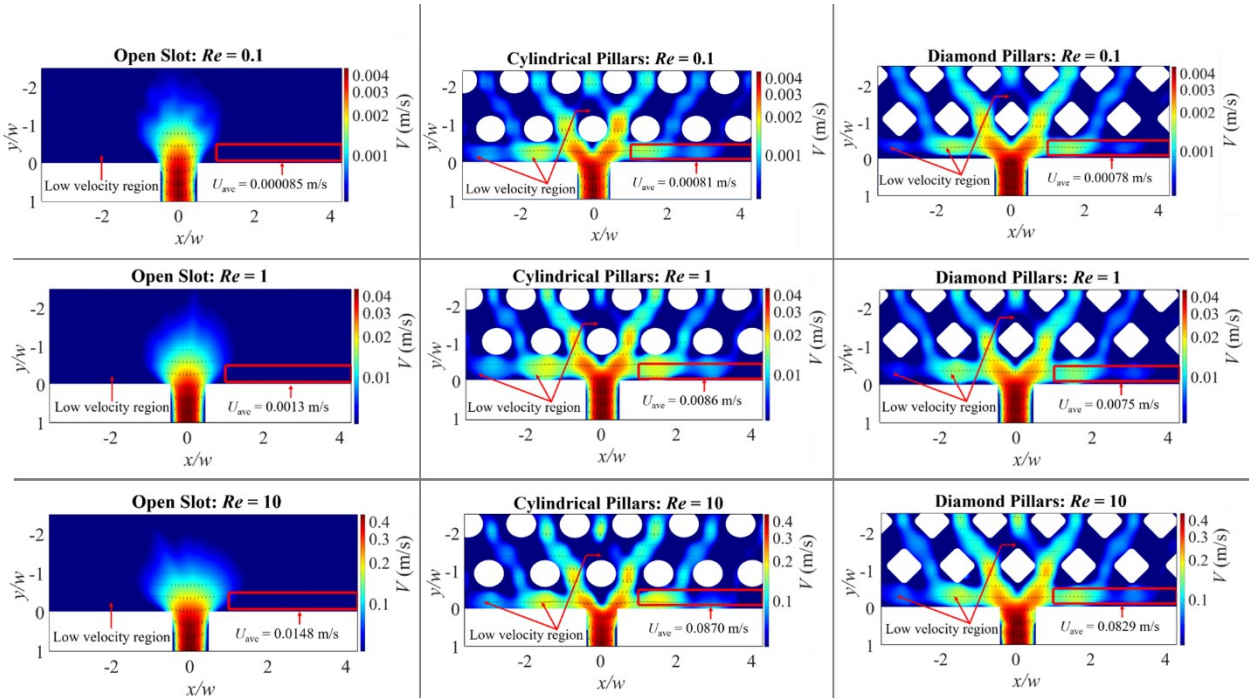


Figure 38 The velocity field within the region of interest for the three flow cell configurations (the open slot and inlet conditions aimed to simulate porous media using cylindrical pillars or diamond shaped pillars). The colors in the background represent the velocity magnitude ($\sqrt{u^2+v^2}$) and the black arrows represent the velocity vector field. The low velocity regions are selected with red boxes and the average velocities U_{ave} within the low velocity regions are shown.[11].

Figure 39 shows the extent to which U_{ave} within the low velocity region changes with respect to the flow geometry. It was noted that that as Re increases U_{ave} increases for the three flow cell configurations. However, it was observed that U_{ave} for the two flow cells with the simulated porous media at the inlet were generally higher than those for the open slot. The cylindrical pillars had a diameter of 1 mm and the diamond shaped pillars were circumscribed within 1 mm diameter circles. Comparing these two flow cells, the diamond shaped pillar flow cell had a greater open flow area. Therefore, U_{ave} within the low velocity region was lower than that for the cylindrical pillars as shown in Figure 39.

However, due to having the largest open flow area, U_{ave} within the low velocity region was the smallest for the open slot compared to all other geometries. By comparing the velocity distributions in different geometries at a given Re , represented by each row in Figure 39, it was observed that the presence of the simulated porous media had a remarkable effect on the flow in the near-slot region.

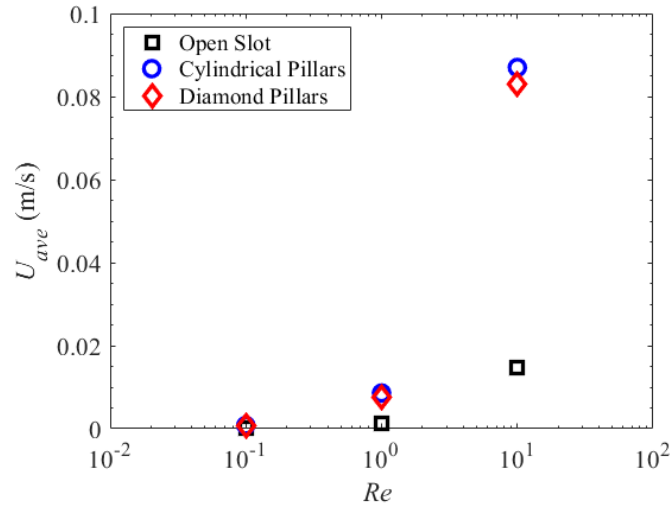


Figure 39 A plot of the average velocity U_{ave} within the low velocity regions, represented by the red boxes in Figure 38, versus Reynolds number ($Re = 0.1, 1.0$ and 10) for the three flow cell configurations (the open slot and inlet conditions aimed to simulate porous media using cylindrical pillars or diamond shaped pillars). [11]

5.5.2 Particle Deposition

Particle deposition occurs when the particles deviate from the fluid flow streamlines and eventually settle on the surface of the flow geometry. The build-up tests were performed in order to identify the factors that lead to particle deposition. The results from the build-up tests corresponds to the flow velocity results from in Figure 38 and Figure 39. Whereby particle deposition occurred within the regions of low velocities as highlighted by the red boxes and red arrows in Figure 38. The particle build-up that occurred during the 12 seconds of data collection, at time $t = 0$ and at time $t = 16$ minutes are shown in Figure 40, Figure 41 and Figure 42. The build-up tests were performed using the 80- μm spherical glass beads and 40- μm irregularly shaped silicon carbide particles within the three flow geometries at $Re = 0.1, 1$ and 10 . The initial layers of particle build-up at time $t = 0$ in Figure 40, Figure 41 and Figure 42 are due to the particles settling during the time to fill the flow cell and preparation for the experiments. There was a variation in thickness of the initial layer of particle build-up at time $t = 0$ because a controlled and uniform particle concentration at the inlet of the flow channel was not achieved. The results from the build-up tests were analyzed based on any visible changes of the initial layer of particles after 16 minutes.

Figure 40 shows that at the lowest flowrate ($Re = 0.1$), the thickness of the deposited layer in all geometries increased after 16 minutes for both types of particles. This corresponds to the data presented in Figure 39 whereby at $Re = 0.1$, U_{ave} within the low velocity region was approximately zero for all the geometries. It was noted that at $Re = 0.1$, U_{ave} for the open slot was 0.000085 m/s which is the lowest value and an order of magnitude lower than the two geometries. This value was followed by the diamond shaped pillars in which the value of U_{ave} was 0.00078 m/s then the cylindrical pillars had a U_{ave} of 0.00081 m/s. Figure 40 shows that the particle build-up thickness at 16 minutes for both the spherical and irregularly shaped particles were the highest at the lowest value of U_{ave} . Whereby the thickest layer of deposited particles at 16 minutes occurred within the open-slot, followed by the diamond shaped pillars then the cylindrical pillars.

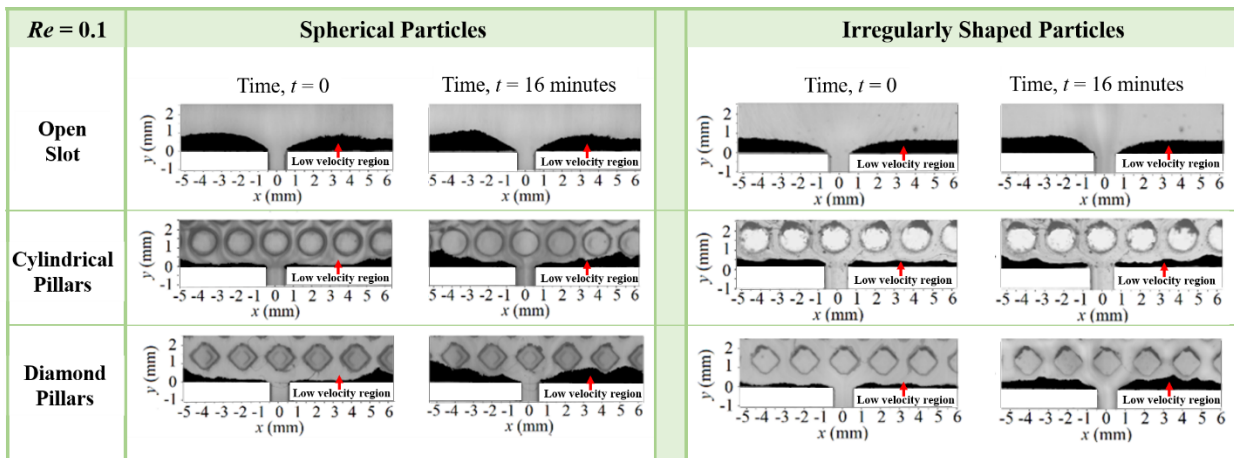


Figure 40 Particle deposition which occurred during the 12 seconds of data collection, starting at time $t = 0$ and then at time $t = 16$ minutes. This figure shows the particle deposition for both spherical and irregularly shaped particles in three flow cell configurations: open slot, cylindrical pillars, and diamond shaped pillars, at $Re = 0.1$ [11].

At $Re = 1$, the values of U_{ave} , within the low velocity regions were calculated to be 0.0013 m/s, 0.0086 m/s and 0.0075 m/s for the open slot, cylindrical pillars, and diamond shaped pillars, respectively as shown in Figure 38 and Figure 39. The values were an order of magnitude higher than the U_{ave} at $Re = 0.1$. At $Re = 1$ the open slot was the only geometry that had a significant particle build-up at 16 minutes as shown in Figure 41. The presence of the simulated porous media (i.e. the cylindrical pillars and the diamond shaped pillars) significantly reduced the open flow area and thereby the values of U_{ave} were higher as a result the particles were washed away after 16 minutes for these flow geometries. It was observed that there was a thicker layer of deposited

particles after 16 minutes for the spherical particles compared to the irregularly particles. This probably occurred because the spherical particles were larger and heavier compared to the irregularly shaped particles.

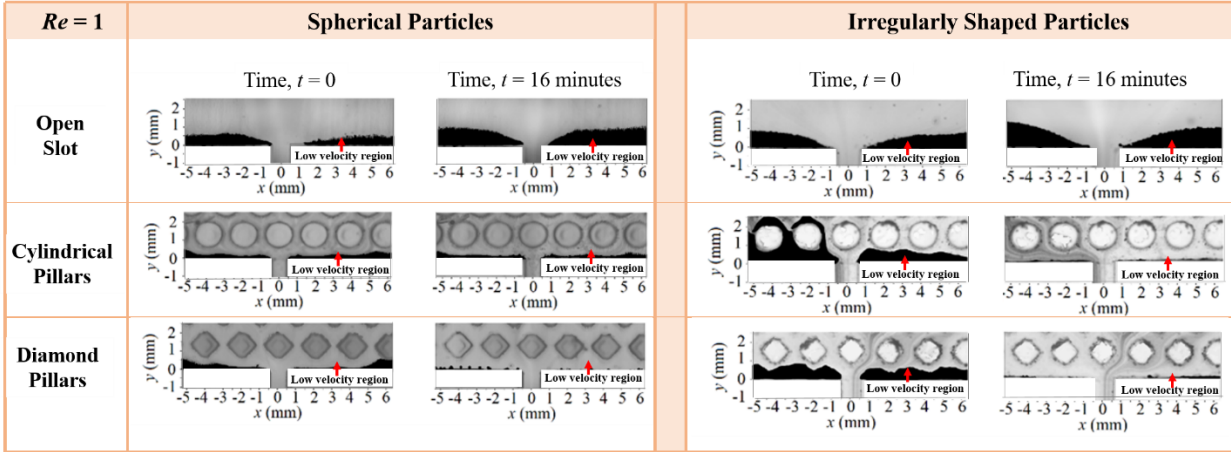


Figure 41 Particle deposition which occurred during the 12 seconds of data collection, starting at time $t = 0$ and then at time $t = 16$ minutes. This figure shows the particle deposition for both spherical and irregularly shaped particles in three flow cell configurations: open slot, cylindrical pillars, and diamond shaped pillars, at $Re = 1$ [11].

U_{ave} within the low velocity regions were 0.0148 m/s, 0.0870 m/s and 0.0829 m/s for the open slot, cylindrical pillars, and diamond shaped pillars respectively at $Re = 10$, which is an order of magnitude higher than the values obtained at $Re = 1$. At $Re = 10$, the high velocity of the fluid washed away the particles almost immediately after the flow was initiated. Therefore in order to demonstrate how quickly the particles washed away, prior to the start of the experiment the particle–fluid mixture was allowed to flow into the flow channels at a low flow rate to allow a large layer of particles to be formed. Then the flow increased to the highest flowrate, $Q = 30$ ml/min, and the data was collected. As described in Section 5.3 the thickness of the deposited layer of particles was found by finding the average of the 432 images collected during the build-up tests for a duration of 12 seconds first at time $t = 0$ then at $t = 16$ minutes. However, at $Re = 10$, the particles washed away so quickly that the average of the entire 432 images dataset over 12 seconds could not capture the phenomena. Therefore, beginning at $t = 16$ minutes the deposited layer of particles shown in Figure 42 was determined by finding the average of the first 35 images which is 8% of the original data set. This shows that approximately within the first minute of pumping the fluids

at a flowrate of $Q = 30$ ml/min at $Re = 10$ a significant amount of particles were washed away as shown in Figure 42.

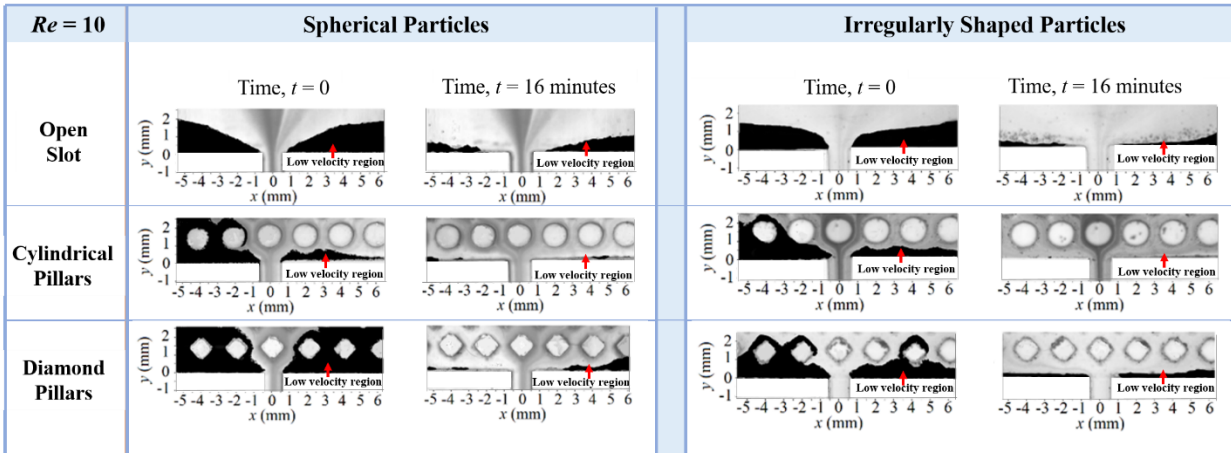


Figure 42 Particle deposition which occurred during the 12 seconds of data collection, starting at time $t = 0$ and then at time $t = 16$ minutes. This figure shows the particle deposition for both spherical and irregularly shaped particles in three flow cell configurations: open slot, cylindrical pillars, and diamond shaped pillars, at $Re = 10$ [11].

Two phenomena that influences particle deposition are (1) inertial effects and (2) gravitational effects. By analyzing the low experimental results and the properties of both the fluids and the particles, it was found that the particle deposition shown in Figure 40, Figure 41 and Figure 42 are mostly attributed to gravitational effects. This was determined by evaluating the values of the Stokes number and the gravitational terminal settling velocity of the particles. The density and viscosity of the 70%–30% glycerol-water fluid that was used in the build-up tests are 1191.6 kg/m^3 and 0.0298 Ns/m^2 respectively. The Stokes numbers for the tracer particles, $80 \mu\text{m}$ spherical glass beads and $40 \mu\text{m}$ irregularly shaped silicon carbide particles at the maximum fluid flow velocity were 3.92×10^{-6} , 1.49×10^{-2} and 5.54×10^{-3} respectively which are all $\ll 1$. At the lowest and intermediate flowrates, the Stokes numbers would be even smaller for the three types of particles. This indicates that particle inertial effects were negligible in this study. A sample calculation for the Stokes numbers is given in Section 8.44 Appendix 44.

However, the particle–fluid density difference between the continuous phase and the tracer particles, $80 \mu\text{m}$ spherical glass beads and $40 \mu\text{m}$ irregularly shaped silicon carbide particles were 0.142 g/cm^3 , 1.308 g/cm^3 and 2.02 g/cm^3 respectively. Additionally, the gravitational







terminal settling velocity, U_t , the 80 μm spherical glass beads and the 40 μm irregularly shaped silicon carbide particles were 1.05×10^{-6} m/s, 1.53×10^{-4} m/s and 6.82×10^{-5} m/s respectively. The U_t for the tracer particles were much less than the average fluid velocities at $Re = 0.1, 1$ and 10 ($Q = 0.0025$ m/s, 0.025 m/s and 0.25 m/s.), this indicates that the tracer particles followed the flow faithfully. The values of U_t and the particle–fluid density difference for the silicon carbide particles indicate that the deviation of the particles from the fluid flow streamlines to be deposited within the flow channel can be attributed to gravitational forces. A sample calculation for the gravitational terminal settling velocity is given in Section 8.44 Appendix 44.

5.5.3 Particle Rotation

Once the velocities were quantified using the tracer particles, a series of separate experiments were carried out at the same flow rates in the same geometries with the difference being that larger particles were used instead of tracer particles. Using the image processing techniques described in Sections 5.4.2 and 5.4.3 each irregularly shaped particle appearing in the images was identified by a fitted ellipse. The angles of rotation, θ , between the major axis of the fitted ellipse and the vertical axis (y) were measured for each particle in each image.

Figure 43 shows the rotations of six selected particles labeled (a) to (f) as they entered the slot section in the open channel at $Re = 1$. The aspect ratio, roundness and the color assigned in Figure 43 to each of the six selected particles are given in Table 14. Each particle shown in Figure 43 is tracked as it is transported throughout the length of the slot. The six grayscale figures illustrate the sequence of the snapshots of selected particles within the flow that includes various shapes of particles. Every 4th frame is shown for each sequence to avoid overlapping images of particles. The snapshots were edited to exclude many other surrounding particles in the flow and to provide a better illustration of the motion of individual particles. The line plots below each pair of grayscale figures show the vertical locations (in every 4th frame) of the selected particles plotted against the absolute value of the difference between the angle of rotation, θ , (in every 4th frame) and the initial angle of rotation, θ_i each of individual particles .

Table 14 The aspect ratio and roundness of the six particles (a)-(f) shown in Figure 43 [11]

Particles (color code)	Aspect Ratio	Roundness
	0.140	0.801
	0.404	0.843
	0.444	0.588
	0.418	0.560
	0.172	0.728
	0.358	0.686

Particles with similar characteristics were paired in Figure 43 that have all but one parameter in common: either the initial angle θ , the particle distance from the wall, or the particle shape. It can be seen that the particles (a) and (b), highlighted with red and blue in Figure 43, were both located at relatively the same distance from the walls. However, particle (b), which is initially not aligned with the flow field, rotates in the direction of the flow much more than particle (a). It was observed that the initial orientation θ at which the particle enters the slot region strongly affected the particle rotation in the section. Particle (b) also has a higher aspect ratio than particle (a), which may have also contributed to particle (b) experiencing a higher rotation.

From the comparison of the rotations of the particles (c) and (d) (highlighted with yellow and green respectively in Figure 43) it can be seen that the distance of the particle from the walls is another important factor in the rotation. Both particles (c) and (d) have a similar shape and both enter the channel with similar orientation. However, particle (c) is closer to the center of the slot where the velocity variation in the cross-stream direction is lower compared to the position of particle (d). Particle (c) is located within the region closer to the peak of the parabolic velocity profile and the gradient in stream-wise velocity is lower. As a result, it moves with a relatively smaller amount of rotation as it passes through the slot towards the exit compared to particle (d) that is in a region of stronger stream-wise velocity gradient, leading to faster rotation rate of the particle.

Finally, the comparison of particles (e) and (f) (highlighted with orange and purple in Figure 43) further confirms that the particle shape (*i.e.* the aspect ratio) has a significant impact on the rotation. Both particles entered the channel with a similar angle as well as a similar initial position with respect to the walls. However, particle (f) with an aspect ratio of 0.358 undergoes a higher level of

rotation compared to particle (e) with an aspect ratio of 0.172, because particle (f) is more exposed to a velocity difference on its surface due to its shape. Particle (e) shows minimal deviation from its initial orientation while passing through the slot compared to particle (f). Comparing all particles (a–f), it can be seen in Figure 43 that particle (d) experienced the highest rotation. This particle is relatively larger than the five other particles and also maintains the smallest distance to the solid wall where a higher gradient in the stream-wise velocity field exists.

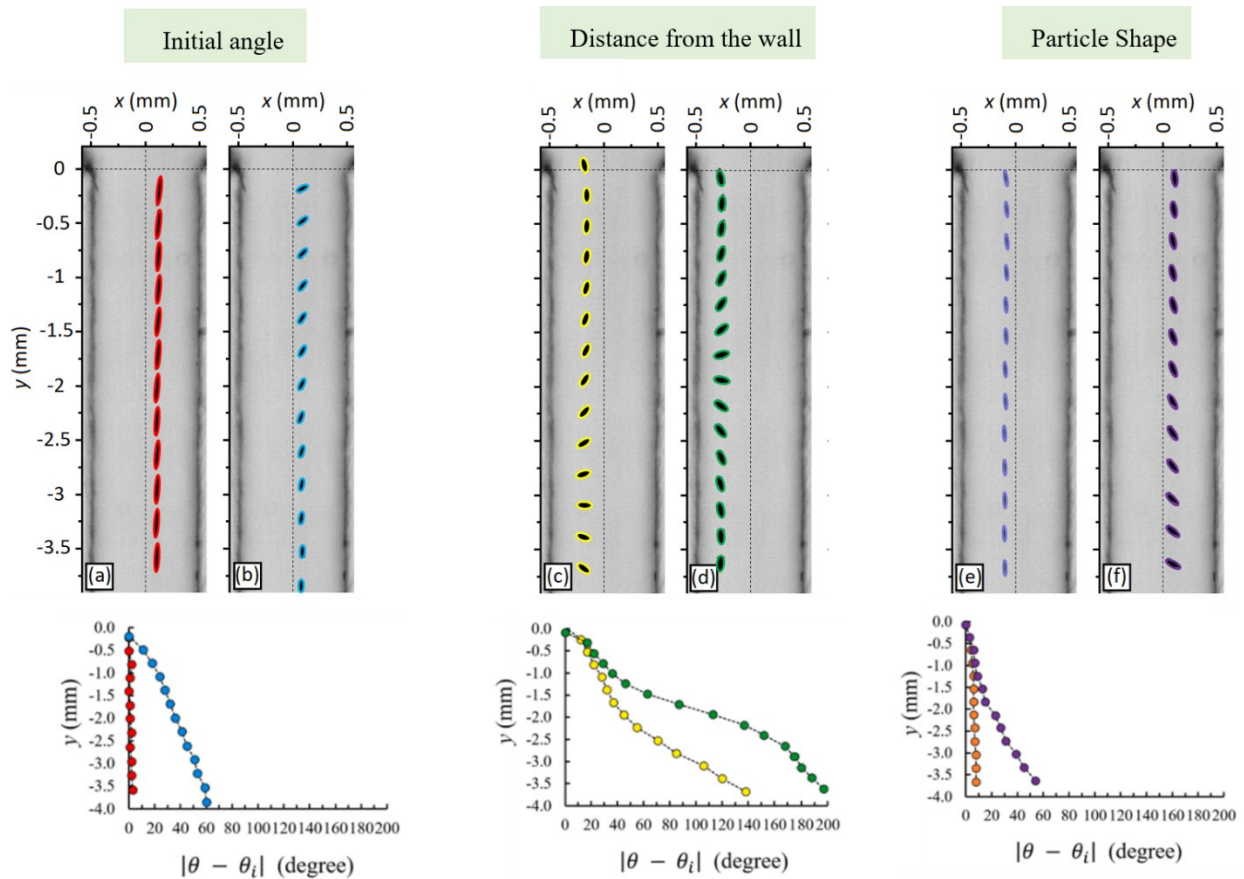


Figure 43 Factors that influenced the rotation of six selected particles flowing through the slot of the open channel at $Re = 1$. The velocity vector field and the streamlines of the continuous phase are shown at left corner. The six grayscale figures are snapshots of selected particles at every 4th frame to avoid overlapping images of particles. The line plots are vertical locations of the center of the fitted ellipse to the particle plotted versus the absolute value of the difference between the angle of rotation of the particles, θ , (in every 4th frame) and the initial angle, θ_i , of each particle [11].

So far, we have discussed some parameters that could potentially affect the rotation of different particles in the slot. However, particles behave differently when they enter a more complex part of the geometry such as the simulated porous region shown in Figure 44. To better illustrate how the rotation of particles can influence the deposition of particles, a sequence of snapshots of two separate particles flowing near the slot entrance is compared in Figure 44. The snapshots in Figure 44 were edited to exclude other surrounding particles in the flow and to provide a better illustration of the motion of individual particles. Note that the trajectories of particles P_1 and P_2 in Figure 44 were captured at two different times and then were overlapped onto one image. Therefore, P_1 and P_2 were not at any time in physical contact.

As shown in Figure 44, even though both particles seemingly have similar aspect ratios, initial orientations, and initial locations in the channel, they showed completely different motions in the near slot region. Both particles almost followed the same streamline in the first three frames. However, particle P_1 begins to cross the streamline and rotates which caused it to collide into the layer of deposited particles on the horizontal surface before the entrance to the slot. Particle P_2 remained oriented along the local velocity vectors (or the streamlines) and followed the flow convergence and flowed through into the slot. It appears that P_2 did not rotate before entering the slot section and maintains its orientation along the fluid flow path before the slot. On entering the slot, it rotates significantly compared to the curvature of the flow.

From the observation of these two particles in Figure 44 it can be seen that the rotation of a particle during its motion is a key factor which affects whether the particle deposits or exits the porous media into the channel. Factors such as the difference in the shapes, which could not be seen clearly in the projected 2D images, higher weight of P_1 compared to P_2 , or interaction with other neighboring particles that have been removed from the images might have affected the deposition of P_1 . This indicates that understanding the detailed behavior of particles in such flows is complex and requires more extensive study.

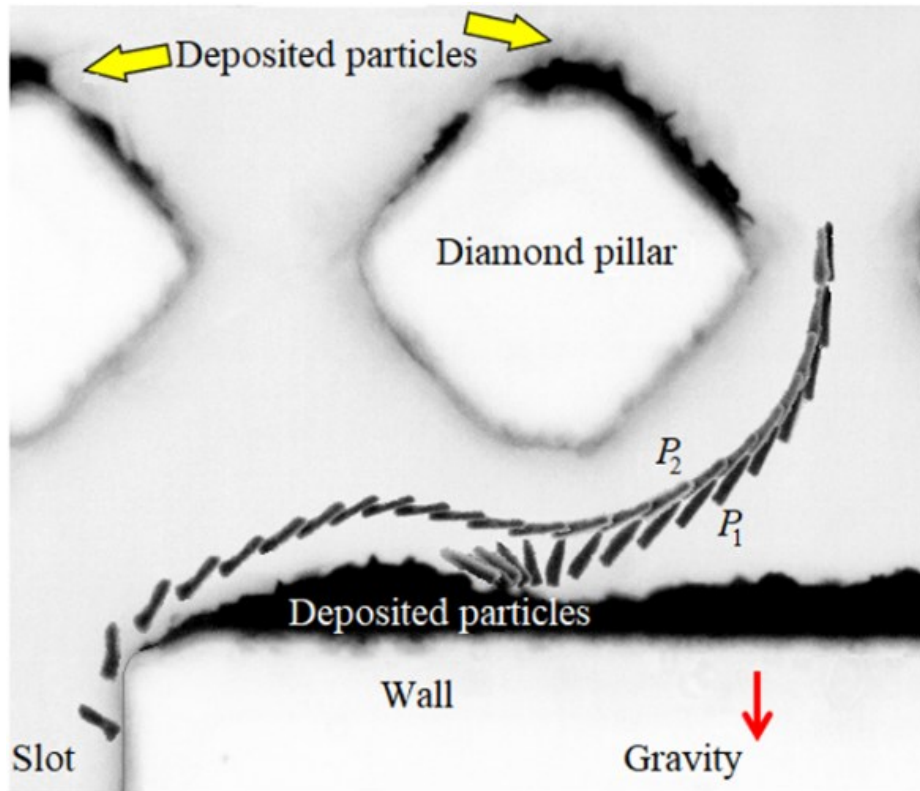


Figure 44 The trajectory of two particles that are transported through a porous network into a narrow slot at $Re = 0.1$. The images were edited to exclude the surrounding particles. P_1 and P_2 flowed at two different times in the experiments and therefore, they were not in physical contact. [11].

5.6 Conclusion

This chapter strictly focuses on the observations made from an experimental study to illustrate the importance of considering the actual shape of particles when modeling particle transport within a fluid. The behavior of solid particles that flow through a porous medium into a narrow slot has been explored using PSV measurements and image processing techniques. Irregularly shaped particles have been traditionally modelled as spheres to reduce the complexity of the mathematical models. This study observed that the differences in the shapes and the sizes of the particles influence their dynamic behaviors in the flow, including their rotation, which in turn affect their tendencies to be deposited on the solid walls.

The results give a visual understanding of the significance of particle shape and rotation on particle deposition even at a microscale. The rotation of particles depends on several factors including their shape, initial orientations, and relative locations in the flow field. These factors can join together and influence particle deposition near the slot entrance. This work also highlights that the particle–fluid density difference driven gravitational settling velocity can have a significant impact on particle deposition. It was observed that particle inertial effects were negligible in the flow regimes investigated.

In general, velocity of the continuous phase has a significant impact on the build-up of the particles. Particle build-up was most likely to occur in regions of lower continuous phase velocity. It was observed that at lower flow rates, the build-up of fine particles in the near-slot region can potentially plug the pore throats and change the local permeability. Cylindrical pillars appear to be slightly more resistant to the formation of a layer of particles near the slot opening. Their geometry generated slightly higher flow rates due to their larger size compared to the diamond shape. However, the presence of the simulated porous media influenced the flow field within the near-slot region. U_{ave} within the low velocity regions for the cylindrical pillars and diamond shaped pillars were generally greater than that of the open slot. As a result, particle build-up within the near-slot region of the open slot after 16 minutes was greater than the build-up within the simulated porous media geometries.

6 Conclusions

The focus of this thesis research was the motion of particles within various flow geometries including: a rectangular channel, a narrow slot and a porous network. Three different particle shapes were studied including spherical particles, cylindrical particles and irregularly shaped particles. Three modifications of a PSV experimental set-up together with various image processing techniques were used to examine various aspects of particle motion such as: the settling velocity, the particle Reynolds number, the coefficient of drag, particle rotation and deposition. This study was also applied to a geometry relevant to an industrial application known as SAGD in which particle motion is of importance.

The importance of selecting an appropriate length scale to define non-dimensional parameters that can be used to model particle motion was one of the main objectives of this work. This was achieved by investigating one of the commonly used correlations in literature to determine the coefficient of drag of non-spherical particles that was developed by Haider and Levenspiel. This model utilized the equivalent diameter as a length scale to define the particle Reynolds number. In the Haider and Levenspiel model, the non-dimensionalized plot of the particle Reynolds number versus the coefficient of drag did not overlap exactly for experimental measurements of particles of various shapes. Additionally, other models in the literature such as Dioguardi et. al and Madhav and Chhabra showed that the plot of the particle Reynolds number versus the coefficient of drag did not overlap exactly for particles Reynolds number greater than 10. These models also used shape parameters that related the particles to a sphere. Therefore, in this thesis research, an experimental study was performed in order to identify an appropriate length scale to model particle motion. It was determined that the ratio of the volume to the surface area of long aspect ratio cylinders is an appropriate length scale to define the particle Reynolds number and the coefficient of drag. The results also showed that the general trajectory of the cylindrical particles differed from the spherical particles. The cylindrical particles generally fell vertically within the few frames and then rotated until the particles reached settling velocity. In the terminal settling velocity region the particle wobbled. The spherical particles moved back and forth in the horizontal direction before reaching terminal settling velocity. The differences in the particle trajectories of the spherical

compared to the cylindrical particles reflected in a difference in the pattern of the particle velocity profile between the spherical particles and the cylindrical particles.

Another objective of this research was to evaluate the use of the spherical assumption to model the motion of non-spherical particles within confined and complex flow geometries in an industrial application known as SAGD. Four particle geometries were considered in the study of particle motion in SAGD operations. These include an open slot, an open flow geometry into a narrow slot, and two patterns of porous media into a narrow slot. Two shapes of particles were considered in each geometry. These include (1) spherical particles and (2) irregularly shaped particles. The results illustrated that particle shape and rotation affects the flow field around the particle. Using the spherical assumption to model the motion of non-spherical particles implies that the velocity profile around the particle should be symmetrical. However, a non-symmetrical velocity profile was observed around the irregularly shaped particles. The velocity profile around the irregularly shaped particle also varied as the particle fell within the slot.

The results of the study that included an open flow geometry into a narrow slot and two patterns of porous media into a narrow slot present a visual understanding of the significance of particle shape and rotation on particle deposition even at a microscale. The rotation of a particle depends on several factors including their shape, initial orientation, and relative locations in the flow field. These factors can combine together to influence particle deposition near the slot entrance. This work also highlights that the particle–fluid density difference driven gravitational settling velocity can have a significant impact on particle deposition. It was observed that particle inertial effects were negligible in the flow regimes investigated. Thereby, the results also demonstrated the limitations of modelling non-spherical particles as spheres. The spherical assumption neglects significant factors such as particle rotation and the corresponding impact on particle deposition and build-up. Particle shape and rotation were also shown to influence the surrounding fluid flow field differently when compared to spheres.

Previously, the analysis in Chapter 3 was performed in an open flow geometry which was more than ten times wider than the diameter of the particles. The results showed that the drag coefficient of non-spherical particles can be modelled as spheres if the correct length scale is used. However, in this chapter, the results demonstrated the limitations of using the spherical assumption to model the motion of irregularly shaped particles a confined flow geometry. It was observed that for

irregularly shaped particles, as small as 2.66 mm, the spherical assumption will not account for the impact of particle shape and rotation on the surrounding fluid flow field. The spherical assumption also implies that the velocity profile around the particle should be symmetrical. However, a non-symmetric velocity profile was also observed around the irregularly shaped particle. This chapter simplifies particle motion within SAGD operation by analyzing individual particles falling within a slot. However, in real conditions in SAGD operations, multiple particles are transported with the fluid flow, therefore the occurrence of particle rotation of non-spherical particles which affects the flow field around the particle can also influence the transport of near-by particles as well.

6.1 Future Work

The experimental study of falling spheres and cylinders within a rectangular channel in Chapter 3 was used to determine the settling velocity of the particles and to select an appropriate length scale to define particle motion. One recommendation for further research is to include tracer particles to the surrounding fluids to better understand the velocity field of the fluid around the spherical particles compared to the cylindrical particles. This analysis should be coupled with: (1) image processing schemes that can detect and describe the flow structures around the particle as it falls within the fluid and (2) further post processing to analyze the forces acting on the particle. Another recommendation for future work of this study is to analyze the motion of multiple particles falling within the channel in order to understand the impact of the motion of one particle on another.

The analysis of particle motion within the near-slot region in SAGD operations as described in Chapters 4 and 5 can be further studied by analyzing particle motion within a packed porous media into a narrow slot. An important consideration to achieve this study would be to select an appropriate optical diagnostic technique to capture the three dimensional effects of particle motion within a densely packed porous media.

7 References

- [1] J. Heyder, Deposition of inhaled particles in the human respiratory tract and consequences for regional targeting in respiratory drug delivery, *Proc. Am. Thorac. Soc.* 1 (2004) 315–320. <https://doi.org/10.1513/pats.200409-046TA>.
- [2] A. Tsuda, F.S. Henry, J.P. Butler, Particle transport and deposition: basic physics of particle kinetics, *Compr. Physiol.* 3 (2013) 1437–1471. <https://doi.org/10.1002/cphy.c100085>.
- [3] W. C. Krumbein, Measurement and geological significance of shape and roundness of sedimentary particles, *Sediment. Res.* 11 (1941) 64–72. <https://doi.org/10.1306/D42690F3-2B26-11D7-8648000102C1865D>.
- [4] W.H. Finlay, Motion of a single aerosol particle in a fluid, in: *Mech. Inhaled Pharm. Aerosols*, Elsevier, 2019: pp. 21–52. <https://doi.org/10.1016/B978-0-08-102749-3.00003-8>.
- [5] A. Melling, Tracer particles and seeding for particle image velocimetry, *Meas. Sci. Technol.* 8 (1997) 1406–1416.
- [6] J. Seville, C.-Y. Wu, Particles in Fluids, in: *Part. Technol. Eng.*, Elsevier, 2016: pp. 67–81. <https://doi.org/10.1016/B978-0-08-098337-0.00004-7>.
- [7] M.C. Shook, C.A., Roco, *Slurry Flow Principles and Practice*, 1991. <https://doi.org/10.1016/B978-0-7506-9110-9.50001-3>.
- [8] W.C. Hinds, *Aerosol Technology Properties, Behavior and Measurement of Airborne Particles*, John Wiley & Sons, Inc, 1999.
- [9] I. Gallily, A.D. Eisner, On the orderly nature of the motion of nonspherical aerosol particles. I. Deposition from a laminar flow, *J. Colloid Interface Sci.* 68 (1979) 320–337. [https://doi.org/10.1016/0021-9797\(79\)90286-8](https://doi.org/10.1016/0021-9797(79)90286-8).
- [10] C.A. Ruzycki, A.R. Martin, R. Vehring, W.H. Finlay, An In Vitro Examination of the Effects of Altitude on Dry Powder Inhaler Performance, *Aerosol Med. Pulm. Drug Deliv.* 31 (2017) 221–236. <https://doi.org/10.1089/jamp.2017.1417>.

- [11] L.K. Kinsale, M.A. Kazemi, J.A.W. Elliott, D.S. Nobes, Transportation and deposition of spherical and irregularly shaped particles flowing through a porous network into a narrow slot, *Exp. Therm. Fluid Sci.* 109 (2019) 109894. <https://doi.org/10.1016/j.expthermflusci.2019.109894>.
- [12] J. Heyder, Deposition of Inhaled Particles in the Human Respiratory Tract and Consequences for Regional Targeting in Respiratory Drug Delivery, *Proc. Am. Thorac. Soc.* 1 (2004) 315–320. <https://doi.org/10.1513/pats.200409-046TA>.
- [13] A.I. Kartushinsky, I.A. Krupensky, S. V Tisler, M.T. Hussainov, I.N. Shcheglov, Deposition of solid particles in laminar boundary layer on a flat plate, *High Temp.* 47 (2009) 892–901. <https://doi.org/10.1134/S0018151X09060170>.
- [14] S. Ghaemi, P. Rahimi, D.S. Nobes, Assessment of parameters for distinguishing droplet shape in a spray field using image-based techniques, *At. Sprays.* 19 (2009) 809–831. <https://doi.org/10.1615/AtomizSpr.v19.i9.10>.
- [15] K. Patchigolla, D. Wilkinson, M. Li, Measuring size distribution of organic crystals of different shapes using different technologies, *Part. Part. Syst. Charact.* 23 (2006) 138–144. <https://doi.org/10.1002/ppsc.200601022>.
- [16] A. Haider, O. Levenspiel, Drag coefficient and terminal velocity of spherical and nonspherical particles, *Powder Technol.* 58 (1989) 63–70. [https://doi.org/10.1016/0032-5910\(89\)80008-7](https://doi.org/10.1016/0032-5910(89)80008-7).
- [17] R. Turton, O. Levenspiel, A short note on the drag correlation for spheres, *Powder Technol.* 47 (1986) 83–86. [https://doi.org/10.1016/0032-5910\(86\)80012-2](https://doi.org/10.1016/0032-5910(86)80012-2).
- [18] D.O. Njobuenwu, M. Fairweather, Effect of Shape on Inertial Particle Dynamics in a Channel Flow, *Flow, Turbul. Combust.* 92 (2014) 83–101. <https://doi.org/10.1007/s10494-013-9503-7>.
- [19] D.A. Edwards, Large Porous Particles for Pulmonary Drug Delivery, *Science* (80-.). 276 (1997) 1868–1872. <https://doi.org/10.1126/science.276.5320.1868>.
- [20] J.S. Patton, P.R. Byron, Inhaling medicines: delivering drugs to the body through the lungs,

- Nat. Rev. Drug Discov. 6 (2007) 67–74. <https://doi.org/10.1038/nrd2153>.
- [21] T.W. Muecke, Formation Fines and Factors Controlling Their Movement in Porous Media, *J. Pet. Technol.* 31 (1979) 144–150. <https://doi.org/10.2118/7007-PA>.
- [22] L. Kinsale, D.S. Nobes, The study of flow through porous media within the near-slot region of SAGD operations using PSV, in: 5th Int. Conf. Exp. Fluid Mech. , Munich, Ger. July 2-4, 2018: pp. 573–578.
- [23] Y. Xie, Z. Chen, Particles migrating and plugging mechanism in loosen sandstone heavy oil reservoir and the strategy of production with moderate sanding, in: 5th Int. Conf. Porous Media Their Appl. Sci. Eng. Ind. Kona, Hawaii, 2014. http://dc.engconfintl.org/porous_media_V%0Ahttp://dc.engconfintl.org/porous_media_V/58.
- [24] J.R. Etherington, I.R. McDonald, Is bitumen a petroleum reserve?, in: SPE Annu. Tech. Conf. Exhib., Society of Petroleum Engineers, Houston, Texas, U.S.A., 2004: pp. 1–7. <https://doi.org/10.2118/90242-MS>.
- [25] J.G. Speight, Thermal Methods of Recovery, in: *Introd. to Enhanc. Recover. Methods Heavy Oil Tar Sands*, Elsevier, 2016: pp. 405–452. <https://doi.org/10.1016/B978-0-12-849906-1.00009-6>.
- [26] J.G. Speight, Heavy Oil and Tar Sand Bitumen, in: *Introd. to Enhanc. Recover. Methods Heavy Oil Tar Sands*, Elsevier, 2016: pp. 3–48. <https://doi.org/10.1016/B978-0-12-849906-1.00001-1>.
- [27] H.A.W. Kaminsky, T.H. Etsell, D.G. Ivey, O. Omotoso, Distribution of clay minerals in the process streams produced by the extraction of bitumen from Athabasca oil sands, *Can. J. Chem. Eng.* 87 (2009) 85–93. <https://doi.org/10.1002/cjce.20133>.
- [28] S. Ansari, Experimental Study of the Geometric Characteristics of Bubbles/Droplets Passing Through a Pore Space, (Ph. D. thesis) University of Alberta, 2021. <https://doi.org/https://doi.org/10.7939/r3-k89t-4r57>.
- [29] P.H. Nadeau, The physical dimensions of fundamental clay particles, *Clay Miner.* 20 (1985)

499–514. <https://doi.org/10.1180/claymin.1985.020.4.06>.

- [30] K.C. Khilar, H.S. Fogler, *Migrations of Fines in Porous Media*, Springer Netherlands, Dordrecht, 1998. <https://doi.org/10.1007/978-94-015-9074-7>.
- [31] Y. Guo, *Effect of Stress Build-up around SAGD Wellbores on the Slotted Liner Performance*, (master's thesis) University of Alberta, 2018. <https://doi.org/https://doi.org/10.7939/R3V98066B>.
- [32] H. Ben Mahmud, V.H. Leong, Y. Lestari, Sand production: A smart control framework for risk mitigation, *Petroleum*. 6 (2020) 1–13. <https://doi.org/10.1016/j.petlm.2019.04.002>.
- [33] D.B. Bennion, S. Gupta, S. Gittins, D. Hollies, Protocols for slotted liner design for optimum SAGD operation, in: *Can. Int. Pet. Conf.*, 2008. <https://doi.org/10.2118/130441-PA>.
- [34] M. Sivagnanam, J. Wang, I.D. Gates, On the fluid mechanics of slotted liners in horizontal wells, *Chem. Eng. Sci.* 164 (2017) 23–33. <https://doi.org/10.1016/j.ces.2017.01.070>.
- [35] J. Xie, S.W. Jones, C.M. Matthews, B.T. Wagg, P. Parker, R. Ducharme, Slotted liner design for SAGD wells, *World Oil*. 228 (2007) 67–75.
- [36] C. Mendez, *The Characterization of High Aspect Ratio Rectangular Jet Flows*, (Master's thesis) University of Alberta, 2020. <https://doi.org/https://doi.org/10.7939/r3-esk9-1e35>.
- [37] D.B. Bennion, S. Gupta, S. Gittins, D. Hollies, Protocols for Slotted Liner Design for Optimum SAGD Operation, *J. Can. Pet. Technol.* 48 (2009) 21–26. <https://doi.org/10.2118/130441-PA>.
- [38] U.G. Romanova, T. Ma, An Investigation on the Plugging Mechanisms in a Slotted Liner from the Steam Assisted Gravity Operations, in: *SPE Eur. Form. Damage Conf. Exhib.*, Society of Petroleum Engineers, 2013. <https://doi.org/10.2118/165111-MS>.
- [39] T. Hallman, V.Y.B. Yung, A. Albertson, Analysis of Wellbore Failures and Re-Design of Slotted Liners for Horizontal Wells Applied in a Heavy Oilfield, in: *SPE West. Reg. Meet.*, Society of Petroleum Engineers, 2015: pp. 1082–1120. <https://doi.org/10.2118/174072-MS>.
- [40] B.P. Erno, J. Christ, K.A. Miller, Carbonate Scale Formation in Thermally Stimulated

- Heavy-Oil Wells Near Lloydminster, Saskatchewan, in: SPE Int. Therm. Oper. Symp., Society of Petroleum Engineers, 1991: pp. 229–240. <https://doi.org/10.2118/21548-MS>.
- [41] A. Kaiser, The experimental and theoretical study of fines migration in porous media under particle-rock repulsion and attraction, (Ph.D. thesis) The University of Adelaide, 2014.
- [42] M. Byrne, E. Rojas, R. Kandasamy, A. Gibb, Fines Migration in Oil and Gas Reservoirs : Quantification and Qualification Through Detailed Study, Spe 168150. (2014).
- [43] O. Karazincir, W. Williams, P. Rijken, Prediction of fines migration through core testing, Proc. - SPE Annu. Tech. Conf. Exhib. (2017) 9–11. <https://doi.org/10.2118/187157-ms>.
- [44] G.L. Kothny, Underground well surveying, directed drilling, side-wall sampling, and polar core orientation, Drill. Prod. Pract. 1941. (1941) 76–90.
- [45] M. Kennedy, Core and Other Real Rock Measurements, in: Dev. Pet. Sci., 2015: pp. 73–88. <https://doi.org/10.1016/B978-0-444-63270-8.00003-7>.
- [46] W.C. Hinds, Aerosol technology - properties, behavior, and measurement of airborne particles, Second Edi, John Wiley & Sons, Linc., 1999.
- [47] W.H. Finlay, Motion of a single aerosol particle in a fluid, in: Mech. Inhaled Pharm. Aerosols, Elsevier, 2001: pp. 17–45. <https://doi.org/10.1016/B978-012256971-5/50004-3>.
- [48] Y. You, Y. Zhao, Discrete element modelling of ellipsoidal particles using super-ellipsoids and multi-spheres: A comparative study, Powder Technol. 331 (2018) 179–191. <https://doi.org/10.1016/j.powtec.2018.03.017>.
- [49] X. Garcia, J.-P. Latham, J. Xiang, J.P. Harrison, A clustered overlapping sphere algorithm to represent real particles in discrete element modelling, Géotechnique. 59 (2009) 779–784. <https://doi.org/10.1680/geot.8.T.037>.
- [50] T.G. Chondros, Archimedes life works and machines, Mech. Mach. Theory. 45 (2010) 1766–1775. <https://doi.org/10.1016/j.mechmachtheory.2010.05.009>.
- [51] G.G. Stokes, On the effect of the internal friction of fluids on motion of pendulums, in: Math. Phys. Pap. Vol.1, Cambridge University Press, Cambridge, 2010: pp. 75–129.

<https://doi.org/10.1017/CBO9780511702242.005>.

- [52] M.R. Maxey, Equation of motion for a small rigid sphere in a nonuniform flow, *Phys. Fluids*. 26 (1983) 883. <https://doi.org/10.1063/1.864230>.
- [53] T.L. Thompson, N.N. Clark, A holistic approach to particle drag prediction, *Powder Technol.* 67 (1991) 57–66. [https://doi.org/10.1016/0032-5910\(91\)80026-F](https://doi.org/10.1016/0032-5910(91)80026-F).
- [54] F. Dioguardi, D. Mele, P. Dellino, A New One-Equation Model of Fluid Drag for Irregularly Shaped Particles Valid Over a Wide Range of Reynolds Number, *J. Geophys. Res. Solid Earth*. 123 (2018) 144–156. <https://doi.org/10.1002/2017JB014926>.
- [55] A. Unnikrishnan, R.P. Chhabra, An experimental study of motion of cylinders in newtonian fluids: Wall effects and drag coefficient, *Can. J. Chem. Eng.* 69 (1991) 729–735. <https://doi.org/10.1002/cjce.5450690315>.
- [56] G. Bagheri, C. Bonadonna, On the drag of freely falling non-spherical particles, *Powder Technol.* 301 (2016) 526–544. <https://doi.org/10.1016/j.powtec.2016.06.015>.
- [57] N.-S. Cheng, Simplified Settling Velocity Formula for Sediment Particle, *J. Hydraul. Eng.* 123 (1997) 149–152. [https://doi.org/10.1061/\(ASCE\)0733-9429\(1997\)123:2\(149\)](https://doi.org/10.1061/(ASCE)0733-9429(1997)123:2(149)).
- [58] S. Tran-Cong, M. Gay, E.E. Michaelides, Drag coefficients of irregularly shaped particles, *Powder Technol.* 139 (2004) 21–32. <https://doi.org/10.1016/j.powtec.2003.10.002>.
- [59] E. Loth, Drag of non-spherical solid particles of regular and irregular shape, *Powder Technol.* 182 (2008) 342–353. <https://doi.org/10.1016/j.powtec.2007.06.001>.
- [60] Y. Çengel, J.M. Cimbala, *Fluid mechanics: fundamentals and applications*, McGraw-Hill, 2006. <https://doi.org/10.1088/1751-8113/44/8/085201>.
- [61] G.V. Madhav, R.P. Chhabra, Drag on non-spherical particles in viscous fluids, *Int. J. Miner. Process.* 43 (1995) 15–29. [https://doi.org/10.1016/0301-7516\(94\)00038-2](https://doi.org/10.1016/0301-7516(94)00038-2).
- [62] M. Raffel, C.E. Willert, F. Scarano, C.J. Kähler, S.T. Wereley, J. Kompenhans, *Particle Image Velocimetry*, Springer International Publishing AG, part of Springer Nature, 2018. <https://doi.org/10.1007/978-3-319-68852-7>.

- [63] A.K. Prasad, Particle image velocimetry, *Curr. Sci.* 79 (2000) 51–60.
- [64] L. Squires, The sedimentation of thin discs, *Trans. Am. Inst. Chem. Eng.* 33 (1936) 1–12.
- [65] E. PettyJohn, E. Christiansen, Effect of Particle Shape on Free Settling Rates of Isometric Particles, *Chem. Eng. Prog.* (1948).
- [66] S. Rushd, I. Hassan, R.A. Sultan, V.C. Kelessidis, A. Rahman, H.S. Hasan, A. Hasan, Terminal settling velocity of a single sphere in drilling fluid, *Part. Sci. Technol.* 37 (2019) 939–948. <https://doi.org/10.1080/02726351.2018.1472162>.
- [67] J.G. Speight, Sediments, Reservoirs, and Deposits, in: *Introd. to Enhanc. Recover. Methods Heavy Oil Tar Sands*, Elsevier, 2016: pp. 85–121. <https://doi.org/10.1016/B978-0-12-849906-1.00003-5>.
- [68] T. Ahmed, Fundamentals of Rock Properties, in: *Reserv. Eng. Handb.*, Elsevier, 2010: pp. 189–287. <https://doi.org/10.1016/B978-1-85617-803-7.50012-2>.
- [69] M.A. Oliveira, A.S.L. Vaz, F.D. Siqueira, Y. Yang, Z. You, P. Bedrikovetsky, Slow migration of mobilised fines during flow in reservoir rocks: Laboratory study, *J. Pet. Sci. Eng.* 122 (2014) 534–541. <https://doi.org/10.1016/j.petrol.2014.08.019>.
- [70] Z. You, Y. Yang, A. Badalyan, P. Bedrikovetsky, M. Hand, Mathematical modelling of fines migration in geothermal reservoirs, *Geothermics.* 59 (2016) 123–133. <https://doi.org/10.1016/j.geothermics.2015.05.008>.
- [71] C. Yin, L. Rosendahl, S. K. Kær, T. J. Condra, Use of numerical modeling in design for co-firing biomass in wall-fired burners, *Chem. Eng. Sci.* 59 (2004) 3281–3292. <https://doi.org/10.1016/j.ces.2004.04.036>.
- [72] M. Byron, The rotation and translation of non-spherical particles in homogeneous isotropic turbulence, (Ph.D. thesis) University of California, Berkeley, 2015.
- [73] R. Castrejón-García, J.R. Castrejón-Pita, G.D. Martin, I.M. Hutchings, The shadowgraph imaging technique and its modern application to fluid jets and drops, *Rev. Mex. Fis.* 57 (2011) 266–275.

- [74] N.S. Cheng, Formula for the Viscosity of a Glycerol–Water Mixture, *Ind. Eng. Chem. Res.* 47 (2008) 3285–3288. <https://doi.org/10.1021/ie071349z>.
- [75] A. Volk, C.J. Kähler, Density model for aqueous glycerol solutions, *Exp. Fluids.* 59 (2018) 75. <https://doi.org/10.1007/s00348-018-2527-y>.
- [76] E.E.G. Rojas, J.S.R. Coimbra, J. Telis-Romero, Thermophysical Properties of Cotton, Canola, Sunflower and Soybean Oils as a Function of Temperature, *Int. J. Food Prop.* 16 (2013) 1620–1629. <https://doi.org/10.1080/10942912.2011.604889>.
- [77] L.M. Diamante, T. Lan, Absolute Viscosities of Vegetable Oils at Different Temperatures and Shear Rate Range of 64.5 to 4835 s^{-1} , *J. Food Process.* 2014 (2014) 1–6. <https://doi.org/10.1155/2014/234583>.
- [78] John D’Errico, A suite of minimal bounding objects, (2022). <https://www.mathworks.com/matlabcentral/fileexchange/34767-a-suite-of-minimal-bounding-objects>), MATLAB Central File Exchange (accessed January 27, 2022).
- [79] K. Bricker, D.S. Nobes, derivativeFit, (2022). <https://www.mathworks.com/matlabcentral/fileexchange/89371-derivativefit>), MATLAB Central File Exchange (accessed January 27, 2022).
- [80] J.F. RICHARDSON, J.H. HARKER, J.R. BACKHURST, Motion of Particles in a Fluid, in: *Chem. Eng.*, Elsevier, 2002: pp. 146–190. <https://doi.org/10.1016/B978-0-08-049064-9.50014-X>.
- [81] L. Kinsale, D.S. Nobes, Development of an online system to measure sand production through mini-slots in SAGD operations using PSV, in: *Okanagan Fluid Dyn. Meet. Kelowna, Br. Columbia, Canada. August 21-24, 2017*: pp. 182–186.
- [82] J.B. Segur, H.E. Oberstar, Viscosity of glycerol and its aqueous solutions, *Ind. Eng. Chem.* 43 (1951) 2117–2120. <https://doi.org/10.1021/ie50501a040>.
- [83] F. Moisy, PIVMat, (2017). <https://www.mathworks.com/matlabcentral/fileexchange/10902-pivmat-4-10> (accessed December 1, 2018).

- [84] S. Ghaemi, P. Rahimi, D.S. Nobes, Evaluation of Digital Image Discretization Error in Droplet Shape Measurement Using Simulation, Part. Part. Syst. Charact. 26 (2009) 243–255. <https://doi.org/10.1002/ppsc.200900069>.
- [85] D. Homeniuk, Development and testing of macro and micro three-dimensional particle tracking systems, (master's thesis) Thesis University of Alberta, 2009.
- [86] S.J. Baek, S.J. Lee, A new two-frame particle tracking algorithm using match probability, Exp. Fluids. 22 (1996) 23–32. <https://doi.org/10.1007/BF01893303>.
- [87] F. Podczec, S.. Rahman, J.. Newton, Evaluation of a standardised procedure to assess the shape of pellets using image analysis, Pharmaceutics. 192 (1999) 123–138. [https://doi.org/10.1016/S0378-5173\(99\)00302-6](https://doi.org/10.1016/S0378-5173(99)00302-6).
- [88] L. Mayor, J. Pissarra, A.M. Sereno, Microstructural changes during osmotic dehydration of parenchymatic pumpkin tissue, Food Eng. 85 (2008) 326–339. <https://doi.org/10.1016/j.jfoodeng.2007.06.038>.
- [89] H.J. Hwang, S.W. Kim, C.P. Xu, J.W. Choi, J.W. Yun, Morphological and rheological properties of the three different species of basidiomycetes *Phellinus* in submerged cultures, Appl. Microbiol. 96 (2004) 1296–1305. <https://doi.org/10.1111/j.1365-2672.2004.02271.x>.
- [90] Y. Takashimizu, M. Iiyoshi, New parameter of roundness R: circularity corrected by aspect ratio, Prog. Earth Planet. Sci. 3 (2016). <https://doi.org/10.1186/s40645-015-0078-x>.
- [91] H. Wadell, Volume, shape, and roundness of quartz particles, Geology. 43 (1935) 250–280. <https://doi.org/10.1086/624298>.
- [92] J. Zheng, R.D. Hryciw, Traditional soil particle sphericity, roundness and surface roughness by computational geometry, Géotechnique. 65 (2015) 494–506. <https://doi.org/10.1680/geot.14.P.192>.
- [93] E.P. Cox, A method of assigning numerical and percentage values to the degree of roundness of sand grains, Paleontology. 1 (1927) 179–183.
- [94] J. Zheng, Wadell_roundness.m Particle roundness and sphericity computation, (2014).

<https://www.mathworks.com/matlabcentral/fileexchange/60651-particle-roundness-and-sphericity-computation> (accessed November 1, 2018).

- [95] J.C. Santamarina, G. Tech, *Advances in Geotechnical Engineering: The Skempton Conference*, Thomas Telford Ltd, 2004. <https://doi.org/10.1680/aigev1.32644>.
- [96] P.P. Lewicki, G. Pawlak, Effect of mode of drying on microstructure of potato, *Dry. Technol.* 23 (2005) 847–869. <https://doi.org/10.1081/DRT-200054233>.
- [97] J.R. Hernandez-Aguilar, R.G. Coleman, C.O. Gomez, J.A. Finch, A comparison between capillary and imaging techniques for sizing bubbles in flotation systems, *Miner. Eng.* 17 (2004) 53–61. <https://doi.org/10.1016/j.mineng.2003.09.011>.
- [98] C.E. Willert, M. Gharib, Digital particle image velocimetry, *Exp. Fluids.* 10 (1991) 181–193. <https://doi.org/10.1007/BF00190388>.
- [99] S. Ansari, *Newtonian and non-newtonian flows through mini-channels and micro-scale orifices for SAGD applications*, (Master's thesis) University of Alberta, 2016. <https://doi.org/https://doi.org/10.7939/R3J09WC3C>.
- [100] B. Wieneke, PIV uncertainty quantification from correlation statistics, *Meas. Sci. Technol.* 26 (2015). <https://doi.org/10.1088/0957-0233/26/7/074002>.
- [101] A. Sciacchitano, B. Wieneke, PIV uncertainty propagation, *Meas. Sci. Technol.* 27 (2016). <https://doi.org/10.1088/0957-0233/27/8/084006>.
- [102] S. Ansari, Y. Yusuf, L. Kinsale, R. Sabbagh, D.S. Nobes, Visualization of fines migration in the flow entering apertures through the near-wellbore porous media, in: *SPE Therm. Well Integr. Des. Symp.*, Society of Petroleum Engineers, 2018. <https://doi.org/10.2118/193358-MS>.
- [103] Y. Yusuf, S. Ansari, M. Bayans, R. Sabbagh, Study of flow convergence in rectangular slots using particle shadowgraph velocimetry, *5th Int. Conf. Exp. Fluid Mech. Munich, Ger.* July 2-4, 2018. (2018) 579–584.
- [104] H.A. Stone, C. Duprat, Chapter 2: Low-reynolds-number flows, in: *Fluid-Structure Interact.*

Low-Reynolds-Number Flows, Royal Society of Chemistry, 2016: pp. 25–77.
<https://doi.org/10.1039/9781782628491-00025>.

8 Appendices

8.1 Appendix 1: 4mm Diameter Delrin Spheres in Water

8.1.1 Particle Displacement, Particle Velocity and Particle Acceleration for 4mm Diameter Delrin Spheres in Water

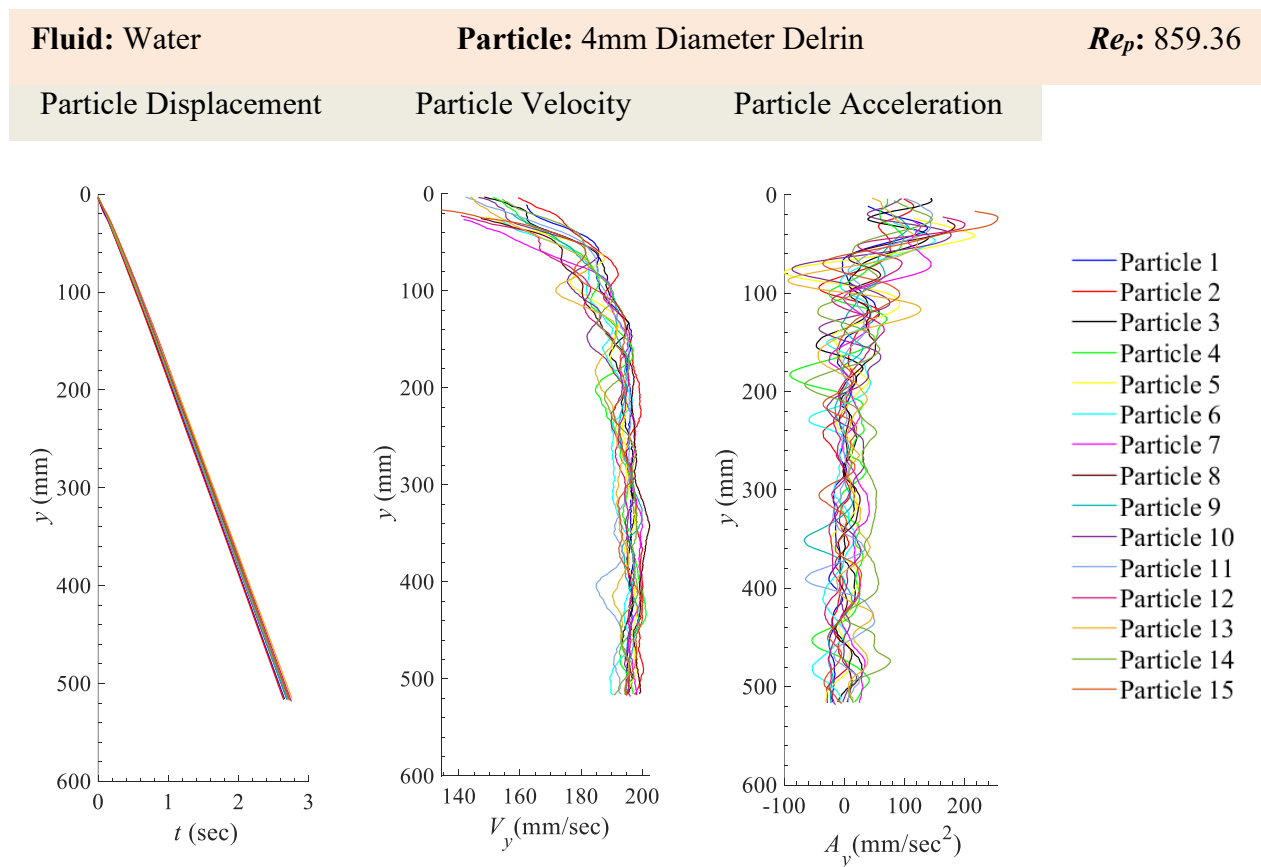


Figure 45 Particle displacement, y , velocity, V_y , and acceleration, A_y , for 4mm Diameter Delrin (15 particles) in Water. Two particles (represented by the light blue and mustard lines) were outliers because the velocity plots exhibited unusual trends within 375 mm and 450 mm of the particle displacement. The outliers in the original data were removed and plotted in Figure 46 and Figure 47 in order to obtain a better estimate of the terminal settling velocity and average constant acceleration.

8.1.2 x -Velocity (V_x), y -Velocity (V_y) and Magnitude of Velocity ($|V|$) for 4mm Diameter Delrin Spheres in Water

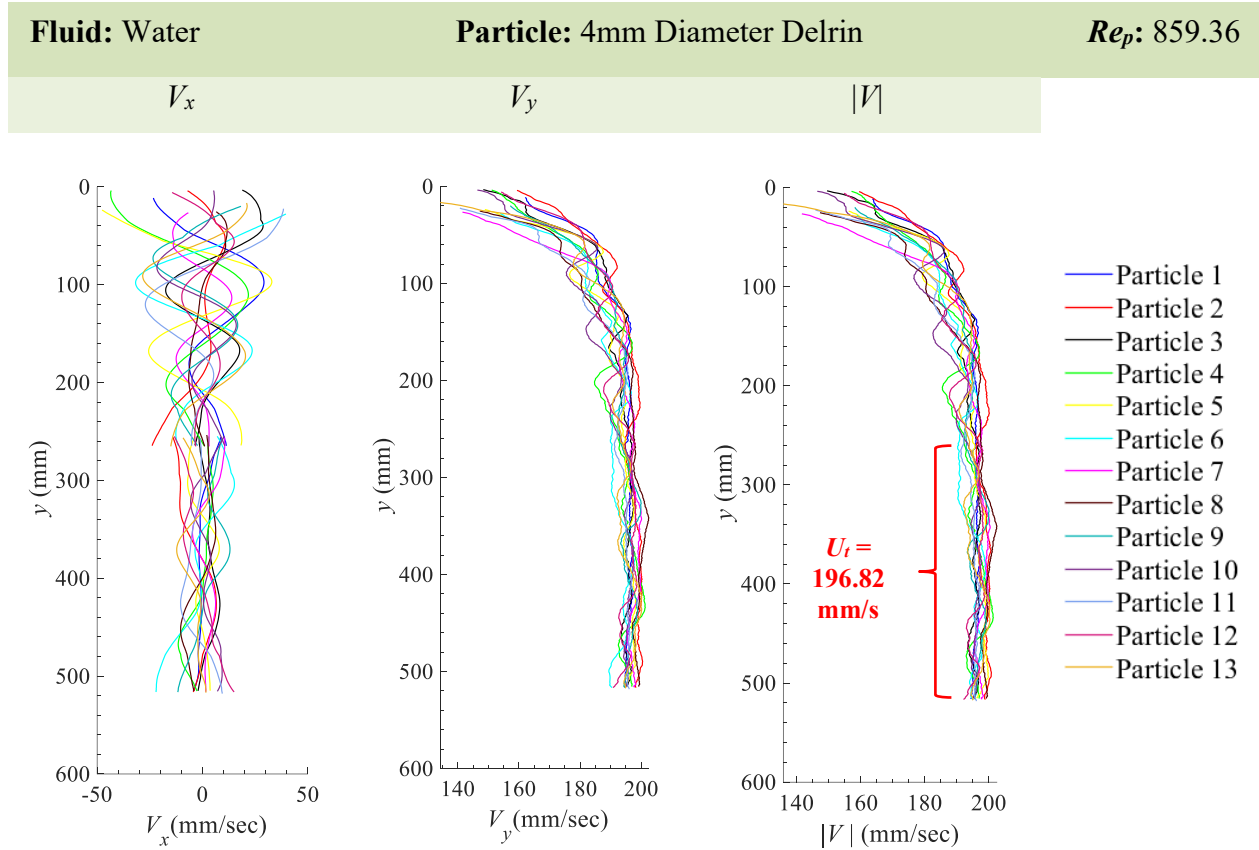


Figure 46 Particle velocity in the x -direction V_x , y -direction V_y , and the magnitude $\sqrt{V_x^2 + V_y^2}$ of the particle velocity $|V|$ for 4mm Diameter Delrin in Water. The average terminal settling velocity, U_t is 196.82 mm/s. Note: the two (2) outliers shown in Figure 45 were omitted in order to obtain a better estimate of the terminal settling velocity. Therefore only 13 particles are shown in this plots.

8.1.3 x -Acceleration (A_x), y -Acceleration (A_y) and Magnitude of Acceleration ($|A|$) for 4mm Diameter Delrin Spheres in Water

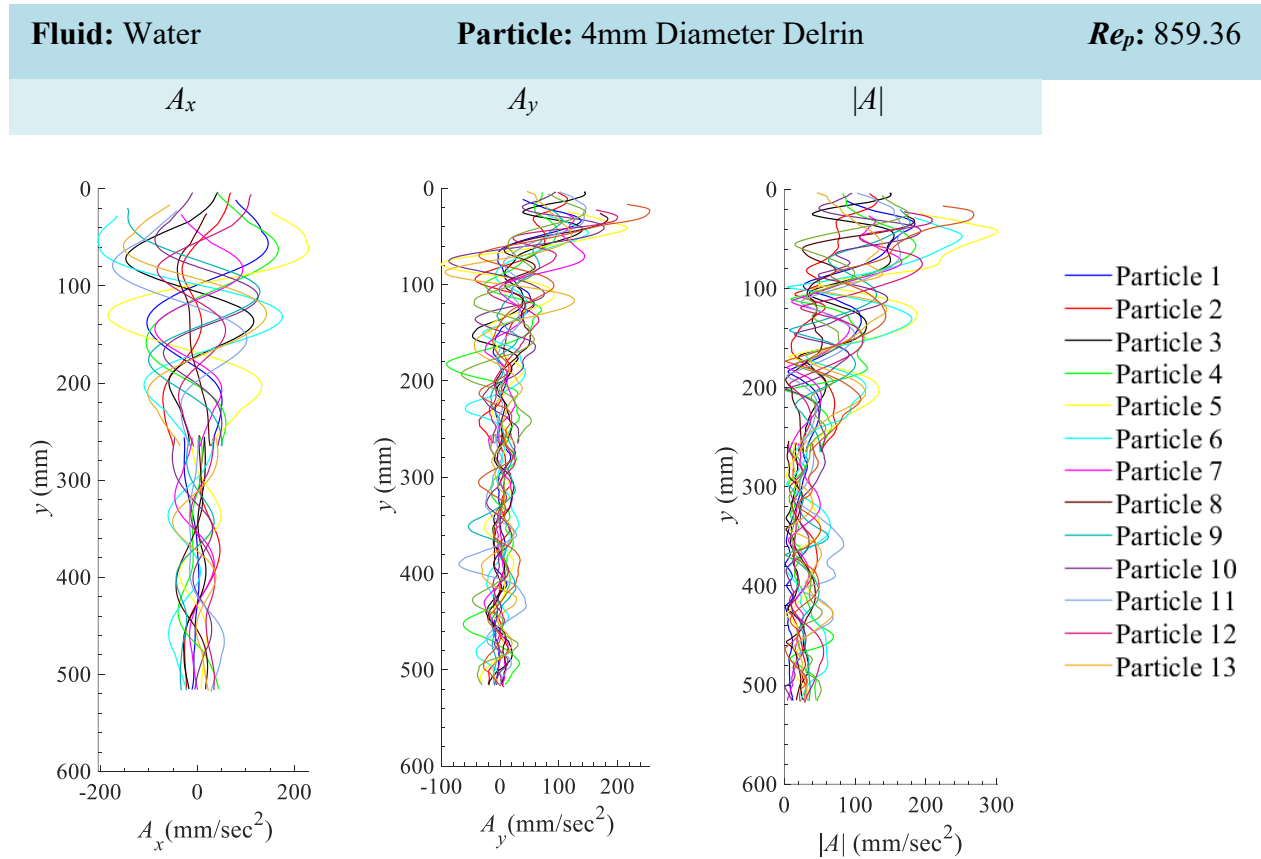


Figure 47 Particle acceleration in the x -direction A_x , y -direction A_y , and the magnitude $\sqrt{A_x^2 + A_y^2}$ of the particle acceleration $|A|$ for 4mm Diameter Delrin in Water. Note: the two (2) outliers shown in Figure 45 were omitted in order to obtain a better estimate of the average acceleration within the terminal velocity region. Therefore only 13 particles are shown in this plots.

8.2 Appendix 2: 4mm Delrin Spheres in 20%–80% Glycerol–Water

8.2.1 Particle Displacement, Particle Velocity and Particle Acceleration for 4mm Diameter Delrin Spheres in 20%–80% Glycerol–Water

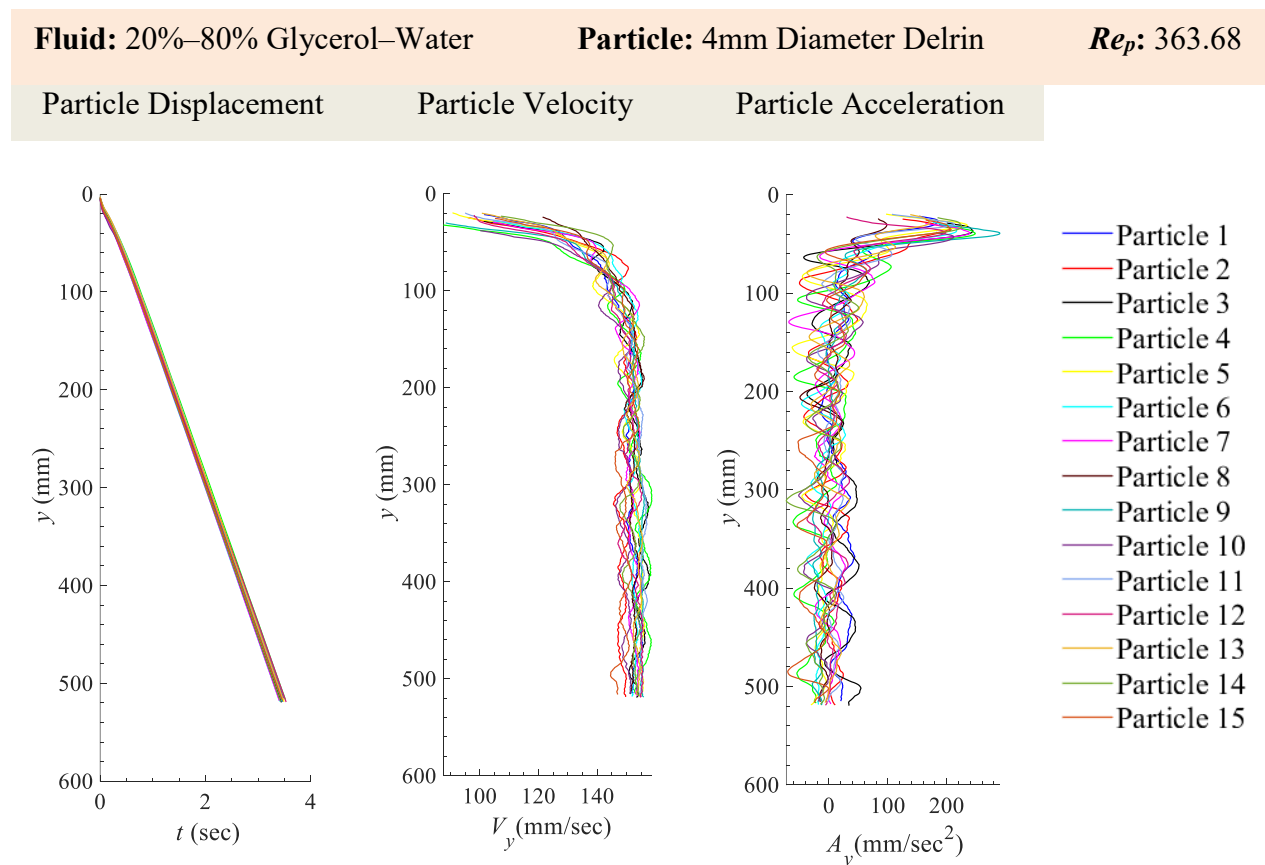


Figure 48 Particle displacement, y , velocity, V_y , and acceleration, A_y , for 4mm Diameter Delrin (15 particles) in 20%–80% Glycerol–Water.

8.2.2 x -Velocity (V_x), y -Velocity (V_y) and Magnitude of Velocity ($|V|$) for 4mm Diameter Delrin Spheres in 20%–80% Glycerol–Water

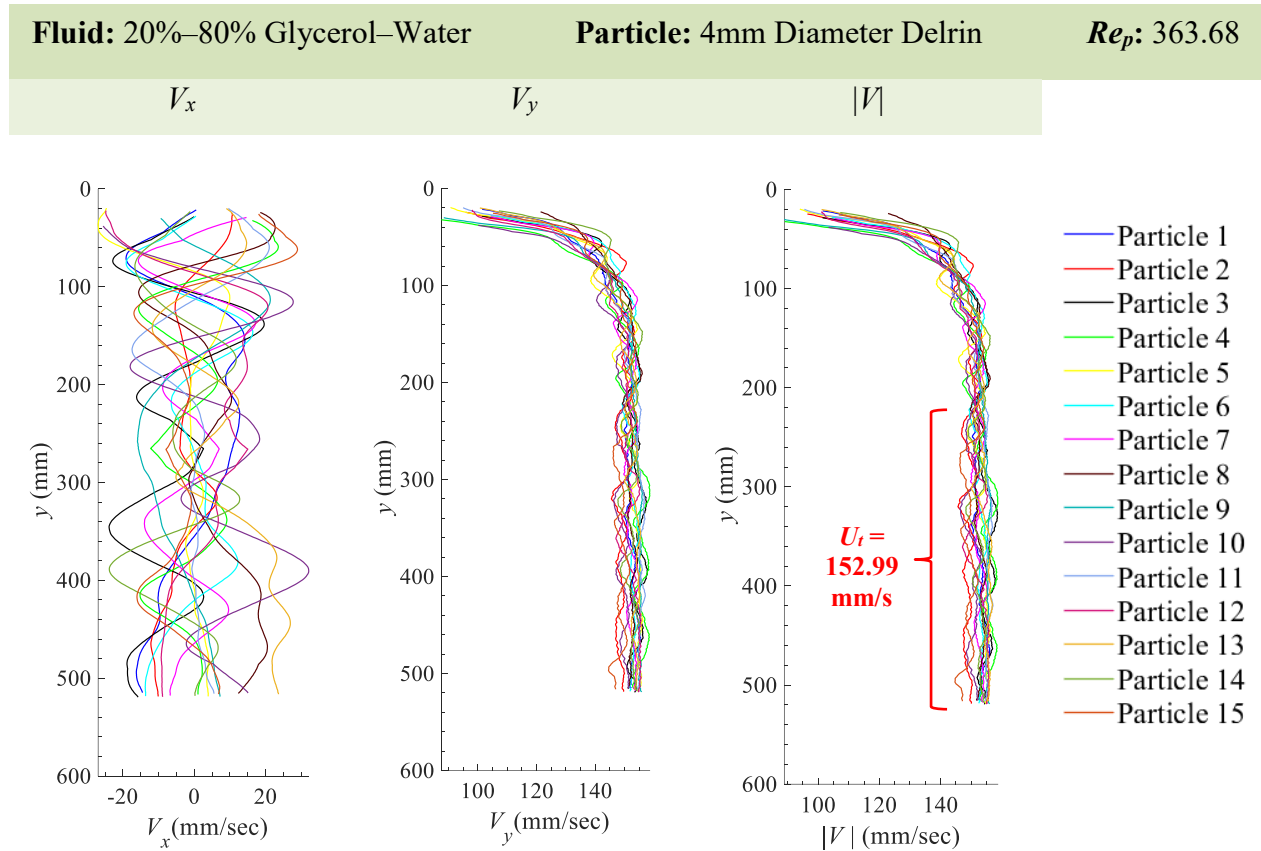


Figure 49 Particle velocity in the x -direction V_x , y -direction V_y , and the magnitude $\sqrt{V_x^2 + V_y^2}$ of the particle velocity $|V|$ for 4mm Diameter Delrin (15 particles) in 20%–80% Glycerol–Water. The average terminal settling velocity, U_t is 152.99 mm/s.

8.2.3 x -Acceleration (A_x), y -Acceleration (A_y) and Magnitude of Acceleration ($|A|$) for 4mm Diameter Delrin Spheres in 20%–80% Glycerol–Water

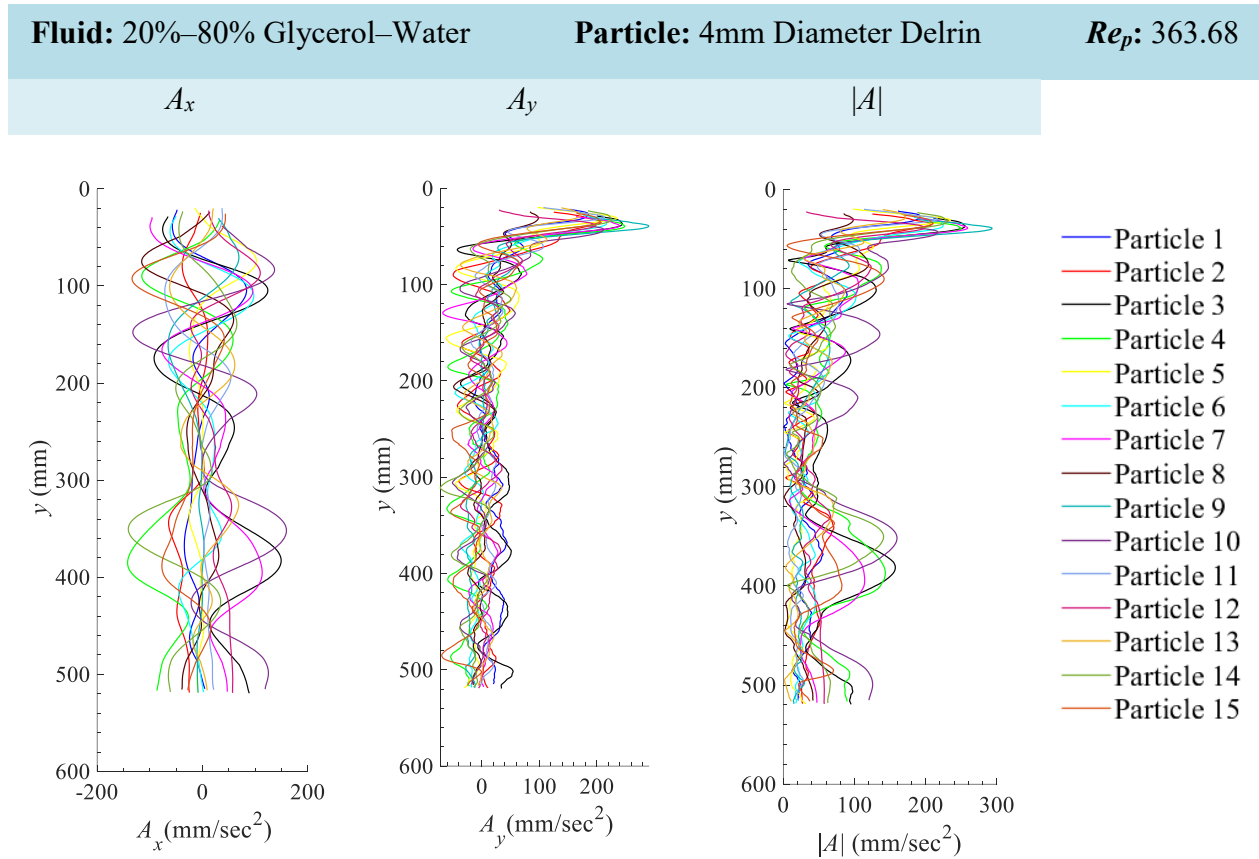


Figure 50 Particle acceleration in the x -direction A_x , y -direction A_y , and the magnitude $\sqrt{A_x^2 + A_y^2}$ of the particle acceleration $|A|$ for 4mm Diameter Delrin (15 particles) in 20%–80% Glycerol–Water.

8.3 Appendix 3: 4mm Delrin Spheres in 40%–60% Glycerol–Water

8.3.1 Particle Displacement, Particle Velocity and Particle Acceleration for 4mm Diameter Delrin Spheres in 40%–60% Glycerol–Water

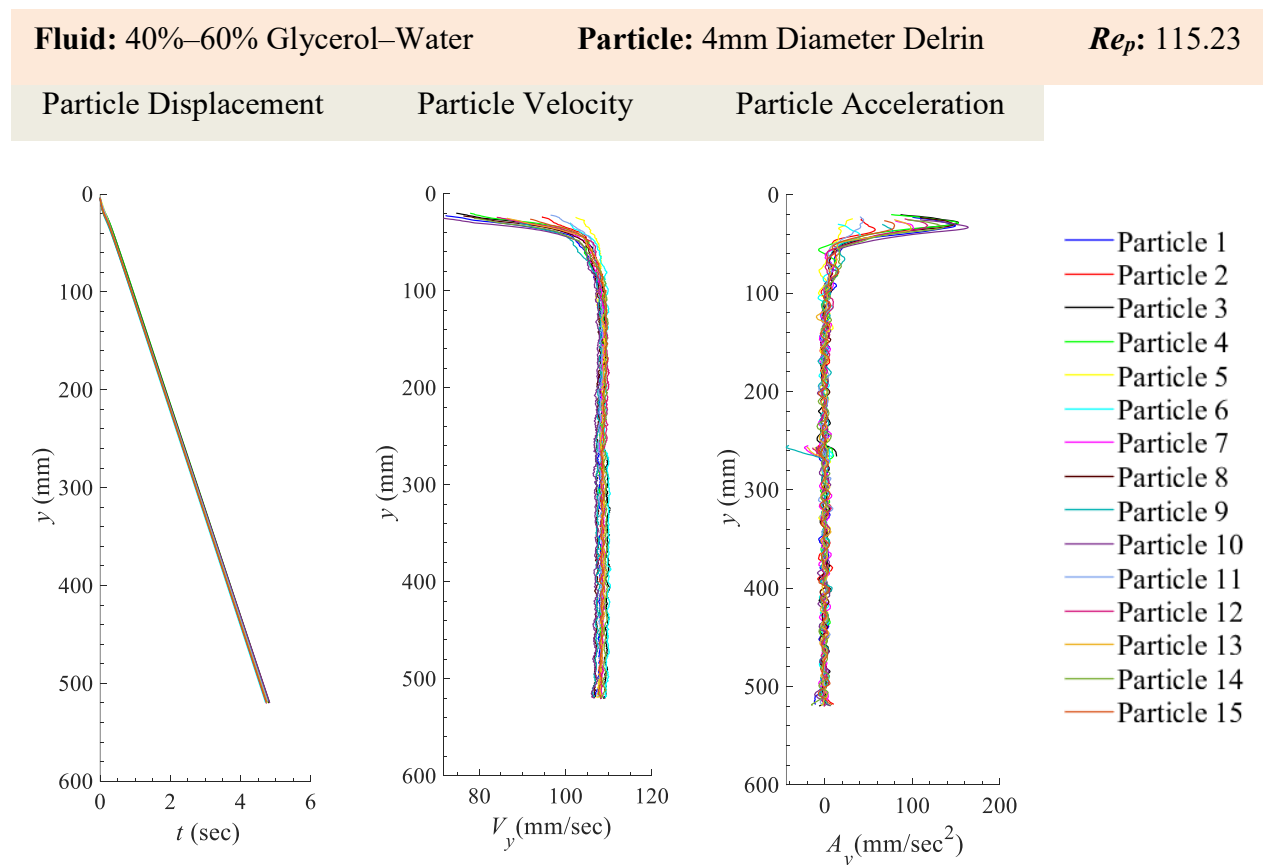


Figure 51 Particle displacement, y , velocity, V_y , and acceleration, A_y , for 4mm Diameter Delrin (15 particles) in 40%–60% Glycerol–Water.

8.3.2 x -Velocity (V_x), y -Velocity (V_y) and Magnitude of Velocity ($|V|$) for 4mm Diameter Delrin Spheres in 40%–60% Glycerol– Water

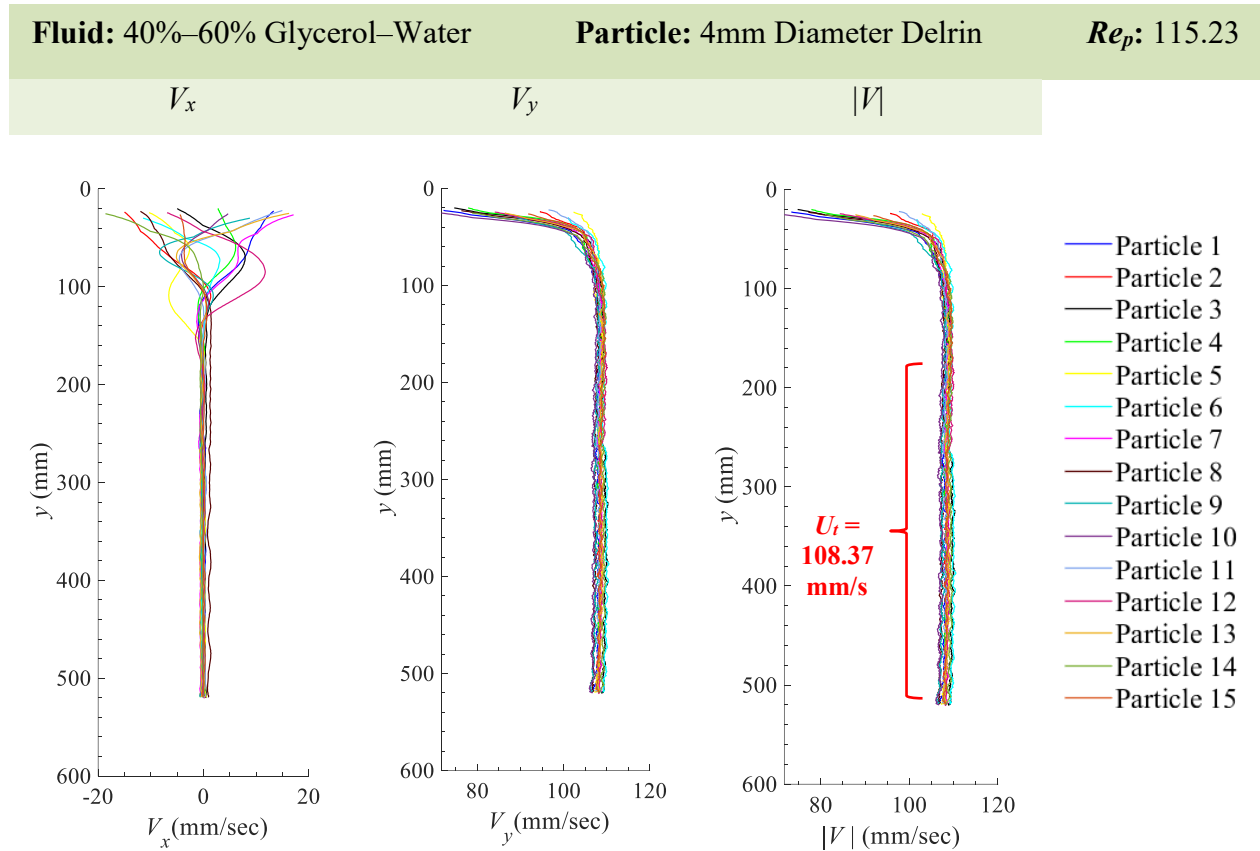


Figure 52 Particle velocity in the x -direction V_x , y -direction V_y , and the magnitude $\sqrt{(V_x^2 + V_y^2)}$ of the particle velocity $|V|$ for 4mm Diameter Delrin (15 particles) in 40%–60% Glycerol–Water. The average terminal settling velocity, U_t is 108.37 mm/s.

8.3.3 x -Acceleration (A_x), y -Acceleration (A_y) and Magnitude of Acceleration ($|A|$) for 4mm Diameter Delrin Spheres in 40%–60% Glycerol–Water

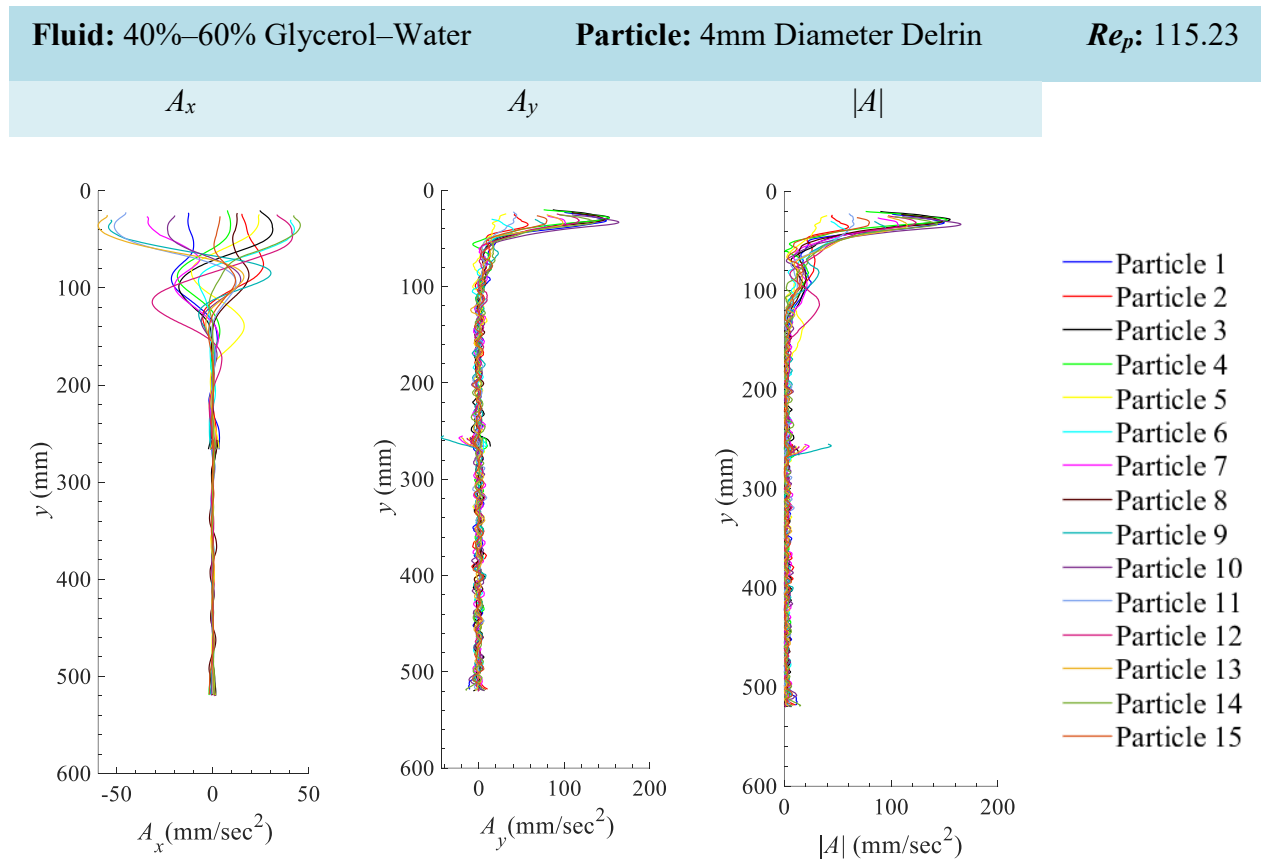


Figure 53 Particle acceleration in the x -direction A_x , y -direction A_y , and the magnitude $\sqrt{A_x^2 + A_y^2}$ of the particle acceleration $|A|$ for 4mm Diameter Delrin (15 particles) in 40%–60% Glycerol–Water.

8.4 Appendix 4: 4mm Delrin Spheres in 70%–30% Glycerol–Water

8.4.1 Particle Displacement, Particle Velocity and Particle Acceleration for 4mm Diameter Delrin Spheres in 70%–30% Glycerol–Water

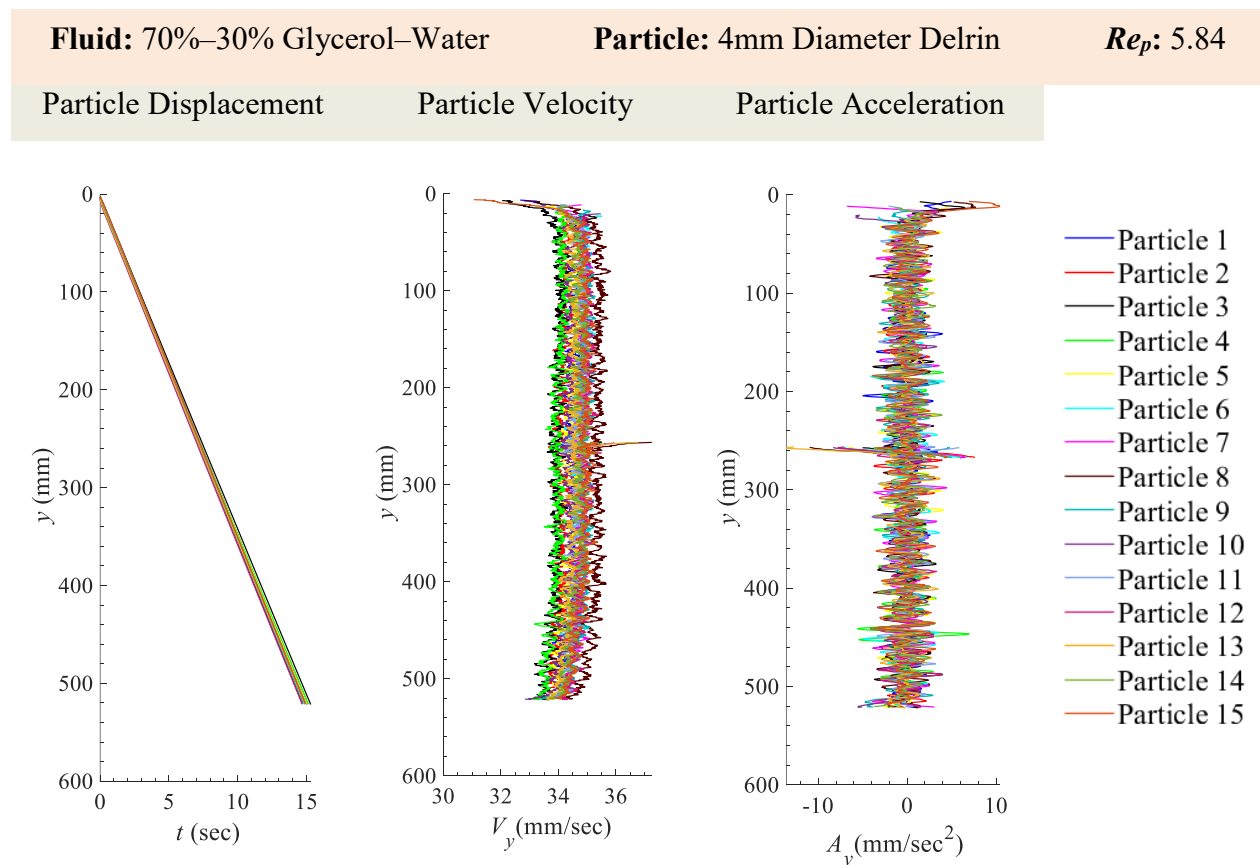


Figure 54 Particle displacement, y , velocity, V_y , and acceleration, A_y , for 4mm Diameter Delrin (15 particles) in 70%–30% Glycerol–Water. The outliers at displacement 260 mm occurred within the overlap between the two cameras. In this region there was a variation in the light distribution compared to the rest of the field of view. A uniform distribution of light was not achieved with the projector and kite paper as shown in Figure 8 and describe in Section 3.5.1. This affected the binarization of the particle within that region and thereby a slight shift in the location of the centroid of the particle from the image processing scheme.

8.4.2 x -Velocity (V_x), y -Velocity (V_y) and Magnitude of Velocity ($|V|$) for 4mm Diameter Delrin Spheres in 70%–30% Glycerol–Water

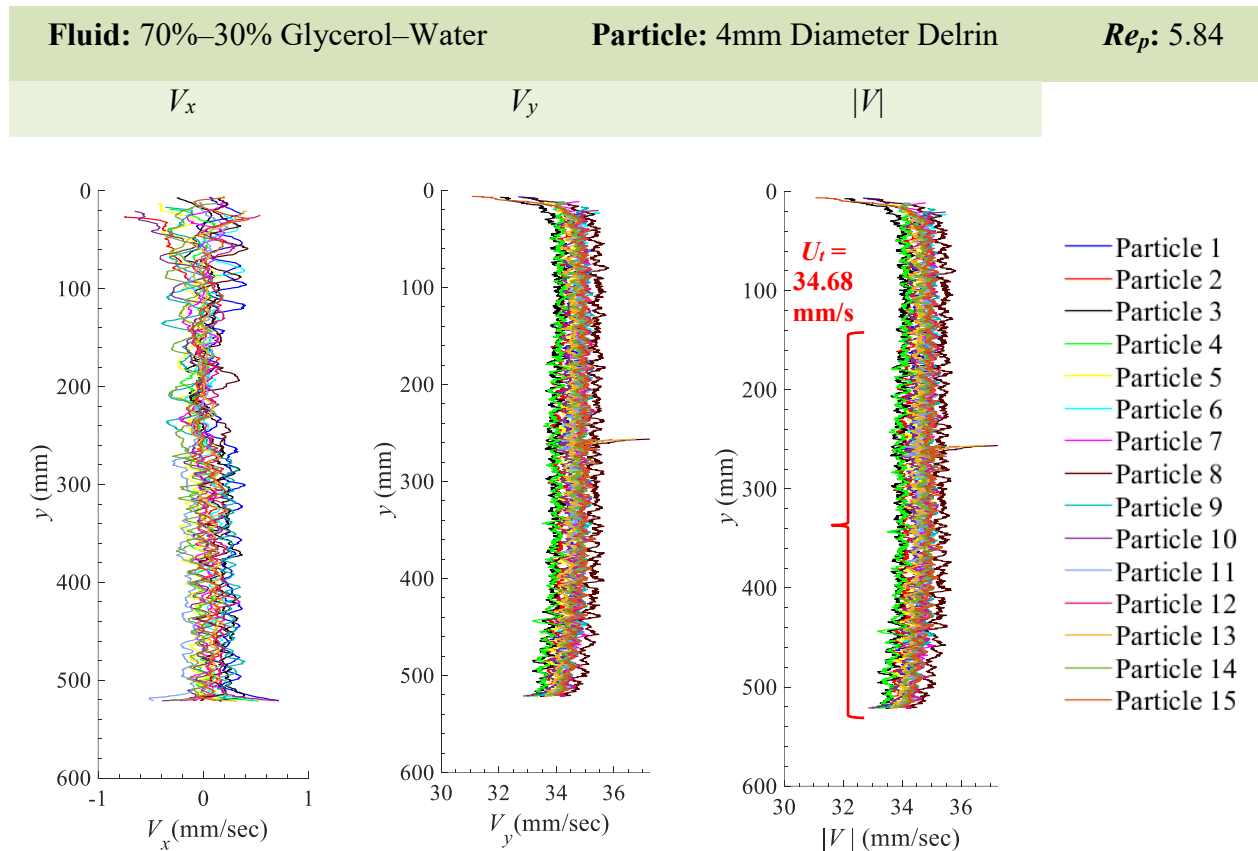


Figure 55 Particle velocity in the x -direction V_x , y -direction V_y , and the magnitude $\sqrt{(V_x^2 + V_y^2)}$ of the particle velocity $|V|$ for 4mm Diameter Delrin (15 particles) in 70%–30% Glycerol–Water. The average terminal settling velocity, U_t is 34.68 mm/s. The outliers at displacement 260 mm occurred within the overlap between the two cameras. In this region there was a variation in the light distribution compared to the rest of the field of view. A uniform distribution of light was not achieved with the projector and kite paper as shown in Figure 8 and describe in Section 3.5.1. This affected the binarization of the particle within that region and thereby a slight shift in the location of the centroid of the particle from the image processing scheme.

8.4.3 x -Acceleration (A_x), y -Acceleration (A_y) and Magnitude of Acceleration ($|A|$) for 4mm Diameter Delrin Spheres in 70%–30% Glycerol–Water

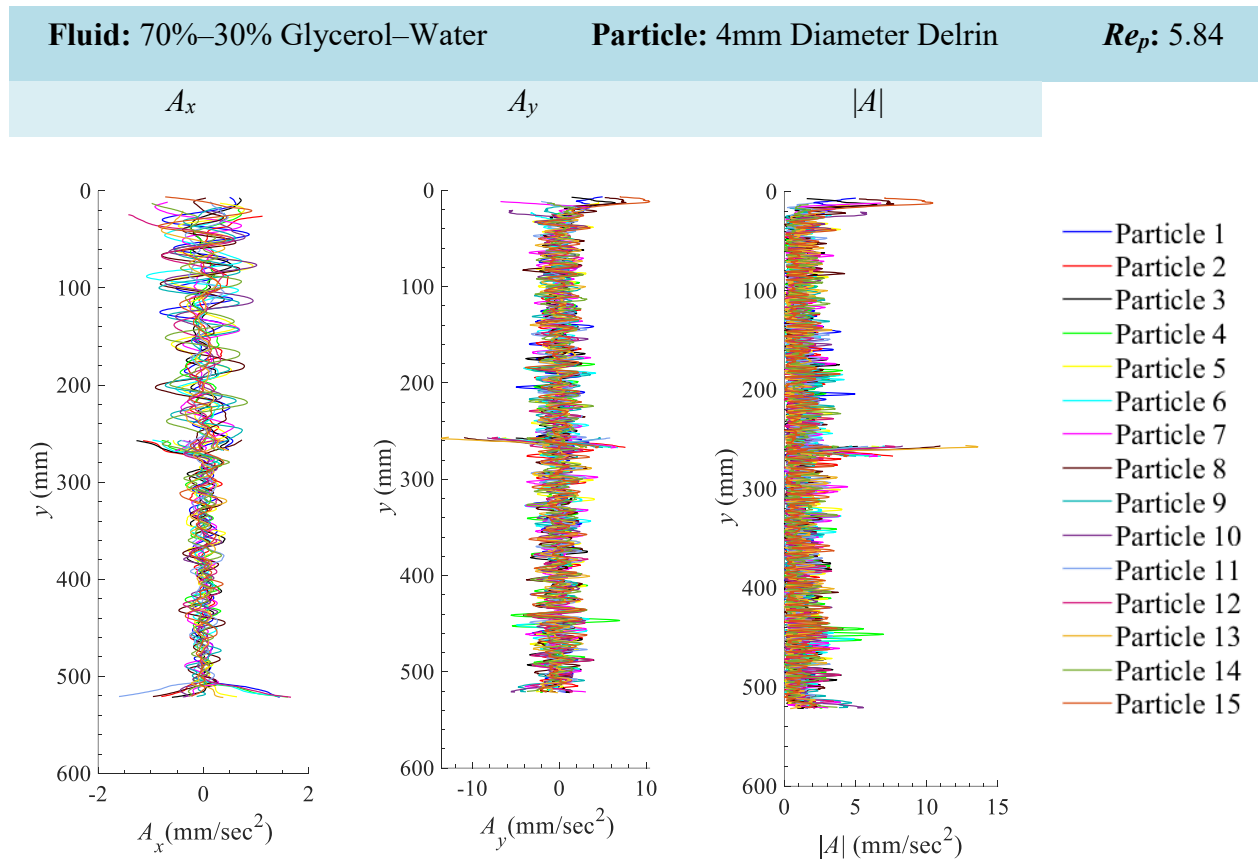


Figure 56 Particle acceleration in the x -direction A_x , y -direction A_y , and the magnitude $\sqrt{A_x^2 + A_y^2}$ of the particle acceleration $|A|$ for 4mm Diameter Delrin (15 particles) in 70%–30% Glycerol–Water. The outliers at displacement 260 mm occurred within the overlap between the two cameras. In this region there was a variation in the light distribution compared to the rest of the field of view. A uniform distribution of light was not achieved with the projector and kite paper as shown in Figure 8 and describe in Section 3.5.1. This affected the binarization of the particle within that region and thereby a slight shift in the location of the centroid of the particle from the image processing scheme.

8.5 Appendix 5: 4mm Delrin Spheres in Canola Oil

8.5.1 Particle Displacement, Particle Velocity and Particle Acceleration for 4mm Diameter Delrin Spheres in Canola Oil

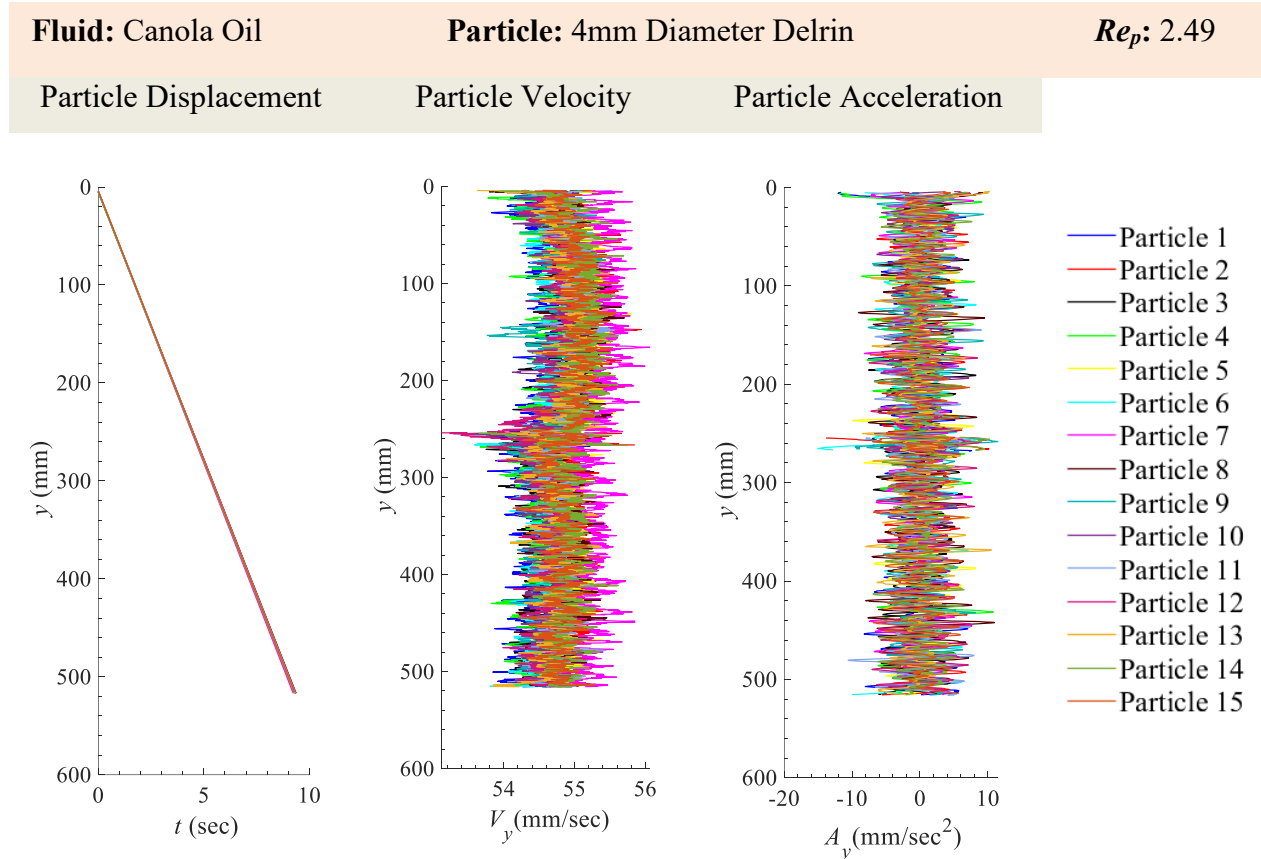


Figure 57 Particle displacement, y , velocity, V_y , and acceleration, A_y , for 4mm Diameter Delrin (15 particles) in Canola Oil. The outliers at displacement 260 mm occurred within the overlap between the two cameras. In this region there was a variation in the light distribution compared to the rest of the field of view. A uniform distribution of light was not achieved with the projector and kite paper as shown in Figure 8 and describe in Section 3.5.1. This affected the binarization of the particle within that region and thereby a slight shift in the location of the centroid of the particle from the image processing scheme.

8.5.2 x -Velocity (V_x), y -Velocity (V_y) and Magnitude of Velocity ($|V|$) for 4mm Diameter Delrin Spheres in Canola Oil

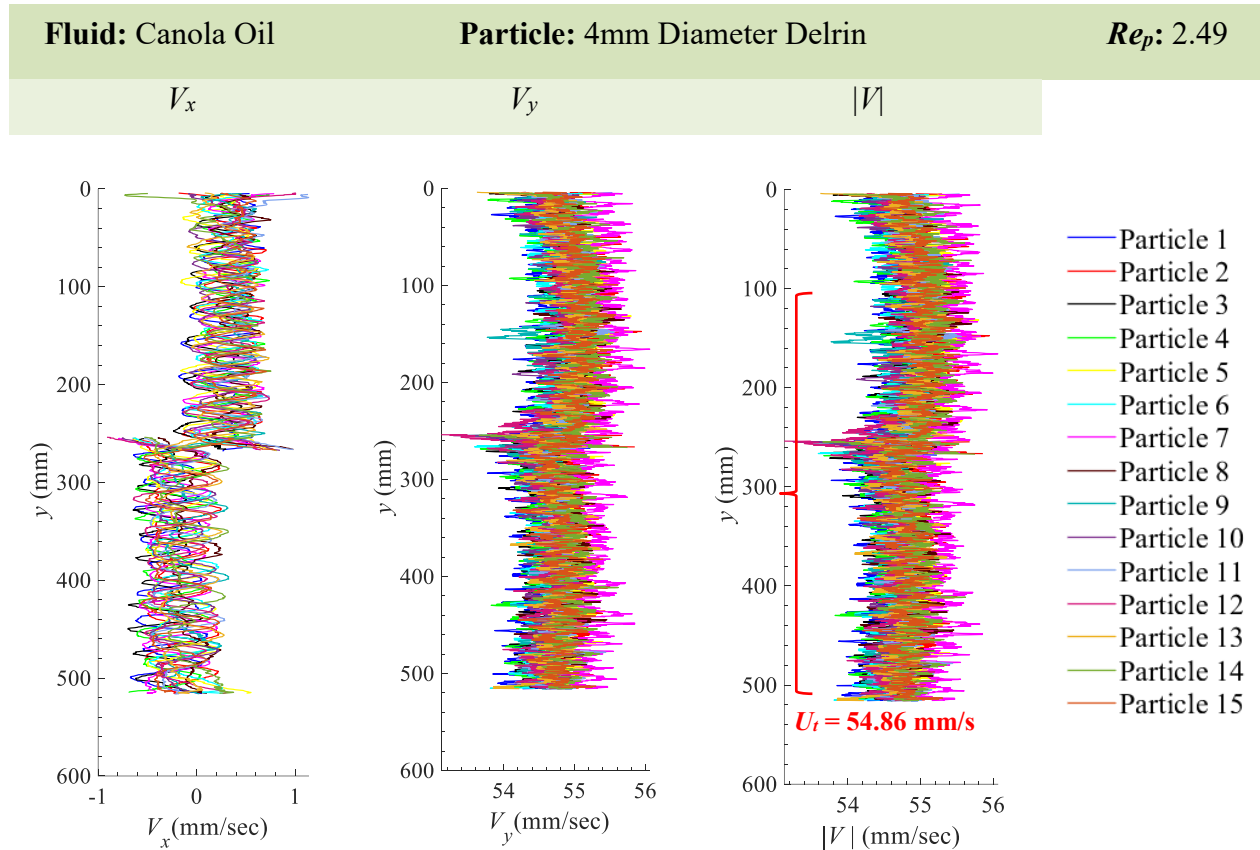


Figure 58 Particle velocity in the x -direction V_x , y -direction V_y , and the magnitude $\sqrt{(V_x^2 + V_y^2)}$ of the particle velocity $|V|$ for 4mm Diameter Delrin in Canola Oil. The average terminal settling velocity, U_t is 54.86 mm/s. The outliers at displacement 260 mm occurred within the overlap between the two cameras. In this region there was a variation in the light distribution compared to the rest of the field of view. A uniform distribution of light was not achieved with the projector and kite paper as shown in Figure 8 and describe in Section 3.5.1. This affected the binarization of the particle within that region and thereby a slight shift in the location of the centroid of the particle from the image processing scheme.

8.5.3 x -Acceleration (A_x), y -Acceleration (A_y) and Magnitude of Acceleration ($|A|$) for 4mm Diameter Delrin Spheres in Canola Oil

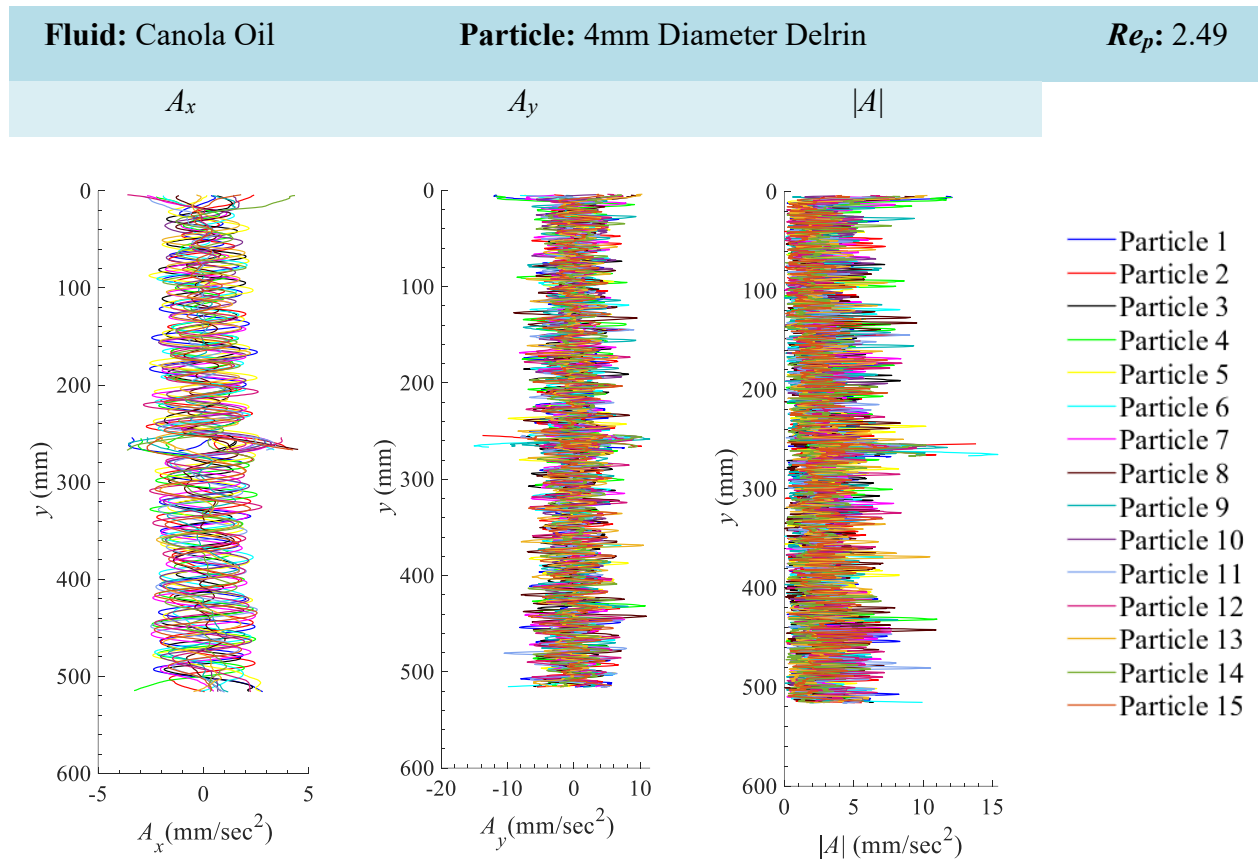


Figure 59 Particle acceleration in the x -direction A_x , y -direction A_y , and the magnitude $\sqrt{A_x^2 + A_y^2}$ of the particle acceleration $|A|$ for 4mm Diameter Delrin in Canola Oil. The outliers at displacement 260 mm occurred within the overlap between the two cameras. In this region there was a variation in the light distribution compared to the rest of the field of view. A uniform distribution of light was not achieved with the projector and kite paper as shown in Figure 8 and describe in Section 3.5.1. This affected the binarization of the particle within that region and thereby a slight shift in the location of the centroid of the particle from the image processing scheme.

8.6 Appendix 6: 2mm Diameter Delrin Spheres in Water

8.6.1 Particle Displacement, Particle Velocity and Particle Acceleration for 2mm Diameter Delrin Spheres in Water

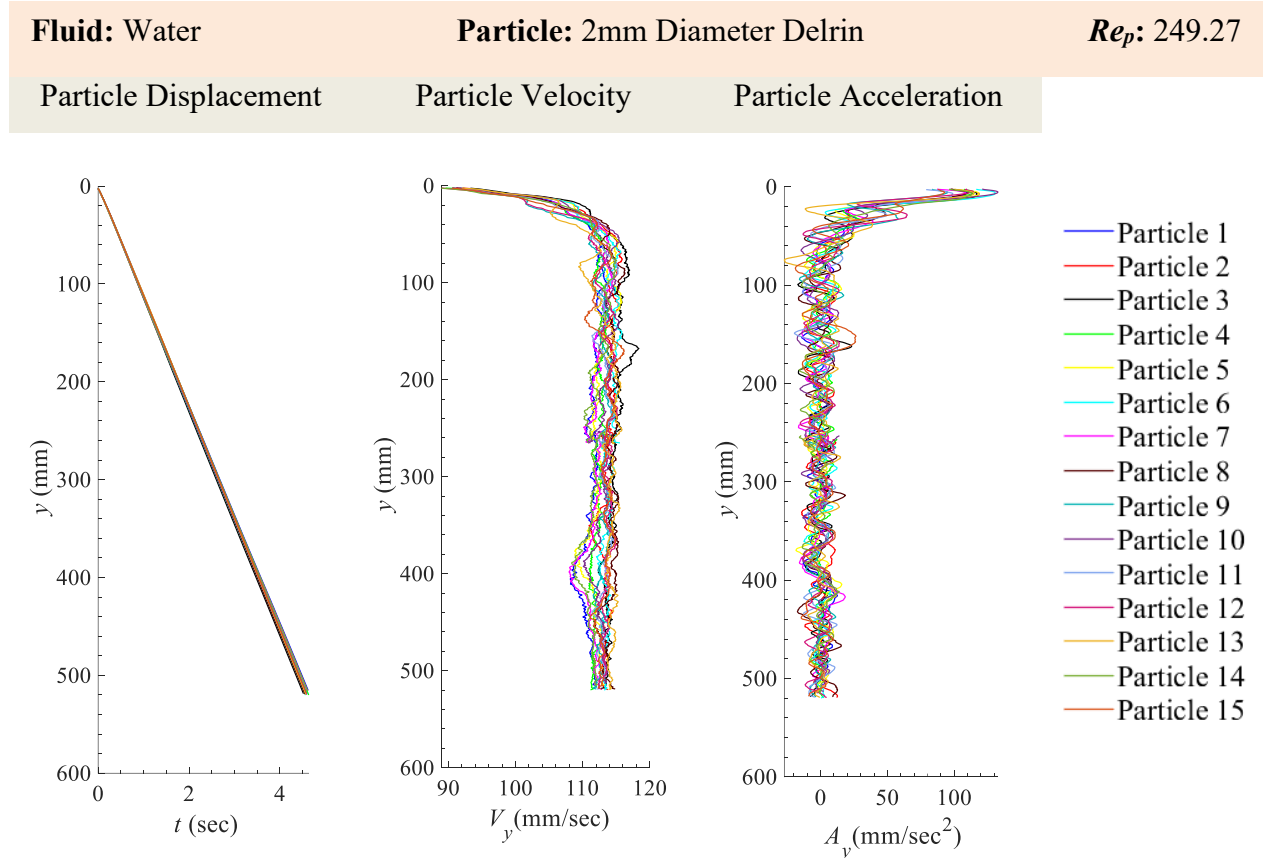


Figure 60 Particle displacement, y , velocity, V_y , and acceleration, A_y , for 2mm Diameter Delrin (15 particles) in Water. Four particles (represented by the pink, blue, light green and purple lines) were outliers because the velocity plots exhibited unusual trends within 360 mm and 420 mm of the particle displacement. The outliers in the original data were removed and plotted in Figure 61 and Figure 62 in order to obtain a better estimate of the terminal settling velocity and average constant acceleration.

8.6.2 x -Velocity (V_x), y -Velocity (V_y) and Magnitude of Velocity ($|V|$) for 2mm Diameter Delrin Spheres in Water

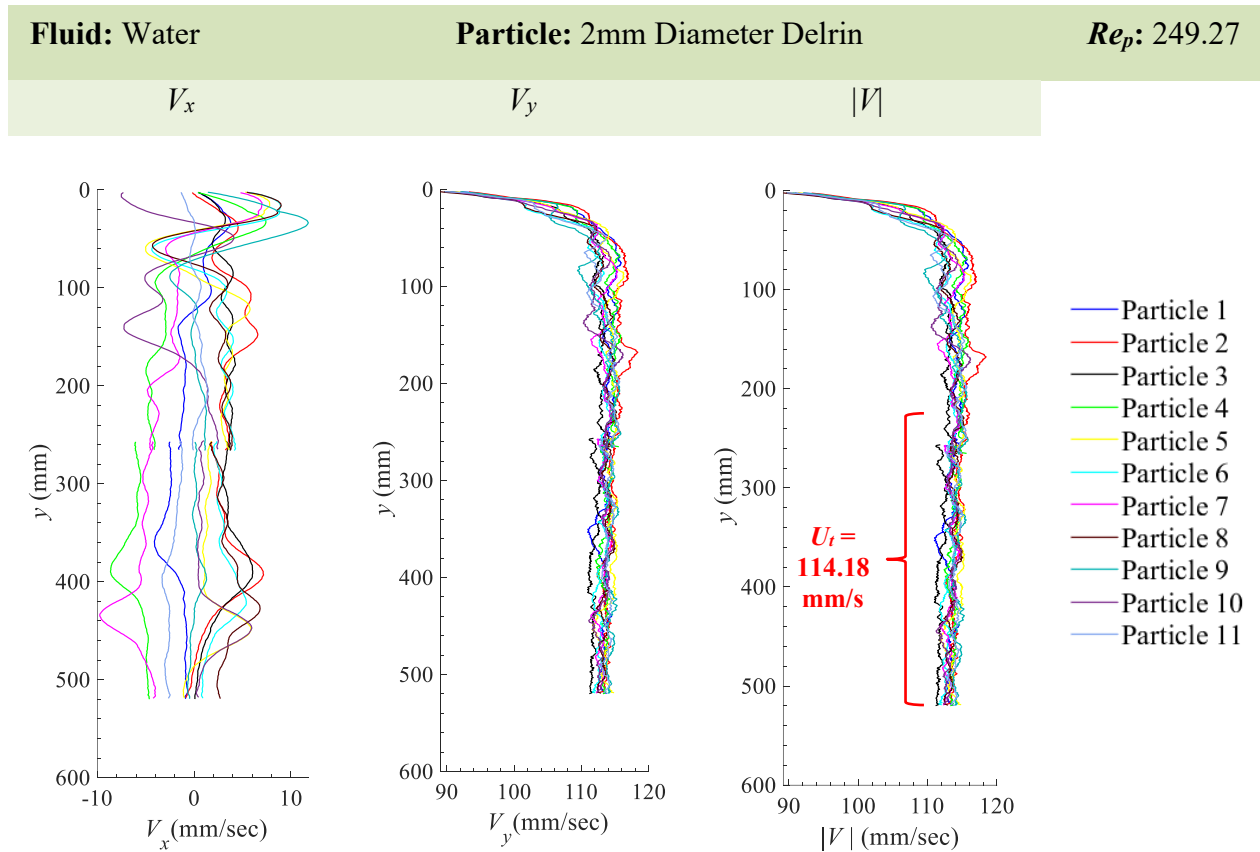


Figure 61 Particle velocity in the x -direction V_x , y -direction V_y , and the magnitude $\sqrt{(V_x^2 + V_y^2)}$ of the particle velocity $|V|$ for 2mm Diameter Delrin in Water. The average terminal settling velocity, U_t is 114.18 mm/s. Note: the four (4) outliers shown in Figure 60 were omitted in order to obtain a better estimate of the terminal settling velocity. Therefore only 11 particles are shown in this plots.

8.6.3 x -Acceleration (A_x), y -Acceleration (A_y) and Magnitude of Acceleration ($|A|$) for 2mm Diameter Delrin Spheres in Water

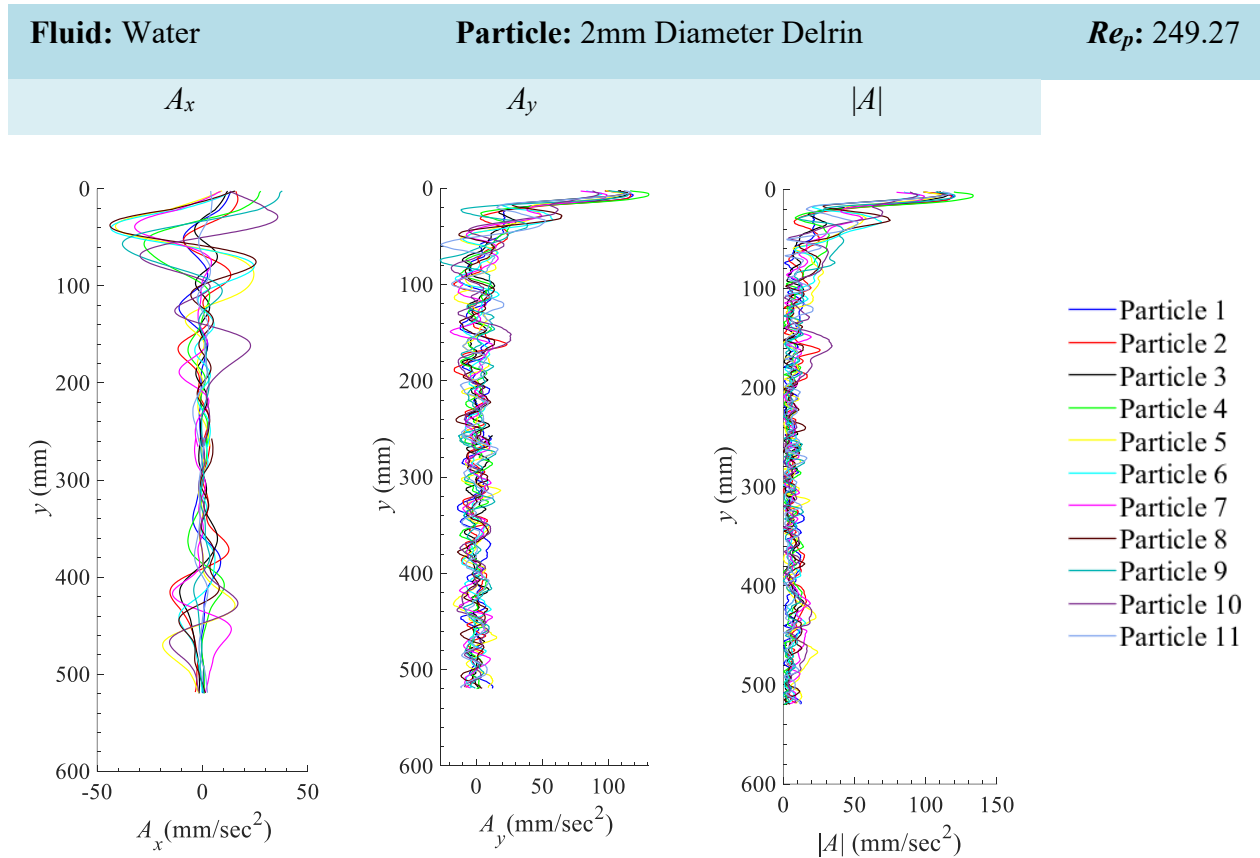


Figure 62 Particle acceleration in the x -direction A_x , y -direction A_y , and the magnitude $\sqrt{(A_x^2 + A_y^2)}$ of the particle acceleration $|A|$ for 2mm Diameter Delrin in Water. Note: the four (4) outliers shown in Figure 60 were omitted in order to obtain a better estimate of the average acceleration within the terminal velocity region. Therefore only 11 particles are shown in this plots.

8.7 Appendix 7: 2mm Delrin Spheres in 20%–80% Glycerol–Water

8.7.1 Particle Displacement, Particle Velocity and Particle Acceleration for 2mm Diameter Delrin Spheres in 20%–80% Glycerol–Water

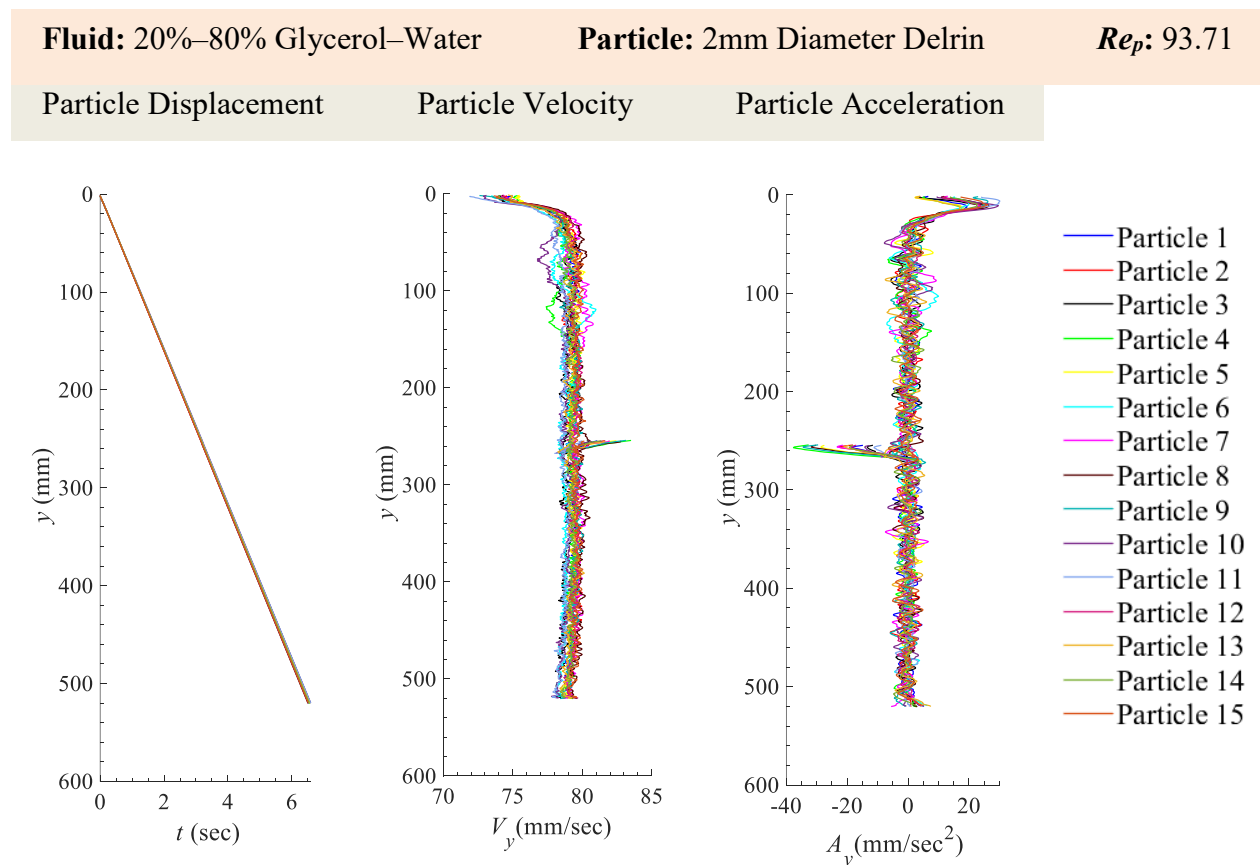


Figure 63 Particle displacement, y , velocity, V_y , and acceleration, A_y , for 2mm Diameter Delrin (15 particles) in 20%–80% glycerol–water. The outliers at displacement 260 mm occurred within the overlap between the two cameras. In this region there was a variation in the light distribution compared to the rest of the field of view. A uniform distribution of light was not achieved with the projector and kite paper as shown in Figure 8 and describe in Section 3.5.1. This affected the binarization of the particle within that region and thereby a slight shift in the location of the centroid of the particle from the image processing scheme.

8.7.2 x -Velocity (V_x), y -Velocity (V_y) and Magnitude of Velocity ($|V|$) for 2mm Diameter Delrin Spheres in 20%–80% Glycerol–Water

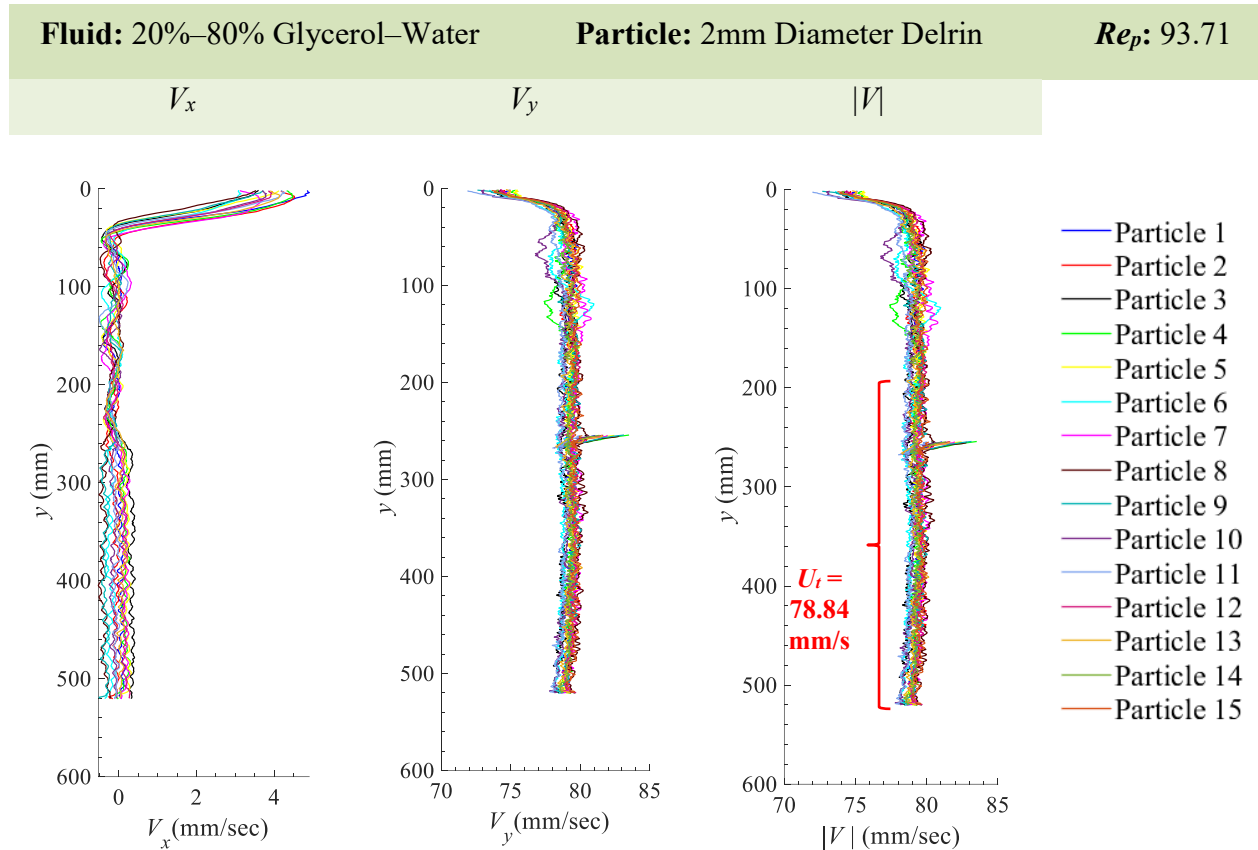


Figure 64 Particle velocity in the x -direction V_x , y -direction V_y , and the magnitude $\sqrt{V_x^2 + V_y^2}$ of the particle velocity $|V|$ for 2mm Diameter Delrin in 20%–80% glycerol–water. The average terminal settling velocity, U_t is 78.84 mm/s. The outliers at displacement 260 mm occurred within the overlap between the two cameras. In this region there was a variation in the light distribution compared to the rest of the field of view. A uniform distribution of light was not achieved with the projector and kite paper as shown in Figure 8 and describe in Section 3.5.1. This affected the binarization of the particle within that region and thereby a slight shift in the location of the centroid of the particle from the image processing scheme.

8.7.3 x -Acceleration (A_x), y -Acceleration (A_y) and Magnitude of Acceleration ($|A|$) for 2mm Diameter Delrin Spheres in 20%–80% Glycerol–Water

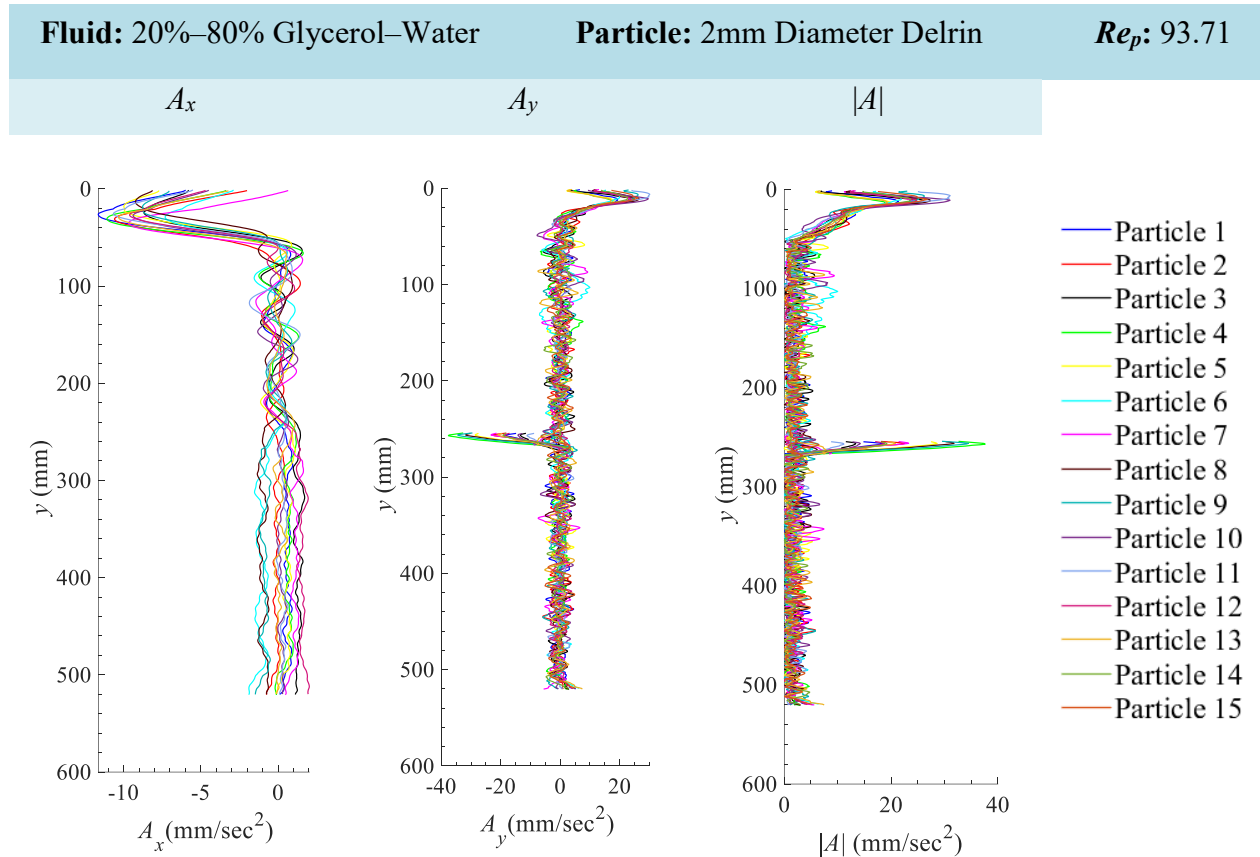


Figure 65 Particle acceleration in the x -direction A_x , y -direction A_y , and the magnitude $\sqrt{A_x^2 + A_y^2}$ of the particle acceleration $|A|$ for 2mm Diameter Delrin in 20%–80% glycerol–water. The outliers at displacement 260 mm occurred within the overlap between the two cameras. In this region there was a variation in the light distribution compared to the rest of the field of view. A uniform distribution of light was not achieved with the projector and kite paper as shown in Figure 8 and describe in Section 3.5.1. This affected the binarization of the particle within that region and thereby a slight shift in the location of the centroid of the particle from the image processing scheme.

8.8 Appendix 8: 2mm Delrin Spheres in 40%–60% Glycerol–Water

8.8.1 Particle Displacement, Particle Velocity and Particle Acceleration for 2mm Diameter Delrin Spheres in 40%–60% Glycerol–Water

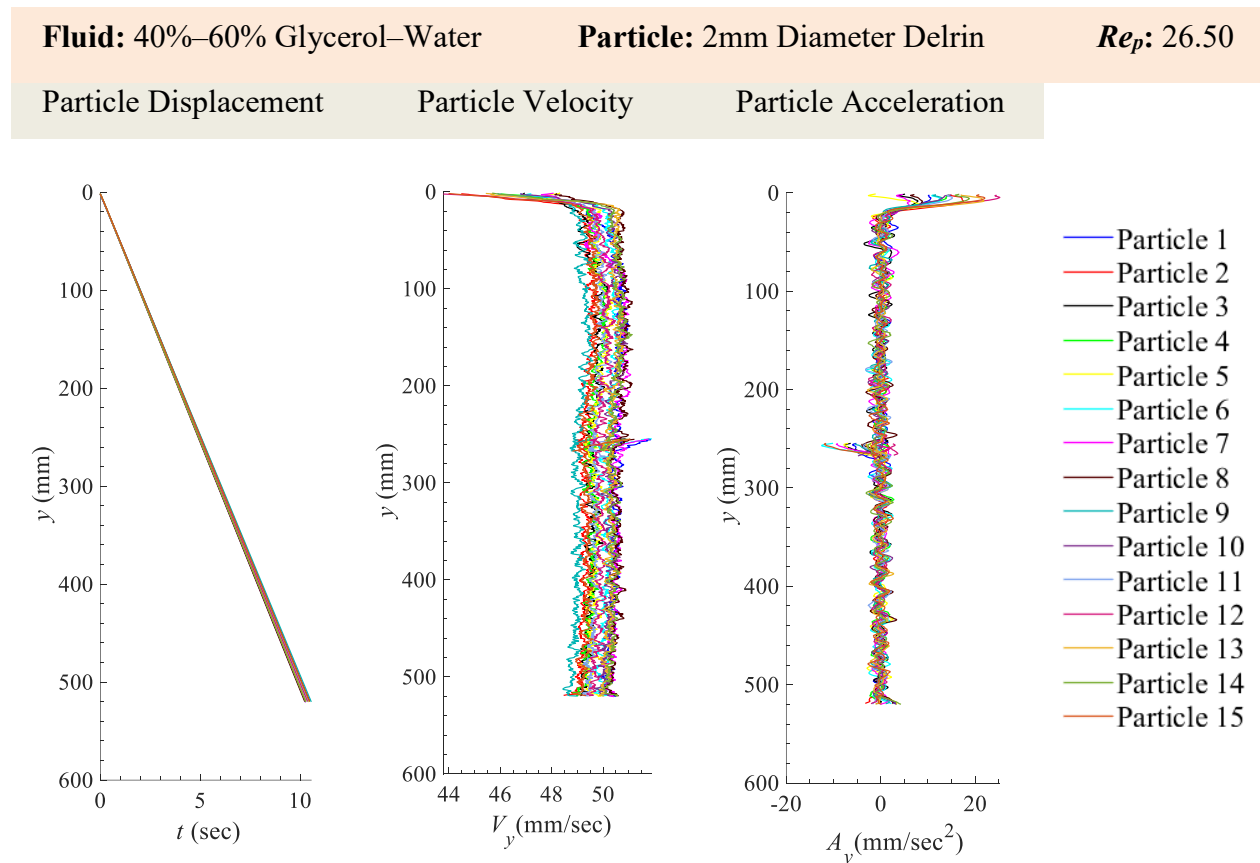


Figure 66 Particle displacement, y , velocity, V_y , and acceleration, A_y , for 2mm Diameter Delrin (15 particles) in 40%–60% glycerol–water. The outliers at displacement 260 mm occurred within the overlap between the two cameras. In this region there was a variation in the light distribution compared to the rest of the field of view. A uniform distribution of light was not achieved with the projector and kite paper as shown in Figure 8 and describe in Section 3.5.1. This affected the binarization of the particle within that region and thereby a slight shift in the location of the centroid of the particle from the image processing scheme.

8.8.2 x -Velocity (V_x), y -Velocity (V_y) and Magnitude of Velocity ($|V|$) for 2mm Diameter Delrin Spheres in 40%–60% Glycerol–Water

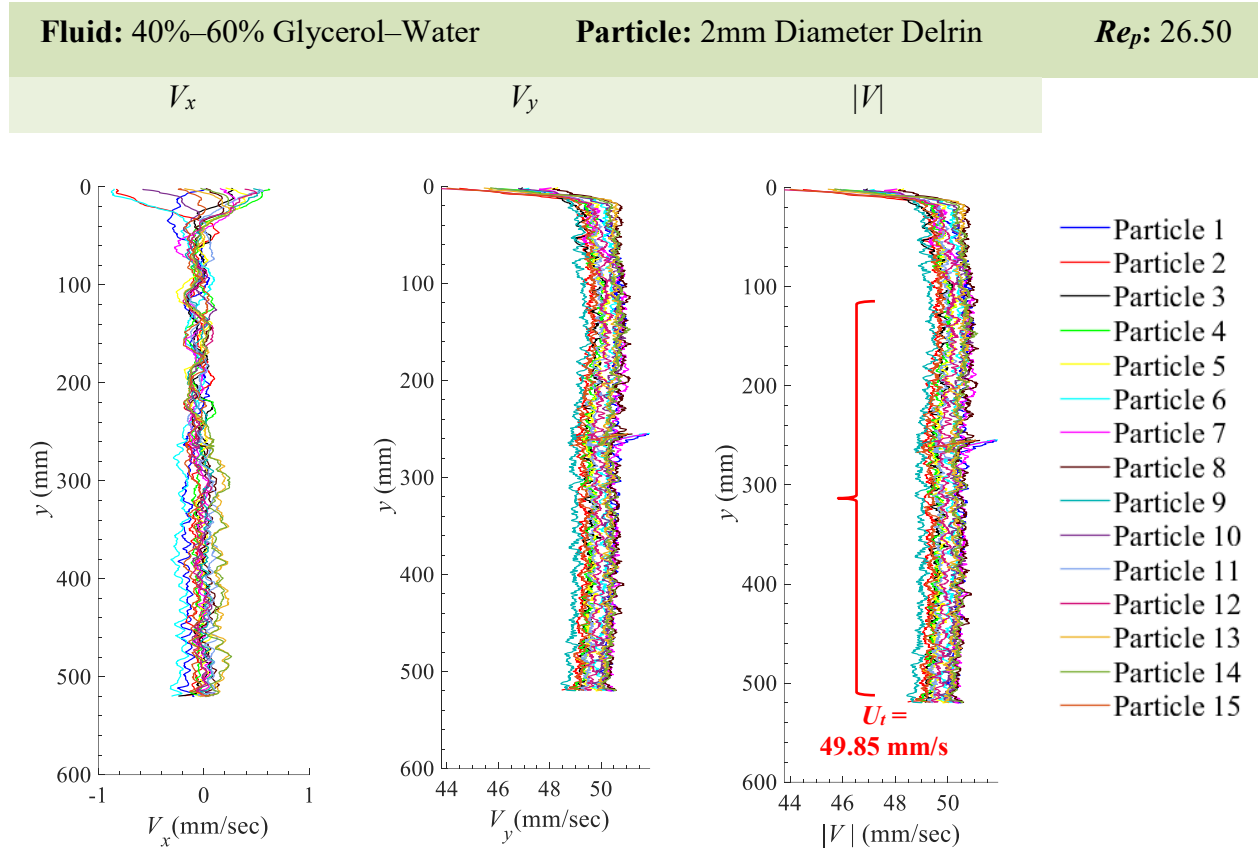


Figure 67 Particle velocity in the x -direction V_x , y -direction V_y , and the magnitude $\sqrt{(V_x^2 + V_y^2)}$ of the particle velocity $|V|$ for 2mm Diameter Delrin (15 particles) in 40%–60% glycerol–water. The average terminal settling velocity, U_t is 49.85 mm/s. The outliers at displacement 260 mm occurred within the overlap between the two cameras. In this region there was a variation in the light distribution compared to the rest of the field of view. A uniform distribution of light was not achieved with the projector and kite paper as shown in Figure 8 and describe in Section 3.5.1. This affected the binarization of the particle within that region and thereby a slight shift in the location of the centroid of the particle from the image processing scheme.

8.8.3 x -Acceleration (A_x), y -Acceleration (A_y) and Magnitude of Acceleration ($|A|$) for 2mm Diameter Delrin Spheres in 40%–60% Glycerol–Water

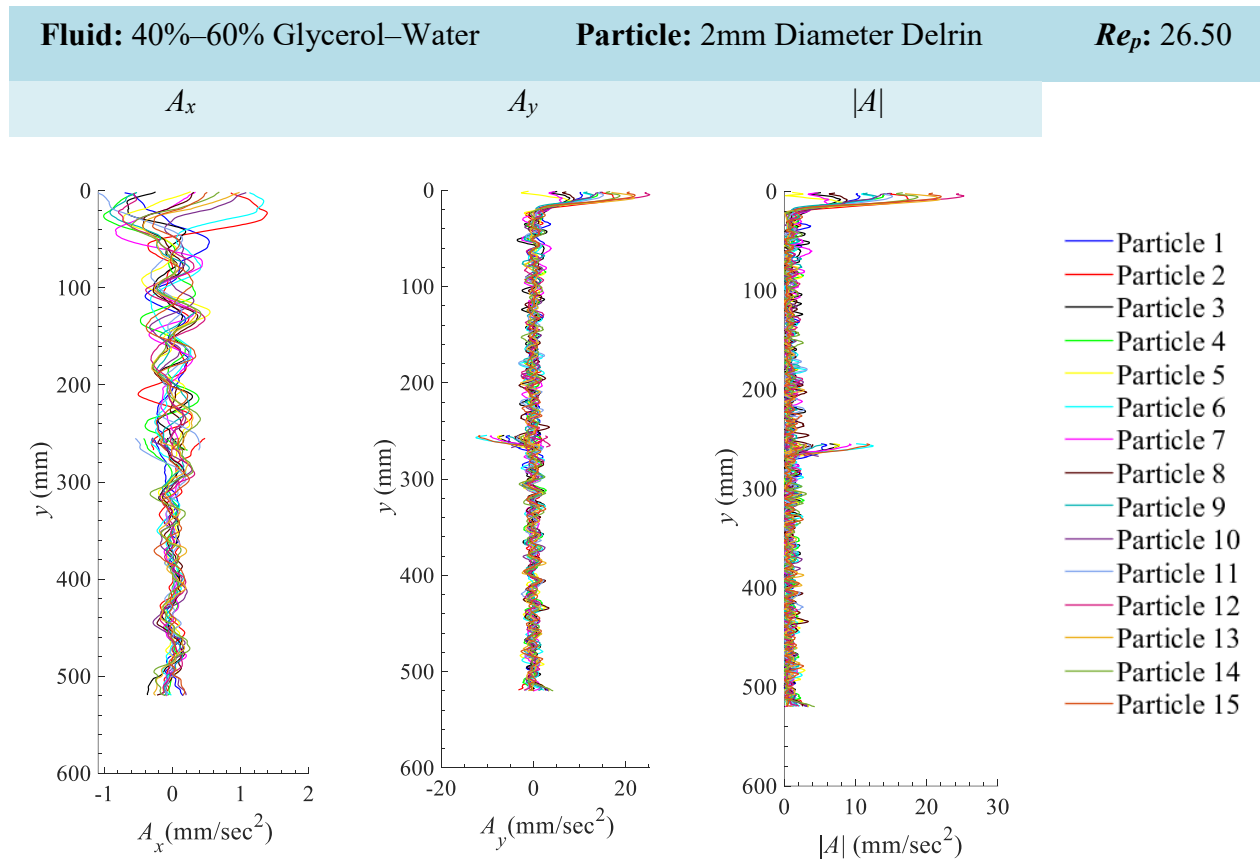


Figure 68 Particle acceleration in the x -direction A_x , y -direction A_y , and the magnitude $\sqrt{A_x^2 + A_y^2}$ of the particle acceleration $|A|$ for 2mm Diameter Delrin (15 particles) in 40%–60% glycerol–water. The outliers at displacement 260 mm occurred within the overlap between the two cameras. In this region there was a variation in the light distribution compared to the rest of the field of view. A uniform distribution of light was not achieved with the projector and kite paper as shown in Figure 8 and describe in Section 3.5.1. This affected the binarization of the particle within that region and thereby a slight shift in the location of the centroid of the particle from the image processing scheme

8.9 Appendix 9: 2mm Delrin Spheres in 70%–30% Glycerol–Water

8.9.1 Particle Displacement, Particle Velocity and Particle Acceleration for 2mm Diameter Delrin Spheres in 70%–30% Glycerol–Water

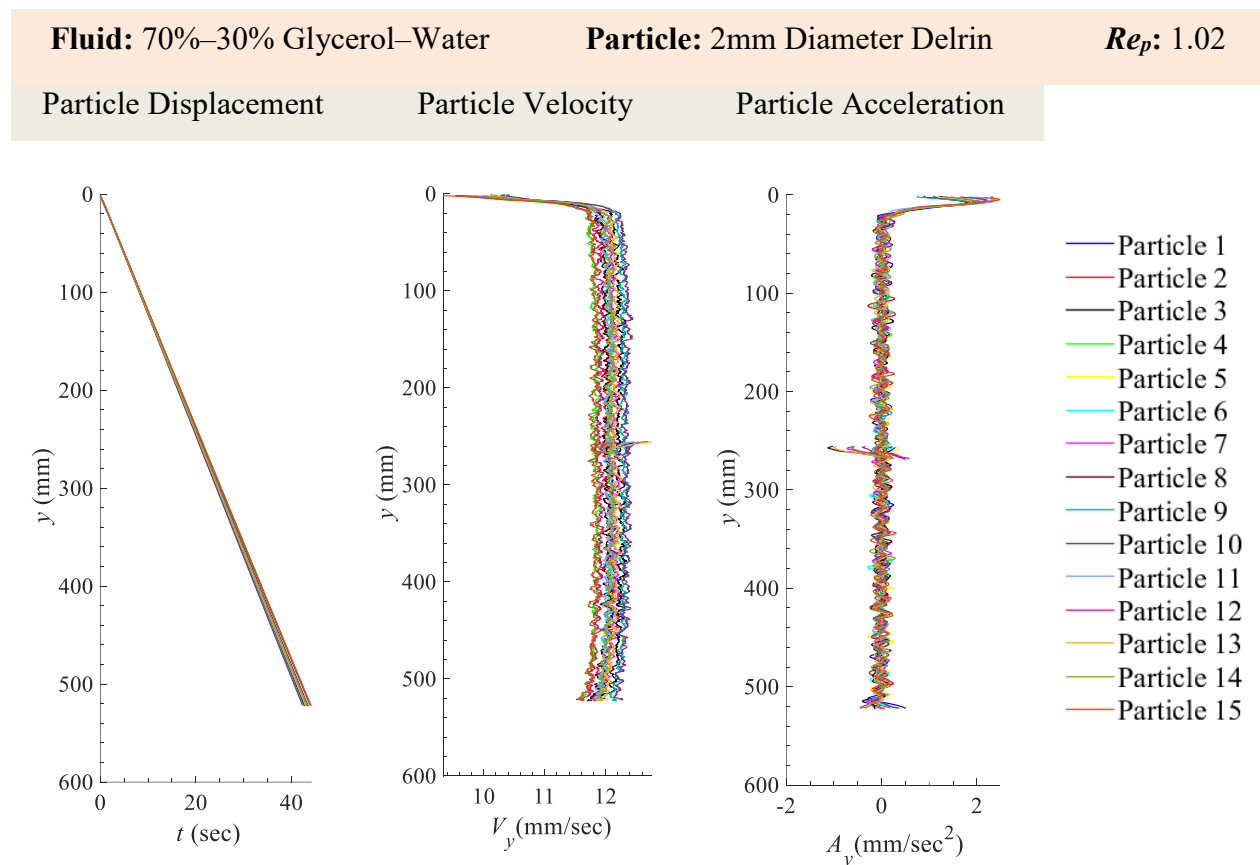


Figure 69 Particle displacement, y , velocity, V_y , and acceleration, A_y , for 2mm Diameter Delrin (15 particles) in 70%–30% glycerol–water. The outliers at displacement 260 mm occurred within the overlap between the two cameras. In this region there was a variation in the light distribution compared to the rest of the field of view. A uniform distribution of light was not achieved with the projector and kite paper as shown in Figure 8 and describe in Section 3.5.1. This affected the binarization of the particle within that region and thereby a slight shift in the location of the centroid of the particle from the image processing scheme.

8.9.2 x -Velocity (V_x), y -Velocity (V_y) and Magnitude of Velocity ($|V|$) for 2mm Diameter Delrin Spheres in 70%–30% Glycerol–Water

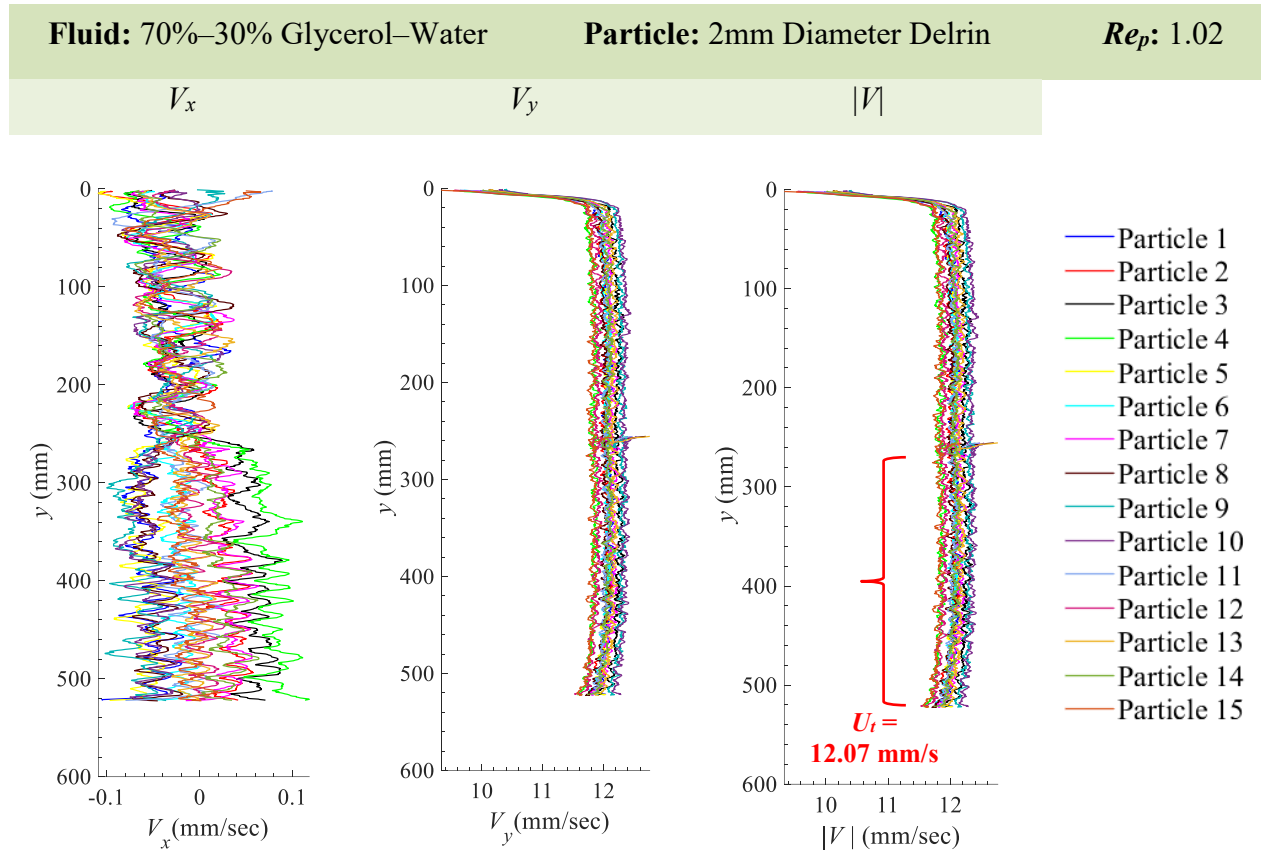


Figure 70 Particle velocity in the x -direction V_x , y -direction V_y , and the magnitude $\sqrt{V_x^2 + V_y^2}$ of the particle velocity $|V|$ for 2mm Diameter Delrin (15 particles) in 70%–30% glycerol–water. The average terminal settling velocity, U_t is 12.07 mm/s. The outliers at displacement 260 mm occurred within the overlap between the two cameras. In this region there was a variation in the light distribution compared to the rest of the field of view. A uniform distribution of light was not achieved with the projector and kite paper as shown in Figure 8 and describe in Section 3.5.1. This affected the binarization of the particle within that region and thereby a slight shift in the location of the centroid of the particle from the image processing scheme.

8.9.3 x -Acceleration (A_x), y -Acceleration (A_y) and Magnitude of Acceleration ($|A|$) for 2mm Diameter Delrin Spheres in 70%–30% Glycerol–Water

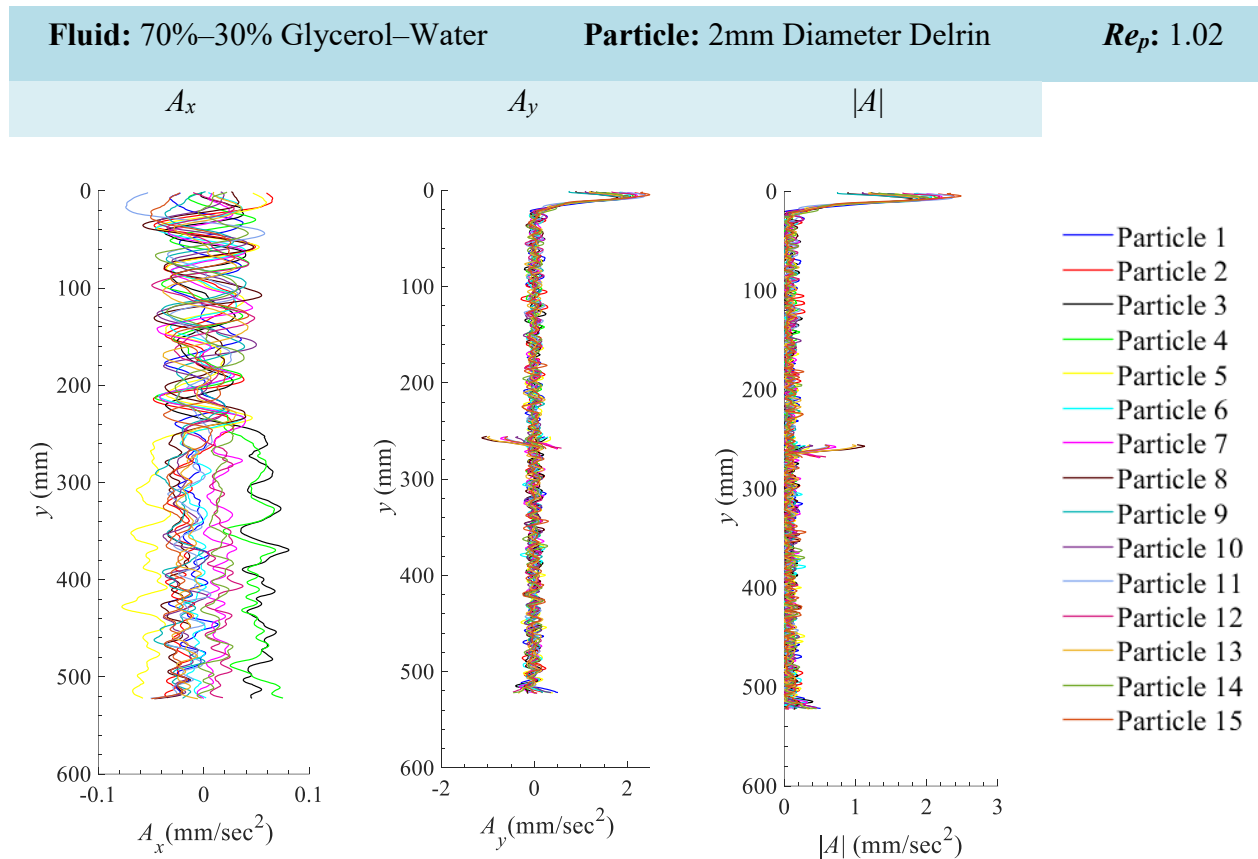


Figure 71 Particle acceleration in the x -direction A_x , y -direction A_y , and the magnitude $\sqrt{A_x^2 + A_y^2}$ of the particle acceleration $|A|$ for 2mm Diameter Delrin (15 particles) in 70%–30% glycerol–water. The outliers at displacement 260 mm occurred within the overlap between the two cameras. In this region there was a variation in the light distribution compared to the rest of the field of view. A uniform distribution of light was not achieved with the projector and kite paper as shown in Figure 8 and describe in Section 3.5.1. This affected the binarization of the particle within that region and thereby a slight shift in the location of the centroid of the particle from the image processing scheme.

8.10 Appendix 10: 2mm Delrin Spheres in Canola Oil

8.10.1 Particle Displacement, Particle Velocity and Particle Acceleration for 2mm Diameter Delrin Spheres in Canola Oil

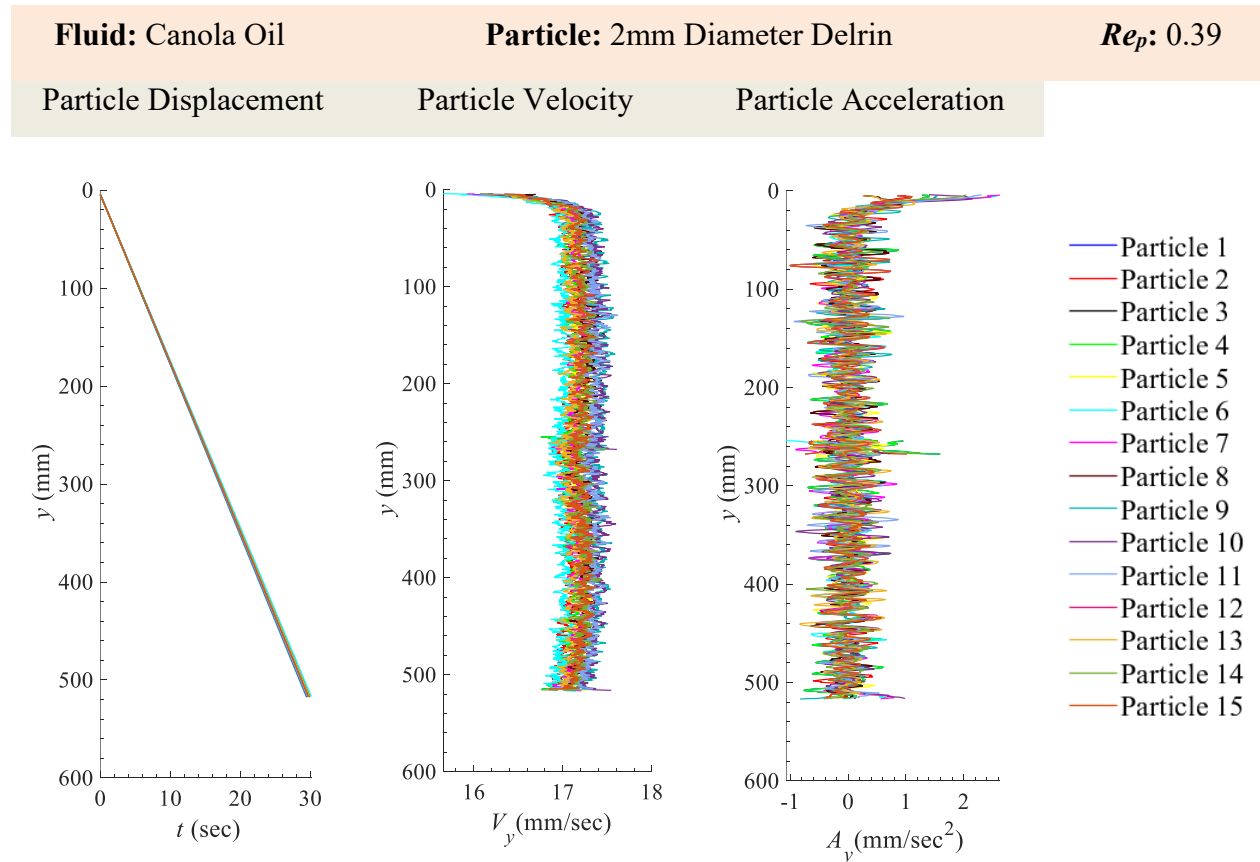


Figure 72 Particle displacement, y , velocity, V_y , and acceleration, A_y , for 2mm Diameter Delrin (15 particles) in Canola Oil. In this region there was a variation in the light distribution compared to the rest of the field of view. A uniform distribution of light was not achieved with the projector and kite paper as shown in Figure 8 and describe in Section 3.5.1. This affected the binarization of the particle within that region and thereby a slight shift in the location of the centroid of the particle from the image processing scheme.

8.10.2 x -Velocity (V_x), y -Velocity (V_y) and Magnitude of Velocity ($|V|$) for 2mm Diameter Delrin Spheres in Canola Oil

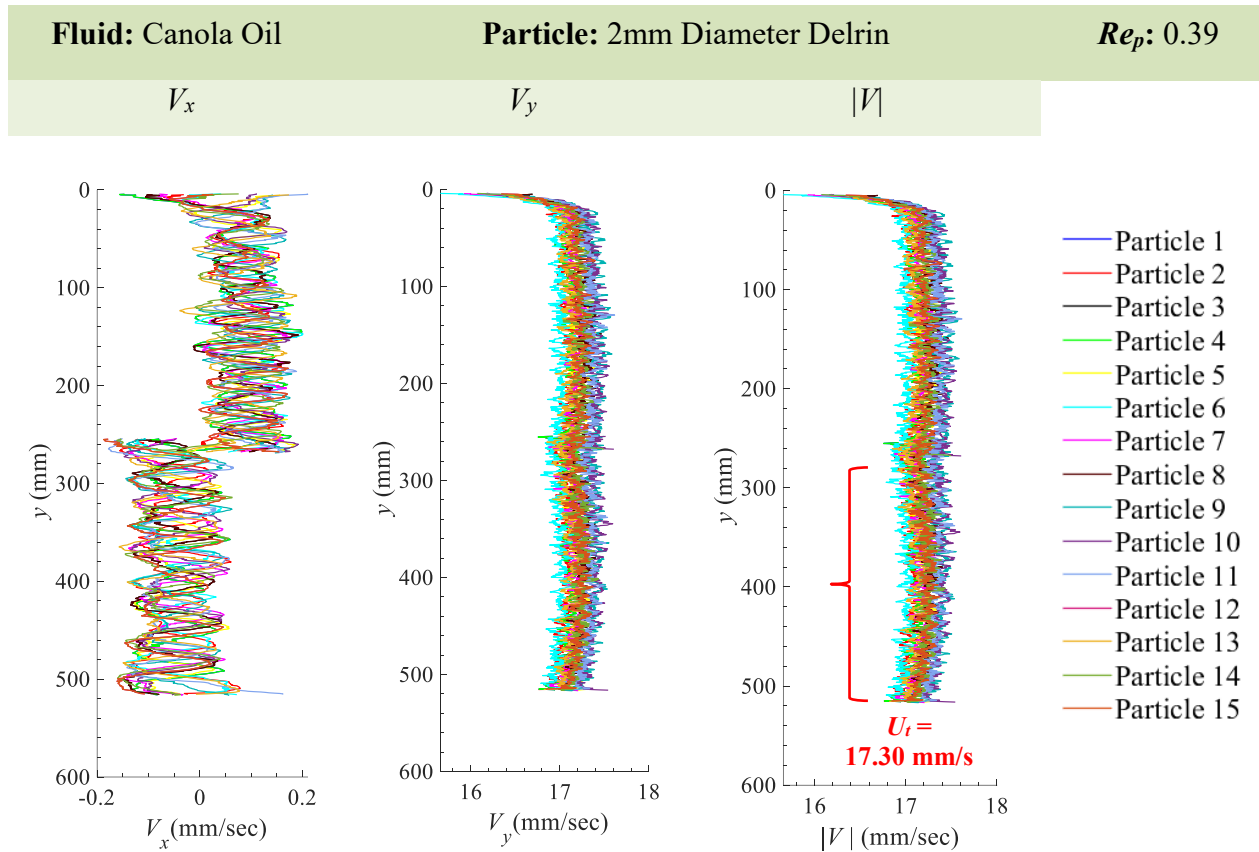


Figure 73 Particle velocity in the x -direction V_x , y -direction V_y , and the magnitude $\sqrt{(V_x^2 + V_y^2)}$ of the particle velocity $|V|$ for 2mm Diameter Delrin (15 particles) in Canola Oil. The average terminal settling velocity, U_t is 17.30 mm/s. In this region there was a variation in the light distribution compared to the rest of the field of view. A uniform distribution of light was not achieved with the projector and kite paper as shown in Figure 8 and describe in Section 3.5.1. This affected the binarization of the particle within that region and thereby a slight shift in the location of the centroid of the particle from the image processing scheme.

8.10.3 x -Acceleration (A_x), y -Acceleration (A_y) and Magnitude of Acceleration ($|A|$) for 2mm Diameter Delrin Spheres in Canola Oil

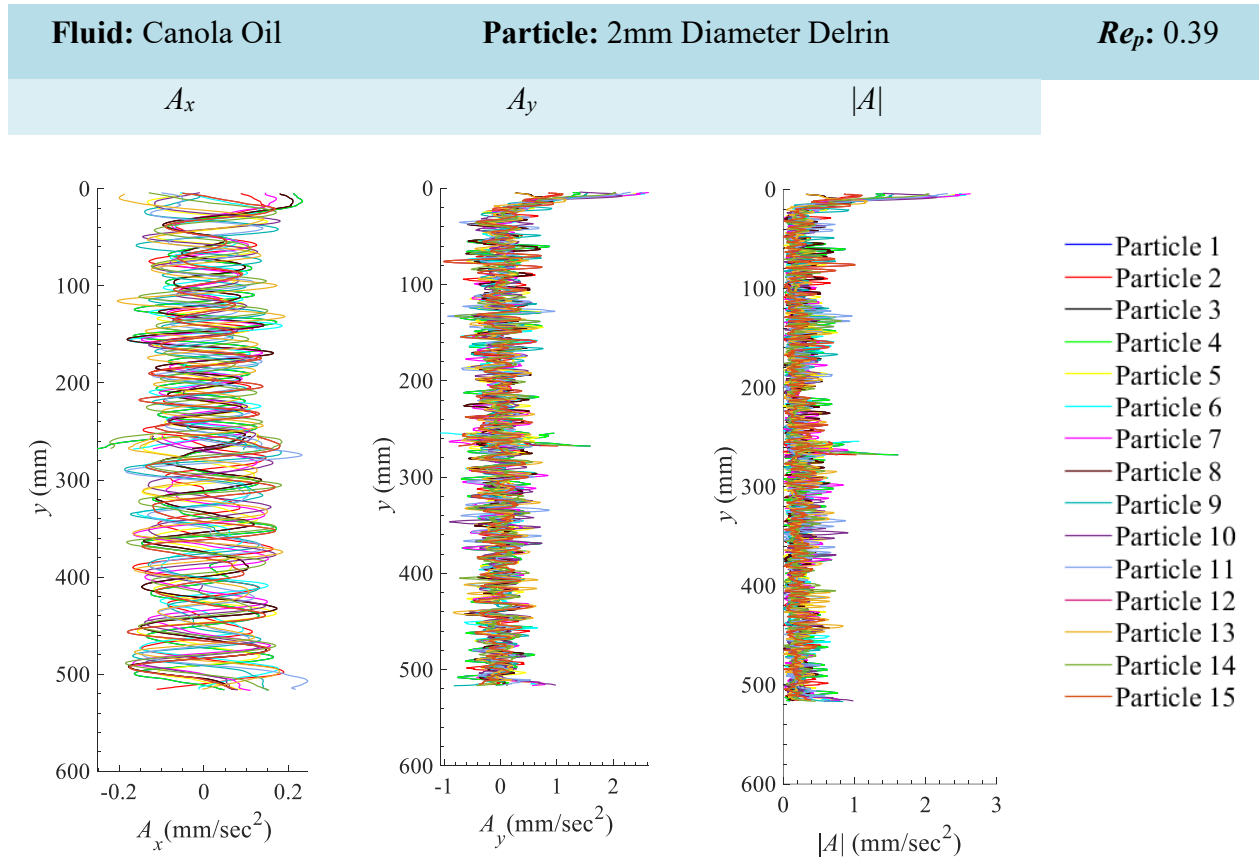


Figure 74 Particle acceleration in the x -direction A_x , y -direction A_y , and the magnitude $\sqrt{A_x^2 + A_y^2}$ of the particle acceleration $|A|$ for 2mm Diameter Delrin (15 particles) in Canola Oil. In this region there was a variation in the light distribution compared to the rest of the field of view. A uniform distribution of light was not achieved with the projector and kite paper as shown in Figure 8 and describe in Section 3.5.1. This affected the binarization of the particle within that region and thereby a slight shift in the location of the centroid of the particle from the image processing scheme.

8.11 Appendix 11: 2mm Diameter Aluminum Spheres in Water

8.11.1 Particle Displacement, Particle Velocity and Particle Acceleration for 2mm Diameter Aluminum Spheres in Water

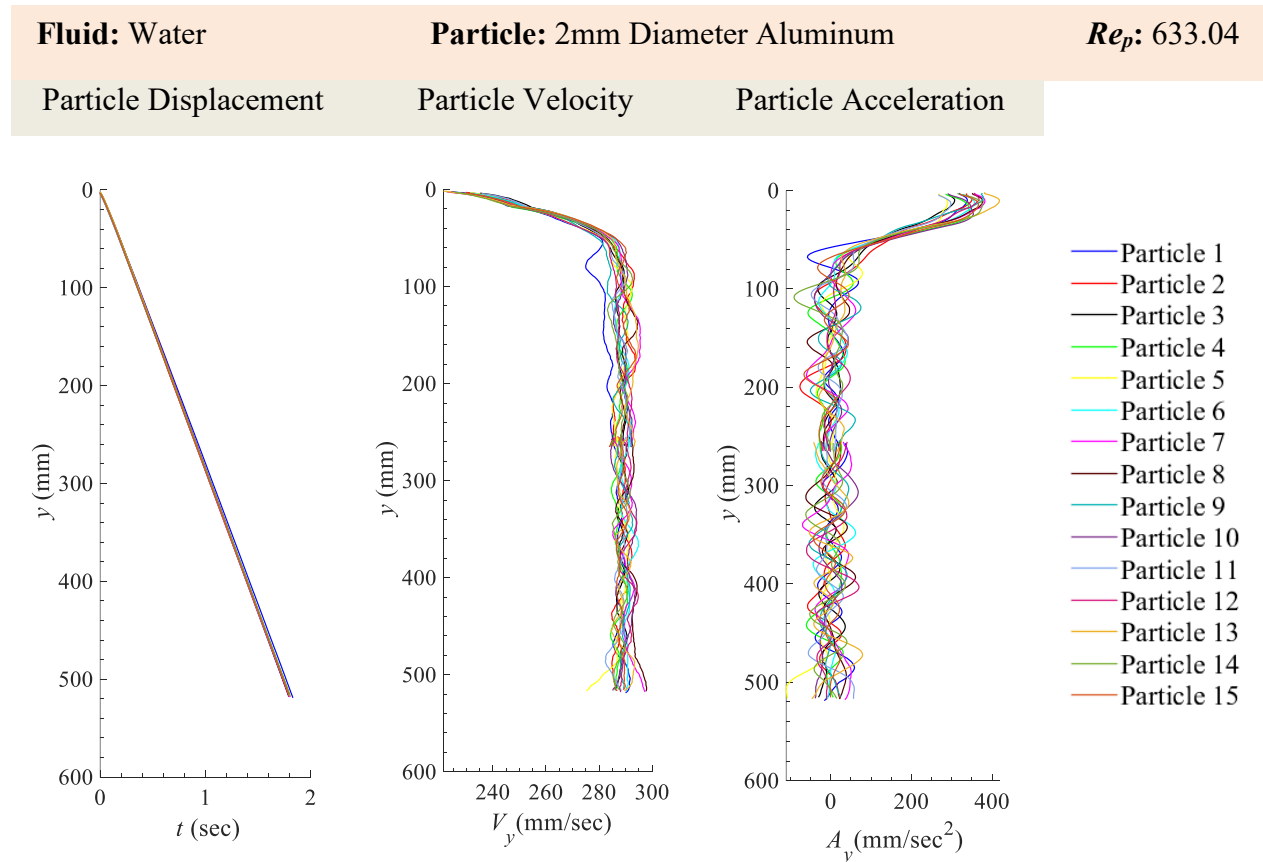


Figure 75 Particle displacement, y , velocity, V_y , and acceleration, A_y , for 2mm Diameter Aluminum (15 particles) in Water.

8.11.2 x -Velocity (V_x), y -Velocity (V_y) and Magnitude of Velocity ($|V|$) for 2mm Diameter Aluminum Spheres in Water

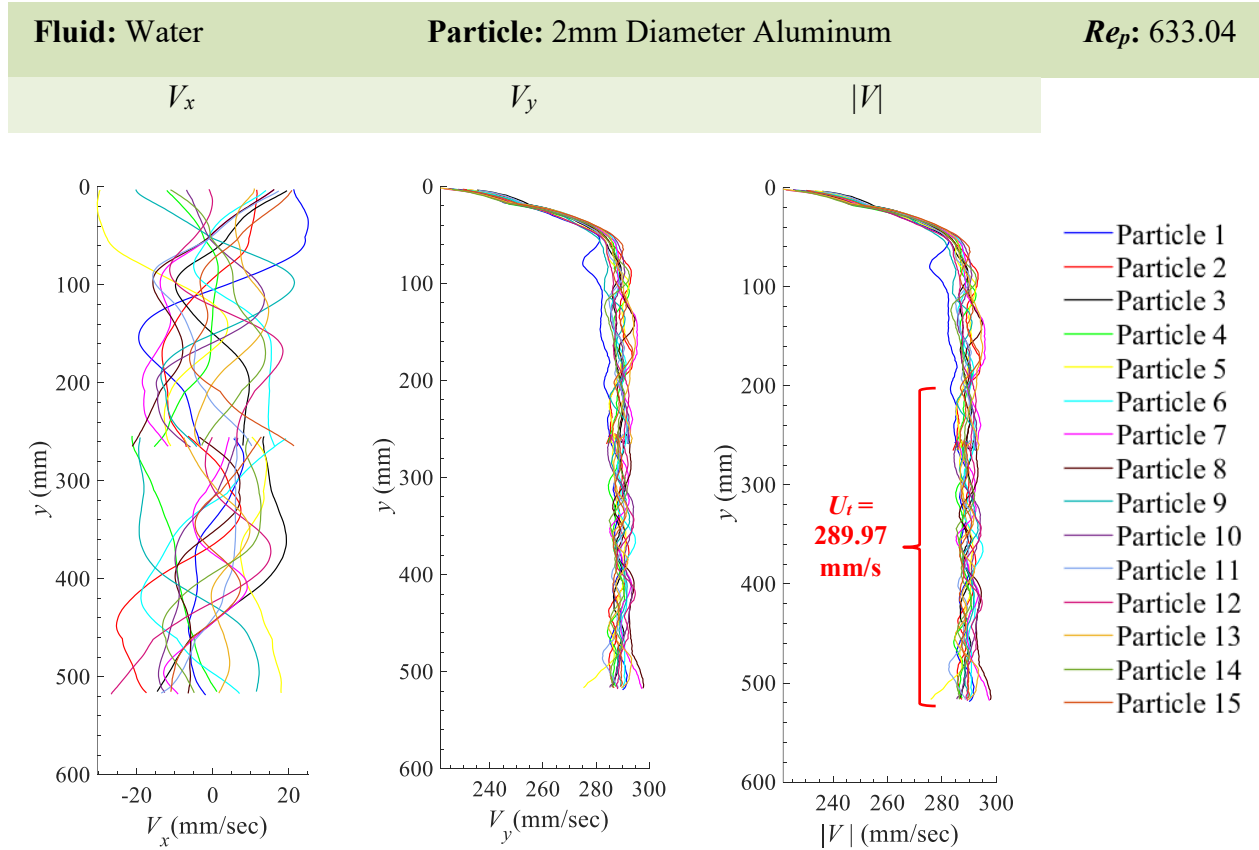


Figure 76 Particle velocity in the x -direction V_x , y -direction V_y , and the magnitude $\sqrt{V_x^2 + V_y^2}$ of the particle velocity $|V|$ for 2mm Diameter Aluminum (15 particles) in Water. The average terminal settling velocity, U_t is 289.97 mm/s.

8.11.3 x -Acceleration (A_x), y -Acceleration (A_y) and Magnitude of Acceleration ($|A|$) for 2mm Diameter Aluminum Spheres in Water

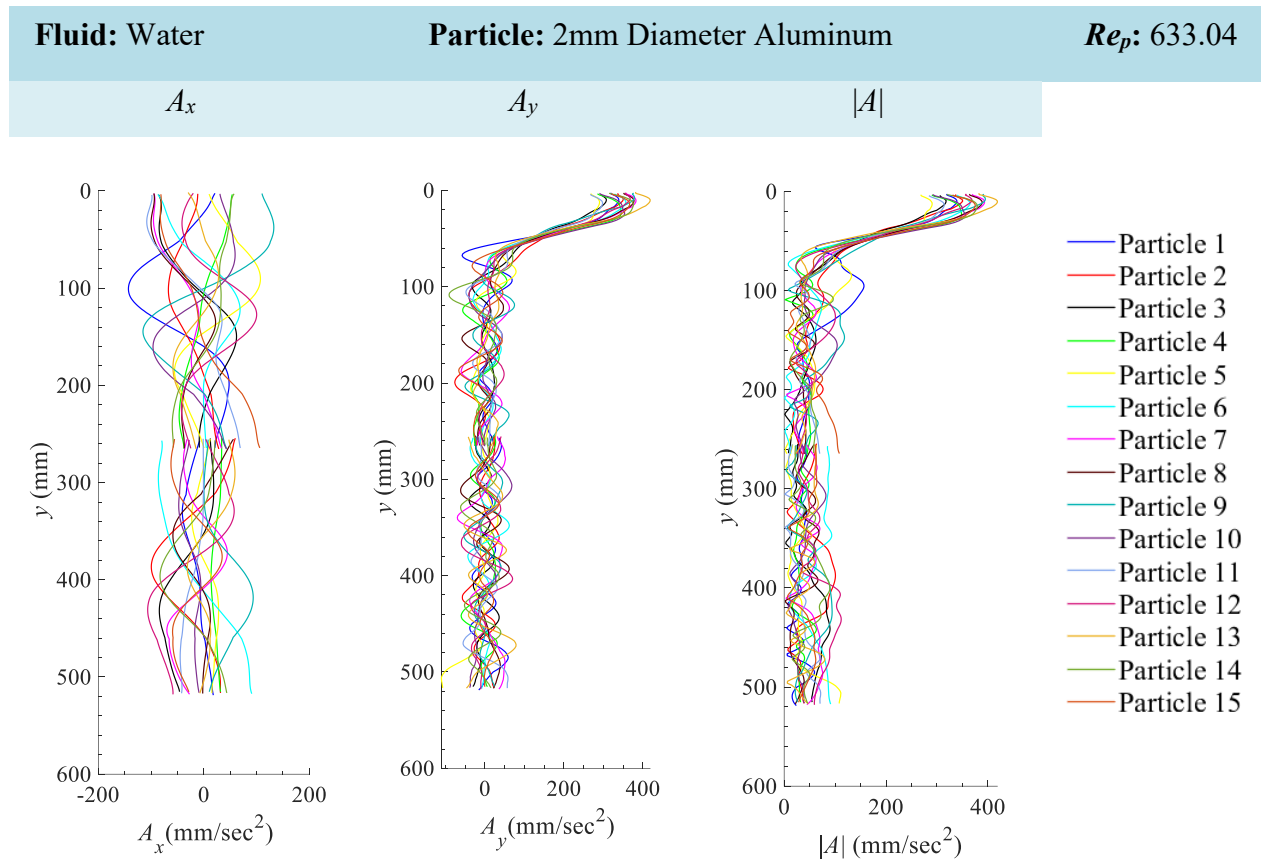


Figure 77 Particle acceleration in the x -direction A_x , y -direction A_y , and the magnitude $\sqrt{(A_x^2 + A_y^2)}$ of the particle acceleration $|A|$ for 2mm Diameter Aluminum (15 particles) in Water.

8.12 Appendix 12: 2mm Diameter Aluminum Spheres in 20%–80% Glycerol–Water

8.12.1 Particle Displacement, Particle Velocity and Particle Acceleration for 2mm Diameter Aluminum Spheres in 20%–80% Glycerol–Water

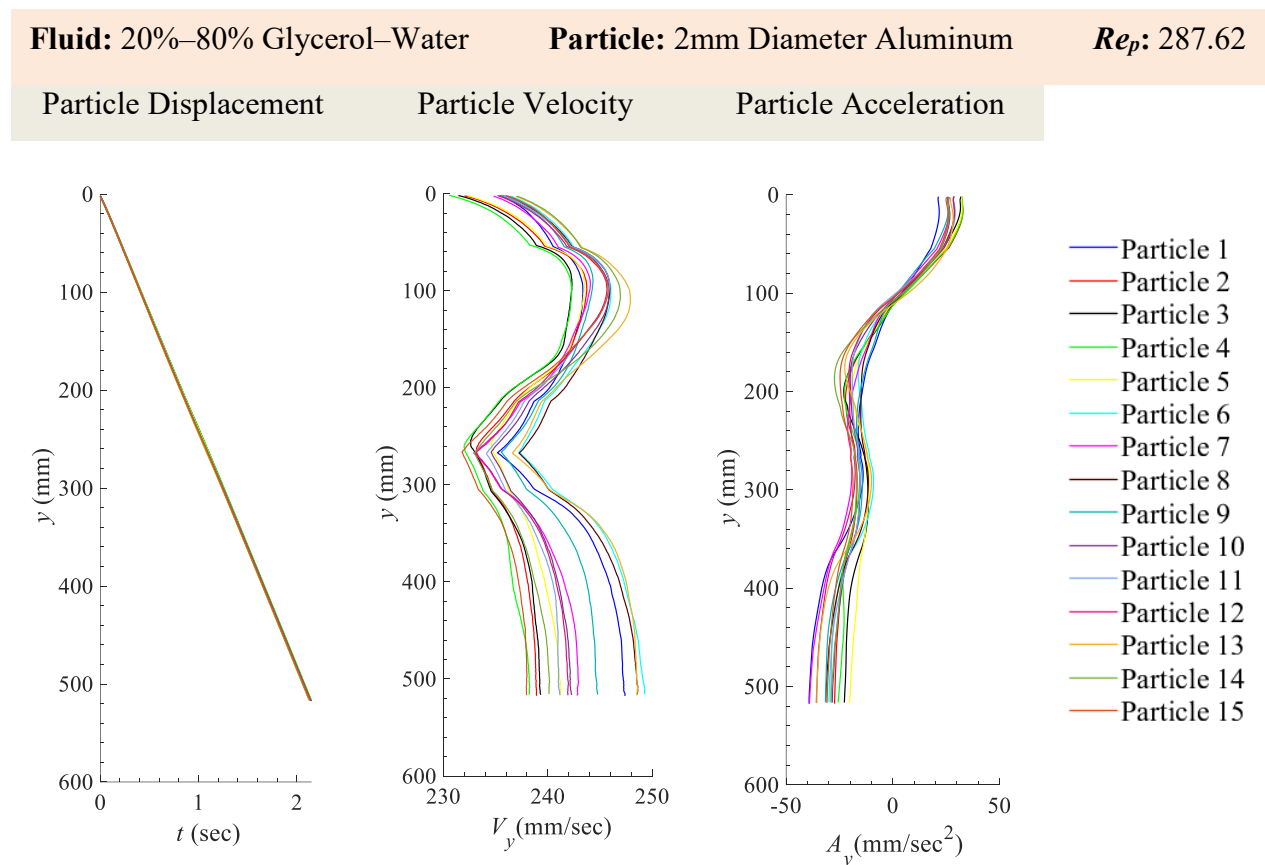


Figure 78 Particle displacement, y , velocity, V_y , and acceleration, A_y , for 2mm Diameter Aluminum (15 particles) in 20%–80% glycerol–water.

8.12.2 x -Velocity (V_x), y -Velocity (V_y) and Magnitude of Velocity ($|V|$) for 2mm Diameter Aluminum Spheres in 20%–80% Glycerol–Water

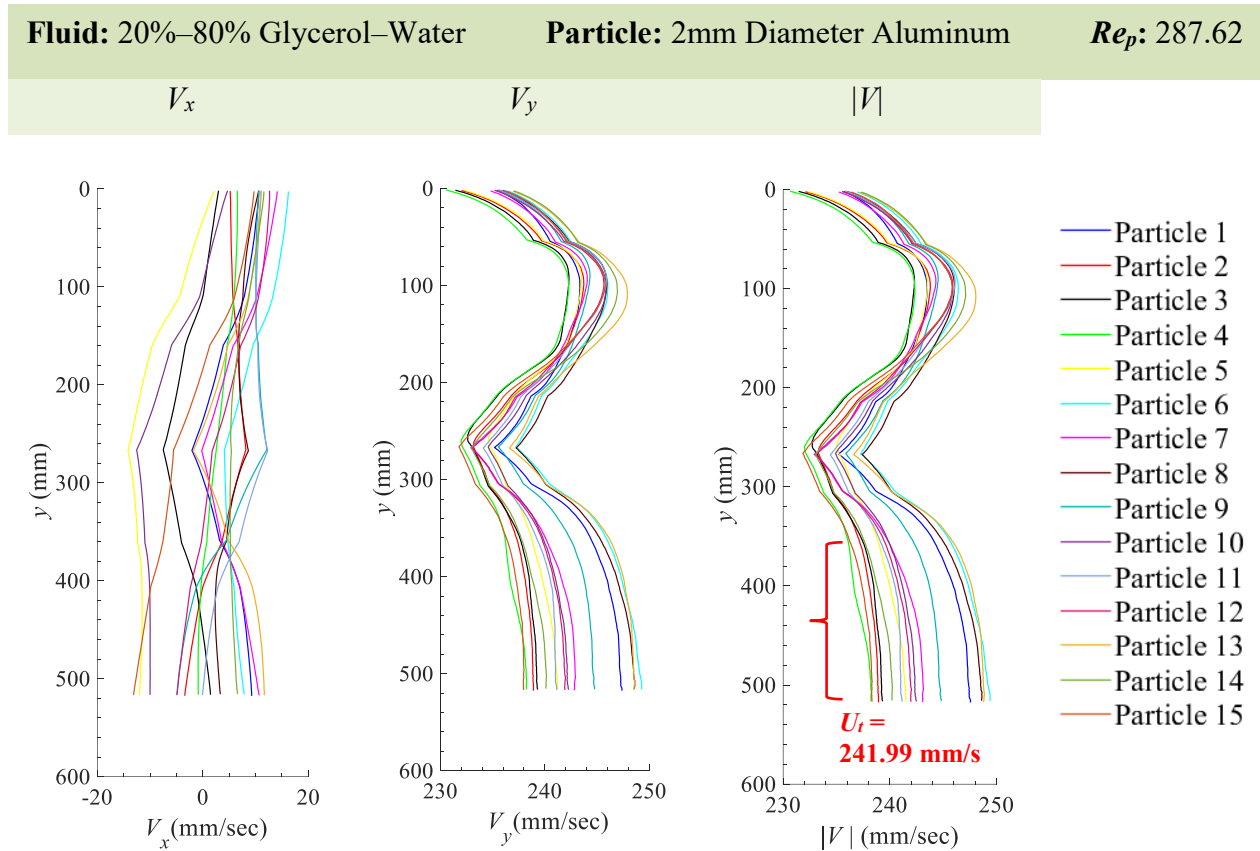


Figure 79 Particle velocity in the x -direction V_x , y -direction V_y , and the magnitude $\sqrt{(V_x^2 + V_y^2)}$ of the particle velocity $|V|$ for 2mm Diameter Aluminum (15 particles) in 20%–80% glycerol–water. The average terminal settling velocity, U_t is 241.99 mm/s.

8.12.3 x -Acceleration (A_x), y -Acceleration (A_y) and Magnitude of Acceleration ($|A|$) for 2mm Diameter Aluminum Spheres in 20%–80% Glycerol–Water

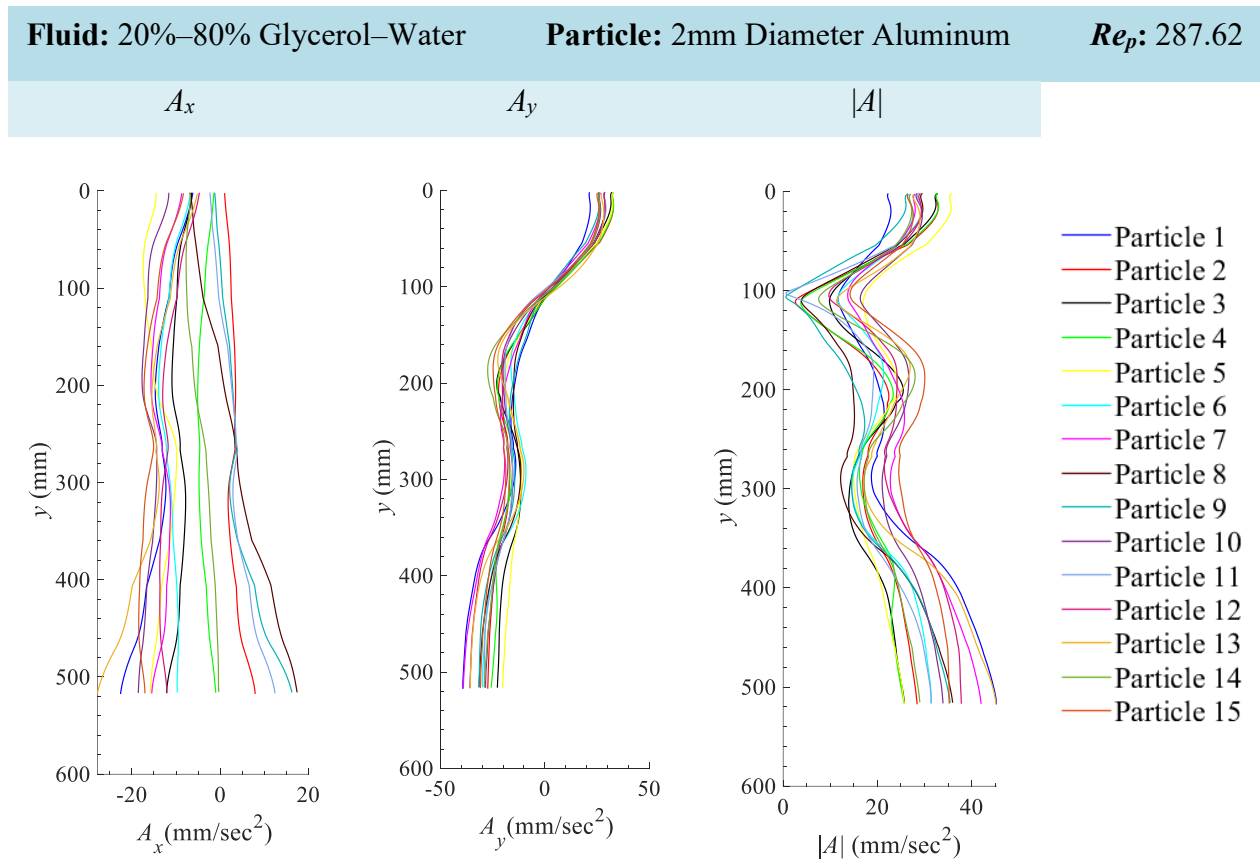


Figure 80 Particle acceleration in the x -direction A_x , y -direction A_y , and the magnitude $\sqrt{(A_x^2 + A_y^2)}$ of the particle acceleration $|A|$ for 2mm Diameter Aluminum (15 particles) in 20%–80% glycerol–water.

8.13 Appendix 13: 2mm Diameter Aluminum Spheres in 40%–60% Glycerol–Water

8.13.1 Particle Displacement, Particle Velocity and Particle Acceleration for 2mm Diameter Aluminum Spheres in 40%–60% Glycerol–Water

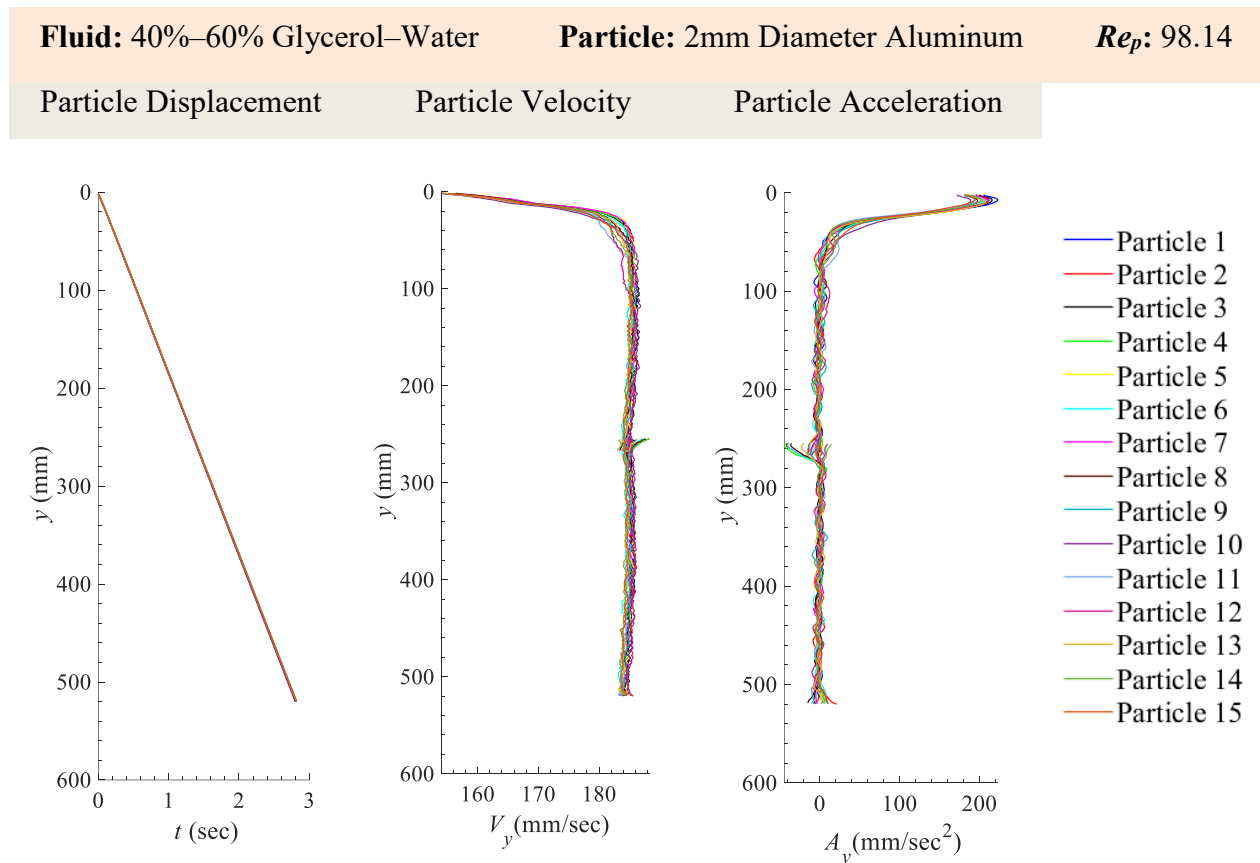


Figure 81 Particle displacement, y , velocity, V_y , and acceleration, A_y , for 2mm Diameter Aluminum (15 particles) in 40%–60% Glycerol–Water. The outliers at displacement 260 mm occurred within the overlap between the two cameras. In this region there was a variation in the light distribution compared to the rest of the field of view. A uniform distribution of light was not achieved with the projector and kite paper as shown in Figure 8 and describe in Section 3.5.1. This affected the binarization of the particle within that region and thereby a slight shift in the location of the centroid of the particle from the image processing scheme.

8.13.2 x -Velocity (V_x), y -Velocity (V_y) and Magnitude of Velocity ($|V|$) for 2mm Diameter Aluminum Spheres in 40%–60% Glycerol–Water

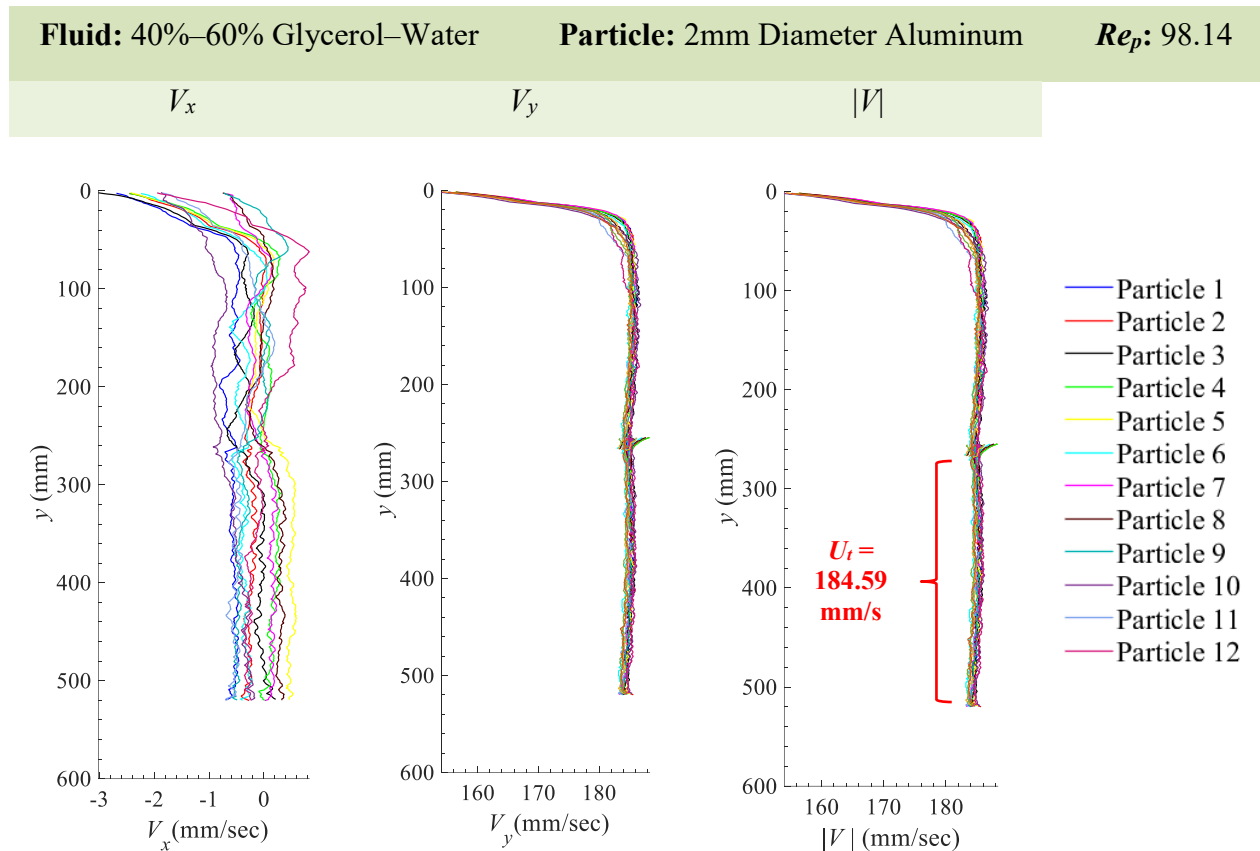


Figure 82 Particle velocity in the x -direction V_x , y -direction V_y , and the magnitude $\sqrt{(V_x^2 + V_y^2)}$ of the particle velocity $|V|$ for 2mm Diameter Aluminum in 40%–60% Glycerol–Water. The average terminal settling velocity, U_t is 184.59 mm/s. The outliers at displacement 260 mm occurred within the overlap between the two cameras. In this region there was a variation in the light distribution compared to the rest of the field of view. A uniform distribution of light was not achieved with the projector and kite paper as shown in Figure 8 and describe in Section 3.5.1. This affected the binarization of the particle within that region and thereby a slight shift in the location of the centroid of the particle from the image processing scheme.

8.13.3 x -Acceleration (A_x), y -Acceleration (A_y) and Magnitude of Acceleration ($|A|$) for 2mm Diameter Aluminum Spheres in 40%–60% Glycerol–Water

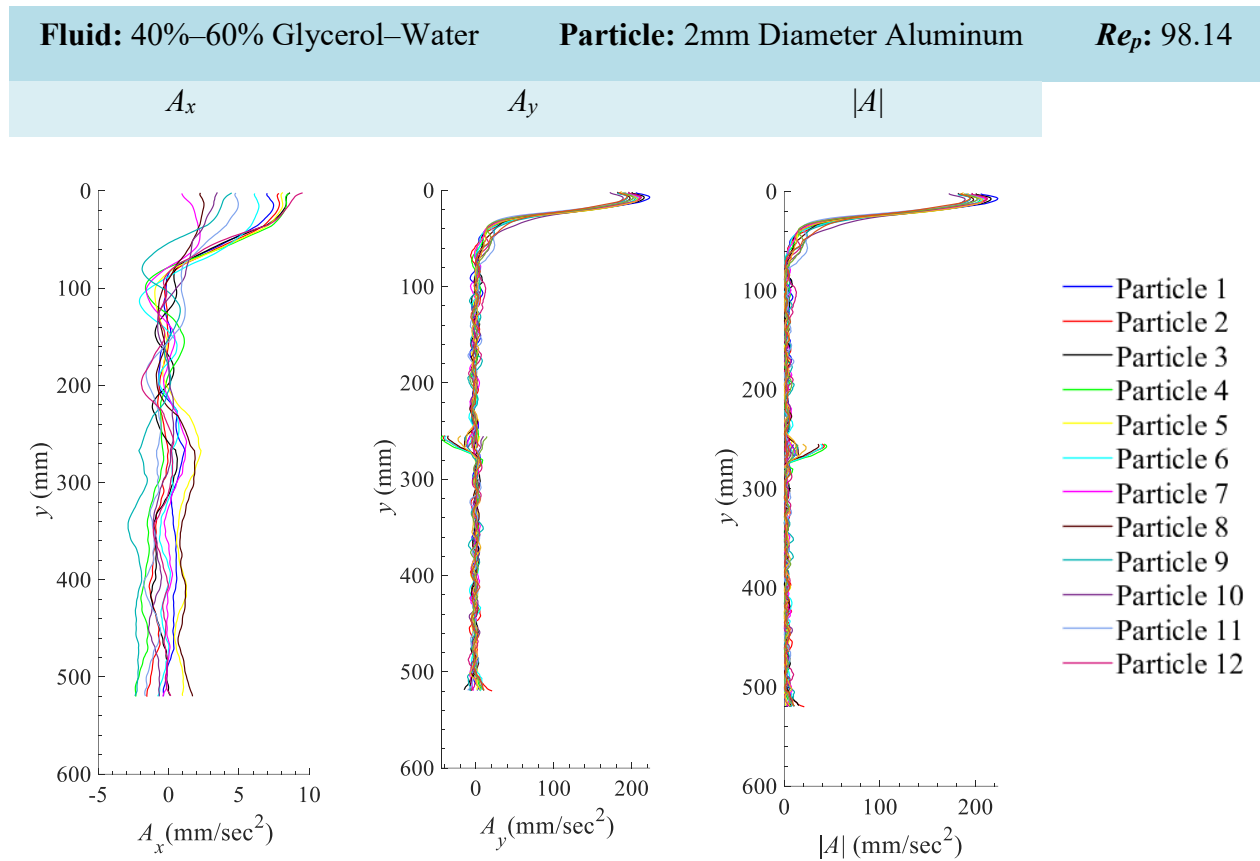


Figure 83 Particle acceleration in the x -direction A_x , y -direction A_y , and the magnitude $\sqrt{A_x^2 + A_y^2}$ of the particle acceleration $|A|$ for 2mm Diameter Aluminum in 40%–60% Glycerol–Water. The outliers at displacement 260 mm occurred within the overlap between the two cameras. In this region there was a variation in the light distribution compared to the rest of the field of view. A uniform distribution of light was not achieved with the projector and kite paper as shown in Figure 8 and describe in Section 3.5.1. This affected the binarization of the particle within that region and thereby a slight shift in the location of the centroid of the particle from the image processing scheme.

8.14 Appendix 14: 2mm Diameter Aluminum Spheres in 70%–30% Glycerol–Water

8.14.1 Particle Displacement, Particle Velocity and Particle Acceleration for 2mm Diameter Aluminum Spheres in 70%–30% Glycerol–Water

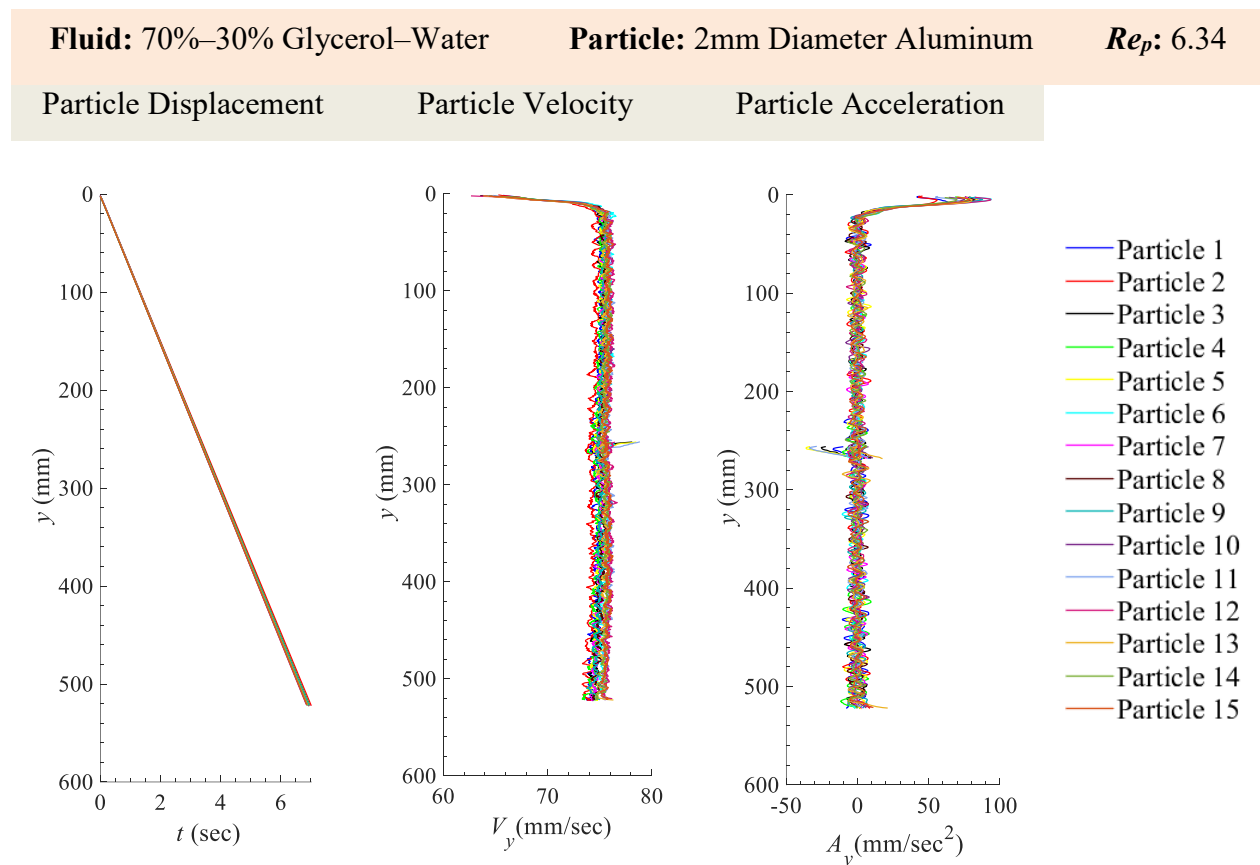


Figure 84 Particle displacement, y , velocity, V_y , and acceleration, A_y , for 2mm Diameter Aluminum (15 particles) in 70%–30% Glycerol–Water. The outliers at displacement 260 mm occurred within the overlap between the two cameras. In this region there was a variation in the light distribution compared to the rest of the field of view. A uniform distribution of light was not achieved with the projector and kite paper as shown in Figure 8 and describe in Section 3.5.1. This affected the binarization of the particle within that region and thereby a slight shift in the location of the centroid of the particle from the image processing scheme.

8.14.2 x -Velocity (V_x), y -Velocity (V_y) and Magnitude of Velocity ($|V|$) for 2mm Diameter Aluminum Spheres in 70%–30% Glycerol–Water

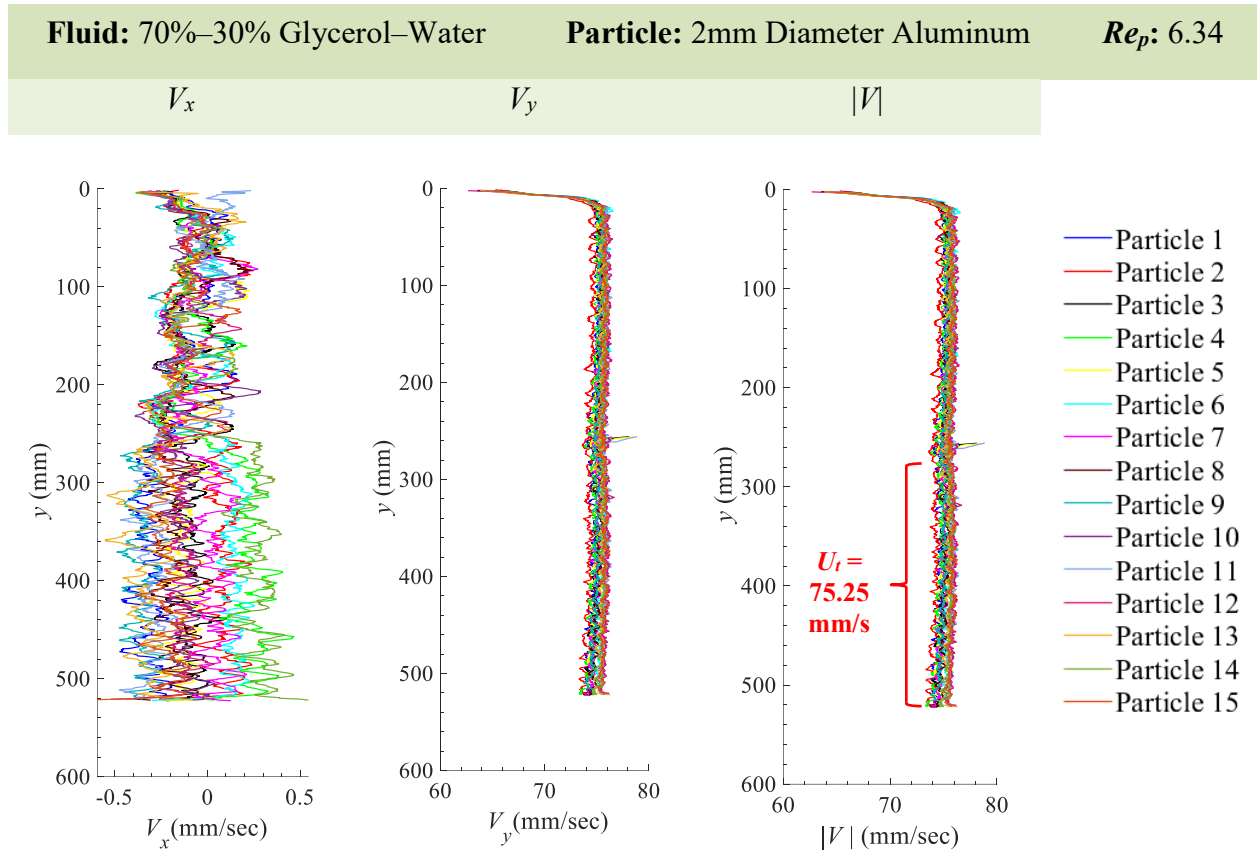


Figure 85 Particle velocity in the x -direction V_x , y -direction V_y , and the magnitude $\sqrt{(V_x^2 + V_y^2)}$ of the particle velocity $|V|$ for 2mm Diameter Aluminum in 70%–30% Glycerol–Water. The average terminal settling velocity, U_t is 75.25 mm/s. The outliers at displacement 260 mm occurred within the overlap between the two cameras. In this region there was a variation in the light distribution compared to the rest of the field of view. A uniform distribution of light was not achieved with the projector and kite paper as shown in Figure 8 and describe in Section 3.5.1. This affected the binarization of the particle within that region and thereby a slight shift in the location of the centroid of the particle from the image processing scheme.

8.14.3 x -Acceleration (A_x), y -Acceleration (A_y) and Magnitude of Acceleration ($|A|$) for 2mm Diameter Aluminum Spheres in 70%–30% Glycerol–Water

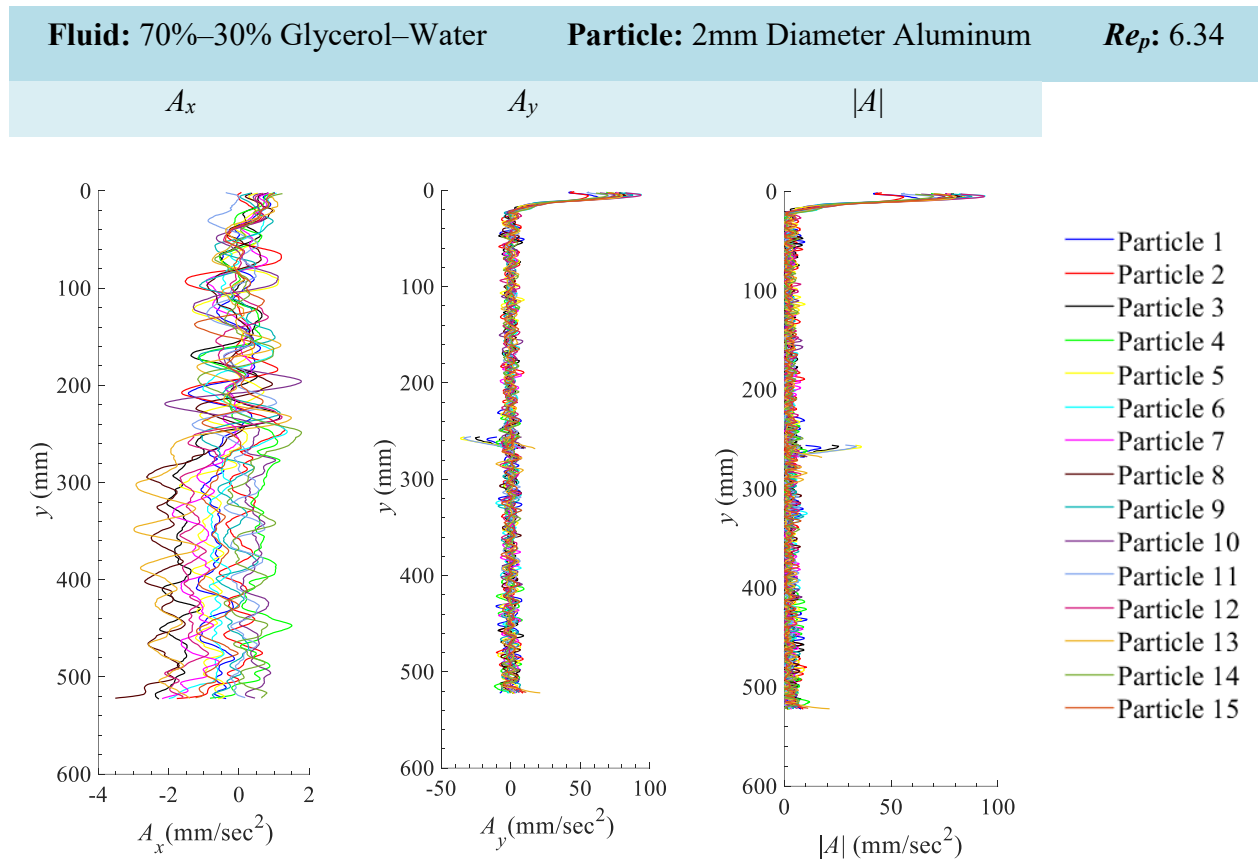


Figure 86 Particle acceleration in the x -direction A_x , y -direction A_y , and the magnitude $\sqrt{(A_x^2 + A_y^2)}$ of the particle acceleration $|A|$ for 2mm Diameter Aluminum in 70%–30% Glycerol–Water. The outliers at displacement 260 mm occurred within the overlap between the two cameras. In this region there was a variation in the light distribution compared to the rest of the field of view. A uniform distribution of light was not achieved with the projector and kite paper as shown in Figure 8 and describe in Section 3.5.1. This affected the binarization of the particle within that region and thereby a slight shift in the location of the centroid of the particle from the image processing scheme.

8.15 Appendix 15: 2mm Diameter Aluminum Spheres in Canola Oil

8.15.1 Particle Displacement, Particle Velocity and Particle Acceleration for 2mm Diameter Aluminum Spheres in Canola Oil

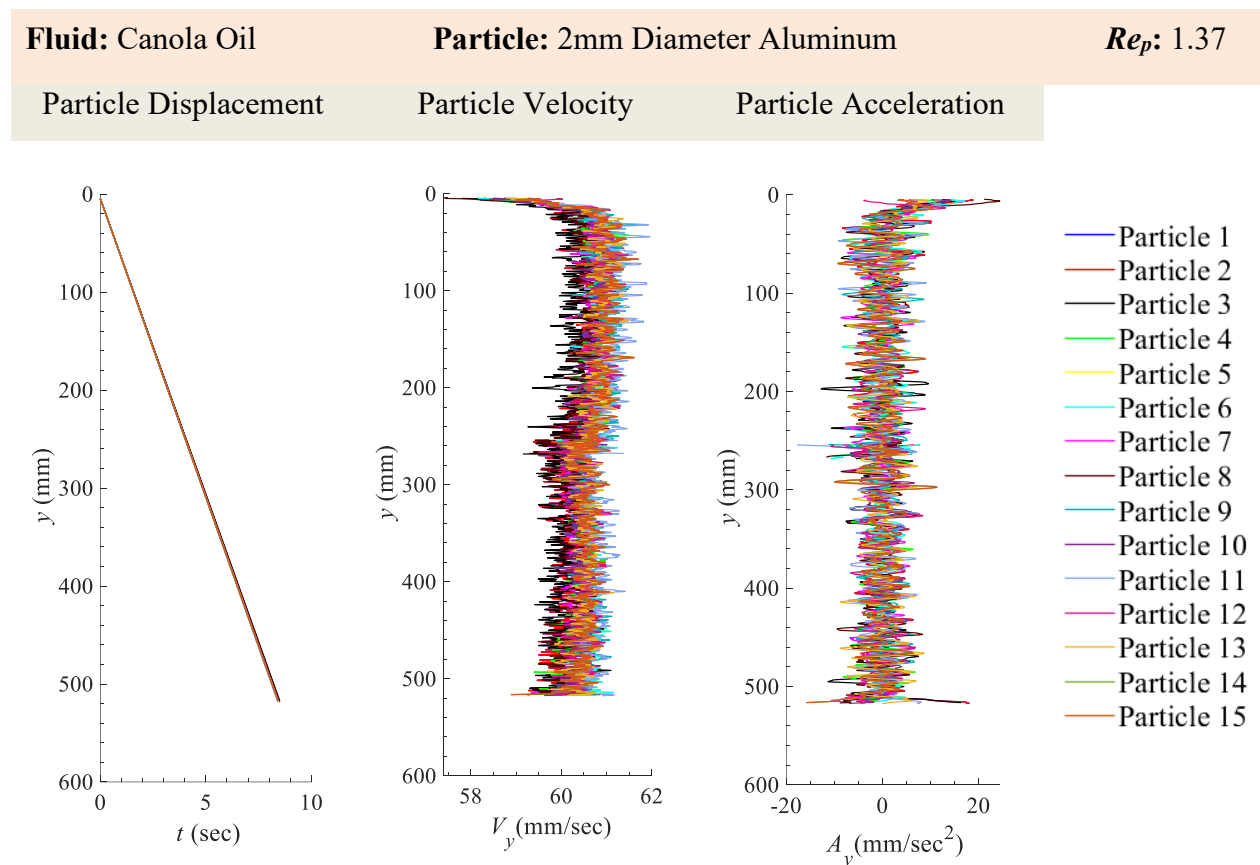


Figure 87 Particle displacement, y , velocity, V_y , and acceleration, A_y , for 2mm Diameter Aluminum (15 particles) in Canola Oil.

8.15.2 x -Velocity (V_x), y -Velocity (V_y) and Magnitude of Velocity ($|V|$) for 2mm Diameter Aluminum Spheres in Canola Oil

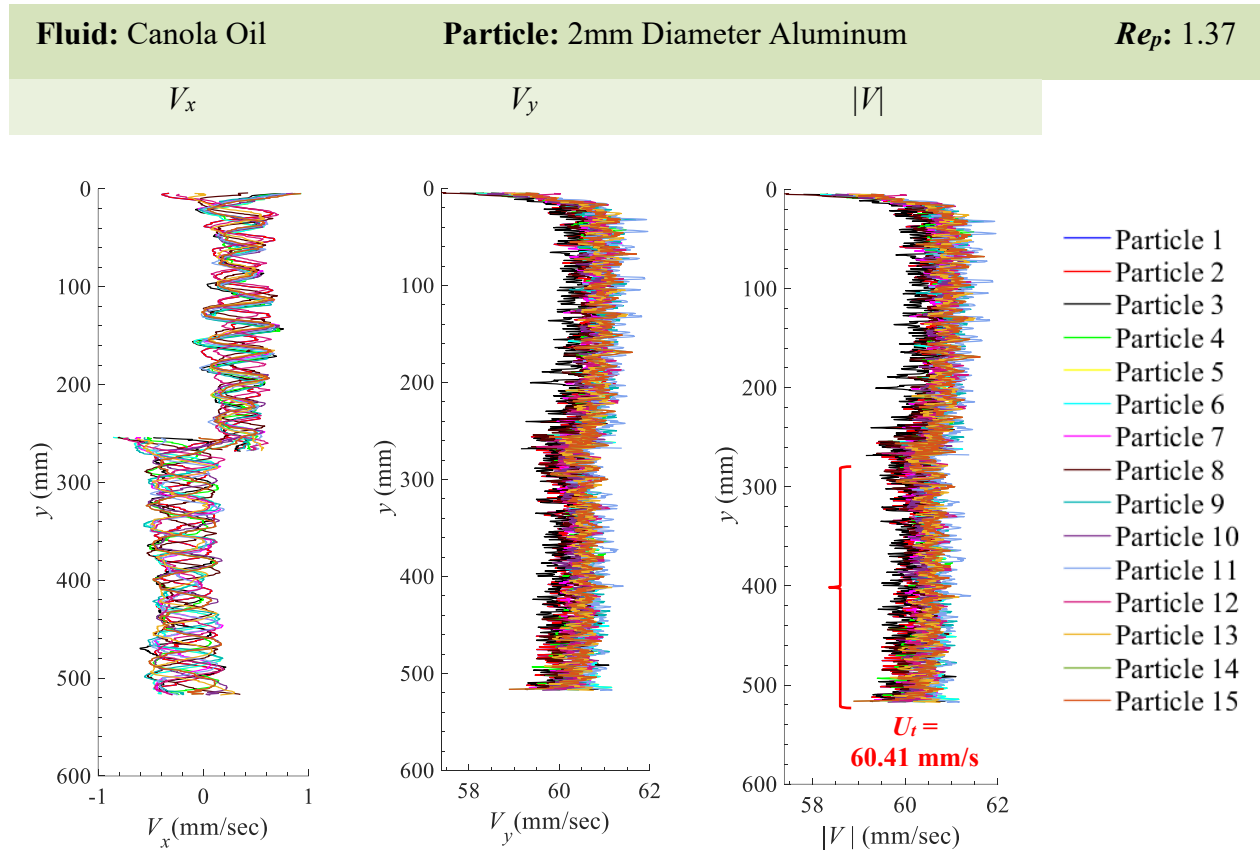


Figure 88 Particle velocity in the x -direction V_x , y -direction V_y , and the magnitude $\sqrt{V_x^2 + V_y^2}$ of the particle velocity $|V|$ for 2mm Diameter Aluminum in Canola Oil. The average terminal settling velocity, U_t is 60.41 mm/s.

8.15.3 x -Acceleration (A_x), y -Acceleration (A_y) and Magnitude of Acceleration ($|A|$) for 2mm Diameter Aluminum Spheres in Canola Oil

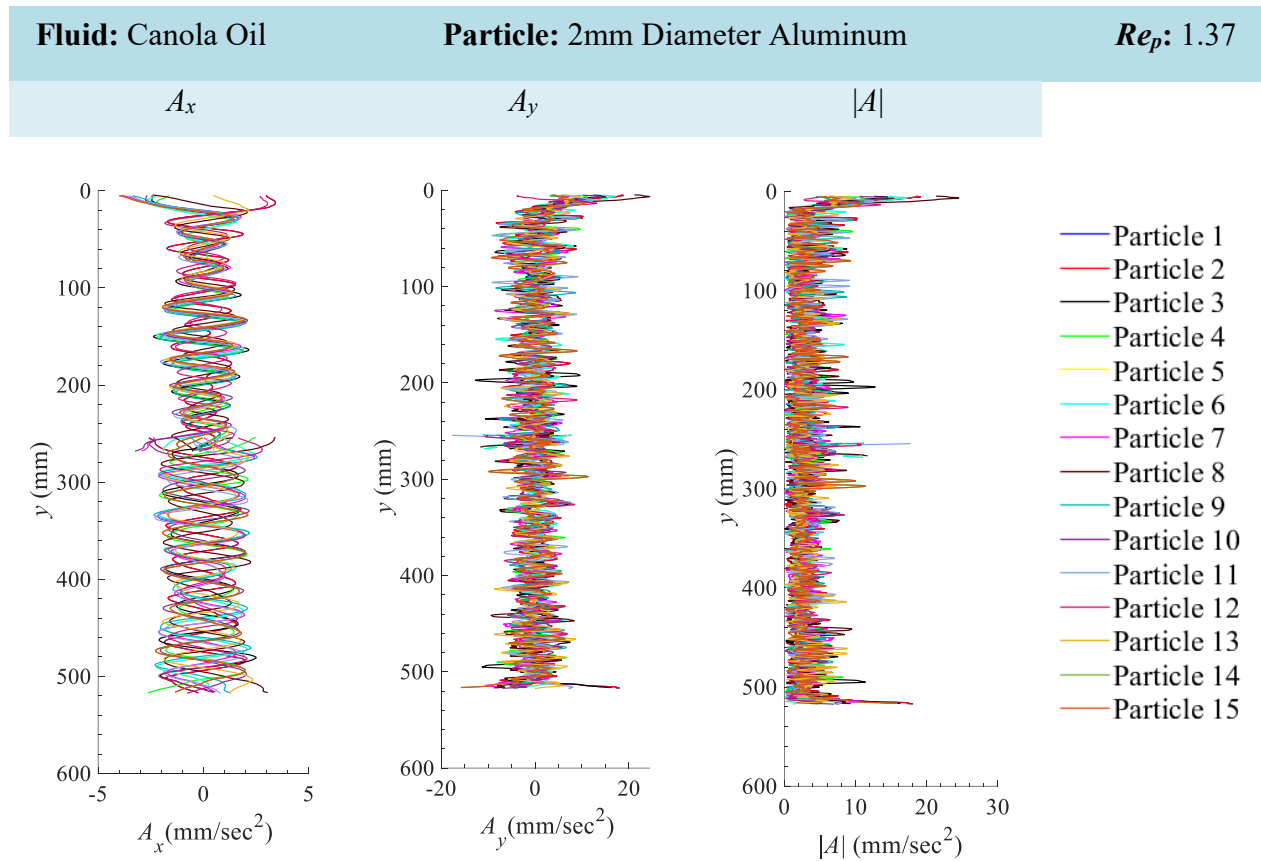


Figure 89 Particle acceleration in the x -direction A_x , y -direction A_y , and the magnitude $\sqrt{(A_x^2 + A_y^2)}$ of the particle acceleration $|A|$ for 2mm Diameter Aluminum in Canola Oil.

8.16 Appendix 16: 1.30 mm Diameter and 1:1 Aspect Ratio ($AR = d_p/l_p$) Nylon Cylindrical Particles in Water

8.16.1 Particle Displacement, Particle Velocity and Particle Acceleration for 1.30 mm Diameter and 1:1 Aspect Ratio ($AR = d_p/l_p$) Nylon Cylindrical Particles in Water

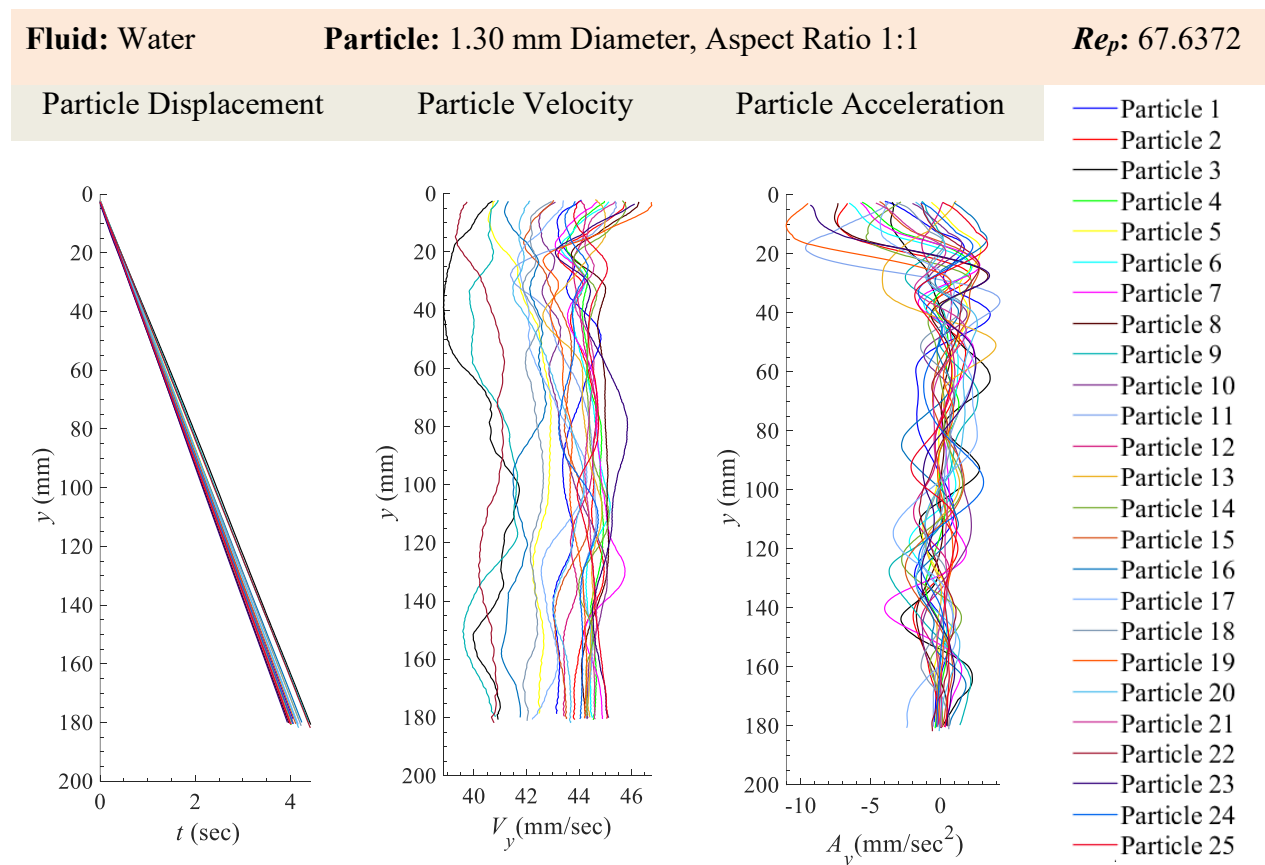


Figure 90 Particle displacement, y , velocity, V_y , and acceleration, A_y , for 1.30 mm Diameter Nylon Cylindrical Particles with Aspect Ratio, A.R. = 1:1 (25 particles) in Water.

8.16.2 x -Velocity (V_x), y -Velocity (V_y) and Magnitude of Velocity ($|V|$) for 1.30 mm Diameter and 1:1 Aspect Ratio ($AR = d_p/l_p$) Nylon Cylindrical Particles in Water

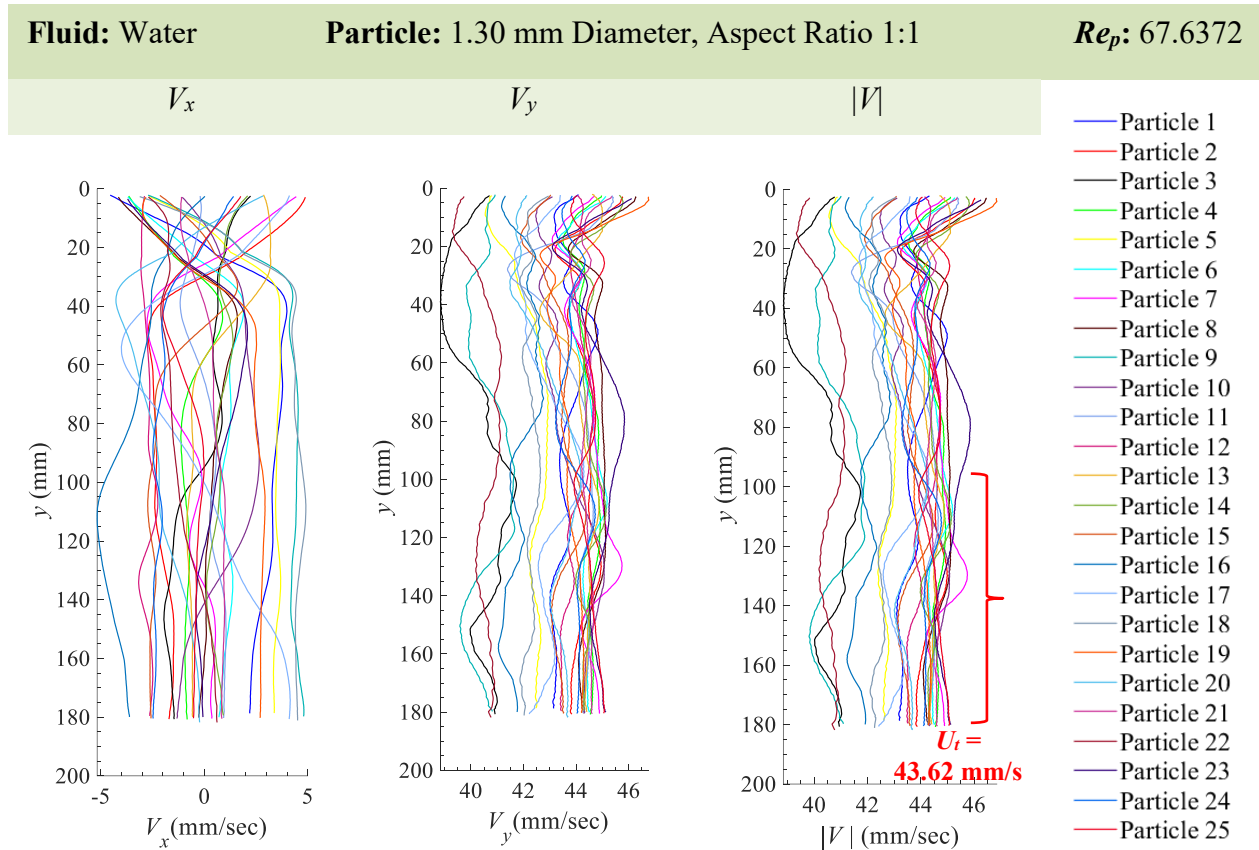


Figure 91 Particle velocity in the x -direction V_x , y -direction V_y , and the magnitude $\sqrt{(V_x^2 + V_y^2)}$ of the particle velocity $|V|$ for 1.30 mm Diameter Nylon Cylindrical Particles with Aspect Ratio, A.R. = 1:1 (25 particles) in Water. The average terminal settling velocity, U_t is 43.62 mm/s.

8.16.3 x -Acceleration (A_x), y -Acceleration (A_y) and Magnitude of Acceleration ($|A|$) for 1.30 mm Diameter and 1:1 Aspect Ratio ($AR = d_p/l_p$) Nylon Cylindrical Particles in Water

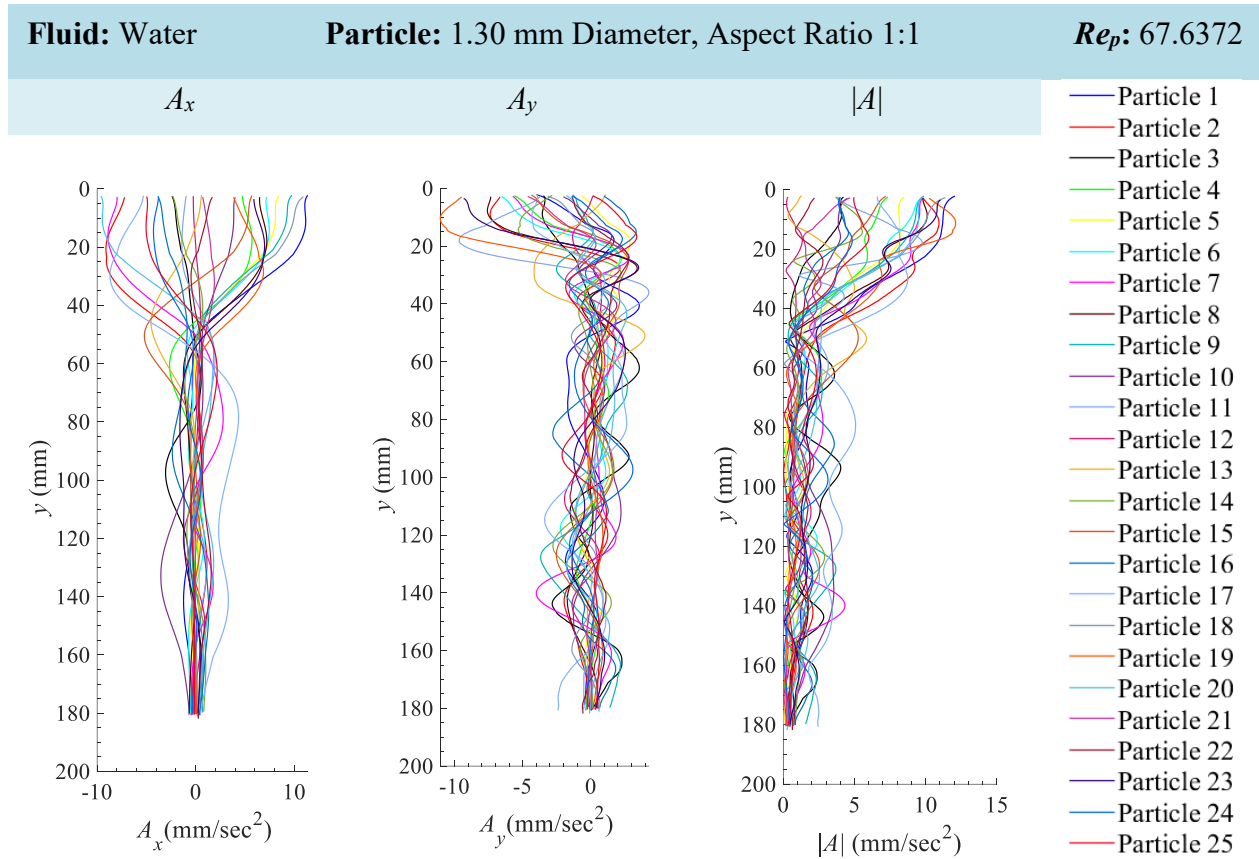


Figure 92 Particle acceleration in the x -direction A_x , y -direction A_y , and the magnitude $\sqrt{A_x^2 + A_y^2}$ of the particle acceleration $|A|$ for 1.30 mm Diameter Nylon Cylindrical Particles with Aspect Ratio, A.R. = 1:1 (25 particles) in Water.

8.17 Appendix 17: 1.30 mm Diameter and 1:1 Aspect Ratio ($AR = d_p/l_p$) Nylon Cylindrical Particles in 20%–80% Glycerol–Water

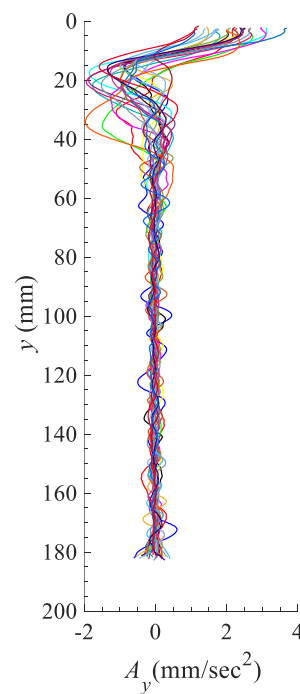
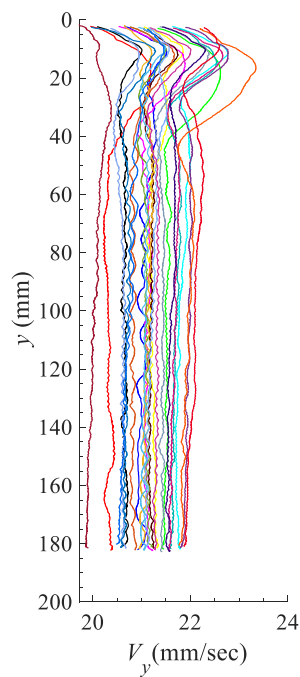
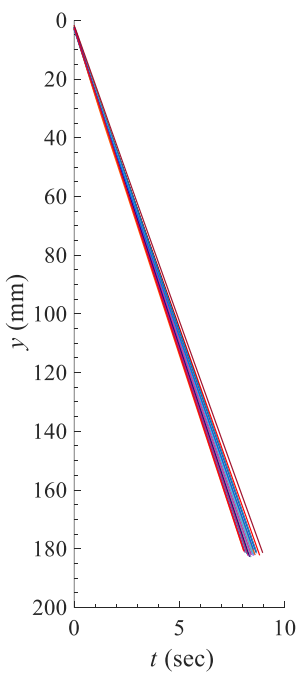
8.17.1 Particle Displacement, Particle Velocity and Particle Acceleration for 1.30 mm Diameter and 1:1 Aspect Ratio ($AR = d_p/l_p$) Nylon Cylindrical Particles in 20%–80% Glycerol–Water

Fluid: 20%–80% Glycerol–Water Particle: 1.30 mm Dia. and Aspect Ratio 1:1 Re_p : 18.73

Particle Displacement

Particle Velocity

Particle Acceleration



- Particle 1
- Particle 2
- Particle 3
- Particle 4
- Particle 5
- Particle 6
- Particle 7
- Particle 8
- Particle 9
- Particle 10
- Particle 11
- Particle 12
- Particle 13
- Particle 14
- Particle 15
- Particle 16
- Particle 17
- Particle 18
- Particle 19
- Particle 20
- Particle 21
- Particle 22
- Particle 23
- Particle 24
- Particle 25

Figure 93 Particle displacement, y , velocity, V_y , and acceleration, A_y , for 1.30 mm Diameter Nylon Cylindrical Particles with Aspect Ratio, A.R. = 1:1 (25 particles) in 20%–80% Glycerol–Water.

8.17.2 x -Velocity (V_x), y -Velocity (V_y) and Magnitude of Velocity ($|V|$) for 1.30 mm Diameter and 1:1 Aspect Ratio ($AR = d_p/l_p$) Nylon Cylindrical Particles in 20%–80% Glycerol–Water

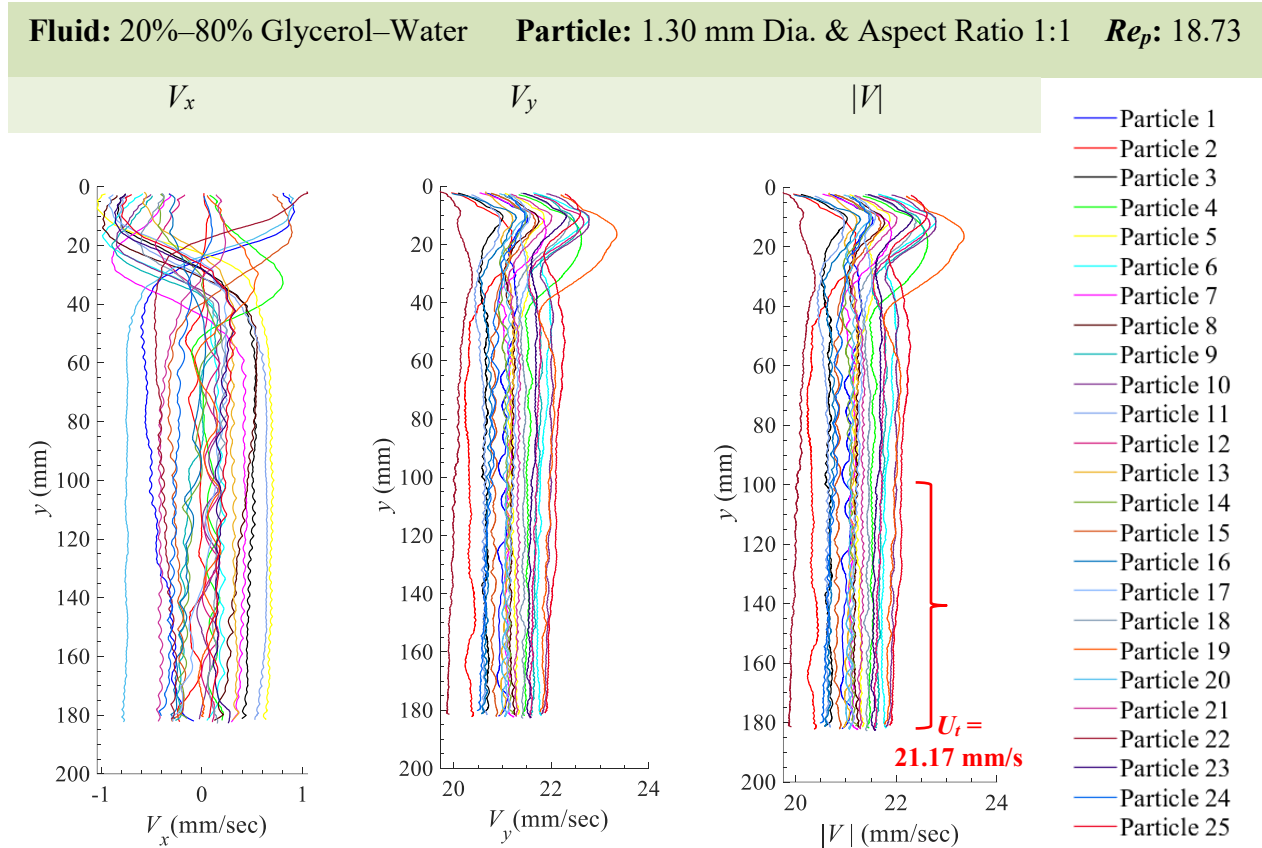


Figure 94 Particle velocity in the x -direction V_x , y -direction V_y , and the magnitude $\sqrt{(V_x^2 + V_y^2)}$ of the particle velocity $|V|$ for 1.30 mm Diameter Nylon Cylindrical Particles with Aspect Ratio, A.R. = 1:1 (25 particles) in 20%–80% Glycerol–Water. The average terminal settling velocity, U_t is 21.17 mm/s.

8.17.3 x -Acceleration (A_x), y -Acceleration (A_y) and Magnitude of Acceleration ($|A|$) for 1.30 mm Diameter and 1:1 Aspect Ratio ($AR = d_p/l_p$) Nylon Cylindrical Particles in 20%–80% Glycerol–Water

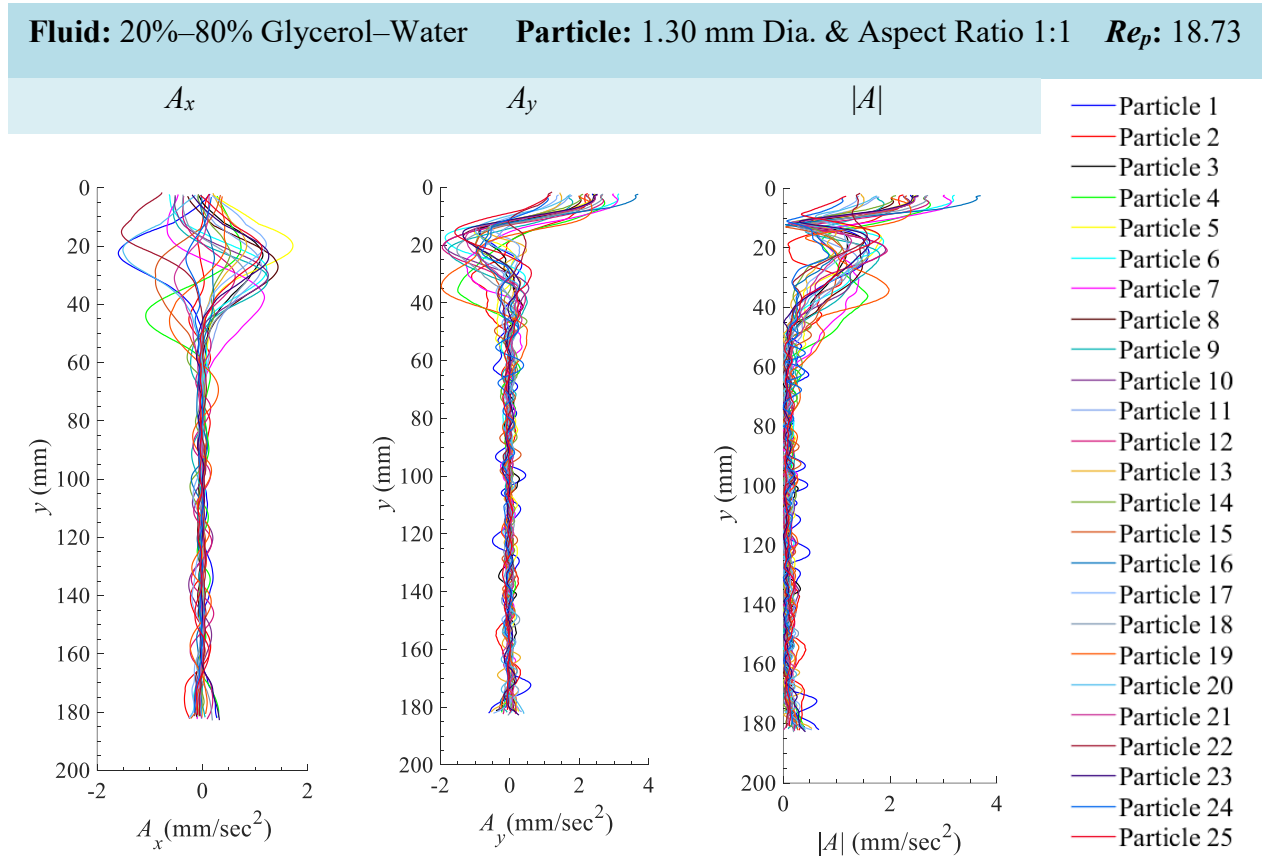


Figure 95 Particle acceleration in the x -direction A_x , y -direction A_y , and the magnitude $\sqrt{A_x^2 + A_y^2}$ of the particle acceleration $|A|$ 1.30 mm Diameter Nylon Cylindrical Particles with Aspect Ratio, A.R. = 1:1 (25 particles) in 20%–80% Glycerol–Water.

8.18 Appendix 18: 1.30 mm Diameter and 1:1 Aspect Ratio ($AR = d_p/l_p$) Nylon Cylindrical Particles in 40%–60% Glycerol–Water

8.18.1 Particle Displacement, Particle Velocity and Particle Acceleration for 1.30 mm Diameter and 1:1 Aspect Ratio ($AR = d_p/l_p$) Nylon Cylindrical Particles in 40%–60% Glycerol–Water

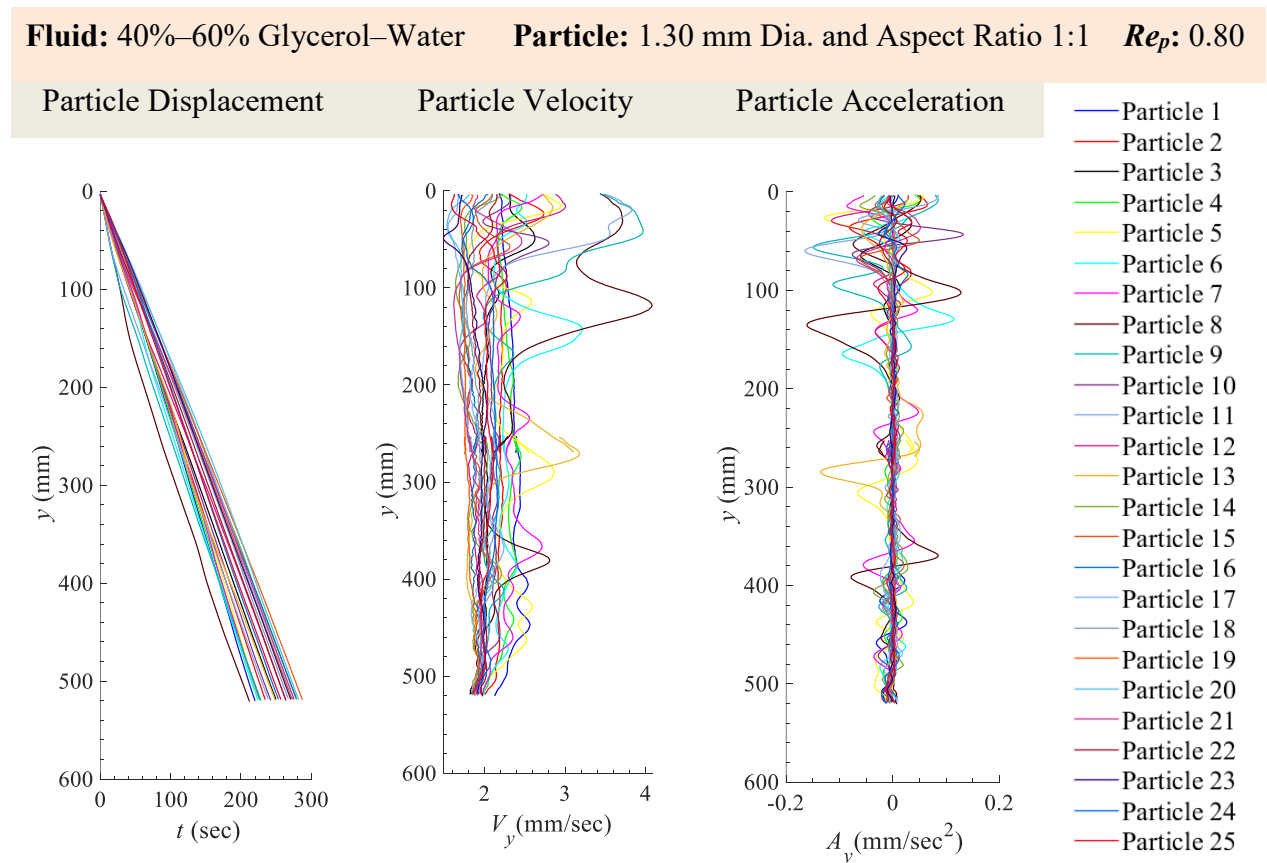


Figure 96 Particle displacement, y , velocity, V_y , and acceleration, A_y , for 1.30 mm Diameter Nylon Cylindrical Particles with Aspect Ratio, A.R. = 1:1 (25 particles) in 40%–60% Glycerol–Water.

8.18.2 x -Velocity (V_x), y -Velocity (V_y) and Magnitude of Velocity ($|V|$) for 1.30 mm Diameter and 1:1 Aspect Ratio ($AR = d_p/l_p$) Nylon Cylindrical Particles in 40%–60% Glycerol–Water

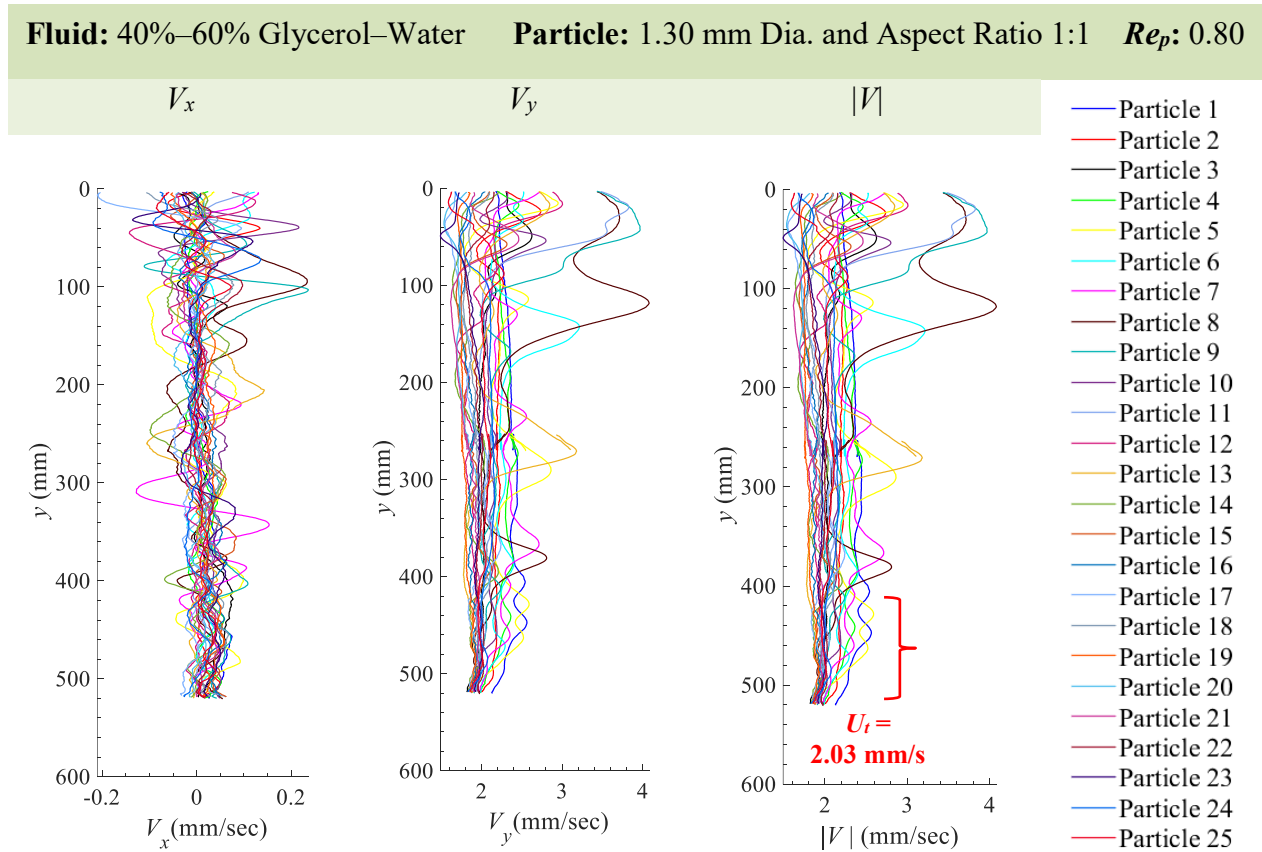


Figure 97 Particle velocity in the x -direction V_x , y -direction V_y , and the magnitude $\sqrt{(V_x^2 + V_y^2)}$ of the particle velocity $|V|$ for 1.30 mm Diameter Nylon Cylindrical Particles with Aspect Ratio, A.R. = 1:1 (25 particles) in 40%–60% Glycerol–Water. The average terminal settling velocity, U_t is 2.03 mm/s.

8.18.3 x -Acceleration (A_x), y -Acceleration (A_y) and Magnitude of Acceleration ($|A|$) for 1.30 mm Diameter and 1:1 Aspect Ratio ($AR = d_p/l_p$) Nylon Cylindrical Particles in 40%–60% Glycerol–Water

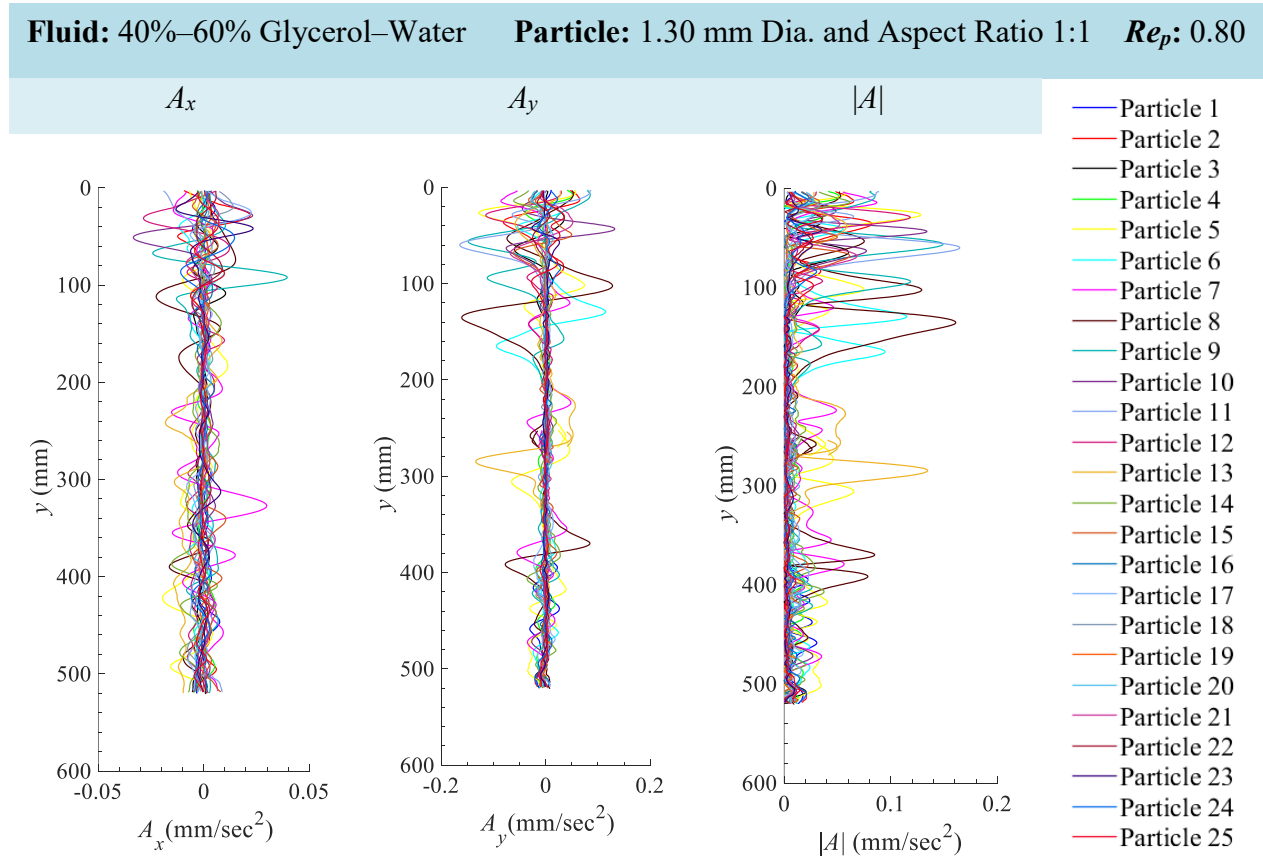


Figure 98 Particle acceleration in the x -direction A_x , y -direction A_y , and the magnitude $\sqrt{(A_x^2 + A_y^2)}$ of the particle acceleration $|A|$ for 1.30 mm Diameter Nylon Cylindrical Particles with Aspect Ratio, A.R. = 1:1 (25 particles) in 40%–60% Glycerol–Water.

8.19 Appendix 19: 1.30 mm Diameter and 1:1 Aspect Ratio ($AR = d_p/l_p$) Nylon Cylindrical Particles in Canola Oil

8.19.1 Particle Displacement, Particle Velocity and Particle Acceleration for 1.30 mm Diameter and 1:1 Aspect Ratio ($AR = d_p/l_p$) Nylon Cylindrical Particles in Canola Oil

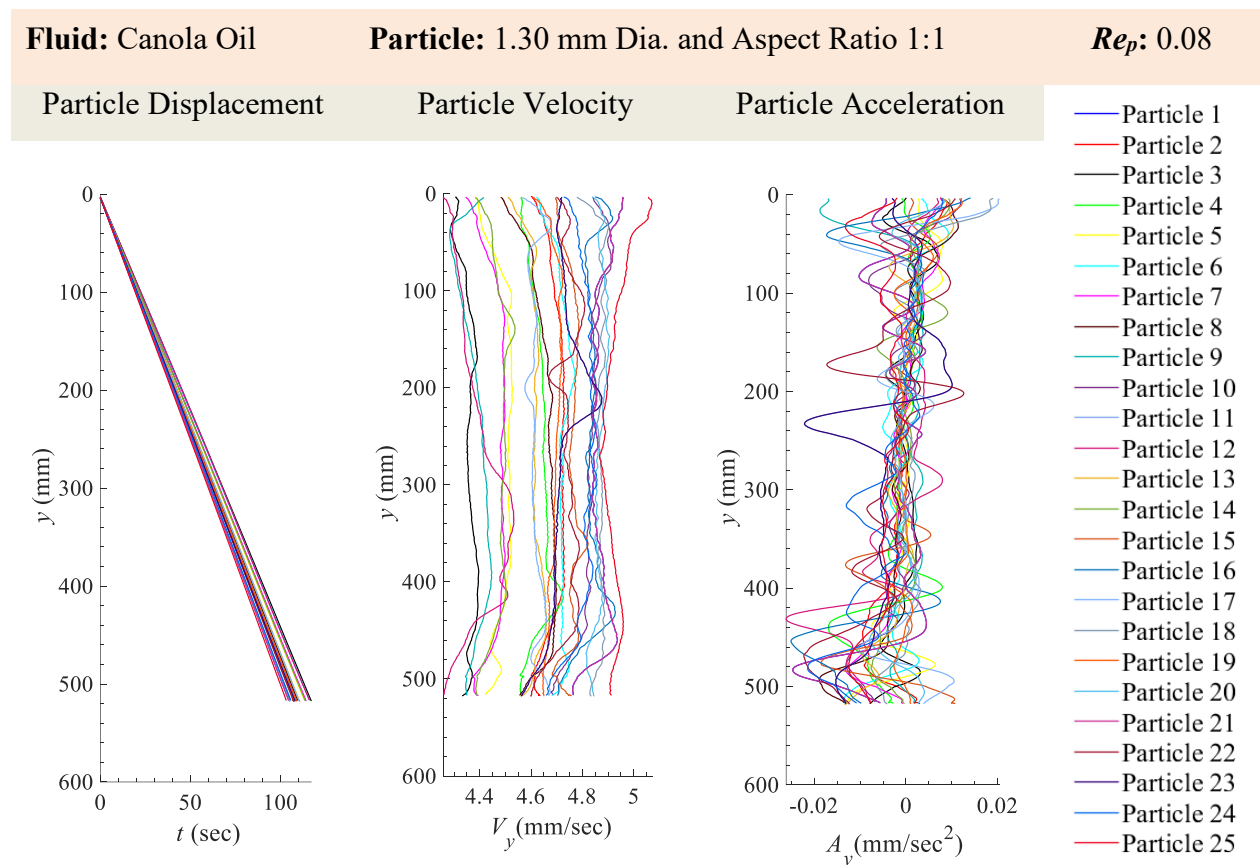


Figure 99 Particle displacement, y , velocity, V_y , and acceleration, A_y , for 1.30 mm Diameter Nylon Cylindrical Particles with Aspect Ratio, A.R. = 1:1 (25 particles) in Canola Oil.

8.19.2 x -Velocity (V_x), y -Velocity (V_y) and Magnitude of Velocity ($|V|$) for 1.30 mm Diameter and 1:1 Aspect Ratio ($AR = d_p/l_p$) Nylon Cylindrical Particles in Canola Oil

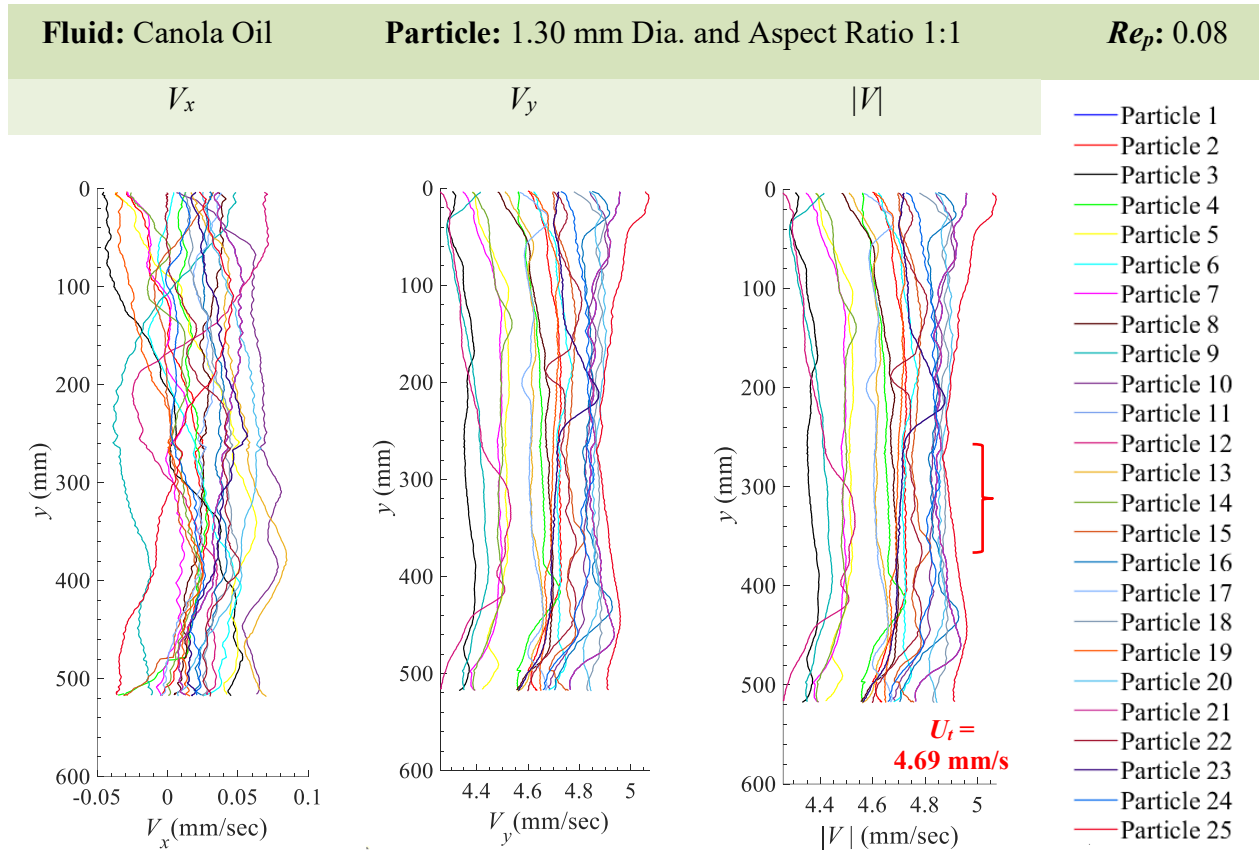


Figure 100 Particle velocity in the x -direction V_x , y -direction V_y , and the magnitude $\sqrt{V_x^2 + V_y^2}$ of the particle velocity $|V|$ for 1.30 mm Diameter Nylon Cylindrical Particles with Aspect Ratio, A.R. = 1:1 (25 particles) in Canola Oil. The average terminal settling velocity, U_t is 4.69 mm/s.

8.19.3 x -Acceleration (A_x), y -Acceleration (A_y) and Magnitude of Acceleration ($|A|$) for 1.30 mm Diameter and 1:1 Aspect Ratio ($AR = d_p/l_p$) Nylon Cylindrical Particles in Canola Oil

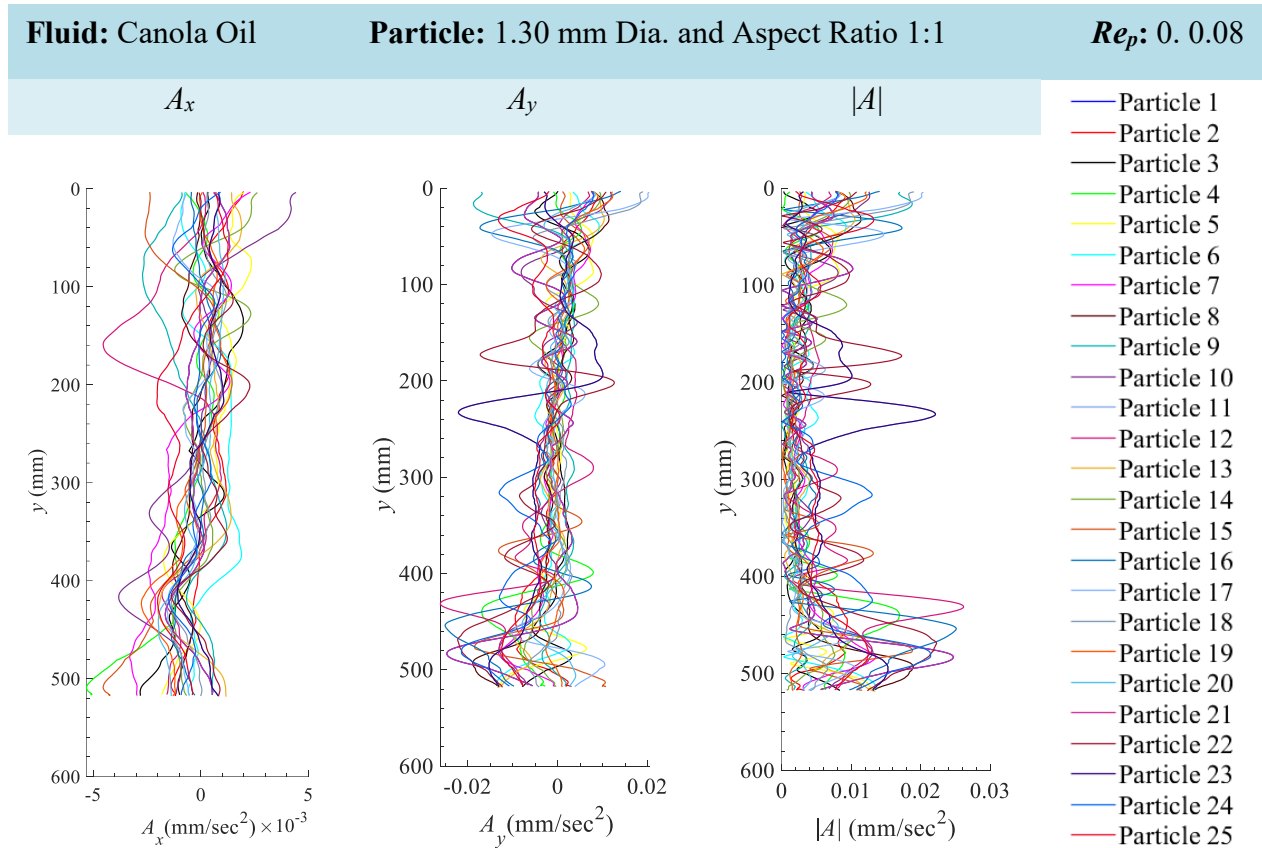


Figure 101 Particle acceleration in the x -direction A_x , y -direction A_y , and the magnitude $\sqrt{(A_x^2 + A_y^2)}$ of the particle acceleration $|A|$ for 1.30 mm Diameter Nylon Cylindrical Particles with Aspect Ratio, A.R. = 1:1 (25 particles) in Canola Oil.

8.20 Appendix 20: 1.30 mm Diameter and 1:3 Aspect Ratio ($AR = d_p/l_p$) Nylon Cylindrical Particles in Water

8.20.1 Particle Displacement, Particle Velocity and Particle Acceleration for 1.30 mm Diameter and 1:3 Aspect Ratio ($AR = d_p/l_p$) Nylon Cylindrical Particles in Water

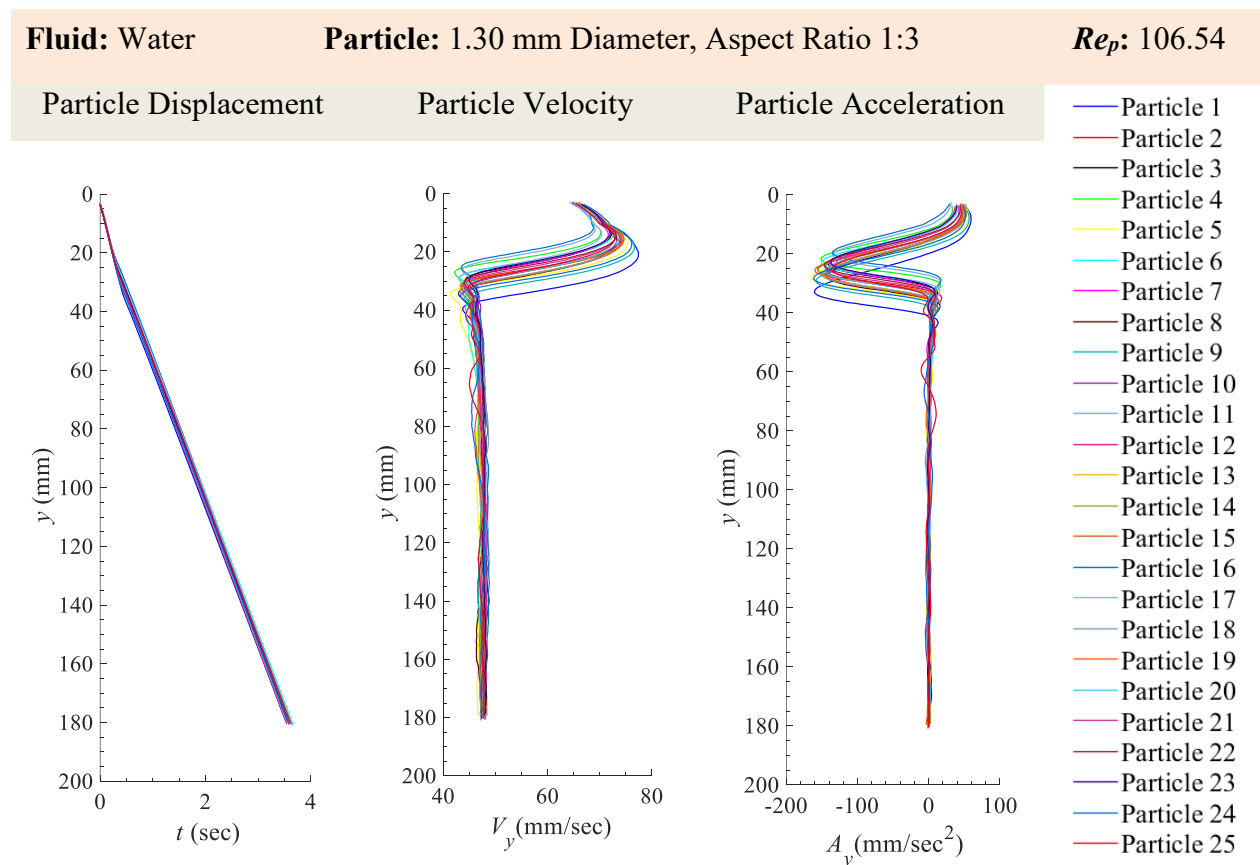


Figure 102 Particle displacement, y , velocity, V_y , and acceleration, A_y , for 1.30 mm Diameter Nylon Cylindrical Particles with Aspect Ratio, A.R. = 1:3 (25 particles) in Water.

8.20.2 x -Velocity (V_x), y -Velocity (V_y) and Magnitude of Velocity ($|V|$) for 1.30 mm Diameter and 1:3 Aspect Ratio ($AR = d_p/l_p$) Nylon Cylindrical Particles in Water

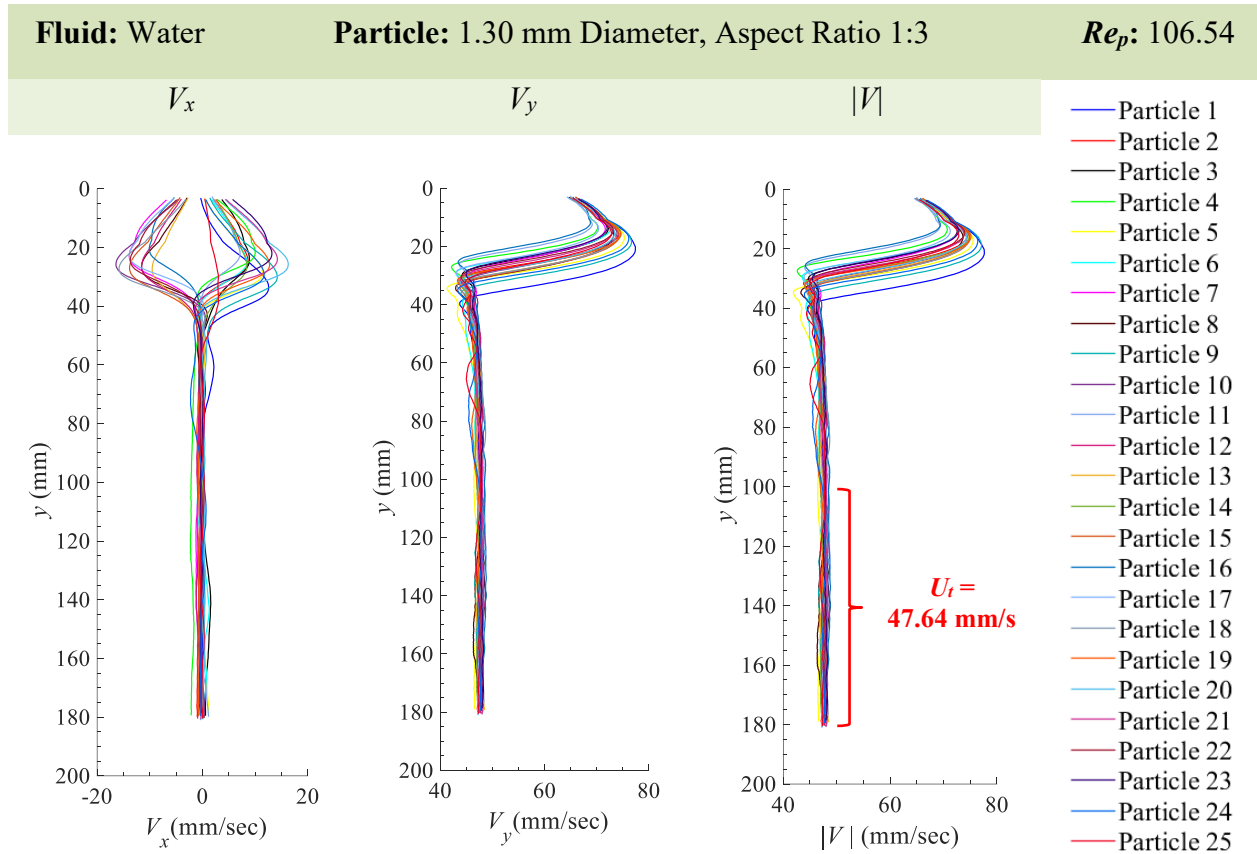


Figure 103 Particle velocity in the x -direction V_x , y -direction V_y , and the magnitude $\sqrt{V_x^2 + V_y^2}$ of the particle velocity $|V|$ for 1.30 mm Diameter Nylon Cylindrical Particles with Aspect Ratio, A.R. = 1:3 (25 particles) in Water. The average terminal settling velocity, U_t is 47.64 mm/s.

8.20.3 x -Acceleration (A_x), y -Acceleration (A_y) and Magnitude of Acceleration ($|A|$) for 1.30 mm Diameter and 1:3 Aspect Ratio ($AR = d_p/l_p$) Nylon Cylindrical Particles in Water

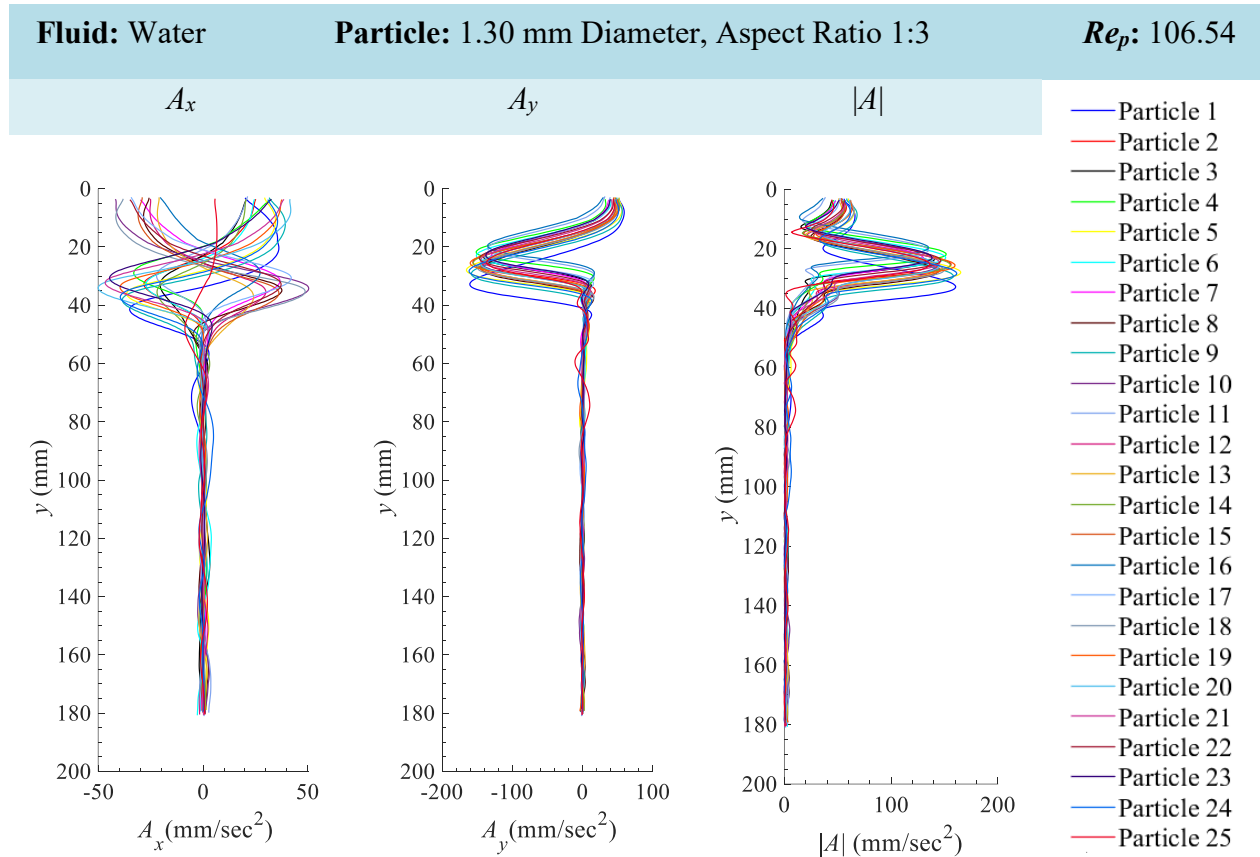


Figure 104 Particle acceleration in the x -direction A_x , y -direction A_y , and the magnitude $\sqrt{(A_x^2 + A_y^2)}$ of the particle acceleration $|A|$ for 1.30 mm Diameter Nylon Cylindrical Particles with Aspect Ratio, A.R. = 1:3 (25 particles) in Water.

8.21 Appendix 21: 1.30 mm Diameter and 1:3 Aspect Ratio ($AR = d_p/l_p$) Nylon Cylindrical Particles in 20%–80% Glycerol–Water

8.21.1 Particle Displacement, Particle Velocity and Particle Acceleration for 1.30 mm Diameter and 1:3 Aspect Ratio ($AR = d_p/l_p$) Nylon Cylindrical Particles in 20%–80% Glycerol–Water

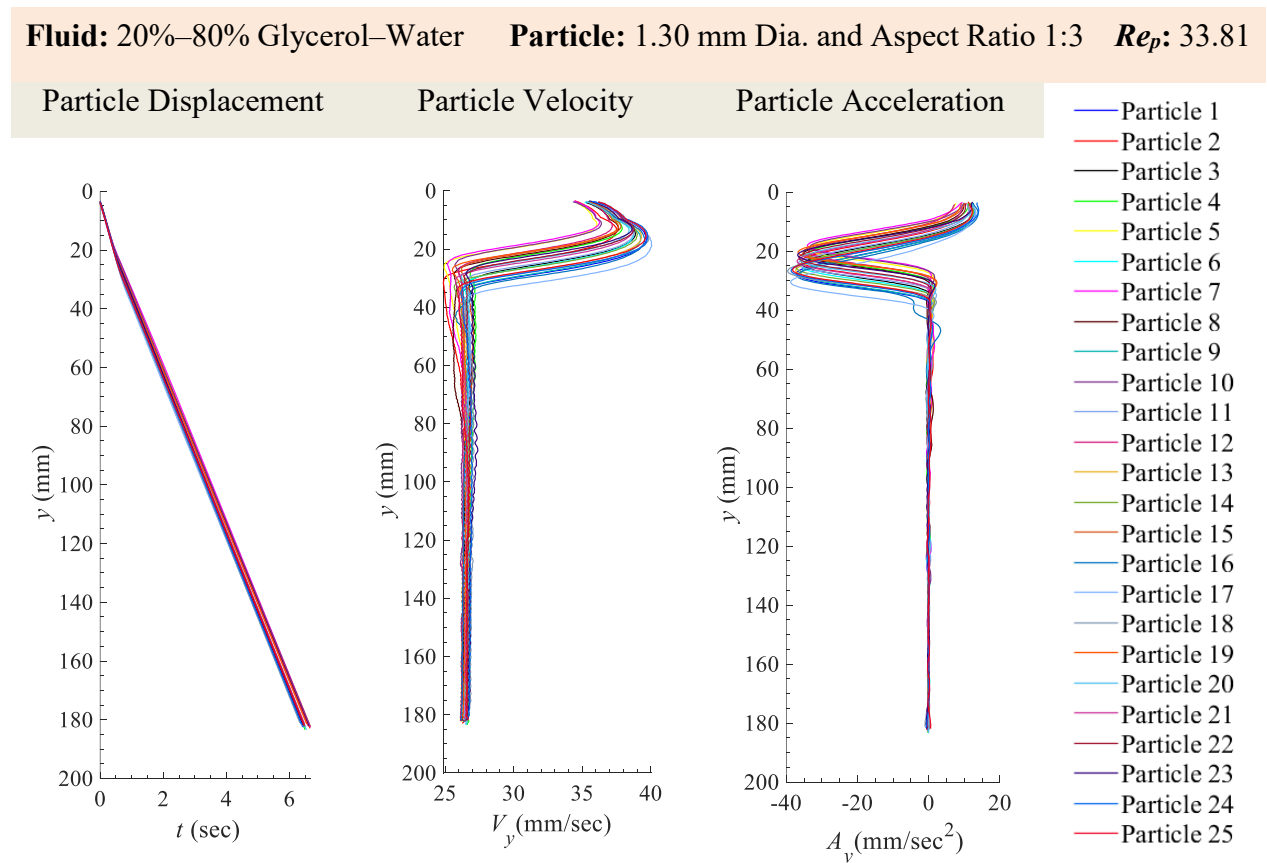


Figure 105 Particle displacement, y , velocity, V_y , and acceleration, A_y , for 1.30 mm Diameter Nylon Cylindrical Particles with Aspect Ratio, A.R. = 1:3 (25 particles) in 20%–80% Glycerol–Water.

8.21.2 x -Velocity (V_x), y -Velocity (V_y) and Magnitude of Velocity ($|V|$) for 1.30 mm Diameter and 1:3 Aspect Ratio ($AR = d_p/l_p$) Nylon Cylindrical Particles in 20%–80% Glycerol–Water

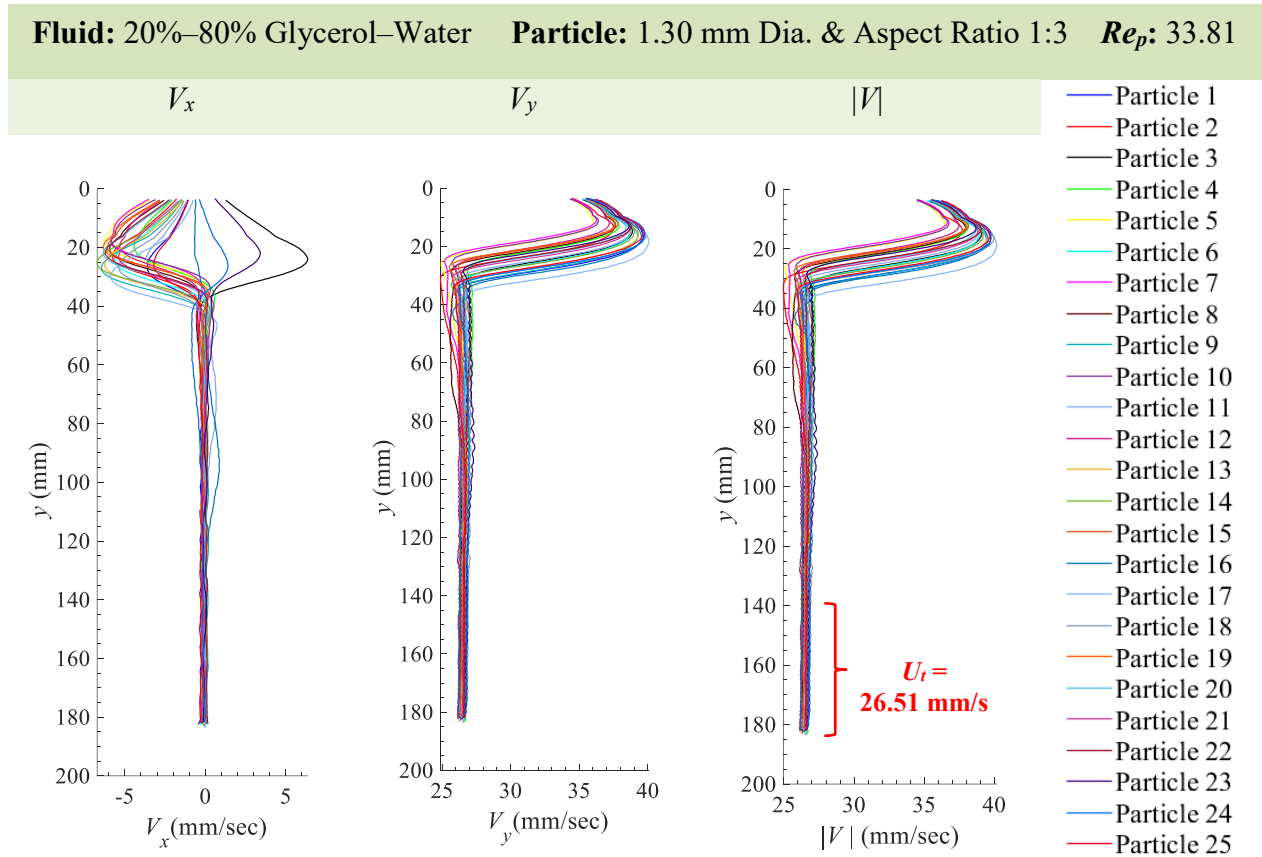


Figure 106 Particle velocity in the x -direction V_x , y -direction V_y , and the magnitude $\sqrt{V_x^2 + V_y^2}$ of the particle velocity $|V|$ for 1.30 mm Diameter Nylon Cylindrical Particles with Aspect Ratio, A.R. = 1:3 (25 particles) in 20%–80% Glycerol–Water. The average terminal settling velocity, U_t is 26.51 mm/s.

8.21.3 x -Acceleration (A_x), y -Acceleration (A_y) and Magnitude of Acceleration ($|A|$) for 1.30 mm Diameter and 1:3 Aspect Ratio ($AR = d_p/l_p$) Nylon Cylindrical Particles in 20%–80% Glycerol–Water

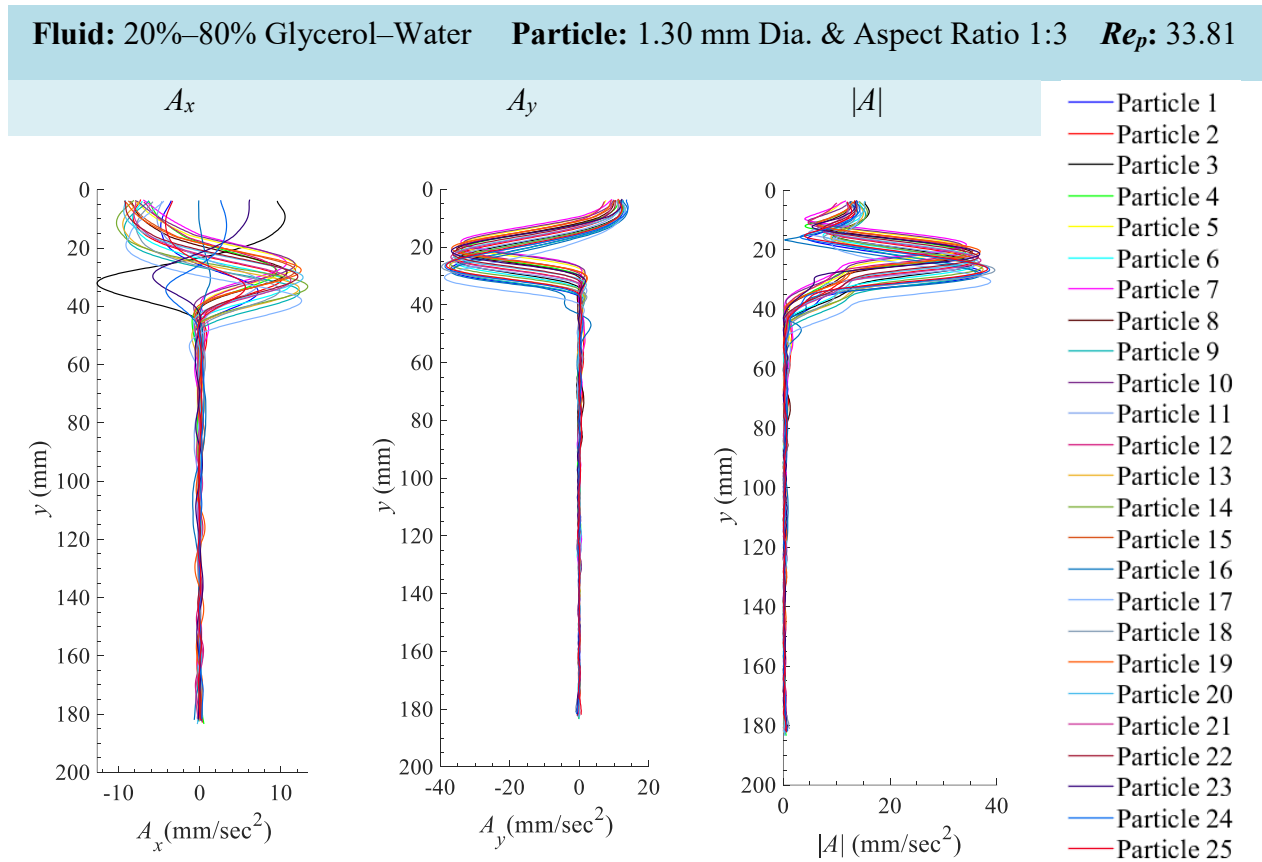


Figure 107 Particle acceleration in the x -direction A_x , y -direction A_y , and the magnitude $\sqrt{A_x^2 + A_y^2}$ of the particle acceleration $|A|$ for 1.30 mm Diameter Nylon Cylindrical Particles with Aspect Ratio, A.R. = 1:3 (25 particles) in 20%–80% Glycerol–Water.

8.22 Appendix 22: 1.30 mm Diameter and 1:3 Aspect Ratio ($AR = d_p/l_p$) Nylon Cylindrical Particles in 40%–60% Glycerol–Water

8.22.1 Particle Displacement, Particle Velocity and Particle Acceleration for 1.30 mm Diameter and 1:3 Aspect Ratio ($AR = d_p/l_p$) Nylon Cylindrical Particles in 40%–60% Glycerol–Water

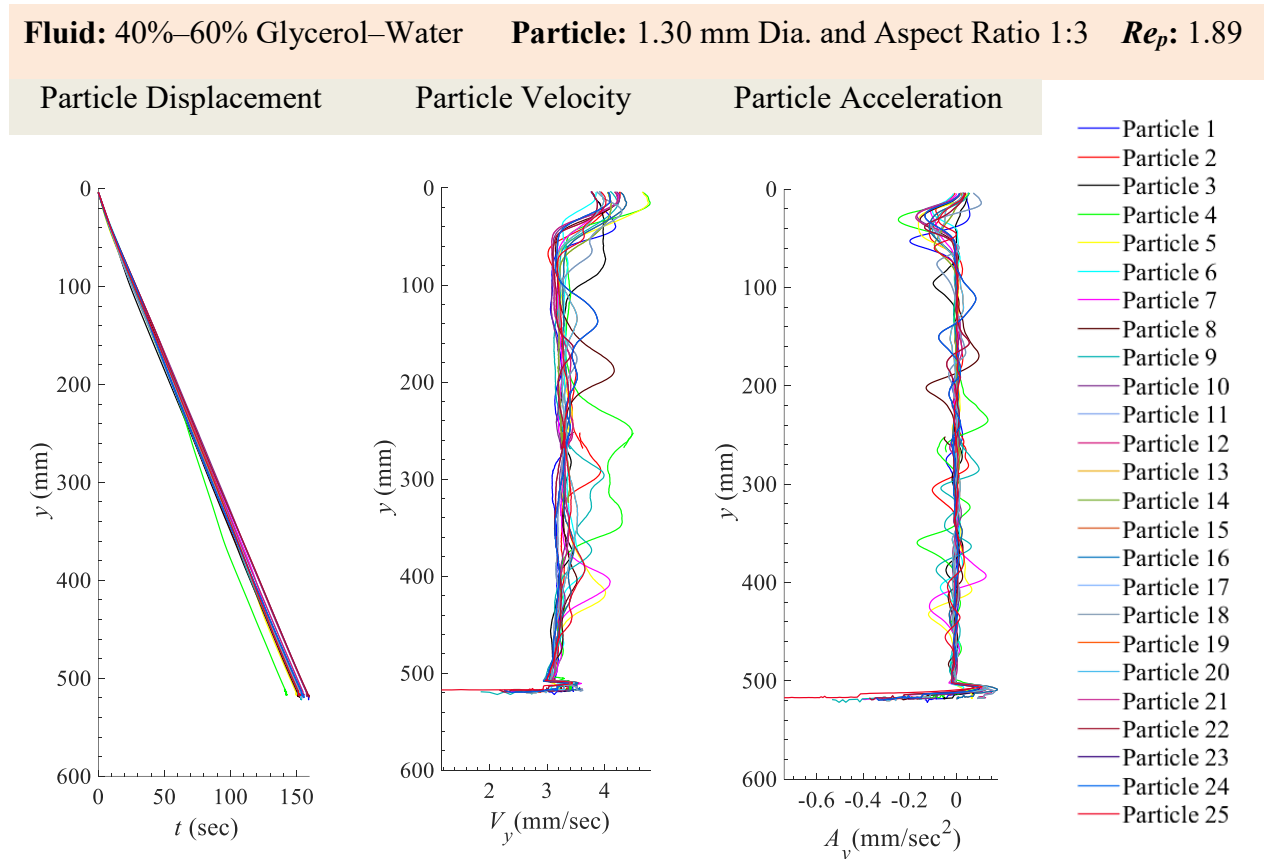


Figure 108 Particle displacement, y , velocity, V_y , and acceleration, A_y , for 1.30 mm Diameter Nylon Cylindrical Particles with Aspect Ratio, A.R. = 1:3 (25 particles) in 40%–60% Glycerol–Water. The outliers at displacement 500 mm occurred in this region there was a low light compared to the rest of the field of view. A uniform distribution of light was not achieved with the projector and kite paper as shown in Figure 8 and describe in Section 3.5.1. This affected the binarization of the particle within that region and thereby a slight shift in the location of the centroid of the particle from the image processing scheme.

8.22.2 x -Velocity (V_x), y -Velocity (V_y) and Magnitude of Velocity ($|V|$) for 1.30 mm Diameter and 1:3 Aspect Ratio ($AR = d_p/l_p$) Nylon Cylindrical Particles in 40%–60% Glycerol–Water

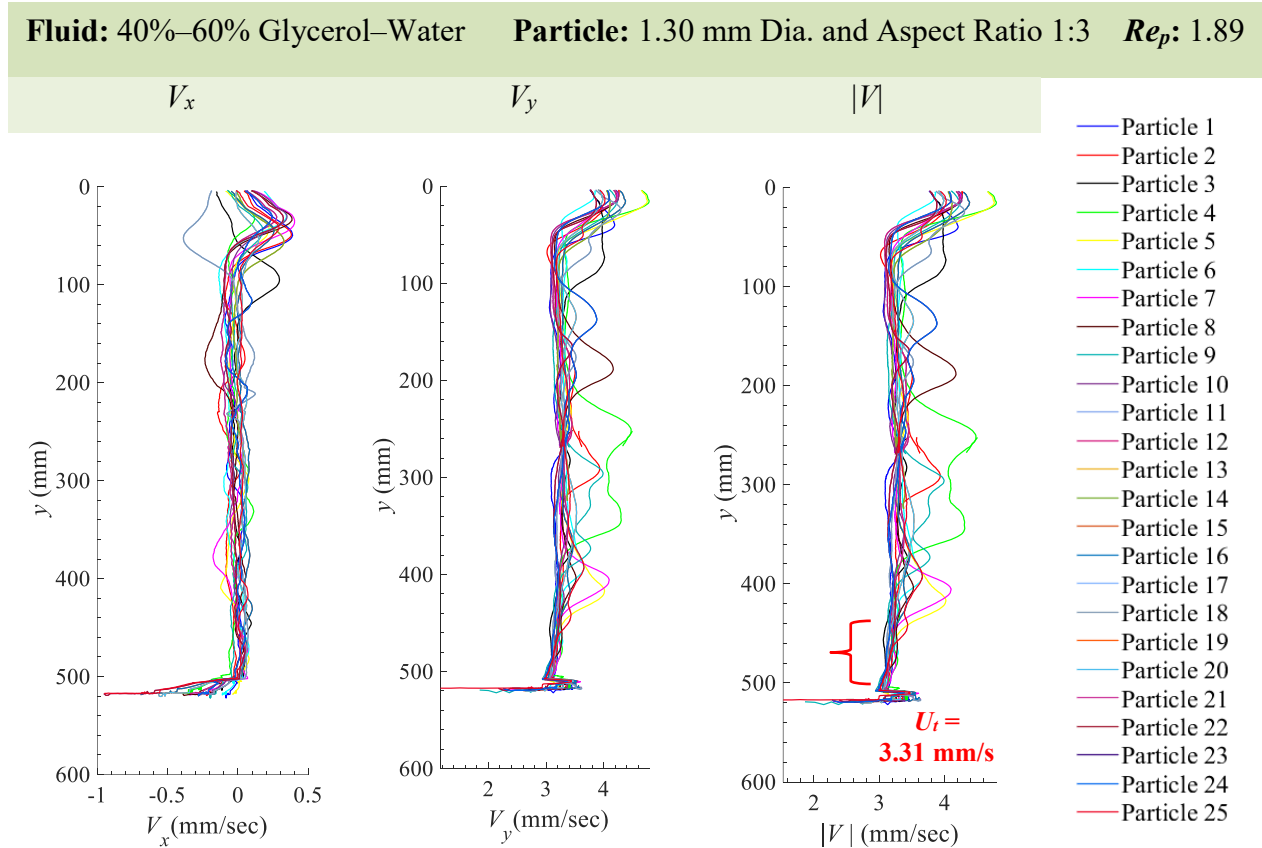


Figure 109 Particle velocity in the x -direction V_x , y -direction V_y , and the magnitude $\sqrt{V_x^2 + V_y^2}$ of the particle velocity $|V|$ for 1.30 mm Diameter Nylon Cylindrical Particles with Aspect Ratio, A.R. = 1:3 (25 particles) in 40%–60% Glycerol–Water. The average terminal settling velocity, U_t is 3.31 mm/s. The outliers at displacement 500 mm occurred in this region there was a low light compared to the rest of the field of view. A uniform distribution of light was not achieved with the projector and kite paper as shown in Figure 8 and describe in Section 3.5.1. This affected the binarization of the particle within that region and thereby a slight shift in the location of the centroid of the particle from the image processing scheme.

8.22.3 x -Acceleration (A_x), y -Acceleration (A_y) and Magnitude of Acceleration ($|A|$) for 1.30 mm Diameter and 1:3 Aspect Ratio ($AR = d_p/l_p$) Nylon Cylindrical Particles in 40%–60% Glycerol–Water

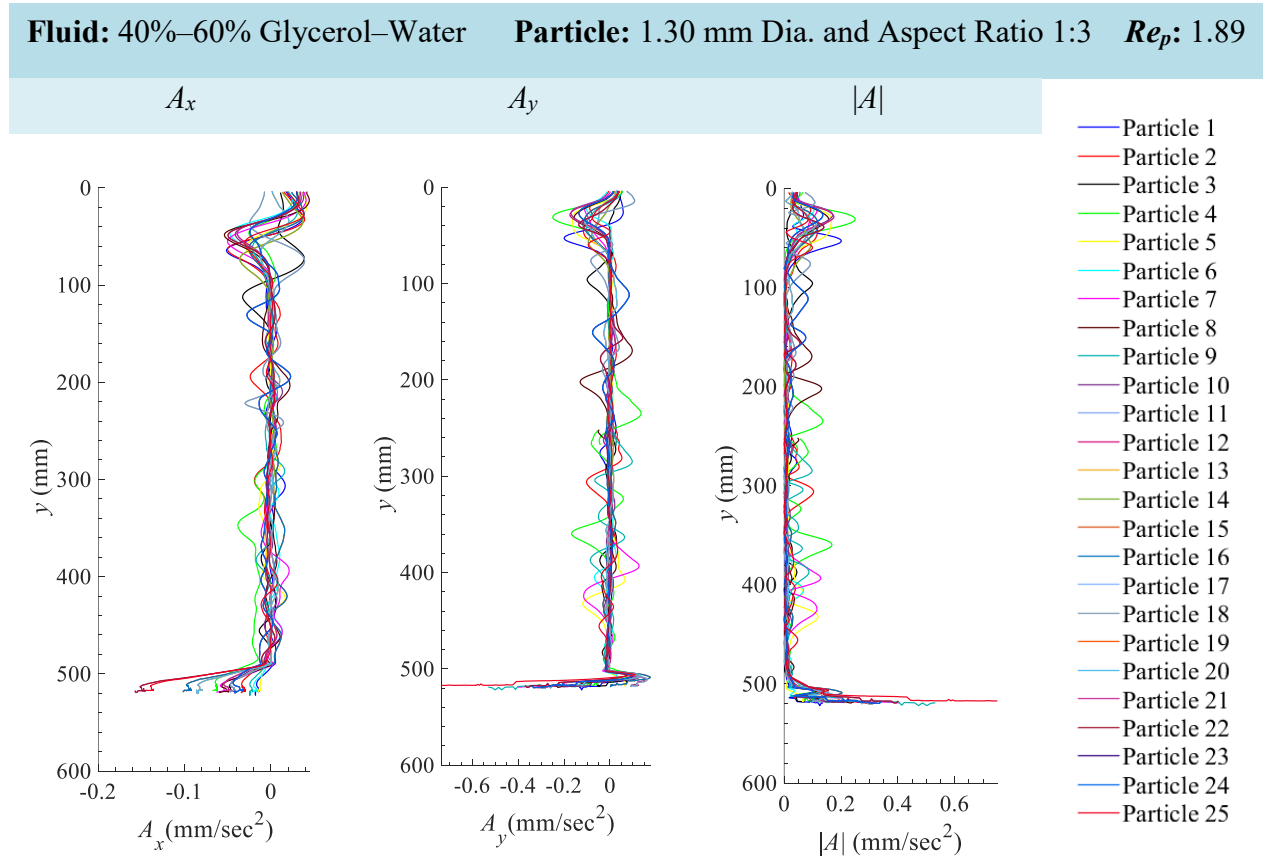


Figure 110 Particle acceleration in the x -direction A_x , y -direction A_y , and the magnitude $\sqrt{(A_x^2 + A_y^2)}$ of the particle acceleration $|A|$ for 1.30 mm Diameter Nylon Cylindrical Particles with Aspect Ratio, A.R. = 1:3 (25 particles) in 40%–60% Glycerol–Water. The outliers at displacement 500 mm occurred in this region there was a low light compared to the rest of the field of view. A uniform distribution of light was not achieved with the projector and kite paper as shown in Figure 8 and describe in Section 3.5.1. This affected the binarization of the particle within that region and thereby a slight shift in the location of the centroid of the particle from the image processing scheme.

8.23 Appendix 23: 1.30 mm Diameter and 1:3 Aspect Ratio ($AR = d_p/l_p$) Nylon Cylindrical Particles in Canola Oil

8.23.1 Particle Displacement, Particle Velocity and Particle Acceleration for 1.30 mm Diameter and 1:3 Aspect Ratio ($AR = d_p/l_p$) Nylon Cylindrical Particles in Canola Oil

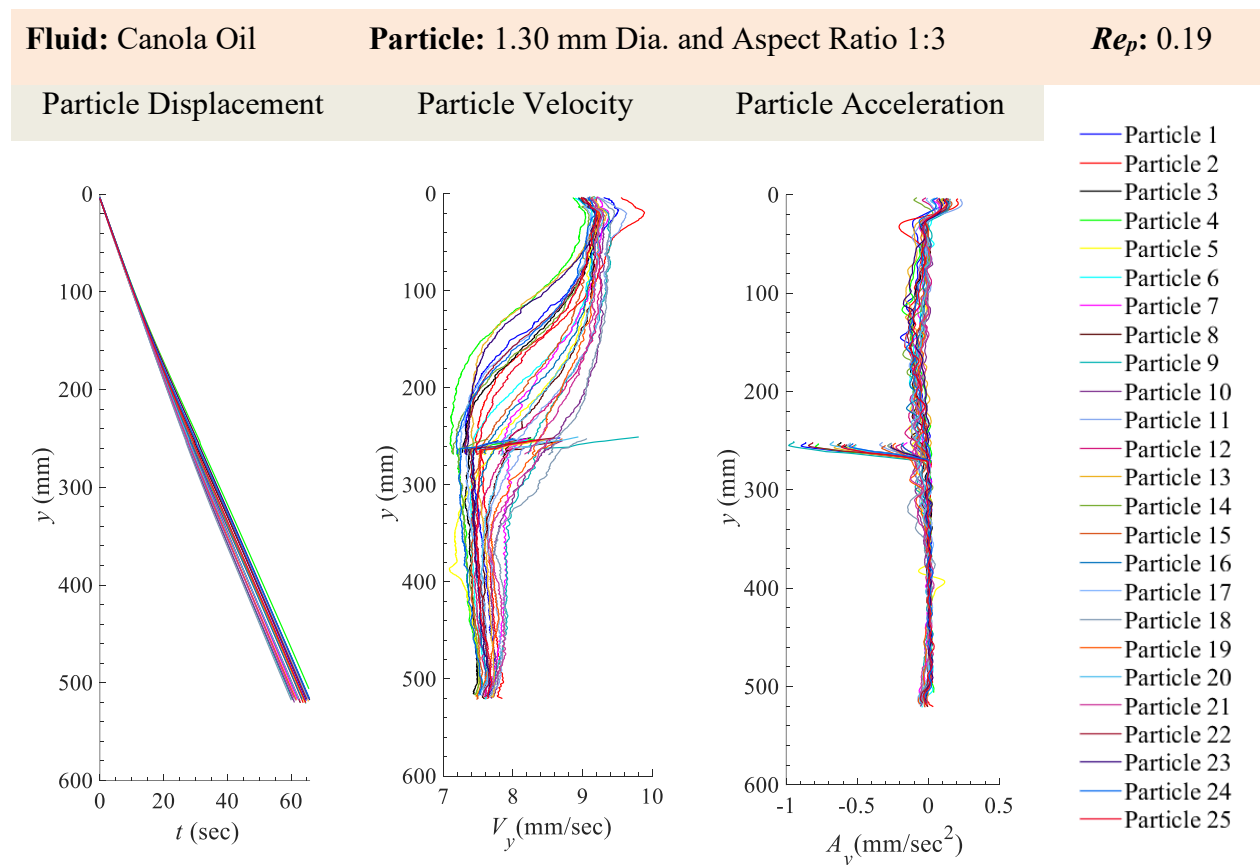


Figure 111 Particle displacement, y , velocity, V_y , and acceleration, A_y , for 1.30 mm Diameter Nylon Cylindrical Particles with Aspect Ratio, A.R. = 1:3 (25 particles) in Canola Oil. The outliers at displacement 260 mm occurred within the overlap between the two cameras. In this region there was a variation in the light distribution compared to the rest of the field of view. A uniform distribution of light was not achieved with the projector and kite paper as shown in Figure 8 and describe in Section 3.5.1. This affected the binarization of the particle within that region and thereby a slight shift in the location of the centroid of the particle from the image processing scheme.

8.23.2 x -Velocity (V_x), y -Velocity (V_y) and Magnitude of Velocity ($|V|$) for 1.30 mm Diameter and 1:3 Aspect Ratio ($AR = d_p/l_p$) Nylon Cylindrical Particles in Canola Oil

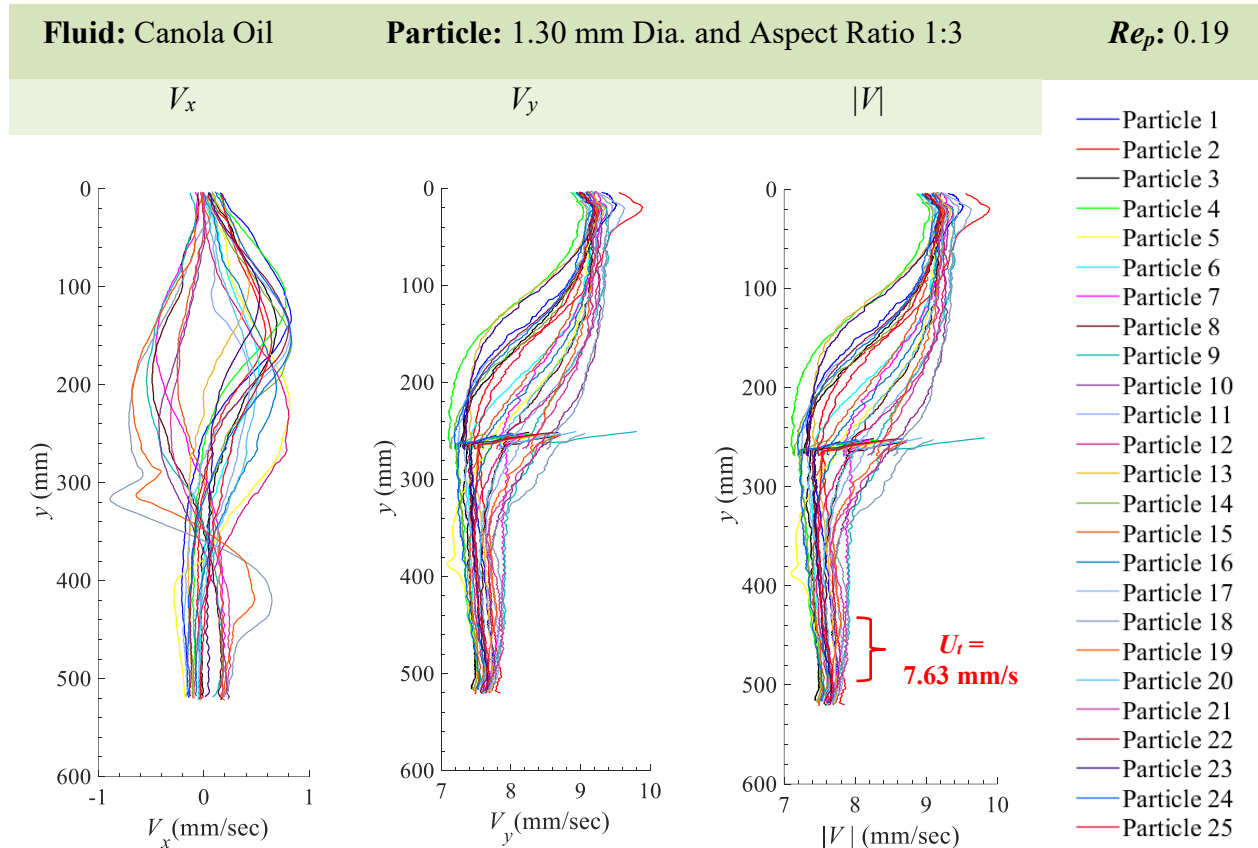


Figure 112 Particle velocity in the x -direction V_x , y -direction V_y , and the magnitude $\sqrt{V_x^2 + V_y^2}$ of the particle velocity $|V|$ for 1.30 mm Diameter Nylon Cylindrical Particles with Aspect Ratio, A.R. = 1:3 (25 particles) in Canola Oil. The magnitude of velocity deviated slightly to the left between 490 mm and 520 mm. Therefore the average was calculated between 430 mm and 475 mm in order to obtain a more accurate representation of the terminal settling velocity. The average terminal settling velocity, U_t is 7.63 mm/s. The outliers at displacement 260 mm occurred within the overlap between the two cameras. In this region there was a variation in the light distribution compared to the rest of the field of view. A uniform distribution of light was not achieved with the projector and kite paper as shown in Figure 8 and describe in Section 3.5.1. This affected the binarization of the particle within that region and thereby a slight shift in the location of the centroid of the particle from the image processing scheme.

8.23.3 x -Acceleration (A_x), y -Acceleration (A_y) and Magnitude of Acceleration ($|A|$) for 1.30 mm Diameter and 1:3 Aspect Ratio ($AR = d_p/l_p$) Nylon Cylindrical Particles in Canola Oil

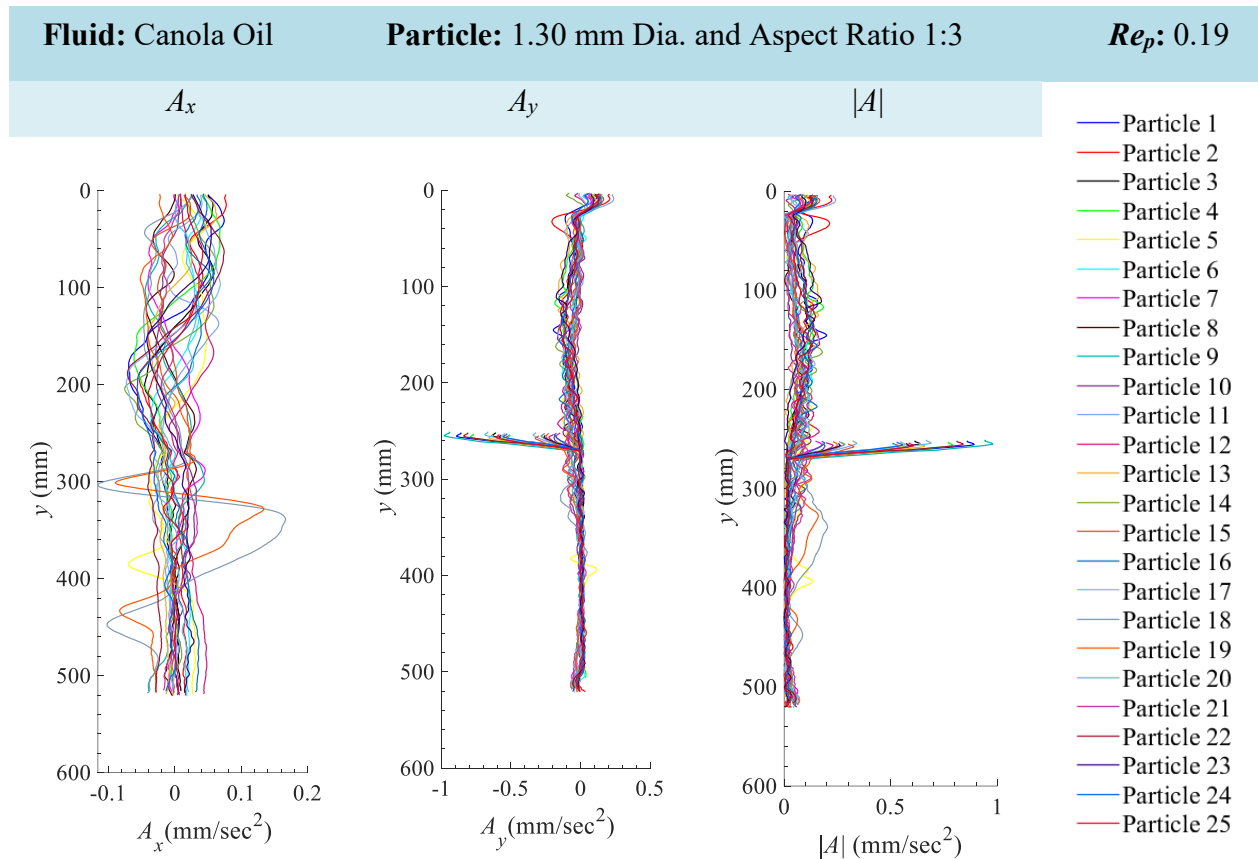


Figure 113 Particle acceleration in the x -direction A_x , y -direction A_y , and the magnitude $\sqrt{(A_x^2 + A_y^2)}$ of the particle acceleration $|A|$ for 1.30 mm Diameter Nylon Cylindrical Particles with Aspect Ratio, A.R. = 1:3 (25 particles) in Canola Oil. The outliers at displacement 260 mm occurred within the overlap between the two cameras. In this region there was a variation in the light distribution compared to the rest of the field of view. A uniform distribution of light was not achieved with the projector and kite paper as shown in Figure 8 and describe in Section 3.5.1. This affected the binarization of the particle within that region and thereby a slight shift in the location of the centroid of the particle from the image processing scheme.

8.24 Appendix 24: 1.30 mm Diameter and 1:5 Aspect Ratio ($AR = d_p/l_p$) Nylon Cylindrical Particles in Water

8.24.1 Particle Displacement, Particle Velocity and Particle Acceleration for 1.30 mm Diameter and 1:5 Aspect Ratio ($AR = d_p/l_p$) Nylon Cylindrical Particles in Water

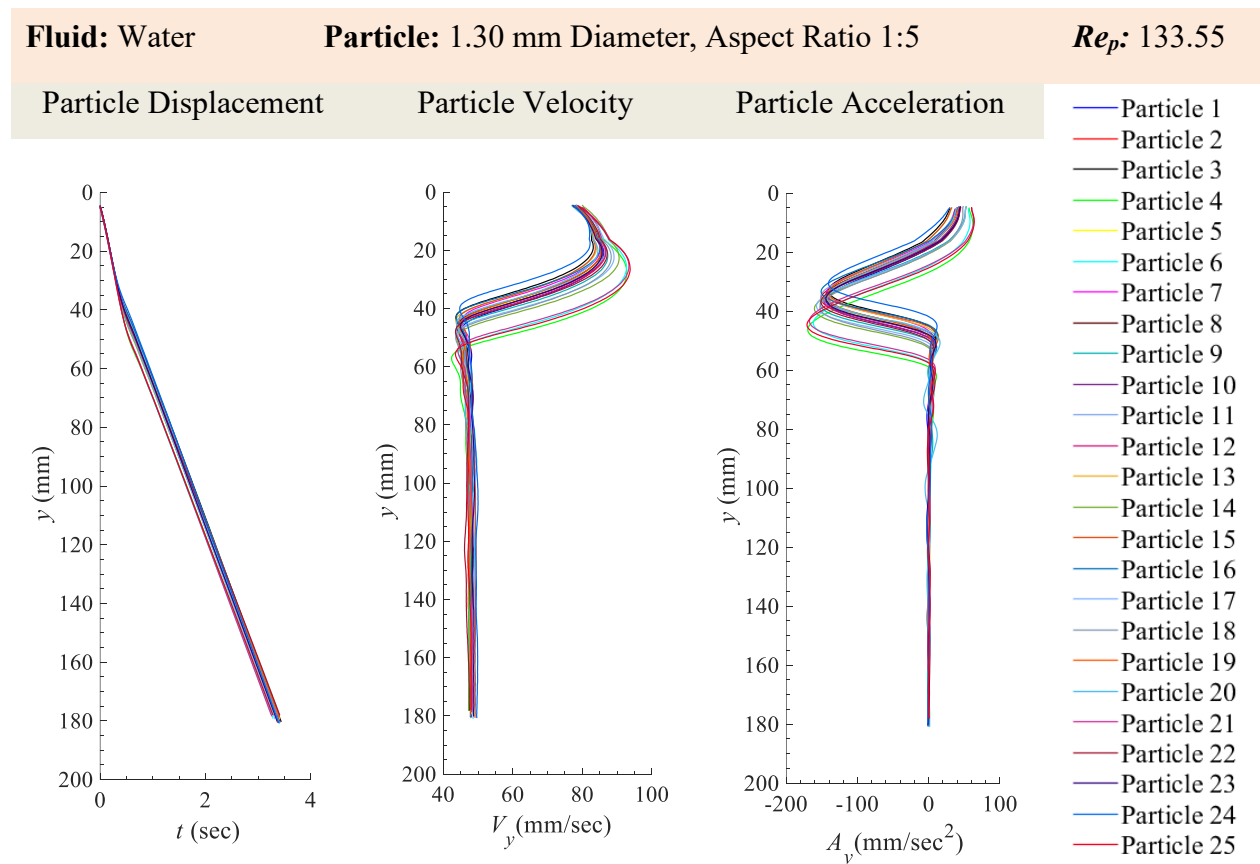


Figure 114 Particle displacement, y , velocity, V_y , and acceleration, A_y , for 1.30 mm Diameter Nylon Cylindrical Particles with Aspect Ratio, A.R. = 1:5 (25 particles) in Water.

8.24.2 x -Velocity (V_x), y -Velocity (V_y) and Magnitude of Velocity ($|V|$) for 1.30 mm Diameter and 1:5 Aspect Ratio ($AR = d_p/l_p$) Nylon Cylindrical Particles in Water

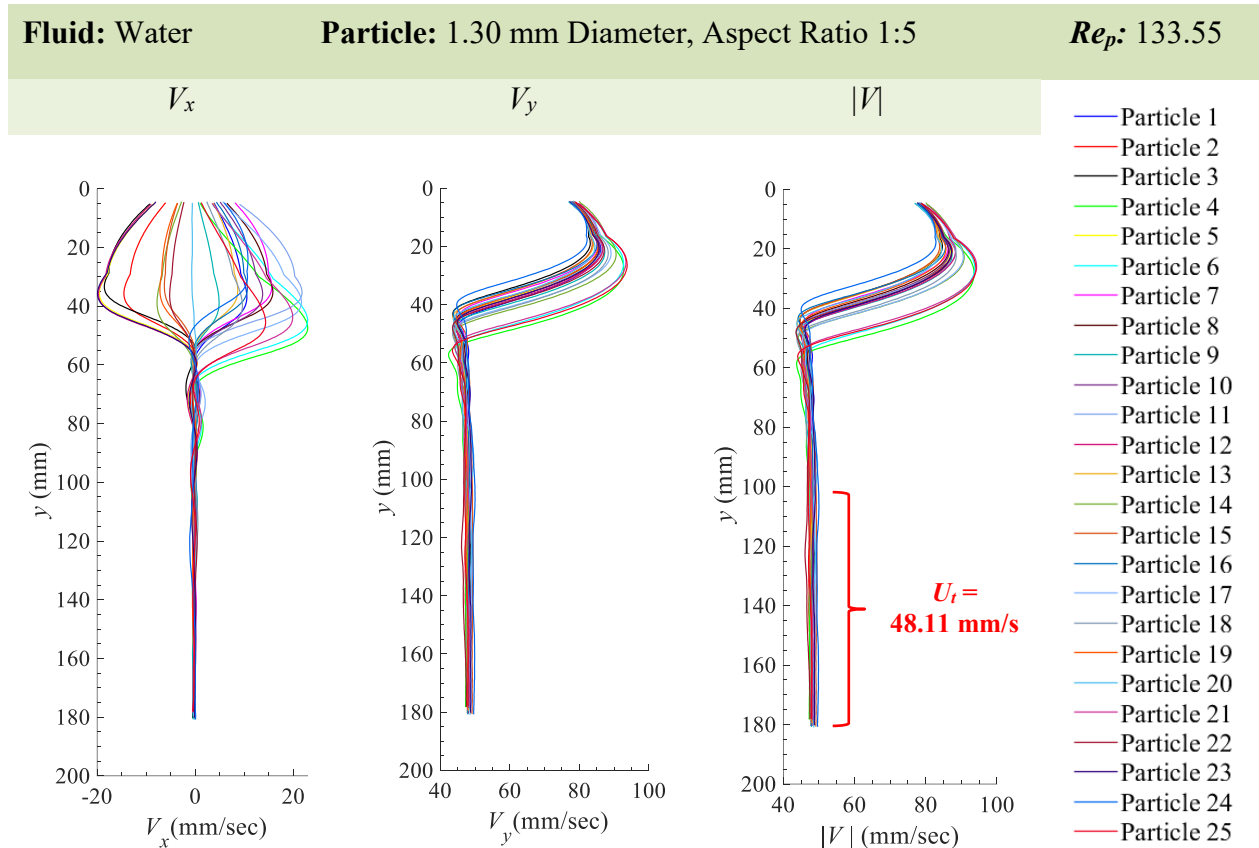


Figure 115 Particle velocity in the x -direction V_x , y -direction V_y , and the magnitude $\sqrt{V_x^2 + V_y^2}$ of the particle velocity $|V|$ for 1.30 mm Diameter Nylon Cylindrical Particles with Aspect Ratio, A.R. = 1:5 (25 particles) in Water. The average terminal settling velocity, U_t is 60.41 mm/s.

8.24.3 x -Acceleration (A_x), y -Acceleration (A_y) and Magnitude of Acceleration ($|A|$) for 1.30 mm Diameter and 1:5 Aspect Ratio ($AR = d_p/l_p$) Nylon Cylindrical Particles in Water

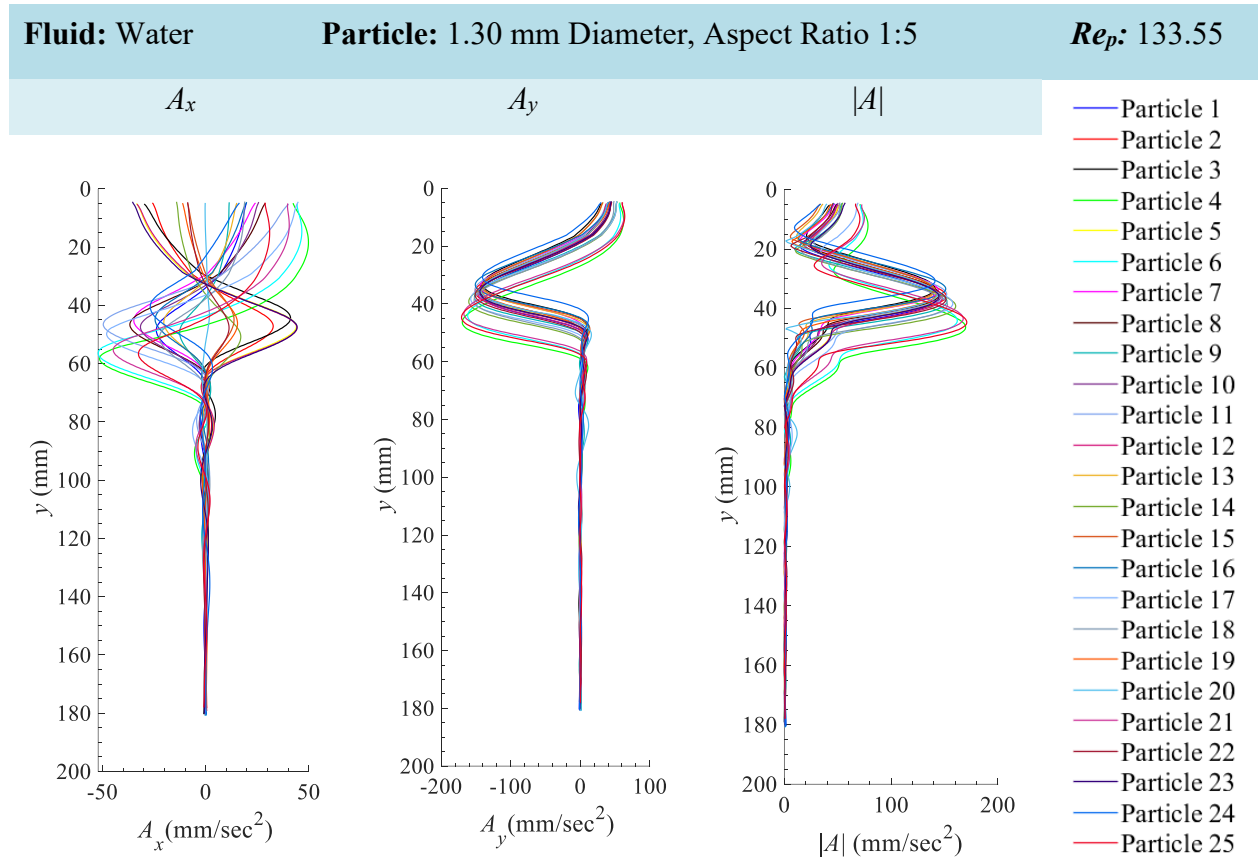


Figure 116 Particle acceleration in the x -direction A_x , y -direction A_y , and the magnitude $\sqrt{(A_x^2 + A_y^2)}$ of the particle acceleration $|A|$ for 1.30 mm Diameter Nylon Cylindrical Particles with Aspect Ratio, A.R. = 1:5 (25 particles) in Water.

8.25 Appendix 25: 1.30 mm Diameter and 1:5 Aspect Ratio ($AR = d_p/l_p$) Nylon Cylindrical Particles in 20%–80% Glycerol–Water

8.25.1 Particle Displacement, Particle Velocity and Particle Acceleration for 1.30 mm Diameter and 1:5 Aspect Ratio ($AR = d_p/l_p$) Nylon Cylindrical Particles in 20%–80% Glycerol–Water

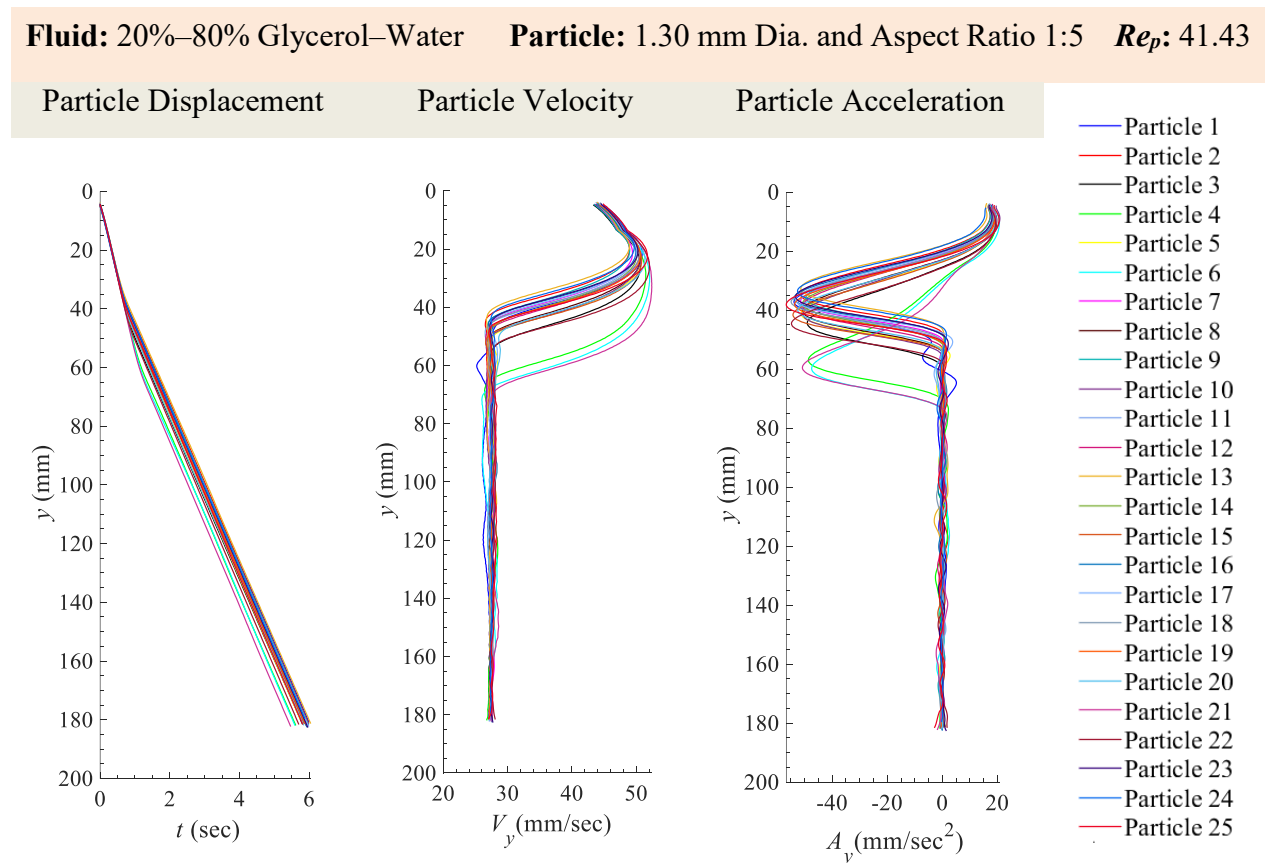


Figure 117 Particle displacement, y , velocity, V_y , and acceleration, A_y , for 1.30 mm Diameter Nylon Cylindrical Particles with Aspect Ratio, A.R. = 1:5 (25 particles) in 20%–80% Glycerol–Water.

8.25.2 x -Velocity (V_x), y -Velocity (V_y) and Magnitude of Velocity ($|V|$) for 1.30 mm Diameter and 1:5 Aspect Ratio ($AR = d_p/l_p$) Nylon Cylindrical Particles in 20%–80% Glycerol–Water

Fluid: 20%–80% Glycerol–Water **Particle:** 1.30 mm Dia. and Aspect Ratio 1:5 Re_p : 41.43

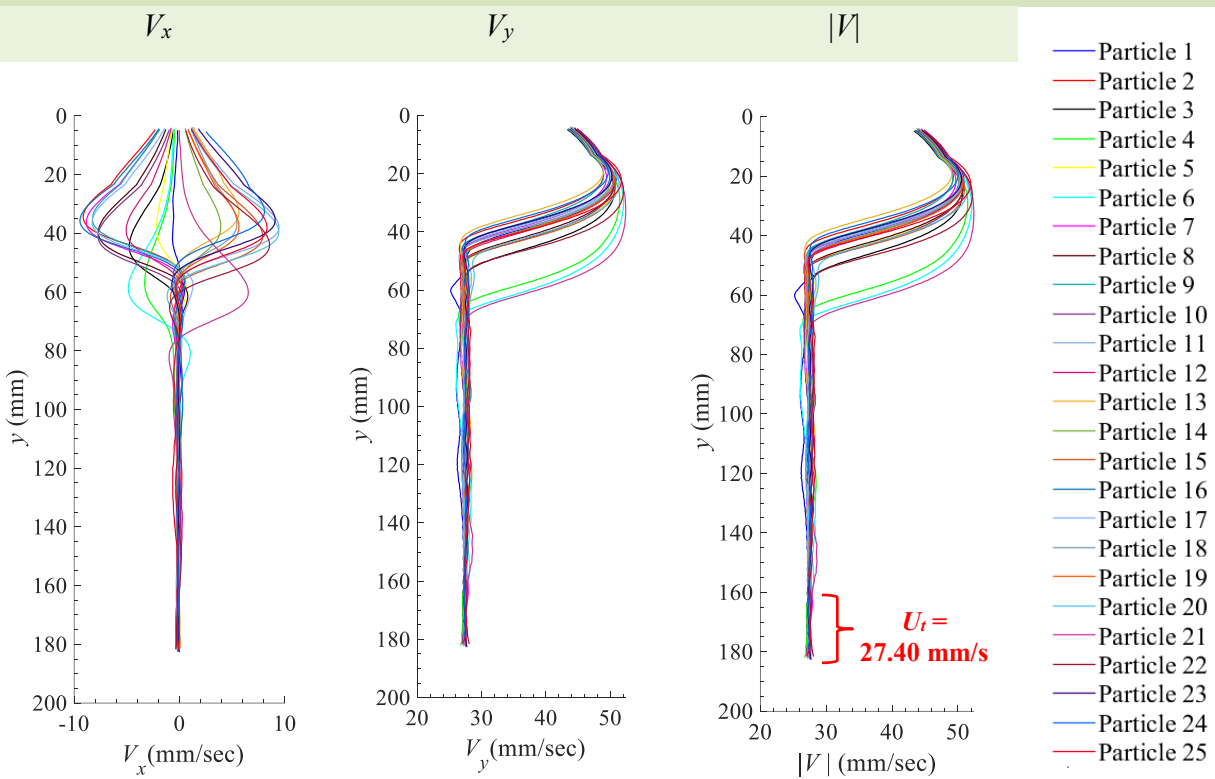


Figure 118 Particle velocity in the x -direction V_x , y -direction V_y , and the magnitude $\sqrt{V_x^2 + V_y^2}$ of the particle velocity $|V|$ for 1.30 mm Diameter Nylon Cylindrical Particles with Aspect Ratio, A.R. = 1:5 (25 particles) in 20%–80% Glycerol–Water. The average terminal settling velocity, U_t is 27.40 mm/s.

8.25.3 x -Acceleration (A_x), y -Acceleration (A_y) and Magnitude of Acceleration ($|A|$) for 1.30 mm Diameter and 1:5 Aspect Ratio ($AR = d_p/l_p$) Nylon Cylindrical Particles in 20%–80% Glycerol–Water

Fluid: 20%–80% Glycerol–Water **Particle:** 1.30 mm Dia. and Aspect Ratio 1:5 Re_p : 41.43

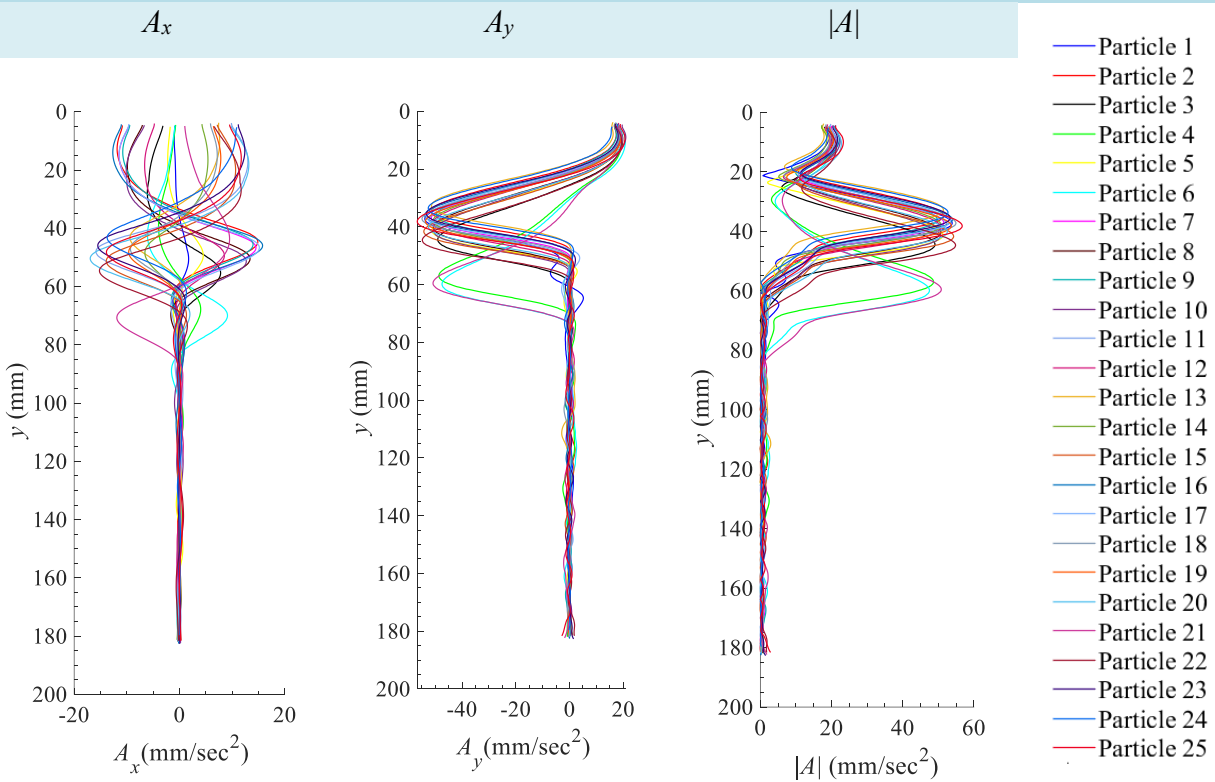


Figure 119 Particle acceleration in the x -direction A_x , y -direction A_y , and the magnitude $\sqrt{(A_x^2 + A_y^2)}$ of the particle acceleration $|A|$ for 1.30 mm Diameter Nylon Cylindrical Particles with Aspect Ratio, A.R. = 1:5 (25 particles) in 20%–80% Glycerol–Water.

8.26 Appendix 26: 1.30 mm Diameter and 1:5 Aspect Ratio ($AR = d_p/l_p$) Nylon Cylindrical Particles in 40%–60% Glycerol–Water

8.26.1 Particle Displacement, Particle Velocity and Particle Acceleration for 1.30 mm Diameter and 1:5 Aspect Ratio ($AR = d_p/l_p$) Nylon Cylindrical Particles in 40%–60% Glycerol–Water

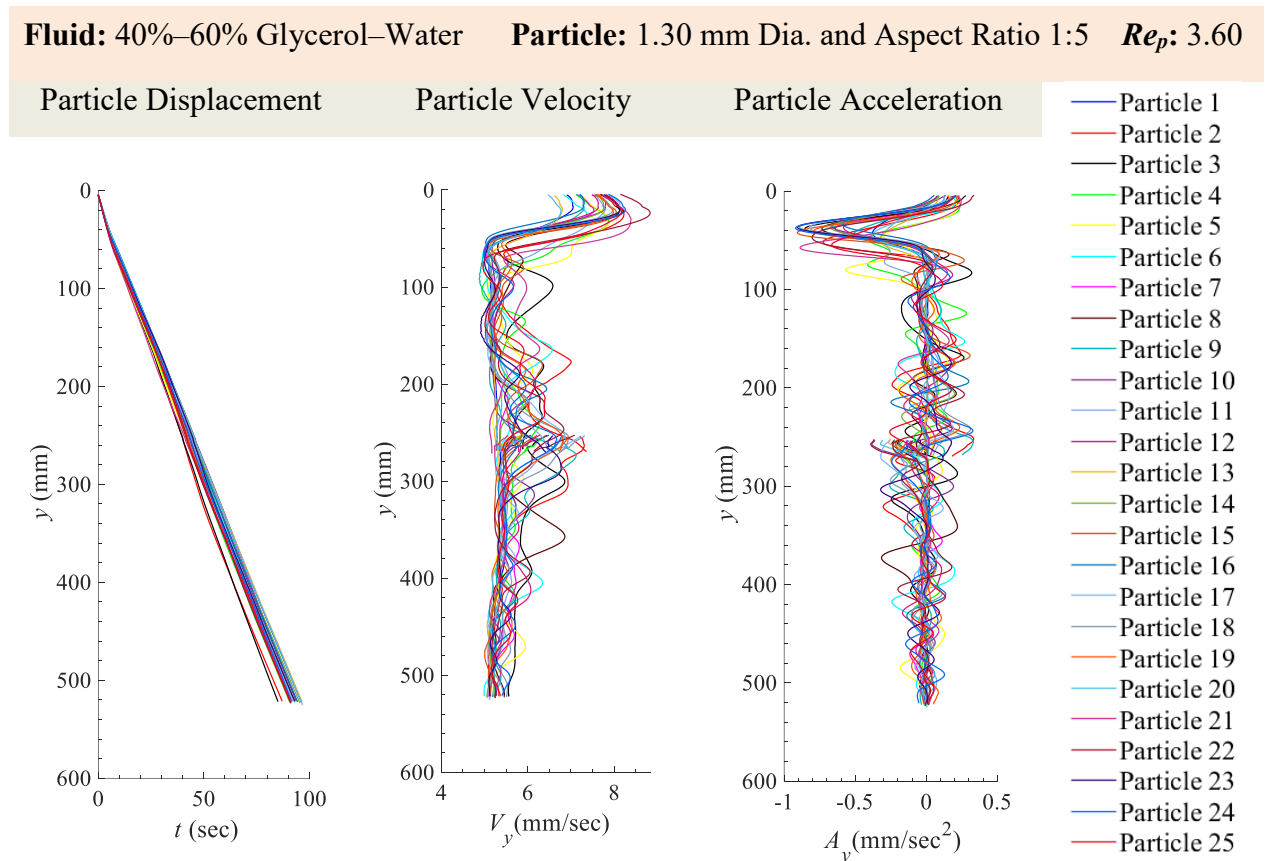


Figure 120 Particle displacement, y , velocity, V_y , and acceleration, A_y , for 1.30 mm Diameter Nylon Cylindrical Particles with Aspect Ratio, A.R. = 1:5 (25 particles) in 40%–60% Glycerol–Water. The outliers at displacement 260 mm occurred within the overlap between the two cameras. In this region there was a variation in the light distribution compared to the rest of the field of view. A uniform distribution of light was not achieved with the projector and kite paper as shown in Figure 8 and describe in Section 3.5.1. This affected the binarization of the particle within that region and thereby a slight shift in the location of the centroid of the particle from the image processing scheme.

8.26.2 x -Velocity (V_x), y -Velocity (V_y) and Magnitude of Velocity ($|V|$) for 1.30 mm Diameter and 1:5 Aspect Ratio ($AR = d_p/l_p$) Nylon Cylindrical Particles in 40%–60% Glycerol–Water

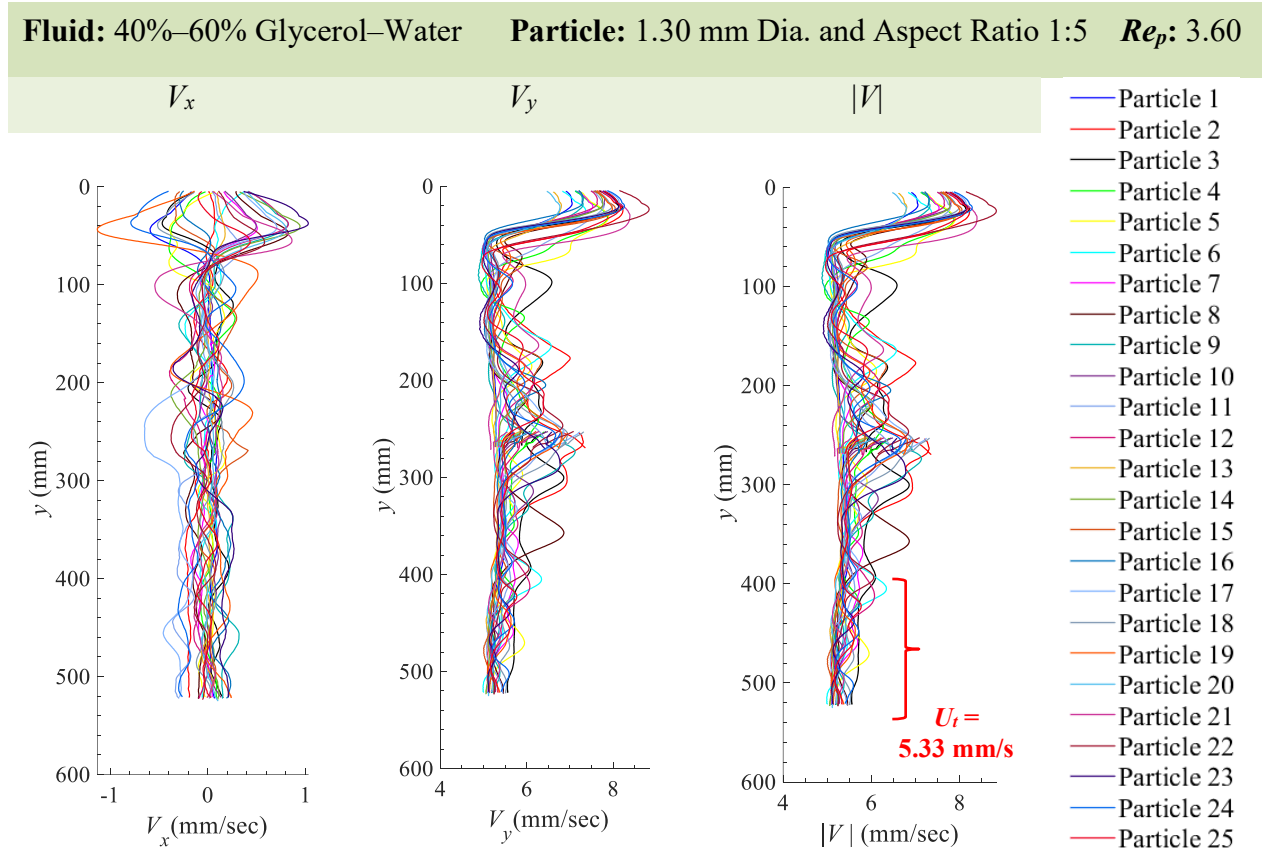


Figure 121 Particle velocity in the x -direction V_x , y -direction V_y , and the magnitude $\sqrt{V_x^2 + V_y^2}$ of the particle velocity $|V|$ for 1.30 mm Diameter Nylon Cylindrical Particles with Aspect Ratio, A.R. = 1:5 (25 particles) in 40%–60% Glycerol–Water. The average terminal settling velocity, U_t is 5.33 mm/s. The outliers at displacement 260 mm occurred within the overlap between the two cameras. In this region there was a variation in the light distribution compared to the rest of the field of view. A uniform distribution of light was not achieved with the projector and kite paper as shown in Figure 8 and describe in Section 3.5.1. This affected the binarization of the particle within that region and thereby a slight shift in the location of the centroid of the particle from the image processing scheme.

8.26.3 x -Acceleration (A_x), y -Acceleration (A_y) and Magnitude of Acceleration ($|A|$) for 1.30 mm Diameter and 1:5 Aspect Ratio ($AR = d_p/l_p$) Nylon Cylindrical Particles in 40%–60% Glycerol–Water

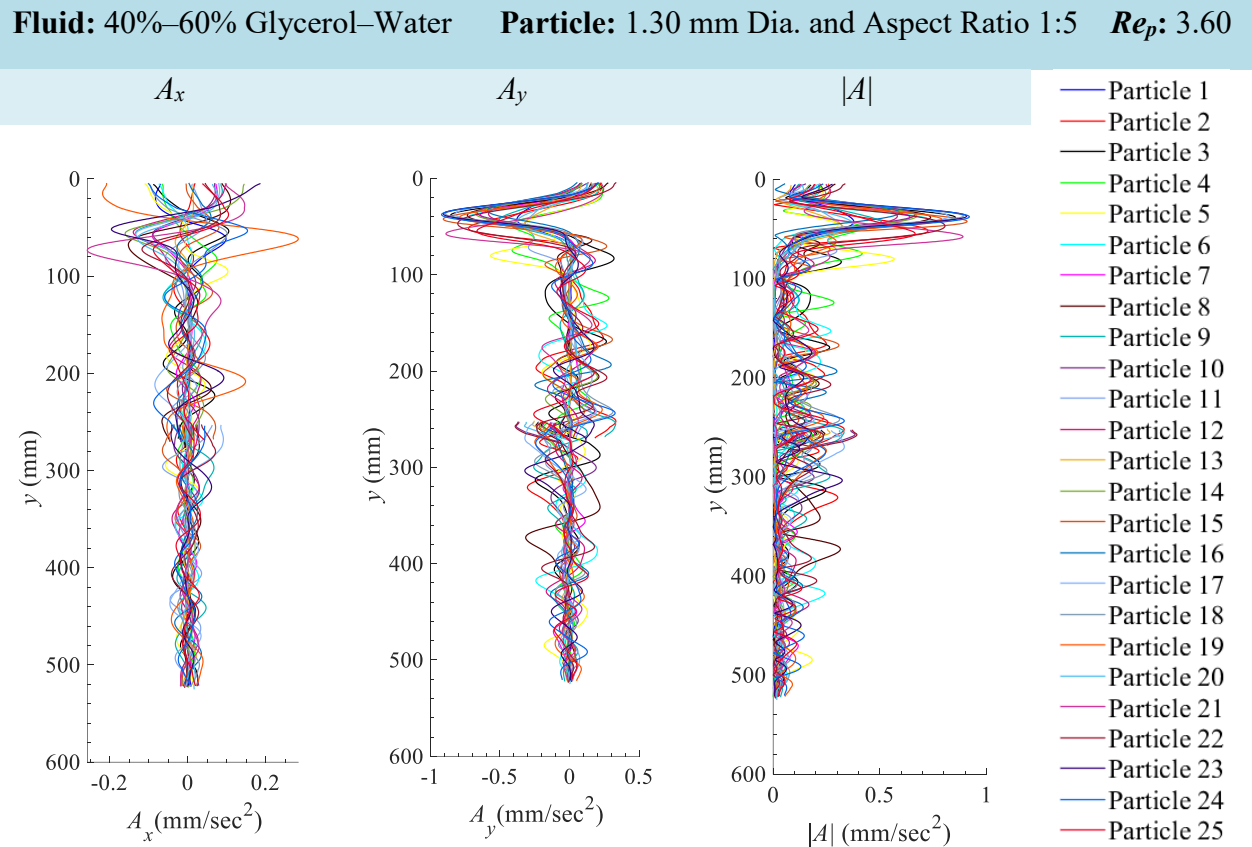


Figure 122 Particle acceleration in the x -direction A_x , y -direction A_y , and the magnitude $\sqrt{(A_x^2 + A_y^2)}$ of the particle acceleration $|A|$ for 1.30 mm Diameter Nylon Cylindrical Particles with Aspect Ratio, A.R. = 1:5 (25 particles) in 40%–60% Glycerol–Water. The outliers at displacement 260 mm occurred within the overlap between the two cameras. In this region there was a variation in the light distribution compared to the rest of the field of view. A uniform distribution of light was not achieved with the projector and kite paper as shown in Figure 8 and describe in Section 3.5.1. This affected the binarization of the particle within that region and thereby a slight shift in the location of the centroid of the particle from the image processing scheme.

8.27 Appendix 27: 1.30 mm Diameter and 1:5 Aspect Ratio ($AR = d_p/l_p$) Nylon Cylindrical Particles in Canola Oil

8.27.1 Particle Displacement, Particle Velocity and Particle Acceleration for 1.30 mm Diameter and 1:5 Aspect Ratio ($AR = d_p/l_p$) Nylon Cylindrical Particles in Canola Oil

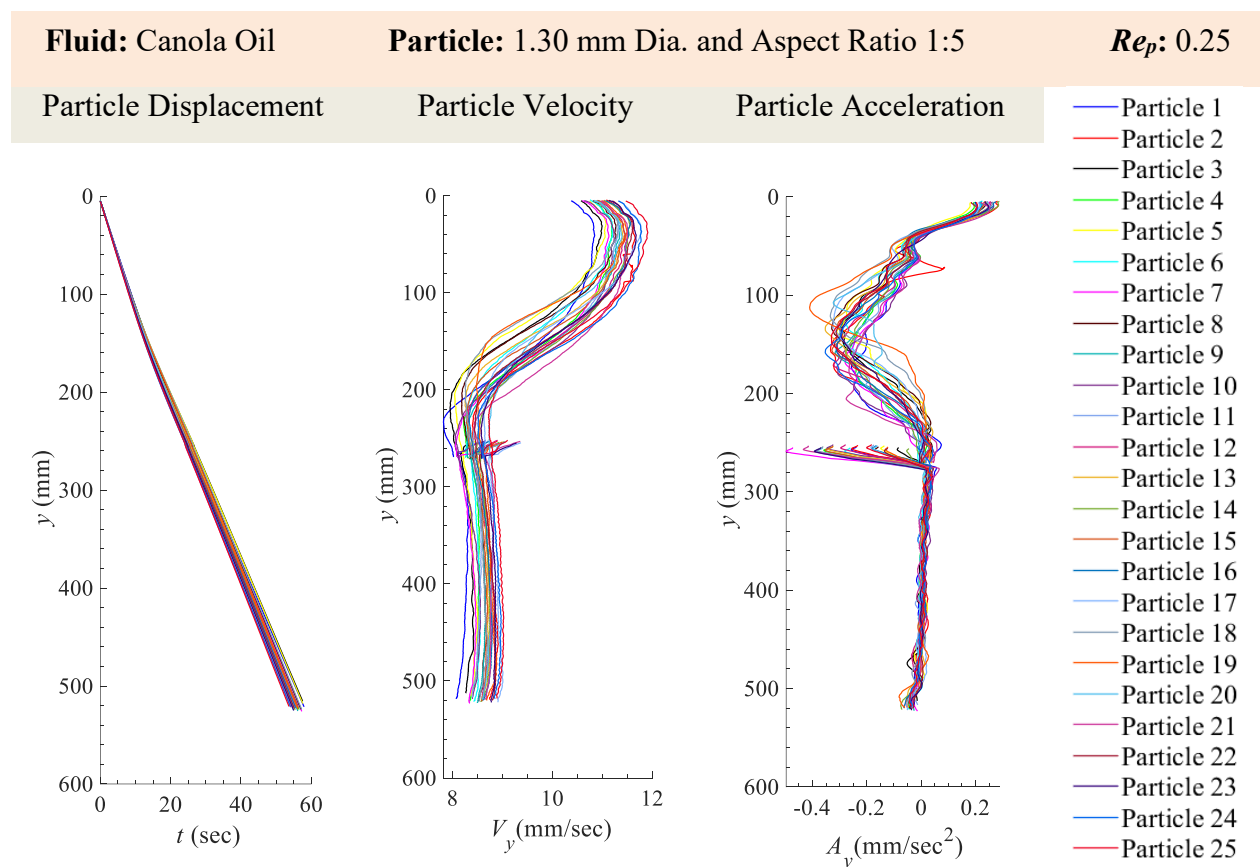


Figure 123 Particle displacement, y , velocity, V_y , and acceleration, A_y , for 1.30 mm Diameter Nylon Cylindrical Particles with Aspect Ratio, A.R. = 1:5 (25 particles) in Canola Oil. The outliers at displacement 260 mm occurred within the overlap between the two cameras. In this region there was a variation in the light distribution compared to the rest of the field of view. A uniform distribution of light was not achieved with the projector and kite paper as shown in Figure 8 and describe in Section 3.5.1. This affected the binarization of the particle within that region and thereby a slight shift in the location of the centroid of the particle from the image processing scheme.

8.27.2 x -Velocity (V_x), y -Velocity (V_y) and Magnitude of Velocity ($|V|$) for 1.30 mm Diameter and 1:5 Aspect Ratio ($AR = d_p/l_p$) Nylon Cylindrical Particles in Canola Oil

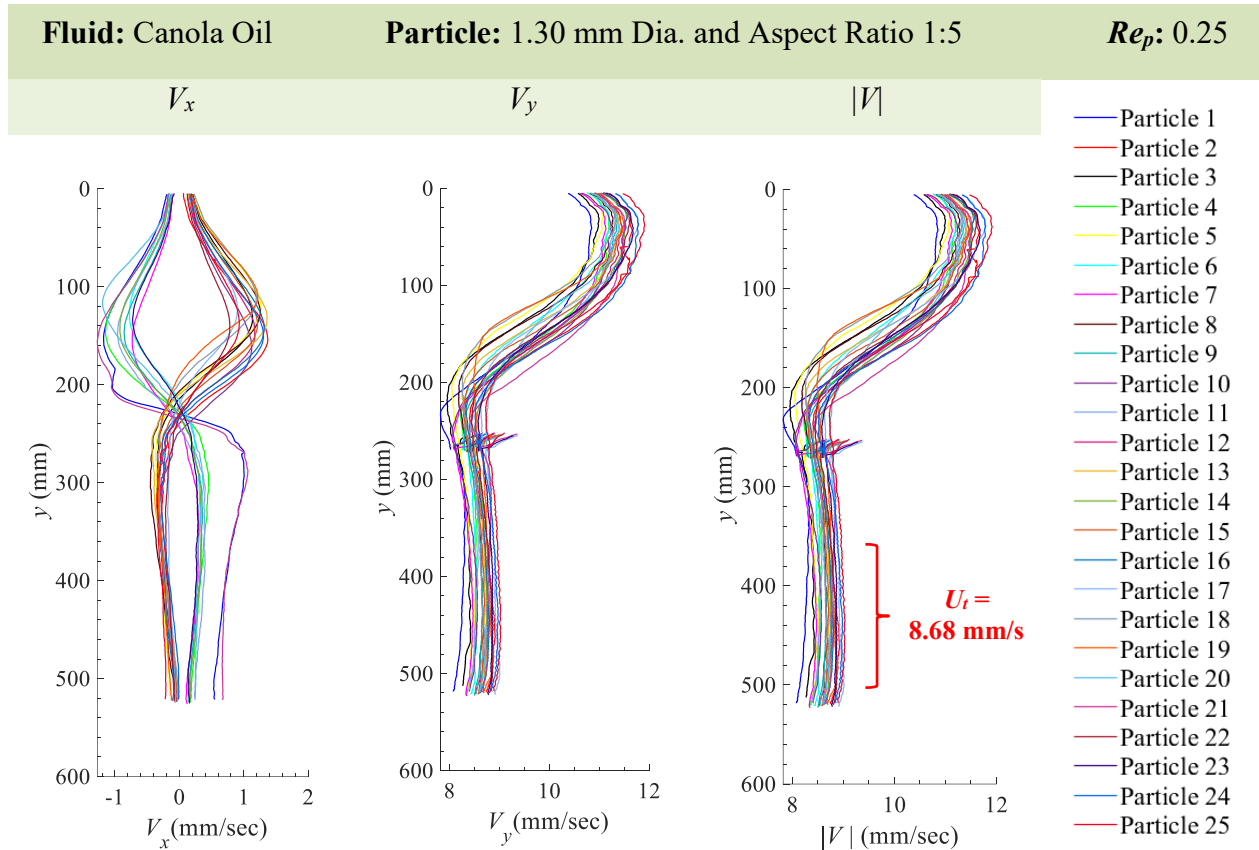


Figure 124 Particle velocity in the x -direction V_x , y -direction V_y , and the magnitude $\sqrt{V_x^2 + V_y^2}$ of the particle velocity $|V|$ for 1.30 mm Diameter Nylon Cylindrical Particles with Aspect Ratio, A.R. = 1:5 (25 particles) in Canola Oil. The magnitude of velocity deviated slightly to the left between 470 mm and 520 mm. Therefore the average was calculated between 340 mm and 460 mm in order to obtain a more accurate representation of the terminal settling velocity. The average terminal settling velocity, U_t is 8.68 mm/s. The outliers at displacement 260 mm occurred within the overlap between the two cameras. In this region there was a variation in the light distribution compared to the rest of the field of view. A uniform distribution of light was not achieved with the projector and kite paper as shown in Figure 8 and describe in Section 3.5.1. This affected the binarization of the particle within that region and thereby a slight shift in the location of the centroid of the particle from the image processing scheme.

8.27.3 x -Acceleration (A_x), y -Acceleration (A_y) and Magnitude of Acceleration ($|A|$) for 1.30 mm Diameter and 1:5 Aspect Ratio ($AR = d_p/l_p$) Nylon Cylindrical Particles in Canola Oil

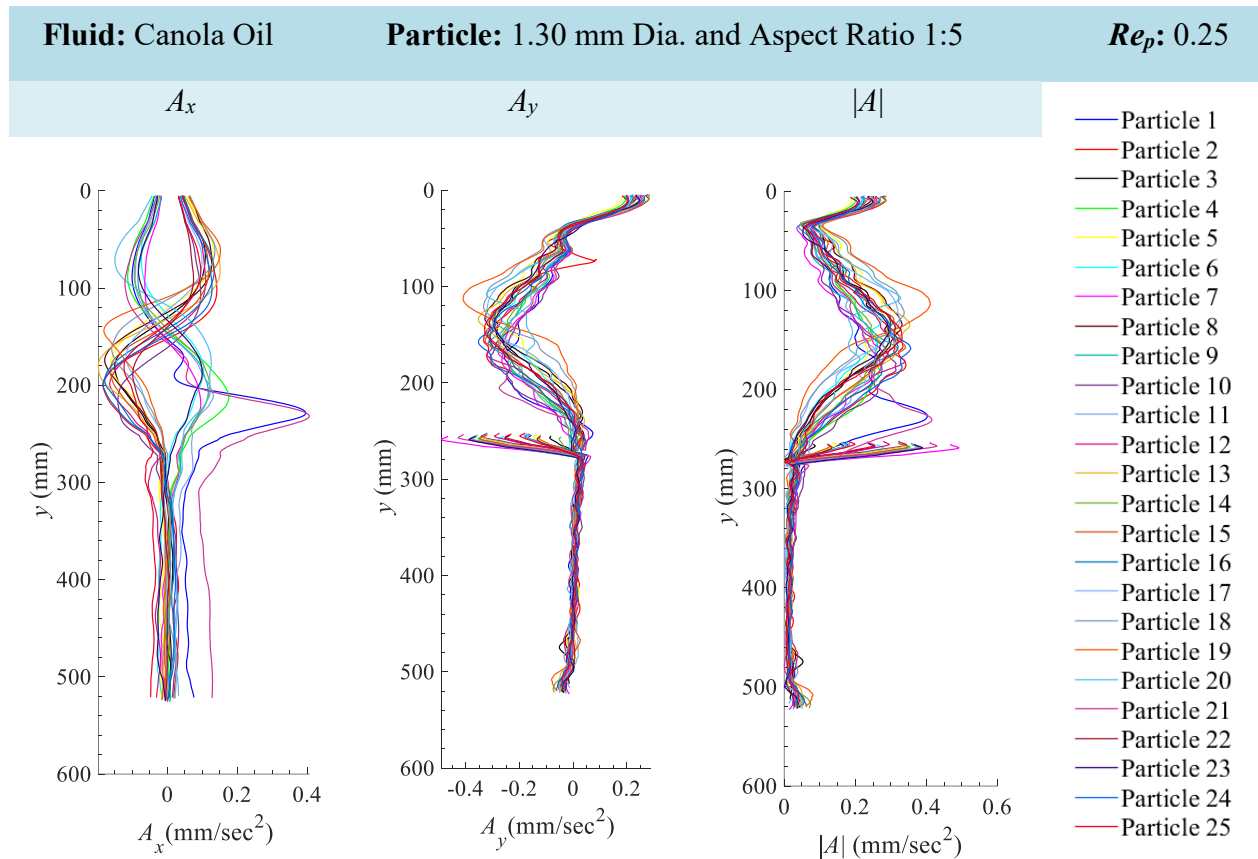


Figure 125 Particle acceleration in the x -direction A_x , y -direction A_y , and the magnitude $\sqrt{(A_x^2 + A_y^2)}$ of the particle acceleration $|A|$ for 1.30 mm Diameter Nylon Cylindrical Particles with Aspect Ratio, A.R. = 1:5 (25 particles) in Canola Oil. The outliers at displacement 260 mm occurred within the overlap between the two cameras. In this region there was a variation in the light distribution compared to the rest of the field of view. A uniform distribution of light was not achieved with the projector and kite paper as shown in Figure 8 and describe in Section 3.5.1. This affected the binarization of the particle within that region and thereby a slight shift in the location of the centroid of the particle from the image processing scheme.

8.28 Appendix 28: 1.50 mm Diameter and 1:1 Aspect Ratio ($AR = d_p/l_p$) Nylon Cylindrical Particles in Water

8.28.1 Particle Displacement, Particle Velocity and Particle Acceleration for 1.50 mm Diameter and 1:1 Aspect Ratio ($AR = d_p/l_p$) Nylon Cylindrical Particles in Water

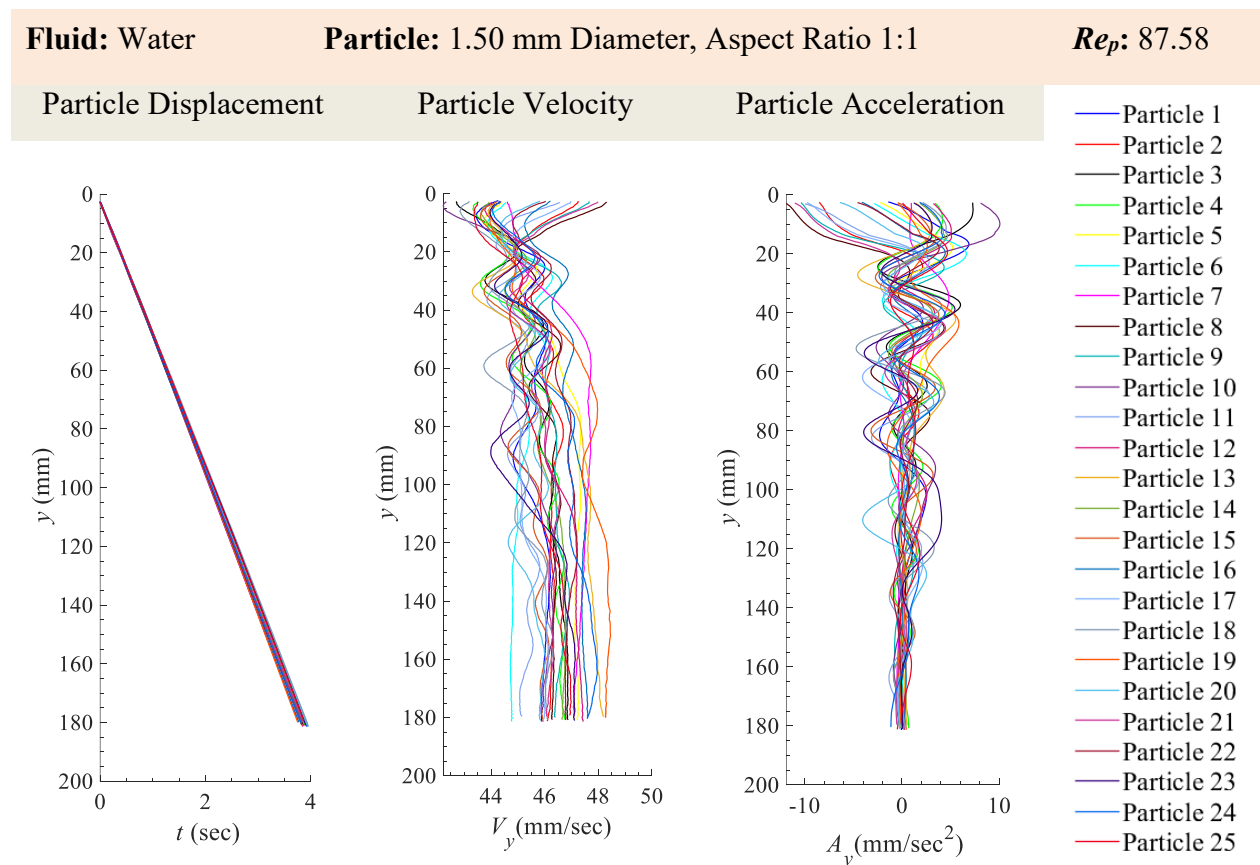


Figure 126 Particle displacement, y , velocity, V_y , and acceleration, A_y , for 1.50 mm Diameter Nylon Cylindrical Particles with Aspect Ratio, A.R. = 1:1 (25 particles) in Water.

8.28.2 x -Velocity (V_x), y -Velocity (V_y) and Magnitude of Velocity ($|V|$) for 1.50 mm Diameter and 1:1 Aspect Ratio ($AR = d_p/l_p$) Nylon Cylindrical Particles in Water

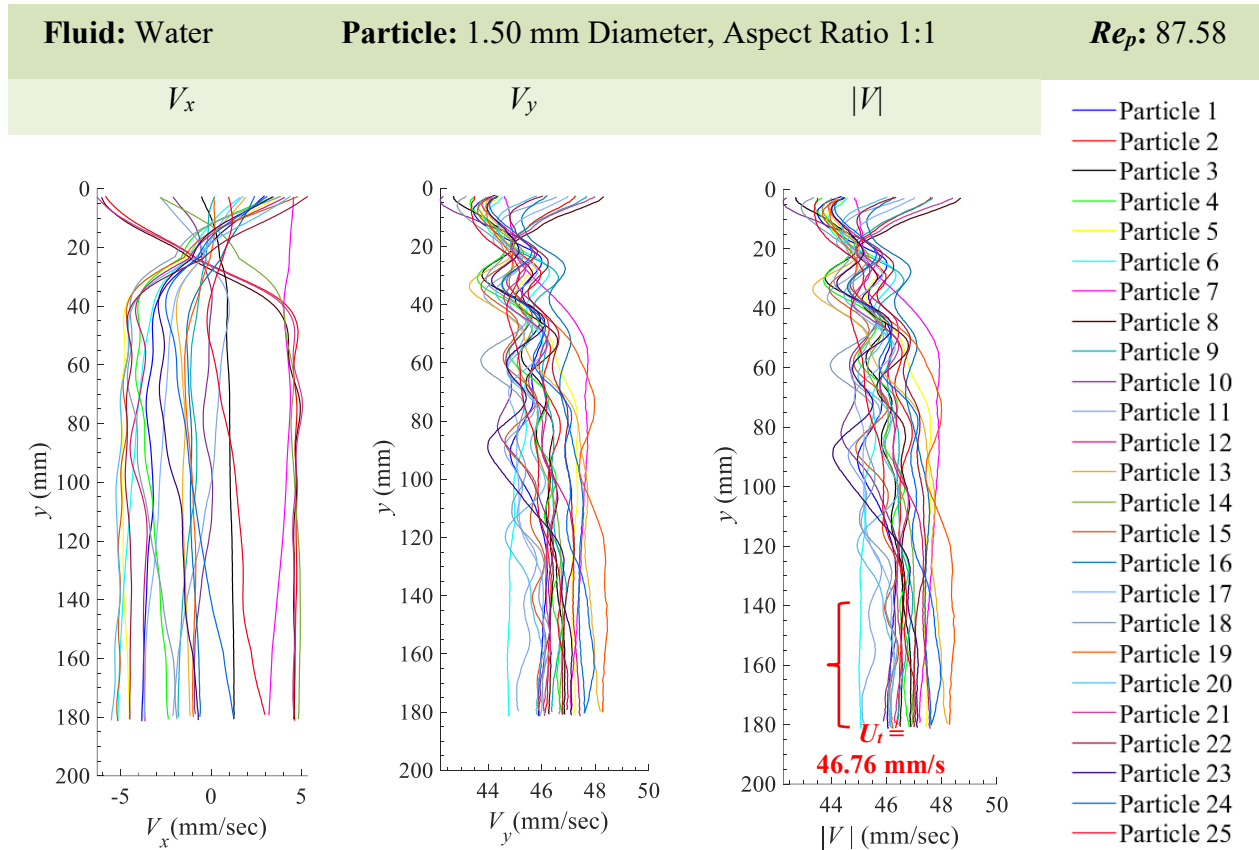


Figure 127 Particle velocity in the x -direction V_x , y -direction V_y , and the magnitude $\sqrt{V_x^2 + V_y^2}$ of the particle velocity $|V|$ for 1.50 mm Diameter Nylon Cylindrical Particles with Aspect Ratio, A.R. = 1:1 (25 particles) in Water. The average terminal settling velocity, U_t is 46.76 mm/s.

8.28.3 x -Acceleration (A_x), y -Acceleration (A_y) and Magnitude of Acceleration ($|A|$) for 1.50 mm Diameter and 1:1 Aspect Ratio ($AR = d_p/l_p$) Nylon Cylindrical Particles in Water

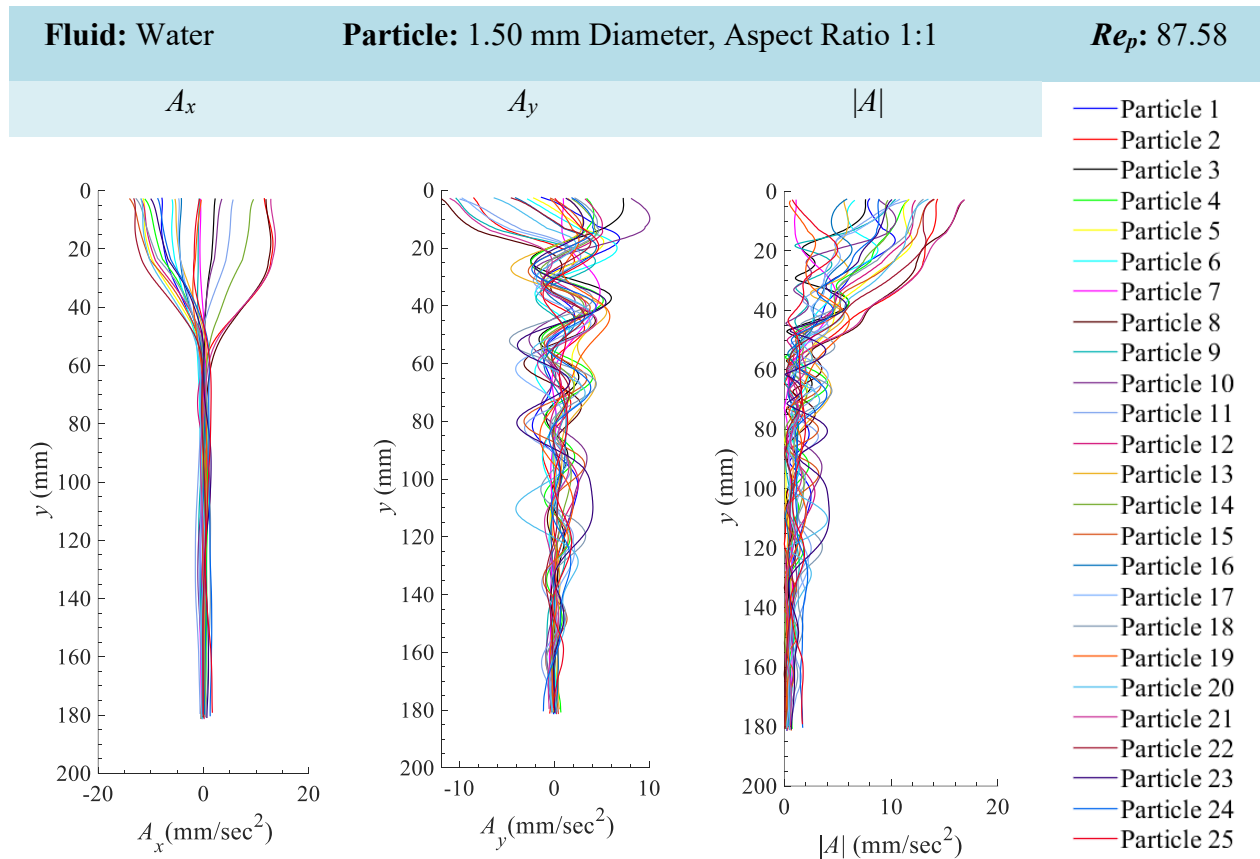


Figure 128 Particle acceleration in the x -direction A_x , y -direction A_y , and the magnitude $\sqrt{(A_x^2 + A_y^2)}$ of the particle acceleration $|A|$ for 1.50 mm Diameter Nylon Cylindrical Particles with Aspect Ratio, A.R. = 1:1 (25 particles) in Water.

8.29 Appendix 29: 1.50 mm Diameter and 1:1 Aspect Ratio ($AR = d_p/l_p$) Nylon Cylindrical Particles in 20%–80% Glycerol–Water

8.29.1 Particle Displacement, Particle Velocity and Particle Acceleration for 1.50 mm Diameter and 1:1 Aspect Ratio ($AR = d_p/l_p$) Nylon Cylindrical Particles in 20%–80% Glycerol–Water

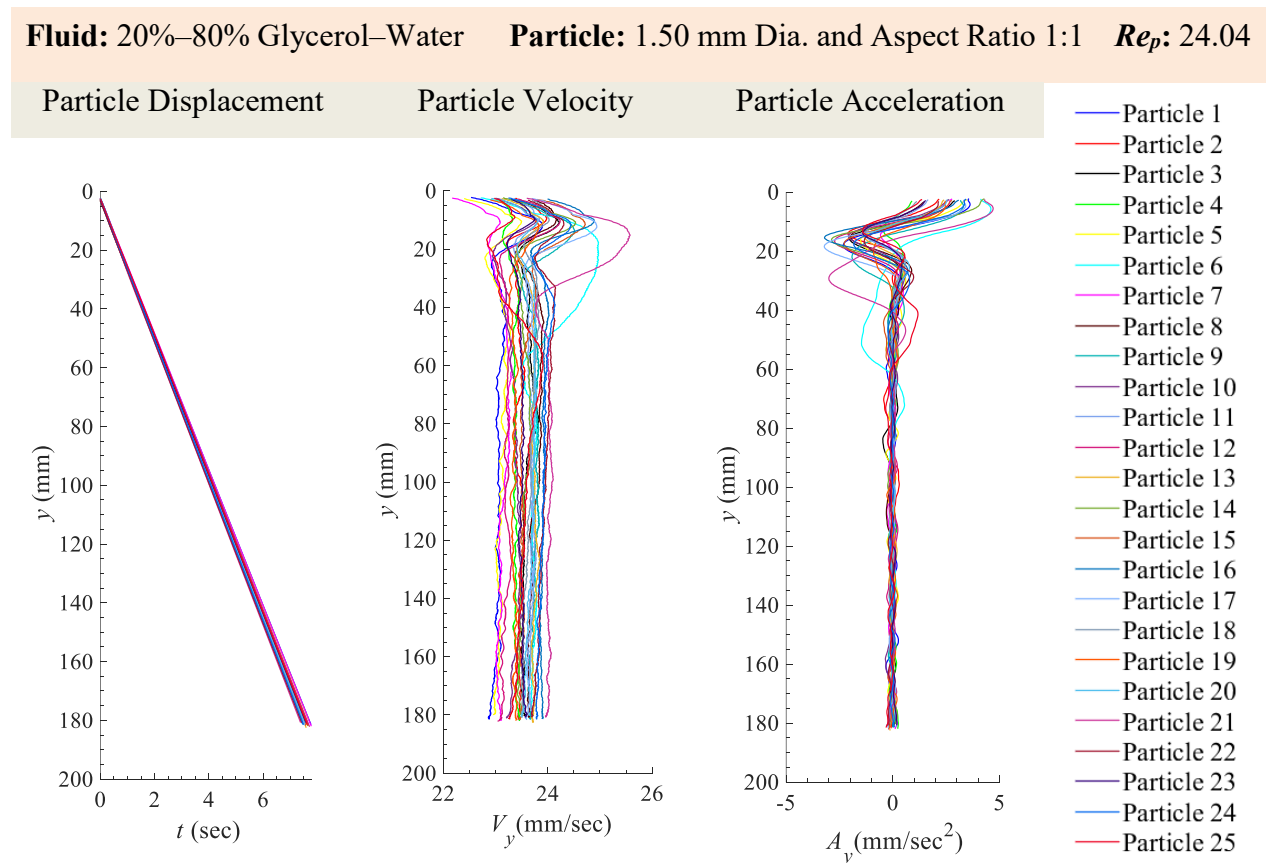


Figure 129 Particle displacement, y , velocity, V_y , and acceleration, A_y , for 1.50 mm Diameter Nylon Cylindrical Particles with Aspect Ratio, A.R. = 1:1 (25 particles) in 20%–80% Glycerol–Water.

8.29.2 x -Velocity (V_x), y -Velocity (V_y) and Magnitude of Velocity ($|V|$) for 1.50 mm Diameter and 1:1 Aspect Ratio ($AR = d_p/l_p$) Nylon Cylindrical Particles in 20%–80% Glycerol–Water

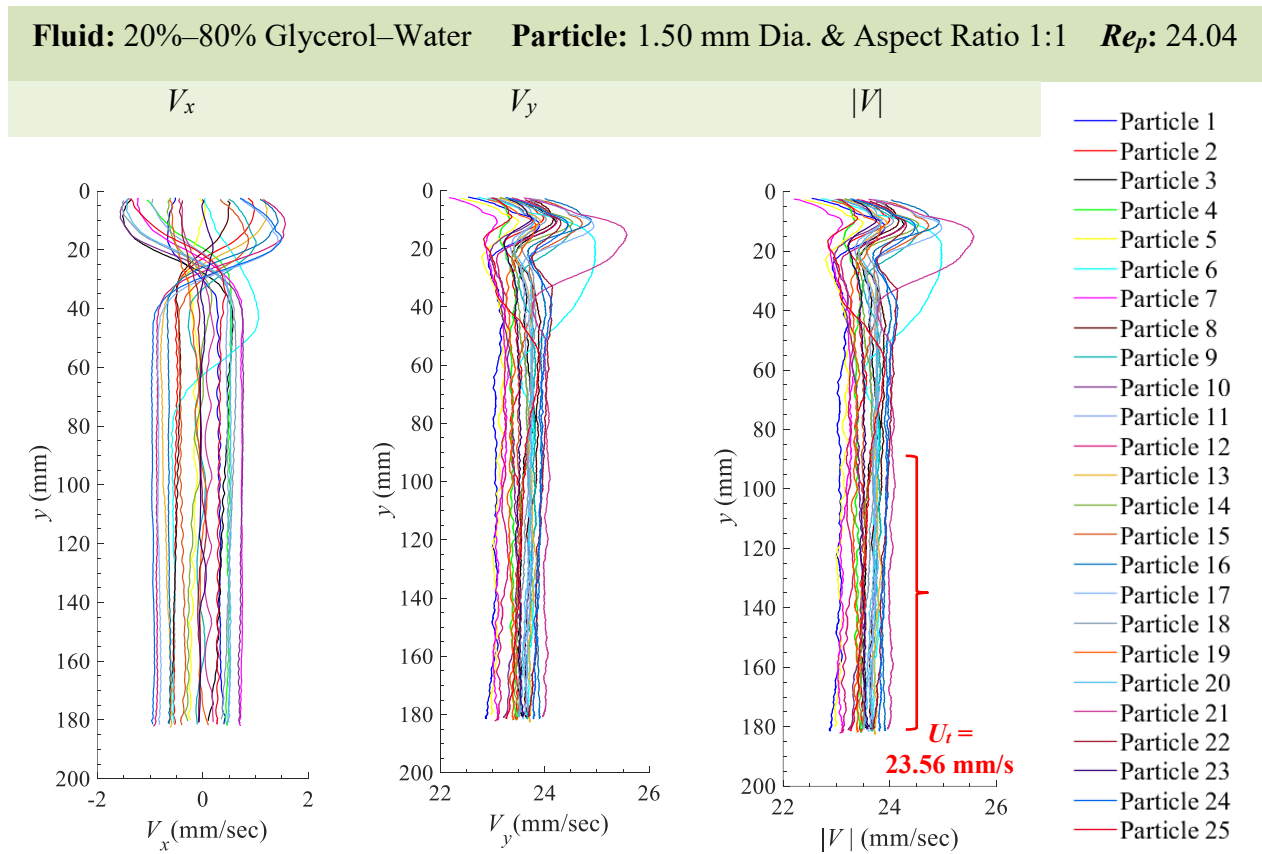


Figure 130 Particle velocity in the x -direction V_x , y -direction V_y , and the magnitude $\sqrt{V_x^2 + V_y^2}$ of the particle velocity $|V|$ for 1.50 mm Diameter Nylon Cylindrical Particles with Aspect Ratio, A.R. = 1:1 (25 particles) in 20%–80% Glycerol–Water. The average terminal settling velocity, U_t is 23.56 mm/s.

8.29.3 x -Acceleration (A_x), y -Acceleration (A_y) and Magnitude of Acceleration ($|A|$) for 1.50 mm Diameter and 1:1 Aspect Ratio ($AR = d_p/l_p$) Nylon Cylindrical Particles in 20%–80% Glycerol–Water

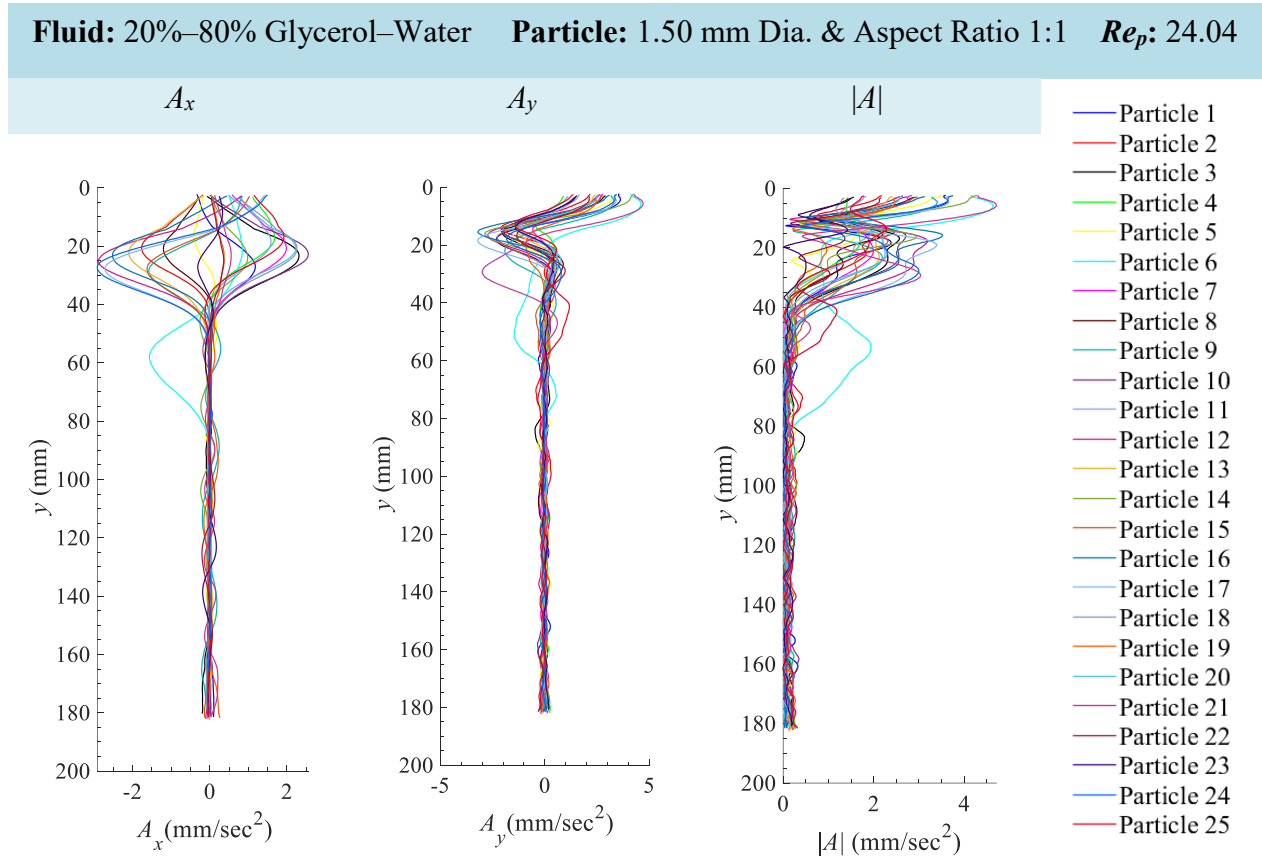


Figure 131 Particle acceleration in the x -direction A_x , y -direction A_y , and the magnitude $\sqrt{(A_x^2 + A_y^2)}$ of the particle acceleration $|A|$ for 1.50 mm Diameter Nylon Cylindrical Particles with Aspect Ratio, A.R. = 1:1 (25 particles) in 20%–80% Glycerol–Water.

8.30 Appendix 30: 1.50 mm Diameter and 1:1 Aspect Ratio ($AR = d_p/l_p$) Nylon Cylindrical Particles in 40%–60% Glycerol–Water

8.30.1 Particle Displacement, Particle Velocity and Particle Acceleration for 1.50 mm Diameter and 1:1 Aspect Ratio ($AR = d_p/l_p$) Nylon Cylindrical Particles in 40%–60% Glycerol–Water

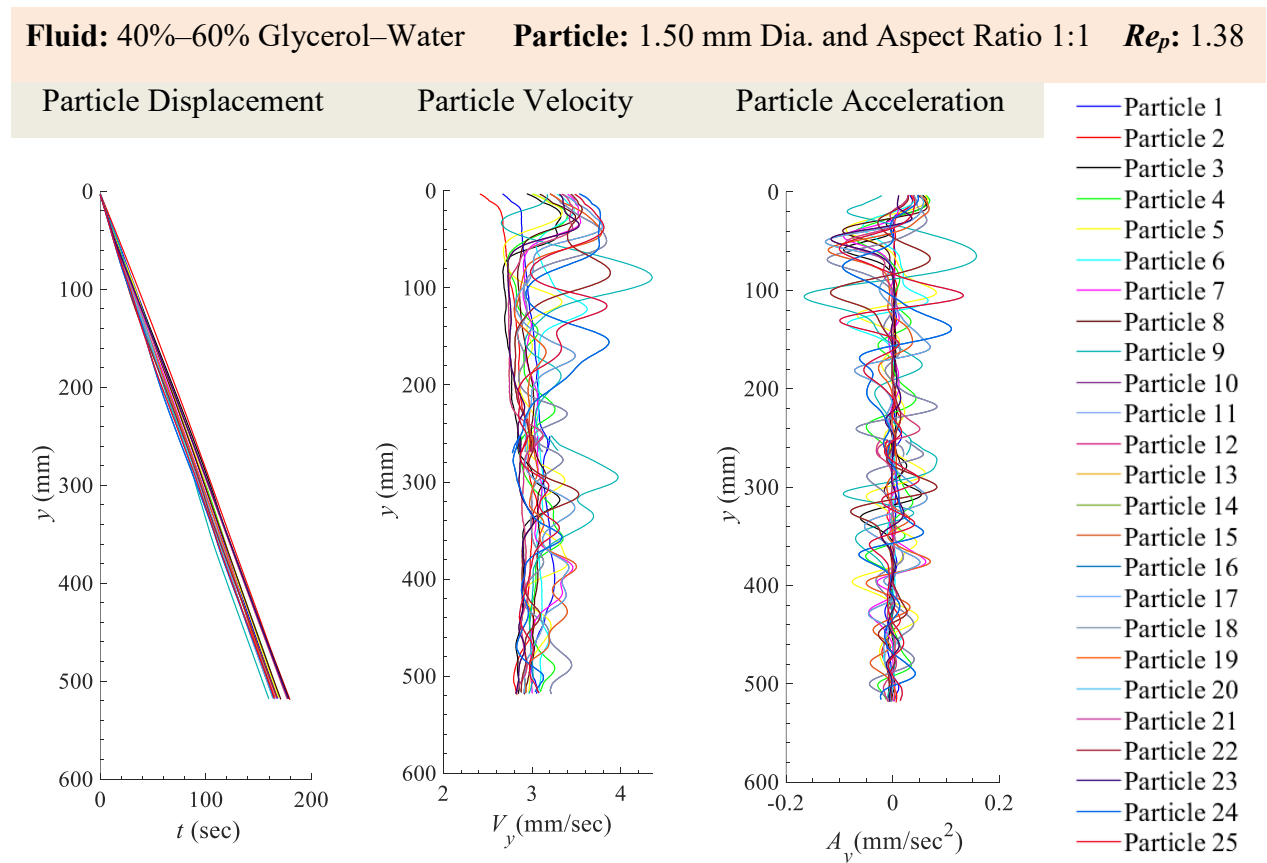


Figure 132 Particle displacement, y , velocity, V_y , and acceleration, A_y , for 1.50 mm Diameter Nylon Cylindrical Particles with Aspect Ratio, A.R. = 1:1 (25 particles) in 40%–60% Glycerol–Water.

8.30.2 x -Velocity (V_x), y -Velocity (V_y) and Magnitude of Velocity ($|V|$) for 1.50 mm Diameter and 1:1 Aspect Ratio ($AR = d_p/l_p$) Nylon Cylindrical Particles in 40%–60% Glycerol–Water

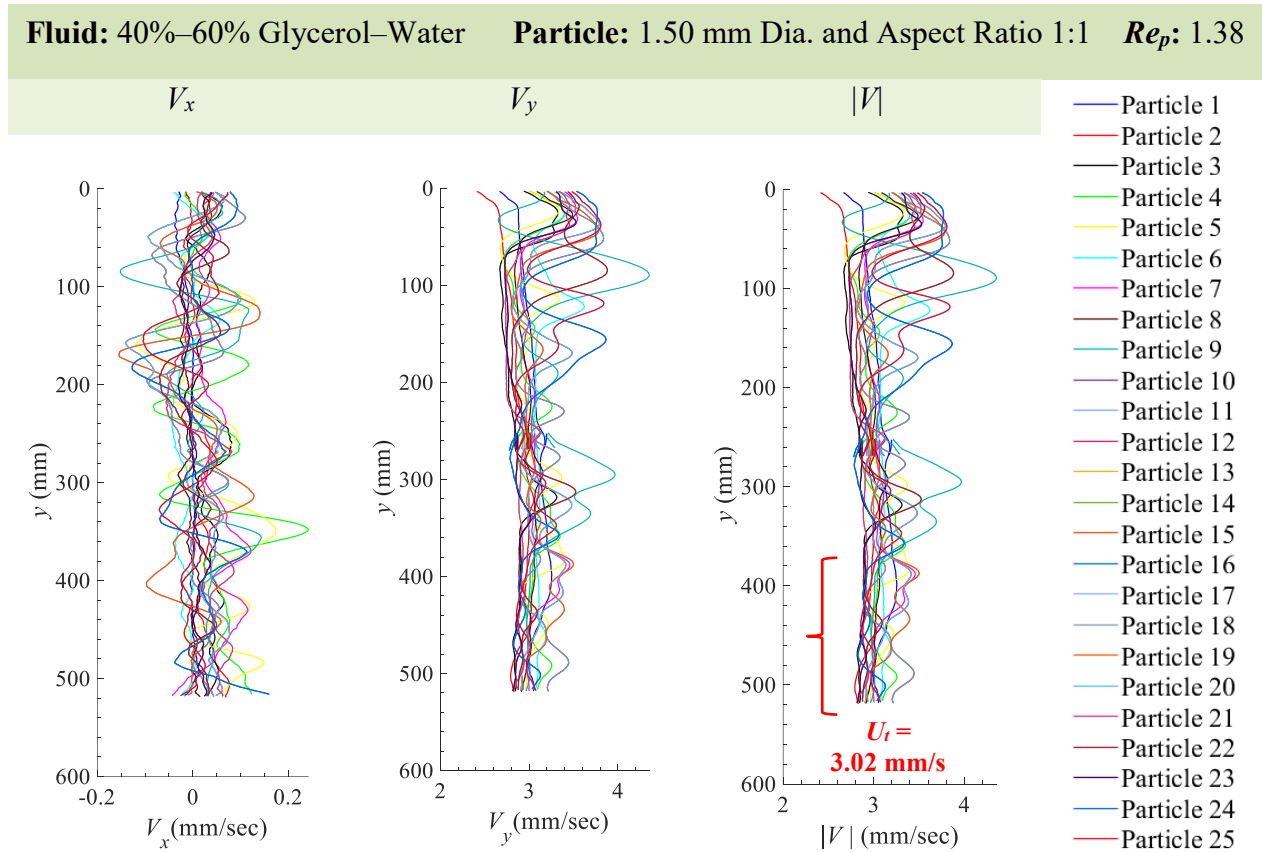


Figure 133 Particle velocity in the x -direction V_x , y -direction V_y , and the magnitude $\sqrt{V_x^2 + V_y^2}$ of the particle velocity $|V|$ for 1.50 mm Diameter Nylon Cylindrical Particles with Aspect Ratio, A.R. = 1:1 (25 particles) in 40%–60% Glycerol–Water. The average terminal settling velocity, U_t is 3.02 mm/s.

8.30.3 x -Acceleration (A_x), y -Acceleration (A_y) and Magnitude of Acceleration ($|A|$) for 1.50 mm Diameter and 1:1 Aspect Ratio ($AR = d_p/l_p$) Nylon Cylindrical Particles in 40%–60% Glycerol–Water

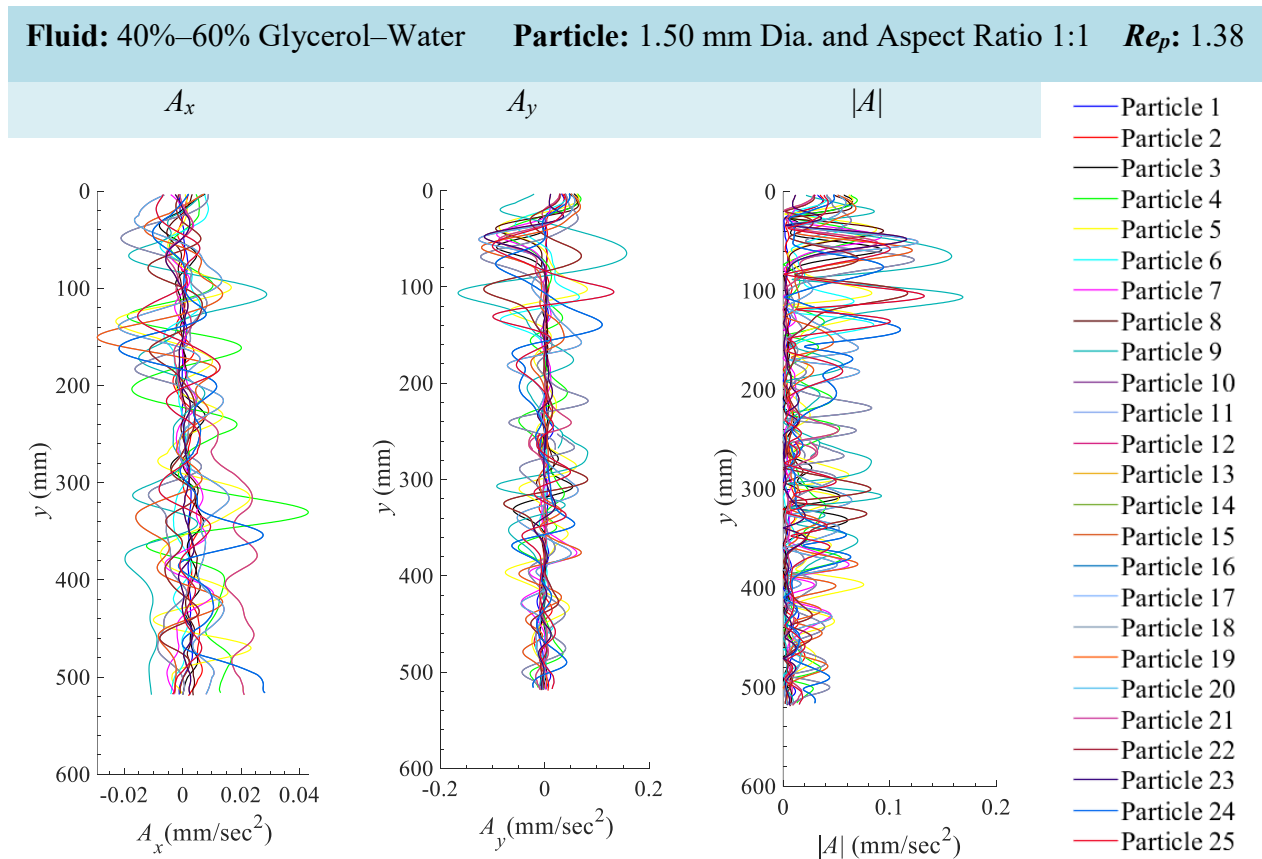


Figure 134 Particle acceleration in the x -direction A_x , y -direction A_y , and the magnitude $\sqrt{(A_x^2 + A_y^2)}$ of the particle acceleration $|A|$ for 1.50 mm Diameter Nylon Cylindrical Particles with Aspect Ratio, A.R. = 1:1 (25 particles) in 40%–60% Glycerol–Water.

8.31 Appendix 31: 1.50 mm Diameter and 1:1 Aspect Ratio ($AR = d_p/l_p$) Nylon Cylindrical Particles in Canola Oil

8.31.1 Particle Displacement, Particle Velocity and Particle Acceleration for 1.50 mm Diameter and 1:1 Aspect Ratio ($AR = d_p/l_p$) Nylon Cylindrical Particles in Canola Oil

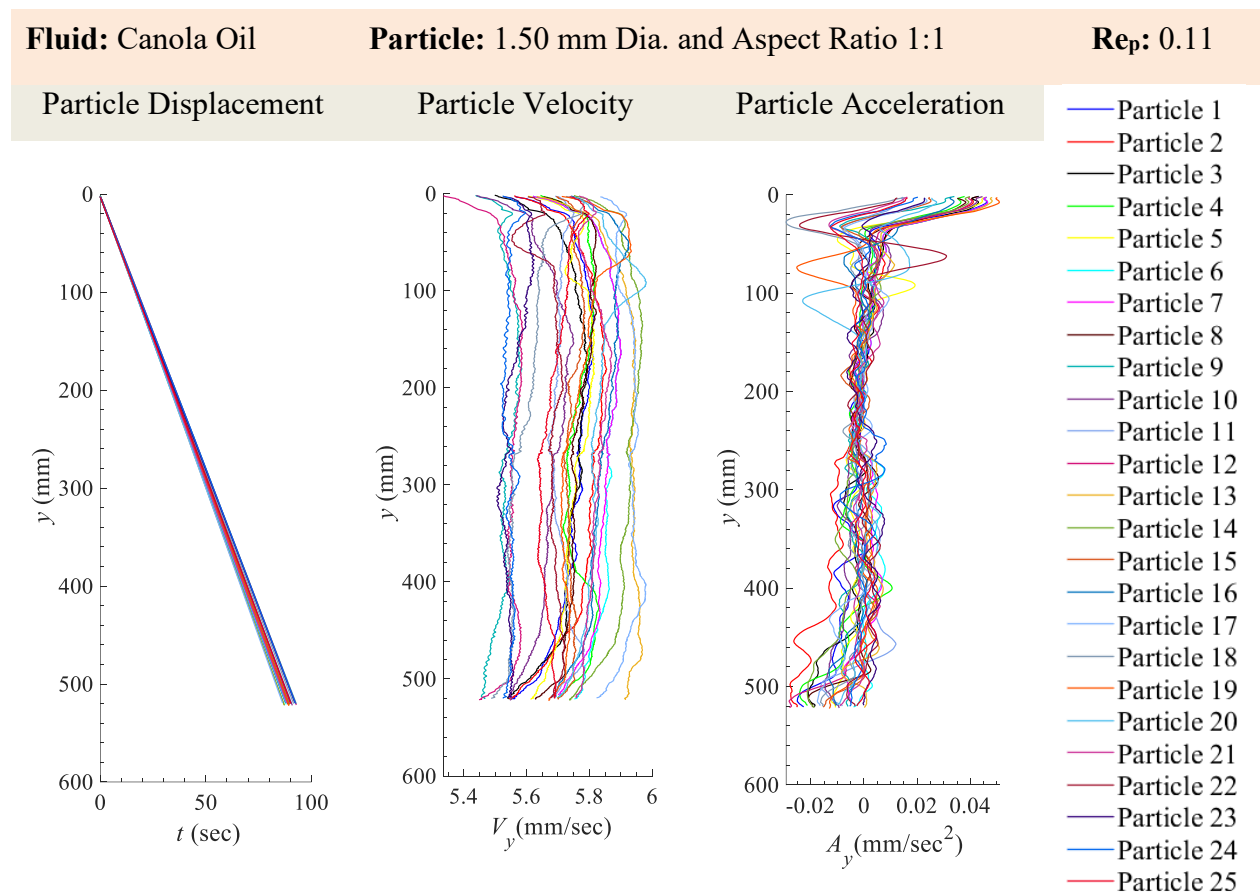


Figure 135 Particle displacement, y , velocity, V_y , and acceleration, A_y , for 1.50 mm Diameter Nylon Cylindrical Particles with Aspect Ratio, A.R. = 1:1 (25 particles) in Canola Oil.

8.31.2 x -Velocity (V_x), y -Velocity (V_y) and Magnitude of Velocity ($|V|$) for 1.50 mm Diameter and 1:1 Aspect Ratio ($AR = d_p/l_p$) Nylon Cylindrical Particles in Canola Oil

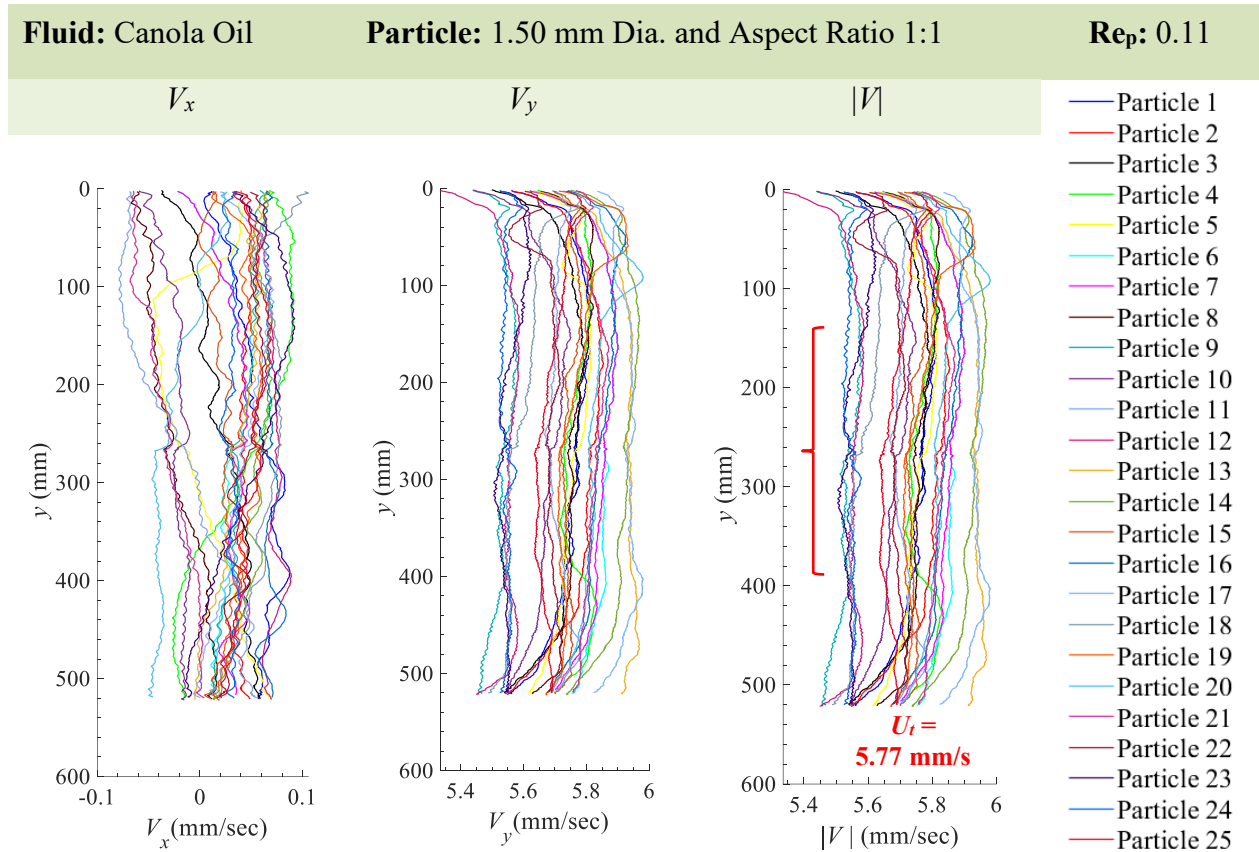


Figure 136 Particle velocity in the x -direction V_x , y -direction V_y , and the magnitude $\sqrt{V_x^2 + V_y^2}$ of the particle velocity $|V|$ for 1.50 mm Diameter Nylon Cylindrical Particles with Aspect Ratio, A.R. = 1:1 (25 particles) in Canola Oil. The magnitude of velocity deviated slightly to the left between 390 mm and 520 mm. Therefore the average was calculated between 140 mm and 380 mm in order to obtain a more accurate representation of the terminal settling velocity. The average terminal settling velocity, U_t is 5.77 mm/s.

8.31.3 x -Acceleration (A_x), y -Acceleration (A_y) and Magnitude of Acceleration ($|A|$) for 1.50 mm Diameter and 1:1 Aspect Ratio ($AR = d_p/l_p$) Nylon Cylindrical Particles in Canola Oil

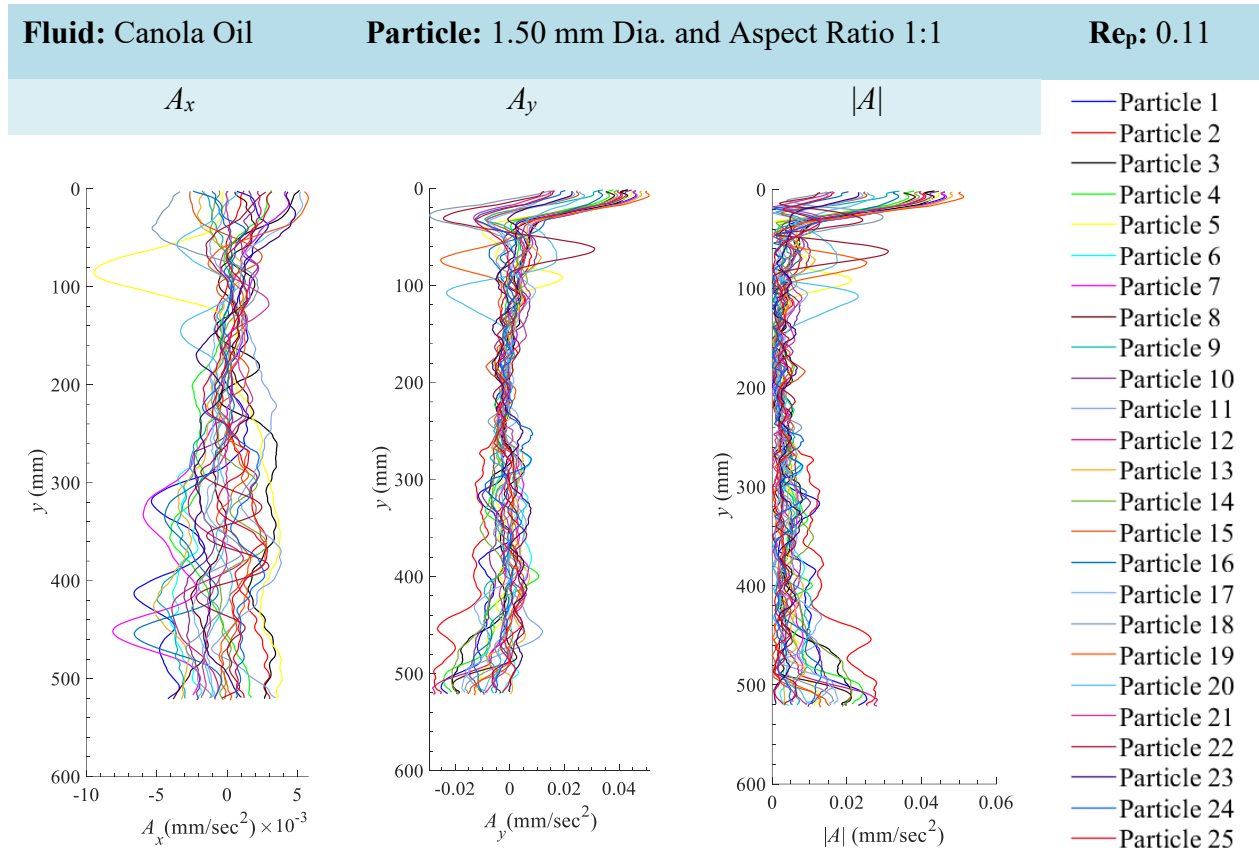


Figure 137 Particle acceleration in the x -direction A_x , y -direction A_y , and the magnitude $\sqrt{(A_x^2 + A_y^2)}$ of the particle acceleration $|A|$ for 1.50 mm Diameter Nylon Cylindrical Particles with Aspect Ratio, A.R. = 1:1 (25 particles) in Canola Oil.

8.32 Appendix 32: 1.50 mm Diameter and 1:3 Aspect Ratio ($AR = d_p/l_p$) Nylon Cylindrical Particles in Water

8.32.1 Particle Displacement, Particle Velocity and Particle Acceleration for 1.50 mm Diameter and 1:3 Aspect Ratio ($AR = d_p/l_p$) Nylon Cylindrical Particles in Water

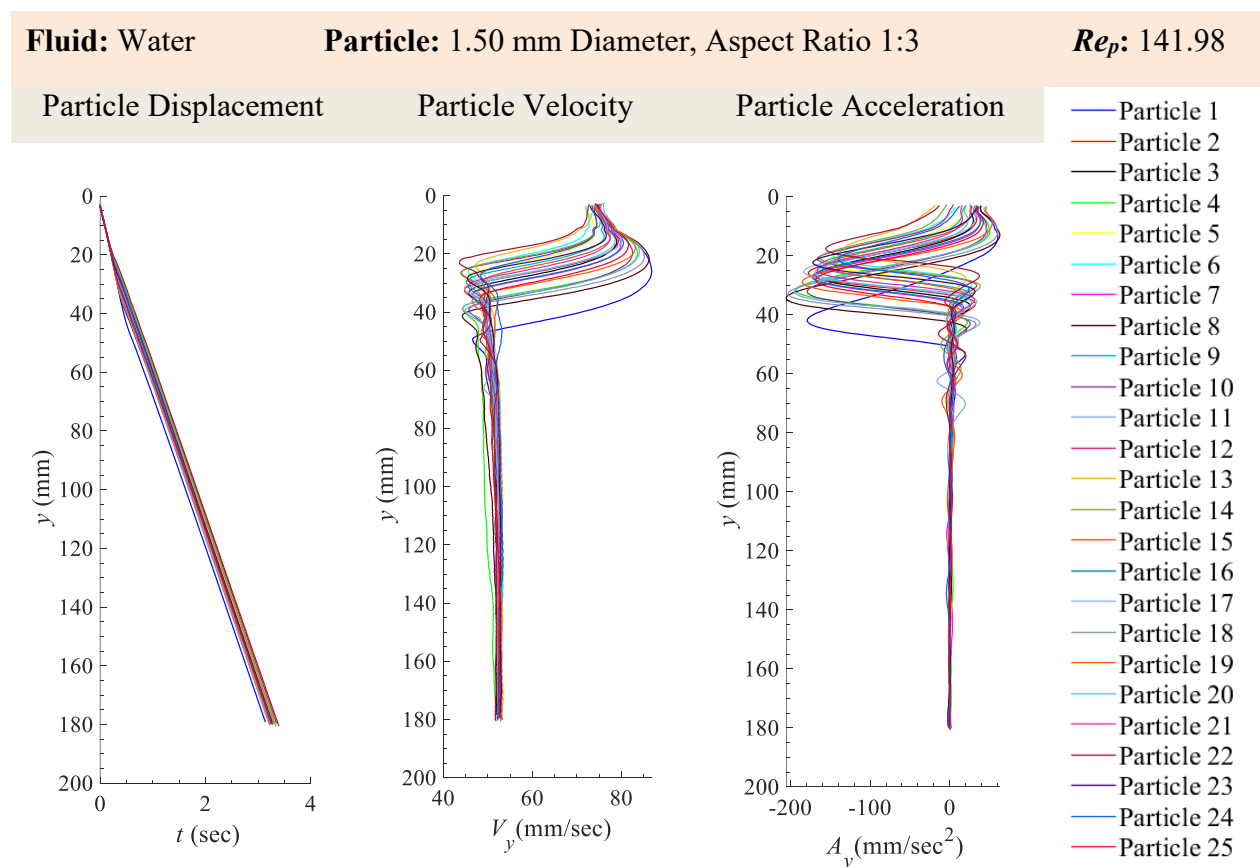


Figure 138 Particle displacement, y , velocity, V_y , and acceleration, A_y , for 1.50 mm Diameter Nylon Cylindrical Particles with Aspect Ratio, A.R. = 1:3 (25 particles) in Water.

8.32.2 x -Velocity (V_x), y -Velocity (V_y) and Magnitude of Velocity ($|V|$) for 1.50 mm Diameter and 1:3 Aspect Ratio ($AR = d_p/l_p$) Nylon Cylindrical Particles in Water

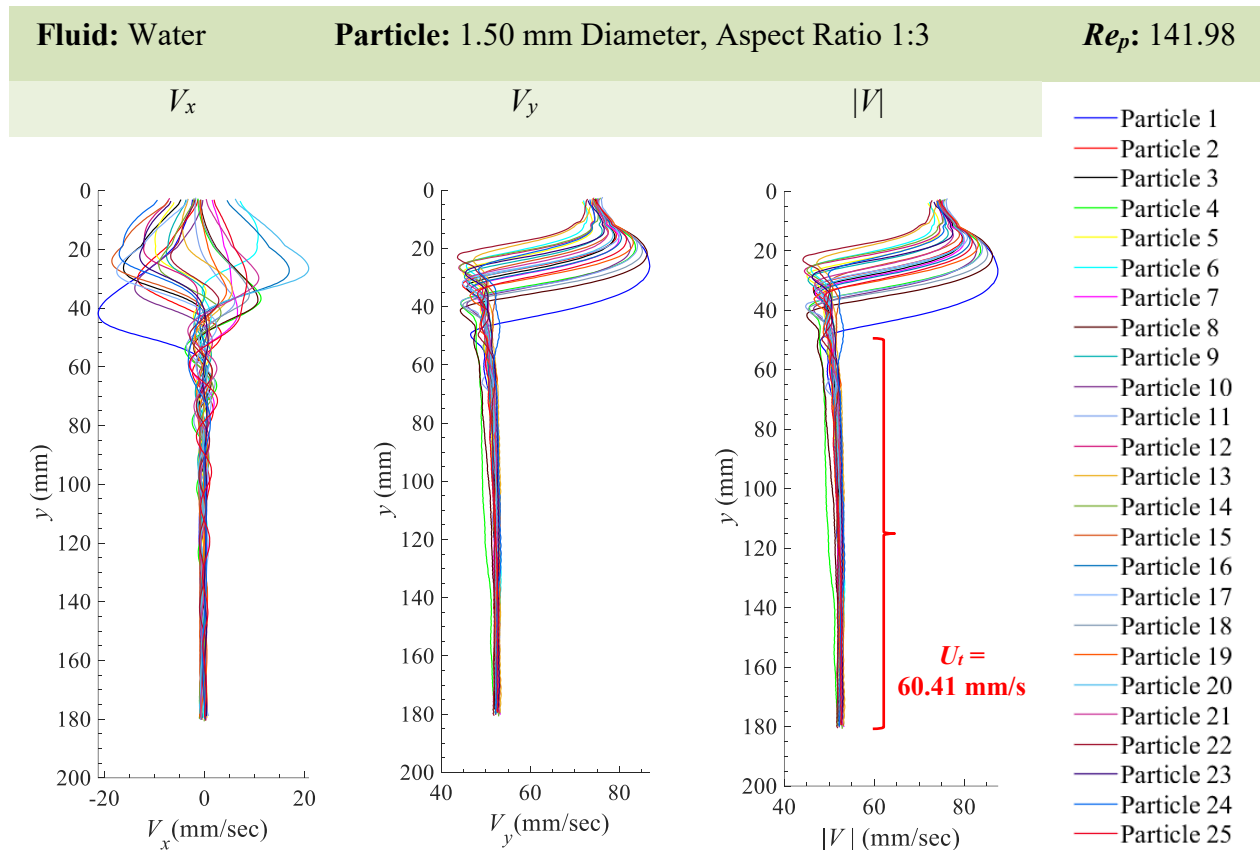


Figure 139 Particle velocity in the x -direction V_x , y -direction V_y , and the magnitude $\sqrt{V_x^2 + V_y^2}$ of the particle velocity $|V|$ for 1.50 mm Diameter Nylon Cylindrical Particles with Aspect Ratio, A.R. = 1:3 (25 particles) in Water. The average terminal settling velocity, U_t is 60.41 mm/s.

8.32.3 x -Acceleration (A_x), y -Acceleration (A_y) and Magnitude of Acceleration ($|A|$) for 1.50 mm Diameter and 1:3 Aspect Ratio ($AR = d_p/l_p$) Nylon Cylindrical Particles in Water

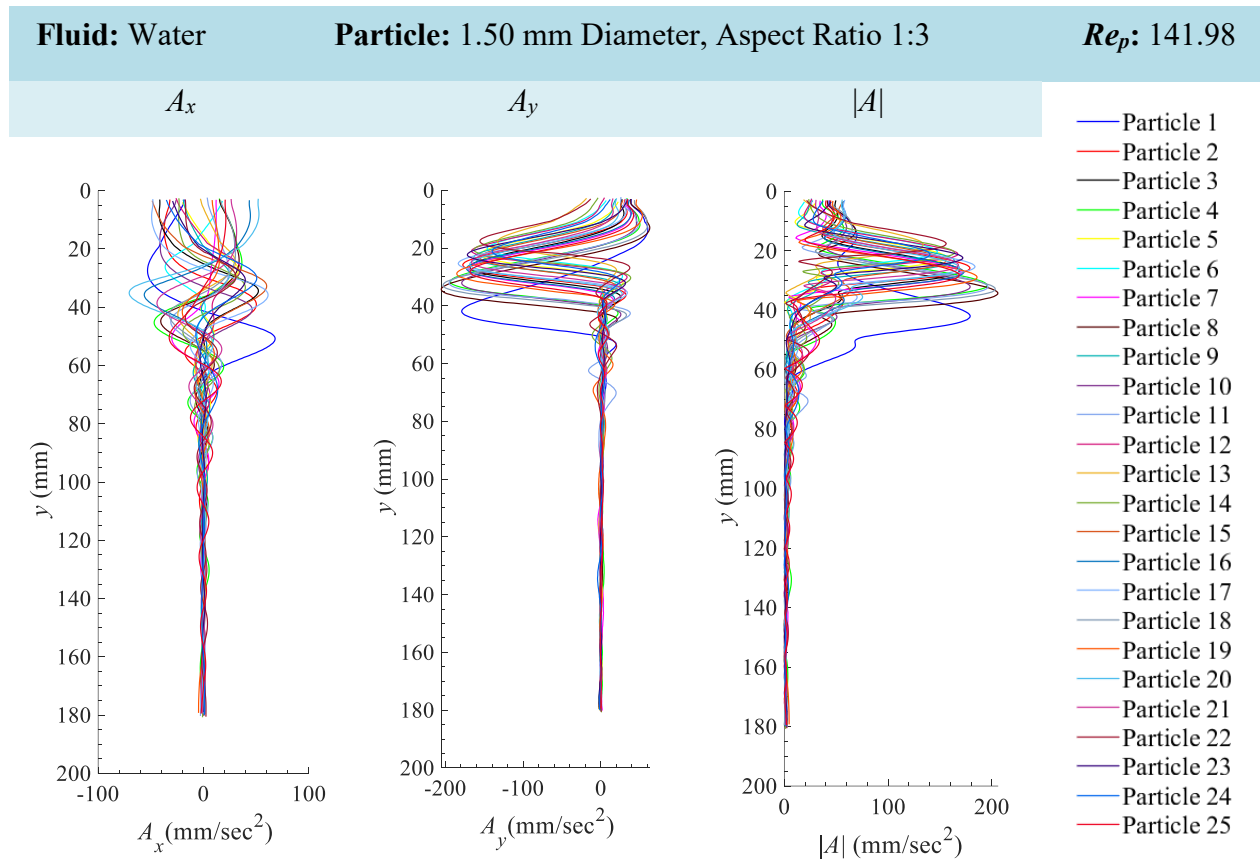


Figure 140 Particle acceleration in the x -direction A_x , y -direction A_y , and the magnitude $\sqrt{(A_x^2 + A_y^2)}$ of the particle acceleration $|A|$ for 1.50 mm Diameter Nylon Cylindrical Particles with Aspect Ratio, A.R. = 1:3 (25 particles) in Water.

8.33 Appendix 33: 1.50 mm Diameter and 1:3 Aspect Ratio ($AR = d_p/l_p$) Nylon Cylindrical Particles in 20%–80% Glycerol–Water

8.33.1 Particle Displacement, Particle Velocity and Particle Acceleration for 1.50 mm Diameter and 1:3 Aspect Ratio ($AR = d_p/l_p$) Nylon Cylindrical Particles in 20%–80% Glycerol–Water

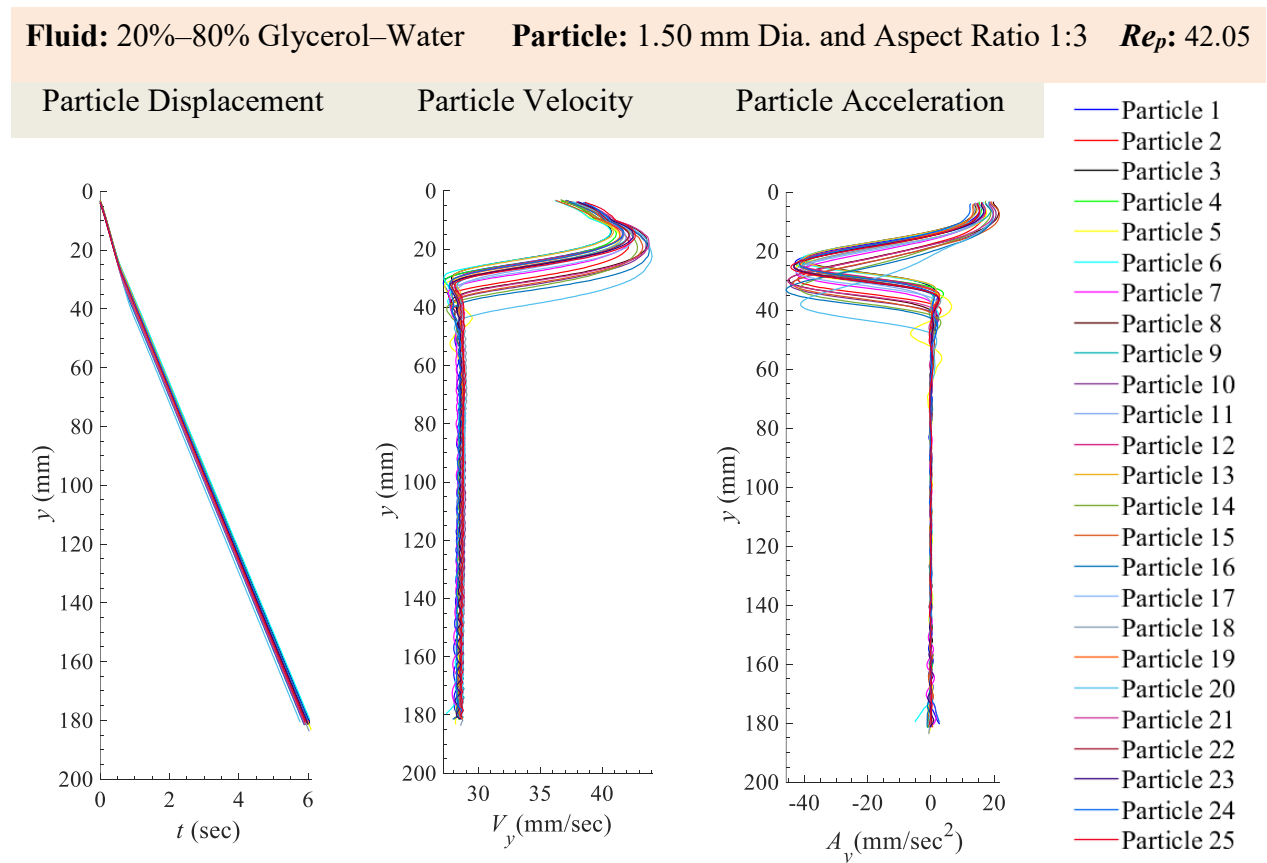


Figure 141 Particle displacement, y , velocity, V_y , and acceleration, A_y , for 1.50 mm Diameter Nylon Cylindrical Particles with Aspect Ratio, A.R. = 1:3 (25 particles) in 20%–80% Glycerol–Water.

8.33.2 x -Velocity (V_x), y -Velocity (V_y) and Magnitude of Velocity ($|V|$) for 1.50 mm Diameter and 1:3 Aspect Ratio ($AR = d_p/l_p$) Nylon Cylindrical Particles in 20%–80% Glycerol–Water

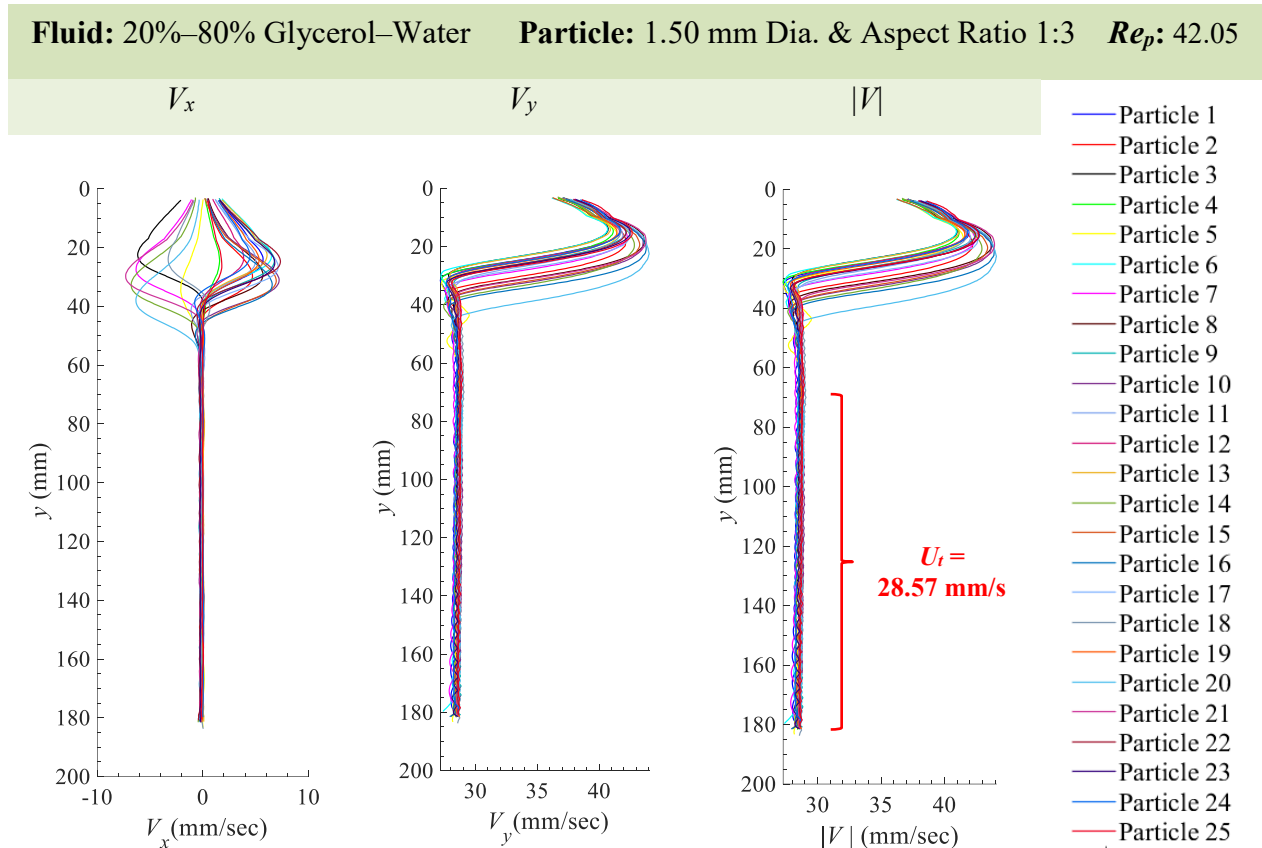


Figure 142 Particle velocity in the x -direction V_x , y -direction V_y , and the magnitude $\sqrt{V_x^2 + V_y^2}$ of the particle velocity $|V|$ for 1.50 mm Diameter Nylon Cylindrical Particles with Aspect Ratio, A.R. = 1:3 (25 particles) in 20%–80% Glycerol–Water. The average terminal settling velocity, U_t is 28.57 mm/s.

8.33.3 x -Acceleration (A_x), y -Acceleration (A_y) and Magnitude of Acceleration ($|A|$) for 1.50 mm Diameter and 1:3 Aspect Ratio ($AR = d_p/l_p$) Nylon Cylindrical Particles in 20%–80% Glycerol–Water

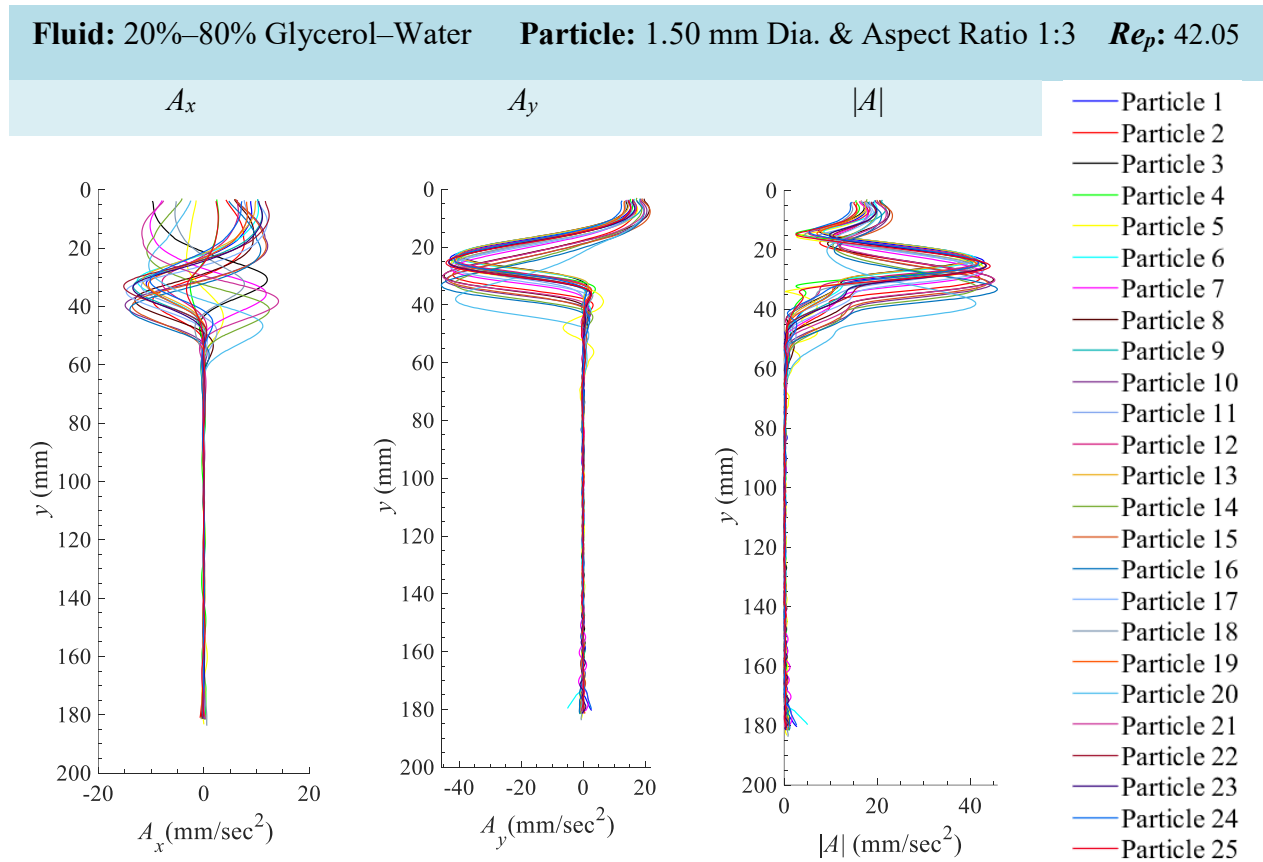


Figure 143 Particle acceleration in the x -direction A_x , y -direction A_y , and the magnitude $\sqrt{(A_x^2 + A_y^2)}$ of the particle acceleration $|A|$ for 1.50 mm Diameter Nylon Cylindrical Particles with Aspect Ratio, A.R. = 1:3 (25 particles) in 20%–80% Glycerol–Water.

8.34 Appendix 34: 1.50 mm Diameter and 1:3 Aspect Ratio ($AR = d_p/l_p$) Nylon Cylindrical Particles in 40%–60% Glycerol–Water

8.34.1 Particle Displacement, Particle Velocity and Particle Acceleration for 1.50 mm Diameter and 1:3 Aspect Ratio ($AR = d_p/l_p$) Nylon Cylindrical Particles in 40%–60% Glycerol–Water

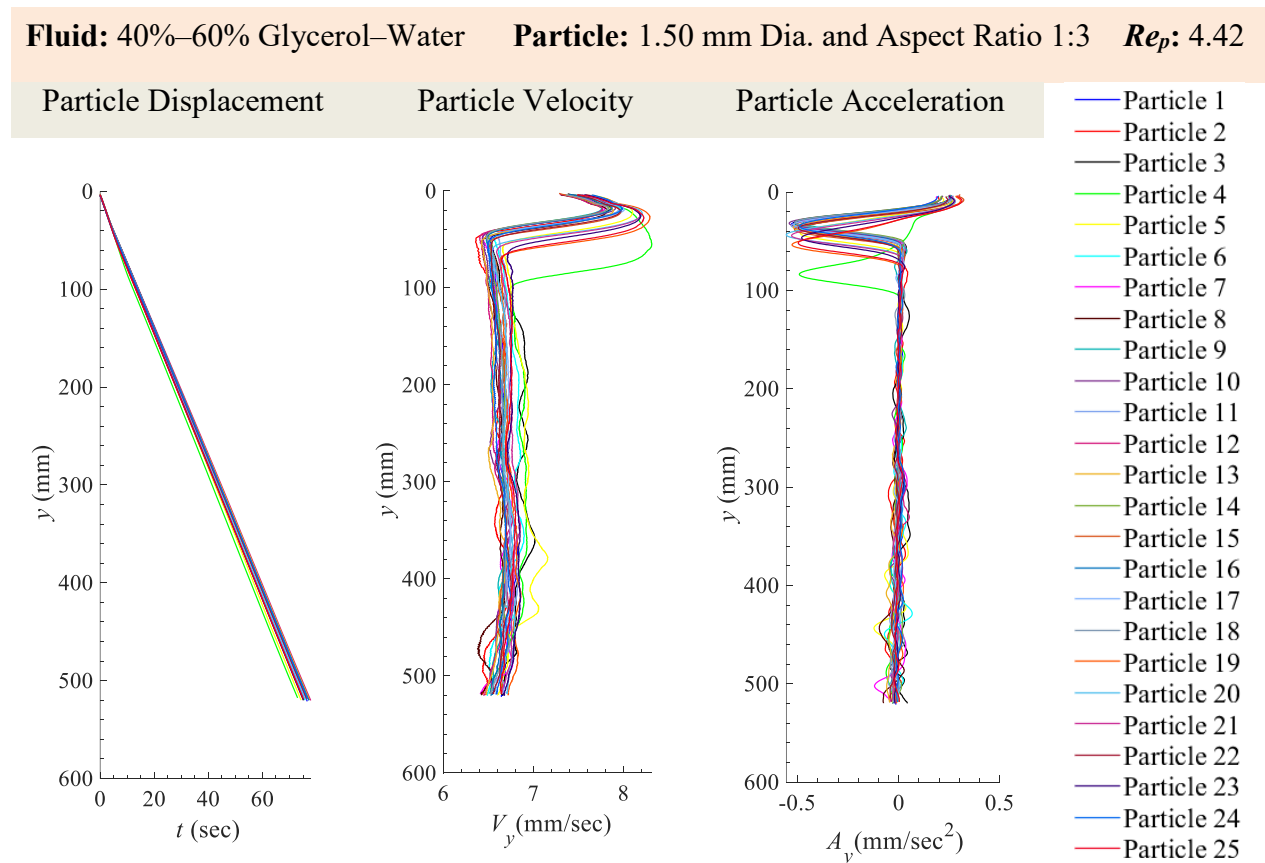


Figure 144 Particle displacement, y , velocity, V_y , and acceleration, A_y , for 1.50 mm Diameter Nylon Cylindrical Particles with Aspect Ratio, A.R. = 1:3 (25 particles) in 40%–60% Glycerol–Water.

8.34.2 x -Velocity (V_x), y -Velocity (V_y) and Magnitude of Velocity ($|V|$) for 1.50 mm Diameter and 1:3 Aspect Ratio ($AR = d_p/l_p$) Nylon Cylindrical Particles in 40%–60% Glycerol–Water

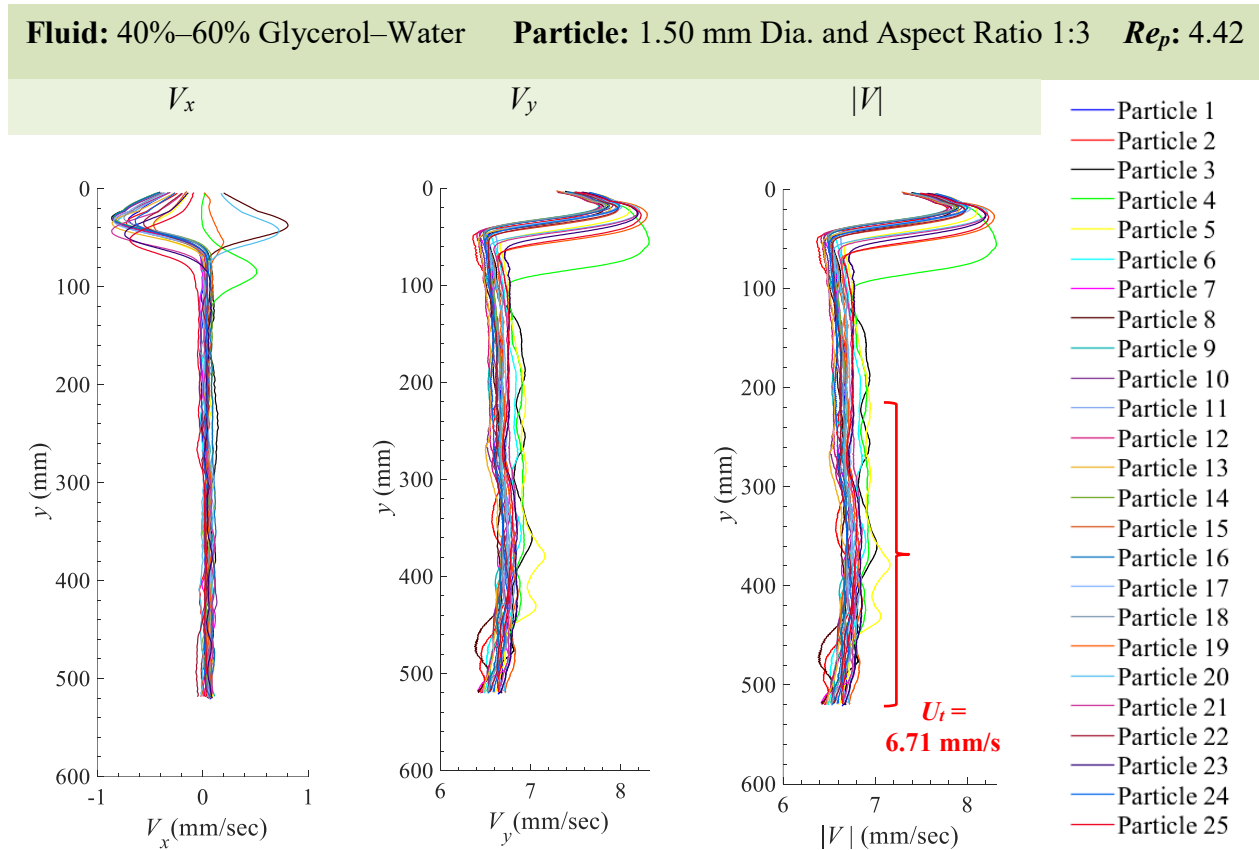


Figure 145 Particle velocity in the x -direction V_x , y -direction V_y , and the magnitude $\sqrt{V_x^2 + V_y^2}$ of the particle velocity $|V|$ for 1.50 mm Diameter Nylon Cylindrical Particles with Aspect Ratio, A.R. = 1:3 (25 particles) in 40%–60% Glycerol–Water. The average terminal settling velocity, U_i is 6.71 mm/s.

8.34.3 x -Acceleration (A_x), y -Acceleration (A_y) and Magnitude of Acceleration ($|A|$) for 1.50 mm Diameter and 1:3 Aspect Ratio ($AR = d_p/l_p$) Nylon Cylindrical Particles in 40%–60% Glycerol–Water

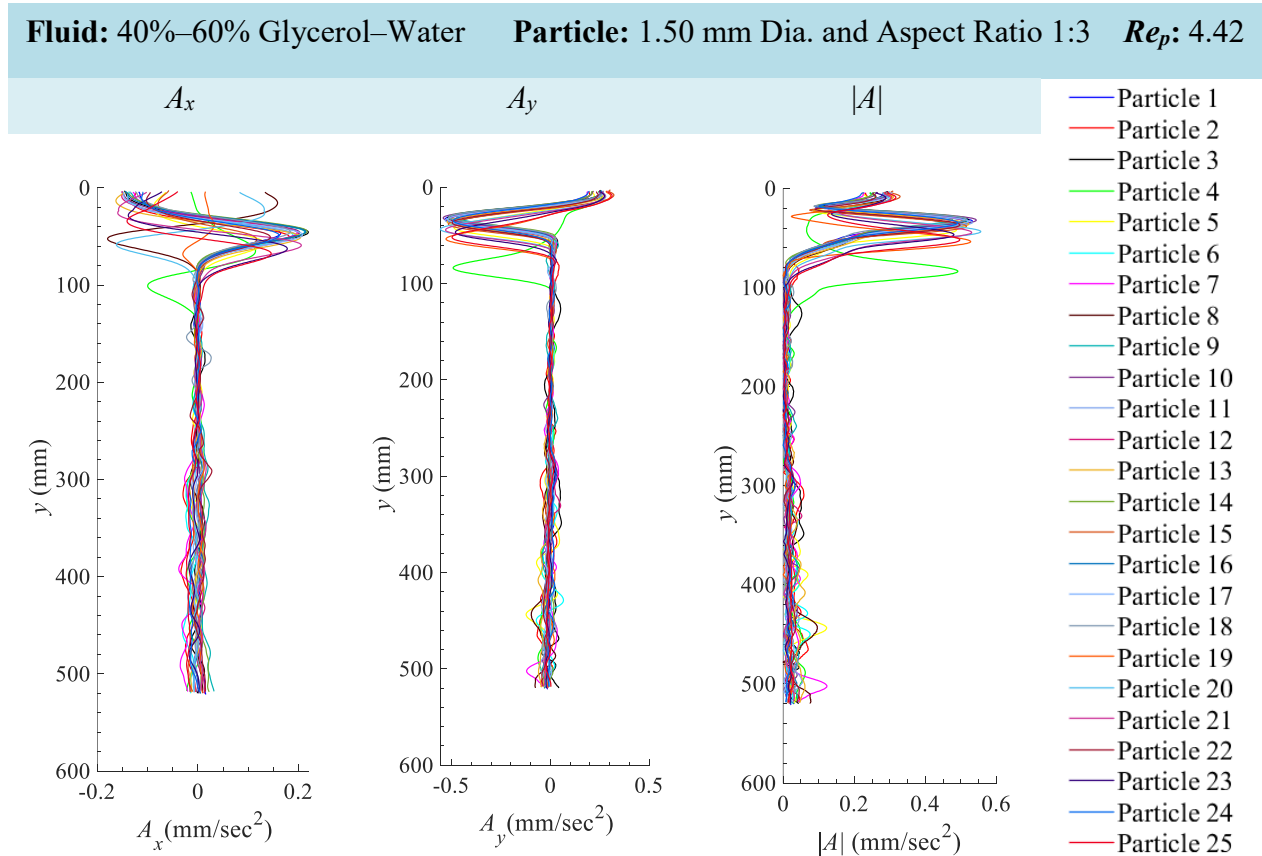


Figure 146 Particle acceleration in the x -direction A_x , y -direction A_y , and the magnitude $\sqrt{(A_x^2 + A_y^2)}$ of the particle acceleration $|A|$ for 1.50 mm Diameter Nylon Cylindrical Particles with Aspect Ratio, A.R. = 1:3 (25 particles) in 40%–60% Glycerol–Water.

8.35 Appendix 35: 1.50 mm Diameter and 1:3 Aspect Ratio ($AR = d_p/l_p$) Nylon Cylindrical Particles in Canola Oil

8.35.1 Particle Displacement, Particle Velocity and Particle Acceleration for 1.50 mm Diameter and 1:3 Aspect Ratio ($AR = d_p/l_p$) Nylon Cylindrical Particles in Canola Oil

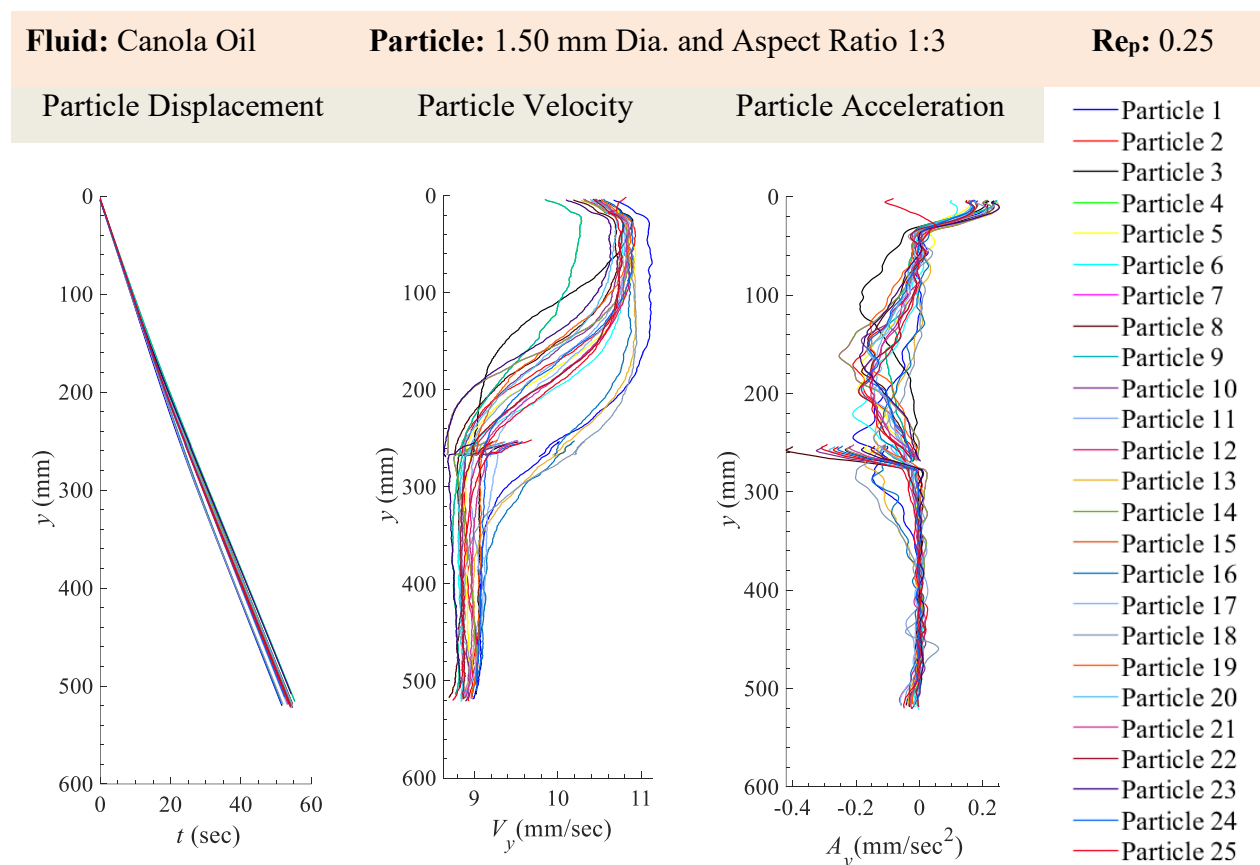


Figure 147 Particle displacement, y , velocity, V_y , and acceleration, A_y , for 1.50 mm Diameter Nylon Cylindrical Particles with Aspect Ratio, A.R. = 1:3 (25 particles) in Canola Oil. The outliers at displacement 260 mm occurred within the overlap between the two cameras. In this region there was a variation in the light distribution compared to the rest of the field of view. A uniform distribution of light was not achieved with the projector and kite paper as shown in Figure 8 and describe in Section 3.5.1. This affected the binarization of the particle within that region and thereby a slight shift in the location of the centroid of the particle from the image processing scheme.

8.35.2 x -Velocity (V_x), y -Velocity (V_y) and Magnitude of Velocity ($|V|$) for 1.50 mm Diameter and 1:3 Aspect Ratio ($AR = d_p/l_p$) Nylon Cylindrical Particles in Canola Oil

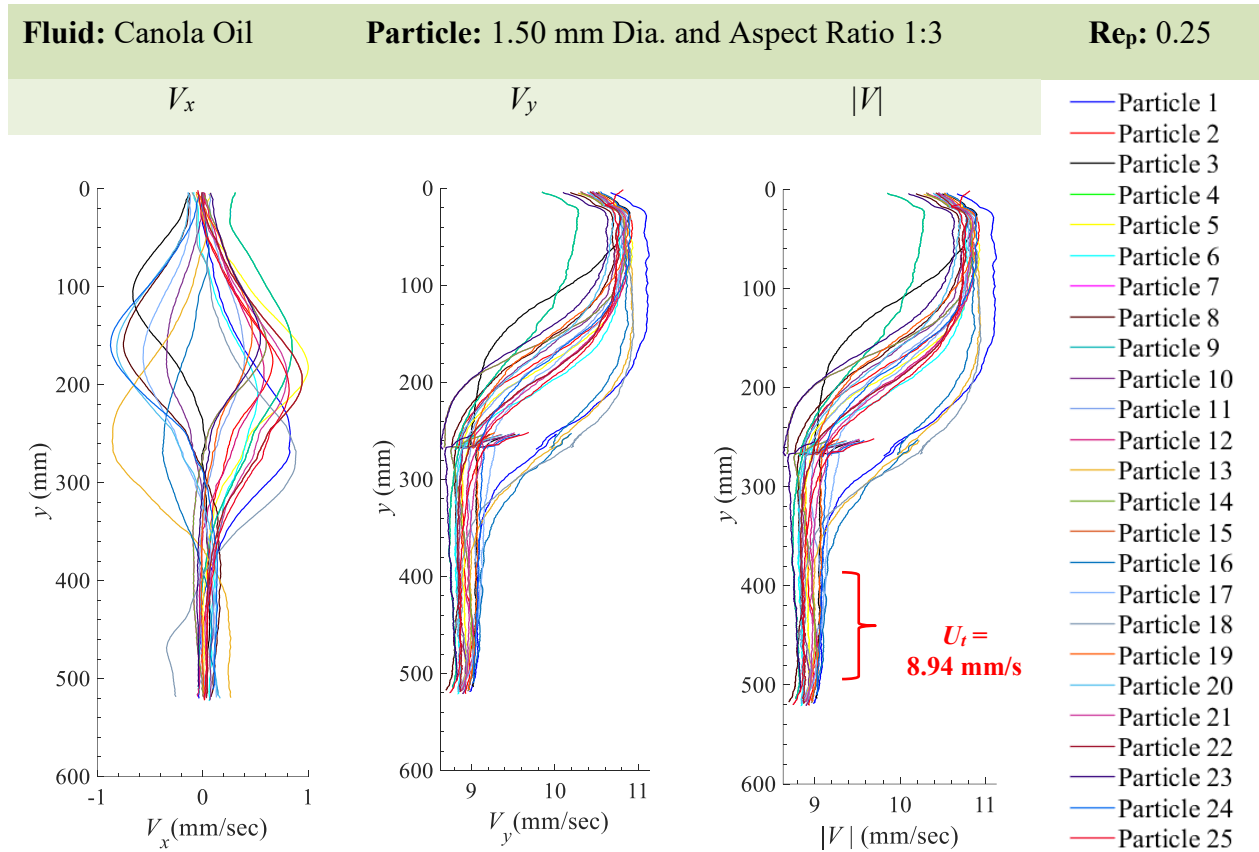


Figure 148 Particle velocity in the x -direction V_x , y -direction V_y , and the magnitude $\sqrt{V_x^2 + V_y^2}$ of the particle velocity $|V|$ for 1.50 mm Diameter Nylon Cylindrical Particles with Aspect Ratio, A.R. = 1:3 (25 particles) in Canola Oil. The magnitude of velocity deviated slightly to the left between 490 mm and 520 mm. Therefore the average was calculated between 390 mm and 480 mm in order to obtain a more accurate representation of the terminal settling velocity. The average terminal settling velocity, U_t is 8.94 mm/s. The outliers at displacement 260 mm occurred within the overlap between the two cameras. In this region there was a variation in the light distribution compared to the rest of the field of view. A uniform distribution of light was not achieved with the projector and kite paper as shown in Figure 8 and describe in Section 3.5.1. This affected the binarization of the particle within that region and thereby a slight shift in the location of the centroid of the particle from the image processing scheme.

8.35.3 x -Acceleration (A_x), y -Acceleration (A_y) and Magnitude of Acceleration ($|A|$) for 1.50 mm Diameter and 1:3 Aspect Ratio ($AR = d_p/l_p$) Nylon Cylindrical Particles in Canola Oil

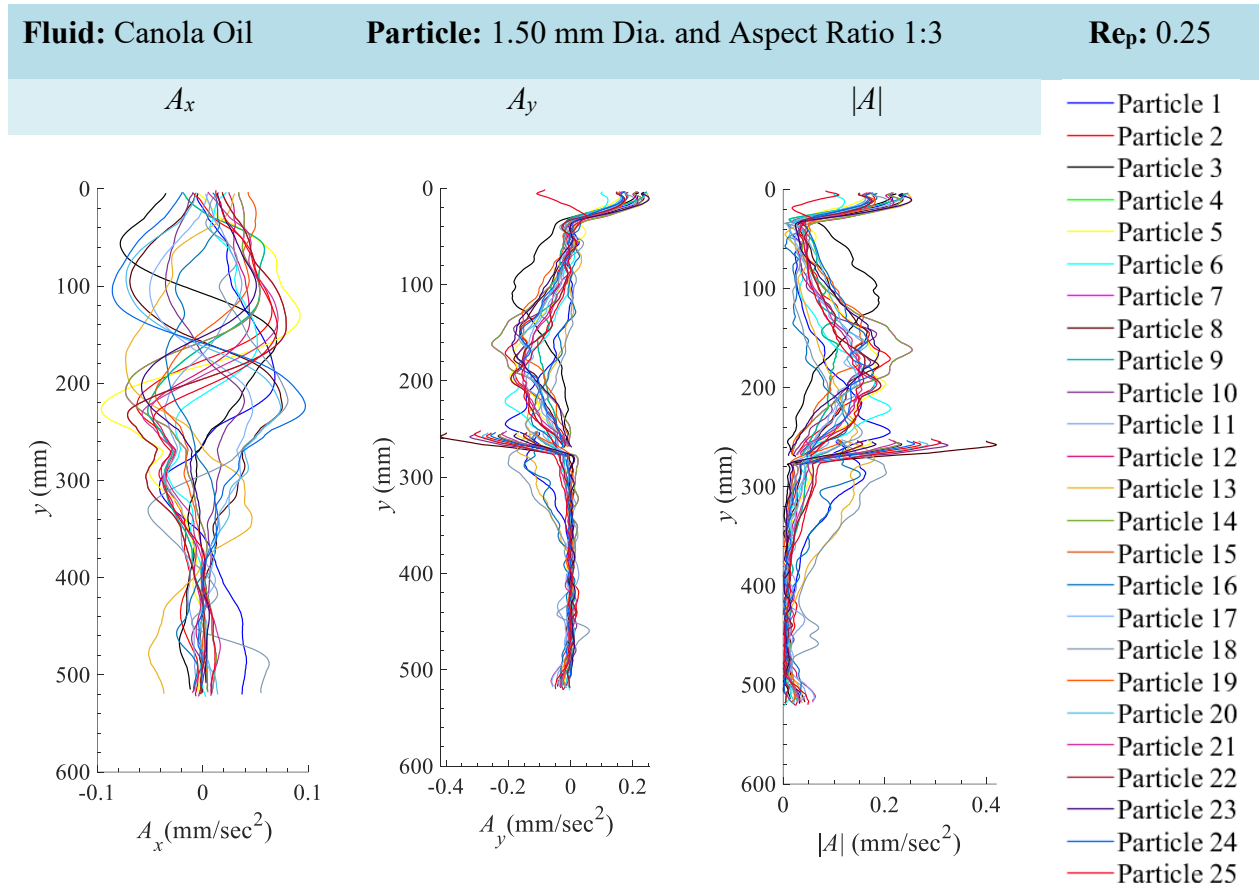


Figure 149 Particle acceleration in the x -direction A_x , y -direction A_y , and the magnitude $\sqrt{(A_x^2 + A_y^2)}$ of the particle acceleration $|A|$ for 1.50 mm Diameter Nylon Cylindrical Particles with Aspect Ratio, A.R. = 1:3 (25 particles) in Canola Oil. The outliers at displacement 260 mm occurred within the overlap between the two cameras. In this region there was a variation in the light distribution compared to the rest of the field of view. A uniform distribution of light was not achieved with the projector and kite paper as shown in Figure 8 and describe in Section 3.5.1. This affected the binarization of the particle within that region and thereby a slight shift in the location of the centroid of the particle from the image processing scheme.

8.36 Appendix 36: 1.50 mm Diameter and 1:5 Aspect Ratio ($AR = d_p/l_p$) Nylon Cylindrical Particles in Water

8.36.1 Particle Displacement, Particle Velocity and Particle Acceleration for 1.50 mm Diameter and 1:5 Aspect Ratio ($AR = d_p/l_p$) Nylon Cylindrical Particles in Water

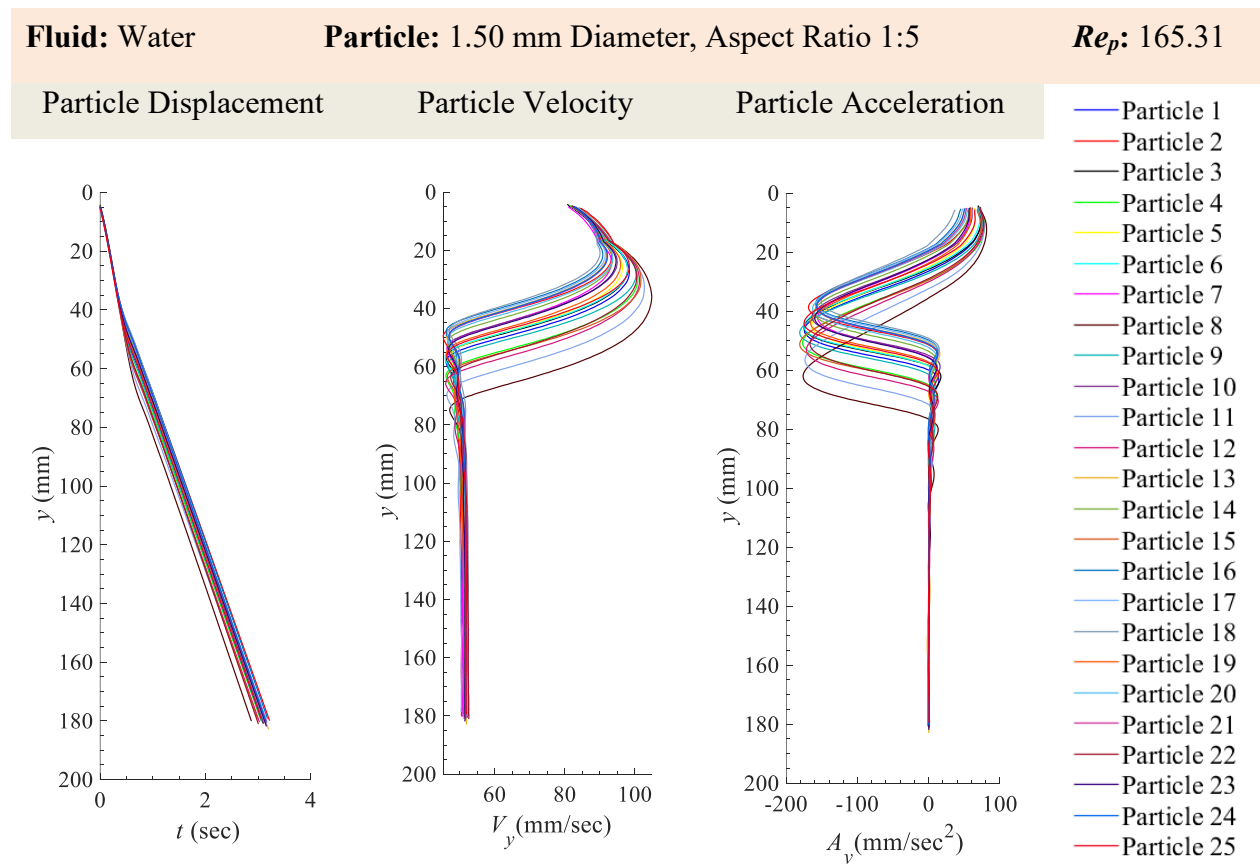


Figure 150 Particle displacement, y , velocity, V_y , and acceleration, A_y , for 1.50 mm Diameter Nylon Cylindrical Particles with Aspect Ratio, A.R. = 1:5 (25 particles) in Water.

8.36.2 x -Velocity (V_x), y -Velocity (V_y) and Magnitude of Velocity ($|V|$) for 1.50 mm Diameter and 1:5 Aspect Ratio ($AR = d_p/l_p$) Nylon Cylindrical Particles in Water

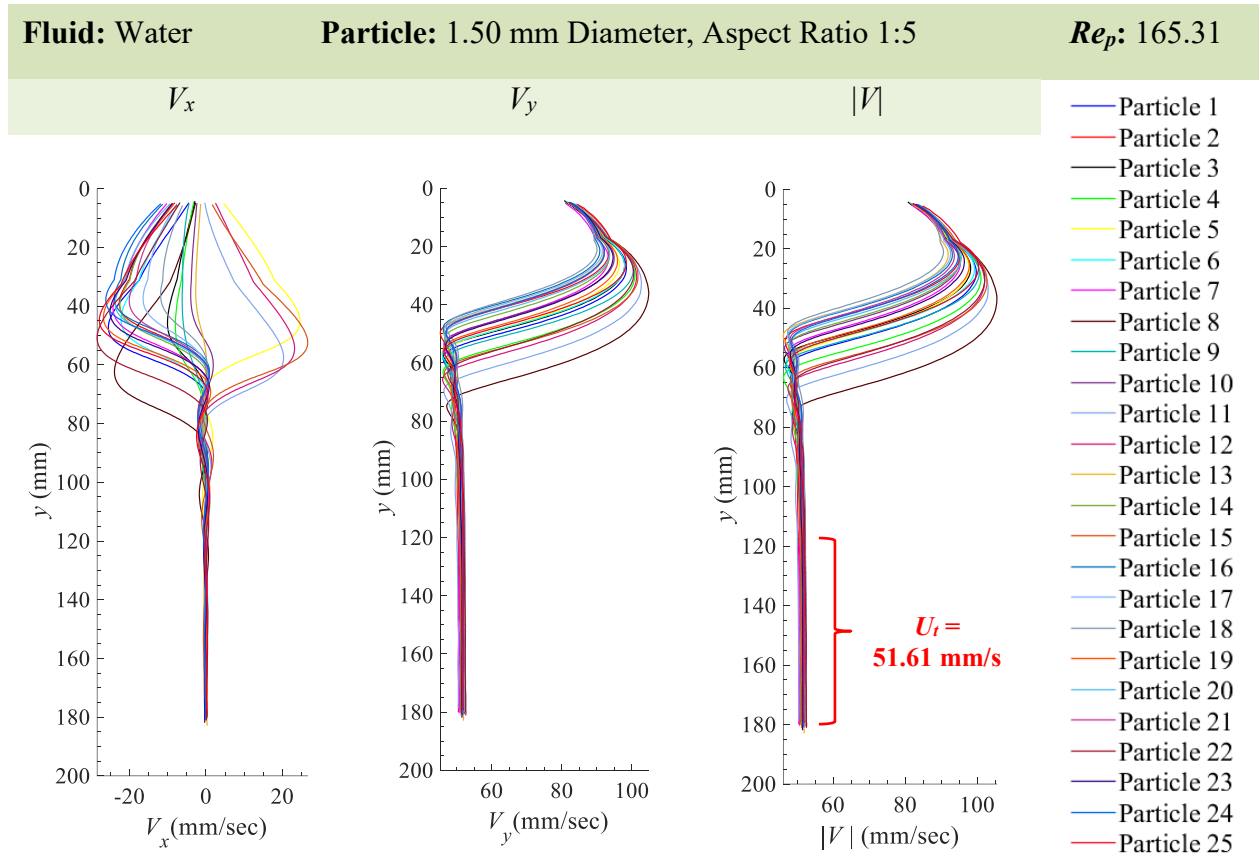


Figure 151 Particle velocity in the x -direction V_x , y -direction V_y , and the magnitude $\sqrt{V_x^2 + V_y^2}$ of the particle velocity $|V|$ for 1.50 mm Diameter Nylon Cylindrical Particles with Aspect Ratio, A.R. = 1:5 (25 particles) in Water. The average terminal settling velocity, U_t is 51.61 mm/s.

8.36.3 x -Acceleration (A_x), y -Acceleration (A_y) and Magnitude of Acceleration ($|A|$) for 1.50 mm Diameter and 1:5 Aspect Ratio ($AR = d_p/l_p$) Nylon Cylindrical Particles in Water

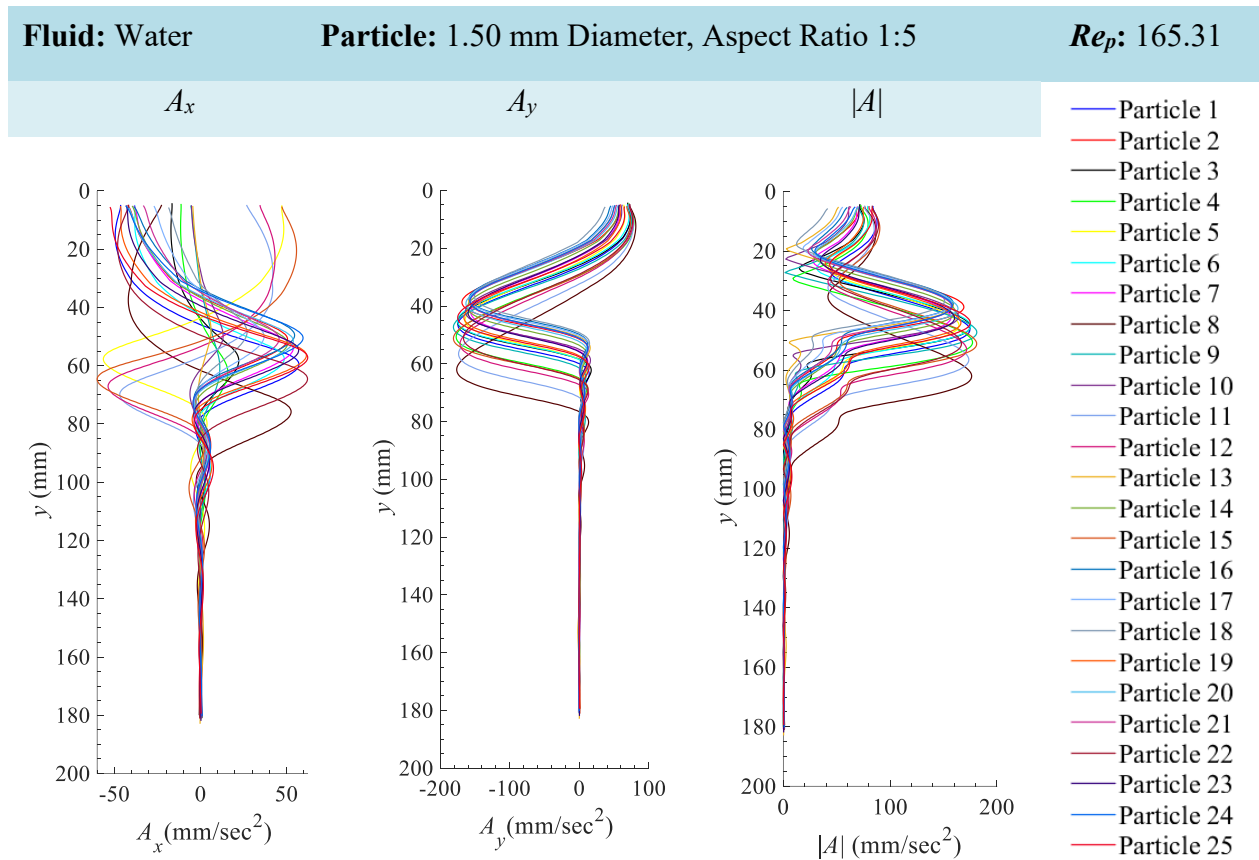


Figure 152 Particle acceleration in the x -direction A_x , y -direction A_y , and the magnitude $\sqrt{(A_x^2 + A_y^2)}$ of the particle acceleration $|A|$ for 1.50 mm Diameter Nylon Cylindrical Particles with Aspect Ratio, A.R. = 1:5 (25 particles) in Water.

8.37 Appendix 37: 1.50 mm Diameter and 1:5 Aspect Ratio ($AR = d_p/l_p$) Nylon Cylindrical Particles in 20%–80% Glycerol–Water

8.37.1 Particle Displacement, Particle Velocity and Particle Acceleration for 1.50 mm Diameter and 1:5 Aspect Ratio ($AR = d_p/l_p$) Nylon Cylindrical Particles in 20%–80% Glycerol–Water

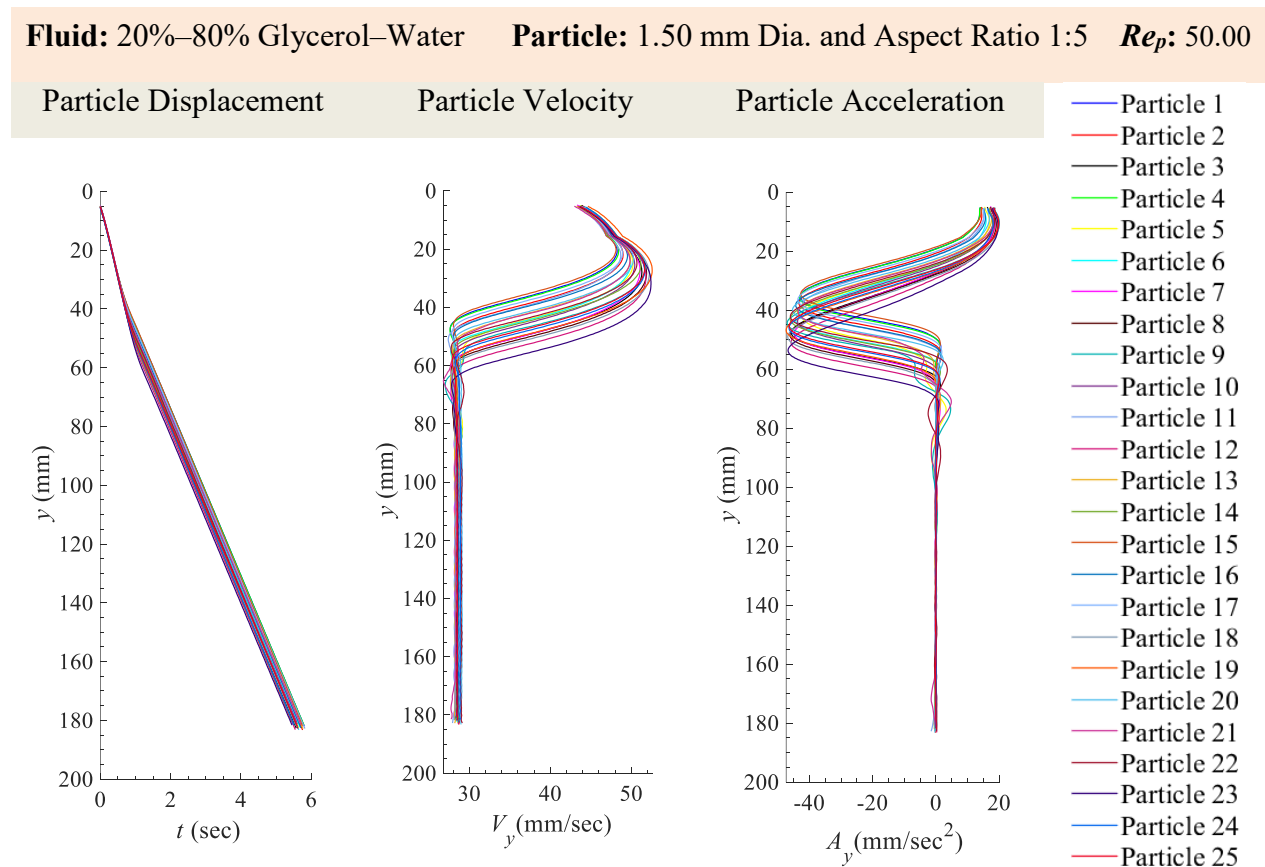


Figure 153 Particle displacement, y , velocity, V_y , and acceleration, A_y , for 1.50 mm Diameter Nylon Cylindrical Particles with Aspect Ratio, A.R. = 1:5 (25 particles) in 20%–80% Glycerol–Water.

8.37.2 x -Velocity (V_x), y -Velocity (V_y) and Magnitude of Velocity ($|V|$) for 1.50 mm Diameter and 1:5 Aspect Ratio ($AR = d_p/l_p$) Nylon Cylindrical Particles in 20%–80% Glycerol–Water

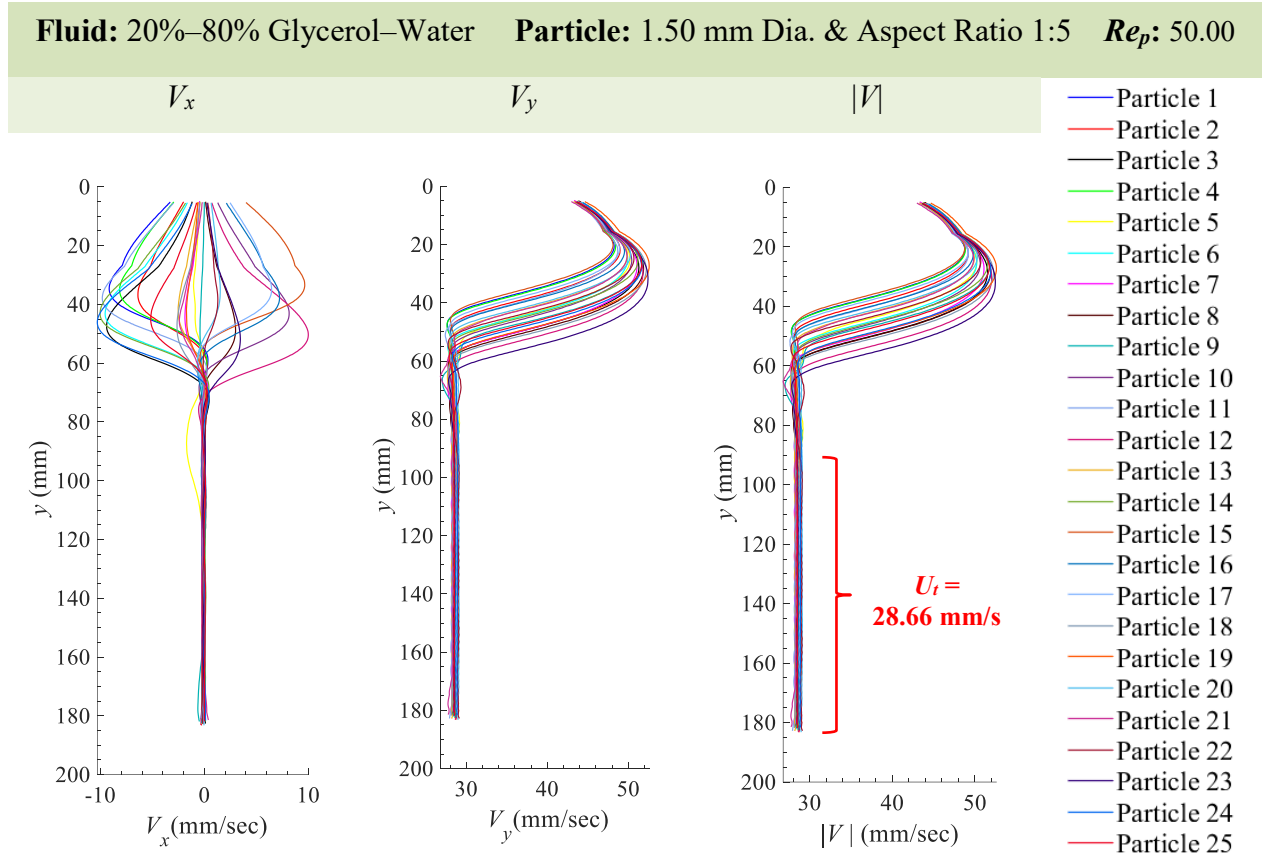


Figure 154 Particle velocity in the x -direction V_x , y -direction V_y , and the magnitude $\sqrt{V_x^2 + V_y^2}$ of the particle velocity $|V|$ for 1.50 mm Diameter Nylon Cylindrical Particles with Aspect Ratio, A.R. = 1:5 (25 particles) in 20%–80% Glycerol–Water. The average terminal settling velocity, U_t is 28.66 mm/s.

8.37.3 x -Acceleration (A_x), y -Acceleration (A_y) and Magnitude of Acceleration ($|A|$) for 1.50 mm Diameter and 1:5 Aspect Ratio ($AR = d_p/l_p$) Nylon Cylindrical Particles in 20%–80% Glycerol–Water

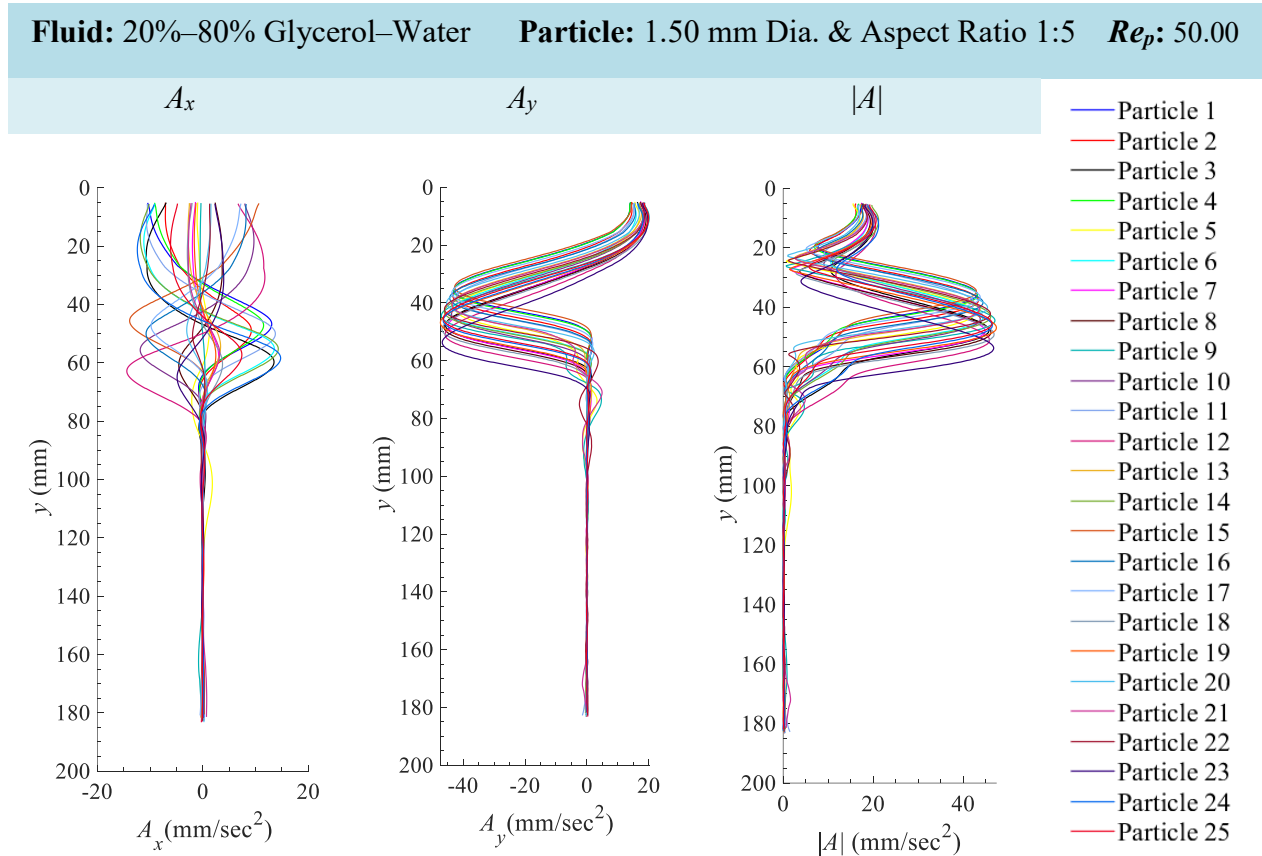


Figure 155 Particle acceleration in the x -direction A_x , y -direction A_y , and the magnitude $\sqrt{(A_x^2 + A_y^2)}$ of the particle acceleration $|A|$ for 1.50 mm Diameter Nylon Cylindrical Particles with Aspect Ratio, A.R. = 1:5 (25 particles) in 20%–80% Glycerol–Water.

8.38 Appendix 38: 1.50 mm Diameter and 1:5 Aspect Ratio ($AR = d_p/l_p$) Nylon Cylindrical Particles in 40%–60% Glycerol–Water

8.38.1 Particle Displacement, Particle Velocity and Particle Acceleration for 1.50 mm Diameter and 1:5 Aspect Ratio ($AR = d_p/l_p$) Nylon Cylindrical Particles in 40%–60% Glycerol–Water

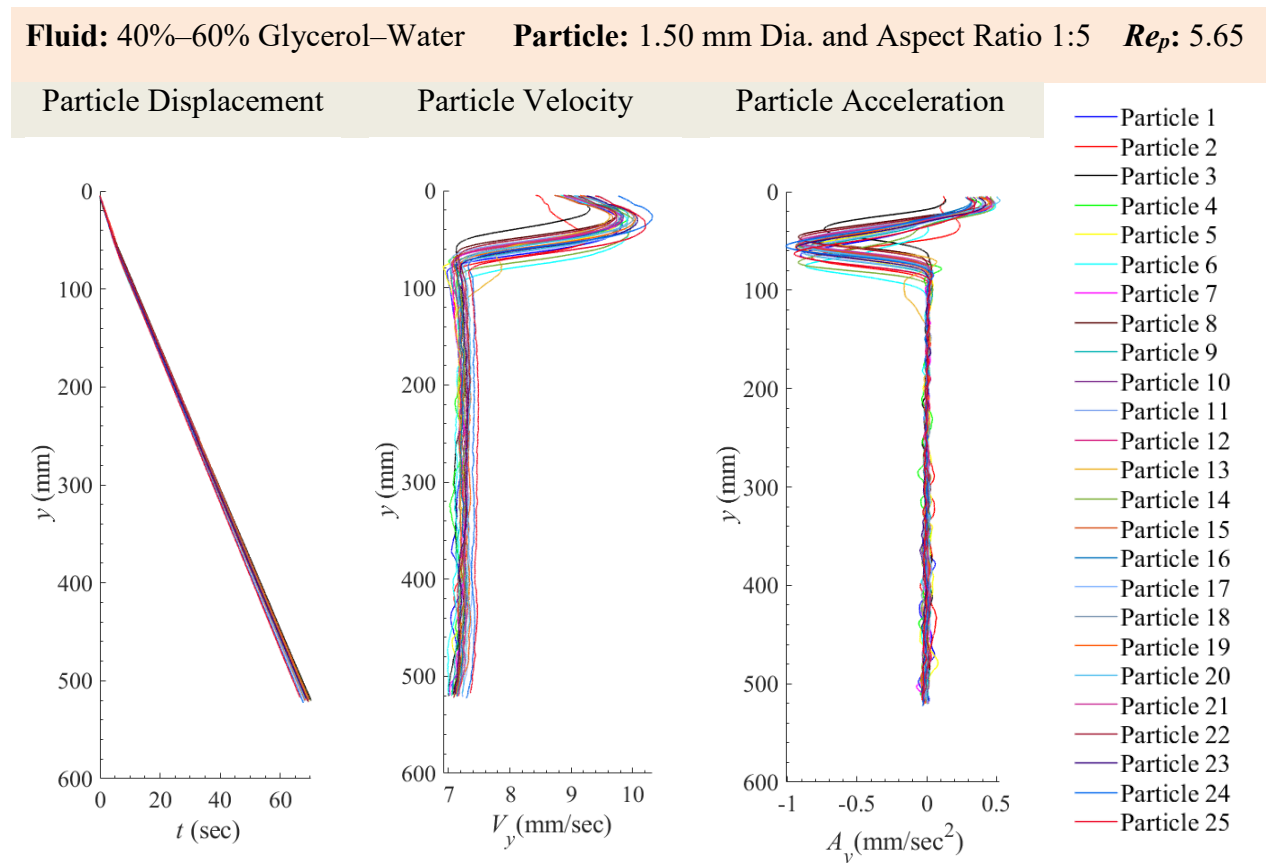


Figure 156 Particle displacement, y , velocity, V_y , and acceleration, A_y , for 1.50 mm Diameter Nylon Cylindrical Particles with Aspect Ratio, A.R. = 1:5 (25 particles) in 40%–60% Glycerol–Water.

8.38.2 x -Velocity (V_x), y -Velocity (V_y) and Magnitude of Velocity ($|V|$) for 1.50 mm Diameter and 1:5 Aspect Ratio ($AR = d_p/l_p$) Nylon Cylindrical Particles in 40%–60% Glycerol–Water

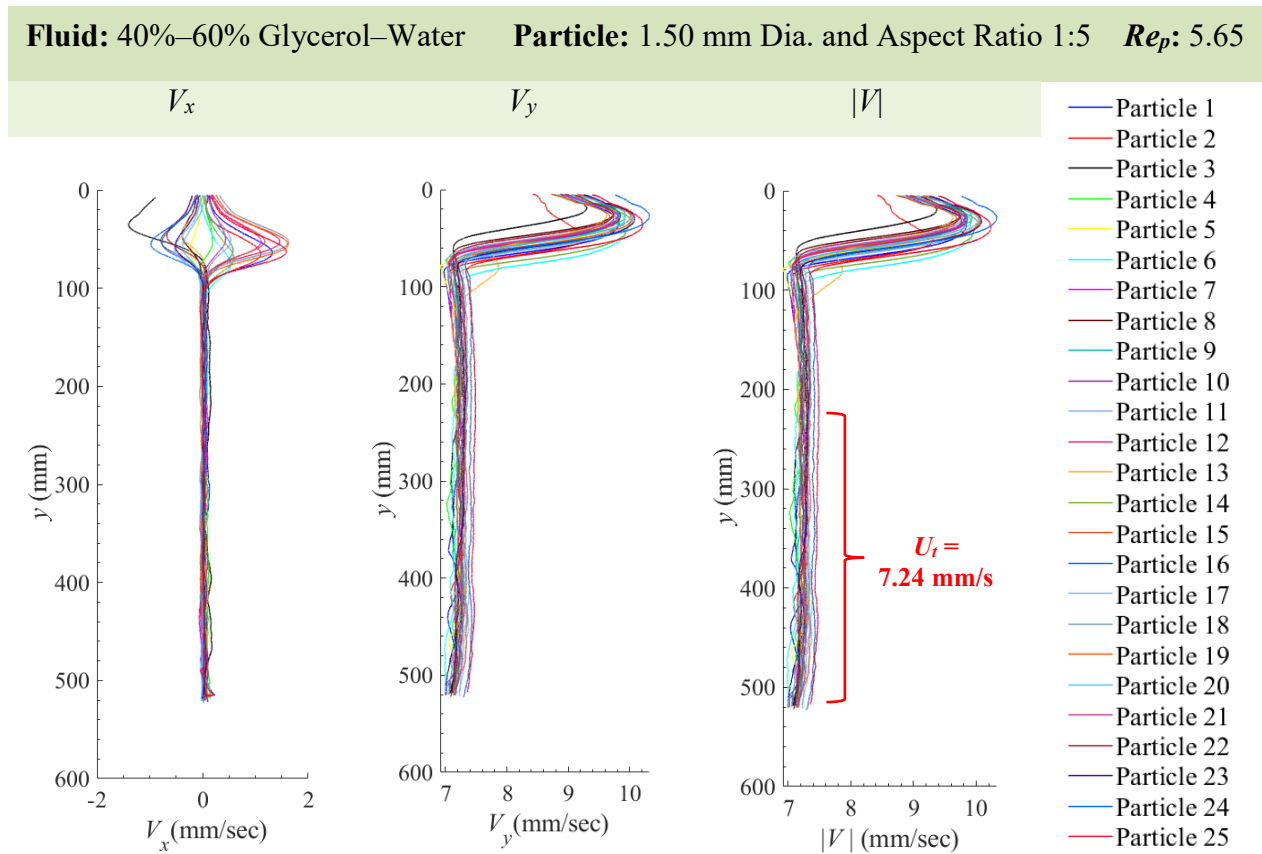


Figure 157 Particle velocity in the x -direction V_x , y -direction V_y , and the magnitude $\sqrt{V_x^2 + V_y^2}$ of the particle velocity $|V|$ for 1.50 mm Diameter Nylon Cylindrical Particles with Aspect Ratio, A.R. = 1:5 (25 particles) in 40%–60% Glycerol–Water. The average terminal settling velocity, U_t is 7.24 mm/s.

8.38.3 x -Acceleration (A_x), y -Acceleration (A_y) and Magnitude of Acceleration ($|A|$) for 1.50 mm Diameter and 1:5 Aspect Ratio ($AR = d_p/l_p$) Nylon Cylindrical Particles in 40%–60% Glycerol–Water

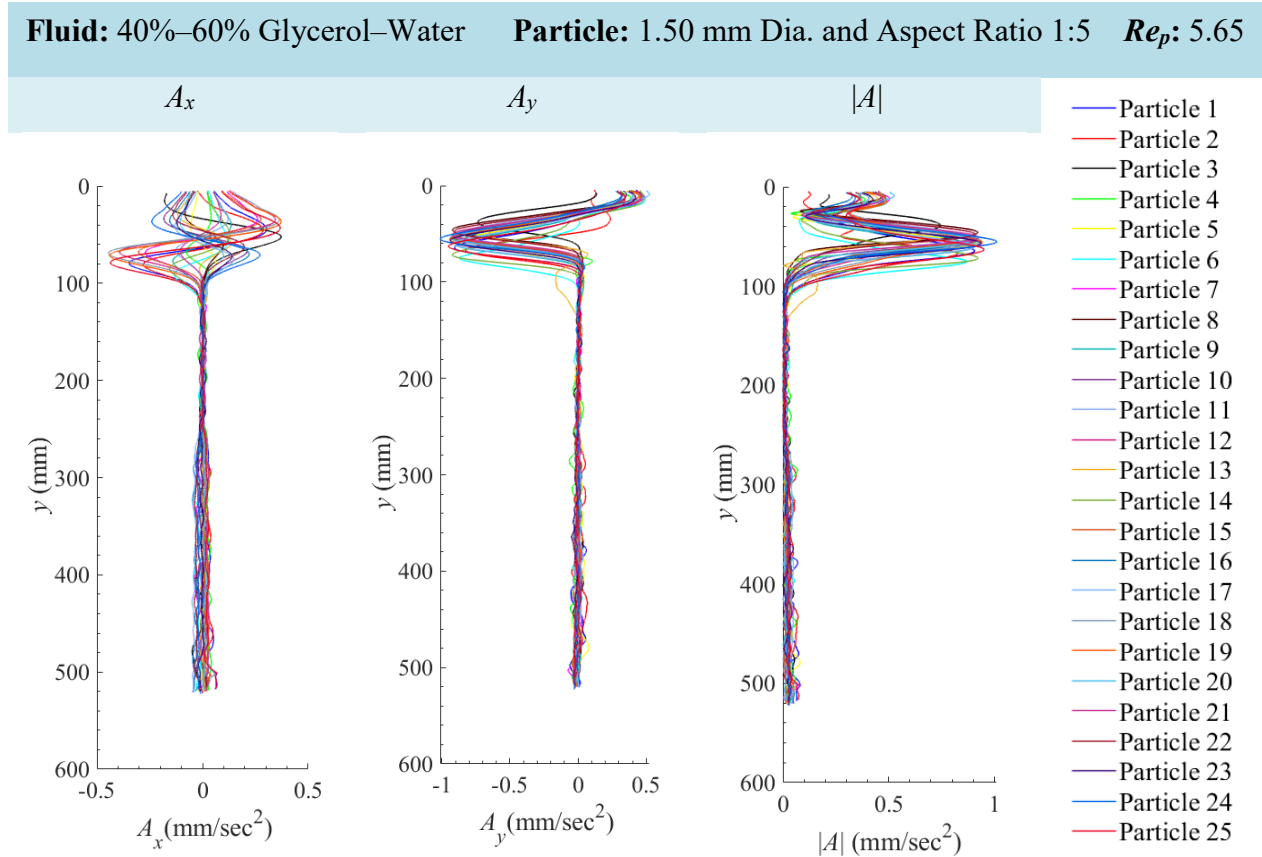


Figure 158 Particle acceleration in the x -direction A_x , y -direction A_y , and the magnitude $\sqrt{(A_x^2 + A_y^2)}$ of the particle acceleration $|A|$ for 1.50 mm Diameter Nylon Cylindrical Particles with Aspect Ratio, A.R. = 1:5 (25 particles) in 40%–60% Glycerol–Water.

8.39 Appendix 39: 1.50 mm Diameter and 1:5 Aspect Ratio ($AR = d_p/l_p$) Nylon Cylindrical Particles in Canola Oil

8.39.1 Particle Displacement, Particle Velocity and Particle Acceleration for 1.50 mm Diameter and 1:5 Aspect Ratio ($AR = d_p/l_p$) Nylon Cylindrical Particles in Canola Oil

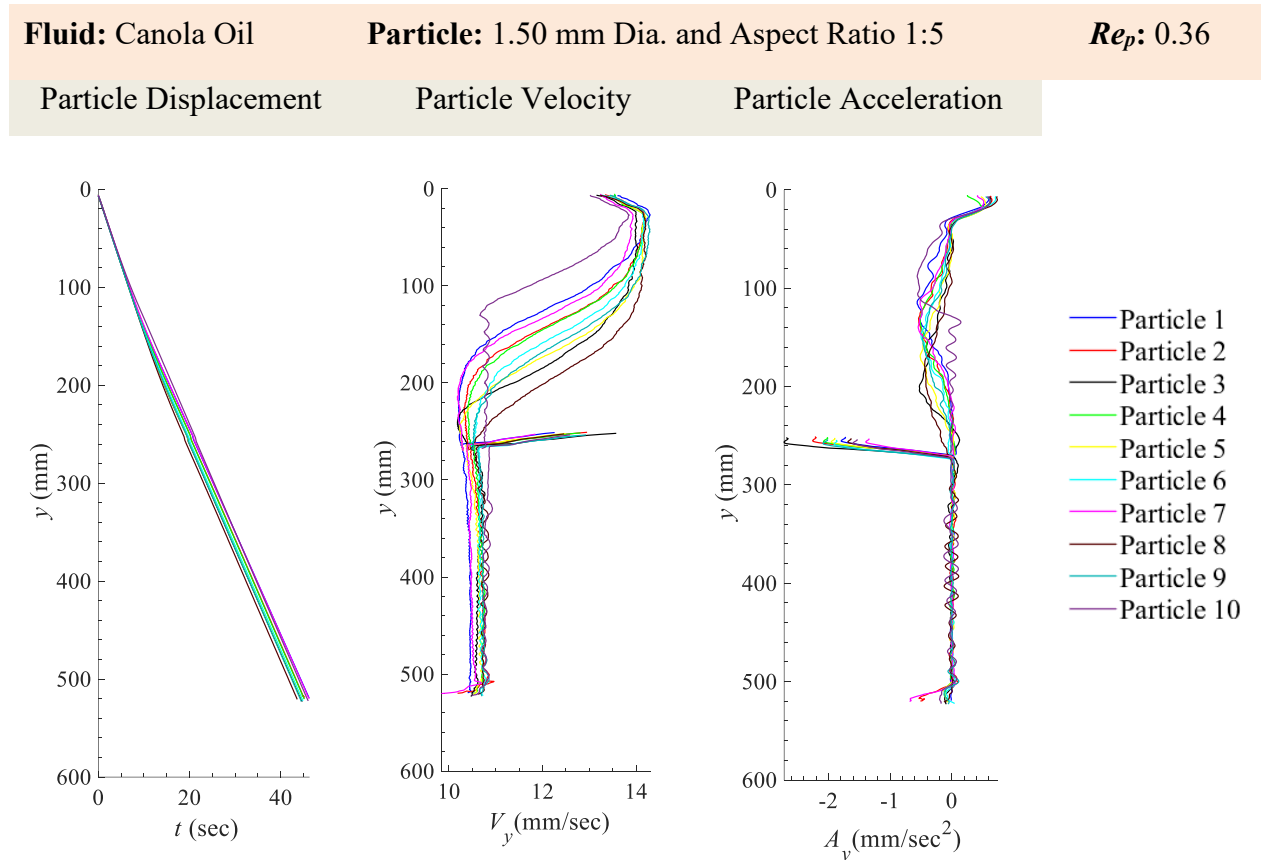


Figure 159 Particle displacement, y , velocity, V_y , and acceleration, A_y , for 1.50 mm Diameter Nylon Cylindrical Particles with Aspect Ratio, A.R. = 1:5 (25 particles) in Canola Oil. The outliers at displacement 260 mm occurred within the overlap between the two cameras. In this region there was a variation in the light distribution compared to the rest of the field of view. A uniform distribution of light was not achieved with the projector and kite paper as shown in Figure 8 and describe in Section 3.5.1. This affected the binarization of the particle within that region and thereby a slight shift in the location of the centroid of the particle from the image processing scheme. Note: 25 particles were used in this experiment however the light distribution was particularly problematic for this experimental condition so there were 15 outliers which were omitted from this plot.

8.39.2 x -Velocity (V_x), y -Velocity (V_y) and Magnitude of Velocity ($|V|$) for 1.50 mm Diameter and 1:5 Aspect Ratio ($AR = d_p/l_p$) Nylon Cylindrical Particles in Canola Oil

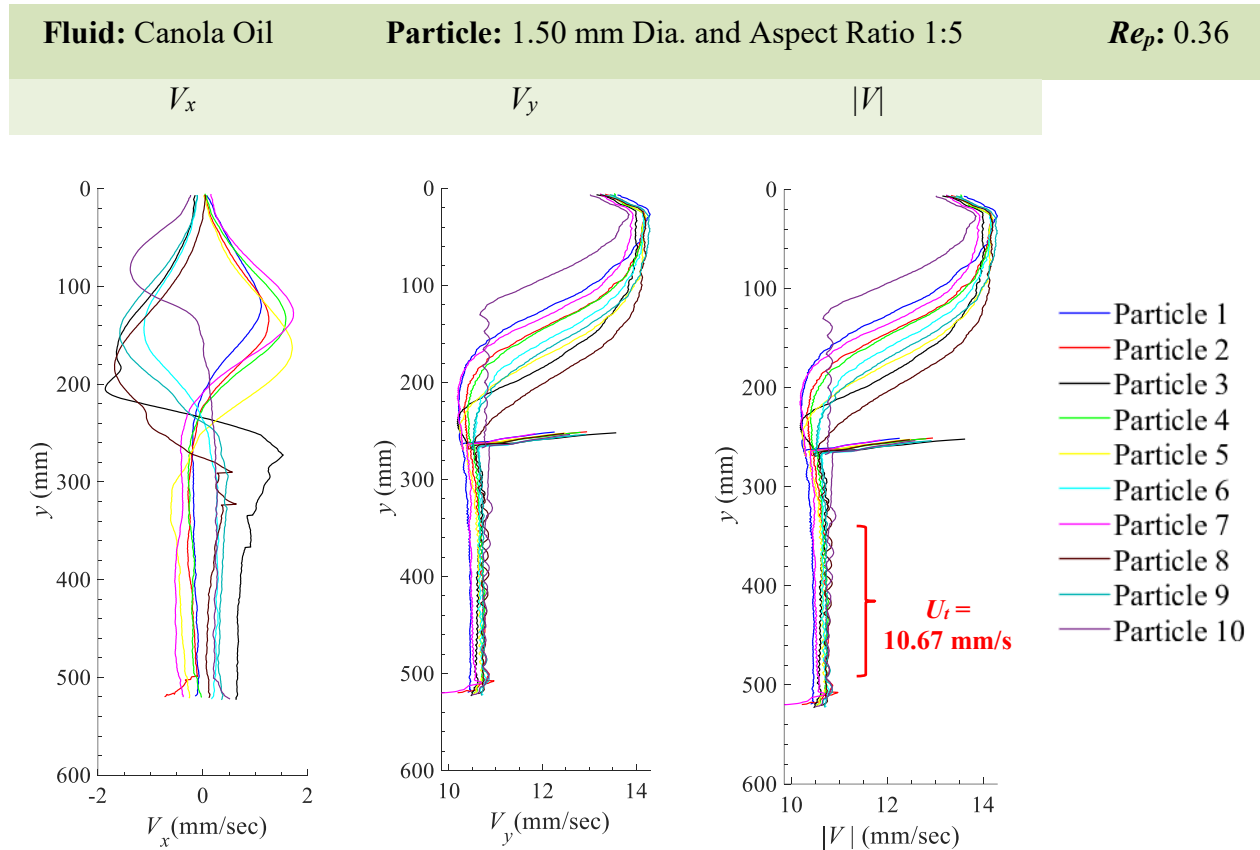


Figure 160 Particle velocity in the x -direction V_x , y -direction V_y , and the magnitude $\sqrt{V_x^2 + V_y^2}$ of the particle velocity $|V|$ for 1.50 mm Diameter Nylon Cylindrical Particles with Aspect Ratio, A.R. = 1:5 (25 particles) in Canola Oil. The average terminal settling velocity, U_t is 10.67 mm/s. The outliers at displacement 260 mm occurred within the overlap between the two cameras. In this region there was a variation in the light distribution compared to the rest of the field of view. A uniform distribution of light was not achieved with the projector and kite paper as shown in Figure 8 and describe in Section 3.5.1. This affected the binarization of the particle within that region and thereby a slight shift in the location of the centroid of the particle from the image processing scheme. Note: 25 particles were used in this experiment however the light distribution was particularly problematic for this experimental condition so there were 15 outliers which were omitted from this plot.

8.39.3 x -Acceleration (A_x), y -Acceleration (A_y) and Magnitude of Acceleration ($|A|$) for 1.50 mm Diameter and 1:5 Aspect Ratio ($AR = d_p/l_p$) Nylon Cylindrical Particles in Canola Oil

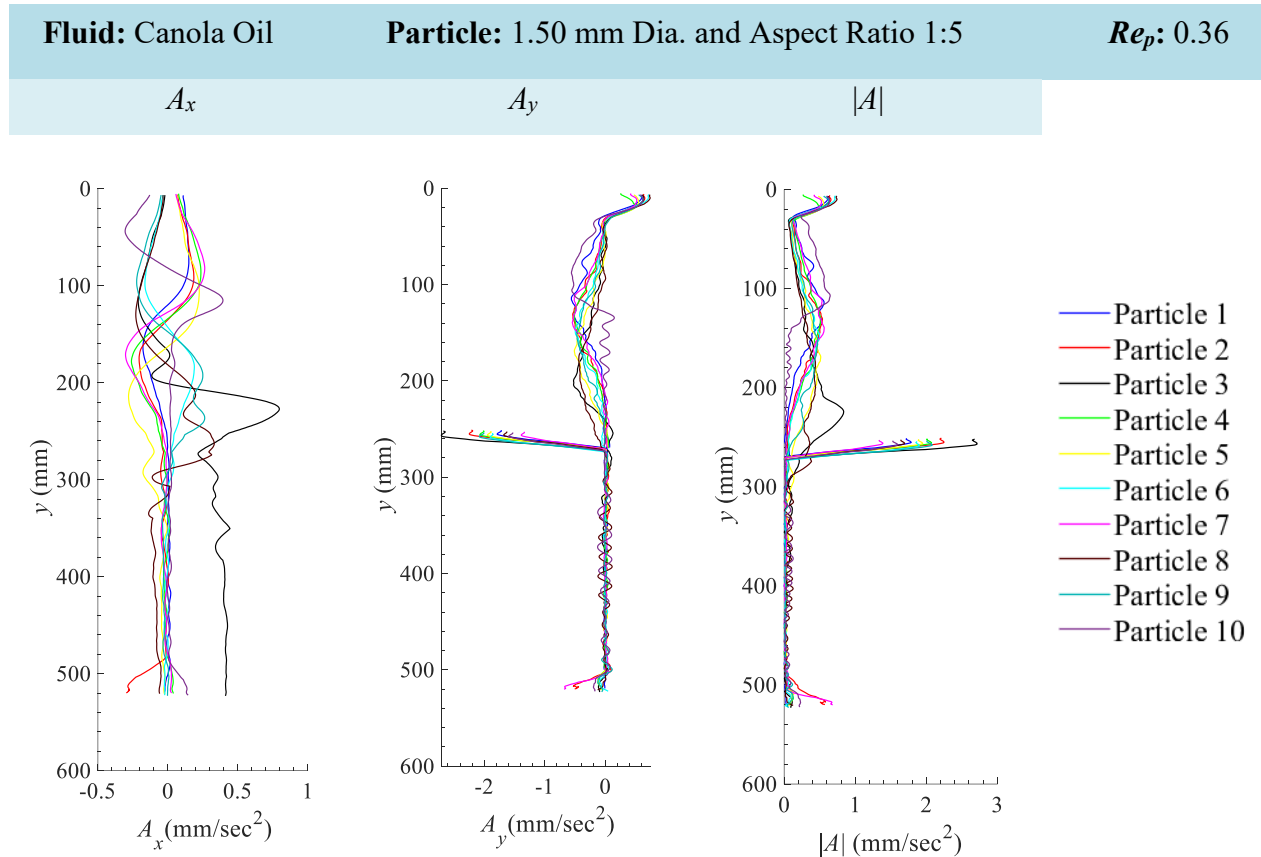


Figure 161 Particle acceleration in the x -direction A_x , y -direction A_y , and the magnitude $\sqrt{(A_x^2 + A_y^2)}$ of the particle acceleration $|A|$ for 1.50 mm Diameter Nylon Cylindrical Particles with Aspect Ratio, A.R. = 1:5 (25 particles) in Canola Oil. The outliers at displacement 260 mm occurred within the overlap between the two cameras. In this region there was a variation in the light distribution compared to the rest of the field of view. A uniform distribution of light was not achieved with the projector and kite paper as shown in Figure 8 and describe in Section 3.5.1. This affected the binarization of the particle within that region and thereby a slight shift in the location of the centroid of the particle from the image processing scheme. Note: 25 particles were used in this experiment however the light distribution was particularly problematic for this experimental condition so there were 15 outliers which were omitted from this plot.

8.40 Appendix 40 The Predicted Theoretical Values of the Terminal Settling Velocity of the 4 mm Delrin Spheres in Water

The predicted theoretical values of the spherical particles used in Chapter 3 were obtained using the iteration procedure described in Section 3.6.4. The predicted theoretical values were compared to the measured values of the terminal settling velocity obtained from the experiments. This comparison was performed in order to evaluate the uncertainty of the experimental measurements. The iterative approach was used to calculate the theoretical terminal settling velocity of the three different spheres i.e. the 4 mm delrin, 2 mm delrin and 2 mm aluminum spheres falling within the five different fluids i.e. water, 20%-80% glycerol–water, 40%-60% glycerol–water, 70%-30% glycerol–water, and canola oil. Table 15 shows an example of the values obtained from the iteration process to determine the theoretical terminal settling velocity the 4 mm delrin particles in water.

Table 15 The predicted theoretical values of the terminal settling velocity and the coefficient of drag of the 4 mm delrin particles in water.

Fluid Density ρ_f (kg/m ³)	Viscosity μ_f (Pa.s)	Particle Diameter d_p (m)	Particle Density ρ_p (kg/m ³)	Theoretical Settling Velocity U_t (mm/s) $\sqrt{\frac{\pi r g (\rho_p - \rho_f)}{c_d \rho_f}}$	Experimental Settling Velocity U_t (mm/s)	Particle Reynolds Number, Re_p	Surface area of the particle, S (mm ²)	Surface area of a sphere with equivalent volume as the particle, s (mm ²)	Particle Sphericity Φ	A	B	C	D	Coefficient of Drag for Spheres, C_D $\frac{24}{Re} [1 + A Re^B] + \frac{C}{[1 + \frac{D}{Re}]}$
997.14	0.000914	0.004	1360		196.82	859.363	50.265	50.265	1	0.186	0.653	0.437	7185.354	0.503033568
997.14	0.000914	0.004	1360	211.163	196.82	921.987	50.265	50.265	1	0.186	0.653	0.437	7185.354	0.493821293
997.14	0.000914	0.004	1360	213.123	196.82	930.548	50.265	50.265	1	0.186	0.653	0.437	7185.354	0.492651752
997.14	0.000914	0.004	1360	213.376	196.82	931.651	50.265	50.265	1	0.186	0.653	0.437	7185.354	0.492502397
997.14	0.000914	0.004	1360	213.409	196.82	931.793	50.265	50.265	1	0.186	0.653	0.437	7185.354	0.492483309
997.14	0.000914	0.004	1360	213.413	196.82	931.811	50.265	50.265	1	0.186	0.653	0.437	7185.354	0.492480869
997.14	0.000914	0.004	1360	213.413	196.82	931.813	50.265	50.265	1	0.186	0.653	0.437	7185.354	0.492480558
997.14	0.000914	0.004	1360	213.413	196.82	931.813	50.265	50.265	1	0.186	0.653	0.437	7185.354	0.492480518
997.14	0.000914	0.004	1360	213.413	196.82	931.813	50.265	50.265	1	0.186	0.653	0.437	7185.354	0.492480513
997.14	0.000914	0.004	1360	213.413	196.82	931.813	50.265	50.265	1	0.186	0.653	0.437	7185.354	0.492480512
997.14	0.000914	0.004	1360	213.413	196.82	931.813	50.265	50.265	1	0.186	0.653	0.437	7185.354	0.492480512

8.41 Appendix 41 Measured Mass, Diameter and Density of 4 mm Delrin Spherical Particles

Table 16 shows the measured mass, diameter, volume and density of the spherical delrin particles which were used in the experimental analysis in Chapter 3. These values were used in the uncertainty analysis in Section 3.6.4. The mass of 20 delrin particles were determined using a scale (Ohaus Explorer Analytical Balance). Each particle was placed within a plastic container with a mass of 2021 mg. Then the mass of the plastic container and the particle were measured as shown in Table 16. The mass of the particle was obtained by subtracting the mass of the plastic container. The diameter of the particles were measured with a digital Vernier caliper. The volume and density of the particles were then calculated using the measured mass and diameter of the particles.

Table 16 The measured mass, diameter, volume and density of the 4 mm delrin spheres.

Particle Number	Mass of the Container and 1 Particle (mg)	Mass of 1 Particle (mg)	Diameter (mm)	Volume (mm ³)	Density (g/cm ³)
1	2066	45	3.98	33.01	1.36
2	2066	45	3.98	33.01	1.36
3	2065	44	3.98	33.01	1.33
4	2066	45	3.98	33.01	1.36
5	2065	44	3.98	33.01	1.33
6	2065	44	3.98	33.01	1.33
7	2065	44	3.98	33.01	1.33
8	2065	44	3.98	33.01	1.33
9	2065	44	3.98	33.01	1.33
10	2065	44	3.98	33.01	1.33
11	2065	44	3.98	33.01	1.33
12	2064	43	3.97	32.76	1.31
13	2066	45	3.98	33.01	1.36
14	2065	44	3.98	33.01	1.33
15	2064	43	3.97	32.76	1.31
16	2064	43	3.97	32.76	1.31
17	2065	44	3.97	32.76	1.34
18	2066	45	3.98	33.01	1.36
19	2067	46	3.98	33.01	1.39
20	2067	46	3.97	32.76	1.40
Average		44.3	3.98	32.95	1.34

8.42 Appendix 42 Measured Diameter, Mass and Density of 2 mm Aluminium Spherical Particles

Table 17 shows the measured mass, diameter, volume and density of the spherical delrin particles which were used in the experimental analysis in Chapter 3. These values were also used in the uncertainty analysis in Section 3.6.4. The mass, diameter, volume and density of the 2 mm aluminum particles were found using the approach described in Section 8.41 – Appendix 41.

Table 17 The measured mass, diameter, volume and density of the 2 mm aluminum spheres.

Particle Number	Mass (Container & 1 Particle) (mg)	Mass of 1 Particle (mg)	Diameter (mm)	Volume (mm ³)	Density (g/cm ³)
1	2030	9	2.01	4.25	2.12
2	2031	10	2.01	4.25	2.35
3	2031	10	2.00	4.19	2.39
4	2031	10	2.00	4.19	2.39
5	2031	10	2.01	4.25	2.35
6	2031	10	2.01	4.25	2.35
7	2031	10	2.00	4.19	2.39
8	2030	9	2.00	4.19	2.15
9	2031	10	2.01	4.25	2.35
10	2030	9	2.00	4.19	2.15
11	2031	10	2.00	4.19	2.39
12	2031	10	2.01	4.25	2.35
13	2031	10	2.01	4.25	2.35
14	2031	10	2.01	4.25	2.35
15	2032	11	2.01	4.25	2.59
16	2031	10	2.00	4.19	2.39
17	2031	10	2.01	4.25	2.35
18	2031	10	2.00	4.19	2.39
19	2031	10	2.00	4.19	2.39
20	2031	10	2.01	4.25	2.35
Average		9.9	2.01	4.22	2.34

8.43 Appendix 43 Particle Reynolds Number and the Coefficient of Drag of the Cylindrical Particles using the Ratio of Volume to the Surface Area of the Particle as a Length Scale

Table 18 This table shows the average terminal settling velocity within the terminal settling velocity region of the 1.30 mm Diameter 25 nylon cylindrical particles for each experimental condition. The terminal settling velocity were obtain from the plots of the particle displacement versus the particle velocity (magnitude) for the spherical particles as shown in Section 8.16 – Appendix 16 to Section 8.27 – Appendix 27. The particle Reynolds Number and the coefficient of drag were calculated based on the average terminal settling velocity values and *the ratio of the volume to the surface area of the particle as a length scale*. The coefficient of drag was calculated based on the model in [16].

Particle	Fluid	Average Terminal settling velocity, U_t (mm/s) (Obtained from Experiments) 25 particles	Particle Reynolds Number, $Re_p = \frac{\rho_f U_t d_p}{\mu_f}$	Coefficient of Drag, $C_D = \frac{24}{Re} [1 + A Re^B] + \frac{C}{[1 + \frac{D}{Re}]}$
Nylon	Water	43.62	10.31	4.48
Cylinders:	20%–80% Glycerol–Water	21.17	2.72	12.55
Dia. 1.30 mm	40%–60% Glycerol–Water	2.03	0.12	219.45
AR 1:1	Canola Oil	4.75	0.02	1186.59
Nylon	Water	47.64	14.48	3.74
Cylinders:	20%–80% Glycerol–Water	26.51	4.38	9.05
Dia. 1.30 mm	40%–60% Glycerol–Water	3.31	0.24	111.98
AR 1:3	Canola Oil	7.63	0.04	592.24
Nylon	Water	48.11	15.51	3.88
Cylinders:	20%–80% Glycerol–Water	27.40	4.80	9.05
Dia. 1.30 mm	40%–30% Glycerol–Water	5.33	0.42	71.52
AR 1:5	Canola Oil	8.68	0.05	506.54

Table 19 This table shows the average terminal settling velocity within the terminal settling velocity region of the 1.50 mm Diameter 25 nylon cylindrical particles for each experimental condition. The terminal settling velocity were obtain from the plots of the particle displacement versus the particle velocity (magnitude) for the spherical particles as shown in Section 8.28 – Appendix 18 to Section 8.39 – Appendix 39. The particle Reynolds Number and the coefficient of drag were calculated based on the average terminal settling velocity values and *the ratio of the volume to the surface area of the particle as a length scale*. The coefficient of drag was calculated based on the model in [16].

Particle	Fluid	Average Terminal settling velocity, U_t (mm/s) (Obtained from Experiments) 25 particles	Particle Reynolds Number, $\frac{Re_p}{\rho_f U_t d_p} \mu_f$	Coefficient of Drag, C_D $\frac{24}{Re} [1 + A Re^B] + \frac{C}{[1 + \frac{D}{Re}]}$
Nylon	Water	46.76	12.75	3.85
Cylinders: Dia. 1.50 mm AR 1:1	20%–80% Glycerol–Water	23.56	3.50	10.24
	40%–60% Glycerol–Water	3.02	0.20	130.94
	Canola Oil	5.77	0.03	850.74
Nylon	Water	52.55	18.43	3.18
Cylinders: Dia. 1.50 mm AR 1:3	20%–80% Glycerol–Water	28.57	5.45	7.64
	40%–60% Glycerol–Water	6.71	0.57	51.18
	Canola Oil	8.94	0.06	441.95
Nylon	Water	51.61	19.19	3.38
Cylinders: Dia. 1.50 mm AR 1:5	20%–80% Glycerol–Water	28.66	5.80	7.83
	40%–60% Glycerol–Water	7.24	0.66	47.82
	Canola Oil	10.67	0.07	362.53

8.44 Appendix 44: Stokes' Number and Gravitational Terminal settling velocity for the Multiple Particles within the Near-Slot Region in SAGD Operations

The appendix includes the particle properties of the 20 μm tracer particles, the 80 μm spherical particles and the 43 μm irregularly shaped particles for the multiple particle analysis used in Section 5.5.2. The density and viscosity of the fluid are given in Section 5.2. The sample calculations for the terminal settling velocity and the Stokes number of the spherical glass beads are shown below.

Table 20 Diameter, density, particle–fluid density difference and terminal settling velocity of the three particles used in Chapter 5 and discussed in Section 5.5.2 namely, tracer particles (polystyrene spherical microbeads), spherical particles (glass beads) and irregularly shaped (silicon carbide). Note the equivalent diameter was used as the length scale to characterize the irregularly shaped particles.

PARTICLES	d_p (μm)	ρ_p (g/cm^3)	$\rho_p - \rho_f$ (g/cm^3)	U_t (m/s)	Stokes Number (at the maximum flow velocity of 0.25m/s)
Tracer particles (polystyrene spherical microbeads)	20	1.05	-0.142	-1.05×10^{-6}	3.92×10^{-6}
Spherical particles (glass beads)	80	2.5	1.308	1.53×10^{-4}	1.49×10^{-2}
Irregularly shaped (silicon carbide) using the Equivalent Diameter	43	3.21	2.018	6.82×10^{-5}	5.54×10^{-3}

Sample Calculations for the terminal settling velocity and Stokes number for the **spherical glass beads**.

$$\text{Terminal settling velocity, } U_t = \frac{g d_p^2 (\rho_p - \rho_f)}{18 \mu}$$

Where g is the acceleration due to gravity, d_p is the diameter of the particles, ρ_p is the density of the particle, ρ_f is the density of the continuous phase and μ is the viscosity of the fluid

$$U_t = \frac{9.81 \text{ m/s} \times (80 \times 10^{-6})^2 \times 1308 \text{ kg/m}^3}{18 \times 0.0298 \text{ Pa.s}}$$

$$U_t = 1.53 \times 10^{-4} \text{ m/s}$$

$$\text{Stokes Number} = \frac{\rho_p d_p^2 U}{18 \mu d_c}$$

Where ρ_p is the density of the particle, d_p is the diameter of the particles, U is the average fluid velocity of the continuous phase, μ is the viscosity of the fluid and d_c is the typical dimension of the geometry containing the fluid flow. The pillar spacing of 0.5 mm was used as the typical dimension of the geometry containing the fluid.

$$\text{Stokes Number} = \frac{2500 \text{ kg/m}^3 \times (80 \times 10^{-6} \text{ m})^2 \times 0.25 \text{ m/s}}{18 \times 0.0298 \text{ Pa.s} \times (0.5 \times 10^{-3}) \text{ m}}$$

$$\text{Stokes Number} = 1.49 \times 10^{-2}$$

Note: The Stokes numbers for all three particles were $\ll 1$ at the maximum flow velocity of 0.25 m/s. Therefore, at the lowest and intermediate flow velocities of 0.0025 m/s and 0.025 m/s (as described in Section 5.2.) the Stokes numbers would be even smaller. The Stokes numbers of the particles in the open slot geometry would be less than the Stokes numbers within for the porous matrix geometries with the cylindrical and diamond shaped pillars. Since the slot width of 1 mm would be used to define d_c . These factors indicate that particle inertial effects for the three different particles are negligible for all three flow conditions and the three flow geometries used in this chapter 5.

8.45 Appendix 45: Image Processing Code – Image Preprocessing and Boundary Fitted Approach

This section presents the customized image processing code that was developed to analysis the motion of the falling spheres and cylinders which were described in Chapter 3, Section 3.5.2. The 2D projected area was obtained and the boundary of the particle was traced using a built-in function (*bwboundaries*, Matlab, The Mathworks). The minimal bounding objects function [78] then fits a square/rectangle to the particles.

```
%% This code was customized by Lisa Kinsale and Professor David S. Nobes
% Date: Wednesday, April 21, 2021

% This code uses the function found in:
% John D'Errico, A suite of minimal bounding objects,
% https://www.mathworks.com/matlabcentral/fileexchange/34767-a-suite-of-
minimal-bounding-objects),
% MATLAB Central File Exchange

function [x_min, y_min, stats, CYLINDER,angle] = LKK_FitBox(img, showImages)
% Will look for a square particle in the provided image
% Will fit a box to it
% Will return the properties of that Box.

if showImages == 1
    figure(3); set(3,'pos',[860 245 420 360]);

    figure(4); set(4,'pos',[1330 610 420 360]);

    figure(6); set(6,'pos',[1330 135 420 360]);

end

%% Image Preprocessing - Course Threshold
% Identifying the particle and cropping a square region around the particle
% This is done to perform the analysis locally instead of throughout the
% entire image

threshold = 0.194; %black and white threshold - typical values: 0.10, 0.12,
0.14, 0.20

bw = im2bw(img,threshold); % binarize the cropped image based on a threshold

inverted_img = imcomplement(bw); % Calculating the inverted image
%The particle appears bright on a dark background
```

```

% (i.e. the reverse of the raw image)

    thres_for_remove_obj = 20; %threshold for removing small objects - typical
values: 2, 4
    bin_img = bwareaopen(inverted_img,thres_for_remove_obj); % Remove small
objects from binary image

%% get outlines of each object
[B_course,L_course,N_course] = bwboundaries(bin_img);
%get stats
stats_preproc= regionprops(L_course, 'Centroid', 'Area', 'Perimeter');
Centroid_preproc = cat(1, stats_preproc.Centroid);
Perimeter_preproc = cat(1,stats_preproc.Perimeter);
Area_preproc = cat(1,stats_preproc.Area);
CircleMetric_preproc = (Perimeter_preproc.^2)./(4*pi*Perimeter_preproc);
%circularity metric
CircleMetric_preproc = CircleMetric_preproc (1:N_course);
SquareMetric_preproc = NaN(N_course,1);
TriangleMetric_preproc = NaN(N_course,1);
CYLINDER_preproc = NaN(N_course,1); % setup a structure to hold the found the
cylinders

%% Detects the particle based on a course threshold and crops an area around
the particle in each frame
if showImages == 1
    % Update the figure image
    figure(3)
    imagesc(bin_img);
    title('Detected Particle wt Course Thres.')
    set(gcf,'color','w')

    squ_size = 50; % defining the square box around the particle in which we
are performing the analysis

    % Defining the limits of the axis
    x_min = Centroid_preproc(1,1)-squ_size;
    x_max = Centroid_preproc(1,1)+squ_size;
    y_min = Centroid_preproc(1,2)-squ_size;
    y_max = Centroid_preproc(1,2)+squ_size;

    Particle_Region_Crop = ([x_min, x_max, y_min, y_max]);
    axis ([Particle_Region_Crop]);

end

%% Crops an area around the particle in the Raw Image based on the region
defined in figure (3) with the course threshold
if showImages == 1

    figure(4)

```

```

width = x_max - x_min;
height = y_max - y_min;
Raw_image_crop = imcrop (img, [x_min y_min width height]);

end

%% Crops an area around the particle in the Raw Image based on the region
defined in figure (3) with the course threshold
if showImages == 1

    inverted_raw_img = imcomplement(Raw_image_crop);

    stretch_img = imadjust(inverted_raw_img, [0.70 0.90]); %might need to
adjust this %[0.6 1] for 2mm delrin

    binarize_newpreproc = imbinarize(stretch_img, 0.45);

    thres_remove_obj_newpreproc = 30; %threshold for removing small objects -
typical values: 2, 4
    bin_img_newpreproc =
bwareaopen(binarize_newpreproc, thres_remove_obj_newpreproc); % Remove small
objects from binary image

    figure(4)
    imagesc(bin_img_newpreproc);
    title('Preprocessed Image')
    set(gcf, 'color', 'w')
    colormap(gray);
    hold on

end

%% get outlines of each object
[B,L,N] = bwboundaries(bin_img_newpreproc);
%get stats
stats= regionprops(L, 'Centroid', 'Area', 'Perimeter');
Centroid = cat(1, stats.Centroid);
Perimeter = cat(1, stats.Perimeter);
Area = cat(1, stats.Area);
CircleMetric = (Perimeter.^2)./(4*pi*Area); %circularity metric
CircleMetric = CircleMetric(1:N);
SquareMetric = NaN(N,1);
TriangleMetric = NaN(N,1);
CYLINDER = NaN(N,1); % setup a structure to hold the found the cylinders

%% Plots the centroid from [B,L,N] = bwboundaries(bin_img_newpreproc) above
% AND the centers of the circle from using viscircles above

if showImages == 1

    figure(4)
    hold on

```

```

    plot(Centroid(1),Centroid(2), 'r+', 'MarkerSize',10);

end

%% now label with results
if showImages == 1
    RGB = label2rgb(L);

    figure(6)
    clf
    % Update the figure image
    imagesc(RGB); hold on;
    title('Colour Coded with wrapped rectangles')
    set(gcf, 'color', 'w')

    axis([Centroid(1,1)-squ_size, Centroid(1,1)+squ_size, Centroid(1,2)-
squ_size, Centroid(1,2)+squ_size]);

end

%% for each boundary, fit to bounding box, and calculate some parameters
clear CYLINDER;
for k=1:N
    boundary = B{k};
    [rx,ry,boxArea] = minboundrect( boundary(:,2), boundary(:,1), 'a'); %x and
y are flipped in images
    %get width and height of bounding box
    width = sqrt( sum( (rx(2)-rx(1)).^2 + (ry(2)-ry(1)).^2));
    height = sqrt( sum( (rx(2)-rx(3)).^2+ (ry(2)-ry(3)).^2));
    aspectRatio = width/height;
    if aspectRatio > 1
        aspectRatio = height/width; %make aspect ratio less than unity
    end
    SquareMetric(k) = aspectRatio; %aspect ratio of box sides
    TriangleMetric(k) = Area(k)/boxArea; %filled area vs box area

    %% Plot a line around the object
    Major_1 = [rx(1)+((abs(rx(2)-rx(1)))/2) ry(1)+((abs(ry(1)-ry(2)))/2)];
    Major_2 = [rx(4)+((abs(rx(3)-rx(4)))/2) ry(4)+((abs(ry(4)-ry(3)))/2)];
    Minor_1 = [rx(1)-((abs(rx(4)-rx(1)))/2) ry(1)+((abs(ry(4)-ry(1)))/2)];
    Minor_2 = [rx(2)-((abs(rx(3)-rx(2)))/2) ry(2)+((abs(ry(3)-ry(2)))/2)];

    dist1 = abs(Major_1(1)-Major_2(1)) + abs(Major_1(2)-Major_2(2));
    dist2 = abs(Minor_1(1)-Minor_2(1)) + abs(Minor_1(2)-Minor_2(2));

    if dist1<dist2 % Setting the major line as the largest
        temp1 = Minor_1;
        temp2 = Minor_2;
        Minor_1 = Major_1;
        Minor_2 = Major_2;
        Major_1 = temp1;
        Major_2 = temp2;
    end
end

```



```

    angle = 360 * atan( (Major_2(2)-Major_1(2)) / (Major_1(1)-Major_2(1)) ) /
(2*pi);

    if showImages == 1
        plot([rx(1) rx(2) rx(3) rx(4) rx(1)], [ry(1) ry(2) ry(3) ry(4) ry(1)],
'r', 'linewidth',1);
        % plot the MAJOR and MINOR Axis
        plot(Major_1(1), Major_1(2), 'b.', 'MarkerSize',8);
        plot(Major_2(1), Major_2(2), 'bo', 'MarkerSize',5);
        plot([Major_1(1) Major_2(1)], [Major_1(2) Major_2(2)], 'b',
'linewidth',1);

        plot(Minor_1(1), Minor_1(2), 'r.', 'MarkerSize',8);
        plot(Minor_2(1), Minor_2(2), 'ro', 'MarkerSize',5);
        plot([Minor_1(1) Minor_2(1)], [Minor_1(2) Minor_2(2)], 'r',
'linewidth',1);
    end

    CYLINDER(k).rx = rx;
    CYLINDER(k).ry = ry;
    if width < height
        CYLINDER(k).width = width;
        CYLINDER(k).height = height;
    else
        CYLINDER(k).width = height;
        CYLINDER(k).height = width;
    end

    CYLINDER(k).aspectRatio = aspectRatio;
end
hold off
%% define some thresholds for each metric
%do in order of circle, triangle, square, rectangle to avoid assigning the
%same shape to multiple objects

isCircle = (CircleMetric < 1.1);
isTriangle = ~isCircle & (TriangleMetric < 0.6);
isSquare = ~isCircle & ~isTriangle & (SquareMetric > 0.9);

isRectangle= ~isCircle & ~isTriangle & ~isSquare; %rectangle isn't any of
these
%assign shape to each object
whichShape = cell(N,1);
whichShape(isCircle) = {'Circle'};
whichShape(isTriangle) = {'aTriangle'};
whichShape(isSquare) = {'Square'};
whichShape(isRectangle)= {'Rectangle'};

if showImages == 1
    hold on;
    title('Colour Coded with particle specs')
    % Plot the centroid.
    plot(Centroid(1,1), Centroid(1,2), 'r+');

```

```

plot(Centroid(1,1), Centroid(1,2), 'bo', 'MarkerSize',5);

Combined = [CircleMetric, SquareMetric, TriangleMetric];
for k=1:N

    Txt = sprintf('C=%0.3f S=%0.3f T=%0.3f', Combined(k,:));
    text( Centroid(k,1)-45, Centroid(k,2)+25, Txt);
    text( Centroid(k,1)-45, Centroid(k,2)+30, whichShape{k});
    angletxt = sprintf('Angle=%0.2f', angle);
    text( Centroid(k,1)-45, Centroid(k,2)+35, angletxt);
end
hold off
end

```

8.46 Appendix 46: Image Processing Code – Tracking the Centroid of the Particles and Calculating the Particle Displacement, Velocity and Acceleration

This section presents the customized image processing code that was developed to calculate the displacement, velocity and acceleration of the falling spheres and cylinders which were described in Chapter 3, Section 3.5.3. A derivativeFit function [79] was used to find the first derivative of the displacement plot in order to obtain the particle velocity, ds , and the second derivative of the displacement plot in order to obtain the particle acceleration, dds .

```
%% This code was developed by Lisa Kinsale, Professor David S. Nobes and Kyle
Bricker
% Date: Wednesday, April 21, 2021

% This code uses two functions:
% (1) A minimal bounding objects function developed in:
% John D'Errico, A suite of minimal bounding objects, (2022).
% https://www.mathworks.com/matlabcentral/fileexchange/34767-a-suite-of-
minimal-bounding-objects),
% MATLAB Central File Exchange

% (2) A derivative fit function developed in:
% K. Bricker, D.S. Nobes, derivativeFit,
% https://www.mathworks.com/matlabcentral/fileexchange/89371-derivativefit,
% MATLAB Central File Exchange

function LKK_ShowImages(varargin)
%% inputs
if isempty(varargin) %% Edit if running file as main
    clear
    close all

    LKK_folder = 'E:\3_40Gly_60Water\1.50mm\AR_1-5_1.50mm\Camera_2\1.50mm_AR1-
5_40Gly_60Water_1'; % Must be a folder containing one data set

    LKK_filename = '1.50mm_AR1-5_40Gly_60Water_1_Flare 2_%04d.png'; % Naming
scheme for images

    start_Im = 3102;
    stop_Im = 3191;
    step = 1;

    N_factor = 5; % curve fitting factor n (increase this for less noise)
    saveData = 1;
```

```

    Im_ROI = [358,9,655-358,2025-9]; % Box to search for particles (Default:
[770,120,1300-770,1736-120])

    output = 'Data\'; % Output folder
    showImages = 1; % Displays additional figures in image processing (takes
much longer to run)
    makeGif = 0;
    trackCorner = 0; % tracks a corner of the particle instead of the centroid
    graphType = 1; % graphType = 0 : Graphs raw acceleration and velocity as
red points, as well as the normalized curves in blue
        % graphType = 1 : Graphs only the normalized velocity and
acceleration curves

    FR = 149.7; %FrameRate in fps (frames per sec)
    CF = 17; %Calibration factor 1mm = 17 pixels

else %% Inputs if running as function
    LKK_folder = varargin{1};
    LKK_filename = varargin{2};
    start_Im = varargin{3};
    stop_Im = varargin{4};
    step = varargin{5};
    N_factor = varargin{6};
    saveData = 1;
    Im_ROI = varargin{7};
    output = varargin{8};
    showImages = varargin{9};
    makeGif = varargin{10};
    trackCorner = varargin{11};
    graphType = varargin{12};
end

%% Set up a figure
if showImages == 1
    figure(1);
    set(1, 'Position', [75 100 500 500])
end
figure(2);
set(2, 'Position', [650 100 250 600])
%% Show some images
clc

for i = start_Im :step: stop_Im
    %clc
    r_Im1 = sprintf( LKK_filename, i);
    Im1 = imread([LKK_folder '\' r_Im1]);
    fprintf(['Processing Image: ' LKK_filename '\n'], i);

    if showImages == 1
        figure(1)
        imagesc(Im1);

        rectangle( 'Position', Im_ROI, ...
            'EdgeColor', 'r', ...

```

```

        'LineWidth', 1, ...
        'LineStyle', '-')

end

cropped_Im1 = imcrop(Im1, Im_ROI);
figure(2)
clf
imagesc(cropped_Im1);

% Fit the particle
[stats,CYLINDER, anglecurrent] = LKK_FitBox(cropped_Im1, showImages);
angle(i) = anglecurrent;
saveStats(i) = stats(1);

%% Calculates off of the top left point of the particle
if trackCorner == 1
    if i==start_Im % Grab first top left point
        px(i) = CYLINDER.rx(1);
        py(i) = CYLINDER.ry(1);
    else % Find where the point has moved to
        for j = 1:4
            dx = abs(px(i-step) - CYLINDER.rx(j));
            dy = abs(py(i-step) - CYLINDER.ry(j));
            if j == 1
                d = dx+dy;
                temp = j;
            else
                if d > dx+dy
                    d = dx+dy;
                    temp = j;
                end
            end
        end
        px(i) = CYLINDER.rx(temp);
        py(i) = CYLINDER.ry(temp);
    end
end
end
%%

figure (2)
clf
imagesc(cropped_Im1);
axis equal
Centroid = stats.Centroid;
Cent_X(i) = Centroid(1);
Cent_Y(i) = Centroid(2);

hold on
plot(Centroid(1),Centroid(2), 'r+', 'MarkerSize', 8);
plot(Cent_X,Cent_Y, 'r.', 'MarkerSize', 5);
if trackCorner == 1
    plot(px(i), py(i), 'b+', 'MarkerSize', 8);
    plot(px,py, 'b.', 'MarkerSize', 5);
end

```

```

    end
    hold off

    drawnow

end
%% If Calculating off top left point
if trackCorner == 1
    Cent_X = px;
    Cent_Y = py;
end

%% Displacement Graph
figure(5)
set(5, 'Position', [75 100 500 500])
I = start_Im:step:stop_Im;
I = I';
s = Cent_Y(start_Im:step:end);
s = (s');

if graphType == 1
    [ds, dds] = derivativeFit( I, s, N_factor, 1);
elseif graphType == 0
    [ds, dds] = derivativeFit( I, s, N_factor, 1);
    Dds = diff(s) / step;
    Ddds = diff(Dds) / step;
end

plot(I, s, '-b. ');
title('Displacement');
xlabel('Time (Frame)');
ylabel('Y-Displacement (Pixels)');
%% Angle
angle = angle(start_Im:step:end);
figure(8)
set(8, 'Position', [75 700 500 500])
plot(I, angle, '-b. ');
yline(0, ':');
title('Angle');
xlabel('Time (Frame)');
ylabel('Angle (degrees)');
%% Velocity
figure(6)
set(6, 'Position', [650 100 500 500])
plot(I, ds, '-b. ');
if graphType == 0
    hold on
    DI = I(1:end-1)+0.5*step;
    plot(DI, Dds, 'r. ');
    hold off
end
title(['Velocity N = ' num2str(N_factor)]);
xlabel('Time (Frame)');
ylabel('Y-Velocity (Pixels / Frame)');
%% Acceleration
figure(7)

```

```

set(7, 'Position', [1225 100 500 500])
plot(I, dds, '-b. ');
if graphType == 0
    hold on
    DI = I(2:end-1);
    plot(DI, Ddds, 'r. ');
    hold off
end
yline(0, ':');
mean_dds = mean(dds);

title(['Acceleration N = ' num2str(N_factor)]);

xlabel('Time (Frame)');
ylabel('Y-Acceleration (Pixels / Frame^2)');
%% Save
if saveData == 1
    status = mkdir(output);
    Cent_X = Cent_X(start_Im:step:end);
    Cent_X = Cent_X(:);
    Cent_Y = Cent_Y(start_Im:step:end);
    Cent_Y = Cent_Y(:);
    Displacement = s(:);
    Velocity = ds;
    Acceleration = dds;
    Frames = I(:);
    stats = saveStats(start_Im:step:end);
    save( [ output 'GraphData' ] , 'Cent_X', 'Cent_Y', 'Velocity',
'Acceleration', 'angle', 'Displacement', 'step', 'N_factor', 'Frames' );
    save( [ output 'Stats' ], 'stats' );
    figure(2)
    savefig([output 'Centroid.fig']);
    figure(5)
    savefig([output 'Displacement.fig']);
    figure(6)
    savefig([output 'Velocity.fig']);
    figure(7)
    savefig([output 'Acceleration.fig']);
    figure(8)
    savefig([output, 'Angle.fig'])

end

%% Gif

if makeGif == 1
    Im_Name = 'raw.gif'; % file name
    F_Name = [output Im_Name]; % file path
    ISFILE = isfile( F_Name ) ;
    if ISFILE == 1
        disp( ['There is already a gif file named ', Im_Name, ' in the
folder!'] ) ;
    elseif ISFILE == 0
        folder = [LKK_folder '\'] ;
        Fol_Proc = dir( fullfile( folder, '*.tif' ) ) ;
    end
end

```

```

        Com = {['Original frame range of ' , num2str(1), ' to ',
num2str(200)]} ;
        for j = start_Im : step : stop_Im
            Name_Proc = sprintf( LKK_filename, j);
            Im_Proc = imread( [folder, Name_Proc] ) ;
            [imind, im] = rgb2ind(Im_Proc, 256);
            if j == start_Im
                imwrite(imind,im,F_Name,'gif','Loopcount',inf,'DelayTime',
0.1,'Comment', Com);
            else

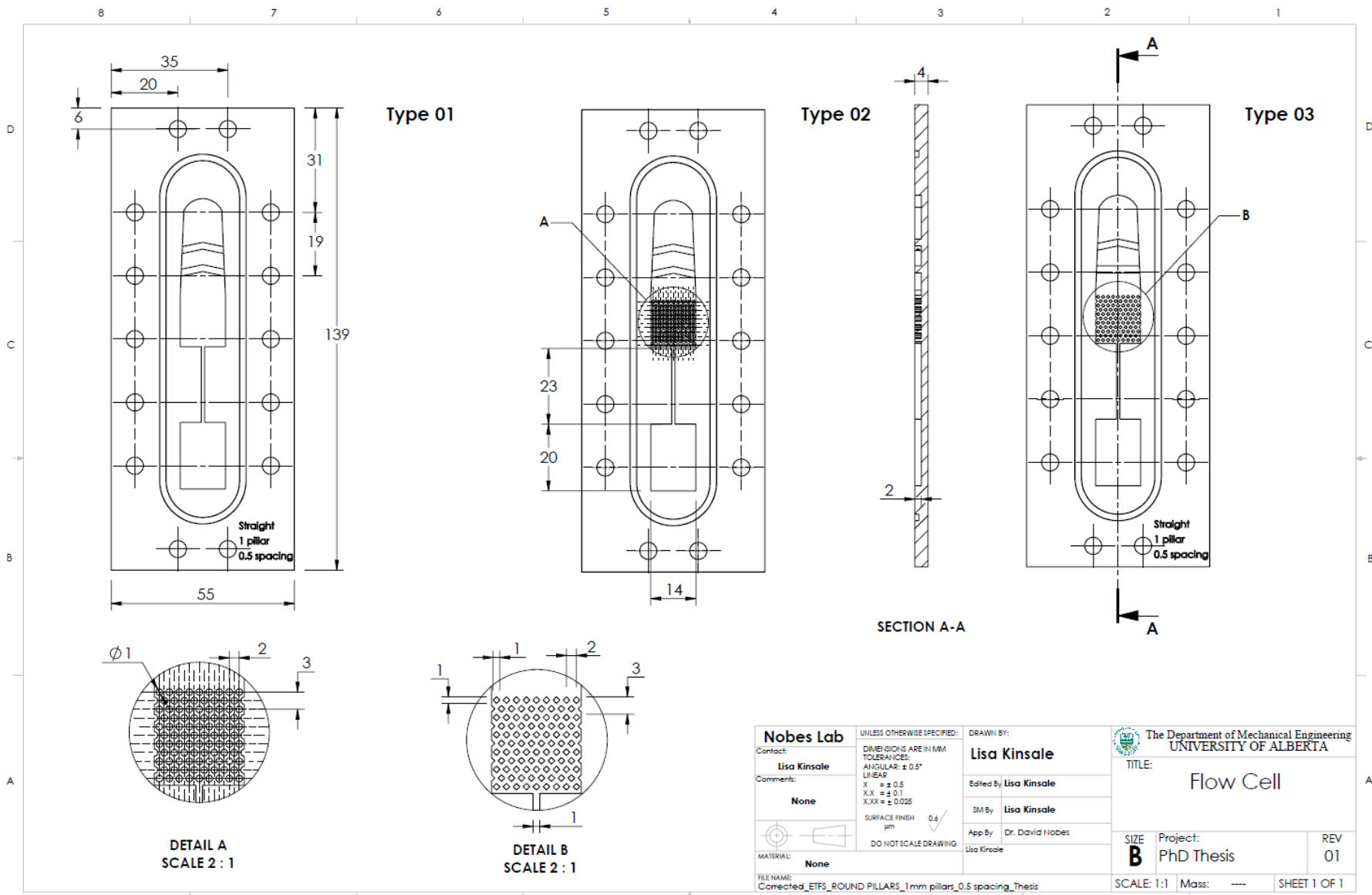
imwrite(imind,im,F_Name,'gif','WriteMode','append','DelayTime', 0.1);
            end
            disp( [ Name_Proc ' has been added to the ' Im_Name ' file' ] ) ;
        end
    end
end

%%
disp('Complete');

```


8.47 Appendix 47: Solid Modeling

This section presents the detail solid modeling drawings of the flow channels that was designed to analyze particle motion within the near-slot region in Chapter 5, Section 5.2. The solid models of the flow channel were developed in SolidWorks 2021, Dassault Systèmes and then 3D printed (Form 2, Formlabs Inc.). In the drawing the three types of flow channel geometries were presented: Type 1 is the open slot geometry, Type 2 is the cylindrical pillars flow geometry which was aimed to simulate porous media at the inlet of the slot and Type 3 is the diamond shaped pillars flow geometry which was aimed to simulate porous media at the inlet of the slot.



SOLIDWORKS Educational Product. For Instructional Use Only.